

Process simulation and optimization of biomass fast pyrolysis

Zur Erlangung des akademischen Grades eines
DOKTORS DER INGENIEURWISSENSCHAFTEN

von der KIT-Fakultät für Chemieingenieurwesen und Verfahrenstechnik des
Karlsruher Instituts für Technologie (KIT)
genehmigte

DISSERTATION

von

M. Sc. Frederico Gomes Fonseca

Aus Lissabon, Portugal

Tag der mündlichen Prüfung: 6. Juni 2023

Erstgutachter: Prof. Dr. Nicolaus Dahmen

Zweitgutachter: PD Dr. Anthony Dufour (CNRS – Université de Lorraine)

*And what
if the universe
is not about us?
Then what?
What
is it about?
And what
about us?*

— *May Swenson (1913-1989), 1963*

Summary

The intensive use of fossil fuels for energy, fuel, and commodity production has engendered global and long-lasting environmental, political, and economic impacts which disproportionately affect poorer populations and countries without easy access to those materials. The need for a transition to renewable sources that do not imply a complete reform of the current energetic system is clear.

Biomass, namely forestry and crop residues, is an underexplored energy source which use may help further valorize rural economies, by using a side-product of low economic value. Amongst competing possibilities, fast pyrolysis is a thermochemical conversion route that can generate energy-dense products and value-added products from biogenic material. Pyrolysis can generate products in three different states: gas, liquid, and solid. This is an important advantage when compared to conventional processes that solely produce one or two of these phases or even only heat. All generated products are immediately usable for energy production, and feature a higher energy density than raw biomass; they can also be further refined into higher-value commodities, including hydrogen, fuels, intermediates, and fine chemicals. This is the primary motivation behind the *bioliq*[®] project.

This doctoral project is focused on the establishment of a rigorous and versatile fast pyrolysis model based on a real industrial-pilot scale materialization of the *bioliq*[®] project. The designed model takes as input the characteristics of lignocellulosic biomass, employs a set of reactors employed to mimic the real biomass degradation, and features rigorous simulations of the quenching loops employed for two-step liquid product recovery.

Initialization of the model was made using wheat straw as model biomass, an uncommon selection due to its high ash content fostering catalytic effects. In that sense, thermogravimetry was used for the characterization of the biomass process degradation, estimation of lignocellulosic content, and pyrolysis kinetics specific to this feedstock. To ensure the versatility of the model in terms of the input data, several reaction networks available in the literature, which convert the lignocellulosic composition of the biomass into the final products, were analyzed and customized; the composition of the produced condensate was tuned by defining secondary and aging reactions to match experimental data. The composition of the condensates was streamlined to facilitate modeling, and the defined chemical species have been fully characterized in terms of thermophysical properties. Several of the selected species lack thermophysical characterization, and existent estimation methods were implemented, for which results were made available in this work.

Final tests considered the variation of moisture content in wheat straw and produced results matching the experimental data. Subsequent models considering different lignocellulosic biomasses confirmed the versatility of the designed model in predicting product distribution and condensate composition. The final model is fully operational on its own and may be further customized in terms of process specifications and up/downstream implementations.

Kurzfassung

Die intensive Nutzung fossiler Brennstoffe für die Energie-, Kraftstoff- und Rohstoffproduktion hat globale und langanhaltende ökologische, politische und wirtschaftliche Auswirkungen, von denen ärmere Bevölkerungsschichten und Länder ohne einfachen Zugang zu diesen Rohstoffen außerordentlich stark betroffen sind. Jedem ist klar, denn ein Übergang zu erneuerbaren Energiequellen ist notwendig, der keine vollständige Reform des heutigen Energiesystems erfordert.

Biomasse, insbesondere forstwirtschaftliche und pflanzliche Rückstände, ist eine wenig erforschte Energiequelle, deren Nutzung zur weiteren Aufwertung der ländlichen Wirtschaft beitragen kann, indem ein Nebenprodukt von geringem wirtschaftlichem Interesse verwendet wird. Unter den konkurrierenden Möglichkeiten ist Schnellpyrolyse ein thermochemischer Umwandlungspfad, der aus biogenem Material energiereiche Produkte und Produkte mit Mehrwert erzeugen kann. Die Pyrolyse kann Produkte in drei verschiedenen Zuständen erzeugen: gasförmig, flüssig und fest. Dies ist ein wichtiger Vorteil gegenüber traditionellen Verfahren, die nur eine oder zwei dieser Phasen oder überhaupt nur Wärme erzeugen. Alle erzeugten Produkte sind sofort für die Energieerzeugung nutzbar und weisen eine vergleichbare oder höhere Energiedichte als Rohbiomasse auf; sie können auch zu höherwertigen Produkten weiterverarbeitet werden, darunter Wasserstoff, Kraftstoffe, Zwischenprodukte und Feinchemikalien. Dies ist die Hauptmotivation für das bioliq[®]-Projekt.

Dieses Promotionsprojekt konzentriert sich auf die Erstellung eines rigorosen und vielseitig verwendbaren Schnellpyrolysemodells, das auf einer realen Materialisation des bioliq[®]-Projekts im industriellen Pilotmaßstab basiert. Das Modell basiert auf den Eigenschaften von lignozellulosehaltiger Biomasse, verwendet eine Reihe von Reaktoren zur Abbildung des realen Biomasseabbaus und bietet strenge Simulationen der Abschreckungsschleifen, die für eine zweistufige Flüssigproduktgewinnung verwendet werden.

Bei der Initialisierung des Modells wurde Weizenstroh als Modellbiomasse verwendet, eine ungewöhnliche Wahl aufgrund seines hohen Aschegehalts, der katalytische Effekte begünstigt. In diesem Sinne wurde Thermogravimetrie für die Charakterisierung des Biomasseabbaus, die Schätzung des Lignozellulosegehalts und der Pyrolysekinetik für dieses Ausgangsmaterial verwendet. Um die Vielseitigkeit des Modells in Bezug auf die Eingabedaten zu gewährleisten, wurden mehrere in der Literatur verfügbare Reaktionsnetzwerke, die die lignozellulosehaltige Zusammensetzung der Biomasse in die Endprodukte umwandeln, analysiert und angepasst; die Zusammensetzung des erzeugten Kondensats wurde durch Sekundär- und Alterungsreaktionen auf die experimentellen Daten angepasst.

Die Zusammensetzung der Kondensate wurde gestrafft, um die Modellierung zu erleichtern, und die definierten chemischen Spezies wurden im Hinblick auf ihre thermophysikalischen Eigenschaften vollständig charakterisiert. Für einige der ausgewählten Spezies mangelt es an experimenteller Charakterisierung, und es wurden bestehende Schätzmethode implementiert, deren Ergebnisse in dieser Arbeit zur Verfügung gestellt wurden.

Die abschließenden Tests berücksichtigten die Variation des Feuchtigkeitsgehalts im Weizenstroh und ergaben Ergebnisse, die mit den experimentellen Daten übereinstimmen. Nachfolgende Modelle, die verschiedene lignozellulosehaltige Biomassen berücksichtigten, bestätigten die Vielseitigkeit des entwickelten Modells bei der Vorhersage der Produktverteilung und der Zusammensetzung des Kondensats. Das endgültige Modell ist eigenständig voll funktionsfähig und kann im Hinblick auf Prozessspezifikationen und vor- und nachgeschaltete Implementierungen weiter angepasst werden.

Acknowledgments

It feels like it was yesterday that I arrived in Karlsruhe on a rainy February afternoon carrying two suitcases and no place to live in. And ever since it took me over 5 years to get to this. Sometimes we make the process more complicated than we need to, and I am all too proficient in complicating things. These were five years of many trials, tribulations, and a somewhat unhealthy dose of mistakes and resets. But at the same time five years filled with experiences, meeting fascinating characters, and getting to know myself a little more each day. I would not have it any other way.

First and foremost, I would like to give my thanks to Prof. Nicolaus Dahmen for providing me the opportunity to perform the Ph.D. study in his research group and enabling the defense of the work at the Faculty of Chemical Engineering of the Karlsruhe Institute of Technology. His assistance not only in all manners of documentation and overseeing was invaluable, but also his contribution to narrative development, manuscript structuring, and those final touches that make a paper worth reading.

As a group leader and supervisor, Dr. Axel Funke provided an insightful perspective that proved useful in many cases, and he always support me in following this doctoral project in my own way. I felt like he had my back all the way through, and for that, I can only express my gratitude.

I must acknowledge the staff team at IKFT for their diligence and warm reception. I would like to name Daniel Richter for preparing and leading the experimental trials; the laboratory team including Pia Griesheimer, Jessica Heinrich, Jessica Meier, Melany Frank, Petra Janke, and Armin Lautenbach; Andreas Niebel for data organization and availability for questions; Cornelius Richter, Norbert Sickinger, and Till Henrich for assistance during modeling; Alexandra Böhm and Monika Zimmer for back-office support. I also must thank the INTL staff for the warm welcome and assistance.

Afterward, thanks must be extended to the colleagues I had the pleasure to befriend during my doctoral period: Dr. Yannik Stark, Dr. Clarissa Baehr, Dr. Caroline Carriel-Schmitt, Dr. Yujie Fan, Dr. Bingfeng Guo, Dr. Anke Kurtorf, Eugen Aschenbrenner, Joscha Zimmermann, Ewelina Brunet, Ana Araújo, George Parku, Si Chen and Bing Wang.

I had the great opportunity to spend three amazing months in Bangkok under a research grant, and I would like to single out Prof. Panmanas Sirisomboon, Prof. Wanphut Saechua, and Dr. Sneha Sharma for their direct support, as well as the Near-Infrared Spectroscopy Research Center for Agricultural Products and Food at the King Mongkut's Institute of Technology Ladkrabang. Back in Germany, I must thank the Karlsruhe House of Young Scientists for financial support, namely Gaby Weick for the bureaucratic assistance.

Being a member of the BBW ForWerts Bioeconomy Graduate Program was a good chance to get to know other junior researchers working in different fields, and expand my scientific knowledge. I had the chance to get to collaborate with external partners Prof. Ana Paula Dias, Dr. Filipe Rego, Prof. Andrés Anca-Couce, and Dr. Umut Ali Şen. I would like to thank Dr. Jens Peters and Dr. Abdul Petersen for their suggestions.

Final thanks go to my friends, who have been my biggest cheerers, namely Teresa Filipe, Pedro Fonseca, Duarte Cecílio, João Falcão, and João Romão. Special thanks to Malte Klöckner for his patience and companionship.

My parents, for unconditionally having my back and being the ultimate refuge.

My partner, Szymon, for being my rock and my biggest supporter. Any place is home as long as you are around. Thank you for believing in me.

Contents

Summary	iii
Kurzfassung	iv
Acknowledgments	v
List of Figures	ix
List of Tables	xiii
Glossary	xv
1. Introduction	1
1.1. Motivation	1
1.2. Objectives of the doctoral project	2
1.3. Academic contributions	3
1.3.1. Manuscripts.....	3
1.3.2. Conference Participations	3
2. Literature Review	5
2.1. Pyrolysis in the context of energy production	5
2.1.1. Greenhouse emissions and energy production trends	5
2.1.2. Biorefining potential of straws.....	8
2.1.3. The pyrolysis process	10
2.1.4. Fast pyrolysis research and large-scale materializations	12
2.1.5. Utilization of the produced fractions	13
2.1.6. The bioliq® project	14
2.2. Reaction pathways of fast pyrolysis	16
2.2.1. Degradation pathways present during the pyrolysis process	16
2.2.2. Reaction networks.....	23
2.2.3. Effect of particle size on thermal degradation	24
2.2.4. Effect of the inorganic content of feedstock on thermal degradation.....	25
2.2.5. Thermogravimetry for lignocellulosic content determination	27
2.2.6. Kinetics derived from dynamic thermogravimetry	29
2.2.7. Principles of chemical reaction equilibrium and kinetics	33
2.2.8. Reaction modeling using process simulation software	33
2.2.9. Summary of the section	35
2.3. Condensation systems	36
2.3.1. Thermodynamic models.....	36
2.3.2. Modeling of condensation systems	38

2.3.3.	Summary of the section	40
2.4.	Species representation in the context of process modeling	40
2.4.1.	Approaches to non-conventional representation	41
2.4.2.	Bio-oil characterization: definition of surrogate mixtures	41
2.4.3.	The high-molecular-weight fraction.....	46
3.	Thermogravimetry and pyrolysis	49
3.1.	Methodology	49
3.1.1.	Feedstock and pyrolysis product analysis	49
3.1.2.	Thermogravimetry	51
3.1.3.	Pyrolysis trials.....	52
3.2.	Thermogravimetry for the estimation of lignocellulosic content in biomass.....	53
3.3.	Thermogravimetry for the estimation of kinetic parameters	56
4.	Modeling of the pyrolysis process	63
4.1.	Auxiliary calculations	65
4.1.1.	Characterization of the reactor	65
4.1.2.	Characterization of the condensation loops	67
4.1.3.	Definition of a condensate surrogate mixture	68
4.1.4.	Decision on property model.....	71
4.1.5.	Thermophysical property estimation	73
4.2.	Furnace, liftpipe, gas cleaning	76
4.3.	Reactor modeling.....	77
4.3.1.	Performance of published reaction networks.....	78
4.3.2.	Secondary pyrolysis.....	89
4.4.	Solid separation section	92
4.5.	Condensation.....	92
4.5.1.	Loop pre-initialization tests.....	94
5.	Final tests.....	97
5.1.	Effect of moisture content.....	98
5.1.1.	Product distribution	99
5.1.2.	Energetic balance	103
5.2.	Comparison of lignocellulosic biomasses	105
5.2.1.	Product distribution	105
5.2.2.	Energetic balance	109
6.	Conclusions and Future Work	111
	References.....	117

List of Figures

Figure 1.1: Scheme of the model preparation, from lignocellulosic biomass (left) to the final products (right).	2
Figure 2.1: Global energy-related carbon emissions by scenario, 2000-2040. Source: [6] IEA (2020). All rights reserved. SPS: Stated Policies Scenario; SDS: Sustainable Development Scenario.	5
Figure 2.2: Energy-related carbon emissions in key regions, 2000-2040. Source: [6] IEA (2020). All rights reserved.	6
Figure 2.3: Global total energy supply by source, 1990-2018. Source: IEA (2020). All rights reserved...	6
Figure 2.4: Global energy supply by biomass/biowastes from 1990-2018. Source: IEA (2020). All rights reserved.	7
Figure 2.5: Average auction price by project commissioning for the generation of electric power, 2012-2023. Source: IEA (2020). All rights reserved...	7
Figure 2.6: Lignocellulosic biorefinery scheme. Source: [13]	9
Figure 2.7: Methods of heating commonly employed. Source: IEA Bioenergy Task 34 [23].	11
Figure 2.8: The bioliq® concept schematized. Source: [66]	15
Figure 2.9: Flowchart of the bioliq® I pyrolysis plant. Source: [53].	16
Figure 2.10: Intra- and extra-particle mass and heat transport events. Source: [79].	17
Figure 2.11: Several anhydrosugars, as reported by Lin et al. [86].	18
Figure 2.12: Chemical structure for hemicellulose extracted from beechwood. Source: [87].	19
Figure 2.13: Structure of initial lignin model tetramer. Source: [93]	20
Figure 2.14: Schematic structures of lignin surrogates. Source: [96].	20
Figure 2.15: Selected bond dissociation energies for typical bonds found in lignin pyrolysis products. Values in kcal/mol. Source: [92].	21
Figure 2.16: Comparison of Py-GC/MS and conventional GC-MS separated by several months. Results were normalized to account for the presence of water and non-detectable heavy compounds. Unknowns are absent from the Py-GC/MS results due to the limitations of the method. Based on results associated with [127].	23
Figure 2.17: Overlaying of the degradation speed profiles of three reaction sets ([131,158]) against the DTG profiles of both wheat straw and beech wood. Ranzi 14 represents a standard reaction network, whereas Trendewicz 15 represents reaction networks that account for potassium content (Beech: 0.13 wt.%, WS: 1.18 wt.%). Based on data associated with [175].	26
Figure 2.18: Use of the second derivative (DDTG, in black) inflection points to determine peak/transition points for the different pseudo-components (PC), based on the work by Gaitán-Álvarez et al. [188] and Wu et al. [184]. Example using wheat straw hull at 10 K·min ⁻¹ , source [175].	28
Figure 2.19: Three-stage reaction scheme for pyrolysis reactions. Adapted from [4] to include lipids and extractives.	34
Figure 2.20: Mass water content in the condensate as a function of the temperature and the molar fraction of non-condensable compounds in the input mixture. Source: [258].	38
Figure 2.21: Solvent fractionation scheme. DCM: Dichloromethane (CH ₂ Cl ₂); WS-DDS: Water soluble-DCM+DEE (Diethyl ether, C ₄ H ₁₀ O) soluble; WS-DDIS: Water soluble-DCM+DEE insoluble; WIS-DIS: Water insoluble, DCM insoluble; WIS-DS: Water insoluble, DCM soluble. Adapted from [55].	42
Figure 2.22: 'Pyrolytic lignin' surrogate based on the	

description by Scholze et al. [97] ($C_{37}H_{44}O_{12}$, $680.74 \text{ g}\cdot\text{mol}^{-1}$).	46	approaches. $\tau = 9.1 \text{ s}$. Source of experimental data: [287].	67
Figure 2.23: Proposal of representative for wheat straw pyrolytic lignin, the conclusions by Scholze et al. [97], Bayerbach and Meier [282], and Del Río et al. [283] ($C_{128}H_{144}O_{50}$, $1450.58 \text{ g}\cdot\text{mol}^{-1}$).	47	Figure 4.4: Isomerization of HAA to acetic acid.	69
Figure 3.1: Comparison of the -DTG behavior divided by feedstock and peak temperature. a) Beech, b) WS-P, c) WS-H. Source: [175].	54	Figure 4.5: T-xy plots for the binary mixture Water-Acetic Acid, at 4 different pressures. Symbols stand for experimental data. Dashed lines stand for dew point curves. Source of experimental data: [311,312].	71
Figure 3.2: Example of deconvolution using Gaussian curves centered at the point devised by the DDTG method. WS-P, $10 \text{ K}\cdot\text{min}^{-1}$. Source: [175].	54	Figure 4.6: Born-Haber scheme for the enthalpy of a compound in a process simulator. ΔH_{IG} stands for the sensible heat departure in the ideal gas state, and ΔH_d for the remaining enthalpy departure, which depends on the thermodynamic models. Adapted from [243]	73
Figure 3.3: Comparison of the curve-fitting $n_3=3$ method (left) and the isoconversional KAS ($n_3=3$) method (right). Experimental data: DTG from WS-P, $10 \text{ K}\cdot\text{min}^{-1}$. Source: [175].	57	Figure 4.7: Flowsheet view of the heat carrier cycle hierarchy in Aspen Plus™ V12. Blue streams correspond to utilities (steam, water, natural gas, sweeping nitrogen, air); dotted streams correspond to gas streams; and thick streams to solid products. Heat carrier (sand) is represented by dashed lines, including loop purges and make-up streams.	77
Figure 3.4: Kinetic parameters obtained using the isoconversional methods. Top: activation energy, bottom: pre-exponential factor. Values for higher conversions were disregarded. Source: [175].	58	Figure 4.8: Aspen Plus™ flowsheet of the models for testing the different reaction networks: top: CSTR, bottom: PFR. Black: feedstock, Ochre: sweeping gas (N_2), Grey: heat carrier (sand). Full lines: CSTR models, Dashed lines: PFR models, Dotted lines: heat transfer to the HC.	78
Figure 3.5: Comparison of the experimental derivative degradation curves with the predictions by the R17a model [133] modified using the Trendewicz model [158] assuming three different potassium contents. A: cellulose curves against WS-H experimental degradation; B: summative curves against WS-H experimental degradation; C: cellulose curves against Beech experimental degradation; D: summative curves against Beech experimental degradation. Source: [175].	62	Figure 4.9: Comparison between a PFR profile (hollow points) and CSTR values (filled points) for both heat demand and residence time.	79
Figure 4.1: Schematic of the bioliq® I process materialization.	63	Figure 4.10: Comparison of the base case product distribution (left) and organic liquid yield composition (right) between the experimental data (base, bioliq® 2015-2018) and the results of the models using CSTR (above) and PFR (below) unit blocks. Legend: R08: Ranzi et al. (2008) [96]; C14: Corbetta et al. [130]; RAC: Anca-Couce and Scharler [135], for which LC: low charring conditions, HC: high-charring conditions; R17a: Ranzi et al. (2017a) [133]; R17b: Ranzi et al. (2017b) [81]; D18: Debiagi et al. [281], for which H: hardwood hemicellulose, C: cereal hemicellulose...	82
Figure 4.2: Main flowsheet of the model in Aspen Plus™ V12. Blue streams correspond to utilities (steam, water, natural gas, sweeping nitrogen, air); dotted streams correspond to gas streams; purple streams to liquid streams, and thick streams to solid products. Heat carrier (sand) is represented by dashed lines, including loop purges and make-up streams.	64	Figure 4.11: Comparison of the base case product	

distribution (left) and organic liquid yield composition (right) between the experimental data (base, bioliq® 2015-2018) and the results of the models presented in Table 3.7 using CSTR (above) and PFR (below) unit blocks. Legend: R08: Ranzi et al. (2008) [96]; C14: Corbetta et al. [130]; RAC: Anca-Couce and Scharler [135]; R17a: Ranzi et al. (2017a) [133]; values in percentage refer to the potassium content in the feedstock..... 84

Figure 4.12: Comparison of the base case (bioliq® 2015-2018) and the product distribution (left) / the composition of the organic liquid phase (right) obtained using the models highlighted in Table 4.9 and Table 4.10. Base networks: R08: Ranzi et al. (2008) [96] and R17a: Ranzi et al. (2017a) [133]. All base networks modified with the cellulose degradation proposed by Trendewicz et al. [158], assuming a potassium content of 0.10 wt.%; D18 indicates hemicellulose degradation modified assuming cereal proportions, as per Debiagi et al. [281]. Unit blocks used CSTR (above) and PFR (below). 86

Figure 4.13: Mapping of the points presented in Table 4.10. Filled points: CSTR, hollow points: PFR. Labels: #; ε; OLY deviation. 87

Figure 4.14: Comparison of the base case (Experimental, bioliq® 2015-2018) and the product distribution (up) / the composition of the organic liquid phase (down), after primary pyrolysis (see section 4.3.2) and secondary pyrolysis. 91

Figure 4.15: Flowsheet view of the solid separation section in Aspen Plus™ V12..... 92

Figure 4.16: Detailed chart of the mass flows in the ORC loop. Source: [381] 92

Figure 4.17: Flowsheet view of the ORC condensation loop hierarchy in Aspen Plus™ V12. 93

Figure 4.18: Flowsheet view of the AC condensation loop hierarchy in Aspen Plus™ V12. 93

Figure 4.19: Comparison on the influence of the surrogate choice on the composition of the condensates. 95

Figure 5.1: Variation of viscosity and density with the

measurement temperature. Sample: miscanthus organic condensate, bioliq® campaign 2020.97

Figure 5.2: Product distribution comparison between experimental data (stripes) and simulation results. The coke in HTC metric does not sum to 100% with the others.99

Figure 5.3: Comparison of the composition of the first condensate between experimental data (stripes) and simulation results.....99

Figure 5.4: Comparison of the composition of the pyrolysis gas between campaign data and simulation results.102

Figure 5.5: Product distribution comparison between experimental data (stripes) and simulation results. The coke in HTC metric does not sum to 100% with the others.106

Figure 5.6: Comparison of the composition of the first condensate between experimental data (stripes) and simulation results.....107

Figure 5.7: Comparison of the composition of the pyrolysis gas between campaign data and simulation results.109

List of Tables

Table 2.1: Expected values for lignocellulosic and proximate compositions of wheat straw. Data for beech wood obtained from the Phyllis2 database (www.phyllis.nl)	9	boiling point at atmospheric pressure (°C). Data taken from the PubChem database (https://pubchem.ncbi.nlm.nih.gov/) unless otherwise stated. Part 2 of 2.	45
Table 2.2: Different pyrolysis classifications based on the heat transfer method. Sources: [3,9,20,21].	10	Table 2.11: Nominal and fractional composition of several FPBOs in the literature, as well as an estimation of its elemental composition.	48
Table 2.3: Types and frequencies (%) of inter-subunit linkages in softwood and hardwood lignin. Source: [88].	19	Table 3.1: Proximate, ultimate, and elemental analysis of wheat straw. All values in dry base. Data for beech wood was obtained from the Phyllis2 database (www.phyllis.nl).	49
Table 2.4: Relationship between the effective activation energies and reactions for pyrolysis. Indices and notation adapted from [70].	29	Table 3.2: Comparison of presented estimates for the lignocellulosic composition of the feedstocks in this study (wt. % daf.). Values in italic represent relative deviations from the literature values. All values were extrapolated to 100%, and the presence of extractives, lipids, and protein content was disregarded. Source: [175].	55
Table 2.5: Literature data of Arrhenius parameters for the non-catalytic degradation of wheat straw (WS). Source: [69].	30	Table 3.3: Fit error of the $d\alpha/dT$ curves produced using kinetics determination methods in simultaneous comparison with all experimental $d\alpha/dt$ curves. Source: [175].	56
Table 2.6: Development of existent methods for surrogate mixtures of pyrolysis oils.	37	Table 3.4: Peak values and kinetic parameters for the different feedstocks and different methods. Cellulose peak @ 10 K·min ⁻¹ . Source: [175].	59
Table 2.7: List of thermodynamic methods used during vapor-liquid modeling of biomass pyrolysis or downstream bio-oil processing.	39	Table 3.5: Peak values and kinetic parameters for the different feedstocks and different methods. Hemicellulose peak @ 10 K·min ⁻¹ . Source: [175]. ...	59
Table 2.8: Nominal bio-oil compositions (water-free) of surrogate mixtures used to model liquid-vapor equilibrium processes in the context of bio-oil separation. Values in brackets correspond to the boiling point at atmospheric pressure (°C). Data taken from the PubChem database (https://pubchem.ncbi.nlm.nih.gov/) unless otherwise stated.	43	Table 3.6: Peak values and kinetic parameters for the different feedstocks and different methods. Lignin peak @ 10 K·min ⁻¹ . Source: [175].	60
Table 2.9: Nominal bio-oil compositions (water-free) of surrogate mixtures employed in reaction networks. Values in brackets correspond to the boiling point at atmospheric pressure (°C). Data taken from the PubChem database (https://pubchem.ncbi.nlm.nih.gov/) unless otherwise stated. Part 1 of 2.	44	Table 3.7: Mass loss and derivative fits for the best performant reaction networks versus experimental data (WS-H, 10 K·min ⁻¹), including estimation of hypothetical optimum potassium contents to model the degradation profile. Source: [175].	61
Table 2.10: Nominal bio-oil compositions (water-free) of surrogate mixtures used to model pyrolysis reactions. Values in brackets correspond to the		Table 3.8: Reaction network from Trendewicz et al. [158] for the degradation of cellulose. ‘Beech’	

represents a potassium content of 0.13 wt.% and 'Wheat Straw' represents a potassium content of 1.21 wt.%. Source: [175].	61	model can be found in Appendix D.	88
Table 4.1: Composition of the condensates (wt.%) based on averaged data from the bioliq® campaigns 2015-2018.	68	Table 4.12: List of secondary reactions considered in this work.	90
Table 4.2: Proposed surrogate for the bioliq® I condensates using wheat straw. Based on data from the bioliq® campaigns 2015-2018.	69	Table 4.13: Values of the cooling water utilities and hot stream discharge for the condensation loops.	94
Table 4.3: Other relevant components that may take part in liquid-vapor equilibrium.	70	Table 4.14: Values of the cooling water utilities and hot stream discharge for the condensation loops.	94
Table 4.4: Average deviations between predicted T-xy/P-xy values and experimental values.	72	Table 4.15: Surrogates tested using the condensation loops shown in Figure 4.17 and Figure 4.18.	94
Table 4.5: Availability of measured thermophysical properties available in the literature. Does not include surrogate species.	75	Table 5.1: Composition of the feedstock as input to the model. Values in wt.%.	98
Table 4.6: Sources of thermophysical properties of individual components considered in the model. Not included: literature sources.	76	Table 5.2: Data estimated for the first condensate and K1 loop, using Aspen Plus 12™	100
Table 4.7: Results of the simulations. Deviation based on difference between base and predicted product distribution. Also shown are the associated heat demand on top of the HC supply, the residence time on both unit blocks, and the mass balance closure. Values in bold indicate best results, while those in italic indicate simulation errors.	80	Table 5.3: Data estimated for the second condensate and K2 loop, using Aspen Plus 12™	101
Table 4.8: Results of the simulations considering the effect of potassium content. Also shown are the associated heat demand on top of the HC supply, the residence time on both unit blocks, and the mass balance closure. Values in bold indicate best results, while those in italic indicate simulation errors.	81	Table 5.4: Data estimated for the pyrolysis gas and coke products using Aspen Plus 12™	103
Table 4.9: Comparison of the deviations between the WS-H thermodynamic curves and the predicted behavior.	85	Table 5.5: Estimation of the reactor energy demand and comparison with the potential supply from combusting the pyrolysis gas, assuming a furnace efficiency of 80% [5]	104
Table 4.10: Comparison of the Aspen Plus™ modelling results using the best results from Table 4.9.	87	Table 5.6: Estimation of cooling water consumption and cost in the system based on all cases.	104
Table 4.11: Primary pyrolysis network employed in the final model. Description of the components of the		Table 5.7: Composition of the feedstock as input to the model. Values in wt.%.	105
		Table 5.8: Data estimated for the first condensate and K1 loop, using Aspen Plus 12™	107
		Table 5.9: Data estimated for the second condensate and K2 loop, using Aspen Plus 12™	108
		Table 5.10: Data estimated for the pyrolysis gas and coke products using Aspen Plus 12™	108
		Table 5.11: Estimation of the reactor demand and comparison with the potential supply from combusting the pyrolysis gas, assuming a furnace efficiency of 80% [5].	110
		Table 5.12: Estimation of cooling water consumption and cost in the system based on all cases.	110

Glossary

Acronym	Meaning	Acronym	Meaning
AC	Aqueous Condensate	MC	Moisture Content
BP	British Petroleum [®]	MHV2	Huron-Vidal Version 2 (mixing rule)
CFD	Computational Fluid Dynamics	MS	Mass Spectroscopy
CI	Confidence Interval	MS	Mass Spectroscopy
COD	Chemical Oxygen Demand	MW	Molecular Weight
CSTR	Continuous Stirred Tank Reactor	NMR	Nuclear Magnetic Resonance
DAEM	Distributed Activation Energy Model	NRTL	Non-Random Two Liquid
DDTG	Second derivative of the thermogravimetric curve	OLY	Organic Liquid Yield
DFT	Density-Functional Theory	ORC	Organic-Rich Condensate
DIN	<i>Deutsches Institut für Normung</i>	PDU	Process Development Unit
DTG	First derivative of the thermogravimetric curve	PDU	Process Development Unit
EN	European Technical Standards	PFD	Process Flowsheet Diagram
EoS	Equation of State	PFR	Plug Flow Reactor
EU	European Union	PLS	Partial Least Squares
FAO	Food and Agriculture Organization	PR	Peng Robinson (EoS)
FC	Fixed Carbon	RMSE	Root Mean Square Error
FCC	Fluid Catalytic Cracking	SAFT	Statistical Associating Fluid Theory
FID	Flame Ionization Detector	SDS	Sustainable Policies Scenario
FID	Flame Ionization Detector	SPS	Stated Policies Scenario
FPBO	Fast Pyrolysis Bio-oil	SRK	Soave-Redlich-Kwong (EoS)
GC	Gas Chromatography	TAC	Thesis Advisory Committee
GC	Gas Chromatography	TGA	Thermogravimetric Analysis
GDP	Gross Domestic Product	TOC	Total Organic Carbon
GHG	Greenhouse Gas	UNIFAC	Universal Quasichemical Functional Group Activity Coefficients
HAA	Hydroxyacetaldehyde	UNIQUAC	Universal Quasichemical
HC	Heat Carrier	USD	United States Dollar
HCE	Hemicellulose	VGO	Vacuum Gas Oil
HHV	Higher Heating Value	VM	Volatile Matter
HMF	5-hydroxymethyl-furfural	WS	Wheat Straw
HMWL	High Molecular Weight Lignin	ar.	As received basis
HPLC	High-Performance Liquid Chromatography	daf.	Dry and ash-free basis
ICP-OES	Inductively Coupled Plasma – Optical Emission Spectroscopy	db.	Dry basis
IEA	International Energy Agency	Eq.	Equation
ISO	International Organization for Standardization	mol. %	Molar fraction
LHV	Lower Heating Value	wt. %	Weight (mass) fraction
LLVE	Liquid-Liquid-Vapor Equilibrium(a)	α	Conversion
LVE	Liquid-Vapor Equilibrium	β	Heating rate

1. Introduction

1.1. Motivation

Despite increasing investment and research on alternative methods, human quotidian activities depend greatly on fossil fuels. The global production of food, electricity, plastics, and chemicals, depends at least partially on petroleum, coal, or natural gas to some extent, and the great majority of transportation relies on petroleum-derived commodities. According to a report from BP, petroleum accounted for a third of all primary energy consumption in the world, followed by coal and natural gas not far behind. [1]

This maintenance situation has environmental, economic, and political repercussions. Although the absolute depletion of resources is a contested topic, the distribution of these resources is not even throughout the world, leading to availability fluctuations, as well as economic and political disparities. On the other hand, the combustion of fossil fuels and their derivatives leads to the emission of carbon dioxide and water vapor at a rate much higher than the normal ecological one. Both these gases are greenhouse gases (GHG) that have the capacity of trapping heat in the atmosphere, leading to global climate warming, in turn leading to ecosystem disruption, species extinction, desertification, flooding of coastal areas, etc. The situation is not expected to improve: while developed countries usually have established infrastructures and can make an effort to phase out fossil fuel consumption, developing countries rely greatly on conventional, proven methods to foment their growth, which increases the demand and use of fossil fuels.

To counter this issue, humanity is called upon to replace fossil fuels with other forms of energy production and storage. Commonly implemented strategies are the harnessing of the driving power of wind and flowing water to rotate fans, or the use of photovoltaic farms to produce electricity. Although very successfully implemented in many countries, these methods only account for a diminutive fraction of the total global electricity production, as their feasibility depends on the availability of these resources, and care has to be given to the impacts that wind farms and hydroelectric dams have on the ecosystem in which they are implemented.

Bioenergy, or energy from biomass, can help address the non-reliability of wind- or solar-based methods, through direct combustion, or the production of surrogates for the petroleum-based industry, like conventional transport fuels, plastics, and chemical precursors [2,3]. The use of waste materials, if possible, can provide an extra source of revenue in different parts of the value chain, while tackling the issue of waste management, most commonly landfilling, a noticeable problem in developing countries.

A wide variety of methods have been developed or repurposed to transform biomass into energy or energy carriers (fuels), but can mostly be divided into two categories: biochemical and thermochemical. The former makes use of bacteria or yeasts to ferment or digest biomass in a water suspension, yielding such products as ethanol, methane, or relevant chemicals. The latter uses high temperatures to degrade a solid material

under different environments, to harness the chemical energy of their combustion (e.g., incineration), or to produce one or more useful phases that can be used for the production of relevant materials (e.g., pyrolysis or gasification).

Pyrolysis has been singled out due to the large range of possible feedstocks it can process, as well as the production of both liquid and solid phases with interesting possibilities (section 2.1). The liquid phase(s), the bio-oil(s), is being studied as a source of fine chemicals, as a precursor for liquid fuels, or as a fuel itself, due to its high energy content. The solid phase, the coke, finds use as a carbon source, a fuel for direct combustion, or is used like activated carbon.

1.2. Objectives of the doctoral project

While pyrolysis models exist in the literature, these tend to employ simplification strategies that avoid the intricate reaction networks of thermal biomass degradation and/or disregard the complexity of the organic liquid phase altogether. Therefore, these models are not suitable for flexible and rigorous process simulation, which would allow for the change of feedstock or operating conditions.

The objective of the work is the development of a flexible and rigorous model of fast pyrolysis, based on fast pyrolysis process materializations in two different scales, and applied for biomass conversion in the *bi-oliq*[®] project at KIT. The final model is expected to reflect changes in feedstock composition and process setup on the liquid product yield and quality. The choice of Aspen Plus[™], a commercial flowsheeting simulator, when compared to open-source options or other types of modeling, is focused on the ubiquity of its use in academia and industry alike, its versatility and ease of use, and the access to the powerful Aspen Properties[™] package and database.

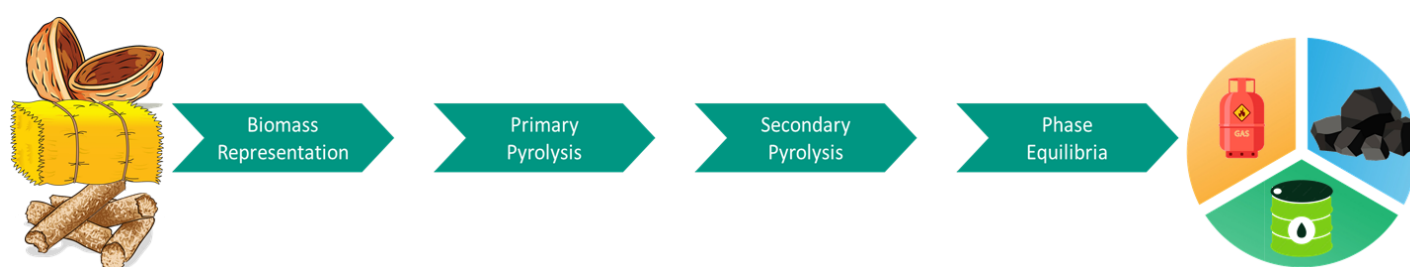


Figure 1.1: Scheme of the model preparation, from lignocellulosic biomass (left) to the final products (right).

The project can be divided into four main stages (Figure 1.1). To ensure versatility in feedstock input, it is important to define the representation of biogenic materials in the model and define the decomposition network for these materials, for which an implementation found in the literature has been adapted [4], which can be obtained with the assistance of thermogravimetry (sections 3.2 and 3.3). The current materialization of this project [5] employs a black-box reaction, but to correctly allow for versatility in feedstock and *in-process* setup, it is important to define how to correctly model the pyrolysis reactor, namely the choice of the kinetic scheme from both biomass and literature (section 4.3.1), not ignoring the presence of secondary pyrolysis and aging

phenomena (section 4.3.2). Finally, a major focus of this project has been the definition of a surrogate mixture for bio-oils (section 4.1.3), the complete thermophysical characterization of all species considered in the model (section 4.1.5), and the rigorous modeling of the condensation loops (section 4.5).

1.3. Academic contributions

1.3.1. Manuscripts

F.G. Fonseca, A. Anca-Couce, A. Funke, N. Dahmen, *Challenges in kinetic parameter determination for wheat straw pyrolysis*, *Energies*. 15 (2022) 7240. doi:10.3390/en15197240.

C.C. Schmitt, F.G. Fonseca, M.C. Fraga, A.W. Jr, S. Karp, Á. Henrique, M. José, C. Rita, R. Moreira, D. Eiji, K. Raffelt, N. Dahmen, *Thermochemical and Catalytic Conversion Technologies for the Development of Brazilian Biomass Utilization*, *Catalysts*. 11 (2021) 1549.

F.G. Fonseca, A.P. Soares Dias, *Almond shells: Catalytic fixed-bed pyrolysis and volatilization kinetics*, *Renew. Energy*. 180 (2021) 1380–1390. doi:10.1016/j.renene.2021.08.104.

A.P. Soares Dias, F.G. Fonseca, M. Catarino, J. Gomes, *Biodiesel Glycerin Valorization into Oxygenated Fuel Additives*, *Catal. Letters*. (2021).

Y. Fan, F.G. Fonseca, M. Gong, A. Hoffmann, U. Hornung, N. Dahmen, *Energy valorization of integrating lipid extraction and hydrothermal liquefaction of lipid-extracted sewage sludge*, *J. Clean. Prod.* (2020).

A.U. Şen, F.G. Fonseca, A. Funke, H. Pereira, F. Lemos, *Pyrolysis kinetics and estimation of the chemical composition of Quercus cerris cork*, *Biomass Convers. Biorefinery*. (2020).

F.G. Fonseca, A. Funke, A. Niebel, A.P. Soares Dias, N. Dahmen, *Moisture content as a design and operational parameter for fast pyrolysis*, *J. Anal. Appl. Pyrolysis*. 139 (2019) 73–86.

A.P. Soares Dias, F. Rego, F.G. Fonseca, M. Casquilho, F. Rosa, A. Rodrigues, *Catalyzed pyrolysis of SRC poplar biomass. Alkaline carbonates and zeolites catalysts*, *Energy*. 183 (2019) 1114–1122.

1.3.2. Conference Participations

F.G. Fonseca, A. Funke, N. Dahmen, *Modeling Fast Pyrolysis of Waste Biomass: Improving Predictive Capability*, in: *Pyroliq 2023, Engineering Conferences International, Hernstein (Austria)*, 2023

F.G. Fonseca, A. Anca-Couce, A. Funke, N. Dahmen, *Kinetic parameter determination for wheat straw pyrolysis*, in: *ePYRO2021, Medicongress, Ghent*, 2021.

F.G. Fonseca, A. Funke, W. Saechua, P. Sirisomboon, *Precision test for the spectral characteristic of FT-NIR for the measurement of water content of wheat straw*, *IOP Conf. Ser. Earth Environ. Sci.* 301 (2019) 012034.

F.G. Fonseca, A. Funke, N. Dahmen, *Aspen PlusTM modeling of Fractional Condensation schemes for the production of Fast Pyrolysis bio-oil*, in: *27th Eur. Biomass Conf. Exhib., ETA-Florence Renewable Energies, Lisbon*, 2019: pp. 681–683.

F.G. Fonseca, A. Funke, A. Niebel, A.P.S. Dias, N. Dahmen, *Moisture content as a design and operational parameter for fast pyrolysis*, in: *1. Dtsch. Doktorandenkolloquium Bioenergie, DBFZ Deutsches Biomasseforschungszentrum gemeinnützige GmbH*, 2018: p. 286.

2. Literature Review

2.1. Pyrolysis in the context of energy production

2.1.1. Greenhouse emissions and energy production trends

In 2018, the global energy-related CO₂ emissions reached a historic high of 33 GTon (variation from 2000-2017 shown in Figure 2.1). Current and planned policies throughout the world do not follow Paris-compliant emissions, and projected scenarios following said politics predict a stabilization of the value (SPS, Figure 2.1), but not a reduction unless energy-related CO₂ emissions drop 52% by 2040. The IEA proposed 2018 a Sustainable Development Scenario (SDS, Figure 2.1), which recommends an annual reduction of 2% by 2020 and 4.6% by 2030. [6]

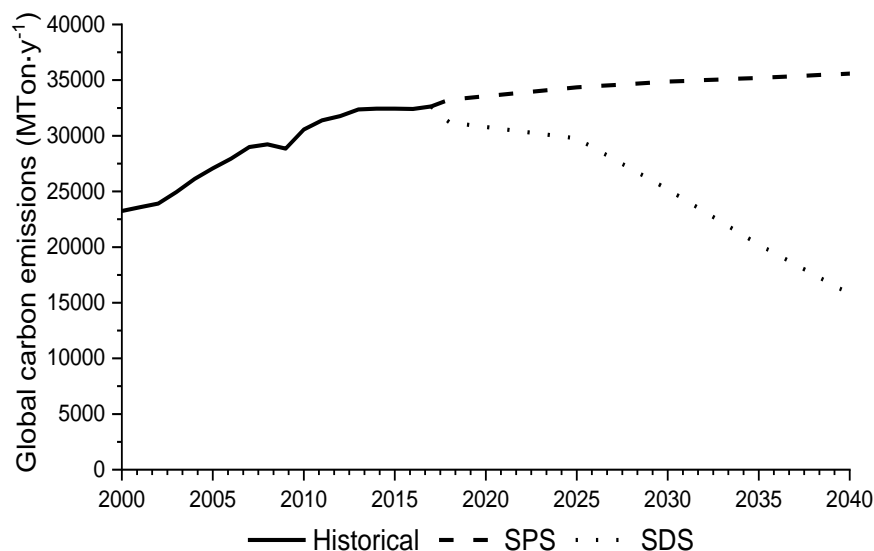


Figure 2.1: Global energy-related carbon emissions by scenario, 2000-2040. Source: [6] IEA (2020). All rights reserved. SPS: Stated Policies Scenario; SDS: Sustainable Development Scenario.

In Figure 2.2, the carbon emissions in key regions following both scenarios are shown. In Europe (EU), policies promoting renewable energy practices and reducing coal power generation have led to a consistent drop, which is expected to continue. A similar trend is expected for Japan and the USA alike. Current published guidelines by the Chinese government indicate an expected further rise in a country that is already the World's greatest contributor to carbon emissions by a large margin. On the other hand, emerging markets, such as India, Brazil, and South Africa, are expected to keep increasing their carbon emissions due to a growth in industrialization, with an open opportunity to reverse their upward trends. [6]

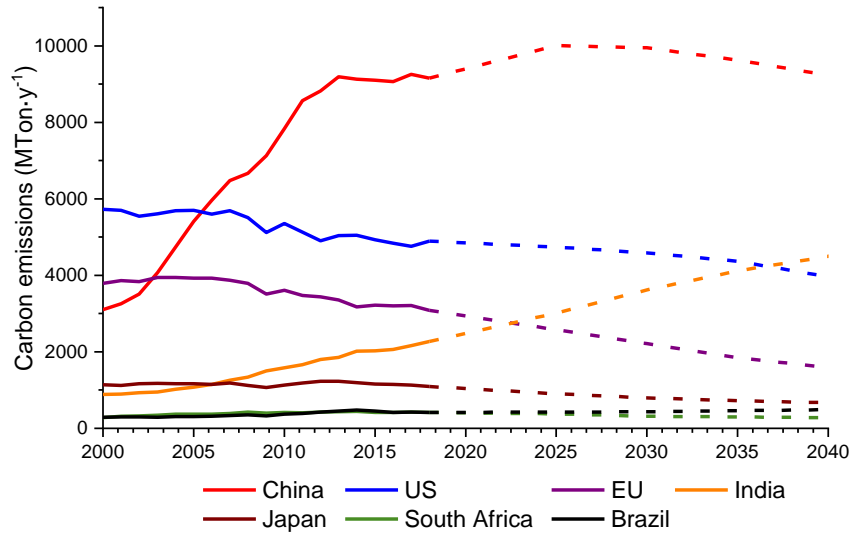


Figure 2.2: Energy-related carbon emissions in key regions, 2000-2040. Source: [6] IEA (2020). All rights reserved.

The use of biomass is considered a short-term carbon-neutral alternative to other renewable energies for the production of hydrocarbons and direct heat and power by displacing fossil fuels with minimal equipment adjustment. It is especially relevant for the production of liquid fuels for use in combustion engines, which are expected to still be the main technology for transportation in the immediate future.

Production of energy (heat and power) has been historically significant for human populations due to its availability and ease of exploitation. Despite the technological advances which permitted the use of higher-production sources, coal, oil, nuclear, and hydro, biofuels are still a relevant source, and the previously mentioned concerns towards carbon emissions kept their share constant in the face of higher global energy demand, as seen in Figure 2.3. From 1990 to 2018, according to data from the IEA ¹, the global energy supply provided by biofuels increased from 10.5 TWh to 15.4 TWh, which translates to a share of 10.3% to 9.3% of the global energy supply.

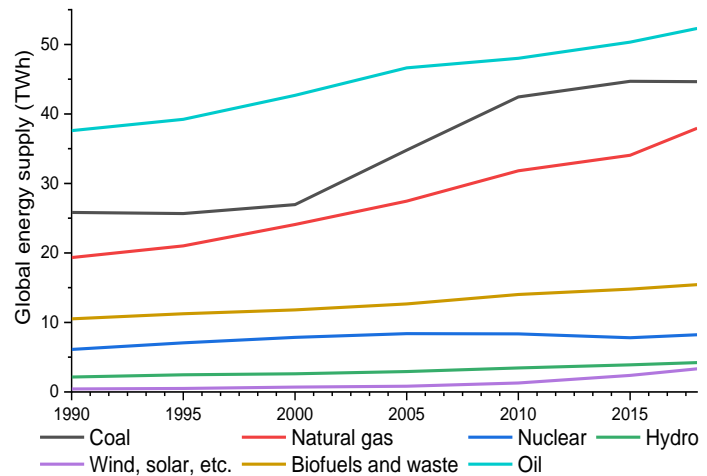


Figure 2.3: Global total energy supply by source, 1990-2018. Source: IEA (2020). All rights reserved.

¹ Source: IEA World Energy Balances 2020 <https://www.iea.org/subscribe-to-data-services/world-energy-balances-and-statistics>

In Figure 2.4, the comparison is narrowed down to biomass and waste as energy sources. Among these, primary solid biofuels, such as wood, have always paid a leading role due to their ease of exploitation. However, the market share of wastes (both industrial and municipal) has grown, in both direct and transformed use. The market share of liquid biofuels is very dependent on national directives and oil prices.

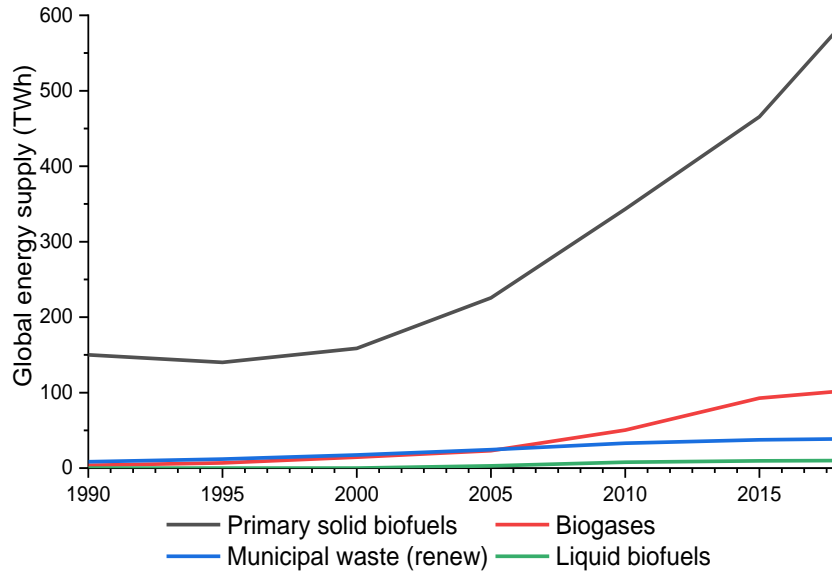


Figure 2.4: Global energy supply by biomass/biowastes from 1990-2018. Source: IEA (2020). All rights reserved.

Recent technological developments led to a substantial auction price reduction for solar and wind, which makes them comparable if not cheaper than bioenergy for electrical power production on a short-term basis, while also featuring lower variable costs, mainly due to not having to source their primary energy source (Figure 2.5). However, Martín et al. [7] discussed the reality of these trends for a series of countries and cast doubts on the ability of these technologies to break even in the case of low/inexistent governmental support.

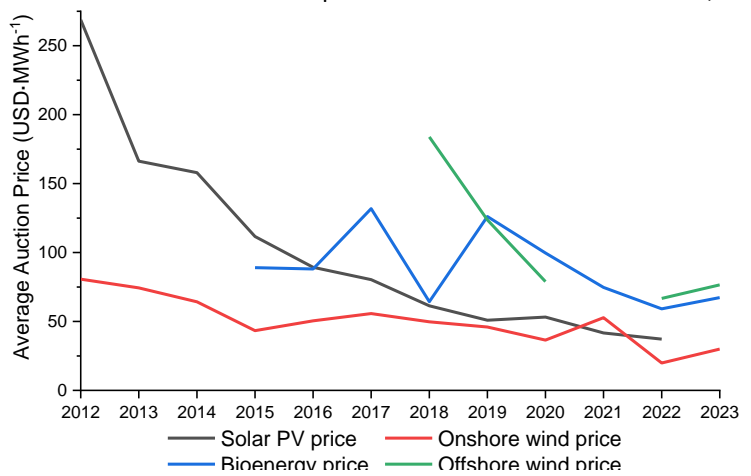


Figure 2.5: Average auction price by project commissioning for the generation of electric power, 2012-2023. Source: IEA (2020). All rights reserved.

2.1.2. Biorefining potential of straws

The definition of biomass can be widely different between available sources and experts, but is defined (Dictionary.com) as “the amount of living matter in a given habitat, expressed either as the weight of organisms per unit area or as the volume of organisms per unit volume of habitat”. However, in terms of energy production, biomass is often considered the amount of matter of biological origin that can be converted into fuel. The use of locally available biomass for the production of energy can reduce the reliance on fossil fuels and the emission of greenhouse gases while promoting economic independence for communities and countries alike [2].

Often, it is divided into four categories: woody, herbaceous, algal, and waste-based. Woody biomass comprises wood itself, and the residues are derived from trees and shrubs and forestry industries (branches, leaves, bark, sawdust, etc.). Herbaceous biomass comes from crops and plant species such as wheat, barley, corn, maize, switchgrass, sugarcane, and many others. The crops themselves can be used for the production of biofuels (so-called first-generation biofuels), but there is concern regarding competition with food production, and other limitations [8,9]. The processing of these herbaceous crops produces a great number of wastes, and biofuels produced from these wastes are part of the second generation of biofuels [8]. Algal biomass produces the so-called third-generation biofuels, with higher energy outputs [10]. Biological waste, from farming, the paper industry, food production residues, and water treatment sludge, is also considered a form of biomass [11].

However, the use of biomass as a carbon/energy source is not without controversy. Many problems associated with agricultural practices and expansion are already a factor for concern, such as deforestation, soil and water contamination, biodiversity reduction, GHG emissions, etc. The use of so-called energy crops, for the production of first-generation biofuels, would increase the extent of these problems, as their market value can sway many landowners to stop producing food and feed products, increasing their price and limiting availability. In this sense, the use of biomass residues, such as wheat straw, can provide the landowners with additional sources of revenue from a low-value by-product, while not competing with the production of food/feed. [2]

Another concern associated with the rapid economic development observed in many countries is the production of waste, mainly plastic and textiles. A study by Hoornweg et al. [12] focuses on the projected trend of waste production, both globally and by region, in which it is made clear that waste production is expected to grow very fast with the growth of population and with the improvement of economic conditions for that same population. Despite the possibility of separation, recycling, and reuse, a great amount of this waste is directed to landfilling, associated with the occupation of land, fire hazards due to methane accumulation, environmental contamination by leaching, foul odors, and the proliferation of disease.

Developing technologies that help process biomass and wastes is in line with the concept of biorefinery, the integrated production of products from biomass sources, maximizing the carbon and energy retrieval from said biomass, as a conventional refinery does with petroleum.

Lignocellulosic biomasses, such as wheat straw, find great potential for biorefining (Figure 2.6). The material situation is favorable, and conversion products can compete in a traditional petrochemical-based market. These materials consist of three main fractions: hemicellulose, cellulose, and lignin. [13]

The cellulose fraction, a polymer of hexoses, can be hydrolyzed to produce glucose which in turn can be used to produce HMF (5-hydroxymethylfurfural, the precursor of nylon-6), and can be fermented to ethanol, acetic or lactic acid, acetone, or butanol, among many. The hemicellulose fraction, a polymer of pentoses, is often processed to plant gum, or hydrolyzed to xylans, with a large assortment of market placements. The lignin scaffold is a copolymer of substituted phenols, with great economic interest, but without any as-of-yet proven industrial isolation pathway. [13]

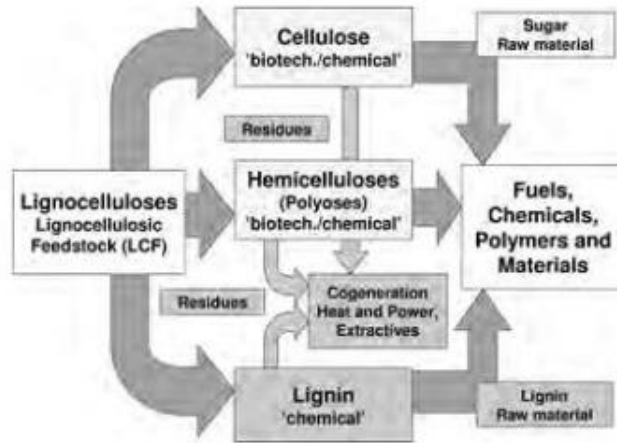


Figure 2.6: Lignocellulosic biorefinery scheme. Source: [13]

Straw, the biomass understudy, is the crop residue constituted by the dry stems and leaves left after the harvest of cereal crops. These materials are available in large quantities and constitute over 50% of the harvestable vegetation. They are coarse, highly fibrous roughage, not fit for human consumption, but find widespread use as livestock feed and bedding material, as well as litter for manure production, and as construction and hand-crafting materials. However, all these uses have been replaced by more profitable alternatives since the advent of the industrial era [14].

Straws are available whenever the production of cereals or legume grains occurs. If one assumes that straw production is slightly higher than the corresponding grain production, it can be estimated that around 3000 million tons of straw were produced in 2018 [15]. Expected values for lignocellulosic, as well as proximate compositions of fully ripe wheat straw, are presented in Table 2.1.

Table 2.1: Expected values for lignocellulosic and proximate compositions of wheat straw. Data for beech wood obtained from the Phyllis2 database (www.phyllis.nl)

Component	Yield (% wt. db.)
Cellulose	39.30 ± 2.40
Hemicellulose	23.47 ± 3.52
Lignin	19.98 ± 2.68
	Yield (% wt.)
Moisture	4.74 ± 1.96
Ash	8.98 ± 2.06
Fixed Carbon	20.08 ± 1.37
Volatile Matter	70.94 ± 2.34

About Germany, data from 2020 from the FAO [15], shows a population of 83.2 million people, with 1.3% of the working-age population employed in agriculture, for a cropland area of around 3.2 Mha. Agriculture in Germany represents around 0.8% of the country's GDP. In this sense, the exploitation of agricultural residues as energy sources could be extremely important. Germany is a net cereal exporter, with a net trade balance of over 11 billion USD on cereals and preparations alone. The biggest areas of production of wheat in Germany

include the Dungau in Bavaria as well as the flatlands surrounding the Harz mountains (Lower Saxony and Saxony-Anhalt). Specific to Baden-Württemberg, the most important areas are the Kraichgau and Zabergäu to the immediate northeast of Karlsruhe. [16]

2.1.3. The pyrolysis process

Pyrolysis (from the Greek $\pi\upsilon\rho$, meaning fire, and $\lambda\acute{\upsilon}\sigma\iota\varsigma$, a loosening) is a thermochemical process of energetic conversion, akin to combustion, gasification, liquefaction, or torrefaction, which occurs in an inert atmosphere, through the application of temperature rising that decomposes macromolecules. The pyrolysis process has been applied to raw wood for charcoal production, as a source of carbon for iron extraction and steel production, before the industrial age and the advent of coal exploration. Kerosene was first obtained through the pyrolysis of coal and was widely employed for public illumination. [3]

The application of this process yields two main products: a char and a vapor, the latter of which is normally condensed to produce a liquid phase, the bio-oil, and a gas phase, the pyrogas. The char phase is rich in carbon, and it retains the vast majority of the inorganic material present on the feedstock, the ash, as well as having a high LHV [3,17]. Pyrogas is mostly made up of gases that do not condensate at normal operation temperatures, like CO, CO₂, and light paraffins [3]. The bio-oil, its composition, and its representation, are further explored in section 2.4.

Heat demand associated with heating the reactor or drying the feedstock is often met with the combustion of pyrolysis by-products, mainly the gas and a fraction of the cokes [3]. Such a situation was calculated for the case of the *bioliq*[®] pyrolysis plant [5,18]. The fast pyrolysis process is considered less energy-intensive than fermentation, within the context of a biorefinery for fuel production [19].

Table 2.2: Different pyrolysis classifications based on the heat transfer method. Sources: [3,9,20,21].

	Heating rate	Temperature	Solid residence time	Vapor residence time
Slow pyrolysis	Low (< 1 °C/s)	Low (> 400 °C)	Long or very long (minutes to days)	Long ($>$ seconds)
Intermediate pyrolysis	Moderate	Moderate	Long (minutes)	Moderate (some seconds)
Fast pyrolysis	Very high (> 100 °C/s)	Moderate or High (425-600 °C)	Short (a few seconds or less)	Very short ($<$ seconds)

The thermal degradation is influenced by a combination of process variables: feedstock, temperature, pressure, residence times of both gas and solid under pyrolysis conditions, heat transfer, reactor design, sweeping gas use and nature, and product recovery systems, among others. Among these, heat transfer is regarded as the most relevant factor, as it governs the selection of the reactor type, heating method, and product recovery. Thus, a pyrolysis process is often classified based on how fast this heat transfer occurs. The most common are presented in Table 2.2.

Fast pyrolysis processes often report high liquid yields, up to 75% wt. db., along with sensitively equal yields in gases and char, which are considered by-products. In this kind of process, heat transfer must occur extremely rapidly within the individual feedstock particles, hence the feedstock is usually supplied grounded to the order of millimeters. In addition, to make the heat transfer fast and efficient, heat carrier systems are often employed, among other options (Figure 2.7). As the bio-oil

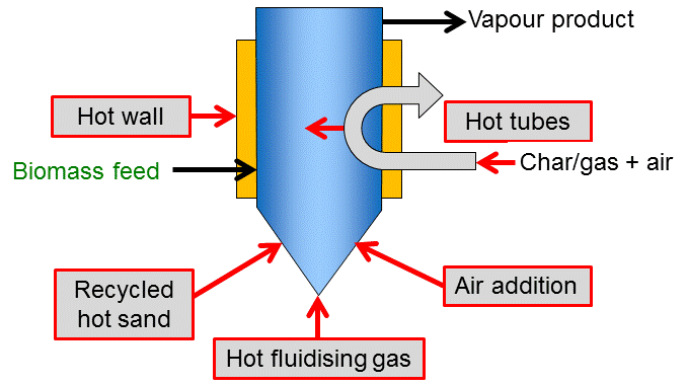


Figure 2.7: Methods of heating commonly employed.
Source: IEA Bioenergy Task 34 [23].

is the main target, the feedstock's moisture content (MC) is usually kept below 10% wt. to minimize the amount of water in the liquid. [20] A small mention of past and current fast pyrolysis projects is mentioned in section 2.1.4. To reach liquid yields over 75% wt. db., a process named flash pyrolysis is in development, featuring residence times that are kept in the range of 30-1500 ms [3]. On the other hand, slow and intermediate pyrolysis feature a more balanced production of the different products, with liquid productions of 30 wt.% and 50 wt.%, respectively [22]. However, definitions based on factors such as heating rate, temperature, and liquid product may not be correct from the point of view of the particle. Ledé and Authier [24] distinguish the heating rate experienced by a particle, and that one supplied by a source, which should be indistinguishable so long as the particle is thermally thin, which corresponds to Biot numbers (Eq. (2-1), for which h stands for the heat transfer coefficient, L stands for the characteristic length of the particle and λ to the thermal conductivity of the material) under 0.1, as long as the thermal gradients within the particle are disregarded.

$$Bi = \frac{hL}{\lambda} \quad (2-1)$$

Defining a characteristic length for a biomass particle can be difficult. Lignocellulosic materials are anisotropic, meaning that heat and mass transfer through one plane of orientation is often dominant versus another. Both Ledé and Authier [24] and Liu et al. [25] define the axial direction as dominating, which is often valid for massive particles such as wood chips. However, in the case of hollow particles like shredded straws, the radial direction is dominating as the particles tend to be very thin, and they do not heat up from the axial ends due to a difference of two orders of magnitude between thickness and length.

Working with fixed external heat source temperatures, as in a pyrolysis reactor, Ledé and Authier [24] modeled the effect of characteristic length and heat transfer to plot the disparity between the external heat source temperature and the internal particle temperature, and found a substantial disparity between those values for large particles (400 μm), with a ΔT (thermal lag) of 620-650 K at a source temperature of 1200 K, and small particles (2 μm), with a ΔT of 700-780 K at a source temperature of 1200 K. These results agree with previous findings regarding a 'biomass fusion-like temperature', and indicates that it is unpractical to increase external heat past this range of temperatures at fast pyrolysis conditions. The authors found that other factors, such as

heat transfer coefficient, the heat of reaction, and heating rate, have a minor effect on the particle temperature even at increasingly higher heat source temperatures.

Analyzing situations in which the heating rate changes, the authors found a high difference between the particle temperature change rate and the external heating rate, with the ratio between these two parameters possibly going as low as 0.03 at very high external heating rates, leading to possible operating error. The authors also found a variation in the particle temperature change rate with the conversion and with time, reaching a minimum during the reaction that can be 10 times lower than the maximum. During the reaction, while not strictly isothermal, the particle temperature does not change greatly as a function of conversion. [24]

The authors recommend criteria such as efficient removal of products (not necessarily residence time) and external heat transfer coefficient ($h \gtrsim 50 \text{ W}\cdot\text{m}^{-2}\cdot\text{K}^{-1}$) as good parameters for characterizing fast pyrolysis and disregard the effect of particle size and residence time. [24]

2.1.4. Fast pyrolysis research and large-scale materializations

The center of a fast pyrolysis process is the reactor. Apart from the reactor, a fast pyrolysis system includes biomass handling and pre-processing, condensation and product collection, and, whenever relevant, upgrading or product processing. [26]

Despite representing a relatively minor fraction of the total capital cost of a whole system (according to Meier et al. [26]), the majority of the research and development in the field of fast pyrolysis has been dedicated to reactor configurations and feedstock testing and only more recently has focus switched to process control and improvement of condensation systems. The type of reactors most often employed for fast pyrolysis is fluidized (fixed, circulating, transported) beds and variants, due to facilitating heat transfer, vapor collection, and heat carrier re-heating [27]. Processes in which a heat carrier is circulated and externally heated can be considered circulating bed systems. In these processes, the residence time of the solids and vapors is minimized to avoid secondary reactions (section 2.2.1), as the char and ash are catalytically active [26], maximizing the extraction of condensable volatiles from the system [20]. For this purpose, considerable flow rates of carrier gas are often used to keep the vapor residence time under 2 s, while aiding with keeping the system free of molecular oxygen; this factor also leads to gas dilution and further lowers its heating value.

Several types of reactors have been devised to carry out fast pyrolysis in different scales, and for different feedstocks and target products, which can be characterized based on the method of mixing solids with the hot heat carrier and removing pyrolysis vapors efficiently. The most common types are fluidized bed reactors often feature the recirculation of a heat carrier and hot air, ensuring a fast degradation and recovery of pyrolysis vapors, while not permitting the recovery of pyrolytic char, as it is combusted to regenerate the heat carrier [28,29]. Screw reactors are common technologies for the handling and modification of solid and highly viscous materials, such as refinery residues or shale oil, as well as lignocellulosic biomass; they are flexible and compact and produce a brittle char [30–34]. Other types of pyrolysis reactors less commonly employed include ablative

pyrolysis [35], rotating cone [20], vortex [29] and rotating kilns [36,37]. A detailed presentation of different types can be found in [38].

Several reviews of the state-of-the-art of fast pyrolysis research and materialization throughout the world have been published in the last decade [20,38–41]. PyroWiki², a Wikipedia-style encyclopedia maintained by experts and enthusiasts of fast pyrolysis, keeps a listing of commercial-scale throughout the world. IEA Bioenergy³, in their Task 34 website, also offers a small introduction to diverse types of reactors. The BIOFIT Project, an EU-financed project supported through the HORIZON 2020 project, published 2021 an overview of bioenergy in Europe, including an analysis of 10 case studies [42].

2.1.5. Utilization of the produced fractions

As stated before, the typical products of a pyrolysis plant are gas and coke, as well as one or more liquid phases, usually named pyrolysis bio-oils. Due to its composition, rich in carbon dioxide and the employed sweeping gas, the gas has little commercial interest. However, it can be used as a sweeping gas, fluidizing gas, or even as a supplementary heat source [3]. Fonseca et al. calculated that the *bioliq*[®] / fast pyrolysis plant energy demand could hypothetically be suppressed by the combustion of its pyrolysis gas alone [5,18].

As the solid product of pyrolysis, (bio-)char retains the totality of the non-volatile inorganics present on the feedstock, making it a solid source of carbon and minerals whose properties can be engineered [43]. Traditional uses include soil additives for agriculture, activated carbon source, and solid fuel [43]. Char is being studied as an alternative to traditional activated carbon for the adsorption for removal of pollutants from water [44,45], or even as a source of carbon for gasification [46,47] or metallurgy [48], though its use is limited by the ash content of the feedstock. In Brazil, biochar is an essential component of *terra preta* (also known as Amazonian dark earth), which is used to facilitate agriculture in deforested lands, mainly in the Amazon Basin, due to the low fertility of the reclaimed soils [36]. Şen and Pereira [49] compiled a review of char production methods focused on tree bark.

Pyrolysis oil production is currently a mature technology (section 2.1.4), frequently as a side stream from the production of coke. Fast pyrolysis bio-oil (FPBO) is currently widely used to fire boilers modified to handle the high water and oxygen content, low pH, and heating power [23], but few standards for its use and production [41], but these deterrents typically dissuade any use as direct petrol fuel replacements [50,51].

Both treated and upgraded pyrolysis oils have been successfully processed in petroleum refineries in co-feeding, with the main goal to lower the fossil-related GHG emissions during refining ⁴, a process at a growing

² PyroWiki, available online at: http://pyrowiki.pyroknown.eu/index.php/Welcome_to_PyroWiki

³ IEA Bioenergy Pyrolysis Reactors Available online: <http://task34.ieabioenergy.com/pyrolysis-reactors/> (accessed on Dec 4, 2019)

⁴ BTG Bioliq, available online at: <https://www.btg-bioliq.com/plant/pyrocell-gavle-sweden/>

level of industrial maturity [52]. Pyrolysis oil can also be blended directly with conventional fuels and employed as transportation fuel [51,53]

Even though pyrolysis technology has been the topic of great scientific interest in the last half a century, there is a relevant issue with the production of large amounts of FPBO with standardized properties for academic and industrial research, a market gap attracting the investment of player in the pyrolysis coke market, such as ProFagus, as well as industrial consortiums, like BTG BioLiquids and Honeywell Envergent. Biomass pyrolysis oil is also appreciated as a biogenic source of platform chemicals and food additives, like aldehydes, acetic acid, methanol, HMF, lignin, and guaiacol (liquid smoke) ⁵ [23].

Upgrading of pyrolysis oil has been centered around hydrotreatment or *in-situ/ex-situ* catalytic pyrolysis, with important shortcomings centered on the degradation of sugar and sugar decomposition species [38,54,55]. More recent industrial demonstration units have made important advances in this area, thus raising the technological readiness level of the process ⁶.

Distillation has also been considered for the processing of pyrolysis condensates, but a high moisture content and the presence of cracking and polymerization reactions at higher temperatures (about 100 °C) lead to the formation of a solid residue. The fraction of the liquid which can therefore be recovered can be improved by performing the separation under vacuum [56,57].

Fractionation of pyrolysis bio-oils often leads to the production of a water-rich phase of low economic and calorific value with a high oxygenate content, meaning it cannot be disposed of costlessly [5,58]. If its formation cannot be avoided, it may be valued as a hydrogen source in gasifiers [59,60], or as a carbon source for microbial cultivation [61]. Brueckner [62] managed to employ pervaporation to valorize an aqueous phase of pyrolysis oil, reducing its water content considerably and increasing the heating value of this phase; the authors point out the composition of the permeate, rich in low molecular weight oxygenates (such as acetic acid and furfural).

2.1.6. The bioliq® project

The *bioliq*® project (www.bioliq.de, [63–65]) concerns the conversion of low-grade lignocellulosic biomass, such as wood rejects or crop residues for the production of synthetic fuels or organic chemical precursors. The process has been operated since 2007, using wheat straw from the beginning due to its nature as a widely available lignocellulosic residue throughout Baden-Württemberg. As of 2019, a wider repertoire of feedstocks is in use, such as *Miscanthus* grass.

⁵ ProFagus, available online at: <https://profagus.de/raucharomen/>

⁶ GTI Energy, available online at: <https://www.gti.energy/producing-alternative-transportation-fuels-from-renewable-resources-with-ih2/>

Lignocellulosic materials, in general, show a very low energy density, meaning they stand at a clear logistical disadvantage versus liquid hydrocarbonates, such as oil derivatives. To tackle this issue, the *bioliq*[®] concept, schematized in Figure 2.8, proposes a geographic separation of the production chain. In the first small-scale level, close to the producing areas, the biomass is thermally liquefied. The resulting “bioslurry” can be economically transported over longer distances to a central conversion plant, in which it is gasified and converted into methanol, DME, and fuels. [60] This decentralized character is one of the biggest advantages of the *bioliq*[®] concept when compared to bigger units specialized in the production of bio-oil, as the small units have a summative effect.

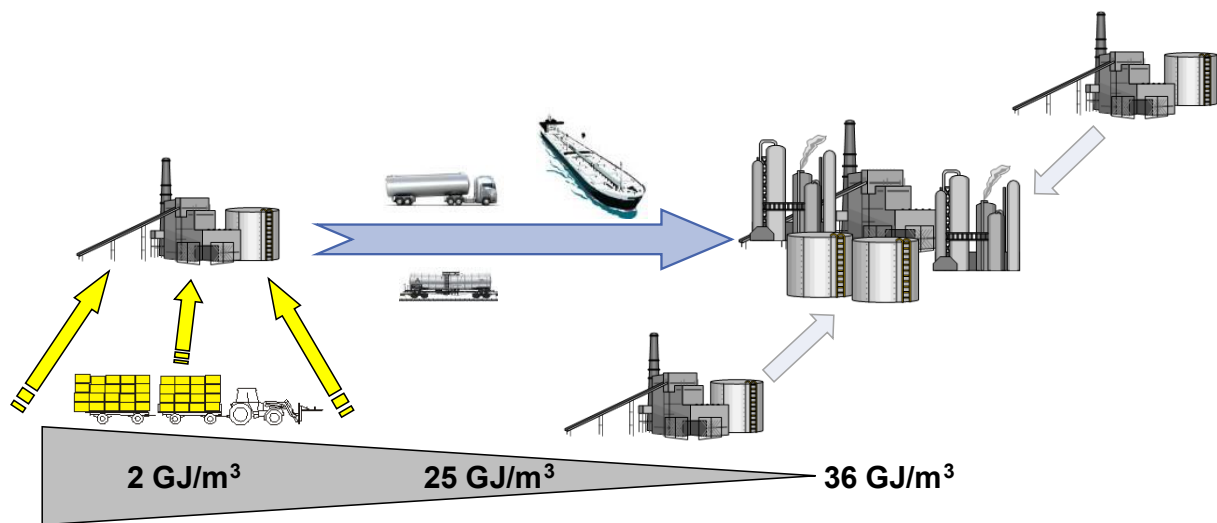


Figure 2.8: The *bioliq*[®] concept schematized. Source: [66]

A pilot that encompasses both stages is materialized in the Campus Nord of the Karlsruhe Institute of Technology, Eggenstein-Leopoldshafen. Our focus lies on the *bioliq*[®] I, the fast pyrolysis plant, that was designed for feed intakes of up to 500 kg/h of shredded lignocellulosic material and was thoroughly described by Funke et al. [67], as well as being visually represented in Figure 2.9. It employs a twin-screw reactor as a reaction medium, as well as quartz sand as a heat carrier. This sand is reheated using flue gas from a natural gas furnace and transported pneumatically to a storage tank above the reactor. Pyrolysis char product conveyed with the sand is employed as an extra heat source by controlling the air flow to the furnace, allowing for rigorous control of the heat carrier temperature. The majority of the coke is carried out of the reactor with the vapors and is mostly removed in a series of cyclones. The vapors are condensed in two stages, leading to two liquid products, henceforth named ORC (organic-rich condensate) and AC (aqueous condensate), respectively. After removal of the majority of the char, the vapor is fed to a quenching spray column, using a liquid excess of 30:1 (liquid: vapor), and the resulting mixture is directed to a column containing an electrostatic precipitator, in which the bottoms are cooled down and recycled as a quenching medium. The water content of this first condensate becomes, therefore, a control parameter, as water is an undesirable trait in hydrocarbon mixtures for further processing, but the viscosity must be kept low enough to allow for pumping, therefore process management targets a content value of 12-16 wt.%. For the case of the second condensate, a single quenching spray column is present with no electrostatic precipitator. Both condensers present a residence time of 6±1 h of the fluid in the loop before being removed from the system.

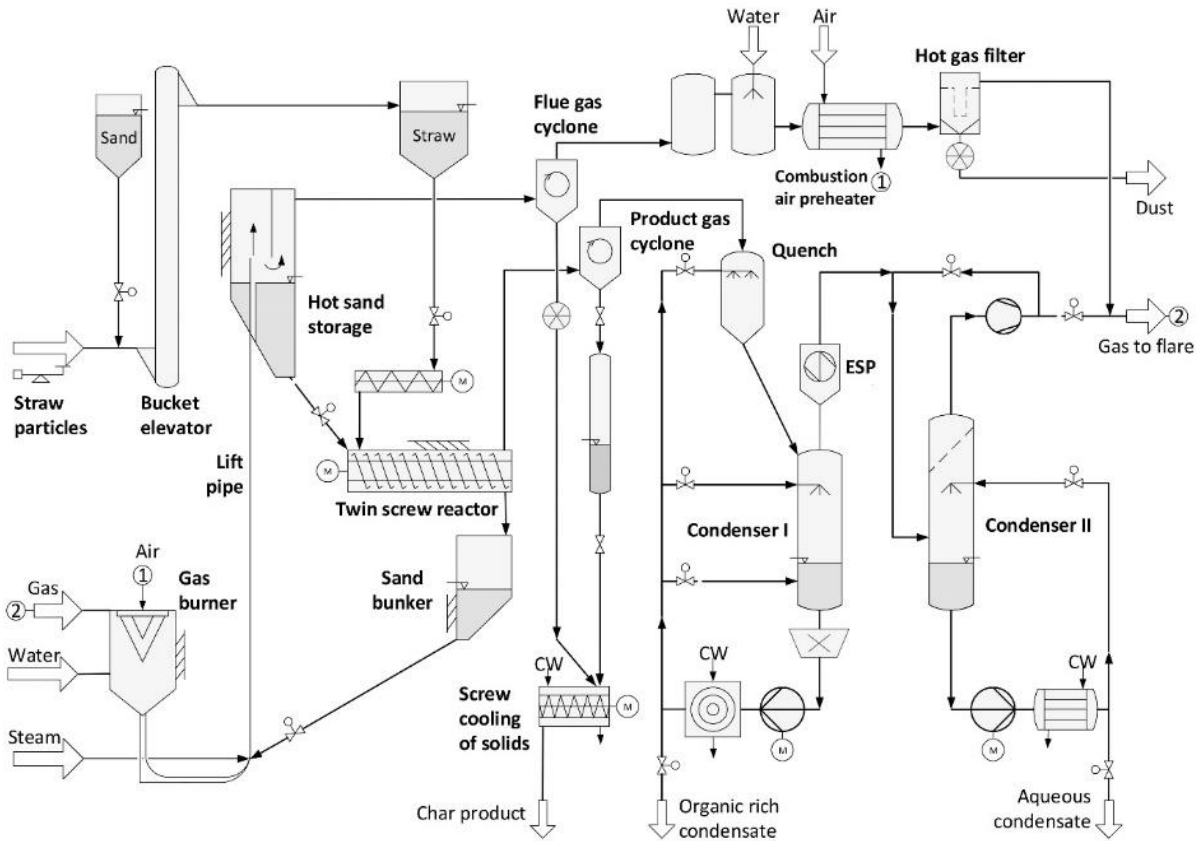
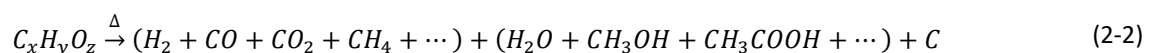


Figure 2.9: Flowchart of the bioliq® I pyrolysis plant. Source: [53].

2.2. Reaction pathways of fast pyrolysis

2.2.1. Degradation pathways present during the pyrolysis process

During the pyrolysis process, a great number of reactions occur in parallel and in series, all featuring different reactants, products, and conditions [3]. An over-simplified reaction for generic biomass is presented in Eq. (2-2), in which the first parcel corresponds to gaseous products, the second the liquids, and the third the char, assuming a lack of ash content, which would otherwise be collected in the solid product [68,69]. Water presents in the resulting products tends to stem mostly from the feedstock moisture content (MC), albeit dehydration reactions occur during pyrolysis, hereby named *reaction water* [50,69], and from condensate aging processes [50,70].



A great variety of mechanisms has been considered to describe this fact, either considering the biomass as a whole or focusing on the degradation of the lignocellulosic substances individually [3,71]. Brennan Pecha et al.[72] compiled a very thorough review of the historical development of pyrolysis reaction modeling, from cellulose-focused to detailed kinetic models which include possible products and intermediates.

Pyrolysis reactions can be categorized into primary and secondary. The former focus on the cracking and devolatilization of the solid matrix by the action of heat, with reactions such as dehydration, decarboxylation, and dehydrogenation [9], plus the formation of tars if the high-molecular-weight low-volatility components are allowed to condensate and polymerize (favored by higher temperatures) [3,20,73]. The latter is based on the thermal and catalytic cracking of the previously formed components, promoting the formation of gas and coke, and are promoted by the ash content contained in the coke [9].

The ash content in the feedstock becomes, therefore, an important parameter to keep in mind, due to the high contents of alkali metals (Groups 1 and 2 in the Periodic Table) that are recognized catalysts for the secondary reactions, especially potassium, and sodium [22,74–77]. Methods to reduce the alkali content on biomass are under development, usually washing with water, or using dilute acid solutions, which may lead to hydrolysis of cellulose and hemicellulose and the diminishing of liquid yields after reaction [20,77,78].

Evans and Milne [79] propose an overarching mechanism (Figure 2.10), which considers three pyrolysis phases for long-lasting residence times, and discuss the polymerization of primary products into soot at high temperatures (900 °C), as well as the degradation of isolated lignocellulosic fractions and conclude that the presence of polysugars catalyzes the release of monolignols from the material. Carrier et al. [80] classify as ‘primary pyrolysis products’ those which result from the fragmentation and shrinkage of particles (residence time < 1 s). If retained in the hot zone, these products undergo secondary pyrolysis, characterized by intra- and inter-particle reactions between solids (unconverted biomass or char, especially its inorganic content) and liquid and/or gas, resulting in secondary char and low molecular weight volatiles.

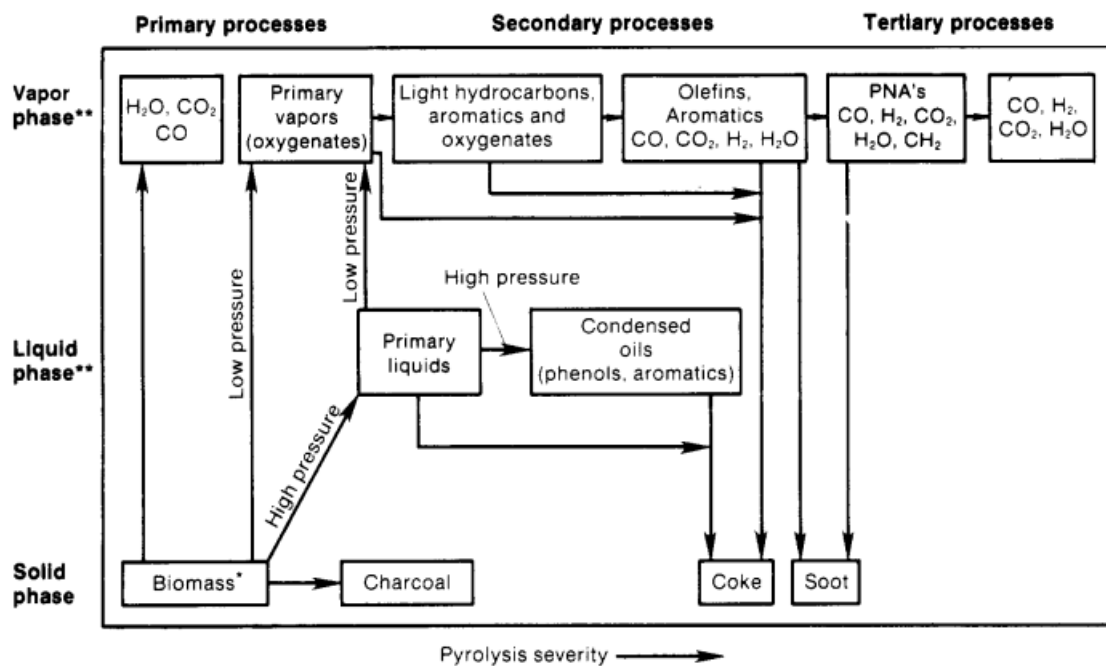


Figure 2.10: Intra- and extra-particle mass and heat transport events. Source: [79].

Py-GC/MS is an analytical process in which a small sample is pyrolyzed under an inert sweeping gas atmosphere which happens upstream of a conventional GC/MS system, presenting the obvious advantage that condensates need not be collected and analyzed, thus avoiding secondary pyrolysis and possible aging phenomena. Carrier et al. [80] employ this technique to shed light on the composition of the products obtained using isolated lignocellulosic fractions versus artificial mixtures and raw biomass. The authors refer to several situations in which the presence of other fractions changed the product distribution (e.g., formation of acetic anhydride), as well as the opposite phenomenon (e.g., heptanal from cellulose does not occur in mixtures), and comment on the high heterogeneity of hemicelluloses in grasses.

Ranzi et al. [81] also consider the gasification of char as a relevant phenomenon taking place during pyrolysis, albeit to a low extent. This can even be extended to include phenomena such as the Boudouard and Water-Gas-Shift (both direct and reverse) reactions, the combustion of hydrogen and methane, and the Sabatier reaction [82,83]. However, the latter reaction is only characterized over group VIII metals (Fe, Ru, Os, Hs), which are not present in appreciable quantities in most lignocellulosic biomasses.

Cellulose

Cellulose is a polysaccharide whose isolation from the lignocellulosic matrix is a widely used and industrially optimized process. Thus, it is no surprise that this material has been the focus of several studies proceeding by far with the other fractions. Mechanisms for the pyrolysis of cellulose based on TGA have been developed at least since the 1970s, such as that by Broido and Shafizadeh [84], featuring an activation step that forms an unstable intermediate, leading to depolymerization and scission reactions forming condensable vapors and heavy tars, as well as char and gases. Diebold et al. [85] reported that, during activation, water and char are formed.

Both Lin et al. [86] and Carrier et al. [80] discuss a more modern approach to these methodologies and consider a first step of intramolecular rearrangement, the activation, followed by successive β -scission until reaching monomeric sugars which dehydrate to yield levoglucosan. Long residence times increase the yield of other anhydrosugars (Figure 2.11), which ring fragmentation phenomena produce hydroxyacetaldehyde and hydroxymethylfurfural as major products, as well as small oxygenates, char, and gases.

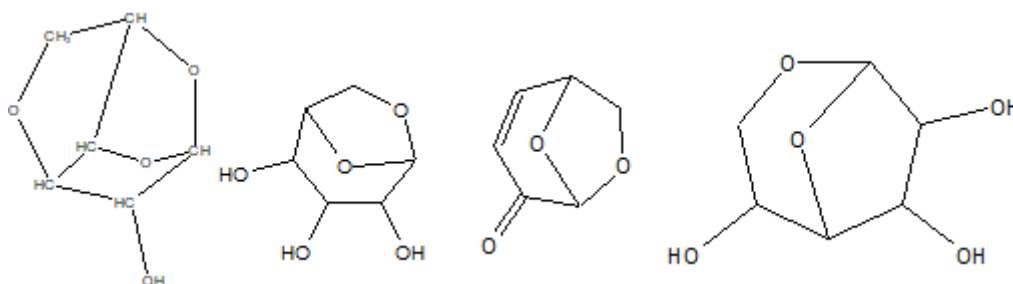


Figure 2.11: Several anhydrosugars, as reported by Lin et al. [86].

Hemicellulose

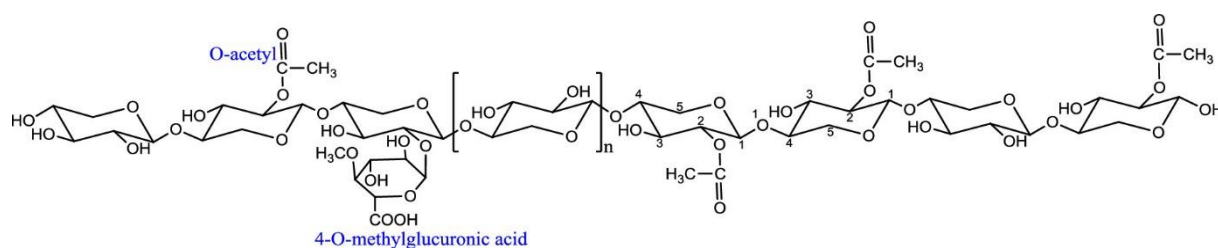


Figure 2.12: Chemical structure for hemicellulose extracted from beechwood. Source: [87].

Hemicellulose is often extracted from the lignocellulosic matrix using alkaline hydrolysis, with a yield of up to 72 wt.% of the original hemicellulose (from partially delignified feedstock) [89]. Both Carrier et al. [80] and Farhat et al. [89] mention the importance of correctly characterizing hemicelluloses, due to the noticeable range of monomer distribution between different plant feedstocks, and the subsequent degradation pathways they follow during pyrolysis. Debiagi [90] considers hemicellulose activation as dependent on this phenomenon, providing different yields of products depending on the nature of the biomass, contrasting glucuroxylan-rich with arabinoxylan-rich hemicelluloses.

Carrier et al. [80] resume the process into three phases: depolymerization of the xylan structure (Figure 2.12) by the breakdown of the glycosidic bond, followed by the production of anhydrosugars and pyrans by rearrangement of the monomers, which themselves degrade into light oxygenates, like carboxylic acids, aldehydes, and furans. Peng and Wu [91] report CO₂, 1-hydroxy-2-propanone, and acetic acid as the majority products of Py-GC/MS at 500 °C, followed by furfural, pentanal, and several cyclopentanediones.

Lignin

Lignin in plant matter is synthesized by radical-driven polymerization of p-coumaryl, coniferyl, and sinapyl alcohols. Due to the unpredictability of radical mechanisms, the obtained molecular structure is cross-linked and irregular, containing several different linkages, of which the phenylpropane β-aryl-ether (β-O-4) bond is the most common [88,92], and other relevant inter-subunit linkages are shown in Table 2.3.

Table 2.3: Types and frequencies (%) of inter-subunit linkages in softwood and hardwood lignin. Source: [88].

Linkage	Softwood lignin	Hardwood lignin
β-O-4	49–51	65
α-O-4	6–8	–
β-5	9–15	6
β-1	2	15
5–5'	10	2
4-O-5	3	2
β-β	2	6

Given the intrinsic heterogeneity of lignin as a polymer, degradation processes are expected to yield a heterogeneous mixture of oxygenated high molecular-weight aromatics, which themselves contain much of the functional groups found in the native pyrolysis [88,92]. The formation of these products seems to stem from the dissociation of the weakest linkages in the biopolymer (β-O-4, α-O-4). Other bonds (Table 2.3) are typically too strong to be broken at pyrolysis temperatures, and form oligomers of low vapor pressure that do not tend to volatilize [92].

Several surrogates have been developed to model the degradation behavior of lignin, often only employing the β -O-4 bond, a fact criticized by Houston and Abdoulmoumine [93]. More complex surrogates have been reported in the literature, such as the one proposed by Quideau and Ralph [94] (Figure 2.13), which presents several types of relevant lignin linkages, such as the β -O-4 (red), α -O-4 (blue), and phenylcoumaran (α -O-4 + β -5, green). The authors reported that ether bonds are the most labile moieties (tendency of bond dissociation: β -5 < α -O-4 < β -O-4). Carrier et al. [80] brought attention to the production of bilignols during pyrolysis, connected by a resistant 5–5' biphenyl bond, and the presence of side chains in biomass lignin that degrade into light carboxylic acids.

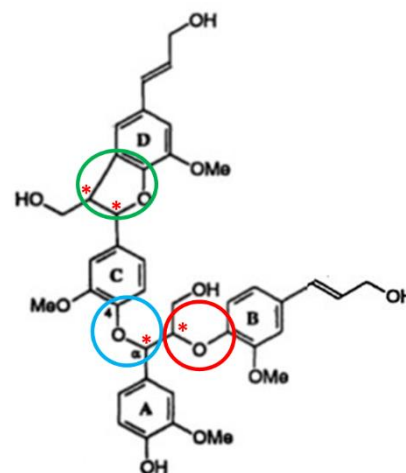


Figure 2.13: Structure of initial lignin model tetramer. Source: [93]

Robichaud et al. [92] remark that the difficulty in determining the cracking mechanism for lignin pyrolysis is related to the presence of multiple functional groups and the general difficulty of identifying products and intermediaries, as these are often unstable species, such as free radicals. Faravelli et al. [95] proposed a radical mechanism to describe the pyrolysis of lignin, featuring seven representative monomers and a long list of intermediate radical compounds, as well as initiation, propagation, and termination reactions.

Ranzi et al. [96] devised a non-radicular reaction scheme that represents the entirety of lignin using three monomers (Figure 2.14), which degrade simultaneously but non-competitively. The authors discuss methodologies to estimate the proportion of these monomers based on the H/G/S (hydroxyphenyl (H), guaiacyl (G), and syringyl (S)) ratio of the feedstock [97] or using error minimization estimation methods relying on the elemental composition of the biomass [4].

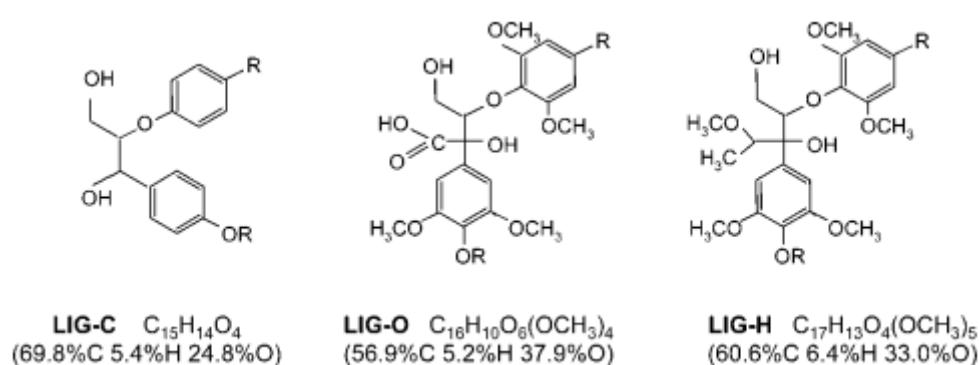


Figure 2.14: Schematic structures of lignin surrogates. Source: [96].

The valorization of lignin is currently underachieved, as the material is mostly used for its bulk heating value, despite the high-value potential of its degradation products. Several strategies making use of catalytic depolymerization and deoxygenation, as well as *organosolv* lignin processing or co-pyrolysis, have had mixed success, but have not made it to the commercial state. [88,98]

Secondary pyrolysis

Secondary pyrolysis reactions occur every time primary pyrolysis products are held in the reaction zone after production; this phenomenon is impossible to prevent intra-particle, but inter-particle phenomena can be mitigated by maintaining low residence times in the reactor [80]. The presence of solid material, especially alkali-containing ashes, catalyzes thermal cracking and hydrogen abstraction reactions. Montoya et al. [99] considered the explicitation of secondary pyrolysis as vital, as well as the presence of typical gasification (water-gas-shift, Boudouard, Sabatier) phenomena, for the correct modeling of the final gas composition.

Due to its role as a primary product of cellulose pyrolysis [86,100], levoglucosan is an important component of pyrolysis oils and its degradation is of utmost importance when modeling secondary biomass pyrolysis. Relevant products of the pyrolysis of levoglucosan include hydroxymethylfurfural (HMF), glycol aldehyde (HHA \equiv hydroxyacetaldehyde), acetol, formic and acetic acids, acetaldehyde, water, and carbon monoxide [101–104]. HMF is known to decompose to furfural and methylfurfural under pyrolysis conditions [105], the latter of which degrades easily into 2-methyl-2-cyclopenten-1-one [106]. Furfural itself may decompose to form vinylketene [107], or decarboxylize into furan (unstable) [108].

Xylose, the primary product of hemicellulose decomposition, degrades to furfural (via the aforementioned HMF-pathway), acetic acid, and water, as well as CO and CO₂. [109–111].

Secondary lignin degradation usually leads to the formation of phenolic components, including phenol, as well as, mono- and dimethoxyphenols, and substituted derivatives [112,113]. Herman-Ware et al. [114] pyrolyzed sinapyl aldehyde and p-coumaryl alcohol, common intermediates of lignin pyrolysis, as surrogates to emulate the primary pyrolysis of lignin. The former was found to degrade mostly into syringol (~80 wt.%), while the latter degrades mostly to guaiacol (71.4 wt.%) and vanillin (8.1 wt.%).

Robichaud et al. [92] studied the degradation of several lignin model compounds and compared it to density functional theory (DFT) estimations, intending to assess the competitiveness of unimolecular pathways. The authors use the bond dissociation energy (Figure 2.15) as a measure of the likelihood of bond dissociation radical mechanisms playing a relevant role in the pyrolysis of a species. Ether bonds in molecules like anisole or (di-)methoxyphenols dissociate easily, while phenol most likely undergoes tautomerization, leading to cyclopentadienes.

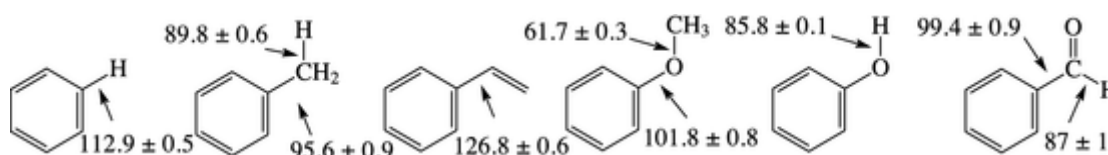


Figure 2.15: Selected bond dissociation energies for typical bonds found in lignin pyrolysis products. Values in kcal/mol. Source: [92].

Ranzi et al. [96,115] proposed a series of secondary gas-phase reactions, dividing them into initiation (25 reactions) and hydrogen abstraction reactions (33 reactions), using kinetic modeling to determine critical pathways (CHEMKIN software). The former group is completely characterized, while the latter provides no kinetic

parameters, but rather the type of abstracting radical and the type of the H to be abstracted. Kinetic modeling and determination of critical pathways were employed by Debiagi et al. [81] to model vapor phase dehydration of glycerol and hydroxypropanal, decarboxylation of phenolics, and reactions of substituted benzenes to produce polyaromatics; and in a different publication the pyrolysis of levoglucosan, glyoxal, and HMF [116].

Aging reactions

As stated before, pyrolysis condensates are inherently unstable due to high oxygen content and pH, and tend to change their composition over time, a fact which is exacerbated by the presence of char/ash in stored material [77,117]. Cai et al. [118] compiled a review on the aging of pyrolysis bio-oils and possible strategies to increase stability, including esterification, filtration, distillation or emulsification. Oasmaa et al. [119] consider the evaporation of water and light organics to be a relevant contributor to the increasing viscosity of bio-oils over time, while others [117,120,121] consider that contact with air may promote oxidation of alcohols and aldehydes, as well as generate radicals which increase the polymerization of olefins. The low pH observed in most pyrolysis condensates exacerbates the reactivity of acids, aldehydes and furans, promoting phenomena like self-condensation, esterification, aldol condensation, and phenol-aldehyde resination [117,118,122,123], which contribute to the presence of high molecular residua.

In Figure 2.16 one can observe the effect of the analysis method and the timespan between gathering and analysis. While differences in GC/MS results can be expected for duplicates, or even between trials employing the same experimental conditions, a clear trend can be observed between the immediate analysis of the vapors and that of a stored condensate. Organic acids are expected to be largely stable in homogeneous secondary pyrolysis reactions and are also expected to be formed by these same reactions, explaining the increased yield. At the same time, aldehydes and pyrans, as well as furans, guaiacols, and syringols are known to be readily degraded at pyrolysis temperatures, hence the considerable diminution in yield when comparing the two methods [124].

Several authors studied the aging of bio-oils either by storing them over long periods or keeping the oil at high temperatures [77,125]. Black and Ferrell [125] correlated keeping the material at 80 °C during different periods with the change in carbonyl content and viscosity observed during room temperature storage over months and proposed the use of exponential decay models to estimate viscosity or molecular weight of pyrolysis condensates over time.

Banks et al. [77] raised attention to the catalytic effects of emulsified solids containing phosphorous or potassium. Gupta et al. [126] discussed polymerization phenomena that occur even at room temperature, which increase the viscosity of the condensate over time.

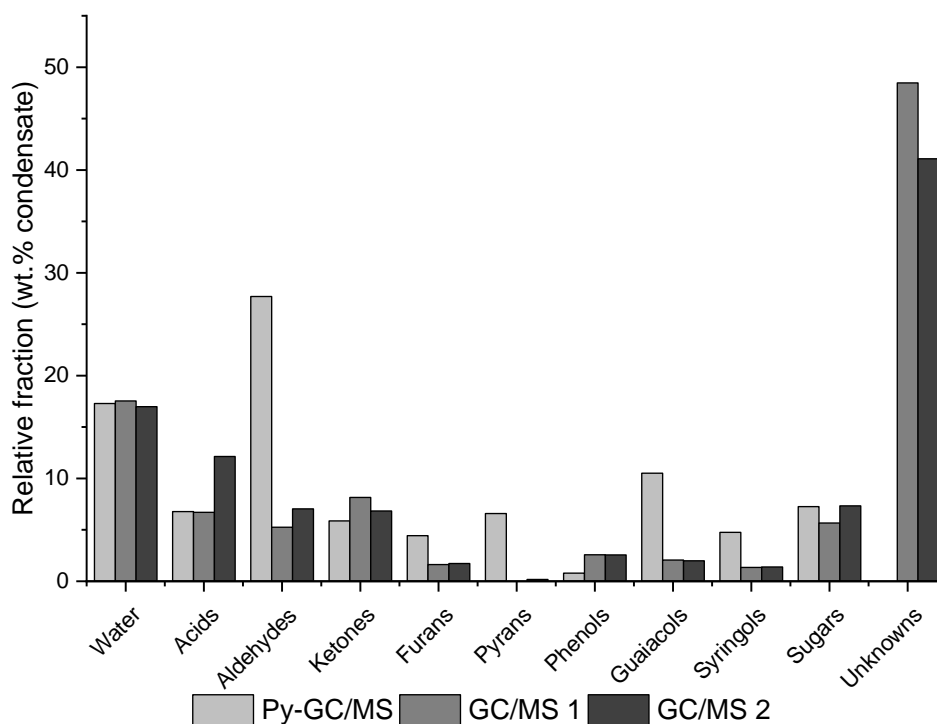


Figure 2.16: Comparison of Py-GC/MS and conventional GC-MS separated by several months. Results were normalized to account for the presence of water and non-detectable heavy compounds. Unknowns are absent from the Py-GC/MS results due to the limitations of the method. Based on results associated with [127].

2.2.2. Reaction networks

As soon as degradation pathways started being considered and explicated, lumped reaction networks that attempt to model the pyrolysis of plant biomasses were developed, with a focus on not only devising pathways but providing kinetic parameters [99,128]. Multicomponent models have been compared to single-component models in their ability to predict the degradation of biomasses and product distribution, and have been found to lead to better estimations, thus enabling the development of reaction networks [129]. However, identifying chemical reactions based on the conversion of model compounds often leads to oversimplified degradation schemes [80].

Ranzi et al. [96] was published in 2008 and is the predecessor to the majority of the reaction networks designed to model the pyrolysis of lignocellulosic biomasses. The model was originally designed to model tar formation during gasification and computes together pyrolysis models of the different lignocellulosic components while employing TGA curve-fitting to estimate kinetic parameters. The authors provide kinetic parameters for all stages on the purposed reaction path of degradation of each component. The model employs 19 bio-oil representatives, char, and several gases, and features 26 primary reactions, as well as 3 delayed volatilization phenomena.

The model was revised by Corbetta et al. [130], Ranzi et al. [131], Trendewicz et al. [132], and most recently by Ranzi et al. [81,133]. The latter publications introduced the effect of different hemicellulose compositions, contrasting the degradation of arabinoxylan-rich materials with that of galactomannan-rich ones, slightly

affecting the downstream reaction network, but not the kinetic parameters. Debiagi et al. [90] further extend the hemicellulose composition contrast, introducing cereal hemicelluloses, as well as considering the presence of extractives and triglycerides, providing surrogate molecular structures and kinetic parameters for their degradation.

Anca-Couce and Scharler [134,135] built upon Ranzi's [96] work, by considering the revision by Corbetta et al. [136] and introducing charring conditions, which affect the product distribution directly, but not kinetic parameters, while featuring 8 delayed volatilization reactions. The authors affirm that the model can better describe the heat evolution of TGA experimental results than the predecessors, as well as the behavior of the degradation of a single biomass particle.

It is important to keep in mind that these models do not take into account the catalytic effect of alkali metals within the ash, which are known to reduce oil yields and alter product composition [5,129].

2.2.3. Effect of particle size on thermal degradation

As mentioned in section 2.1.4, various types of pyrolysis reactors have been developed, in which design and optimization require an understanding of the reactions and transport phenomena involved during the degradation of the solid particles. One area of direct impact that still requires further research is the effect of particle shape and size on product distribution. [137]

It has been reported several times that setups using small dimension particles and low vapor residence times lead to high bio-oil yields, by mitigating secondary reactions [20,138–140]. Mechanical particle size reduction has been found to lead to high oil yields due to the disruption of the internal particle structure [141,142]. Zhou et al. [143] studied the effect of particle size on the removal of water-insoluble condensates and the nature of monolignols formed; the authors indicate that larger particles produce oils with a lower content in guaiacols and syringols, and propose a mechanism in which oil jets contact other sections of the cell wall and lead to a higher formation of char, due to higher heat transfer limitations.

An important factor that determines product distribution is the residence time of the product volatiles amidst the reacting particle before they leave the reacting particle by vaporization/sublimation or physical entrainment (aerosols) [141,144,145]. Teixeira et al. [146] employed a fast-speed camera to prove that the collapse of a bubble of liquid intermediates is the main mechanism in the formation of jets, which break down to form aerosols. Westerhof et al. [137] discussed the influence of the type of vapor flow stemming from the pyrolyzing particle, comparing isotropic and anisotropic flows, and revealed that the release of vapor in larger particles is mostly independent of microstructure. Haas et al. [145] have performed real-time microscopic analysis of pyrolysis of single particles of poplar wood, where liquid droplets of partially depolymerized material were formed throughout the heating process, which stem mostly from the lignin-rich section of the wood material, and cross-link into chars if trapped within the particle.

The heating rate of the biomass particles is of utmost importance for the pyrolysis process, impacting process control, product yields, and product quality [137,138,147–149]. Kersten et al. [147] affirm that individual particle decomposition is controlled by external heat transfer and thermal diffusivity for wood particles larger than 1 mm, where this decomposition takes place very close to the reactor temperature for smaller particles, being, therefore, kinetics driven, an opinion shared with other authors [150–153]. Funazukuri et al. [154] estimate a heat transfer rate of ~ 100000 K/s for cellulose particles of 0.06 mm vs ~ 1000 K/min for 0.6 mm, using microfluidized bed flash pyrolysis.

2.2.4. Effect of the inorganic content of feedstock on thermal degradation

The main inorganic components in lignocellulosic biomass are usually silicon, calcium, potassium, sodium, and magnesium, occurring in the form of oxides, carbonates, sulfates, chlorides, and phosphates [155]. It has been noted that the inorganic content is not distributed evenly during the mechanical size reduction of the particles, with finer sieves presenting a higher average ash content and a different thermal degradation behavior [156,157].

Although silica is the highest inorganic component of grasses, potassium is of particular interest due to its reported catalytic effect during biomass pyrolysis [77,155,158,159]. Potassium in biomass can be mostly found in the form of inorganic salts, like KCl, K_2SO_4 , and K_2CO_3 , and is released from the matrix as KCl or K_2O [160]. Christensen et al. [161] claim that on average only 18% of the potassium in the feedstock is volatilized during combustion and that the amount of potassium retained in the ash phase is intensified by a rising fraction of silica in the material, due to interactions between these elements.

Several authors report that higher levels of alkali metals in the feedstock lead to the amorphization of the cellulosic matrix, a decreased rate of volatilization, and a delay in degradation temperature, promoting the formation of gas and char [74,77,155,162–164], although the effect is not even between the different lignocellulosic fractions and surrogate compounds [165,166]. Potassium-treated feedstocks present lower apparent activation energies for hemicellulose [167], cellulose [158,168], and wood [169] compared to non-treated feedstocks, indicating a more aromatic and complex solid structure.

The high levels of alkali metals on chars were found to contribute more to their reactivity than the surface area, as they catalyzed the oxidation of fixed carbon in the char [170]. Ion presence in ash also promotes the degradation of relevant components of the bio-oil, with different degrees of intensity (effect of cations: $K^+ > Na^+ > Ca^{2+} > Mg^{2+}$, effect of anions: $Cl^- > NO_3^- \approx OH^- > CO_3^{2-} > PO_4^{3-}$) [100,171].

Removal of ash content is possible using several methods, including acid/alkaline pretreatment, ozonolysis, fiber explosion, microwaving, and ionic liquids, all of which require downstream processing of corrosive or acid effluents [172]. Singh et al. [172] propose hot water to promote depolymerization of the lignocellulosic matrix and removal of ash content, but Hu et al. [173] refer to the lower effectiveness of this method compared to acid washing.

Trendewicz et al. [158] modified the cellulose part of the degradation network proposed by Ranzi et al. [131] to consider the effect of potassium, by adjusting the energy of activation to the mass fraction of this component, illustrated in Figure 2.17. Higher potassium concentrations, such as the ones found in wheat straw, lead to a lower energy of activation, hence a faster degradation speed and deviation to a lower temperature, a result consistent with the degradation of wheat straw when compared to beech wood, standard biomass [165,174,175].

It is, to this date, difficult to quantify precisely the effect of inorganics on the extent of secondary pyrolysis. Peters et al. [4] implemented linear regression models based on experimental results to estimate the char fraction due to polymerization as a function of the alkali content on the biomass and the residence time on the reactor, the water content on the condensates as a function of the alkali content on the biomass, and the gas fraction as a function of the process temperature and the residence time. This method, albeit of easy implementation, disregards the nature of the reactions happening during secondary pyrolysis and the composition of the bio-oil, as it only varies the water content and the phase distribution.

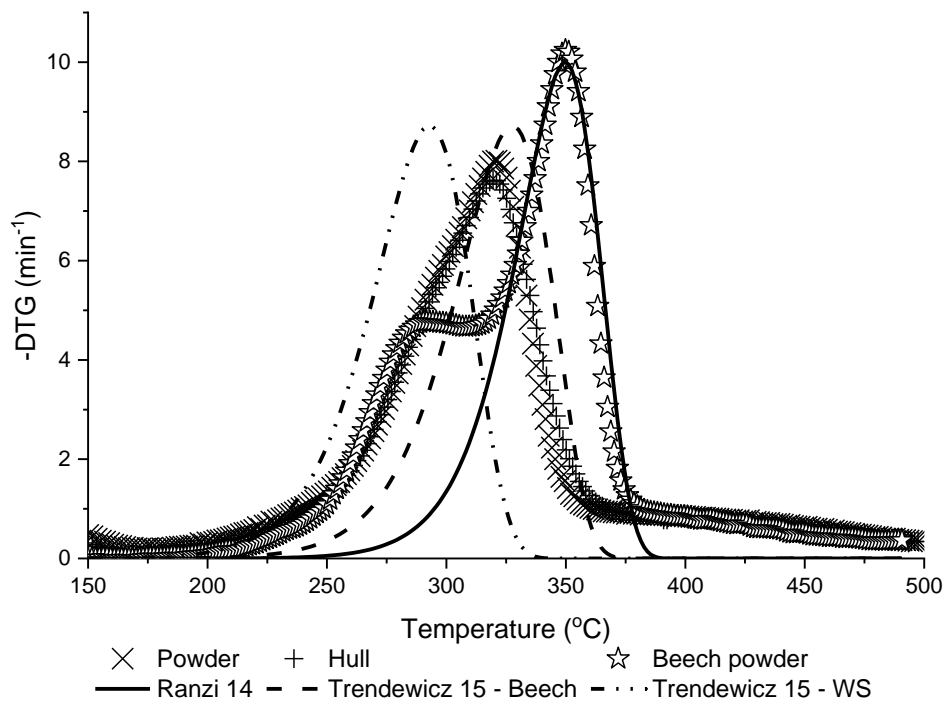


Figure 2.17: Overlaying of the degradation speed profiles of three reaction sets ([131,158]) against the DTG profiles of both wheat straw and beech wood. Ranzi 14 represents a standard reaction network, whereas Trendewicz 15 represents reaction networks that account for potassium content (Beech: 0.13 wt.%, WS: 1.18 wt.%). Based on data associated with [175].

2.2.5. Thermogravimetry for lignocellulosic content determination

Thermogravimetric analysis (TGA) operates by weighing the mass variation of a small solid sample upon controlled temperature profiles, as well as sweeping flow and composition. This method is often employed to study the decomposition of solid materials and permits the dynamic or isothermal study of phenomena such as combustion or pyrolysis [157]. Standards for analysis of volatile, water, extractive, and ash content in biomass samples make extensive use of TGA.

The degradation behavior of the major components of biomass, the so-called lignocellulosic pseudo-components, can be extrapolated to that of the original feedstock, and in Eq. (2-3) an example is shown which estimates the behavior of biomass as a weighted sum of the behavior of the constituents [176,177]. However, in the raw material, these pseudo-components are bound in a structural matrix, meaning that interactions between phases contribute to material properties and degradation behavior in a way the isolated fractions do not [178,179]. As the isolation of the different fractions is a costly process, conventional determination methods are ultimately inaccurate [180,181].

$$[\text{Biomass}] = a[\text{Cellulose}] + b[\text{Hemicellulose}] + c[\text{Lignin}] \quad (2-3)$$

Despite the inaccuracy of indirect lignocellulosic estimation methods, TGA offers a reliable, simple, and cheap method to achieve the desired data [163,175,182,183]. Modern TGA devices come bundled with software that enables the tracking of the mass loss (TG curve), as well as the first (DTG curve) and second (DDTG curve) derivatives or this curve, to time or temperature.

TGA curves of lignocellulosic biomasses present stages of material loss interleaved by periods or negligible mass loss, which are observed as peaks/valleys in the DTG curve. The first stage around 100 °C corresponds to the vaporization of moisture and extractives, and the following ones are often associated with the thermal decomposition of lignocellulosic components. A final stage at high temperatures may correspond to the calcination of in-situ catalysts, especially in fixed-bed pyrolysis. [163,184]

The lignocellulosic mass loss stage appears as a series of peaks in the derivative curve, which correspond to different phases complex network of parallel competitive reactions, which are often assigned to different fractions of the biological matrix [185], within the range 220-500 °C, or even up to 900 °C if charring reactions are considered [69,186]. Frequently, DTG curves of lignocellulosic biomasses feature two DTG peaks in this phase [184], corresponding to hemicellulose-lignin and cellulose-lignin decompositions, which present different degrees of overlap, for example, minimal overlap in almond shells [157] and noticeable overlap in beech [183] and poplar woods [182] (known as a shoulder). However, other biomasses, including wheat straw, present a single 'holocellulosic' peak [163,187]. Local minima of the second derivative curve correspond to inflection points in the DTG curve and have been proposed by Gaitán-Álvarez et al. [188] to detect minor peaks in 'holocellulosic peak' situations. Fonseca et al. [175] employed it successfully to estimate the location of hemicellulose peaks in wheat

straw thermograms, and an example is shown in Figure 2.18. This method features an error proportional to the square of the step size ($O(h^2)$); a description of the mathematical proof can be found at [189].

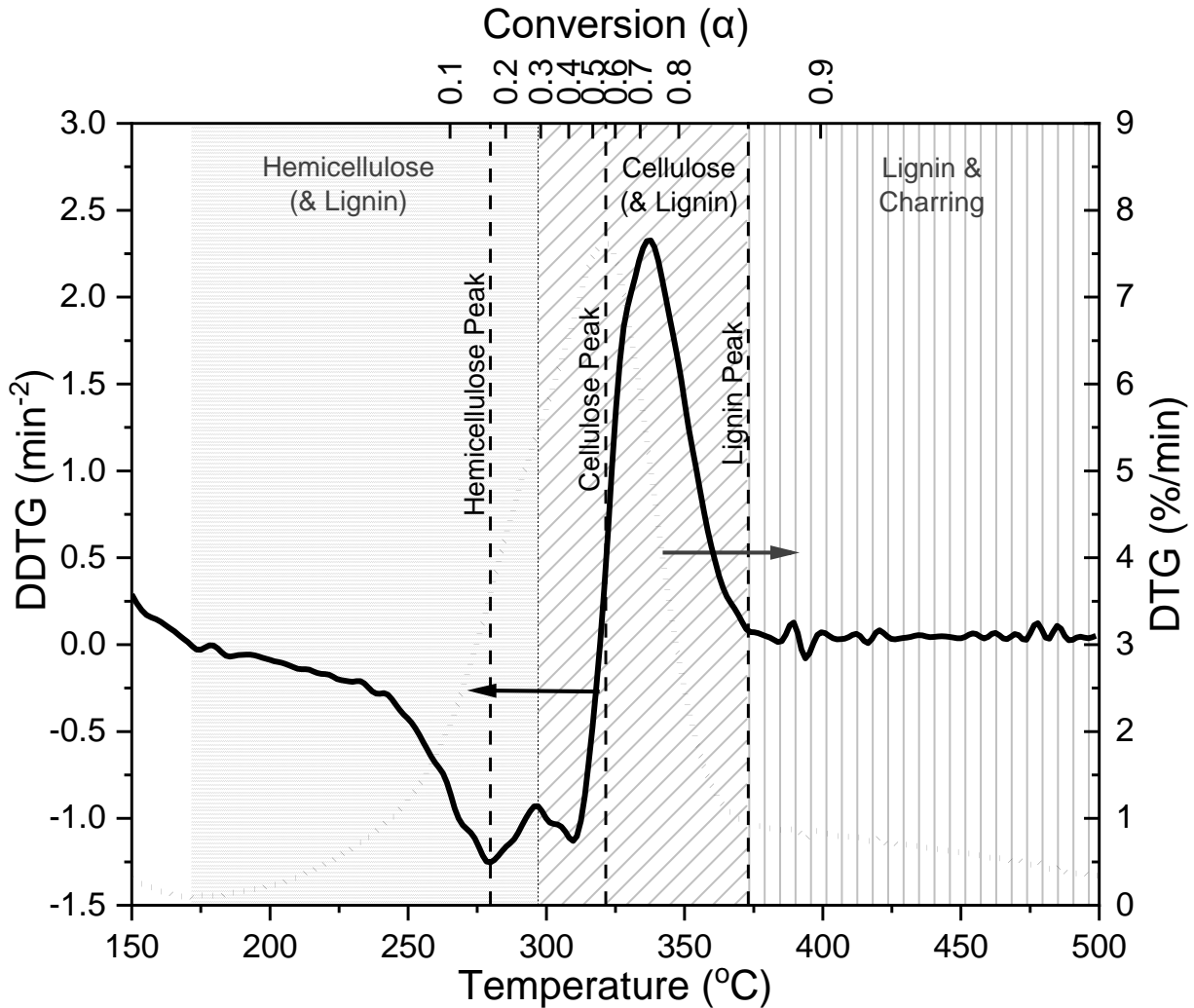


Figure 2.18: Use of the second derivative (DDTG, in black) inflection points to determine peak/transition points for the different pseudo-components (PC), based on the work by Gaitán-Alvarez et al. [188] and Wu et al. [184]. Example using wheat straw hull at $10 \text{ K}\cdot\text{min}^{-1}$, source [175].

Deconvolution methods, for which the experimental curve is expressed as a linear combination of individual curves, either sinusoidal approximations or Arrhenius curves, each of which is assumed to correspond to the isolated decomposition of each pseudo-component [69,175,190,191]. Area integration of the individual curves has also been previously used to estimate the relative fraction of these pseudo-components, i.e., estimate the lignocellulosic content in different biomasses [175,182,191–193].

Wu et al. [184] propose a division of the DTG curve into a series of ranges that divide the weight loss profile into regions, characterized by temperature/conversion pairs, but disregard the concurrence of degradation of different pseudo-components (Table 2.4). This method faults as well by considering the decomposition of lignin as occurring after the temperature at which the DTG curve flattens (transition between the active and passive pyrolysis zones), where exothermic charring reactions dominate [194] that may not be completely attributed to lignin degradation, but also secondary pyrolysis.

The validity of these deconvolution-based methods is contested, due to lack of accuracy. Maschio et al. [195] refer to the complexity of this kind of structure but consider its potential after hydrolysis to remove the hemicellulosic content. Caballero et al. [178] consider the heterogeneity of lignocellulosic materials as a major deterrent to generalizing results obtained using this kind of method; the authors mention features varying between samples of the same crop, such as age, growth factors, and soil characteristics.

Table 2.4: Relationship between the effective activation energies and reactions for pyrolysis. Indices and notation adapted from [70].

Conversion range	Temperature range	Reactions
$\alpha < \alpha_{p3}$	$T_0 - T_{p3}$	Decomposition of hemicellulose
$\alpha_{p2} \in [\alpha_0, \alpha_{p3}]$	T_{p2}	Peak of hemicellulose decomposition
$\alpha_{p3} < \alpha_{p5}$	$T_{p3} - T_{p5}$	Decomposition of cellulose
$\alpha_{p4} \in [\alpha_{p3}, \alpha_{p5}]$	T_{p5}	Peak of cellulose decomposition
$\alpha > \alpha_{p5}$	$T_{p5} - T_f$	Decomposition of lignin, and charring

2.2.6. Kinetics derived from dynamic thermogravimetry

State-of-the-art models of biomass thermal decomposition are often established as a complex set of concurrent reactions, which are approximated as reaction networks starting with the activation of the different pseudo-components [96]. Despite the low heating rates displayed by thermogravimetry when compared to the actual heating rates during fast pyrolysis, it is the most employed method for kinetic parameter determination [196]. White et al. [75] discuss TGA analysis of biomass, including experimental and data treatment methods, while Cai et al. [197] discuss the importance of mathematical consistency when estimating kinetic parameters.

Anca-Couce et al. [183] analyzed 17 publications employing different data treatment methodologies and lignocellulosic biomasses and reported a wide range of activation energies for each pseudo-component. A complication of literature data of kinetic parameters specific to the non-catalytic degradation of wheat straw is presented in Table 2.5. Vyazovkin [198] upholds that the effective activation energy of a lignocellulosic feedstock has the meaning of a collective parameter linked to the activation energies of the individual processes, which themselves involve a distribution of activation energies [199].

Relevant disadvantages of using TGA data for the determination of thermal decomposition kinetics lay in equipment limitations. The low heating rates achievable, already mentioned, mean that the kinetic parameters obtained this way may not be suitable for the modeling of a fast pyrolysis process. On the other hand, crucible size, sample morphology, and sweeping gas rate affect the heat/mass transport and may lead to situations of thermal lag [129,200]. Even when employing samples from the same batch and equipment, low sample sizes mean that natural heterogeneity may lead to low repeatability to these methods [129].

Thermal decomposition is an intrinsically heterogeneous process, as it concerns the incomplete volatilization of a solid material. Tracking of the decomposition over time/temperature is performed using the concept of mass conversion (α , Eq. (2-4), for which m_0 stands for the initial sample mass, m for the mass at the current temperature, and m_f for the residue mass after TGA) [197]. Molar composition could be performed if the molar mass of the solid was known.

$$\alpha = 1 - \frac{m_0 - m}{m_0 - m_f} \quad (2-4)$$

Table 2.5: Literature data of Arrhenius parameters for the non-catalytic degradation of wheat straw (WS). Source: [69].

Method	Temperature range (°C)	Heating rates (K·min ⁻¹)	E _a (kJ·mol ⁻¹)	log ₁₀ [A (s ⁻¹)]	Reference
KAS	α 0.10-0.70 a	1, 2.5, 5	214-353	19.1-32.8	[36]
FWO	α 0.10-0.70 a	1, 2.5, 5	215-347	19.2-32.3	[36]
Friedman	α 0.10-0.70 a	1, 2.5, 5	218-535	19.7-48.4	[36]
Curve Fitting	100-900	1, 2.5, 5	226.90	21.03	[36]
FWO	315-392	5, 10, 20	130-175	-	[37]
Kissinger	220-400	10, 20, 30, 40, 50	93.92	3.03	[38]
Coats-Redfern	198-338	30	115.59	11.97	[39]
Coats-Redfern	338-840	30	24.26	3.42	[39]
Coats-Redfern ^a	220-260	10	69	-	[10]
Coats-Redfern	251-347	20	8.81	-	[40]
Coats-Redfern (1st order model)	250-400	5	40.84	5.55	[41]
Coats-Redfern (3D diffusion model)	250-400	5	82.44	6.99	[41]
Coats-Redfern (Geometric contraction)	250-400	5	36.53	9.06	[41]
Coats-Redfern (Avrami-Erofe'ev)	250-400	5	15.73	5.53	[41]
Coats-Redfern (Power Law)	250-400	5	9.70	5.53	[41]
Modified Friedman	α 0.05-0.60 ^b	2.5, 5, 10, 20	154-176	-	[42]
Modified Friedman	α 0.60-0.85 ^b	2.5, 5, 10, 20	176-379	-	[42]
DAEM	177-527	40, 45, 50	236-382	2.95	[43]
Unrecognized ^c	215-315	20	98.98	-	[8]

a: Referred to by the authors as “linear regression method”

b: No temperature data has been provided, just the variation with the conversion.

c: Referred to by the authors as “based on Arrhenius equation”, based on Mureddu et al. [44].

Kinetic analysis of TGA makes use of fitting methods to match mathematical curves to the experimental data. Font et al. [29] and Caballero et al. [28], for example, employ non-Arrhenius multicomponent concurrent degradations; but the most common method employs Arrhenius curves (Eq. (2-5)), allowing the activation energy (E_a) and the pre-exponential factor (A) to be used as parameters when comparing results using different methods or feedstocks (Table 2.5). The position and shape of a curve are very sensitive to either of these parameters. When assuming multicomponent concurrent degradation, which employs pseudo-components representing the three lignocellulosic polymers: cellulose, hemicellulose, and lignin, simultaneous and non-competitive degradation is assumed (Eq. (2-6), c_i and α_i stand for the relative fraction and conversion of each pseudo-component i) [175].

$$\frac{d\alpha}{dt} = \sum_{i=1}^n c_i \frac{d\alpha_i}{dt} \quad (2-5)$$

$$\frac{d\alpha_i}{dt} = A_i \exp\left(\frac{E_{a,i}}{RT}\right) f(\alpha_i) \quad (2-6)$$

Šesták and Berggren [203] were able to define the conversion function ($f(\alpha_i)$) as being exclusively dependent on the momentaneous conversion of the material (Eq. (2-7)), for which the different exponents are dependent on the phenomena that conduct the reaction, but it is a common approach to assume $m=p=0$. The most common function assumes a first-order ($n=1$) dependence on the temperature Eq. [203], while Manyà et al. [204,205] reported improvements when modeling the degradation of lignin assuming $n=3$, and Anca-Couce [183,196] reports the lowest fitting error assuming the order is allowed to vary during fitting. Other functions devised to model the pyrolysis of biomasses include the contracting spheres ($f(\alpha) = 3(1 - \alpha)^{2/3}$) and three-halves order ($f(\alpha) = (1 - \alpha)^{3/2}$) models [206].

$$f(\alpha_i) = \alpha_i^m (1 - \alpha_i)^n [-\ln(1 - \alpha_i)]^p \quad (2-7)$$

The application of curve-fitting methods can be cumbersome; therefore, several methods have been developed to more easily estimate kinetic parameters from TGA data. Among these, isoconversional methods determine parameters using linear regression and are often employed due to their ease of applicability and comparable results [197,207,208]. Due to making use of data at different heating rates, it may be feasible to employ them at high heating rates for which kinetic determination is unpractical [175]. However, these methods base themselves on the assumption that the reaction speed is exclusively dependent on the temperature for a given conversion value and disregard the complexity of the material to any extent which does not affect any of those parameters [208,209].

It is common practice to employ a single constant heating rate, β , when performing TGA for kinetic determination, which can be stated to represent dT/dt . Hence, one can rewrite Eq. (2-6) as Eq. (2-8), assuming a single component. [209]

$$\frac{d\alpha}{dT} = \frac{A}{\beta} \exp\left(-\frac{E_a}{RT}\right) f(\alpha) \quad (2-8)$$

Which after variable separation and integration, can be integrated, from a null conversion and the starting temperature, as seen in Eq.(2-9) [209]:

$$\int_{\alpha=0}^{\alpha} \frac{1}{f(\alpha)} d\alpha = \int_{T=T_0}^T \frac{A}{\beta} \exp\left(-\frac{E_a}{RT_{\alpha,i}}\right) dT \quad (2-9)$$

The integral on the right side of Eq.(2-9) has no analytic solution. For the case of materials constituted by several substances, such as lignocellulosic biomasses, non-discriminatory methods analyze the kinetic model according to the conversion, regardless of the complexity of the reaction mechanism [208]. These methods base themselves on the assumption that the reaction speed depends only on the temperature for a given conversion value, therefore being known as isoconversional methods. A common representation of the methods is given in Eq. (2-10). [208,209]

$$\ln\left(\frac{\beta_i}{T_{\alpha,i}^B}\right) = -C \left(\frac{E_{a,\alpha}}{RT_{\alpha,i}}\right) + const. \quad (2-10)$$

Different authors have proposed different values for the parameters B and C, and different ways to estimate the pre-exponential factor from the y-intercept. The Flynn-Wall-Ozawa (FWO) method (Eq. (2-11)) assumes a value of B of 0 and C of 1.052, with $g(\alpha)=-\ln(1-\alpha)$, while the Kissinger-Akahira-Sunose (KAS) method (Eq. (2-12)) employs a B of 2 and C of 1 while reorganizing the y-intercept [208].

$$\ln(\beta_i) = -1.052 \left(\frac{E_{a,\alpha}}{RT_{\alpha,i}}\right) + \ln\left(\frac{A_{\alpha} E_{a,\alpha}}{g(\alpha) R}\right) - 5.331, g(\alpha) = -\ln(1 - \alpha) \quad (2-11)$$

$$\ln\left(\frac{\beta_i}{T_{\alpha,i}^2}\right) = -\frac{E_{a,\alpha}}{RT_{\alpha,i}} + \ln\left(\frac{A_{\alpha} R}{g(\alpha) E_{a,\alpha}}\right), g(\alpha) = -\ln(1 - \alpha) \quad (2-12)$$

A third method, the Friedmann differential method (Eq. (2-13)), is widely employed due to its simplicity and high accuracy [197,210]. While not being *per se* an isoconversional method, it is often lumped in together with these, due to a similar methodology.

$$\ln\left(\beta_i \left(\frac{d\alpha}{dT}\right)_{\alpha,i}\right) = -\frac{E_{a,\alpha}}{RT_{\alpha,i}} + \ln(A_{\alpha} f(\alpha)) \quad (2-13)$$

2.2.7. Principles of chemical reaction equilibrium and kinetics

As an example of a thermal chemical process, the core of any pyrolysis process is the reactor. In terms of process modeling, one can loosely divide reactor types into stoichiometric, kinetic, and equilibrium models. Flowsheeting simulation software, such as Aspen Plus™ provides the user with a repertoire of models that mostly follow the aforementioned three-fold division. It is also possible to define several types of reaction, including equilibrium and power-law models, and use them outside of a reactor unit block, but rather in the context of a rigorous distillation unit, for example.

Thermodynamics in the chemical context deals mostly with the tendency of products within a mixture to transform into reactants, allowing the prediction of the composition of the mixture at equilibrium, disregarding the mechanism of the reaction. Spontaneity, the measure of the viability of this change, can be predicted by making use of the Gibbs Free Energy (G) of a system. This Gibbs energy of reaction, $\Delta_r G$, can be interpreted as the difference in chemical potentials of the products and the reactants, which is dependent on the momentary composition of the mixture. A spontaneous reaction, $\Delta_r G < 0$, favors the conversion of the reactants, while a non-spontaneous reaction, $\Delta_r G > 0$, favors the reverse reaction. Both reactions proceed until $\Delta_r G = 0$, when equilibrium is achieved at a set temperature and pressure, in such a way that a small $\Delta_r G$ leads to a small conversion extent on the reaction [58]. Within Aspen Plus™, available equilibrium-based reactors include *RGibbs* and *REquil*, the latter employing stoichiometric equations, while the former employs the entire reacting system without defining reaction paths.

Another approach to chemical reaction is kinetics, which deals with the speed of a reaction, how fast products and reactants are consumed and produced, the response to the presence of a catalyst, and the identification of steps. Aspen Plus™ supplies three basic unit blocks which consider the use of kinetics: *RCSTR*, *RPlug*, and *RBatch* (the latter designed for dynamic operation).

It is also possible to define stoichiometric relations based on known fractional conversions or extents of reaction (*RStoic*), as well as *black-box* models, i.e., nonstoichiometric reactors based on user-inputted yield distribution (*RYield*).

2.2.8. Reaction modeling using process simulation software

Wooley and Putsche [211] discussed how to create a database for biomass products in Aspen Plus™, focused on the use of the substances for combustion or fermentation modeling, thus providing characterization for cellulose, hemicellulose, and lignin, as well as glucose and ash components, and provide some physical properties for these components. Visconti et al. [212] model the biomass as a non-conventional component, and employ a black box model paired with a FORTRAN routine split the feedstock into reference components before the reaction.

Ahmed et al. [213] compiled a review of kinetic and equilibrium concepts to aid in the rigorous modeling of gasification units. The tar phase is modeled as aromatics of increasing complexity. The authors compare the

use of equilibrium reactor models that assume complete conversion of the input, and that employ minimization of the Gibbs free energy of the system, with the use of kinetic models (*CSTR* or plug-flow) due to the accuracy of the results, and the possibility of using optimization to improve the predictions. The authors also discuss the use of FORTRAN subroutines to program complex issues and design specifications and the shortcomings associated with the use of ideal mixing models for kinetic-based simulations. Gupta et al. [214] refer to the limited ability of commercially available process simulation tools to model complex biomass matrices and discuss the simplicity of the equilibrium approach in modeling situations like the gasification of hemicellulose in the context of torrefaction, based on its sugar composition.

Gibbs energy minimization reactor models have been extensively used to simulate gasification [213], and have been adapted to model pyrolysis phenomena as well, due to the advantage of not requiring the input of reaction data, but only of the final possible products [212,215–220]. Neves et al. [221] did not obtain physically significant results using this type of reactor when modeling pyrolysis, which produced exclusively water and light volatiles, which were easily separated from the effluent downstream, while a kinetic reactor model predicted the occurrence of several organics and solids in a downstream condensate.

Models directly linking the feedstock with a product distribution have also been employed to model pyrolysis, either using stoichiometric relations [222] or black box models with the final product distribution [5,223,224]. Ward et al. [225] state that it is unfeasible to consider any other type of reactor simulation other than a black-box model to simulate processes that involve solid, liquid, and gas-phase components. However, black box models lack flexibility and are not predictive when considering changes in feedstock composition or operating conditions.

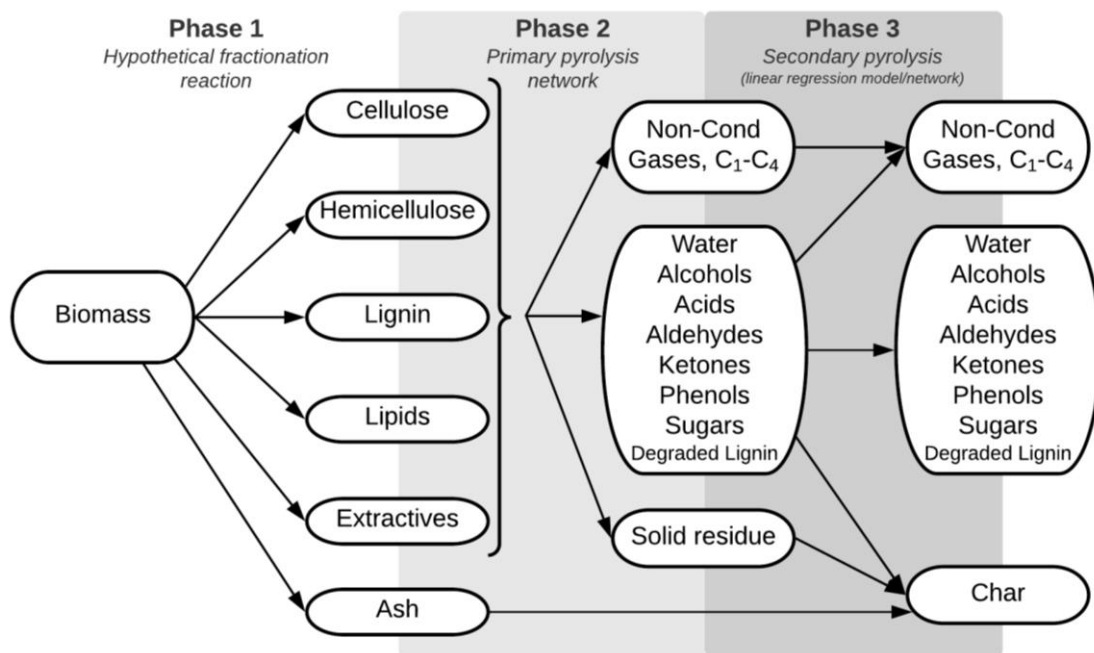


Figure 2.19: Three-stage reaction scheme for pyrolysis reactions. Adapted from [4] to include lipids and extractives.

Kinetic reactor models have also been adopted, often employing lumped reaction networks like those described in section 2.2.2 [4,129,226–231], as well as these models implementing biomass splits similar to that used by Visconti et al. [212]. Several authors also proposed pyrolysis kinetics derived from a mixture of sources [221,232,233] or based on the analysis of fixed-bed pyrolysis product streams over time [234,235]. Novel approaches go beyond current reactor model paradigms and focus on developing custom models to simulate situations involving transport, thermodynamic and reactive phenomena [129,227]; Demol et al. [236] modeled a pyrolysis process in Aspen Plus™ and coupled it with a kinetic modeling tool (CHEMKIN) for the simulation of the pyrolysis process

Secondary pyrolysis or aging phenomena are not often considered during the modeling of pyrolysis or are passively contemplated when using stoichiometric or black box modeling. Peters et al. [4,228,229] modeled primary and secondary pyrolysis phenomena within the same reactor unit (*CSTR*) and employed downstream a linear regression model to estimate the effect of ash and alkali contents in the biomass to adjust the product distribution of the phases, but not the identity of the compounds (Figure 2.19).

2.2.9. Summary of the section

In this chapter, several mechanisms that take part during pyrolysis, i.e., the concurrent degradation of the different lignocellulosic pseudo-components, as well as operational parameters which may lead to results outside of those obtained in lab scale tests using a small amount of powdered ash-free feedstock (particle size, potassium content). Thermogravimetry has been singled out as the main technique to study solid biomass degradation phenomena, mainly as its low-cost and ease of use make it ubiquitous in the field.

Making use of thermogravimetry and downstream analytics, several authors have been able to devise and characterize reaction pathways that convert ash-free lignocellulosic biomass into primary pyrolysis products; the reaction networks build on each other, but new versions do not necessarily lead to better fits to real biomass. The effect of ash has only been considered for cellulose and a narrow range of potassium contents. Secondary pyrolysis and aging phenomena have been reported, but the development of a secondary reaction network that bridges the products of the first network(s) and the experimental product is still missing.

Modeling of pyrolysis in the context of flowsheeting simulators is in great part rudimentary, mostly employing black-box reactors or equilibrium phenomena that favor the gas fraction. Nonetheless, several authors have been able to design predictive reactions, but not establish a state-of-the-art.

Thus, it is necessary to make a selection between different reaction networks published in the literature, as well as consider the ash content to the possible extent. Thermogravimetry can be used to predict lignocellulosic degradation kinetics, as well as provide a baseline to compare the behavior of the reaction networks. Process simulation focused on kinetic modeling implements the selected networks to evaluate product distribution.

2.3. Condensation systems

The yield and composition of recovered liquid fractions are dependent at first glance on the reaction conditions, including residence time, catalytic effects (e.g., alkali in ash, see section 2.2.4), and moisture content of the feedstock [237]. After exiting the reactor, the produced vapors must be quickly separated from any entrained solids and cooled down rapidly to hamper the further occurrence of secondary reactions. In an industrial setting, rapid cooling of the vapors is achieved using quenching systems (showering hot vapors with a relatively cool liquid in great excess), and/or electrostatic precipitators to promote aggregation of liquid droplets, especially relevant at higher gas flow rates [238].

Fractionated condensation strategies, including condensers in series [63,239,240], multistage vapor quenching, cold traps at low temperatures [241], and manipulation of the sweeping flow rate inside the condensation vessels [5,242], can be employed to enhance the recovery of target components or control the flow and composition of different liquid phases.

2.3.1. Thermodynamic models

Thermodynamic models include those which describe the properties of a system and include equations of state (EoS), equilibrium equations, and associated models which help model the system properly, including heat of mixing, activity coefficients in the liquid phase, association in liquid and vapor phases, solvation, hydrogen bonding, Van der Waals forces, and Poynting effect.

The decision of which of these to use during the modeling of a process is paramount for the correct modeling of the phenomena taking place. Process simulators, for example, include ‘property methods’ which are essentially pre-built packages of models that are known to work well together, and are often customizable. Aspen Plus™ includes a great variety of property methods, many of which cater specifically to certain processes, like amines, steam production, pyrometallurgical processes, and polymers, among others. For chemical processes that involve neither of these specifications, the simulator provides several property methods developed for organic compounds that do not fit into any specific categories. It is possible to isolate certain parts of the system within sections, allowing these to be modeled using different property methods.

All thermodynamic methods, apart from ideal gas behavior and Raoult’s law, require the definition of extra properties including critical point properties (temperature, pressure, volume, diameter, compression factor) for cubic and vapor-phase association EoS methods, binary interaction parameters in both phases (calculated from experimental data, and available in several databases⁷) for several EoS and activity coefficient methods.

⁷ It is possible to estimate binary interaction parameters using UNIFAC group contribution distributions for the NRTL, UNIQUAC, Wilson and Soave-RK models, and Huron-Vidal and Wong-Sandler EoS mixing rules.

Several methods have been designed for the estimation of these properties whenever experimental data is absent, which are explored by more depth in section 4.1.5.

Most equation-of-state methods can predict the behavior of liquid phases using similar equations, but they are often disregarded due to misestimating several properties [243]. Carlson [244] recommends the use of liquid-phase activity coefficient models (e.g., variants of NRTL, UNIQUAC, UNIFAC, Wilson) for systems operating at near-atmospheric conditions, mild temperatures, and rich with non-electrolytic polar substances, like pyrolysis oil condensation systems. The author does not advise the use of EoS models (e.g., variations of Redlich-Kwong or Peng-Robinson) at low pressures and low temperatures, such as those found during pyrolysis product recovery. Specific to pyrolysis oils and common components thereof, existent methods have been developed by estimating binary parameters or developing new structural groups for group contribution methods, of which several are presented in Table 2.6.

Table 2.6: Development of existent methods for surrogate mixtures of pyrolysis oils.

Reference	Process	Vapor-phase Method	Liquid-phase Method	Development
Li et al. [245]	Extraction of anisole and guaiacol using butyl acetate	SRK EoS without binary association	NRTL, UNIQUAC, and Wilson	Binary interaction parameters for NRTL, UNIQUAC, and Wilson equations; Proposal of a new UNIFAC-DMD group: aromatic methoxyl.
Ille et al. [246]	Multiphase modeling of FPBO	GCA-EoS	GCA-EoS	Association parameters for aromatic methoxyl and hydroxyl groups.
Sánchez et al. [247]	Multiphase modeling of FPBO	GCA-EoS	GCA-EoS	Parameters for phenol ethers.

A variety of thermodynamic methods have been applied by different authors to model LVE for FPBO processing. A non-extensive list is presented in Table 2.7.

2.3.2. Modeling of condensation systems

Stark [258] studied the process of condensation of a hot pyrolysis vapor within a vessel, from reaction conditions to room temperature, while varying the fraction of non-condensables in the cooling mixture. The author divides the condensation process of a hot pyrolysis vapor into three phases, including an intermediate phase (120 °C-240 °C) where the condensation of heavy species is mostly concluded, but that of lighter species is not dominant.

The author also studied the impact of the non-condensable (NC) intake in the composition of the obtained composition. An example is shown in Figure 2.20, for the water fraction; a higher NC intake would promote easier water content control, but a lower water content in the condensate (thus a higher viscosity) and a larger vessel size. [258]

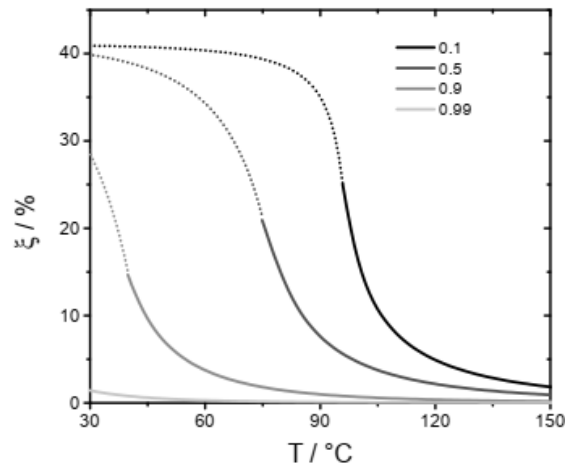


Figure 2.20: Mass water content in the condensate as a function of the temperature and the molar fraction of non-condensable compounds in the input mixture.

Source: [258].

Westerhof et al. [259] assert that the equilibria stages for the pyrolysis process, such as condensers, can be represented by simple flash distillation models, and places the focus on defining adequate surrogate mixtures.

Aspen Plus™, with its focus on conventional chemical project simulation, features a large range of unit blocks suitable for liquid-vapor equilibrium simulations. Categorized under “Separators” are flash distillation unit blocks for LVE (*Flash2*) or LLVE (*Flash3*) systems, at fixed operating conditions (temperature, heat duty, or vapor fraction). Column blocks permit recovering streams of different temperatures and include shortcut models permitting the easy first-step design of a distillation column as long as desired recoveries and key products are defined (variants of the Fenske equation [260]); as well as the rigorous multipurpose *RadFrac*, in which condensers and reboilers are removable, filling and side streams are specifiable, and can simulate reactive distillation.

The modeling of a flash unit implies the choice of two between four operational parameters: temperature, pressure, vapor fraction, and heat duty. A simple flash often operates at a defined temperature and pressure [5], while employing a temperature adjusting unit followed by a flash [212,215,217,222,255] allows for the easier estimation of heat flows or requirements, by defining the selected temperature in one block and operating the flash defining the intended heat flows (or even adiabatic operation). Rigorous separation has also been successfully applied in the context of pyrolysis modeling, although no specifications of the model are provided [223].

Table 2.7: List of thermodynamic methods used during vapor-liquid modeling of biomass pyrolysis or downstream bio-oil processing.

Reference	Process	Vapor-phase Method	Liquid-phase Method	Reference	Process	Vapor-phase Method	Liquid-phase Method
Brigagão et al. [241]	Pyrolysis of corncob	PR EoS	UNIQUAC ^c	Ille et al. [248]	Fast pyrolysis (wheat straw)	Ideal gas	Dortmund-modified UNIFAC
Campos-Franzani et al. [249]	Liquid-liquid extraction of guaiacol from hydrocarbons	- ^a	NRTL	Ille et al. [248]	Fast pyrolysis (wheat straw)	GCA EoS	GCA EoS
Cesari et al. [250]	LLE of phenolic components in water	- ^a	NRTL	Jaspersen et al. [251]	LLE of model FPBO components	- ^a	Dortmund-modified UNIFAC
Dutta et al. [252].	Fast Pyrolysis + <i>In Situ/Ex Situ</i> Vapor Upgrading	PR EoS with Boston-Matthias	PR EoS with Boston-Matthias	Kabir et al. [224]	Pyrolysis of municipal green waste	PR EoS with Boston-Matthias	PR EoS with Boston-Matthias
Feng et al. [253]	Fast Pyrolysis Bio-oil Surrogate	- ^a	SAFT	Krutof and Hawboldt [57]	Distillation curve modeling for FPBO	Ideal gas	UNIQUAC
Fardhyanti et al. [254]	Liquid-liquid extraction of phenol from pyrolysis bio-oil (coconut shell)	- ^a	UNIFAC	Mohammed et al. [231]	Pyrolysis of Napier grass bagasse	Ideal gas	NRTL
Fardhyanti et al. [254]	Liquid-liquid extraction of phenol from pyrolysis bio-oil (coffee shell)	- ^a	NRTL	Neves [233]	Pyrolysis and hydrotreatment of sugarcane bagasse	SRK EoS with Boston-Matthias	SRK EoS with Boston-Matthias
Fonseca et al. [5]	Fast pyrolysis (wheat straw)	Redlich-Kwong EoS	UNIFAC	Onarheim et al. [223]	Fast pyrolysis of pine wood and forest residue	Ideal gas	UNIQUAC ^c
Gorenssek et al. [226]	Lignocellulosic biomass pyrolysis	PR EoS with Boston-Matthias	PR EoS with Boston-Matthias	Peters et al. [4]	Fast pyrolysis of lignocellulosics (pine, eucalyptus, poplar, wheat straw)	PR EoS with Boston-Matthias	PR EoS with Boston-Matthias
Gupta et al. [255]	Fast pyrolysis multi-step condensation	Ideal gas	UNIQUAC	Shahbaz et al. [220]	Slow pyrolysis of cellulose, hemicellulose, and lignin	PR EoS with Boston-Matthias	PR EoS with Boston-Matthias
Gura [235]	Fast pyrolysis of lignin	Redlich-Kwong EoS	Dortmund-modified UNIFAC	Shemfe et al. [230]	Fast-pyrolysis + hydroprocessing for electrical generation (pine wood)	Nothnagel EoS	UNIQUAC
Gustavsson and Nilsson [238]	Flash pyrolysis of forest residues for boiler	Ideal gas	Wilson ^b	Stephan et al. [256]	Ternary LLE equilibria of water, isopropyl acetate/toluene, and bio-oil surrogate	- ^a	UNIQUAC, NRTL
Hammer et al. [222]	Fast Pyrolysis of equine waste for boiler	Ideal gas	NRTL	Žilnik and Jazbinšek [257]	Solvation of fast pyrolysis oils	RK EoS	UNIFAC
Humbird et al. [129]	Custom FP reactor for pyrolysis (softwood, corn stover, switchgrass)	PR EoS with Boston-Matthias	PR EoS with Boston-Matthias				

a: The system did not consider the presence of a vapor phase.

b: The authors defined the bio-oil as a binary mixture of water and a non-water pseudo-component, for which Wilson binary parameters were determined.

c: Component-specific parameters estimated in the Aspen Properties™ software using the UNIFAC group contribution method.

2.3.3. Summary of the section

The variety of thermodynamic models employed during vapor-liquid modeling of FPBO processing focuses greatly on the use of activity coefficient methods to model the liquid phase and the use of ideal gas modeling for the vapor phase. While group contribution methods like UNIFAC greatly facilitate the input of components frequently absent from databases, such as many of the components often found in FPBOs, modeling of the vapor phase to consider non-ideal behavior requires the input of substance-specific data, which must be determined experimentally or can be estimated.

Thus, it is important to decide on the thermodynamic model to employ in an FPBO downstream processing model, as well as ensure the complete thermophysical characterization of the components considered in the mixture (discussed in the following section).

2.4. Species representation in the context of process modeling

One of the most important challenges during the preparation of any kind of simulation model is the definition of the individual species present in the system that can play a role in either reaction or equilibrium calculations. The focus of this section lies in exploring both the different strategies of inputting complex solid materials and the complexity of pyrolysis liquid products.

Unit-by-unit simulation of a process makes use of abstractions called unit blocks, which contain the routines necessary to model the reality of a certain apparatus. Simulation unit by unit permits obtaining optimal operation conditions for each unit operation, but it must be kept in mind that a sequence of optimal units will not necessarily lead to a global optimum for the whole process. [261]

Flowsheeting program packages are especially suited for the design of a process, as each unit block is developed to represent and model a typical chemical industry apparatus, requiring the user to solely input the required parameters. Established commercial systems include Aspen Plus™, Aspen HYSYS™, SuperPro, and ChemCad, and open-source versions like COCO are slowly conquering a sizable share of the market. This can be seen as a step up from other unit-by-unit options available on the market, such as gPROMS that require each block to be fully programmed, but allow for a greater degree of flexibility, especially when modeling complex processes that do not necessarily fit into a common paradigm.

Aspen Plus™, the simulator of choice for this work, was chosen due to its relative ease of use, as well as ubiquity in both academia and industry. Aspen Tech™ has conquered and established market-share by approaching the academic market and becoming a habitual presence in university courses; the company also grew by integrating competitor solutions in its products, such as units and property methods designed for methods using electrolytes, metallurgy, polymers, and solids processing. As a simulator, Aspen Plus™ is praised for the ability to implement optimization and design specification constraints, the ability to modify parameters using FORTRAN routines, and the integration with external software. Further extensions include dynamic-state simulation using

Aspen Dynamics™, and the creation of custom unit blocks using the Aspen Custom Modeler™.

The Aspen Simulator™ package also includes the powerful Aspen Properties™ database, which includes not only an enormous variety of chemical species but also the ability to estimate *in-situ* (and during simulation) properties based on structural and group contribution methods.

2.4.1. Approaches to non-conventional representation

Despite the common use of flowsheeting simulators to design processes involving fluids, the simulation of processes involving solids used to be lagging. This is mostly due to the need for a more complex description of the solid fraction, for example, measures of dispersity, e.g., particle size, which requires a parameter distribution, increasing the complexity of the information to be distributed between the different units of a flowsheet. [261]

Non-conventional materials are, per definition, solids that cannot participate in the reaction. Defining materials this way requires several parameters to be defined, including elemental and proximal analysis, and the methods to calculate enthalpy and density of the solid material. This is the approach used by methods that employ black box models (section 2.2.8). It can be considered a good approach to model ash [175] or coke [5].

Several authors define the biomass or the lignocellulosic fractions using mixtures of monomers [4,211,233] This approach has the obvious advantage of allowing the use of the components directly without requiring characterization, keeping in mind that thermochemical properties for these components are often lacking in commercial databases [211,226], as well as making use of dryer unit blocks. The disadvantage of this method lies in disregarding the complexity of biological materials, and the need to employ extra components to model moisture and ash content.

2.4.2. Bio-oil characterization: definition of surrogate mixtures

As a single liquid product, fast pyrolysis bio-oil (FPBO) is a dark brown, free-flowing complex organic liquid with over 1000 detectable organic compounds, and with a distinctive smoky odor due to the presence of guaiacols [22]. It features a LHV similar to the feedstock ($16-19 \text{ MJ}\cdot\text{h}^{-1}$) [22,70], and a water content between 15-50 wt.% [17,20]. High acid content can lower the pH down to 2, making it very corrosive for many metals, and its high oxygen content makes it prone to 'aging' over time, especially in the presence of ash, leading to condensation reactions and increasing the viscosity, water content and average molecular weight [50,70]. Due to these characteristics, FPBO currently mostly sees commercial use as boiler fuel, with minor uses as a source of high-value chemicals [262], and the possibility of being upgraded [54] or blended with petroleum fractions [53].

Solvent fractionation (Figure 2.21) splits an FPBO into fractions that can be analyzed separately. The oil is divided into water-soluble and -insoluble phases, each of which can be further extracted using dichloromethane (DCM) or similar solvents [263]. The water-insoluble phase makes up 3-29 wt.% (wet) of the FPBO yield [264], and each extracted phase can be associated with low-molecular (DCM insoluble) and high-molecular (DCM

soluble) weight lignin [263]. Relevant methods for the analysis of bio-oil and bio-oil fractions include chromatography methods, such as GC (MS, FID) and HPLC, as well as NMR variants, carboxylic and total acid number estimation, or colorimetric methods [55,265].

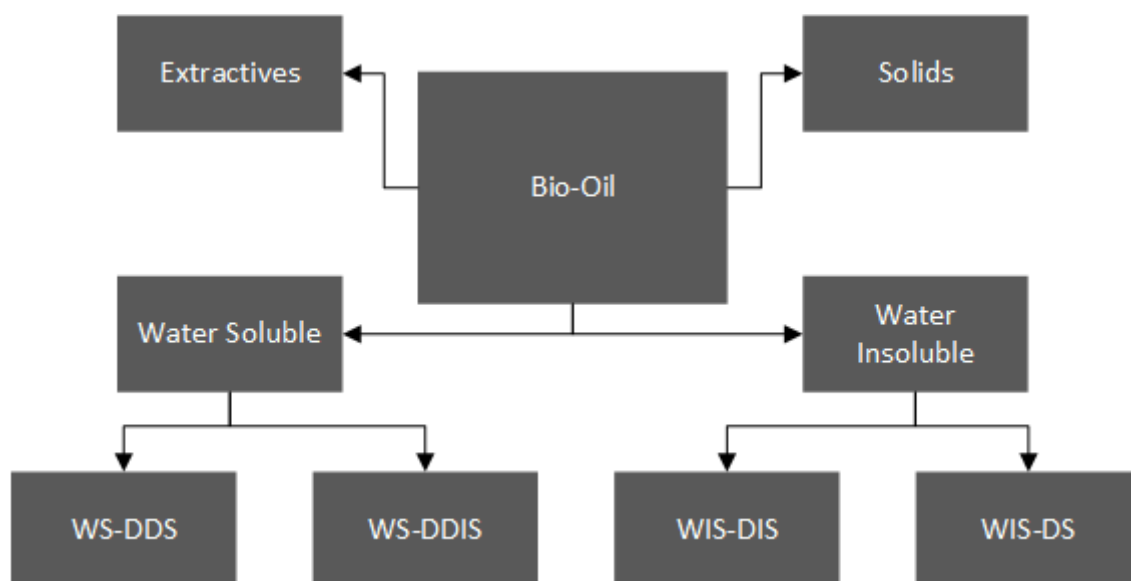


Figure 2.21: Solvent fractionation scheme. DCM: Dichloromethane (CH_2Cl_2); WS-DDS: Water soluble-DCM+DEE (Diethyl ether, $\text{C}_4\text{H}_{10}\text{O}$) soluble; WS-DDIS: Water soluble-DCM+DEE insoluble; WIS-DIS: Water insoluble, DCM insoluble; WIS-DS: Water insoluble, DCM soluble. Adapted from [55].

Due to low operational costs, the requirement of only small sample sizes, and the ability to both quality and quantify chemical species without requiring complex setups, GC/MS and GC/FID (and increasingly often Pyrolysis-GC/MS) became commonplace for the analysis of FPBOs, providing indirect information about the lignocellulosic composition of the material and its decomposition behavior [266]. However, this method is unable to detect components not volatile under the column temperature (often 280-350 °C [267,268]), meaning that only up to 60% of the composition can be identified, depending on the experimental setup, feedstock, calibrations, quality of the analytics, and storage time before analysis [5,127,269]. Moreover, chemometric methods for detection and quantification require spectra databases that often lack data permitting the identification of a considerable fraction, even within the temperature limits of the equipment.

The composition of a condensate surrogate mixture depends on its purpose. Mixtures designed to model LVE phenomena are often a direct simplification of analytic results (Table 2.8), developed focusing specifically on the boiling point range of components that participate in LVE to characterize pyrolysis condensates [259,270], reduce the complexity of GC/MS results [56,57,223,248] or ad initio basing the composition in choosing individual components to represent typical groups present in FPBO [79,271–273]. Those designed to model both pyrolysis reaction phenomena (section 2.2.2) and downstream separation often make use of intermediate components whose presence in the final product compositions may not be attested by analytic methods [4,96,117,118,122–124,127,274,275] (Table 2.9 and Table 2.10), and which presence and characterization must be considered when developing a surrogate mixture for the process.

Table 2.8: Nominal bio-oil compositions (water-free) of surrogate mixtures used to model liquid-vapor equilibrium processes in the context of bio-oil separation. Values in brackets correspond to the boiling point at atmospheric pressure (°C). Data taken from the PubChem database (<https://pubchem.ncbi.nlm.nih.gov/>) unless otherwise stated.

	Evans and Milne [79]	Westerhof et al. [259]	Westerhof et al. [270]	Ille et al. [248,258]	Krutof and Humboldt [57]	Adolf [56]	Jones et al. [271]	Onarheim et al. [223]
Feedstock	Several feedstocks	Pinewood, three condensates	Pinewood, three condensates	Wheat straw, heavy (organic) condensate	Softwood shavings, single condensate	Wheat straw, light (aqueous) condensate	Pinewood sawdust	Pinewood / Forest residue
Acids		Formic acid (101), propionic acid (141), n-butyric acid (164)	Formic acid (101), acetic acid (118), propionic acid (141), n-butyric acid (164)	Acetic acid (118), propionic acid (141)	Acetic acid (118)	Acetic acid (118)	Crotonic acid (185)	Acetic acid (118)
Ketones	Formic acid (101), acetic acid (118)			Acetol (147)	Acetol (147)	Acetol (147)	Acetol (147)	Acetol (147)
Alcohols	Acetone (56), 2-methyl-2-cyclopenten-1-one (160)	Ethanol (78)	Ethanol (78)	Ethylene glycol (197)	Methanol (65)	Methanol (65)		Ethylene glycol (197)
Aldehydes		Formaldehyde (-19), propionaldehyde (49)	Formaldehyde (-19)	Glycol aldehyde (131)	Glycol aldehyde (131)			Glycol aldehyde (131)
Furans	Acetaldehyde (20), glycol aldehyde (131)			Furfural (162)	Furfural (162), Furfuryl alcohol (171)	Furfural (162)	Furfural (162)	Furfural (162)
Lignin derived	Furan (32), furfural (162), furfuryl alcohol (171), 5-methylfurfural (187), α -angelicalactone (198), 2-(5H)-furanone (204), 3-methyl-2(5H)-furanone (222), HMF (270), 2-hydroxy-5,6-dihydropyran-4-one (280)	p-cresol (202), eugenol (254)	p-cresol (202), eugenol (254)	Phenol (182), Guaiacol (205), Syringol (261)	Guaiacol (205), 4-methylguaiacol (221), 4-ethylguaiacol (237), Eugenol (254), Syringol (261), 4-propylguaiacol (264), Vanillin (285)	Phenol (182)	Dimethoxybenzene (206), Isoeugenol (266), Vanillin (285), Dibenzofuran (287), Dimethoxystilbene (338)	Guaiacol (205)
Sugar derived	Guaiacol (205), vinylphenol (209), 4-methylguaiacol (221), guaiacol, 4-vinyl- (224), catechol (245), eugenol (254), syringol 261, isoeugenol (267), maltol (267), resorcinol (280), vinylsyringol (281), vanillin (285), p coumaryl alcohol (297), 4 propenylsyringol (302), coniferyl alcohol (326), synapyl aldehyde (336), sinapyl alcohol (350), ferulic acid (354)	Hydroquinone (287)		Levoglucosan (385)**	Levoglucosan (385)**		Hydroquinone (286), Levoglucosan (385)***, Cellobiose (592)*	Levoglucosan (385)**
Extractives	Hydroquinone (286), α -D-glucose (381)						Dehydroabietic acid (403)*	Oleic acid (360)
High MW residue			"pyrolytic lignin"	3,4,4'-biphenyltriol (389)*	3,4,4'-biphenyltriol (389)*		Phenylcoumarans (> 307), oligomers with β -O-4 bond	"pyrolytic lignin"

*: Estimated using the Adapted Stein & Brown method by the US Environmental Protection Agency's EPISuite™.

***: Levoglucosan data obtained from Shoji et al. [279].

Table 2.9: Nominal bio-oil compositions (water-free) of surrogate mixtures employed in reaction networks. Values in brackets correspond to the boiling point at atmospheric pressure (°C). Data taken from the PubChem database (<https://pubchem.ncbi.nlm.nih.gov/>) unless otherwise stated. Part 1 of 2.

Functional Group	Ranzi et al. [96] ^a	Corbetta et al. [130]	Anca-Couce et al. [280]	Peters et al.[4] ^b	Trendewicz et al. [158] ^c	Ranzi et al. [81,133] ^d	Gorensek et al. [226] ^e
Alkanes			Methane (-162), ethylene (-104)	C1-C4 (-162 - -1), C5-C18 (36-316), cyclopentane (49), methylcyclopentane (72), cyclohexane (81), cyclohexene (83), methylcyclohexane (101), cyclopropylcyclohexane (156), n-propylcyclohexane (157), bicyclohexyl (238)			Methane (-162), ethylene (-104)
Acids	Acetic acid (118)	Acetic acid (118)	Acetic acid (118)	Formic acid (101), Acetic acid (118), Propionic acid (141), Levulinic acid (246)	Formic acid (101)	Acetic acid (118)	Formic acid (101), Acetic acid (118)
Acetons	Ketene (-56), Acetone (56), Diacetyl (88)	Acetone (56)	Acetone (56)	Ketene (-56), Acetone (56), Acetol (147)	Acetone (56)	Acetone (56)	
Alcohols	Methanol (65), Ethanol (78), iso-propanol (82), n-propanol (97), Ethylene glycol (197), 1,3-propanediol (214)	Methanol (65), ethanol (78)	Methanol (65), ethanol (78)	C1-C6,C9 (65-213), Ethylene glycol (197), Propanediol (214)	Methanol (65), ethanol (78)	Methanol (65), ethanol (78)	Methanol (65), ethanol (78)
Aldehydes	Formaldehyde (-19), Acetaldehyde (20), Glyoxal (50), Acrolein (52), Propanedial (122)*, 3-hydroxypropanal (149)*, hydroxyoxopropanal (183)*	Formaldehyde (-19), Acetaldehyde (20), Glyoxal (50)	Formaldehyde (-19), Acetaldehyde (20), Propanal (48), Propanedial (122)*, Glycol aldehyde (131)	Formaldehyde (-19), Acetaldehyde (20), Glyoxal (50), Propanedial (122)*, Glycol aldehyde (131)	Formaldehyde (-19), Acetaldehyde (20), Glycol aldehyde (131)	Formaldehyde (-19), Acetaldehyde (20), Glyoxal (50)	Formaldehyde (-19), Propanal (48), Glyoxal (50), Acrolein (52), Glycol aldehyde (131), 3-hydroxypropanal (149)*
Furans	Furan (32) THF (65) Furfural (162) HMF (270)**		HMF (270)**	Furan (32), Dimethylfuran (108)*, Furfural (162), Furfuryl alcohol (171), HMF (270)**	HMF (270)**		Furfural (162), HMF (270)**

*: Estimated using the Adapted Stein & Brown method by the US Environmental Protection Agency's EPISuite™.

** : Estimated using the ACD/Labs Percepta Platform - PhysChem Module.

***: Levoglucosan data obtained from Shoji et al. [279].

a: Including secondary reactions reported in the Supplementary Information of the manuscript

b: Holocellulosic degradation taken from Ranzi et al. [96], lignin represented by a radical degradation mechanism taken from Faravelli et al. [95]

c: Adapted from Corbetta et al. [130]

d: Both reaction networks feature the same pathways, with slightly distinct kinetic parameters

e: Adapted from Humbird et al. [129]

Table 2.10: Nominal bio-oil compositions (water-free) of surrogate mixtures used to model pyrolysis reactions. Values in brackets correspond to the boiling point at atmospheric pressure (°C). Data taken from the PubChem database (<https://pubchem.ncbi.nlm.nih.gov/>) unless otherwise stated. Part 2 of 2.

Functional Group	Ranzi et al. [96] ^a	Corbetta et al. [130]	Anca-Couce et al. [280]	Peters et al. [4] ^b	Trendewicz et al. [158] ^c	Ranzi et al. [81,133] ^d	Gorenssek et al. [226] ^e
Lignin derived	Phenol (182), Syringol (261), p-Coumaryl alcohol (297)*, Synapyl aldehyde (336)*	Phenol (182), p-Coumaryl alcohol (297)*, Synapyl aldehyde (336)*	Phenol (182), p-Coumaryl alcohol (297)*, Synapyl aldehyde (336)*	Benzene (80), Toluene (111), Ethylbenzene (136), Xylene (139), Phenol (182), p-Cresol (202), 2-ethylphenol (205), Guaiacol (205), Dimethylphenol (217), 4-isopropenylphenol (218), p-Coumaryl alcohol (297)*, Synapyl aldehyde (336)*, Synapyl alcohol (350)*	Phenol (182), p-Coumaryl alcohol (297)*, Synapyl aldehyde (336)*	Phenol (182), p-Coumaryl alcohol (297)*, Synapyl aldehyde (336)*	Anisole (154), Phenol (182), p-Coumaryl alcohol (297)*, Synapyl aldehyde (336)*
Sugar derived	Dihydrolevoglucosan (203)*, Xylose (328)*, Xylofuranose (331)*, Levoglucosan (385)***	Xylose (328)*, Levoglucosan (385)***	Xylose (328)*, Levoglucosan (385)***	Xylose (328)*, Levoglucosan (385)***, Glucose (411)	Levoglucosan (385)***	Xylose (328)*, Levoglucosan (385)***	Xylosan (247)*, Levoglucosan (385)***
Extractives						3,5-dihydroxy-benzofuranone (366)*, Galocatechol (686)	3,5-dihydroxy-benzofuranone (366)*, Galocatechol (686)
Polycyclics				Naphtalene (218), Chrysene (448)			
High MW residue						trans-3-(3,4-dimethoxyphenyl)-4-((E)-3,4-dimethoxystyryl)-cyclohex-1-ene (465)	trans-3-(3,4-dimethoxyphenyl)-4-((E)-3,4-dimethoxystyryl)-cyclohex-1-ene (465)

*: Estimated using the Adapted Stein & Brown method by the US Environmental Protection Agency's EPISuite™.

** : Estimated using the ACD/Labs Percepta Platform - PhysChem Module.

***: Levoglucosan data obtained from Shoji et al. [279].

a: Including secondary reactions reported in the Supplementary Information of the manuscript

b: Holocellulosic degradation taken from Ranzi et al. [96], lignin represented by a radical degradation mechanism taken from Faravelli et al. [95]

c: Adapted from Corbetta et al. [130]

d: Both reaction networks feature the same pathways, with slightly distinct kinetic parameters

e: Adapted from Humbird et al. [129]

Major degradation pathways leading to the final product distribution have been discussed in section 2.2.1. Disregarding water, the final composition of an FPBO determined by GC/MS is rich in organic acids and ketones, as well as sugars if quick condensation methods are employed [276–278]. Minor amounts of aldehydes, esters, furans, and aromatics are expected; aldehydes and furans are often labile, while esters are known to form during aging [117,118,122–124,127,274,275].

However, considering a single surrogate for this phase may not be considered a wise choice, especially when using a reaction-based model for the pyrolysis reactor. Pinheiro Pires et al. [272] considered a very similar setup with both a water-soluble fraction: humins derived from the condensation of HMF (18/12 wt.% of the high molecular weight residue) and a hybrid oligomer derived from all types of lignocellulosic matrix components (28/36 wt.% of the high molecular weight residue), and a water-insoluble fraction: pyrolytic lignin derived from both uncracked lignin or repolymerized material (54/52 wt.% of the high molecular weight residue).

When employing the reaction networks but also attempting to model real condensates, it is important to consider surrogate mixtures that include not only primary reaction products but also important FPBO representatives, as well as the selection of secondary pyrolysis to bridge this gap.

2.4.3. The high-molecular-weight fraction

As stated in section 2.4.2, GC/MS features a relevant shortcoming in being unable to quantify the complete bio-oil. This non-detectable phase, either due to deficiencies in the database or low volatility, is mostly comprised of by-products of lignin decomposition, substituted sugars, and polyaromatics, which are frequently left unidentified. This phase is often associated with the water-insoluble fraction of pyrolysis bio-oils (Figure 2.21) and is often equated with the ‘pyrolytic lignin’ concept. Disregarding the presence of this phase reduces the rigorosity of the model and can lead to skewed results due to constituting a considerable fraction of the condensate, thus indubitably influencing the behavior of the liquid-vapor equilibrium calculations [5,18,206,238]. If considered a single molecule, Elliott et al. [264] proposed a range of molecular weight between 1000-2500 g/mol.

High molecular weight lignin (HMWL) surrogates have been devised to represent this non-detectable phase, as can be seen in Table 2.8, Table 2.9, and Table 2.10. Of these, several have been defined as compounds of null vapor pressure [223,270], while other have been devised per the analysis of the nature of isolated lignin [97,272,273,281]. Ille et al. [248] selected 3,4,4'-biphenyltriol ($C_{12}H_{10}O_3$, 202.2 g·mol⁻¹) as a compromise between a lignin-like molecular structure and functional group distribution, and a correct modeling of the activity of water in fast pyrolysis condensates.

Scholze et al. [97] characterize pyrolytic lignin as having the following characteristics: molecular weight of 684-692 g·mol⁻¹, H/G/S ratio of 6%/73%/21%, the elemental composition of 65.22% C, 6.13% H, 27.63% O, a ratio of 7.5% of phenylic methoxy (CH_3-O-Ph) groups, a ratio of 11.9% of phenylic hydroxyl ($OH-Ph$) groups,

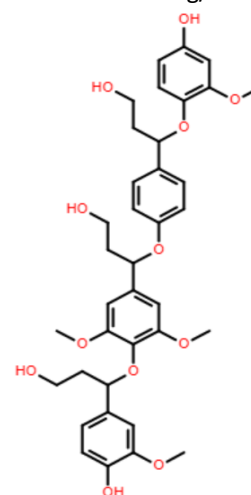


Figure 2.22: ‘Pyrolytic lignin’ surrogate based on the description by Scholze et al. [97] ($C_{37}H_{44}O_{12}$, 680.74 g·mol⁻¹).

and from which a molecular structure has been designed (Figure 2.22). Bayerbach and Meier [282] bring attention to acid (COOH–Ph, around 5% prevalence) and acetyl (CH₃CO–Ph) substituents, as well as resinol groups and biphenyl bonds, often lacking in surrogate molecules.

Del Río et al. [283] classified wheat straw (*Triticum durum*) lignin as a p-hydroxyphenyl-guaiacyl-syringyl biopolymer with a molar H:G:S ratio of 6%:64%:30%, and a molar p-coumarate:ferulate ratio of 4%:11%. 2D-NMR showed a preponderance of 75% of β-O-4 ethers, followed by phenylcoumarans (11%) and resinols (4%). End-groups detected a prevalence of side-chain γ-acylation of 10%. A proposal based on these conclusions is presented in Figure 2.23.

Fortin et al. [284] report the occurrence of carbohydrate contamination in pyrolytic lignin bonded through ester links to lignols. Pires et al. [253] consider the presence of a 2,5-dioxo-6-hydroxyhexanal (DHH) backbone within a hybrid oligomer structure feasible as an insoluble high-molecular weight pyrolysis product.

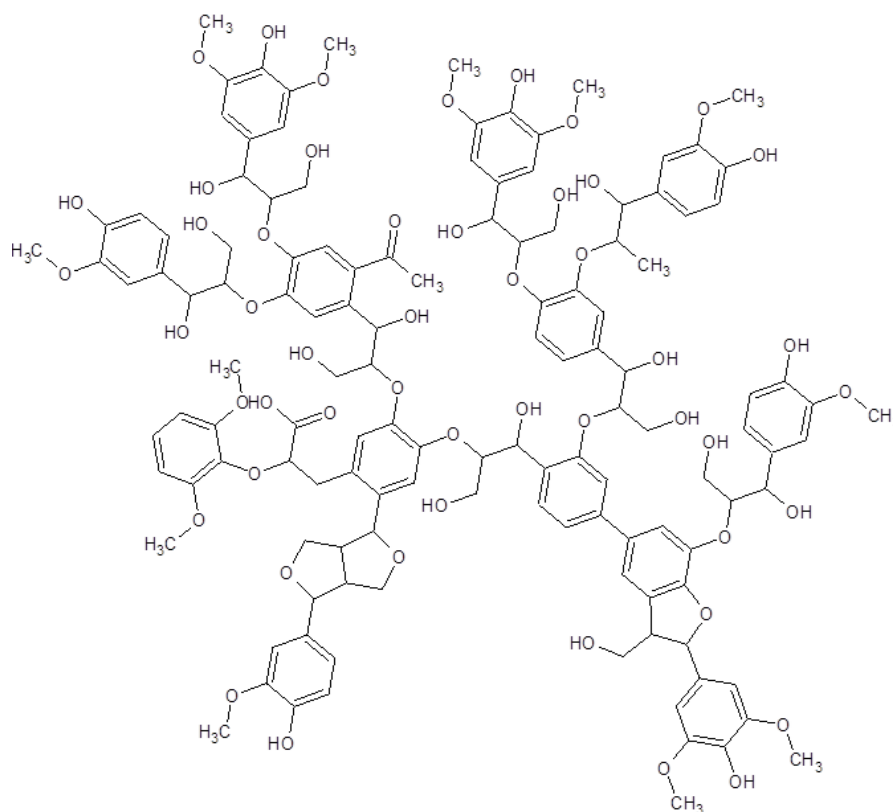


Figure 2.23: Proposal of representative for wheat straw pyrolytic lignin, the conclusions by Scholze et al. [97], Bayerbach and Meier [282], and Del Río et al. [283] (C₁₂₈H₁₄₄O₅₀, 1450.58 g·mol⁻¹).

Pinheiro Pires et al. [272] and Fonts et al. [273] make use of a tripartite surrogate to represent the non-detectable phase. Both surrogate mixtures make use of humins (18/12 wt.% of the high molecular weight residue), water-soluble structures that arise from the condensation of sugars, pyrolytic lignin structures (54/52 wt.% of the high molecular weight residue) that derive from the incomplete degradation of the lignin structure, and hybrid oligomers (28/36 wt.% of the high molecular weight residue), that arise from the reaction between lignin and holocellulose, containing both furanic units, monolignol units, and sugar units. Structures for all these components have been proposed by Pires et al. [272].

In Table 2.11, apart from the aforementioned mixtures, tailor-made to model the *bioliq*[®] organic condensate [5,248], two other surrogates mixtures developed to fit a wide range of lignocellulosic biomasses have been included for the sake of comparison [272,273].

Table 2.11: Nominal and fractional composition of several FPBOs in the literature, as well as an estimation of its elemental composition.

Ille et al. [248]			Fonseca et al. [5]		
Composition	wt.%	mol.%	Composition	wt.%	mol.%
Water	13.3%	53.6%	Water	16.9%	47.4%
Acetic Acid	5.1%	1.2%	Acetic Acid	14.6%	6.6%
Propionic Acid	1.3%	6.1%	Propionic Acid	3.7%	12.3%
HAA	1.0%	1.3%	Acetaldehyde	2.6%	2.5%
Acetol	9.0%	8.8%	Acetol	23.7%	3.0%
Furfural	1.6%	1.2%	Furfural	4.1%	16.2%
Phenol	1.6%	1.2%	Phenol	4.0%	2.2%
Guaiacol	2.7%	1.6%	Guaiacol	6.6%	2.2%
Syringol	2.4%	1.1%	Syringol	5.8%	2.7%
Levogluconan	3.7%	1.7%	Levogluconan	9.9%	1.9%
Pyrolytic Lignin ^a	57.1%	20.5%	Ethylene Glycol	8.1%	3.1%
Ethylene Glycol	1.4%	1.7%			
Elemental Analysis C/H/O	55.8%/6.5%/37.8%	34.7%/47.7%/17.6%	Elemental Analysis C/H/O	41.8%/8.0%/50.2%	24.0%/54.5%/21.6%
Fonts et al. [273]			Pinheiro Pires et al. [272]		
Composition	wt.%	mol.%	Composition	wt.%	mol.%
Water	23.2%	73.0%	Water	21.3%	73.0%
Glycoaldehyde	1.0%	1.3%	Glycoaldehyde	6.4%	1.3%
Acetol	6.7%	5.1%	Acetic acid	4.9%	5.1%
2-Cyclopentenone	0.5%	0.3%	Acetol	4.9%	0.3%
3-met-1,2-cyclopentenedione	0.5%	0.3%	Propanoic acid	1.3%	0.3%
Acetic acid	8.7%	8.2%	2-cyclopenten-1-one	0.1%	8.2%
Propionic acid	2.8%	2.1%	Furfural	0.3%	2.1%
Formic acid	1.0%	1.2%	2(5H)-furanone	0.4%	1.2%
Furfural	0.6%	0.4%	3-met-1,2-cyclopentenedione	0.3%	0.4%
2(5H)-furanone	0.8%	0.5%	Methyl-2(5H)-furanone	0.1%	0.5%
Phenol	0.9%	0.5%	Phenol	0.4%	0.5%
Guaiacol	0.2%	0.1%	Guaiacol	0.3%	0.1%
Creosol	0.5%	0.2%	Creosol	0.3%	0.2%
4-ethylguaiacol	0.2%	0.1%	2,4-xilenol	0.0%	0.1%
Eugenol	0.6%	0.2%	4-ethylguaiacol	0.0%	0.2%
Catechol	0.3%	0.1%	Eugenol	0.7%	0.1%
Syringol	0.1%	0.0%	Catechol	0.5%	0.0%
4-methylcatechol	0.5%	0.2%	Syringol	0.2%	0.2%
Vanillin	1.5%	0.6%	4-methylcatechol	0.2%	0.6%
Syringaldehyde	0.2%	0.1%	Vanillin	0.7%	0.1%
Levogluconan	6.5%	2.3%	Syringaldehyde	0.0%	2.3%
Cellobiosan	3.5%	0.6%	Levogluconan	21.3%	0.6%
HMM PL ^c	11.0%	0.4%	Pyrolignin ^c	18.3%	0.4%
LMM PL ^d	10.2%	1.0%	Hybrid oligomer ^g	12.6%	1.0%
Humin ^e	7.0%	0.6%	Humins ^e	4.4%	0.6%
Oligomer ^f	11.0%	0.4%			
Elemental Analysis C/H/O	42.6%/7.3%/50.1%	25.5%/52.0%/22.5%	Elemental Analysis C/H/O	43.2%/7.3%/49.4%	25.8%/52.0%/22.2%

a: 3,4,4'-bisphenoltriol (C₁₂H₁₀O₃, 202.22 g·mol⁻¹), b: C₃₇H₄₄O₁₂ (680.81 g·mol⁻¹), c: C₈₁H₇₈O₂₅, d: C₃₀H₃₄O₁₁, e: C₃₆H₃₂O₁₆, f: C₇₀H₈₂O₃₄, g: C₇₁H₈₂O₃₃.

3. Thermogravimetry and pyrolysis

3.1. Methodology

3.1.1. Feedstock and pyrolysis product analysis

Wheat straw (*Triticum aestivum* L.) was supplied by a local farmer (Dörrmann, Kraichtal-Münzesheim, Germany), collected from a harvest of spring wheat and supplied in large bales (250-300 kg each). Before the experiments, the wheat straw was cut to a particle size of <5 mm with a disintegrator (HZR 1300) and a subsequent cutting mill (LM 450/1000-S5-2), both supplied and installed by 'Neue Herbold Maschinen- und Anlagenbau GmbH' (Sinsheim/Reihen, Germany). Beechwood powder (*Fagus sylvatica*) was supplied in the context of a previous collaboration [183]. A summary of the proximate and ultimate analyses of the feedstocks considered can be found in Table 3.1.

Table 3.1: Proximate, ultimate, and elemental analysis of wheat straw. All values in dry base. Data for beech wood was obtained from the Phyllis2 database (www.phyllis.nl).

	Beech	WS-P	WS-H
Moisture (wt.%)	9.4	9.3	9.2
Ash (wt.%)	1.0	6.9	7.0
Volatile Matter (wt.%)	83.1	67.5	67.5
Ultimate Analysis			
C (wt.%)	48.8	43.8	43.8
H (wt.%)	6.02	6.1	6.1
N (wt.%)	0.30	< 1	< 1
S (wt.%)	0.02	0.09	0.09
Ca (ppm)	8834	3780	3780
K (ppm)	1314	11800	11800
Si (ppm)	1170	22600	22600

Definitive values for MC of the biomass and char are measured according to the DIN EN 18134-3, drying at 105 °C ($\pm 0.2\%$ for biomass, $\pm 0.1\%$ for char). Ash content of the biomass ($\pm 0.2\%$) and solids ($\pm 0.5\%$) is quantified according to the DIN EN ISO 18122: the samples are subjected to 250 °C for 60 min, followed by 550 °C for 120 min. The elementary analysis was performed according to the DIN EN 15104 for the biomass and the DIN EN 51732 for the char.

For each condensate, volumetric Karl-Fischer titration using methanol with Hydranal Composite-V is used to determine the water content ($\pm 1.5\%$). The elementary analysis is performed according to the DIN EN 15104, akin to the biomass. The first (organic, OC) condensate is submitted to extraction with methanol, filtration, and drying to determine its solids content. It is required to determine the content of ethylene glycol in the first (organic) condensate due to the experimental procedure, which is done using ^1H NMR ($\pm 2.0\%$). Due to the characteristics of the second (aqueous, AC) condensate, chemical oxygen demand (COD) and total organic carbon content (TOC) are determined to estimate the heating values; these values are determined according to the DIN EN 15705 and DIN EN 1484 respectively.

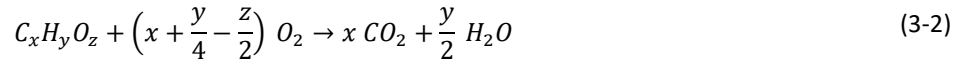
Higher heating value (HHV) determination for biomass was made according to the DIN EN ISO 18125, while for char according to DIN 51900-3, both applying the dynamic mode. No corrections to acid content were

performed, due to the low amounts of acids formed. The Lower Heating Value (LHV) for both cases was calculated assuming an enthalpy of vaporization of water of 2257 J·g⁻¹, according to Eq. (3-1).

$$LHV_{char} = HHV_{char} - \left(\frac{MM_{H_2O}}{MM_{H_2}} \times \%W_H + \%W_{H_2O} \right) \times \Delta H_{vap,H_2O} \quad (3-1)$$

The gas composition is measured online through gas chromatography, calibrated using a commercial mixture employing helium as its carrier gas. Neon is injected with the injected gas at a constant flow rate (10 L/h) and is used as gas chromatography tracer, due to having an easily distinguishable peak allowing to measure the other components by area proportionality. The volumetric flow rate of the gas is measured through the use of an online flowmeter.

Assuming the combustion of a generic organic compound (Eq. (3-2)), the stoichiometric oxygen demand can be estimated using Eq. (3-3), and the water produced by combustion can be estimated using Eq. (3-4). After that, the LHV of each species can be estimated in a similar way to the char (Eq. (3-5)), and the total LHV of the gas is the weighted average of each component (Eq. (3-6)).



$$O_{2,demand,i} = \frac{\left(x + \frac{y}{4} - \frac{z}{2} \right) \times MM_{O_2}}{MM_i} \quad (3-3)$$

$$w_i = \frac{\frac{y}{2} \times MM_{H_2O}}{MM_i} \quad (3-4)$$

$$LHV_i = HHV_i - w_i \times \Delta H_{vap,H_2O} \quad (3-5)$$

$$LHV_{gas} = \sum_i x_i LHV_i \quad (3-6)$$

GC-MS analyses of the pyrolysis condensates have been conducted by Thünen Institute, Hamburg, Germany. The method is described in detail elsewhere [285].

For tests with particles of very low dimensions, a SPEX SamplePrep Freezer-Mill 6875 is employed to powder samples of up to 10 g, using 2-3 cycles of 10 min (precool 5 min, 3 cycles of 1 min grinding, 1 min cool time, at a rate of 10 cps) to a particle size of around 100 mesh (149 μm). As of the writing of this section, it is not possible to estimate the size distribution of the formed powders.

Elementary characterization of the inorganic ash fraction of biomass was achieved by using Inductively Coupled Plasma Optical Emission Spectroscopy (ICP-OES), performed using an Agilent 725 spectrometer coupled with a simultaneous echelle spectrometer with radial plasma observation. Argon is employed as both plasma gas (15 L/min, excitation at 40 MHz, 2 KW) and auxiliary gas (1.5 L/min). Samples are dissolved in hydrofluoric acid (HF) analyzed using a feed rate of 1.3 mL/min, for a total of 3 measurements over 8 sec. Before measurement,

each sample is dissolved in an acid mixture: HNO₃ (65%), HCl (37%), HF (40%), H₂O₂ (35%), on a prepared glass beak.

Volatiles (VM) estimation was performed based on the standard DIN EN ISO 18123 for the determination of volatile matter content on solid biofuels. Fixed carbon (FC) is estimated as the difference to the remaining proximate analysis properties, according to Eq. (3-7).

$$MC(\text{wt } \%) + \text{Ash}(\text{wt } \%) + FC(\text{wt } \%) + VM(\text{wt } \%) \quad (3-7)$$

3.1.2. Thermogravimetry

Thermogravimetric (TGA) data of wheat straw at two different particle sizes (powder, 'WS-P', hull, 'WS-H') was analyzed and compared to data gathered for **beech** wood using the same equipment in the context of another publication [183]. The comparison is warranted due to the differences in ash content, especially potassium, due to its catalytic effects (see section 2.2.4). The TGA data were obtained *in-house* using a Netzsch STA-409 vertical thermal analysis system, with a sensitivity of 1 µg, temperature accuracy of 1 K, a sample mass of up to 200 mg in an alumina holder, employing sweeping gas flows of 70 ml·min⁻¹ [183]. The following linear heating rates were employed (up to 900 °C): 1, 5, 10, 20, 50 K·min⁻¹. The 10 K/min WS-P sample was submitted to 5 replicas, to estimate measurement error during TGA. [175]

The method proposed by Wu et al. [184] was paired with the second-derivative method by Gaitán-Álvarez et al. [188] (section 2.2.5), and applied to all the DTG curves, to estimate the position of the center of the peak before deconvolution, as well as estimate the conversion at those phases for kinetic analysis.

To perform deconvolution, the temperature of the center of each Gaussian peak was set to these values, although defining the peak point for the lignin curve on the slope change after the cellulose peak may lead to a large contribution of charring phenomena. The effect of ash and moisture in the feedstock is only accounted for indirectly, and the degree of overlap between curves may not reflect the reality of the interweaving of the ligno-cellulosic fractions in the matrix.

Methods for estimation of kinetic parameters in this work are the isoconversional KAS, FWO, and Friedman, and curve-fitting using first-order, third-order for lignin, and free-order [175]; all of these have been discussed in section 2.2.6. Application of the isoconversional methods, as well as the estimation of the derivative of the conversion ($d\alpha/dt$), was performed according to the guidelines by Cai et al. [197]. For each conversion value, the kinetic parameters were determined considering the distance to the closest multiple of α 0.05 (e.g., for a peak conversion of 0.37, the value is estimated by taking 3/5 of the α 0.35 value and 2/5 of the α 0.4 value) [175].

Summative curve-fitting was performed based on the recommendations by Anca-Couce [196]. The fit was performed using least-squares minimization of the objective function (Eq. (3-8)) over N=250 experimental points, and the fit was estimated over all the -DTG curves of the same feedstock (Eq. (3-9)), previously normalized by dividing the values by the peak maximum.

$$S = \sum_{i=1}^N \left(\left(\frac{d\alpha_i}{dt} \right)_{exp} - \left(\frac{d\alpha_i}{dt} \right)_{sim} \right)^2 \quad (3-8)$$

$$fit(\%) = \frac{\sqrt{\frac{S}{N}}}{\left(\frac{d\alpha_i}{dt} \right)_{exp,max} - \left(\frac{d\alpha_i}{dt} \right)_{exp,min}} \quad (3-9)$$

To compute the mass loss curves based on kinetic parameters (Eq. (3-8) and (3-9)), integration was performed using Euler's method. Estimation of the deviation (ε , root sum of square errors, results are best when approaching zero) is done as shown in Eq. (3-10). Mass loss comparison (TGA) was made against the experimental $1-\alpha$ curves to disregard the presence of residual solid content, and derivative mass loss (DTG) was made against the experimental $d\alpha/dt$ curves for consistency. For the case of DTG-based comparisons, $(1-\alpha)_{exp}$ is replaced by the $(d\alpha/dt)_{exp}$ curve at the time i :

$$\varepsilon = RSSE = \sqrt{\frac{\sum_{i=1}^N ((1-\alpha)_{exp,i} - (1-\alpha)_{kin,i})^2}{N}} \quad (3-10)$$

3.1.3. Pyrolysis trials

Pyrolysis trials performed to validate the developed process model took place in the process development unit (PDU)'Python' with a feed capacity of $10 \text{ kg}\cdot\text{h}^{-1}$ [286]. They have been initially used to supply experimental data for a black box model to investigate the energetic integration of biomass drying and hence were designed to observe the influence of feedstock moisture content on fast pyrolysis yield distribution [5]. At the beginning of an experiment, pre-conditioned biomass is fed to a buffer silo, which feeds a screw that controls the feed rate to the reactor of $7-8 \text{ kg}\cdot\text{h}^{-1}$. Samples of the biomass are either taken immediately before feeding, from each different sack/bag/barrel in which the feedstock may be stored or additionally from the biomass lock hopper, i.e., directly before biomass is fed into the reactor to account for changes during handling and storage in the silo.

The pyrolysis carries out in a twin-screw reactor, thermally isolated, in which the biomass is mixed with steel beads of 1.5 mm diameter as a heat carrier, which is heated electrically and recirculated around using bucket elevators. The reactor is heated up by starting the preheated heat carrier cycle and biomass feeding is started once a reactor temperature of $500\pm 5 \text{ }^\circ\text{C}$ was reached. It takes around 10 min to ramp up biomass feeding to the desired feed rate. One can safely assume that pyrolysis operates in steady-state as the reactor temperature is reached before startup and maintained throughout the runtime at $500\pm 5 \text{ }^\circ\text{C}$. Via an exhaust hood on top of the reactor, the pyrolysis products are fed into a double cyclone system to recover the dry char at reactor temperature.

The pyrolysis vapors enter the first condensation loop, in which they are quenched with cooled condensate at around 90 °C forming the ORC, which is collected in a first condensation vessel. Uncondensed vapors and gases are directed through an electrostatic precipitator to remove aerosols and particles. The produced condensate is recirculated, cooled down and injected into the quench for contact cooling of the vapors. To start up this condensation system, ethylene glycol is used because it is readily miscible with the ORC. Consequently, the ORC produced from the experiments contains a significant amount of ethylene glycol. The second condensation loop to recover the AC is designed similarly to the first one but operates at lower temperatures of around 28 °C. The start-up medium of this condensate loop is water. The remaining non-condensable gas is removed and analyzed by an online gas chromatograph, before being vented out.

Condensation temperature in the first loop starts at 70 °C and takes typically around 20 min to reach the desired condensation temperature of 90±5 °C. The second condenser does not experience significant temperature changes during startup/operation and is kept at 28±2 °C.

At the end of each trial, both quenching systems are emptied. Both condensates and char are weighed, and yields of the condensates for effects of mass balance are calculated by discounting the initial condensation loop filling. The products are kept in vessels specialized for the storage of pyrophoric material, and are sampled with scoops to smaller bottles for analytics and shipping. Leftovers are kept for a matter of years before disposal. Sampling during operation is possible via a port located directly downstream from the pumps.

Each experiment is conducted in duplicate. In case of high uncertainty between two experimental runs, a third is conducted and the outlier is omitted from further analysis.

3.2. Thermogravimetry for the estimation of lignocellulosic content in biomass

This section presents data published in MDPI Energies [175].

In Figure 3.1, the DTG profile for each feedstock is shown with higher peaks corresponding to higher heating rates, with a deviation to higher temperatures as the heating rate increases; numerical values associated with each curve can be found in Appendix B. Char yields (at 900 °C) for beech wood averaged to 25.2±0.6 wt.%, for WS-P to 26.2±0.7 wt.% and WS-H to 25.9±0.8 wt.%; these values both show little variance between each other and are lower than a range previously found using the same equipment (28.5±0.6 wt.%) [287]. Differences in peak shape can be attributed to heat/mass limitation and catalytic effects, especially comparing beech and wheat straw, and between the different particle sizes. Wheat straw is naturally a hollow fiber contrary to dense beech wood, indicating that anisotropic effects are at play. [175]

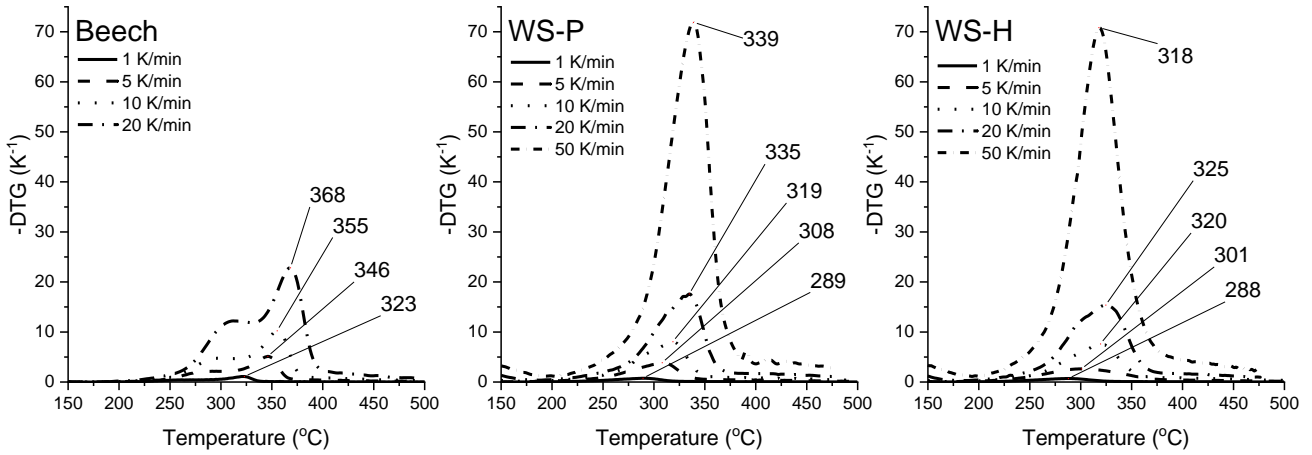


Figure 3.1: Comparison of the $-DTG$ behavior divided by feedstock and peak temperature. a) Beech, b) WS-P, c) WS-H. Source: [175].

In Table 3.2, a comparison between the estimated values for each lignocellulosic pseudocomponent using the different methods is presented (simple deconvolution and as a variable during model-fitting). A visual representation of one deconvolution method can be seen in Figure 3.2.

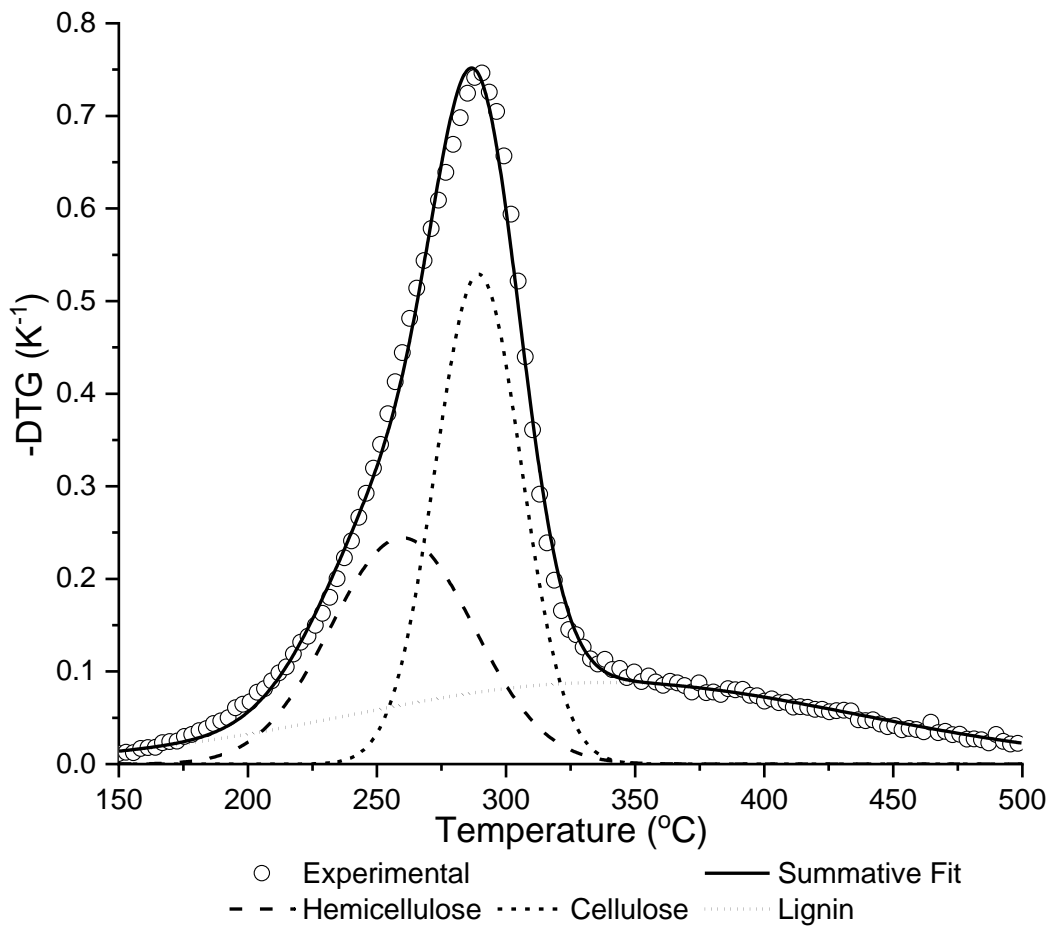


Figure 3.2: Example of deconvolution using Gaussian curves centered at the point devised by the DDTG method. WS-P, 10 K·min⁻¹. Source: [175]

Most values shown in Table 3.2 are within a margin of +10%/-10% of literature values. Both the deconvolution and the model-fitting free order methods presented high overestimations of the lignin fraction for all feedstocks, the former being particularly noticeable for the wheat straw fractions (WS-P and WS-H); however, no noticeable differences between the two particle sizes can be pointed. Cellulose presents the overall lowest error of estimation, followed by hemicellulose and lignin. As all methods operate by minimization of square error, misestimations of lignin content usually have a higher effect on the hemicellulosic fraction than cellulose, due to its underlying position under all other curves (Figure 3.2) [175].

Table 3.2: Comparison of presented estimates for the lignocellulosic composition of the feedstocks in this study (wt. % daf.). Values in *italic* represent relative deviations from the literature values. All values were extrapolated to 100%, and the presence of extractives, lipids, and protein content was disregarded. Source: [175].

		Cellulose	Hemicellulose	Lignin
Beech	<i>Literature^a</i>	<i>47.9 ± 5.0</i>	<i>28.9 ± 2.5</i>	<i>23.2 ± 2.7</i>
	Model-fitting Anca-Couce ^b	54.2 (13.2%)	33.1 (14.5%)	12.8 (-44.8%)
	Deconvolution	43.8 ± 1.2 (-8.6%)	38.0 ± 1.4 (31.5%)	18.1 ± 1.7 (-22.0%)
	Model-fitting first-order	54.7 (14.2%)	28.2 (-2.4%)	17.1 (-26.3%)
	Model-fitting n _{Lig} =3	46.9 (-2.1%)	24.9 (-14.0%)	28.2 (21.7%)
	Model-fitting free-order	45.6 (-4.7%)	19.3 (-33.1%)	35.0 (51.0%)
Wheat straw Powder (WS-P)	<i>Literature^c</i>	<i>45.5 ± 1.4</i>	<i>32.6 ± 2.5</i>	<i>21.9 ± 1.0</i>
	Deconvolution	36.4 ± 1.3 (-20.0%)	26.4 ± 1.1 (-19.0%)	37.2 ± 0.4 (69.9%)
	Model-fitting first-order	47.2 (3.8%)	24.7 (-24.2%)	28.1 (28.1%)
	Model-fitting n _{Lig} =3	44.3 (-2.7%)	31.4 (-3.8%)	24.4 (11.3%)
	Model-fitting free-order	42.5 (-6.6%)	32.5 (-0.3%)	25.0 (14.2%)
Wheat straw Hull (WS-H)	<i>Literature^c</i>	<i>45.5 ± 1.4</i>	<i>32.6 ± 2.5</i>	<i>21.9 ± 1.0</i>
	Deconvolution	47.4 ± 1.0 (4.2%)	18.7 ± 1.8 (-42.6%)	33.9 ± 1.2 (54.8%)
	Model-fitting first-order	43.2 (-5.0%)	32.1 (-1.4%)	24.6 (12.5%)
	Model-fitting n _{Lig} =3	41.7 (-8.4%)	31.7 (-2.9%)	26.7 (21.8%)
	Model-fitting free-order	39.0 (-14.3%)	31.5 (-3.4%)	29.5 (34.7%)

a: Sourced from the Phyllis2 database (www.phyllis.nl), using 4 samples.

b: Obtained using a free-order model-fitting method for simultaneous kinetic and lignocellulosic determination. Source: [183].

c: Sourced from the Phyllis2 database (www.phyllis.nl), using 19 samples.

3.3. Thermogravimetry for the estimation of kinetic parameters

This section presents data published in MDPI Energies [175].

Determination of the shape of a degradation curve from thermogravimetry using Arrhenius parameters can be elusive due to the often unpredictable effect of small changes in the values of said parameters. In this section, the curves obtained using the isoconversional methods, and the curve-fitting methods are overlapped with the da/dT curve for the sake of comparison [175]. The values of the curve-fitting methods presented are obtained by simultaneous fitting with all curves of the same material. All numeric values can be found in Appendix B, as well as the graphical demonstration of the model-fitting procedures.

The kinetic parameters obtained using all methods are collected in Table 3.4 (cellulose), Table 3.5 (hemicellulose), and Table 3.6 (lignin).

Table 3.3: Fit error of the da/dT curves produced using kinetics determination methods in simultaneous comparison with all experimental da/dt curves. Source: [175].

Method	Beech Wood Powder	Wheat Straw Powder	Wheat Straw Hull
KAS $n_3=1$	17.0% \pm 1.8%	19.4% \pm 2.8%	21.5% \pm 3.4%
KAS $n_3=3$	13.4% \pm 1.6%	15.9% \pm 2.8%	18.4% \pm 4.7%
FWO $n_3=1$	16.8% \pm 1.6%	19.9% \pm 4.0%	21.2% \pm 3.6%
FWO $n_3=3$	13.3% \pm 1.5%	16.6% \pm 3.3%	18.2% \pm 4.7%
Friedman $n_3=1$	19.4% \pm 1.1%	25.3% \pm 3.9%	24.2% \pm 6.2%
Friedman $n_3=3$	16.0% \pm 1.2%	22.3% \pm 4.5%	21.6% \pm 7.9%
First-order to all	3.9% \pm 2.0%	6.2% \pm 5.9%	9.6% \pm 8.9%
Third order to lignin ($n_3=3$)	3.5% \pm 1.4%	5.8% \pm 6.5%	8.8% \pm 9.3%
Free-order to all	2.9% \pm 0.6%	5.3% \pm 5.6%	8.1% \pm 9.5%

Table 3.3 shows the fit error between the experimental results and curves traced using the kinetic parameters obtained. At a first glance, it is clear that the curve-fitting methods lead to a lower error than the isoconversional methods, being determined directly from experimental data, with the lowest error being found using a free-order fitting, due to having the fewest optimization constraints. As seen in Table 3.6, the optimum found for the order of lignin is around 5 for wheat straw and 8 for beech wood; the intermediate position tested by setting the order of lignin to 3 (following Manyà et al. [205]) does lead to an improvement when contrasted to first-order modeling, but expectedly worse results than the free-order optimum. Phenomena of curve overlap should not be discarded when interpreting these values, which indicate the presence of concurrent reactions, thus lowering the estimated activation energy of each phenomenon.

Isoconversional kinetic parameters derived from powder samples (**Beech** and **WS-P**) are more similar to each other than with the hull sample (**WS-H**), at least partially attributable to differences in particle size and may be associated with heat/mass-transfer limitations because of unconventionally high sample sizes, or even with

the use of the DDTG method for peak identification. Despite leading to higher errors and substantially different kinetic parameters, the curves traced using the isoconversional parameters show similar graphic behavior and peak position.

Both methods can be regarded as complementary, and the difference in errors should not be enough to discard the use of isoconversional methods, as these are a viable low-effort alternative to determining degradation kinetics on lignocellulosic biomass. A graphic comparison is shown in Figure 3.3.

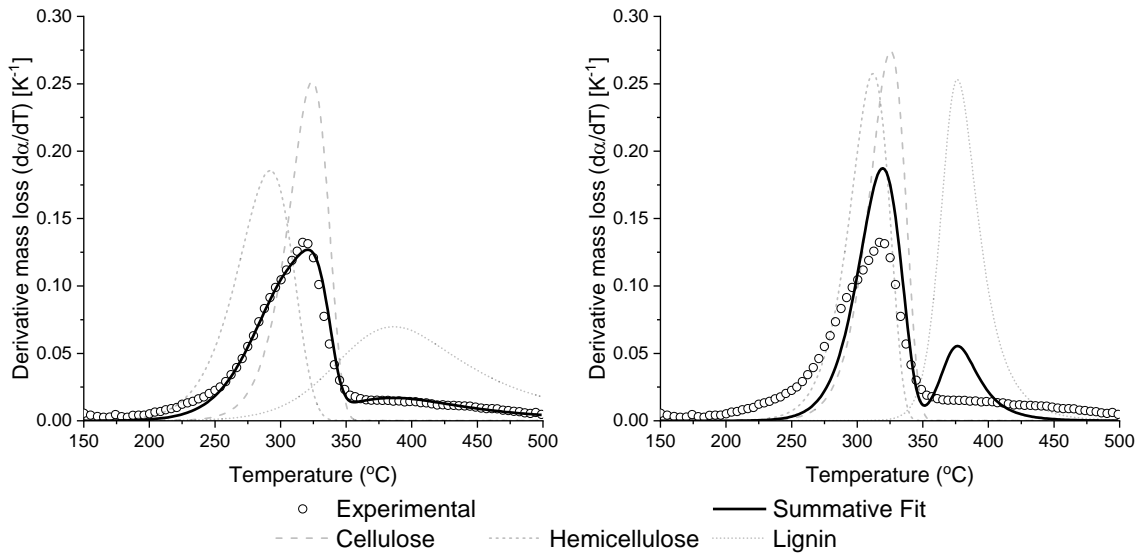


Figure 3.3: Comparison of the curve-fitting $n_3=3$ method (left) and the isoconversional KAS ($n_3=3$) method (right). Experimental data: DTG from WS-P, $10 \text{ K}\cdot\text{min}^{-1}$. Source: [175].

The ability to model beech wood is better than for any of the wheat straw particle sizes. This result is expected as detailed degradation schemes are often based on low-ash feedstocks like beech wood as references. The difference between powder and hull is consistently lower than 2%. Focused exclusively on the ability to model the degradation of the wheat straw hull (Table 3.7), the best results were found for models by Ranzi et al. [96], Corbetta et al. [130], and Ranzi et al. [133]. [175]

Modifications to the model accounting for the presence of inorganic content may lead to improvements. Trendewicz et al. [158] proposed alternative kinetic parameters for the degradation of active cellulose and the charrification of crystal cellulose as a function of the potassium content of the feedstock. Partially replacing the original cellulose degradation with this model led to important improvements to the modeling of wheat straw (Figure 3.5). While the estimation of beech wood improved marginally using experimental results, the experimental content of wheat straw (1.18 wt.%) is outside the validity range of the model, leading to inferior fits, as shown in Table 3.7; an *optimum* value was estimated within the constraints of the model, and the best results were found for the **RAC** and **C14** networks [175].

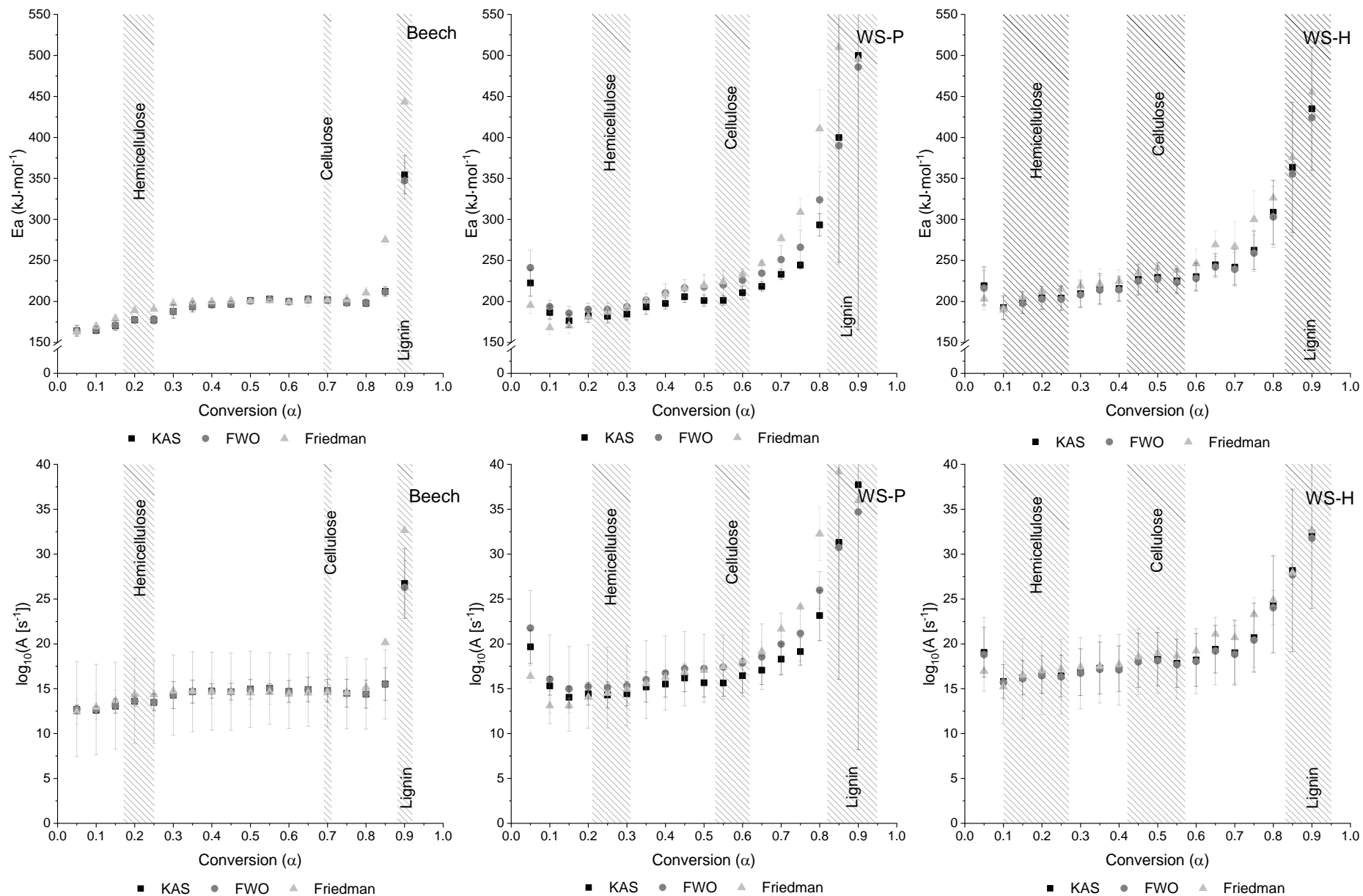


Figure 3.4: Kinetic parameters obtained using the isoconversional methods. Top: activation energy, bottom: pre-exponential factor. Values for higher conversions were disregarded. Source: [175].

Table 3.4: Peak values and kinetic parameters for the different feedstocks and different methods. Cellulose peak @ 10 K·min⁻¹. Source: [175].

		Beech Wood Powder			Wheat Straw Powder			Wheat Straw Hull		
		Peak Temperature (°C)	E _a (kJ/mol)	log ₁₀ [A(s ⁻¹)]	Peak Temperature (°C)	E _a (kJ/mol)	log ₁₀ [A(s ⁻¹)]	Peak Temperature (°C)	E _a (kJ/mol)	log ₁₀ [A(s ⁻¹)]
Cellulose	DTG Peak	357.3			318.2			319.4		
	Isoconversional KAS	355.9	201.4	14.75	325.5	206.9	16.12	323.5	226.6	17.97
	Isoconversional FWO	355.9	201.2	14.75	323.6	224.8	17.79	322.1	224.6	17.81
	Isoconversional Friedman	364.2	201.5	14.56	334.5	231.6	17.99	333.2	239.8	18.77
	Model-fitting First-order	353.1	198.4	14.55	323.3	185.2	14.24	325.0	191.6	14.78
	Model-fitting n ₃ =3	353.1	208.6	15.44	324.1	188.2	14.49	323.5	195.9	15.20
	Model-fitting Free-order	354.5	211.0	15.61	322.8	190.6	14.74	322.1	201.4	15.71
	KAS RR ^a		199.9							
	Model-fitting Free-order RR ^a	354.5	199.6	14.63						

a: Sourced from the aforementioned round-robin using the same equipment as that employed in the context of this work. [183]

Table 3.5: Peak values and kinetic parameters for the different feedstocks and different methods. Hemicellulose peak @ 10 K·min⁻¹. Source: [175].

	Beech Wood Powder				Wheat Straw Powder				Wheat Straw Hull			
	T Peak (°C)	E _a (kJ/mol)	log ₁₀ [A(s ⁻¹)]	Order	T Peak (°C)	E _a (kJ/mol)	log ₁₀ [A(s ⁻¹)]	Order	T Peak (°C)	E _a (kJ/mol)	log ₁₀ [A(s ⁻¹)]	Order
DTG Peak	298.2				283.2				279.8			
Isoconversional KAS	326.8	178.3	13.59	1	312.0	183.7	14.43	1	304.3	203.6	16.51	1
Isoconversional FWO	324.0	178.5	13.61	1	309.9	192.2	15.28	1	304.3	202.2	16.39	1
Isoconversional Friedman	336.4	190.1	14.34	1	320.6	189.1	14.67	1	312.5	211.4	16.95	1
Model-fitting First-order	298.9	136.3	10.41	1	289.0	125.5	9.58	1	288.8	147.3	11.68	1
Model-fitting n₃=3	297.5	139.3	10.72	1	292.3	119.8	8.96	1	287.4	147.6	11.72	1
Model-fitting Free-order	288.8	156.2	12.55	1.62	287.9	138.8	10.87	1.74	286.0	172.5	14.14	1.48
KAS RR^a		185.7		1								
Model-fitting Free-order RR^a	296.1	161.7	12.86	1.79								

a: Sourced from the aforementioned round-robin using the same equipment as that employed in the context of this work. [183]

Table 3.6: Peak values and kinetic parameters for the different feedstocks and different methods. Lignin peak @ 10 K·min⁻¹. Source: [175].

	Beech Wood Powder				Wheat Straw Powder				Wheat Straw Hull			
	T Peak (°C)	E _a (kJ/mol)	log ₁₀ [A(s ⁻¹)]	Order	T Peak (°C)	E _a (kJ/mol)	log ₁₀ [A(s ⁻¹)]	Order	T Peak (°C)	E _a (kJ/mol)	log ₁₀ [A(s ⁻¹)]	Order
DTG Peak	390.2				366.7				369.5			
Isoconversional KAS	390.5	423.9	31.65	1	377.1	434.2	33.20	1	375.5	387.5	29.49	1
	389.2			3	376.3			3	374.1			3
Isoconversional FWO	390.5	413.2	30.82	1	387.4	430.0	32.31	1	371.2	378.5	28.97	1
	389.2			3	386.1			3	369.9			3
Isoconversional Friedman	408.8	508.3	37.26	1	394.4	506.8	38.00	1	400.7	404.0	29.58	1
	408.8			3	394.2			3	399.3			3
Model-fitting First-order	444.2	58.2	1.60	1	421.4	54.4	1.45	1	411.7	69.7	2.79	1
Model-fitting n₃=3	351.8	105.0	6.43	3	386.1	119.9	7.20	3	369.9	126.0	7.96	3
Model-fitting Free-order	304.7	222.6	18.09	7.73	376.6	160.5	10.71	4.93	356.2	185.9	13.26	5.68
KAS RR^a		412.6										
Model-fitting Free-order RR^a	397.1	347.6	25.17	7.26								

a: Sourced from the aforementioned round-robin using the same equipment as that employed in the context of this work. [183].

b: Peak outside of the temperature limits for this work.

Table 3.7: Mass loss and derivative fits for the best performant reaction networks versus experimental data (WS-H, 10 K·min⁻¹), including estimation of hypothetical optimum potassium contents to model the degradation profile. Source: [175].

	K-content	Mass loss fit	Derivative fit
R08	Original	5.7%	21.5%
	Experimental	16.3%	34.1%
	<i>Optimum = 0.071 wt.%</i>	7.1%	15.7%
C14	Original	10.4%	20.6%
	Experimental	13.3%	26.7%
	<i>Optimum = 0.086 wt.%</i>	6.6%	12.8%
RAC	Original	6.0%	25.2%
	Experimental	12.0%	28.1%
	<i>Optimum = 0.393 wt.%</i>	5.6%	10.7%
R17	Original	7.6%	26.1%
	Experimental	16.4%	34.8%
	<i>Optimum = 0.119 wt.%</i>	8.1%	13.8%

*: Including modifications and charring estimations by Pecha et al. [24].

The model presented by Trendewicz et al. [158] is, however, intrinsically unviable to model pyrolysis phenomena for real biomasses, not only due to a very short validity range (1 wt.%) but also due to have been designed using isolated cellulose and potassium impregnation. Possible improvements of this model pass by testing with larger ranges, more metals (see section 2.2.4), or even whole biomasses/different lignocellulosic fractions.

Implementation of the Trendewicz [158] model can be achieved by replacing the cellulose portion of a reaction network (see Appendix C) with the reaction paths and kinetics found in Table 3.8. Between different feedstocks, the authors assumed only the energies of activation change.

Table 3.8: Reaction network from Trendewicz et al. [158] for the degradation of cellulose. 'Beech' represents a potassium content of 0.13 wt.% and 'Wheat Straw' represents a potassium content of 1.21 wt.%. Source: [175].

Group	#		Beech	Wheat Straw	log ₁₀ [A (s ⁻¹)]	T ⁿ
			E _a (kJ/mol)	E _a (kJ/mol)		
Cellulose	1	From original network				
	2	$CELLA \rightarrow 0.8 \text{ HAA} + 0.2 \text{ GLYOxAL} + 0.1 \text{ ACETALDY} + 0.25 \text{ HMF} + 0.3 \text{ ACETONE} + 0.21 \text{ CO}_2 + 0.1 \text{ H}_2 + 0.4 \text{ FORMALDY} + 0.16 \text{ CO} + 0.83 \text{ WATER} + 0.02 \text{ FORMICAC} + 0.61 \text{ C}$	96.28	100.44	9.58	0
	3	$CELLA \rightarrow LEVOGLUC$	104.33	120.10	9.42	0
	4	$CELL \rightarrow WATER + 3 \text{ C} + 2 \text{ CO} + \text{CO}_2 + 4 \text{ H}_2$	133.61	123.90	9.30	0

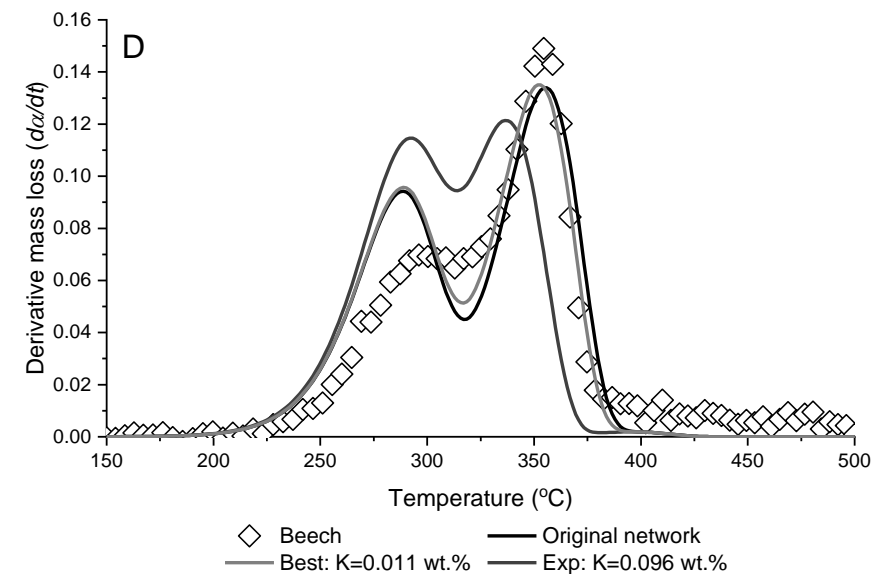
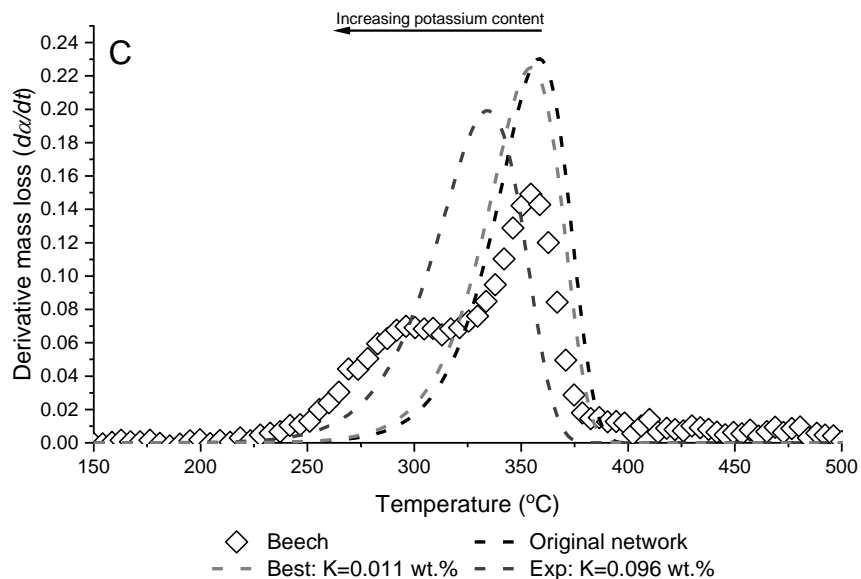
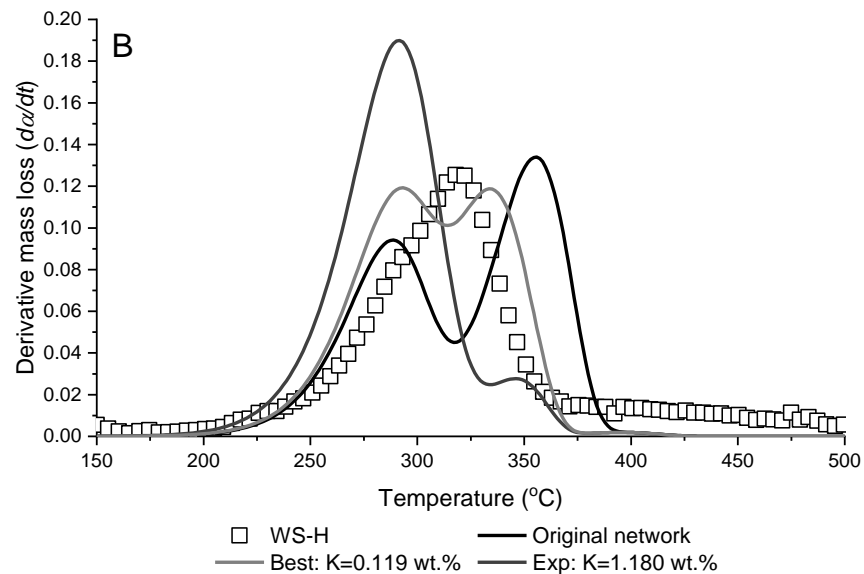
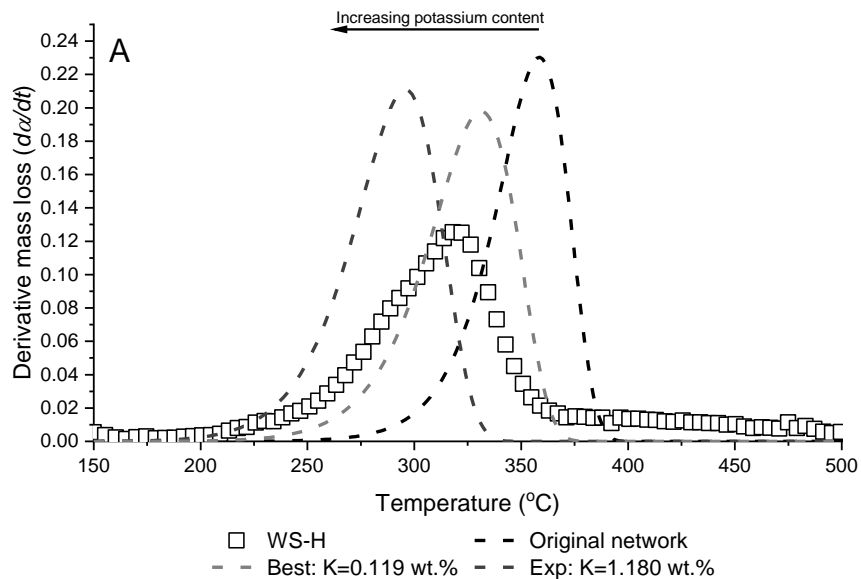


Figure 3.5: Comparison of the experimental derivative degradation curves with the predictions by the R17a model [133] modified using the Trendewicz model [158] assuming three different potassium contents. A: cellulose curves against WS-H experimental degradation; B: summative curves against WS-H experimental degradation; C: cellulose curves against Beech experimental degradation; D: summative curves against Beech experimental degradation. Source: [175].

4. Modeling of the pyrolysis process

The implementation of a model for any kind of processual situation, allows for the carrying out of sensitivity analysis and testing of hypothesis, without the investment or analytical costs usually associated with the design or modification of an industrial unit. A schematic of the process to be modeled is shown in Figure 4.1.

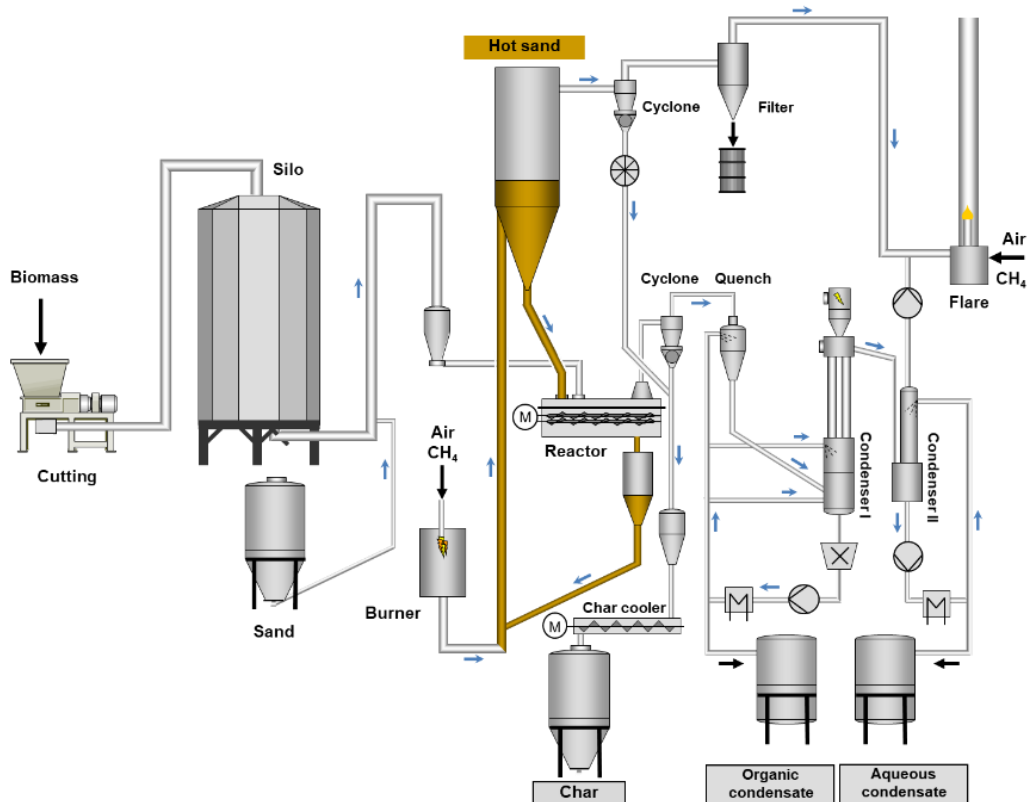


Figure 4.1: Schematic of the *bioliq*® I process materialization.

Prior to the materialization of the *bioliq*® concept, an Aspen Plus™ model had already been developed *in-house* by Treppe et al. [289], to perform techno-economic studies and estimate energetic efficiency. Said model consisted of simplified representations of the system, avoiding the complexity of the liquid phases by modeling only gases and pseudo-components.

The first iteration of the current model was developed in the context of a Master Thesis [290] that took place between IDMEC-IST, Technical University of Lisbon, Portugal, and IKFT-KIT, Eggenstein-Leopoldshafen, Karlsruhe, Germany. This is a descriptive model, for which trials were conducted at the Python-PDU using three different moisture contents (1.1, 9.2, 24.0 wt.%) and two different sweeping gas (N_2) flow rates for the 9.2 wt.% moisture feedstock ($1.3 \text{ Nm}^3 \text{ h}^{-1}$ to $3.2 \text{ Nm}^3 \text{ h}^{-1}$), to help identify whether the vapor residence time at the reactor has any effect on process behavior and product distribution, and which results have been published in an article [5].

The second interaction of the model moves away from a descriptive model of a snapshot version of the process, intending to function as a predictive model. For that, black box models for reaction are disregarded in favor of reaction networks, followed by the definition of secondary and aging reaction phenomena to bridge the gap between the product distribution considered in reaction networks, and the experimental composition of the condensates. A great focus was put on the definition of condensate surrogate mixtures that contain components on both sides of the gap, and the thermophysical characterization of said components. Development of pyrolysis models in Aspen Plus™ in the context of this document assumes steady-state conditions. No custom unit blocks have been developed, and any modifications to the default operation of blocks or streams were made using FORTRAN routines or design specifications. The final model presented in this document makes heavy use of hierarchies, unit blocks that contain models within themselves, as shown in Figure 4.2, and the different hierarchies are detailed in the following subsections. Process values taken from previous *bioliq*® campaigns are processed and used as input values and can be found in Appendix A.

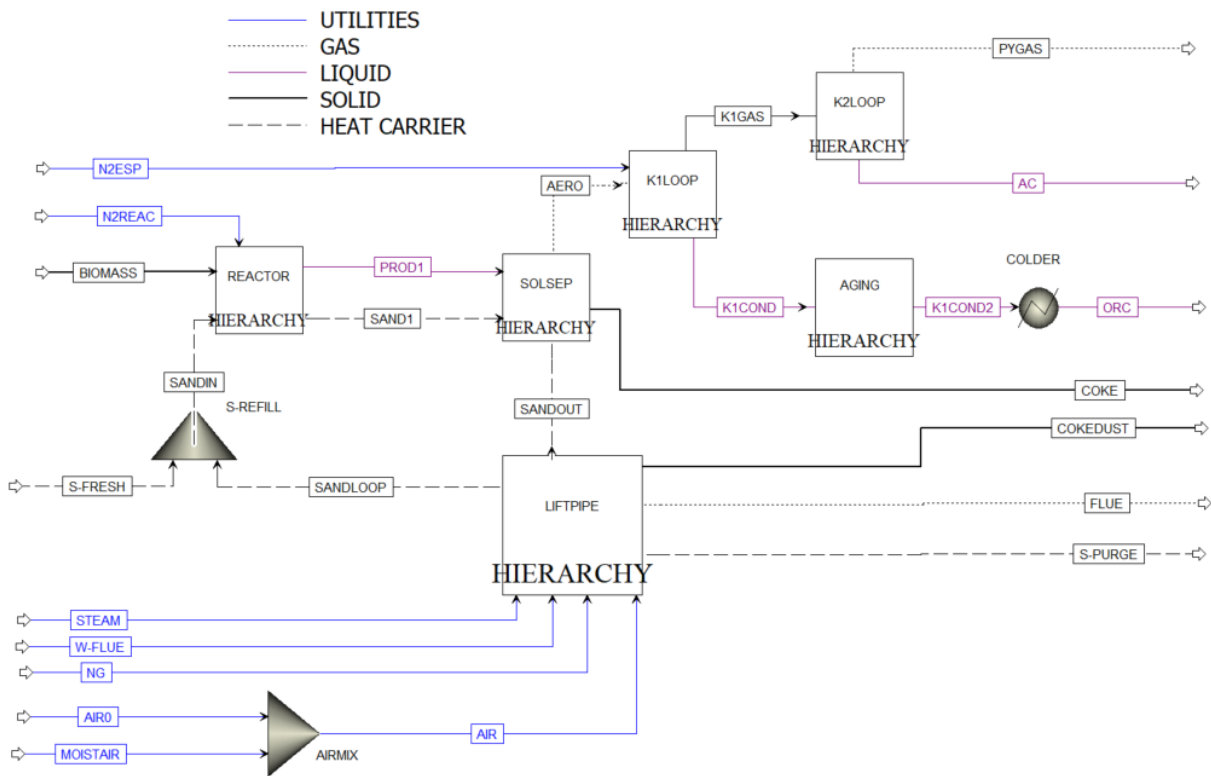


Figure 4.2: Main flowsheet of the model in Aspen Plus™ V12. Blue streams correspond to utilities (steam, water, natural gas, sweeping nitrogen, air); dotted streams correspond to gas streams; purple streams to liquid streams, and thick streams to solid products. Heat carrier (sand) is represented by dashed lines, including loop purges and make-up streams.

4.1. Auxiliary calculations

4.1.1. Characterization of the reactor

The core of a chemical process is the reactor. In the case of the *bioliq*[®] I unit, said core is a twin-screw reactor, in which heat demand is supplied by a heat carrier loop that is constituted by two containers, one before and one after the reactor, which are connected by a liftpipe. The liftpipe employs hot flue gas from a natural gas furnace to reheat the spent heat carrier while providing pneumatic transport. Two additional injections of steam (superheated at 5 bar) help control temperature and transport conditions.

The reaction products exit the reactor through the top, and sweeping gas (N₂) is employed to ensure proper removal. A fraction of the formed coke is not entrained and integrates the heat carrier loop. The majority of the coke is removed using a cyclone immediately downstream from the reactor.

Henrich et al. [31] estimated the Bodenstein number of a reactor similar in operation to the one under study in this document ($Bo = uL/D_{ax}$, in which u stands for the solid flow velocity, L for the length of the reactor and D_{ax} for the axial dispersion coefficient); this number describes the ratio of the amount of substance introduced in a reaction volume by convection to that introduced by diffusion, and can be used to characterize the backmixing in a system. Low values ($Bo < 50$) correspond to preponderant backmixing, hence favoring modeling using CSTRs; high values ($Bo > 50$) indicate diminutive backmixing, hence favoring modeling using PFRs [287]. For a mixture of 600 kg/h of steel balls and wheat straw (50:1), the authors [31] reported a Bo of 121 as the best fit to model the residence time distribution studies, indicating that a plug flow reactor model (PFR) should suffice.

Reactor energy supply

The Python-PDU employs steel balls as heat carriers (1.5 mm, bulk density 4600 kg/m³) at a rate of approximately 50:1 HC to feedstock fed into the reactor [31,286]. The current materialization of the *bioliq*[®] I unit employs quartz sand (1 mm, specific gravity **1.4-1.7** [291]) at an unknown feed rate. More recent internal studies by the *bioliq*[®] I team attempted to quantify this value. During operation, the flow rate of the heat carrier to the liftpipe is controlled based on the filling level of both collecting bins placed up- and downstream from the reactor. A linear regression between the filling level of the bottom bin (Φ) and the flow rate (F_{HC}) was obtained, shown in Eq. (4-1). Based on a Φ of 55%, a value of 5112 kg/h was obtained, equivalent to a HC:feedstock ratio of **14.4:1** (based on a feedstock feed rate of 355 kg/h, see Appendix A), lower than the supposed 50:1. More operation data can be found in Appendix B.

$$F_{HC} \left[\frac{kg}{h} \right] = 56.651 \times \Phi[\%] + 1990.2, R^2 = 0.97 \quad (4-1)$$

It is important to keep in mind that neither in the current *bioliq*[®] materialization nor in the Python-PDU, is there a completely definite way to measure the energy consumption of the reactor part. In the former, heat is provided to the biomass particles via direct contact with sand (the heat carrier), which is heated mostly by flue

gases from a natural gas furnace, plus a controllable contribution of chars that are dragged by the heat carrier. In the case of the Python-PDU, the latter, heating of the heat carrier, steel beads, happens exclusively electrically, and the reactor bed is also electrically heated. Better descriptions of the mechanism can be found in [287].

Several methods to estimate the specific energy demand of the pyrolysis process have been devised. Yang et al. [292] propose a simple energy balance accounting for the heat potential of the products and biomass and proposes a method to estimate the heat capacity of the different products. On the other hand, Polin et al. [293] or Henrich et al. [31] analyze factors like temperature and electrical consumption to estimate the energy loss of the process; assuming energy losses are null, the value can be used to estimate the energy demand of the process. Polin et al. [293] propose a range of 0.75-1.75 MJ·kg⁻¹ for woody biomasses, while Zheng et al. [294] reached a range of 1.16-3.06 MJ·kg⁻¹ for wheat straw in the context of an LCA analysis.

Henrich et al. [31] studied the process using a twin-screw reactor similar to the one currently discussed, and proposes a value of 1.25 MJ·kg⁻¹ before accounting for the moisture content of biomass, corresponding to a value of 1.45 MJ·kg⁻¹ for the wheat straw presented in Table 2.1. Employing the logic proposed by Yang et al. [292], based on experimental mass balance data (section 5.1), one can reach a specific energy demand of 1.10 MJ·kg⁻¹ for the wheat straw process.

However, if one considers the heat carrier as the single energy source in the process, assuming the process is adiabatic, one can perform an energy balance to this heat carrier based on the temperature drop experienced (see Appendix B), a value of 49.0±2.4 °C according to bioliq® campaign data. The heat capacity was assumed to be that of quartz sand (0.80 kJ·K⁻¹·kg⁻¹), leading to a value of 55.60±2.72 kW assuming a ratio of 14.4:1, and 193.07±9.46 kW assuming the originally presumed 50:1 ratio, corresponding to specific energy demands of 0.56 MJ·kg⁻¹ and 0.14 MJ·kg⁻¹, respectively. This value is around a third of the value estimated by Henrich et al. [31], indicating that about two-thirds of the energy potential of the heat carrier loop is not effectively transferred to the biomass.

Reactor dimensions

While the dimensions of the current materialization of the bioliq® reactor are known, the residence time of both phases (solid and gas) is unknown. The reactor has a total length of 2030 mm and a volume of 210 dm³ (after discounting the screws), corresponding to a diameter of **362.5 mm**, and operates at a filling grade of around 70%. Of this original length, the first 430 mm are dedicated to the conveying of the heat carrier, followed by a reaction section of **1253.1 mm** of mixing with the biomass until the product gas is recovered and the heat carrier is recycled, corresponding to a volume of **129.4 dm³**.

The solid flow rate of biomass and heat carrier is assumed to be 15.4 × 360 kg·h⁻¹, or 5544 kg·h⁻¹ = 1.54 kg·s⁻¹. Assuming the solid occupies a volume equal to its filling grade, the cross-section of the solid fraction is estimated at around 90.5 dm², corresponding to a solid residence time of **258.4 s**. Kornmeyer [287] performed residence time tests in a model reactor similar to the *bioliq*® I materialization, assuming a feedstock flow rate of 12.89 kg·h⁻¹ and a 50:1 excess heat exchanger flow rate, and reached a residence time of **9.1 s**. Assuming the

solid occupies a volume equal to its filling grade, the cross section of the solid fraction is estimated at around 90.5 dm², corresponding to a solid residence time of **76.8 s** (assuming a flow rate of 360 kg·h⁻¹, and a heat carrier flow rate of 5184 kg·h⁻¹). The vapor residence time is unknown but assumed to be around **1.5 s**, as no tests as of yet have been conducted in either reactor at operating conditions for the vapor residence time and its dependence on the sweeping flow rate.

In the context of Bo number and residence time estimation, Kornmeyer [287] provided residence time distribution profiles (Figure 4.3). The profile with a Bo number of 121 was compared with CSTR-in-series abstractions (Eq. (4-2), [295]), with the results indicating a series of 22 reactors. This value is considered inviable for simulations using Aspen Plus™ and computationally demanding reaction networks such as the ones employed in this one (section 4.3).

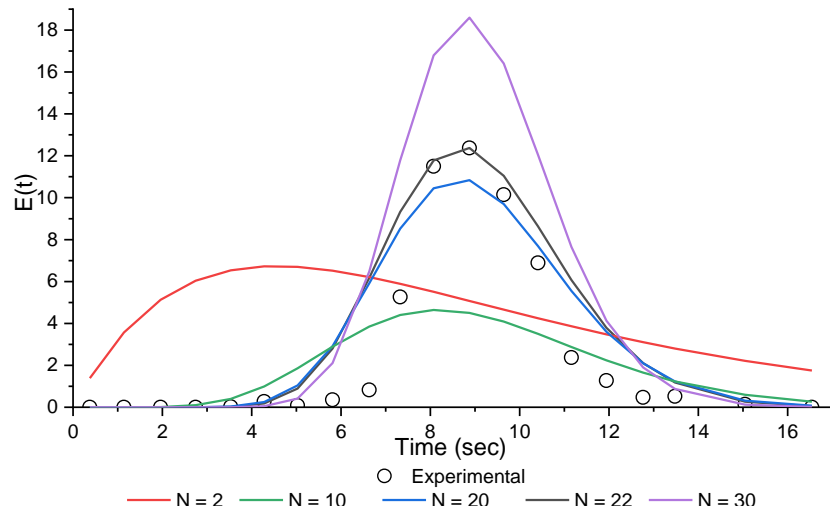


Figure 4.3: Comparison of $E(t)$ profiles of an experimental residence time test and N CSTR-in series approaches. $\tau = 9.1$ s. Source of experimental data: [287].

$$\frac{C_{out}}{C_{in}} = \frac{N^N}{(N-1)!} \left(\frac{t}{\tau}\right)^{N-1} e^{-\frac{N}{\tau}t} \quad (4-2)$$

4.1.2. Characterization of the condensation loops

After exiting the reactor, the mostly gaseous product enters the first condensation loop (refer to Figure 4.1). This is comprised of a quenching unit, a condenser unit, a homogenizer, a pump, and a set of two spiral heat exchangers in series. The loop is constituted by two loops, both making use of the condenser bottoms, which are homogenized and cooled down, with one fraction of the cooled condensate being channeled to the condenser unit as showers, and the other fraction being used to quench the incoming gases. The condenser is equipped with an electrostatic precipitator which employs an electric field to promote the coagulation of droplets forming an aerosol and makes use of a sweeping gas injection. A more complete characterization of the condensation and aerosol formation phenomena can be found in [258]. One of the most important control parameters during operation is a water content of **12 wt.%** in the column bottoms (a collection port is available for sampling and emptying), which is controlled by adjusting the heat exchanger output temperature.

The gas stemming out of the electrostatic precipitator is channeled to the second condensation loop. This is comprised of a condenser unit, a pump, and two parallel heat exchangers. Contrary to the first condensation loop, this one does not feature a quench system, with the entirety of the gas quenching proceeding within the condenser making use of cooled bottoms. The column tops (pyrolytic gas) are passed through a demister to recover entrained droplets, characterized using online gas chromatography, and channeled to a flare.

Fonseca et al. [5] attempted to integrate a hypothetical dryer (9.1 wt.% to 1.1 wt.% moisture) to be placed upstream from the feedstock silo (or directly upstream the reactor feed). The authors were able to make use of a fraction of the first condenser heat duty (23% of 107 kW) due to its hypothetically usable temperature range (90-84 °C), assuming a drying temperature of 80 °C. Due to a very low-temperature range (30-28 °C), the heat potential of the second condenser heat exchangers (62 kW) was considered unusable.

4.1.3. Definition of a condensate surrogate mixture

The definition of a correct surrogate mixture for the different condensates is important for the initialization of the condensation loops, but also for the characterization of the mixture and possible parallel utilizations of the products.

In the *bioliq*[®] pilot plant, both condensates are recycled to quench incoming vapors. The organic condensate is recycled at 80-90 °C with a mean residence time of around 6±1 h [63]. The combination of looping and moderate temperatures is believed to result in the aging of the condensate, meaning the components constituting the pyrolysis vapors may not be the same present on the final process mass balance. The elemental composition of this mixture is C 54.8%±0.6%, H 7.5%±0.4%, O 37.6%±0.4% (N/S contents were neglected (<1 wt.%) to simplify the surrogate), based on the product distribution of the *bioliq*[®] (campaigns 2015-2018) and associated analytics.

Table 4.1: Composition of the condensates (wt.%) based on averaged data from the *bioliq*[®] campaigns 2015-2018.

	Water	Solid	Organics	Unknown	Glycol
Organic Condensate	13.47%	11.99%	20.61%	52.77%	1.14%
Aqueous Condensate	80.82%	-	14.82%	3.88%	0.48%

Table 4.1 shows the composition of the two condensates obtained during normal operation. The number of unknowns, i.e., the fraction not characterizable using GC/MS (section 2.4.3), amounts to the majority of the dry-solid-free fraction of the organic condensate. Regarding the aqueous condensate, the majority is water, it is assumed that there are no solids present, and the unknown phase is disregarded during simulation. (Ethylene) Glycol is assumed to be the fraction of these compounds left in the condensation loop once a steady state is achieved after it has been mostly replaced by pyrolysis products.

The phenomenon of isomers having similar GC/MS signatures must be kept in mind. For example, hydroxyacetaldehyde (HAA, an aldehyde) is a common product in several networks and presents an m/z of 79 amu, as well as being an isomer of acetic acid (Figure 4.4). [296]

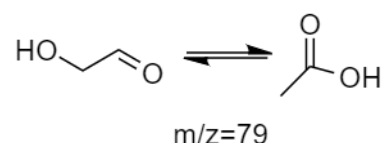


Figure 4.4: Isomerization of HAA to acetic acid.

New surrogates (Table 4.2) are then compiled from GC/MS data and proposed for the first and second *bioliq*[®] condensates, using the same possible composition. This surrogate is a trimmed-down list that includes only one representative molecule for a component family, except for aliphatic ketones (acetol and 3-methylcyclopentanone), furans (furfural and HMF), and guaiacols (guaiacol and vanillin). The nature of the heavy fraction is described in detail in the following sub-section.

Table 4.2: Proposed surrogate for the *bioliq*[®] I condensates using wheat straw. Based on data from the *bioliq*[®] campaigns 2015-2018.

	ID	Formula	CAS	ORC		AC	
				wt.	mol. ^a	wt.	mol.
Water	WATER	H ₂ O		13.12%	73.19%	84.38%	95.10%
Acetic Acid	ACETICAC	C ₂ H ₄ O ₂	64-19-7	5.90%	9.87%	5.55%	1.88%
Ethylene Glycol Monoacetate	EGACET	C ₄ H ₈ O ₃	542-59-6	0.02%	0.02%	0.09%	0.02%
Methanol	METHANOL	CH ₄ O	67-56-1	0.00%	0.00%	0.98%	0.62%
Formaldehyde	FORMALDY	CH ₂ O	50-00-0	0.00%	0.00%	0.00%	0.00%
Acetaldehyde/HAA	HAA	C ₂ H ₄ O ₂	141-46-8	0.46%	1.04%	0.20%	0.09%
Ethylene Glycol	EG	C ₂ H ₆ O ₂	107-21-1	1.11%	1.80%	0.06%	0.02%
Acetol/Acetone	ACETOL	C ₃ H ₆ O ₂	116-09-6	4.64%	6.29%	6.36%	1.74%
3-Methylcyclopenten-2-one	METC5ONE	C ₆ H ₈ O	14963-40-7	1.73%	2.12%	1.13%	0.28%
Furfural	FURFURAL	C ₅ H ₄ O ₂	98-01-1	0.89%	0.93%	0.73%	0.15%
Phenol	PHENOL	C ₆ H ₆ O	108-95-2	1.17%	1.25%	0.18%	0.04%
Guaiacol	GUAIACOL	C ₇ H ₈ O ₂	90-05-1	0.78%	0.63%	0.24%	0.04%
Vanillin	VANILLIN	C ₈ H ₈ O ₃	121-33-5	0.50%	0.33%	0.01%	0.00%
Syringol	SYRINGOL	C ₈ H ₁₀ O ₃	91-10-1	1.53%	1.00%	0.10%	0.01%
Levoglucosan	LEVOGLUC	C ₆ H ₁₀ O ₅	498-07-7	2.46%	1.52%	--	--
Heavy Fraction ^b	--			61.15%	--	--	--
Coke ^c	--			11.68%	--	--	--

a: Value estimated disregarding the presence of the heavy fraction

b: Identity discussed in the following sub-section.

c: The solid fraction comprises several species and depends on the decision of the reaction network (section 4.3.1).

Deciding between these three approaches to model the heavy fraction has ties with the thermodynamic property model, and will be discussed in section 4.1.4.

High molecular weight surrogate

As discussed in section 2.4.3, several strategies have been developed to model the high molecular weight surrogate. The section contrasted the absence of a surrogate (e.g. [5]), a single surrogate (e.g. [273]), the surrogate based on the description by Scholze et al. [82] (Figure 2.22)), and a tripartite surrogate (e.g. [253])

Ille et al. [273] studied mixtures similar to the ORC obtained using fast pyrolysis of wheat straw. For a water mass fraction of 14.98 wt.% in the mixture, the authors report an experimental activity coefficient for a water of 1.540, as well as a calculated value of 1.441, when using 3,4,4'-biphenyltriol as a surrogate for the FPBO heavy fraction, when operating at 70 °C.

Apart from these species, it is important to include compounds that take part in the reaction network but are not detected using GC/MS, such as the ones presented in Table 4.3.

Table 4.3: Other relevant components that may take part in liquid-vapor equilibrium.

	ID	Formula	CAS
Acetaldehyde	ACETALDY	C ₂ H ₄ O	75-07-0
Acetone	ACETONE	C ₃ H ₆ O	67-64-1
Acrolein	ACROLEIN	C ₃ H ₄ O	107-02-8
Anisole	ANISOLE	C ₇ H ₈ O	100-66-3
p-Coumaryl Alcohol	CMRYLALC	C ₉ H ₁₀ O ₂	3690-05-9
p-Cresol	CRESOL	C ₇ H ₈ O	106-44-5
Ethanol	ETHANOL	C ₂ H ₆ O	64-17-5
Linoleic Acid	FFA	C ₁₈ H ₃₂ O ₂	60-33-3
Formic Acid	FORMICAC	CH ₂ O ₂	64-18-6
Glyoxal	GLYOXAL	C ₂ H ₂ O ₂	107-22-2
n-Hexadecane	HEXADEC	C ₁₆ H ₃₄	544-76-3
5-Hydroxymethylfurfural	HMF	C ₇ H ₈ O ₃	67-47-0
Ethenone	KETENE	C ₂ H ₂ O	463-51-4
Levoglucosan	LEVOGLUC	C ₆ H ₁₀ O ₅	498-07-7
5-Methylfurfural	MF	C ₆ H ₆ O ₂	620-02-0
Synapaldehyde	SYNAPALD	C ₁₁ H ₁₂ O ₄	2316-26-9
Vinylketene	VINYLKET	C ₄ H ₄ O	50888-73-8
Xylosan	XYLOSAN	C ₅ H ₈ O ₄	89-91-8

4.1.4. Decision on property model

Within the premises of this doctoral work, Fonseca et al. [297] performed a study using 28 different property methods (a combination of a vapor-phase and liquid-phase method), to estimate deviations in the estimation of the liquid-phase mass flow, as well as the water and guaiacol content. Four different fractionated condensation systems (simple flash distillation, atmospheric pressure) from the literature [5,298–300] were considered, and surrogate mixtures were designed based on GC/MS data reported on each reference. The authors reported the lack of thermophysical property data and binary interaction parameters as important deterrents, thus favoring the use of UNIFAC [301,302] variants that require solely the division of relevant molecules to structures.

Unbeknownst to the authors of the aforementioned work, Aspen Plus™ [297] is able to estimate binary parameters for several thermodynamic models based on the UNIFAC molecular structure division, including UNIQUAC [303,304], NRTL [305], the Wilson [306] model and the Soave-Redlich-Kwong (SRK) [307] model. On the other hand, the Wong-Sandler (WS) [308] and Huron-Vidal (MHV2) [309] mixing rules, applicable to equation of state models, employ UNIFAC structures to estimate binary parameters; the same logic is employed by the Predictive SRK [310] model, but using a different algorithm.

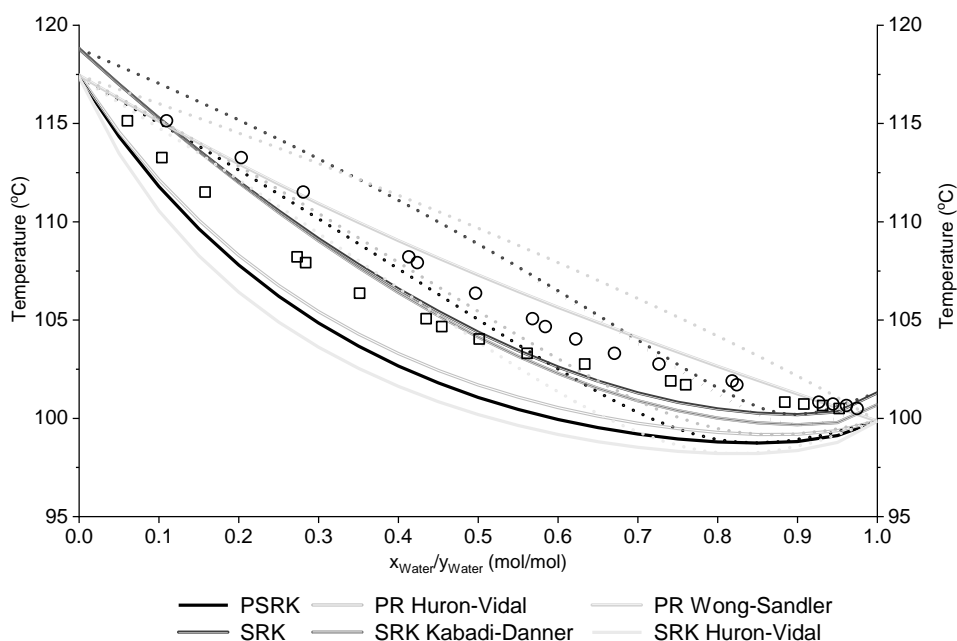


Figure 4.5: T - xy plots for the binary mixture Water-Acetic Acid, at 4 different pressures. Symbols stand for experimental data. Dashed lines stand for dew point curves. Source of experimental data: [311,312].

The most common way to evaluate the usefulness of a vapor-liquid equilibrium model is to compare experimental VLE data with the curves produced by said models, for which an example is provided in Figure 4.5. The comparison was made for a set of binary mixtures featuring oxygenates at different pressure and temperature conditions, based on experimental data from several sources. The results presented in Table 4.4 presents the deviations between estimated and experimental T - xy / P - xy , and the lowest average deviations are found

when using the SRK model modified using the Kabadi-Danner (KD) mixing rules, followed by either the PR or SRK models with Wong-Sandler mixing rules (PR-WS).

Studies of which thermodynamic property model to use has ties with the composition of the surrogate mixture. A study of several models was performed in Aspen Plus™ using the surrogate mixtures presented in Table 4.2, but considering three options for heavy fraction surrogates: 3,4,4'-biphenyltriol [246], the surrogate designed based on the description by Scholze et al. [97] (Figure 2.22), and the three component approach by Pires et al. [272] using a custom pyrolytic lignin based on the findings by del Río et al. [283], whilst keeping the original humin and hybrid oligomer surrogates. The tests were performed using one-step atmospheric flash distillation operated at 86 °C (ORC) and 30 °C (AC), and no quenching phenomena were considered, and the results were presented in Appendix D.

The results in general favor the use of equation-of-state models for the system under study. At the chosen operational conditions, activity coefficient methods fail to predict the existence of an aqueous condensate, and predict organic-rich condensates comprised almost exclusively by the heavy surrogate, regardless of the choice of heavy surrogate. This result mimics results presented by Fonseca et al. [4,304], although in such cases heavy surrogates were not considered, and may imply a fault of the method/software (Ille et al. [246] did employ flash calculations) or the wrong choice of the unit block.

Table 4.4: Average deviations between predicted T-xy/P-xy values and experimental values.

Pair (i-j)	Source Exp. Data	Predictive SRK [310]	SRK [307]	SRK Kabadi Danner [307,313]	SRK Huron Vidal [307,309]	PR Huron-Vidal [309,314]	PR Wong-Sandler [308,314]
Water – Acetic Acid	[311,312]	3.5%	3.8%	3.8%	4.3%	2.7%	1.7%
Acetone - Water	[315,316]	5.7%	12.4%	12.2%	7.9%	4.6%	5.9%
Methanol – Water	[317,318]	5.6%	4.4%	4.2%	5.5%	4.0%	4.3%
Phenol – Water	[319,320]	176.4%	147.3%	75.3%	24.7%	193.3%	76.6%
Acetaldehyde – Water	[321,322]	49.9%	39.9%	27.4%	37.0%	36.0%	42.4%
Acetaldehyde – Acetic Acid	[323]	17.2%	9.6%	9.6%	11.4%	15.1%	13.9%
Acetic Acid – Methanol	[324,325]	35.5%	36.4%	36.4%	35.3%	35.6%	35.8%
Acetone – Phenol	[326,327]	24.0%	274.6%	29.2%	44.0%	20.6%	28.8%
Acetone – Methanol	[328–331]	28.2%	22.9%	18.6%	3.6%	26.7%	23.5%
Acetaldehyde – Acetone	[332,333]	42.6%	35.8%	35.8%	17.9%	42.8%	40.0%
Acetic Acid – Furfural	[334]	2.5%	1.2%	2.4%	1.4%	2.4%	2.3%
Furfural – 5-methylfurfural	[334,335]	32.4%	23.3%	21.9%	34.1%	23.0%	24.8%
Guaiacol – Anisole	[336]	45.9%	47.2%	47.2%	36.7%	46.2%	46.3%
Guaiacol – Ethanol	[337]	10.2%	11.2%	11.2%	2.7%	13.1%	13.3%
Average		20.7%±4.1%	20.4%±3.6%	18.7%±3.2%	19.0%±4.0%	19.0%±3.6%	20.3%±3.7%

The results of the flash tests (criterion: lowest deviations in ORC modeling) favor the use of the SRK Huron Vidal model for both the Ille [246] and the Scholze-based [97] single surrogate approaches, and Predictive SRK for the three-component approach. The lowest deviations of ORC modeling were achieved while employing the Scholze-based [97] surrogate, which also provided the best results for water content and activity coefficient, as well as levoglucosan, aromatic, and heavy surrogate content (and good results for the oxygenates). For the case of AC modeling, the choice of heavy surrogate is irrelevant, and the results favor the SRK-KD model. Both of these models present good results in Table 4.4.

4.1.5. Thermophysical property estimation

Based exclusively on the conventional name, it is often difficult to specify the nature of an organic molecule. Whereas IUPAC rules are usually viable for simple molecules, this is no longer the case for high molecular weight compounds with several substituents and intra-molecular interactions. Therefore, molecules are often cataloged using codes, such as the CAS number, or alphanumeric structure mnemonics, like the SMILES or SMARTS notations.

Several techniques have been used to estimate the physical properties of organic substances, among which Quantitative Structure-Property Relationship (QSPR) methods have been analyzed by Dearden [338] and Mackay et al. [339]. These models make use of advanced molecular descriptors, such as topological, topochemical, electrotopical, geometric, and hydrogen-bonding, as well as computational techniques for optimization like linear regression, non-linear regression, multiple linear regression, and neural networks, but do not allow for a streamlined estimation of physical properties based on group contributions and other easily-determined characteristics [340]. Of these, group contribution methods have been singled out due to their ease of use and accuracy [341], there being frequently multiple options to establish a single property, and it is ultimately the responsibility of the user to select the most reliable value of a physical property in their simulations [342].

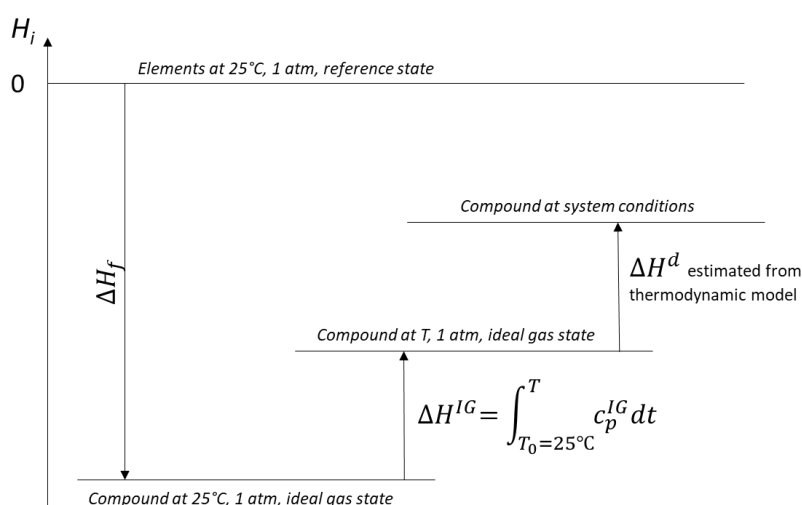


Figure 4.6: Born-Haber scheme for the enthalpy of a compound in a process simulator. ΔH^{IG} stands for the sensible heat departure in the ideal gas state, and ΔH^d for the remaining enthalpy departure, which depends on the thermodynamic models. Adapted from [243]

Estimation of the stream characteristics, for example enthalpy (difference in comparison to a reference state, usually considering isolated elements at 25 °C and 1 atm), is dependent on the choice of thermodynamic methods selected to describe each phase and phase equilibria and can be done assuming the validity of the Born-Haber rules (Figure 4.6 and Eq. (4-3), in which y_i stands for the molar fraction of component i , $\Delta H_{f,i}^{IG}$ for the enthalpy of formation of component i , $C_{p,i}^{IG}$ for the heat capacity of i , and ΔH_i^d for the enthalpy of phase change of component i) [243]

$$H_{mix} = \sum_i y_i \left(\Delta H_{f,i}^{IG} + \int_{T_0}^T C_{p,i}^{IG} dT + \Delta H_i^d \right) \quad (4-3)$$

The simulation of any chemical process and downstream liquid-vapor separation requires the supply of a series of thermodynamic properties for each substance considered in the process, including molecular weight, vapor pressure, heat capacity (ideal gas, at the required phases), enthalpy and entropy/Gibbs energy of formation, enthalpy and entropy/Gibbs energy of phase change, and liquid molar volume.

All thermodynamic methods, apart from ideal gas and Raoult law, require the definition of extra properties including critical point properties (temperature, pressure, volume, diameter, compression factor) for cubic and vapor-phase association EoS methods, binary interaction parameters in both phases (calculated from experimental data, and available in several databases⁸) for several EoS and activity coefficient methods.

In Table 4.5 are included the components proposed in Table 4.2, as well as those which participate in the reaction network and liquid-vapor equilibria. One can see that solely a fraction of these is fully characterized in the literature in terms of thermodynamic property data. For the remaining that do not have this luxury, it comes to the responsibility of the user to input the data required, to ensure the physical viability of the results obtained [342]. Several publications have discussed property estimation for pyrolysis products, including Gorensek et al. [226] and Fonts et al. [273]. In the context of this work, several methods were employed to estimate the lacking values, presented in Table 4.6, and their comparison is shown in Appendix D, where one can find tables listing component data, including estimated properties, group distributions, and property estimation parameters.

⁸ It is possible to estimate binary interaction parameters using UNIFAC group contribution distributions for the NRTL, UNIQUAC, Wilson and Soave-RK models, and Huron-Vidal and Wong-Sandler EoS mixing rules.

Table 4.5: Availability of measured thermophysical properties available in the literature. Does not include surrogate species.

	Normal Boiling Point	Critical Parameters				Acentric Factor	Heat Capacity	Formation		Vapor Pressure	Enthalpy of Vaporization	Liquid Molar Volume	Viscosity	
		Temperature	Pressure	Volume	Compression Factor			Enthalpy	Gibbs Energy				Gas	Liquid
Acetaldehyde	✓	✓	✓	✓	✓	✓	✓	✓	✓	✓	✓	x	✓	
Acetic Acid	✓	✓	✓	✓	✓	✓	✓	✓	✓	✓	✓	✓	✓	
Acetol	✓	x	x	x	x	x	x	✓	x	✓	x	✓	x	
Acetone	✓	✓	✓	✓	x	✓	✓	✓	✓	✓	✓	✓	✓	
Acrolein	✓	x	x	x	x	x	x	x	x	✓	x	x	x	
Anisole	✓	✓	✓	✓	x	x	x	✓	x	✓	x	x	✓	
p-Coumaryl Alcohol	✓	x	x	x	x	x	x	x	x	x	x	x	x	
p-Cresol	✓	✓	✓	✓	✓	✓	✓	✓	✓	✓	✓	x	✓	
Ethylene Glycol	✓	✓	✓	✓	x	✓	✓	✓	✓	✓	✓	x	✓	
Ethylene Glycol Monoacetate	✓	x	x	x	x	x	x	✓	x	✓	x	x	x	
Ethanol	✓	✓	✓	✓	x	✓	✓	✓	✓	✓	✓	✓	✓	
Linoleic Acid	✓	✓	✓	x	x	✓	x	✓	x	x	x	x	x	
Formaldehyde	✓	✓	✓	✓	✓	✓	✓	✓	✓	✓	✓	x	x	
Formic Acid	✓	✓	✓	✓	✓	✓	✓	✓	✓	✓	✓	x	✓	
Furfural	✓	✓	✓	x	x	x	✓	✓	x	✓	x	x	✓	
Glyoxal	✓	x	x	x	x	x	x	x	x	✓	x	x	x	
Guaiacol	✓	x	x	x	x	x	✓	✓	x	✓	x	x	✓	
Hydroxyacetaldehyde	x	x	x	x	x	x	x	x	x	✓	x	x	x	
n-Hexadecane	✓	✓	✓	✓	✓	✓	✓	✓	✓	✓	✓	x	x	
5-Hydroxymethylfurfural	✓	x	x	x	x	x	✓	x	x	✓	x	✓	x	
Ethenone	✓	x	x	x	x	x	x	x	x	✓	✓	x	x	
Levogluconan	✓	x	x	x	x	x	✓	✓	x	✓	x	x	x	
3-Methylcyclopenten-2-one	✓	x	x	x	x	x	x	x	x	x	x	x	x	
Methanol	✓	✓	✓	✓	✓	✓	✓	✓	✓	✓	✓	✓	✓	
5-Methylfurfural	✓	x	x	x	x	x	x	x	x	x	x	x	x	
Phenol	✓	✓	✓	✓	✓	✓	✓	✓	✓	✓	✓	x	✓	
Synapaldehyde	x	x	x	x	x	x	x	x	x	x	x	x	x	
Syringol	✓	x	x	x	x	x	x	✓	x	✓	✓	✓	x	
Vanillin	✓	x	x	x	x	x	x	✓	x	x	x	x	✓	
Vinylketene	x	x	x	x	x	x	x	x	x	x	x	x	x	
Xylosan	x	x	x	x	x	x	x	x	x	x	x	x	x	

Table 4.6: Sources of thermophysical properties of individual components considered in the model. Not included: literature sources.

	Estimation methods	External sources
Normal Boiling Point	Joback [343], Gani [344], Mani ^a , Cordes-Rarey [345]	ACD/Labs ^b , EPISuite ^c , TDE ^d , Fonts [273]
Critical Temperature	Joback [343], Gani [344], Lydersen [346], Fedors [347], Ambrose [348], Klincewicz-Reid [349], Mani ^a , Nannoolal-Rarey [350]	TDE ^d , Fonts [273]
Critical Pressure	Joback [343], Gani [344], Lydersen [346], Ambrose [348], Nannoolal-Rarey [350]	TDE ^d , Fonts [273], Gorenssek [226]
Critical Volume	Joback [343], Gani [344], Lydersen [346], Ambrose [348], Riedel, Fedors[351], Nannoolal-Rarey [350]	TDE ^d , Fonts [273]
Acentric Factor	Lee-Kesler [352]	TDE ^d , Gorenssek [226]
Ideal Gas Heat Capacity	Benson [353], Joback [343]	TDE ^d , Fonts [273], Gorenssek [226]
Liquid Heat Capacity	Růžička [354–356]	TDE ^d , Fonts [273]
Standard Enthalpy of Formation	Joback [343], Gani [344], Benson [353]	TDE ^d , Fonts [273], Gorenssek [226]
Standard Gibbs Energy of Formation	Joback [343], Gani [344], Benson [353]	TDE ^d , Fonts [273]
Vapor Pressure	Riedel [357], Li-Ma [358], Mani ^a , Nannoolal-Rarey [359]	ACD/Labs ^b , EPISuite ^c , TDE ^d , Fonts [273], Gorenssek [226]
Enthalpy of Vaporization	Gani [344], Vetere [360,361], Ducros [362–364], Li-Ma [358]	ACD/Labs ^b , TDE ^d , Fonts [273]
Liquid Molar Volume	Gunn-Yamada [365], Le Bas [366]	ACD/Labs ^b , TDE ^d , Fonts [273]
Gas Viscosity	Reichenberg [367]	TDE ^d
Liquid Viscosity	Letsou-Stiel [368], Orrick-Erbar [369], Nannoolal-Rarey [370]	TDE ^d

a: The Mani method was developed by Aspen Technologies™;

b: Method not disclosed. ACD/Labs™ and ChemSketch™ were developed by Advanced Chemistry Development, Inc.;

c: Adapted Stein & Brown method. The EPISuite™ was developed by the United States Environmental Protection Agency;

d: Method not disclosed. The ThermoDataEngine was developed by the National Institute of Standards and Technology, a subsidiary of the U.S. Department of Commerce;

e: Mean between the Antoine and Grain methods. The EPISuite™ was developed by the United States Environmental Protection Agency.

4.2. Furnace, liftpipe, gas cleaning

Modeling of this section follows an improved version of the model described by Fonseca et al. [5], and is shown in Figure 4.7. Entry air (FRESH1) was set at of 15° C and a relative humidity of 0.77%, and pre-heated with the system flue gas (HE1). The furnace is defined as a Gibbs energy minimization reaction (RGIBBS), set at a temperature of 898° C as per operational data (Appendix A), while disregarding the formation of nitrous oxides (N₂ was defined as an inert). Apart from air, the furnace is supplied with steam and natural gas, both using flows set as per operational data.

The flue gas of the reactor is channeled to the liftpipe (LIFT1, LIFT2) where it is mixed with steam and water and secondary fluidization air. Heat carrier (sand, SAND0) containing a fraction of char, which is decomposed (COKEDECO) into its elemental fraction at 501° C (C, H, O), and the product is channeled to a second RGIBBS (LIFT2) set at 557° C in which N₂ was again defined as an inert. The thermodynamic model employed was Peng-Robinson EoS using Huron-Vidal (PRMHV2) mixing rules, due to its ability of generating binary interaction data making use of UNIFAC groups.

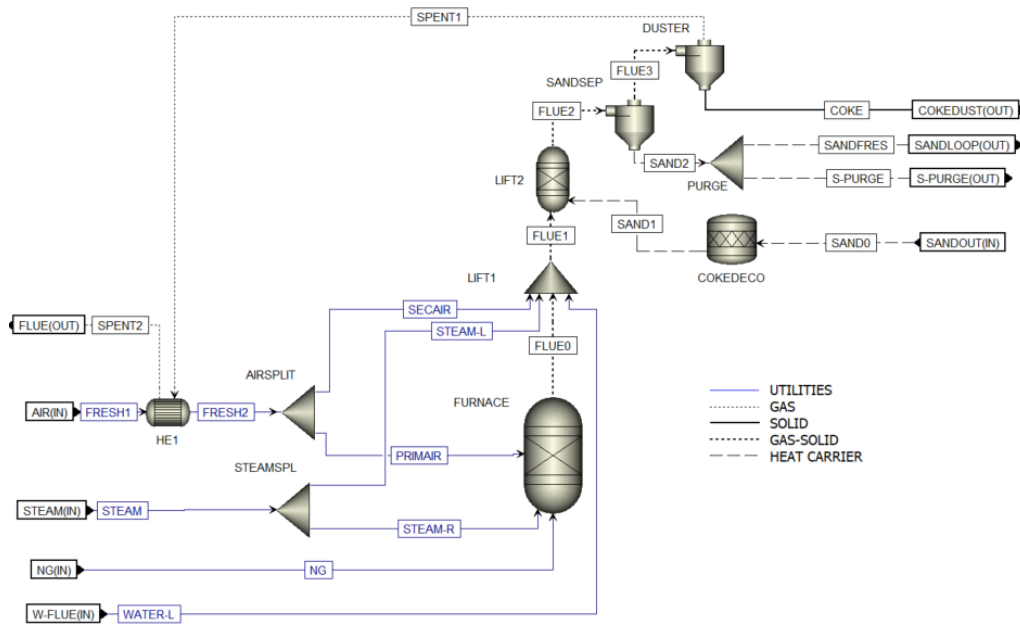


Figure 4.7: Flowsheet view of the heat carrier cycle hierarchy in Aspen Plus™ V12. Blue streams correspond to utilities (steam, water, natural gas, sweeping nitrogen, air); dotted streams correspond to gas streams; and thick streams to solid products. Heat carrier (sand) is represented by dashed lines, including loop purges and make-up streams.

The lifted sand is removed from the material using a stream split (SANDSEP), in which the gas phase entrains a fraction of dusts (around 10 wt.% of the total coke) which is recovered and considered for the overall mass balance; this solid-laden flue gas passes through a cyclone (DUSTER) defined as a perfect solid separator. The coke dust is cooled using water, and the details on the cooler are discussed in section 4.4.

Before recycling, the sand suffers a purge equal to the flow rate of ash in the stream. A make-up of sand is defined (S-FRESH in Figure 4.2) so that the flow of fresh sand is always 14.4 times the amount of fresh biomass.

4.3. Reactor modeling

The ultimate objective of this work lays, as stated before, in the establishment of a predictive model. In that sense, reaction modeling lays either in the use of reaction networks, or the definition of multivariable regression models. The latter requires calibration, for which experimental data is lacking.

Despite the claims by Henrich et al. [31] that a PFR model is a good fit to the *bioliq*® reaction reality, PFR models in Aspen Plus™ tend to have convergence issues and lead to frequent errors and mass balance problems, especially when employing complex mixtures and reaction pathways. In addition, Peters et al. [4] claims that a single CSTR model is the best option to model primary and secondary fast pyrolysis. The results of the residence time study indicate a series of 22 CSTRs would be feasible to model the behavior of the solid phase, but it is unreasonable to consider this value when employing such complex reaction networks.

The thermodynamic model employed is PRMHV2. The calculations assumed a feed of feedstock (wheat straw) of $360 \text{ kg}\cdot\text{h}^{-1}$, characterized as a non-conventional solid with a heat of combustion of $18.26 \text{ MJ}\cdot\text{kg}^{-1}$. Nitrogen feed rate was defined as $16 \text{ kg}\cdot\text{h}^{-1}$. Sand (SiO_2) is supplied with a feed rate $14.4 \times 360 \text{ kg}\cdot\text{h}^{-1}$ at $556 \text{ }^\circ\text{C}$, with a

density of $1440 \text{ kg}\cdot\text{m}^{-3}$, and a heat capacity of $0.80 \text{ kJ}\cdot\text{kg}^{-1}\cdot\text{K}^{-1}$ [291]; assuming a temperature drop of $49 \text{ }^\circ\text{C}$ and the defined flow rate, the heat supplied is expected to be around **56.4 kW**. Assuming the estimated solid residence time (76.8 s) the heat carrier is expected to occupy a volume of **76.8 dm³**, leaving a volume of **13.8 dm³** for the biomass entrained.

Each reactor was divided into three sections, each modeled using a different unit block. The first unit block is the same for both cases, being a black box emulating the decomposition into lignocellulosic monomers (see Table 3.2, values in this section used based on the reference data), as well as extractives (represented by taxifolin, $\text{C}_{15}\text{H}_{12}\text{O}_7$), lipids (represented by trilinolein, $\text{C}_{57}\text{H}_{98}\text{O}_6$), ash (non-conventional solid), and water, with the protein content being disregarded; heat capacity and solid enthalpy of formation for the biomass decomposition products was taken from the work by Gorensek et al. [226], the heat of formation of the feedstock is calculated based in its heat of combustion, and the heat capacity of the biomass is estimated using correlations estimated by Dupont et al. [371].

The second unit block emulates the primary pyrolysis, which happens at $505 \text{ }^\circ\text{C}$ assuming liquid+solid phase reaction (as per Peters et al. [4]). The final reactor simulates the vaporization of the primary products, the partial release of delayed devolatilization solids, and vapor-phase secondary pyrolysis phenomena.

4.3.1. Performance of published reaction networks

The performance of published reaction networks in modeling the actual behavior of TGA degradation was already discussed in section 3.3, but it is relevant to compare how well the product distribution of these networks can reflect the actual data obtained for wheat straw pyrolytic bio-oil using GC/MS. GC/MS and report data from *bioliq*[®] campaigns spanning 2015 to 2018 was averaged for the ‘*Experimental*’ case. Water and the organic fraction of the bio-oils was separated to facilitate comparison, and reflect the totality of components assumed to take part in LVE, as well as the coke and ash. The complete reaction networks, characterized with the Arrhenius parameters for each reaction can be found in Appendix D.

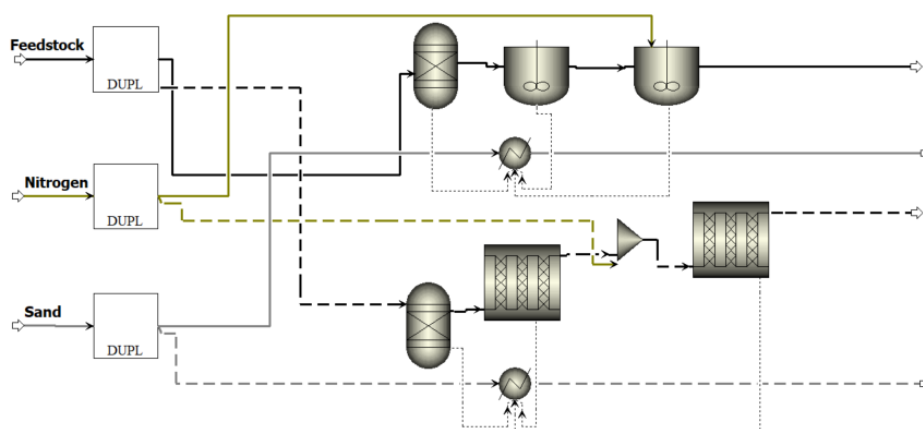


Figure 4.8: Aspen Plus™ flowsheet of the models for testing the different reaction networks: top: CSTR, bottom: PFR. Black: feedstock, Ochre: sweeping gas (N₂), Grey: heat carrier (sand). Full lines: CSTR models, Dashed lines: PFR models, Dotted lines: heat transfer to the HC.

The study contrasted the PFR models with CSTR models operating at similar conditions (Figure 4.8). The CSTR units are modeled with a volume of 13.8 dm³ while the PFR units are modeling as single tubes with a length of 1253.1 mm and a diameter of 118.3 mm (corresponding to a volume of 13.8 dm³). For this comparison step, the presence of secondary reactions was disregarded, and a CSTR unit (volume: 38.8 dm³) was contrasted with a PFR unit (single tube, length: 1253.1 mm, diameter: 198.6 mm, volume 38.8 dm³). Both models are setup at 505 °C and atmospheric pressure.

Correct estimation of the heat of reaction is important when conducting this type of analysis, and it was estimated in the context of this work as the temperature drop the heat carrier suffers (ΔT_{HC}) when considering the energy demand of the different reactors, assumed to be of 49 °C in the base case (section 4.1.1). Neglecting heat losses and assuming adiabatic conditions in the system, the value depends on the reaction network and the unit block employed.

Both types of unit blocks require the specification of kinetics to function, or the definition of a conversion routine. The CSTR model, as the name implies, assumes perfect mixing in a single volume fraction, and estimates all parameters assuming the residence time of the mixture in the volume. In the other hand, the PFR model divides the inputted length into fractions and estimates component generation rate, liquid fraction and energy demand by numerical integration. These two methods may lead to conflicting results which lead to differences in mass balance closure and product/component distribution, an example seen in Figure 4.9.

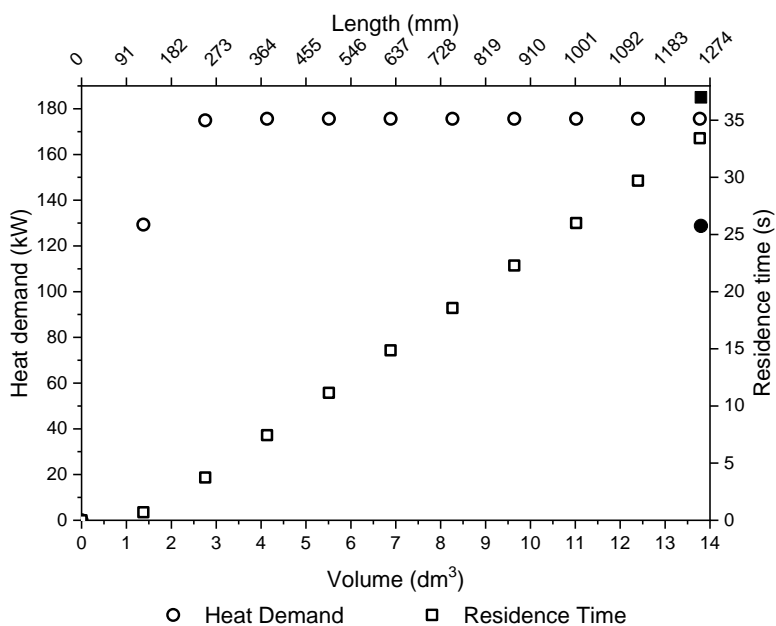


Figure 4.9: Comparison between a PFR profile (hollow points) and CSTR values (filled points) for both heat demand and residence time.

The results can be compared visually in Figure 4.10 (left). Firstly, the underestimation of gas, water and coke is attributed to not considering the occurrence of secondary reactions at this stage. As can be observed, the product distribution is not very impacted by the type of reactor considered, with average deviations of 4.5% (CSTR) vs 5.7% (PFR). CSTR models present better mass balance closures than PFR models (average 2.5 wt.% vs. 4.7 wt.%).

Not only is it relevant to compare the product distribution, but also the composition of a potential organic liquid yield (OLY), presented in Figure 4.10 (right), in this case both blocks lead to a better OLY composition prediction (average deviation 18.6% vs 18.8%), where aromatics stands for the sum of phenolics, methoxyph-

nolics (guaiacols) and dimethoxyphenolics (syringols). However, differences between predicted and experimental values are more relevant than differences between models. These are attributed to the absence of secondary pyrolysis (section 2.2.1). Important reaction pathways include the decomposition of lignin into phenolics, as a relevant fraction of char corresponds to unreacted lignin, followed by the cracking of these phenolics into cyclopentenones, which are absent from these reaction networks. Aldehydes, furans and sugars are expected to decompose during secondary pyrolysis, as well as during storage due to ‘aging’ phenomena (section 2.2.4).

Table 4.7: Results of the simulations. Deviation based on difference between base and predicted product distribution. Also shown are the associated heat demand on top of the HC supply, the residence time on both unit blocks, and the mass balance closure. Values in bold indicate best results, while those in italic indicate simulation errors.

Network	CSTR					PFR				
	Deviation	Demand (kW)	τ_{R1} (s)	τ_{R2} (s)	ϵ	Deviation	Demand (kW)	τ_{R1} (s)	τ_{R2} (s)	ϵ
R08	7.3%±1.1%	98.3	4.0	0.2	0.0%	7.4%±0.6%	105.1	4.1	0.2	0.0%
C14	3.6%±0.9%	166.8	30.6	0.2	7.5%	3.9%±0.4%	161.7	28.5	0.2	7.9%
RAC LC	6.2%±0.9%	60.7	32.4	0.2	4.0%	7.4%±0.6%	46.2	30.1	0.2	5.7%
RAC HC	5.4%±1.5%	-2.5	32.4	0.2	8.7%	5.4%±0.8%	-6.4	30.9	0.2	9.3%
R17a	2.6%±0.5%	39.9	33.1	0.2	3.6%	3.4%±0.3%	40.5	31.4	0.2	4.2%
R17b	5.4%±1.5%	91.4	31.7	0.3	-0.9%	6.6%±0.7%	115.1	30.4	-	-1.0%
D18-H	3.0%±0.6%	99.7	24.9	0.2	-1.5%	6.0%±0.5%	134.7	22.9	-	4.1%
D18-C	0.9%±0.4%	106.8	32.3	0.2	-1.5%	5.3%±0.5%	99.5	27.5	0.2	7.7%

The best results (Table 4.7) in terms of product distribution can be found for the D18-C, R17a, and C14 networks (in this order) when employing a CSTR block, and only two PFR cases present deviations under 5%. Reactor demand was estimated by summing the demand of each unit block and removing the heat already supplied by the heat carrier loop; the best results are found for the RAC model assuming high charring. In terms of residence times of the phases in the defined volumes, the values indicate the unfeasibility of these types of models. Mass balance closure is associated with molar imbalances in the chemical equations that constitute the reaction networks; they are present to some extent in all reaction networks analyzed in the context of this work, and rebalancing was not considered at this stage.

Regarding residence time estimations (Table 4.7), when compared to the target values of 76.8 s and 1.5 s for the first and second reactor blocks, respectively, both models fail to predict good values. This is mostly attributed to shortcomings of using such simplified models, which do not properly consider solid flow during volume estimation, and/or to issues when estimating the density of the reacting mixture at such high temperatures.

Effect of potassium content

Not disregarding the results presented in Table 4.7 and Figure 4.10, TGA curve analysis results (section 3.3) must be considered for further narrowing down [96]. In that sense, further analysis disregards the D18 and R17b networks for inferior TGA deviations, as well as the RAC-HC [72,135] because of the lack of sugar content in the produced oil.

Table 4.8 presents the results of the networks considered for this second stage of choice. It includes results from Table 4.7, as well as networks in which the cellulose degradation was replaced by the Trendewicz model [158]. Like in the case of Table 4.7, it is important to compare both unit blocks (CSTR vs PFR) for the same base network/K-content; while differences in mass balance closure (max. 3.1%, R17a-0.12 wt.%) and OLY composition (max. 3.8%, RAC-1.18 wt.%, Figure 4.11 (right)) may be disregarded, product distribution deviation (max. 5.6%, R17a-1.18 wt.%), and excess heat demand (max. 23.9%, RAC-no K) are important to keep in mind. Disregarding values with simulation error, the lowest excess heat demand is found for all cases using the RAC network, namely the RAC-PFR-0.39 wt.% combination (44 kW), while the higher values are found for all cases using the C14 network. The R17a features a higher heat demand than the R08.

Table 4.8: Results of the simulations considering the effect of potassium content. Also shown are the associated heat demand on top of the HC supply, the residence time on both unit blocks, and the mass balance closure. Values in bold indicate best results, while those in italic indicate simulation errors.

Network	Potassium Content	CSTR			PFR		
		Deviation	Demand (kW)	ϵ	Deviation	Demand (kW)	ϵ
R08	0.00 wt.%	<i>7.3%±1.1%</i>	98.3	<i>-0.05%</i>	<i>7.4%±0.6%</i>	105.1	<i>-0.04%</i>
	0.09 wt.%	<i>5.2%±0.9%</i>	86.9	-1.19%	<i>5.5%±0.5%</i>	85.1	-1.14%
	1.18 wt.%	<i>3.0%±0.8%</i>	84.4	-1.19%	<i>3.2%±0.3%</i>	81.9	-1.03%
C14	0.00 wt.%	<i>3.6%±0.9%</i>	166.8	7.51%	<i>3.9%±0.4%</i>	161.7	7.94%
	0.09 wt.%	<i>6.5%±1.5%</i>	218.8	4.64%	<i>6.0%±0.7%</i>	213.3	5.93%
	1.18 wt.%	<i>3.0%±0.8%</i>	223.0	4.76%	<i>2.2%±0.3%</i>	219.8	4.99%
RAC	0.00 wt.%	<i>6.2%±0.9%</i>	60.7	4.05%	<i>7.4%±0.6%</i>	46.2	5.69%
	0.39 wt.%	<i>6.5%±2.5%</i>	53.5	4.10%	<i>2.6%±0.3%</i>	44.1	5.20%
	1.18 wt.%	<i>7.5%±2.9%</i>	53.0	4.08%	<i>2.9%±0.2%</i>	45.4	4.38%
R17a	0.00 wt.%	<i>2.6%±0.5%</i>	39.9	3.64%	<i>3.4%±0.3%</i>	40.5	4.23%
	0.12 wt.%	<i>4.7%±1.5%</i>	111.6	-0.43%	<i>4.9%±0.5%</i>	111.1	2.71%
	1.18 wt.%	<i>7.7%±2.7%</i>	110.2	-0.49%	<i>2.1%±0.2%</i>	103.7	2.59%

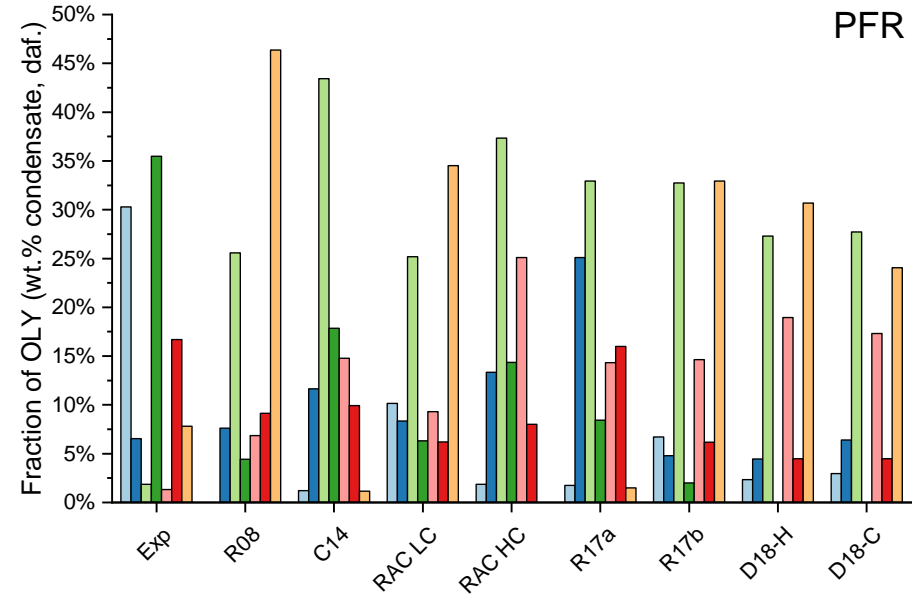
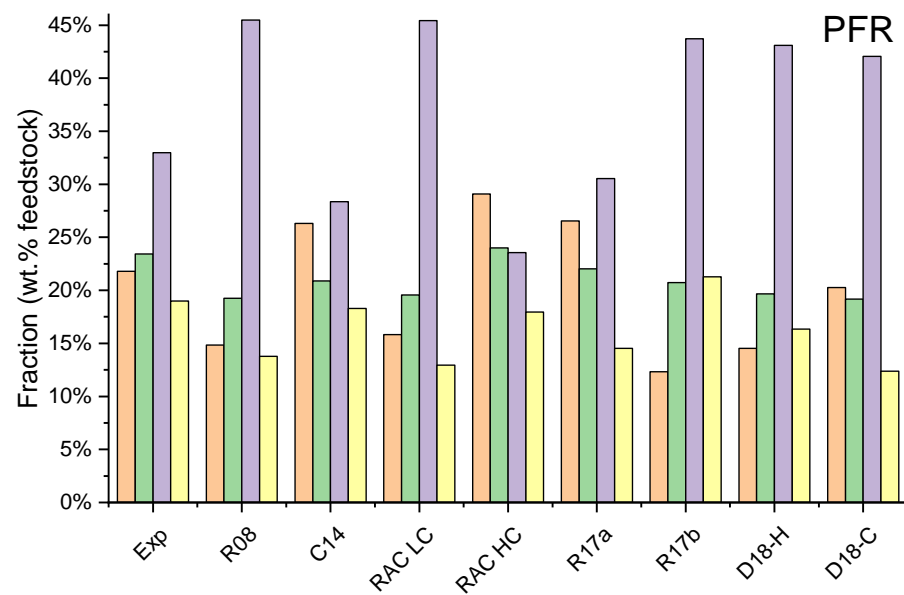
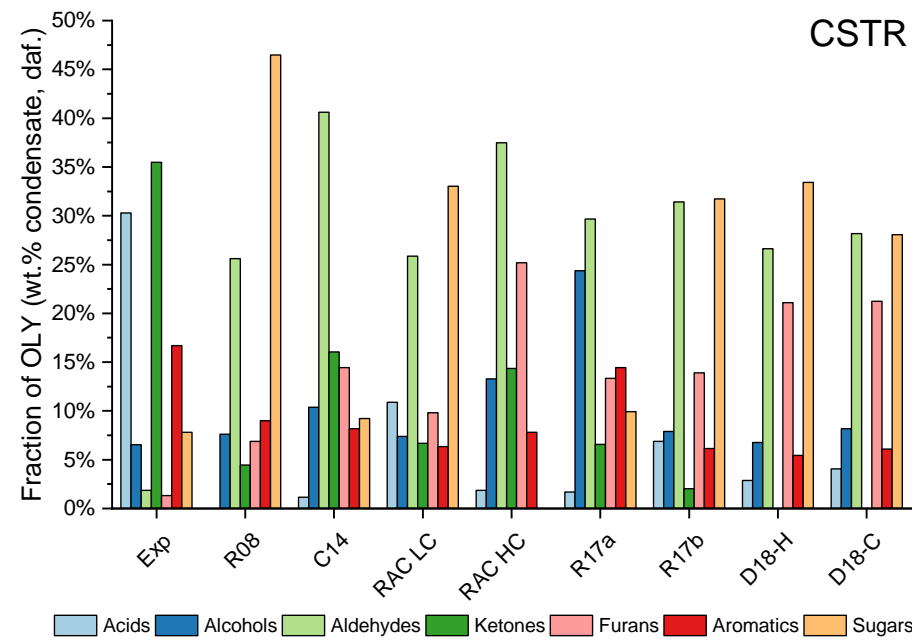
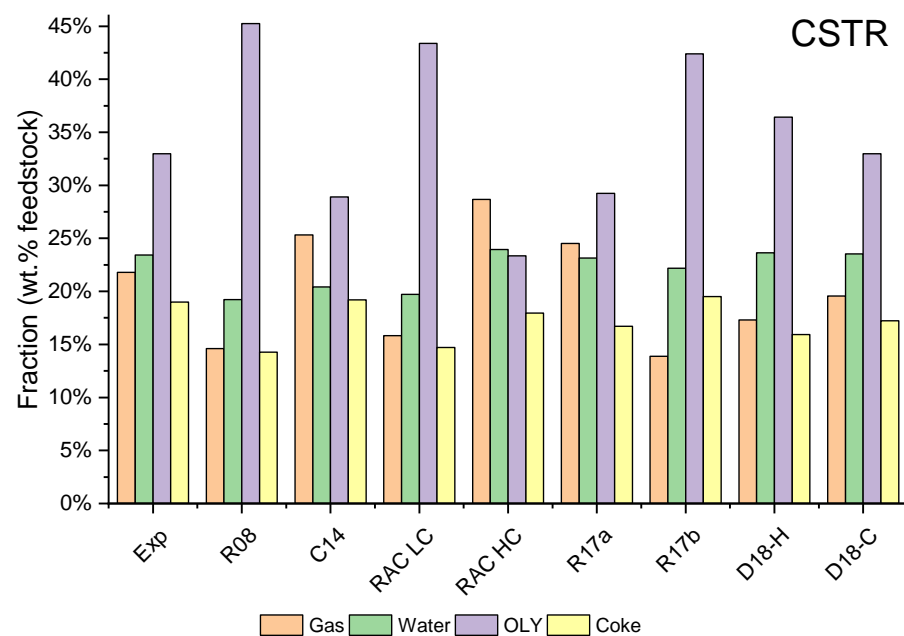


Figure 4.10: Comparison of the base case product distribution (left) and organic liquid yield composition (right) between the experimental data (base, bioliq® 2015-2018) and the results of the models using CSTR (above) and PFR (below) unit blocks. Legend: R08: Ranzi et al. (2008) [96]; C14: Corbetta et al. [130]; RAC: Anca-Couce and Scharler [135], for which LC: low charring conditions, HC: high-charring conditions; R17a: Ranzi et al. (2017a) [133]; R17b: Ranzi et al. (2017b) [81]; D18: Debiagi et al. [281], for which H: hardwood hemicellulose, C: cereal hemicellulose.

As predicted, the production of OLY (Figure 4.11, left) is diminished by an increasing presence of potassium on the feedstock, accompanied by an increase in the gas, water, and coke content. However, this pattern does not hold true consistently, due to differences in reaction kinetic parameters due to the calibration method employed by Trendewicz et al. [158]. As seen in Figure 4.10, the composition of the OLY (Figure 4.11, right) is still dominated by aldehydes and sugars. Within the same model, the production of aldehydes and alcohols seems to increase with an increased potassium content in the feedstock, while an opposing trend can be found for sugars. For the case of furans and aromatics, an upwards trend can be attributed to the lower production of OLY from the decomposition of cellulose, which increases the relative contribution of the fractions.

Decision of reaction network

The findings from section 3.3, place the choice between the RAC or C14 networks, using an optimum potassium content, whereas the experimental K-content performed poorly. The results in Table 4.8 show that RAC-0-39 wt.% is the third-best performant network by product distribution deviation while presenting the best heat demand calculation values. From the C14 network, the only representative in the top 5 employs the experimental potassium content (1.18 wt.%), and all cases present inferior heat demand calculation values. In view of this, only variants of the RAC network were considered for the final decision.

The results presented in section 3.3 show that, for the determination of kinetic parameters for each lignocellulosic component, curve-fitting methods give better results when compared to those obtained using isoconversional methods. However, the viability of the latter should not be overlooked, which is why both KAS and curve-fitting free-order cellulose/hemicellulose are contrasted to the original values. Moreover, the RAC networks employs three pseudo-components to model the degradation of lignin, for which a fit of the values obtained for the degradation of lignin is outside the scope of this work. The degradation of tannins and triglycerides was also considered to improve the modeling range of biomass thermal degradation, as was the cereal hemicellulose decomposition ratios studied by Debiagi et al. [281] (cereal: HCE1/HCE2 = 12%:88%, hardwood: HCE1/HCE2 = 35%:65%) versus the original proportion of the network.

In a first glance, the results reunited in Table 4.9 indicated that incorporating the degradation of tannins and triglycerides leads to a small improvement in deviation compared to the base case (first row, Table 4.9). Applying the Trendewicz method [158] led in average to worse results than using the original network, after applying the modifications to the model, with a minor impact when using the optimum value (av. dev. 1.5%±4.4%) a more pronounced when using the experimental value (av. dev. 7.8%±3.5%). Applying the Debiagi hemicelluloses produced slightly better results than the original hemicellulosic division, slightly favoring the use of the cereal hemicellulose (av. dev. 0.7%±2.1% vs. 0.5%±0.9%). Regarding the source of the kinetic parameters, the use of isoconversional parameters produced slightly worse results (av. dev. 1.5%±3.3%), while the curve-fitting ones produced lower deviations (av. dev. 3.0%±4.1%).

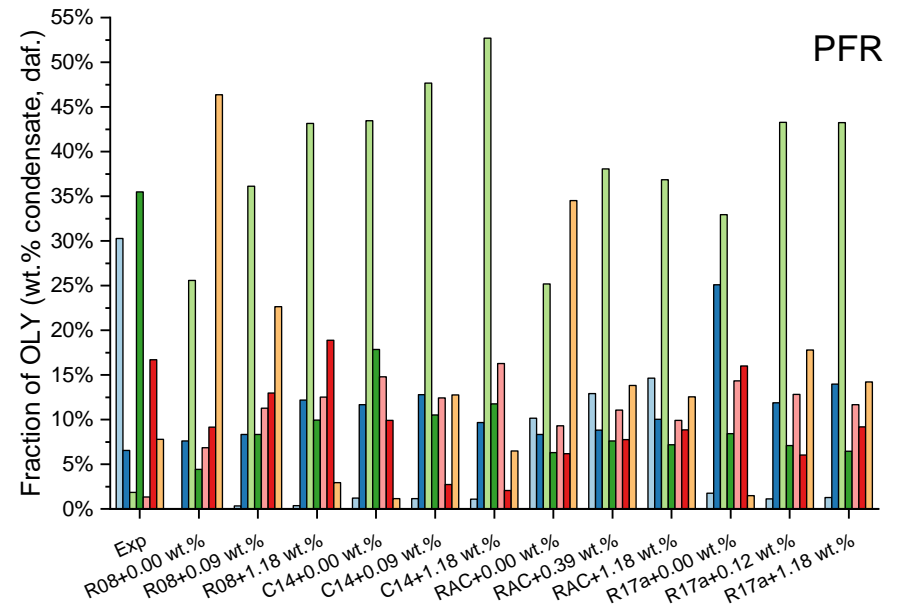
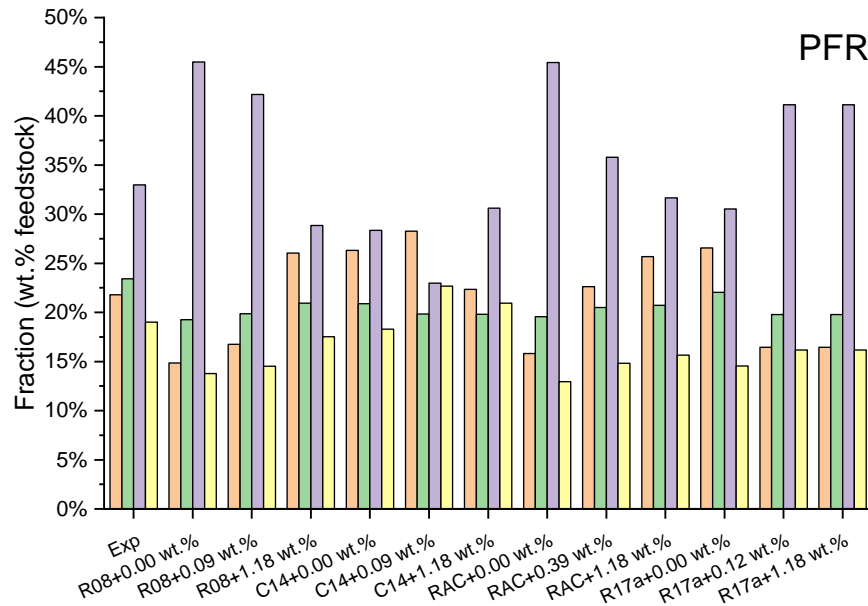
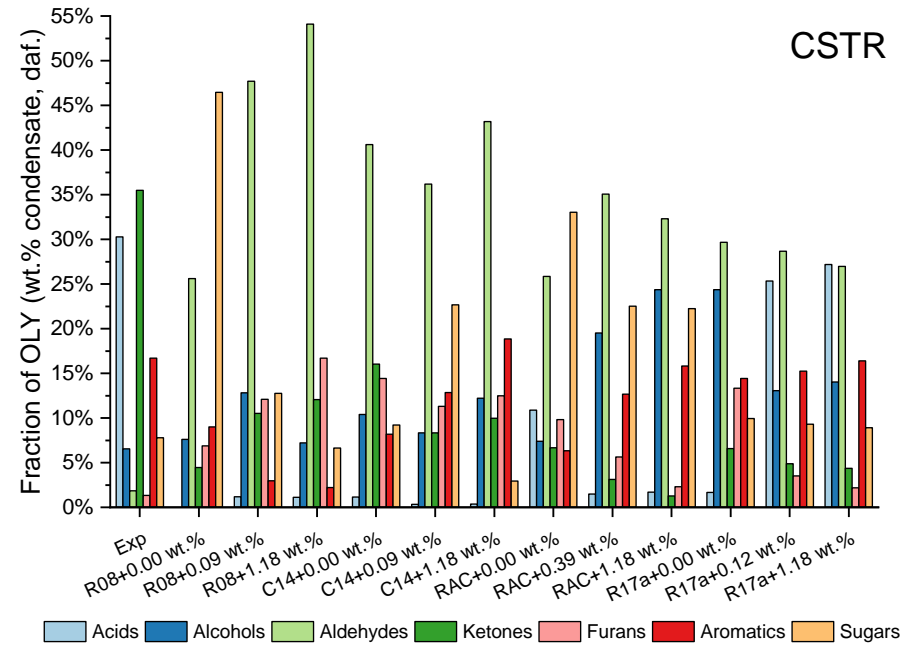
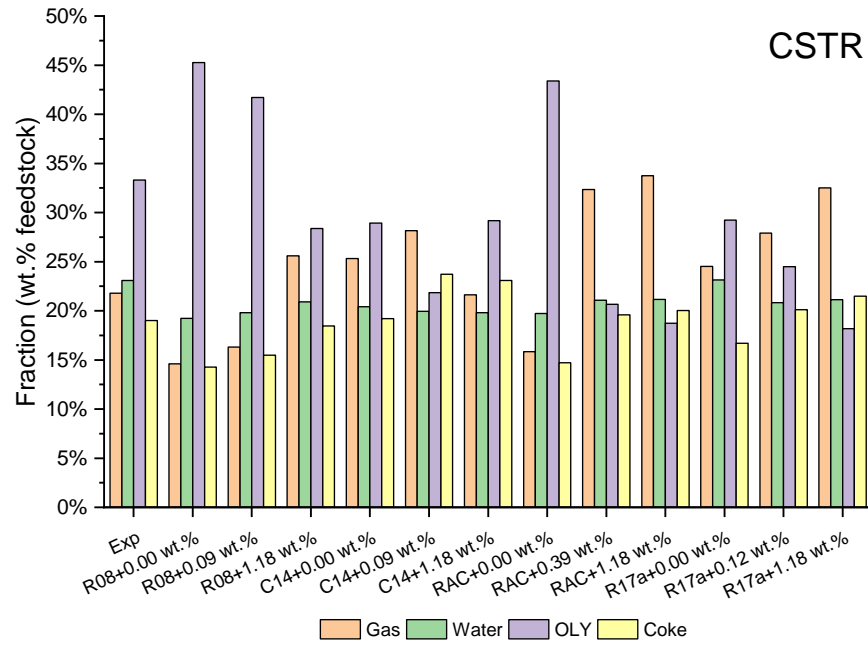


Figure 4.11: Comparison of the base case product distribution (left) and organic liquid yield composition (right) between the experimental data (base, bioliq[®] 2015-2018) and the results of the models presented in Table 3.7 using CSTR (above) and PFR (below) unit blocks. Legend: R08: Ranzi et al. (2008) [96]; C14: Corbetta et al. [130]; RAC: Anca-Couce and Scharler [135]; R17a: Ranzi et al. (2017a) [133]; values in percentage refer to the potassium content in the feedstock.

Table 4.9: Comparison of the deviations between the WS-H thermodynamic curves and the predicted behavior.

K-content ^a	D18 ^b	Source ^c	RMSE TGA	RMSE DTG	K-content ^a	D18 ^b	Source ^c	RMSE TGA	RMSE DTG
Original	None	Original	6.30%	25.60%	Optimum	Cereal	CF free-order	7.50%	22.00%
Original	None	KAS	8.10%	22.40%	Optimum	Hardwood	Original	9.00%	19.40%
Original	None	CF free-order	7.60%	13.30%	Optimum	Hardwood	KAS	9.30%	27.70%
Original	Cereal	Original	9.70%	29.10%	Optimum	Hardwood	CF free-order	9.80%	22.80%
Original	Cereal	KAS	7.00%	24.70%	Experimental	None	Original	14.70%	31.80%
Original	Cereal	CF free-order	6.40%	17.90%	Experimental	None	KAS	13.20%	31.70%
Original	Hardwood	Original	7.00%	26.70%	Experimental	None	CF free-order	14.50%	31.50%
Original	Hardwood	KAS	7.50%	22.80%	Experimental	Cereal	Original	9.80%	28.40%
Original	Hardwood	CF free-order	6.90%	15.70%	Experimental	Cereal	KAS	9.30%	28.70%
Optimum	None	Original	10.80%	20.40%	Experimental	Cereal	CF free-order	9.00%	26.30%
Optimum	None	KAS	10.80%	29.10%	Experimental	Hardwood	Original	12.70%	30.00%
Optimum	None	CF free-order	11.60%	24.10%	Experimental	Hardwood	KAS	11.60%	30.10%
Optimum	Cereal	Original	6.90%	19.50%	Experimental	Hardwood	CF free-order	12.60%	30.00%
Optimum	Cereal	KAS	7.30%	26.80%					

a: Original: no use of the Trendewicz model; Optimum: Trendewicz model using 0.39 wt.% (RAC); Experimental: Trendewicz model using 1.18 wt.%

b: None: no modification of the hemicellulose degradation; Cereal: HCE1/HCE2 = 12%:88%; Hardwood: 45%:55%.

c: Original: values from reaction network; others: replace activation kinetic parameters with the KAS or curve-fitting (CF) free-order values

The 5 best performant combinations shown in Table 4.9 were tested again in a simulation environment. Again, CSTR and PFR reactors were contrasted. The results are presented in Table 4.10 and Figure 4.12. The lowest product distribution deviation is found for the **#4-PFR** combination, and except for the #4 and #5 combinations, CSTR blocks predict slightly lower deviations; this arises due to the excessive water production for the combinations #1, #2 and #3. Prediction of mass balance errors did not vary appreciably between the different unit blocks (av. 0.51% vs. 1.7%), and the lowest value is found for the **#5** combination. CSTR blocks produce marginally better predictions of the heat demand (57.4 kW vs 63.5 kW), and the best result is found for **#4-CSTR**. In terms of the OLY composition, again CSTR blocks perform marginally better (16.1% vs 17.1%), with the best point being **#4-CSTR**.

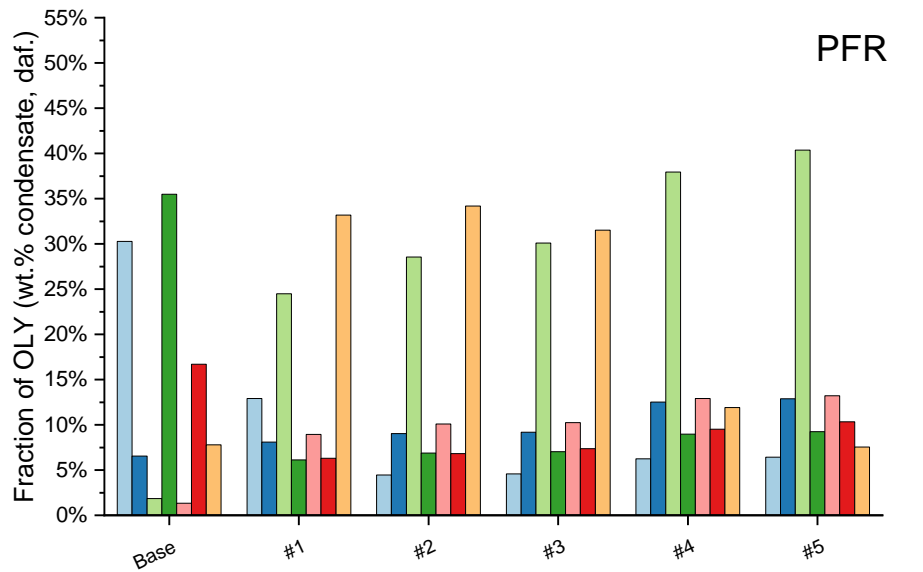
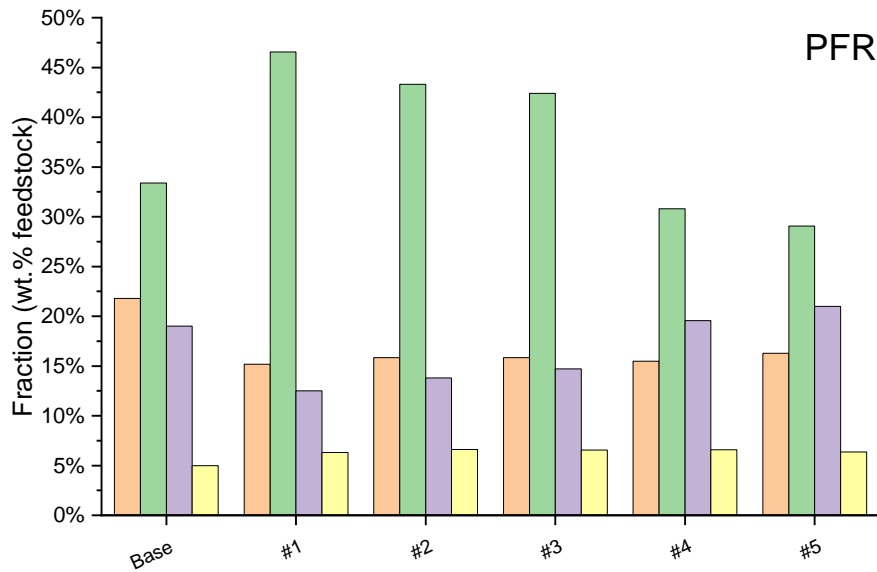
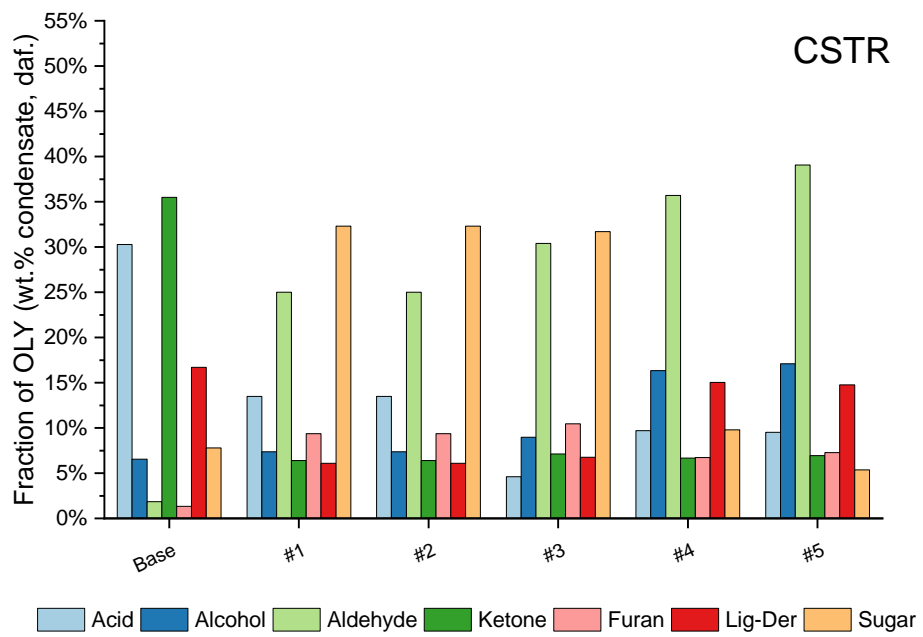
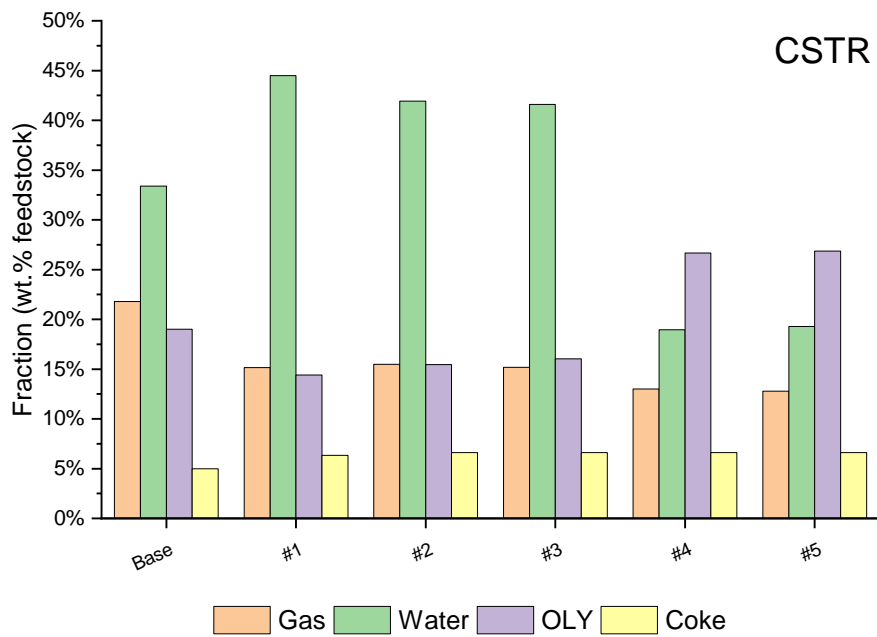


Figure 4.12: Comparison of the base case (bioliq® 2015-2018) and the product distribution (left) / the composition of the organic liquid phase (right) obtained using the models highlighted in Table 4.9 and Table 4.10. Base networks: R08: Ranzi et al. (2008) [96] and R17a: Ranzi et al. (2017a) [133]. All base networks modified with the cellulose degradation proposed by Trendewicz et al. [158], assuming a potassium content of 0.10 wt.%; D18 indicates hemicellulose degradation modified assuming cereal proportions, as per Debiagi et al. [281]. Unit blocks used CSTR (above) and PFR (below).

Table 4.10: Comparison of the Aspen Plus™ modelling results using the best results from Table 4.9.

#	Network			CSTR			PFR		
	K-content ^a	D18 ^b	Source ^c	Prod Dist. Deviation	Demand (kW) ^d	ε ^e	Prod Dist. Deviation	Demand (kW) ^d	ε ^d
1	0.00 wt.%	None	CF fo	6.5%±1.4%	64.7	4.0%	7.6%±0.9%	55.1	4.6%
2	0.00 wt.%	Hardwood	CF fo	5.3%±1.1%	91.2	-0.4%	6.0%±0.6%	84.3	-0.1%
3	0.39 wt.%	Cereal	CF fo	5.2%±1.1%	90.5	-0.3%	5.5%±0.6%	83.8	0.6%
4	0.39 wt.%	Hardwood	Original	10.5%±1.3%	20.1	-0.4%	3.4%±0.5%	51.6	0.2%
5	0.39 wt.%	Cereal	Original	10.5%±1.2%	20.6	-0.3%	3.9%±0.3%	42.5	3.5%

a: Original: no use of the Trendewicz model; Optimum: Trendewicz model using 0.20 wt.% (C14) or 0.39 wt.% (RAC); Experimental: Trendewicz model using 1.18 wt.%

b: None: no modification of the hemicellulose degradation; Cereal: HCE1/HCE2 = 12%:88%; Hardwood: 45%:55%.

c: Original: values from reaction network; others: replace activation kinetic parameters with the KAS or curve-fitting free-order (CF-fo) values.

d: Excess heat demand estimated as the sum of the heat demands of the different unit blocks minus the heat provided by the heat carrier.

e: Mass balance error. Positive values indicate an overestimation of the mass flow of the product stream.

The ultimate decision must fall on a model that is able to predict the product distribution, while minimizing excess heat and mass balance errors (Figure 4.13). The #4-PFR combination presents the lowest distribution deviation, while also presenting a low mass balance error and average heat demand.

Table 4.11 presents the best performing network. Several chemical equations have been re-estimated to ensure atomic balance. Instances of hydroxyacetaldehyde have been replaced by a mixture of acetic acid, itself and acetol based on the molar ratio between these species in the final condensates.

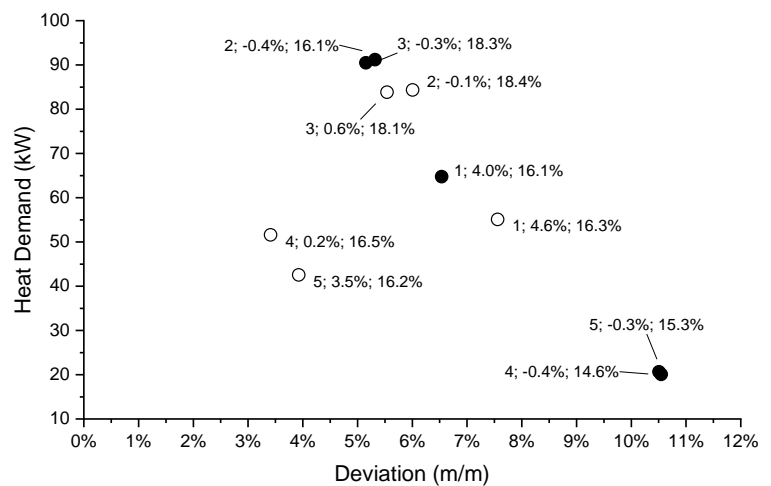


Figure 4.13: Mapping of the points presented in Table 4.10. Filled points: CSTR, hollow points: PFR. Labels: #; ε; OLY deviation.

Table 4.11: Primary pyrolysis network employed in the final model. Description of the components of the model can be found in Appendix D.

		E_a (kJ·mol ⁻¹)	$\log_{10}(A)$ [s ⁻¹]			E_a (kJ·mol ⁻¹)	$\log_{10}(A)$ [s ⁻¹]		
Cellulose	1	CELLULOS → CELL-ACT	188.37	13.60	Lignin	7	LIG → 0.216 ACETONE + 0.643 CO + 0.210 CH ₄ + 0.184 FORMALDY + 0.426 METHANOL + 0.200 ACETALDY + 1.326 WATER + 0.044 FORMICAC + 0.353 GCO + 0.469 GCOH ₂ + 0.479 GCH ₄ + 0.932 GC ₂ H ₄ + 9.234 C + 0.0482 CO ₂ + 0.337 H ₂	125.58	8.60
	2	CELL-ACT → 0.253 ACETICAC + 0.021 HAA + 0.190 ACETOL + 0.197 GLYOXAL + 0.255 ACETONE + 0.224 HMF + 0.073 H ₂ + 0.310 CO + 0.450 CO ₂ + 0.383 FORMALDY + 0.143 METHANOL + 0.095 ACETALDY + 0.885 WATER + 0.020 FORMICAC + 0.049 GH ₂ + 0.183 GCH ₄ + 0.704 C	98.60	9.58		8	LIG → 0.262 CO + 0.232 CH ₄ + 0.360 FORMALDY + 0.779 WATER + 0.156 GCO + 1.894 GCOH ₂ + 0.568 GCH ₄ + 0.458 GCH ₃ OH + 0.792 GC ₂ H ₄ + 9.442 C + 0.046 CO ₂ + 0.368 H ₂	125.58	-1.08 × T
	3	CELL-ACT → 0.975 LEVOGLUC + 0.138 C + 0.1 WATER + 0.013 CO ₂ + 0.025 H ₂	112.93	9.42					
	4	CELLULOS → 5 WATER + 6 C	128.06	9.30	Extractives	1	TANN → PHENOL + ITANN + FORMICAC	46.02	1.70
	5	HEMICELL → 0.35 HEMCELL1 + 0.65 HEMCELL2	129.77	10.00		2	ITANN → 4 C + 3 CO + GCOH ₂ + H ₂	25.52	3.79
	6	HEMICELL1 → 0.475 CO + 0.500 CO ₂ + 0.309 CH ₄ + 0.760 FORMALDY + 0.095 METHANOL + 0.238 C ₂ H ₄ + 0.119 ETHANOL + 0.174 WATER + 0.024 FORMICAC + 0.261 GCO ₂ + 0.380 GCOH ₂ + 0.119 GH ₂ + 0.428 GCH ₃ OH + 1.056 C + 1.050 H ₂	125.58	9.08		3	TGL + WATER → ACROLEIN + 3 FFA	191.20	12.85
	7	HEMICELL1 → 0.095 CO + 0.785 CO ₂ + 0.285 FORMALDY + 0.388 WATER + 0.048 FORMICAC + 0.143 GCO ₂ + 0.143 GCO + 1.140 GCOH ₂ + 0.190 GH ₂ + 0.594 GCH ₄ + 0.357 GC ₂ H ₄ + 1.056 C + 1.050 H ₂	46.05	-0.82 × T					
	8	HEMICELL1 → 0.950 XYLOSAN + 0.225 C + 0.150 WATER + 0.025 CO ₂ + 0.100 H ₂	138.14	0.48 × T	Delayed Volatilization	1	GCO ₂ → CO ₂	100.46	5.00
	9	HEMICELL2 → 0.108 ACETICAC + 0.009 HAA + 0.081 ACETOL + 0.146 CO + 0.190 CO ₂ + 0.475 FORMALDY + 0.106 ETHANOL + 0.344 WATER + 0.023 FORMICAC + 0.208 GCO ₂ + 1.354 GCOH ₂ + 0.304 GCH ₄ + 0.335 GCH ₃ OH + 0.339 GC ₂ H ₄ + 0.596 C + 0.052 H ₂	33.50	9.70		2	GCO → 0.900 CO + 0.050 C + 0.05 CO ₂	209.30	13.48
Lignin	1	LIGNIN-C → 0.350 LIGN-CC + 0.100 CMRYLALC + 0.080 PHENOL + 0.320 CO + 0.300 FORMALDY + WATER + 0.700 GCOH ₂ + 0.495 GCH ₄ + 0.410 GC ₂ H ₄ + 5.735 C	203.02	15.12		3	GCOH ₂ → 0.750 G ₂ COH ₂ + 0.250 H ₂ + 0.125 CO + 0.063 CO ₂ + 0.0623 C	100.46	6.00
	2	LIGNIN-H → LIGN-OH + 0.141 ACETICAC + 0.012 HAA + 0.105 ACETOL + 0.485 ACETONE + 0.463 GC ₂ H ₄	156.97	12.83		4	GH ₂ → H ₂	313.96	12.00
	3	LIGNIN-O → LIGN-OH + CO ₂	106.74	8.52		5	GCH ₄ → CH ₄	300.00	13.30
	4	LIGN-CC → 0.171 ACETICAC + 0.014 HAA + 0.128 ACETOL + 0.262 CMRYLALC + 0.178 PHENOL + 0.364 CO + 0.562 CH ₄ + 0.520 C ₂ H ₄ + 1.046 WATER + 0.364 GCO + 0.899 GCOH ₂ + 7.598 C + 0.297 H ₂	131.86	7.48		6	GCH ₃ OH → 0.900 METHANOL + 0.100 C + 0.100 WATER + 0.100 H ₂	100.46	13.08
	5	LIGN-OH → 0.725 LIG + 0.734 CO + 0.053 CO ₂ + 0.095 CH ₄ + 0.651 METHANOL + 1.253 WATER + 0.053 FORMICAC + 0.819 GCO + 1.120 GCOH ₂ + 0.098 GH ₂ + 0.285 GCH ₄ + 0.313 GCH ₃ OH + 0.177 GC ₂ H ₄ + 3.651 C	50.20	8.00	7	GC ₂ H ₄ → 0.300 C ₂ H ₄ + 0.700 CH ₄ + 0.700 C	209.30	6.00	
	6	LIG → 0.900 SYNAPALD + 4.200 C + 0.200 WATER + 0.100 CO ₂ + 0.300 H ₂ + 0.800 CH ₄	203.02	0.60 × T	8	G ₂ COH ₂ → 0.200 G ₃ COH ₂ + 0.800 CO + 0.800 H ₂	209.30	9.18	

4.3.2. Secondary pyrolysis

Secondary reactions are essential to the correct modeling of a fast pyrolysis process, as can be seen through the deviations between the *Base* case and the predicted outcomes from the reaction networks. It is important to distinguish between secondary reactions in this chapter and secondary pyrolysis. While the latter refers to phenomena that degrade medium/high-molecular-weight components that are product of thermal depolymerization, catalyzed by alkali content in the feedstock, the former refers to a set of reactions designed to mimic stages of the pyrolysis of lignocellulose that are not reflected in the reaction networks.

Modeling of the reactors employs the same reactors (38.3 m³) discussed in section 4.3.1. The reactor operates in vapor-phase, at atmospheric pressure and 500 °C. Reactions are presented in Table 4.12, and include phenomena associated to both secondary pyrolysis and aging (section 2.2.1):

1. Cracking of p-coumaryl alcohol and synapaldehyde, two relevant intermediaries for the depolymerization of lignin, which are end products in primary pyrolysis reaction networks in the literature, but are virtually absent from GC/MS analysis [114];
2. Production of methylcyclopentenones from the pyrolysis of hydroxymethylfurfural (HMF), an important product of the primary pyrolysis of cellulose and hemicellulose [106];
3. Partial decomposition of several species to levels closer to those observed in GC/MS analysis, and the complete degradation of glyoxal [232] and fatty acid (from the degradation of triglyceride);
4. The formation of high molecular weight lignin residue based on the condensation of formaldehyde.

Figure 4.14 presents the comparison of the product distribution and composition of the condensates between experimental data, the predictions obtained using the primary pyrolysis network (Table 4.11), and those obtained using the secondary pyrolysis network (Table 4.12). CSTR and PFR unit blocks were again also compared.

The formation of water and gas is often higher using PFR blocks, while CSTR models overproduce cokes (due to non-reacted lignocellulosics and delayed volatilization solids) and organics, thus leading to a better approximation of the experimental distribution (av. dev. 5.3% vs 8.3%), despite being accompanied by a higher excess heat demand (48.31 kW vs 25.10 kW) and presenting simulation errors. The average deviation in the composition of the condensates also favors PFR blocks (av. dev. 5.0% vs 6.7%). The best scenario seems to favor the implementation of **PFR** models going forward.

All models overestimate the different fractions of the condensates to the detriment of the formation of water. Due to a high volatility, it is expected that a fraction of aldehydes formed during pyrolysis will not be recovered in either experimental condensate, but were not detected due to shortcomings in the gas analysis setup.

Table 4.12: List of secondary reactions considered in this work.

#		E _a (kJ/mol)	log ₁₀ [A (s ⁻¹)]	Reference
1 *	C16H34 → 0.302 H ₂ + 0.770 CH ₄ + 2.612 C ₂ H ₄ + 0.812 C ₃ H ₆ + 1.499 C ₄ H ₁₀ + 1.575 C	161.65	15.53	[372]
2 *	ACETICAC → 2 FORMALDY	250.80	17.70	[4]
3 *	ACETOL → FORMALDY + ACETALDY	221.54	15.30	[373]
4	ACETONE → KETENE + CH ₄	145.00	12.30	[4,374]
5 *	CMRYLALC → 0.560 GUAIACOL + 0.050 VANILLIN + 0.060 HMWL + 0.180 H ₂ + 0.360 CH ₄ + 0.330 C ₂ H ₂ + 1.410 C	13.00	4.35	[114,375]
6 *	ETHANOL → 0.5 C ₂ H ₄ + 0.5 WATER + 0.125 CO ₂ + 0.25 CO + 0.25 H ₂ + 0.625 CH ₄	389.98	4.98	[232]
7	FFA + 0.250 WATER → 3.634 CH ₄ + 0.376 CO ₂ + 0.233 H ₂ + 0.32 C16H34 + 0.49 PHENOL + 0.084 HMWL + 2.832 C	275.26	27.63	[376,377]
8 *	37 FORMALDY + 10 H ₂ → HMWL + 25 WATER	70.84	6.92	New, based on [125]
9 *	FURFURAL → VINYLKET + CO	280.06	19.30	[107]
10	GLYOXAL → CO + FORMALDY	60.27	10.39	[96]
11	HAA + H ₂ → METHANOL + FORMALDY	342.76	20.48	[96]
12 *	HMF → 0.79 MF + 0.17 WATER + 1.25 CO + 0.46 H ₂	246.62	18.00	[96,378]
13	KETENE → 0.571 CO + C ₂ H ₄ + 0.036 HMWL + 0.107 CH ₄	55.50	9.98	[379]
14	LEVOGLUC → HMF + 2 WATER	250.80	12.10	[4]
15	METHANOL → CO + 2 H ₂	195.00	13.90	[4]
16 *	MF → 0.5 FURFURAL + 0.5 METC5ONE + 0.5 CO	278.70	21.70	[96,378,380]
17 *	SYNAPALD → 0.782 SYRINGOL + 0.077 HMWL + 0.304 CO + 0.211 CO ₂ + 0.39 C ₂ H ₂ + 0.59 C	13.00	4.35	[114,375]
18 *	VINYLKET + H ₂ → CO + 0.5 CH ₄ + 0.5 C + C ₂ H ₄	273.79	25.05	[379]
19 *	XYLOSAN → FURFURAL + 2 WATER + H ₂	13.00	1.87	[4]

*: Pre-exponential factor modified from original source to match expected extent of reaction.

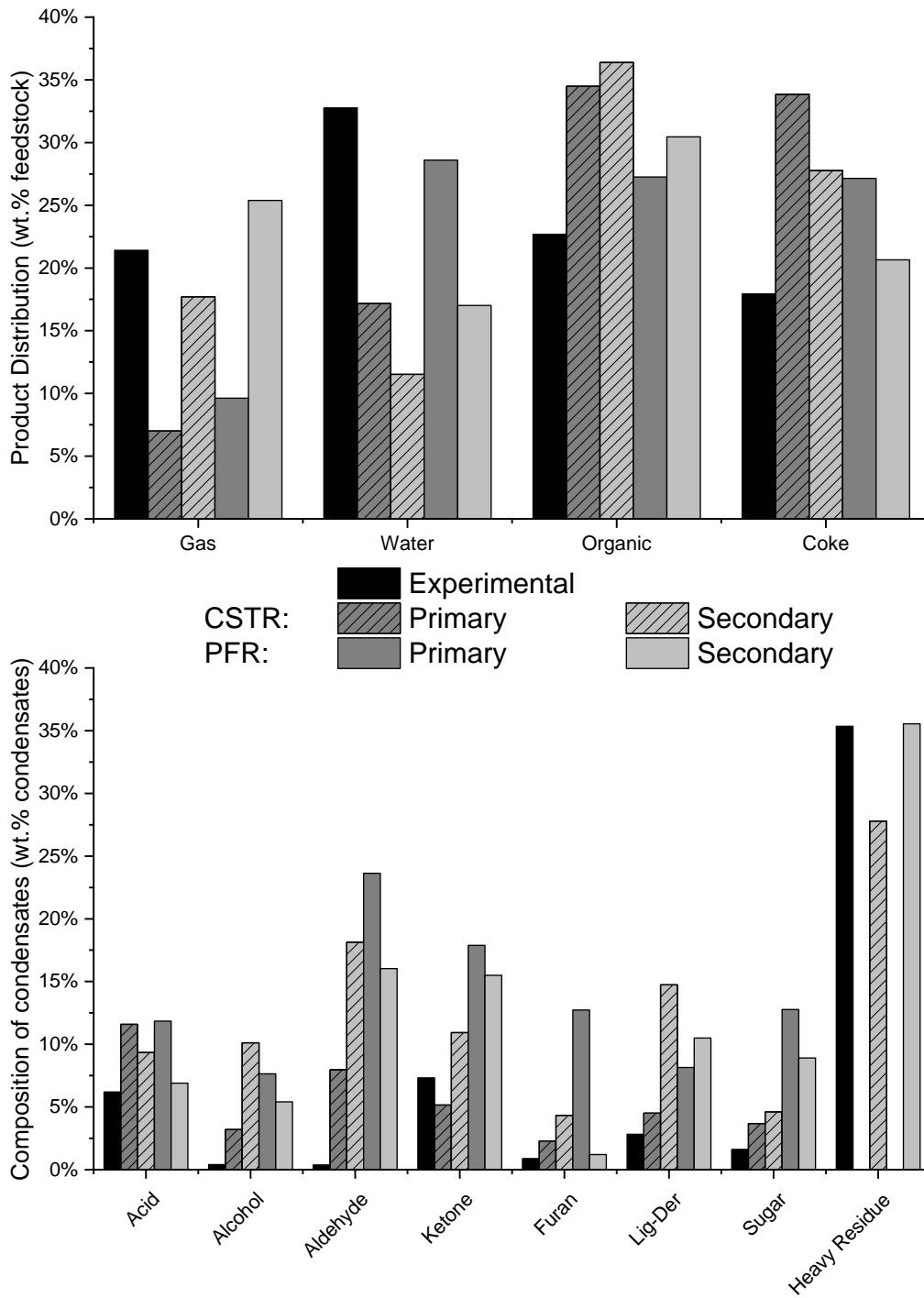


Figure 4.14: Comparison of the base case (Experimental, bioliq® 2015-2018) and the product distribution (up) / the composition of the organic liquid phase (down), after primary pyrolysis (see section 4.3.2) and secondary pyrolysis.

4.4. Solid separation section

The scheme of the solid separation section is presented in Figure 4.15. The spent heat carrier drags a fraction of the formed coke, and this separation was modeled as a *SEP* unit block (*SANDSEP*), in which the user is able to specify the individual distribution of all outward streams. The dragged coke was mixed (*SANDBUF*) with the cold heat carrier prior to reintroduction to the liftpipe hierarchy, while the vapor phase is passed by another *SEP* unit block that mimics the materialization cyclone, and the accrued gas is channeled to the first condenser loop. The distribution of coke in the system is presented in Appendix A.

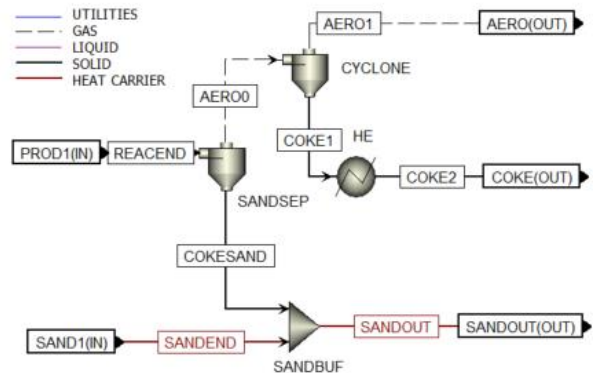


Figure 4.15: Flowsheet view of the solid separation section in Aspen Plus™ V12.

The utility cooling water is defined as a cooling tower water for sake of simplicity, entering at 26° C and exiting at 30° C. Heat exchange with this cooling water is performed using a simplified heater, with a target exit temperature of 50° C; this value which has no experimental meaning, but ensures a high temperature gradient, as the coke is stored in a nitrogen-flushed environment and left to cool down indefinitely, until further use is made of this product.

4.5. Condensation

The condensation loops were modeled separately within hierarchy blocks that permit each condenser model to be a semi-isolated structure, communicating with the rest of the model through input/output streams.

Operation of the ORC condensation loop has been described in detail by Weih et al. [381] (Figure 4.16). Nonetheless, both condenser-loop models (ORC condensation: Figure 4.17, AC condensation: Figure 4.18) share several characteristics, namely the modeling of the columns and the cooling of the bottoms. The differences lay mostly in the condensation method and the position of the condensate collection (before or after cooling). The first condensation loop receives the aerosol stemming from the solid separation hierarchy (section 4.4), and simulates the quenching within a mixing unit block (*QUENCH*) employing a condensate recycling stream (*REFQ-2*). The quench product is passed through a stoichiometric reactor (*ESTERF*) that emulates the esterification of ethylene glycol with acetic acid; this unit also sets temperature and pressure for the mixture to be fed into the separation column. In opposition, the second condensation loop feeds the gas product directly to the column.

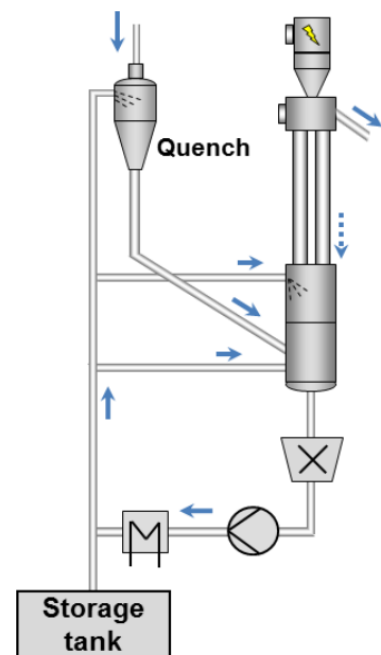


Figure 4.16: Detailed chart of the mass flows in the ORC loop. Source: [381]

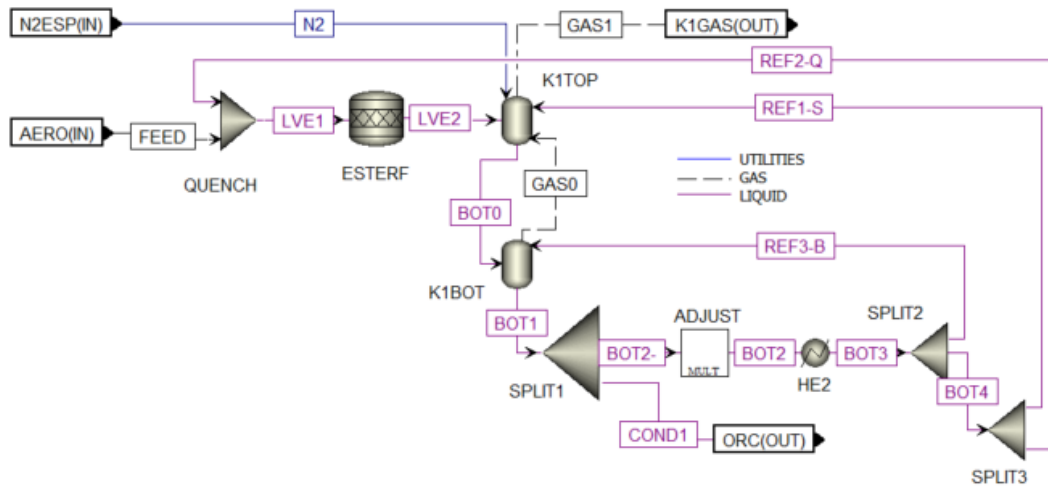


Figure 4.17: Flowsheet view of the ORC condensation loop hierarchy in Aspen Plus™ V12.

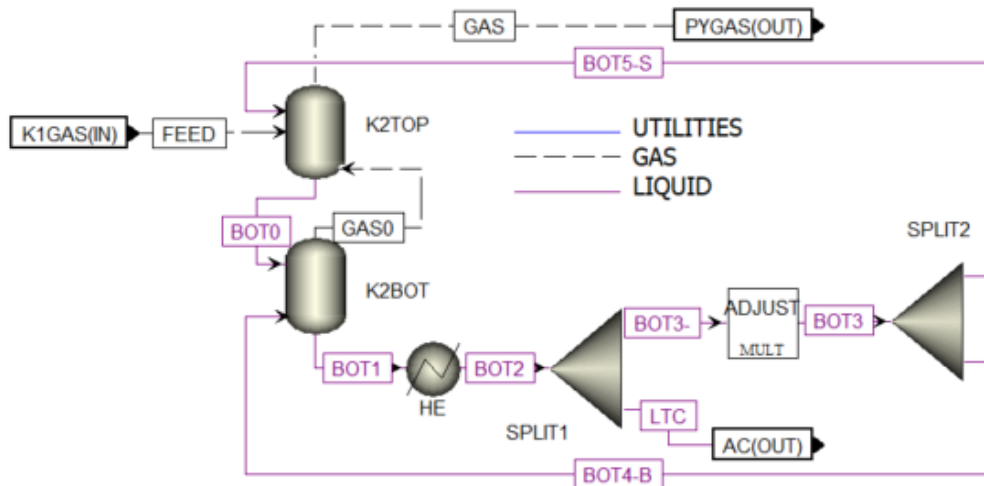


Figure 4.18: Flowsheet view of the AC condensation loop hierarchy in Aspen Plus™ V12.

Following the suggestion of Westerhof et al. [259], modeling of the liquid-vapor separation is performed using flash distillation. Both devices operate like stripping columns using condensate showers (*REF1-S*, *BOT5-S*) with tall liquid levels supplied by bypass recirculation (*REF3-B*, *BOT4-B*). To correctly model the differing operating conditions within the condensers, the device was modeled using two connected flash blocks operating at different temperatures (Table 4.13). The presence of filters, demisters and electrostatic precipitators on the gas stream was disregarded. The ORC loop also employs a stream of sweeping gas (*N2*) fed to the first stage, to emulate the sweeping gas on the electrostatic precipitator (the effect of the electrostatic precipitator was disregarded). Due to the presence of loops, streams *BOT2* in the ORC loop and *BOT3* in the AC loop were defined as pre-initialized tear streams. *ADJUST* represents a multiplier block coupled with a calculator block (*ADJUCALC*) to ensure the correct mass flow in the loop.

Table 4.13: Values of the cooling water utilities and hot stream discharge for the condensation loops.

Loop	Top (C)	Bottom (C)
ORC	88	91
AC	27	31

The coke cooling situation likewise, the cooling waters employed in the loop exchangers are defined as cooling tower water. The values of the cooling water temperatures, as well as the target temperature for the hot stream are given in Table 4.14.

Table 4.14: Values of the cooling water utilities and hot stream discharge for the condensation loops.

	Cooling water Entry (C)	Cooling water Exit (C)	Hot stream Exit (C)
ORC	51	76	86
AC	26	28	30

4.5.1. Loop pre-initialization tests

To ensure convergency into the desired values, a pre-initialization of the loops is required. However, the selection of the initialization mixture is relevant, due to scale effects (the looping liquid flow rate is around 85 times the feedstock flow rate). In that sense, preliminary tests considered the use of different surrogate mixtures, presented in Table 4.15. Solid content is modeled assuming graphite. ORC and AC flow rate are fixed parameters (42 wt.% and 12 wt.% of the feedstock, respectively). Simulation takes place assuming steady-state, directly downstream from the solid separation section (section 4.4). Parameters can be found in Appendix A

Table 4.15: Surrogates tested using the condensation loops shown in Figure 4.17 and Figure 4.18.

	Case 1	Case 2	Case 3	Case 4
ORC	Ethylene Glycol	Water (17%), acetic acid (13%), acetol (10%), HMWL (60%) *	Average of results from internal database *	Table 4.2
Sum of deviations	165%	48%	47%	41%
AC	Water	Water (92%), acetic acid (2%), acetol (3%), Methanol (3%) *	Average of results from internal database *	Table 4.2
Sum of deviations	9%	1%	7%	1%

* Source: data associated with [5], plus results associated with the *bioliq*[®] campaigns of 2015, 2017, 2018, 2019.

Due to the sheer volume of condensate in the loop compared to the feedstock or to the removed flow rate, a difference of almost 2 orders of magnitude, the effect it has in the composition of the condensates is readily noticeable. In Figure 4.19 one can see the effect of the choice of loop starter on this parameter, and in Table 4.15 the sum of deviations is provided as a numerical reference.

Case 1 considers starting the loops using the entrainers (ethylene glycol, water) that the bioliq® materialization employs. As expected, simulating in steady-state does not emulate the correct replacement of the entrainers (matter accumulation is not considered). The simulated ORC presents an excessively high glycol content (64 wt.%) compared to the target (1 wt.%), as well as very low values of any other groups, except and excess of water, attributed to the reaction network and the thermodynamic method. The simulated AC presents a water content of 100 wt.%, thus a virtual absence of other compounds.

The other cases (2, 3, 4) consider increasingly more complex mixtures based in experimental data, starting with a 4-component mixture (Case 2), to an average of the different sources (Case 3), to a mixture based in GC/MS analysis (Case 4). Based on the patterns in Figure 4.19 and the numerical values in Table 4.15, all cases presented similar overall results. Employing the mixture based in GC/MS data provides the best results, but would require the definition of a mixture for each feedstock, leading to a loss of predictive capacity in the model. The Case 3 mixture presented underwhelming results for modeling the AC loop, while leading to negligible improvements when compared to Case 2.

Case 2, due to its nature, having been designed to be a simplified surrogate based on several feedstocks, led to satisfactory results and minimizes the loss of predictive capacity, and is taken as the best option going forward. Despite the good results in modeling the AC, as well as acid/ketone/HMWL content in the ORC, the lack of glycol, ester, aldehyde, furane, aromatic and sugar content in this mixture leads to underestimations of the presence of these types of compounds in the simulated condensates. As stated before, the excessive water content is due to the reaction network and the thermodynamic method.

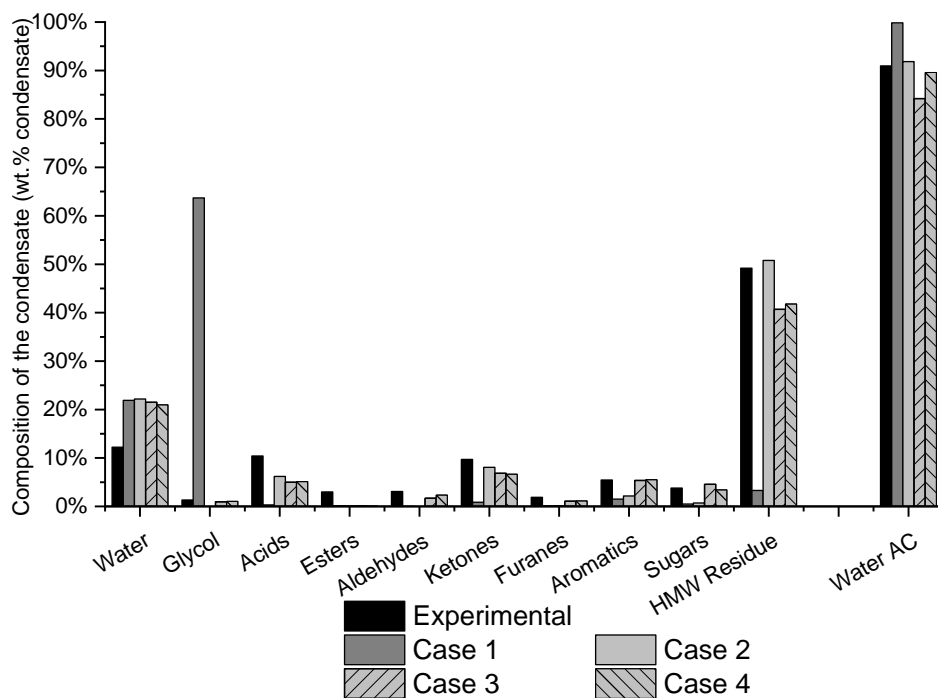


Figure 4.19: Comparison on the influence of the surrogate choice on the composition of the condensates.

5. Final tests

Two series of tests were conducted, the first focused on simulating the effect of varying the moisture content of wheat straw, according to the results presented in [5]; the second compares the feasibility of the model, which was designed with wheat straw in mind, to model the degradation of three other lignocellulosic biomasses. For all cases, condensates are assumed to be constituted of a single liquid phase, thus disregarding the possibility of spontaneous phase separation. It is relevant to notice the data for both bagasse and beech wood were sourced exclusively from the Python-PDU ($10 \text{ kg} \cdot \text{h}^{-1}$), as no *bioliq*[®] campaign data is available for these feedstocks as of September 2022.

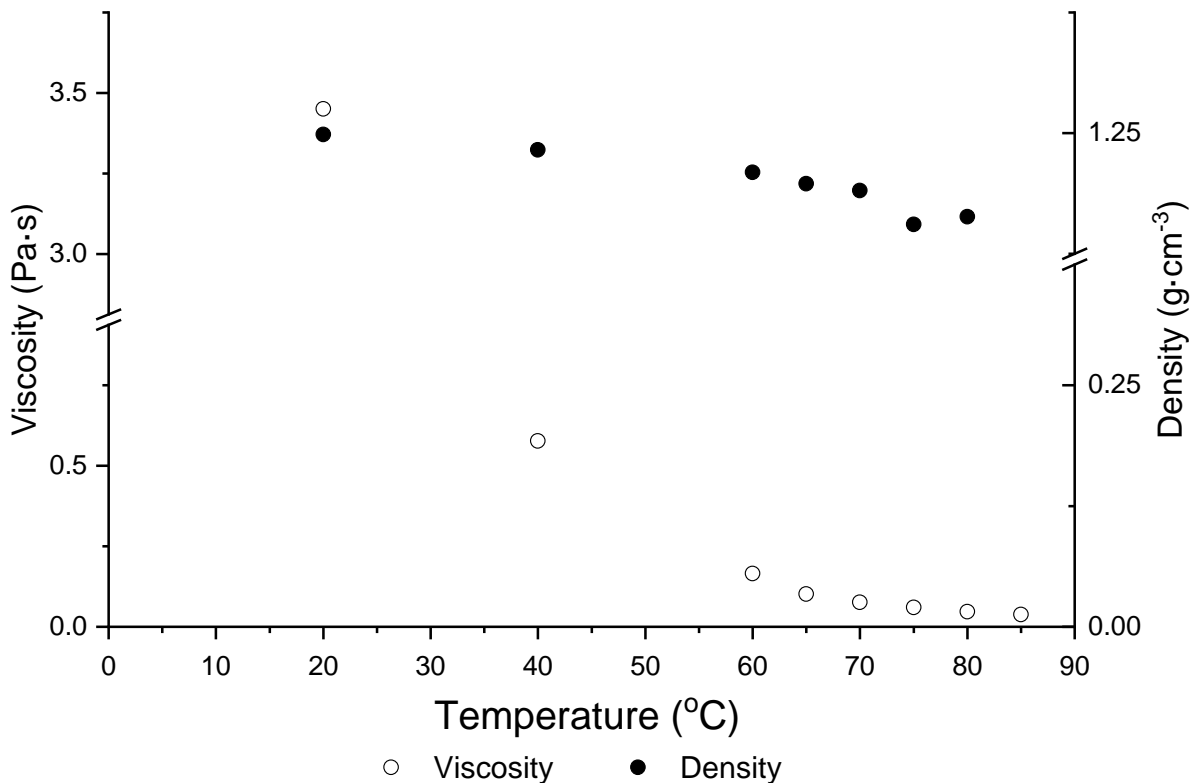


Figure 5.1: Variation of viscosity and density with the measurement temperature. Sample: miscanthus organic condensate, *bioliq*[®] campaign 2020.

The temperature of the condensate loops and the flow rate of the retrieved fractions (ORC and AC) are pre-defined parameters dependent on experimental data, Liquid-liquid-vapor equilibrium was not considered. The loop starters were taken to be **Case 2** presented in section 4.5.1. Reference parameters for the viscosity, density, and heat capacity of the ORC are 38.4 cP (85 °C), $1.16 \text{ g} \cdot \text{cm}^{-3}$ (85 °C), and $2.51 \text{ kJ} \cdot \text{kg}^{-1} \cdot \text{K}^{-1}$ (88.1 °C, water content of 13.3 wt.% solid-free [273]), respectively, and the evolution of the viscosity and heat capacity with the temperature of analysis can be seen in Figure 5.1. A very high fraction of water indicates that the properties of the AC are not expected to differ substantially from those of pure water (at 30 °C: $995.65 \text{ kg} \cdot \text{m}^{-3}$ [270], $4.18 \text{ kJ} \cdot \text{kg}^{-1} \cdot \text{K}^{-1}$ [270], 0.80 cP [357]), but no reference values are available.

Due to the flow rates of the condensates being fixed for each simulation, deviations in product distribution between estimated values and experimental references are focused on the final coke and gas flow rates, as well as mass balance deficits. Differences in composition are also highlighted and discussed.

Apart from the stream composition of the condensate streams, data estimated for this section included parameters like density, heat capacity and viscosity, the fraction (mass and molar), and activity coefficients of relevant components. Elemental composition was estimated for all products by atom balance, but not reported for the second condensate due to a very high water content. These values allowed for the estimation of the heating value (HHV) for organic condensate, coke and gas, using the Channiwala and Parikh [382] method for the first two, and a mass-fraction estimation for the latter.

Cooling water was defined as a utility for the purposes of the simulation, and the yearly early cost of utility was estimated assuming 8500 hours of operation per year, and a cost of 14.8 \$/1000 m³, according to Turton [383].

5.1. Effect of moisture content

Table 5.1: Composition of the feedstock as input to the model. Values in wt.%.

Lignocellulosic Analysis				Proximate Analysis			
	<i>Dry</i>	<i>As Received</i>	<i>Moist</i>		<i>Dry</i>	<i>As Received</i>	<i>Moist</i>
Cellulose ^{a,b}	39.7%	36.5%	30.6%	Moisture	1.2%	9.5%	23.6%
Hemicellulose ^{a,b}	28.3%	26.0%	21.8%	Ash	6.5%	5.6%	5.3%
Lignin-C ^{a,c}	4.6%	4.3%	3.6%	Fixed Carbon ^a	26.6%	24.5%	20.5%
Lignin-H ^{a,c}	8.2%	7.5%	6.3%	Volatile Matter ^a	65.7%	60.5%	50.6%
Lignin-O ^{a,c}	6.6%	6.0%	5.1%	Elemental Analysis			
Triglyceride [358] ^{a,b}	1.7%	1.6%	1.3%	Carbon	47.1%	47.6%	47.7%
Tannin [359] ^{a,b}	3.1%	2.9%	2.4%	Hydrogen	5.9%	5.1%	6.0%
				Oxygen	40.5%	40.9%	41.02%
HHV (MJ·kg⁻¹)	18.53	18.73	19.06				

a: Adapted from the original values to sum to 100% with the ash and moisture content.

b: Values obtained from the Phyllis2 database (www.phyllis.eu).

c: Values obtained from the Phyllis2 database (www.phyllis.eu), and recalculated according to Peters et al. [4].

5.1.1. Product distribution

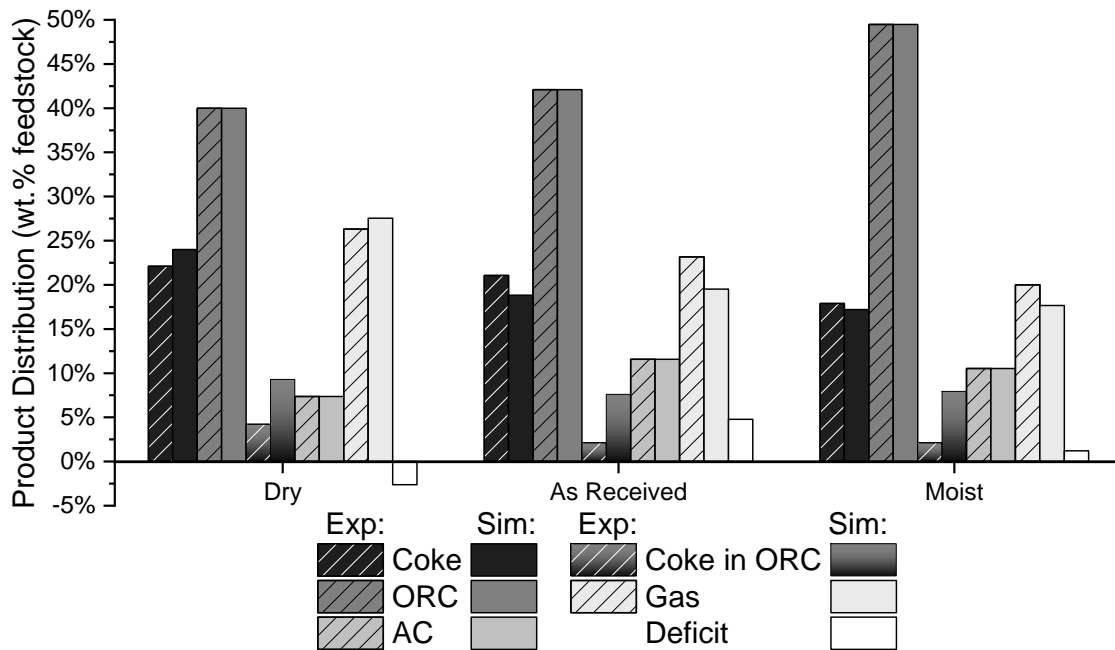


Figure 5.2: Product distribution comparison between experimental data (stripes) and simulation results. The coke in HTC metric does not sum to 100% with the others.

Following the predictions made by Fonseca et al. [5] and the experimental trends, the simulated values (Figure 5.2) follow the experimental trend (coke formation decreases with increased moisture content, and gas follows an opposing trend). The fraction of coke in the HTC, dry coke, and gas are misestimated, within an error of less than 10 wt.% for all cases. The deficit measures the degree of closure of the mass balance (versus the feedstock mass flow, negative values indicate excess product generation), with the error consistently under 5 wt.%.

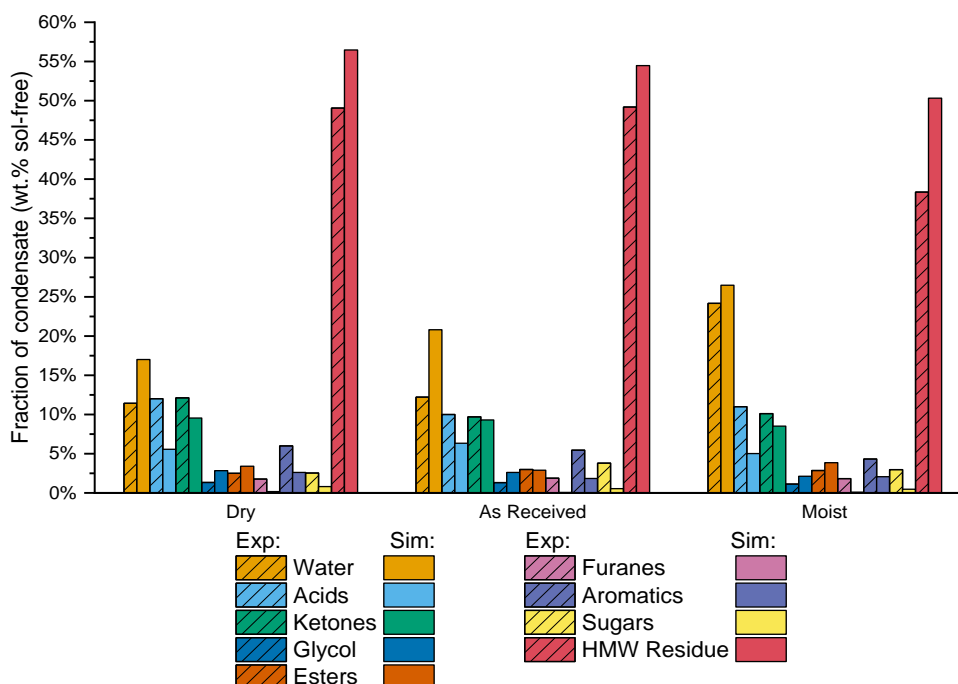


Figure 5.3: Comparison of the composition of the first condensate between experimental data (stripes) and simulation results.

Due to the low mass contents of individual component groups, it is difficult to conclude the existence of an actual influence of the feedstock moisture content and the recovery of different components. Results presented by Fonseca et al. [5] and the experimental values presented in Figure 5.3 indicate there may be a trend at least for acids and aromatics. However, the simulated composition of the bio-oil indicates an under-recovery of most relevant groups attributable in large part to the choice of loop pre-initialization, as the effect is less noticeable for the components that were considered in this loop (acids, ketones, glycol, HMW residue).

Table 5.2: Data estimated for the first condensate and K1 loop, using Aspen Plus 12™.

	Unit	Dry	As Received	Moist
Condensate Produced	kg·h ⁻¹	144.00	151.58	178.11
Density	kg·m ⁻³	255.29	258.81	269.28
Heat Capacity	kJ·kg ⁻¹ ·K ⁻¹	2.41	2.54	2.74
Viscosity	cP	3.77	3.19	2.58
Loop Flow: Mass Balance Error *	kg·h ⁻¹ / kg·h ⁻¹	0.01%	0.28%	0.55%
Elemental composition (C/H/O)	wt.%	49.54%/7.66%/42.80%	47.14%/7.81%/45.05%	43.84%/8.06%/48.10%
	mol.%	28.68%/52.72%/18.60%	27.11%/53.44%/19.45%	24.94%/54.51%/20.54%
Higher Heating Value **	MJ·kg ⁻¹	21.58	20.66	19.45
Water	Frac.	wt.%	17.0%	20.8%
		mol.%	68.8%	73.7%
	Act. coeff.	–	0.94	1.06
Acetic Acid	Frac.	wt.%	5.6%	6.3%
		mol.%	6.8%	6.7%
	Act. coeff.	–	0.67	0.76
Acetol	Frac.	wt.%	9.2%	9.0%
		mol.%	9.1%	7.8%
	Act. coeff.	–	0.60	0.63
Levoglucosan	Frac.	wt.%	0.8%	0.5%
		mol.%	0.4%	0.2%
	Act. coeff.	–	0.04	0.02

* Compared to the target mass flow of 85.37 times the feedstock mass flow (around 30733 kg·h⁻¹).

** Estimated by mass balance, using the Channiwala and Parikh [360] method.

As expected, (Table 5.2), a lower moisture content on the feedstock produces a condensate with a lower water content, as well as a more carbon-rich composition [5]. The properties of the organic condensate seem to be moderately dependent of its water content [384] (properties of pure liquid water at 91 °C: 964.65 kg·m⁻³ [291], 4.21 kJ·kg⁻¹·K⁻¹ [291], 0.31 cP [385]). The software was not able to correctly model any of the mixture properties, which can be attributed to incorrect estimation of physical properties for components without experimental data

(Figure 5.3); for the case of viscosity, the property estimation software was unable to produce viable results for all three high molecular weight lignin representatives, among other relevant molecules (e.g., acetol).

Per definition, the activity coefficient of a component indicates its deviation from the Raoult law relating the partial pressure of the vapor with the vapor pressure of the liquid; values under 1 indicate a volatility lower than the ideal case would indicate, whereas values above 1 indicate a higher than ideal tendency to volatilize. Ille et al. [246] reported an activity coefficient of water between 1.3 and 1.5 in wheat straw condensates at different temperatures, while the computed values (Aspen Plus™, Peng-Robinson using Huron-Vidal mixing rules, activity coefficient in liquids based on UNIFAC) produced values not higher than 1.16; this parameter increased with the water content in the solution for both water and acetic acid, while presenting opposite results for levoglucosan and negligible effect for acetol.

The results of Table 5.3 indicate that estimation of the composition and properties of the AC do not take into consideration the effect of a varying feedstock moisture content, as the model produced condensates with negligible variations between the different cases, and a considerable excess of water content, compared to the target value of 85 wt.%. This is attributed to the choice of initialization pre-loop, necessary due to the volume of looping liquid in comparison to what is removed. As expected, the high water content leads to a unity activity coefficient, and the properties approach those of water at the same temperature (properties of pure liquid water at 30 °C: 995.65 kg·m⁻³ [291], 4.18 kJ·kg⁻¹·K⁻¹ [291], 0.80 cP [385]).

Table 5.3: Data estimated for the second condensate and K2 loop, using Aspen Plus 12™.

	Unit	Dry	As Received	Moist
Condensate Produced	kg·h ⁻¹	26.53	41.68	37.89
Density	kg·m ⁻³	937.65	937.79	937.85
Heat Capacity	kJ·kg ⁻¹ ·K ⁻¹	3.57	3.57	3.57
Viscosity	cP	0.85	0.85	0.85
Loop Flow: Mass Balance Error *	kg·h ⁻¹ / kg·h ⁻¹	-0.49%	-0.37%	-0.48%
Elemental composition (C/H/O)	wt.%	3.41%/11.07%/85.52%	3.40%/11.07%/85.53%	3.39%/11.07%/85.54%
	mol.%	1.71%/66.07%/32.22%	1.71%/66.07%/32.22%	1.70%/66.07%/32.23%
Higher Heating Value **	MJ·kg ⁻¹	4.57	4.57	4.57
Water	Frac.	wt.%	91.8%	91.8%
		mol.%	96.8%	96.8%
	Act. coeff.	–	1.00	1.00
Acetic Acid	Frac.	wt.%	2.0%	2.0%
		mol.%	0.6%	0.6%
	Act. coeff.	–	5.69	5.67

* Compared to the target mass flow of 84.49 times the feedstock mass flow (around 30416 kg·h⁻¹).

** Estimated by mass balance, using the Channiwala and Parikh [360] method.

The results presented in Figure 5.2 also indicate that the simulation is able to predict the production of coke and gas as a function of different moisture contents, a close approximation of the results presented by Fonseca et al. [5]. The simulated characteristics of the coke and gas as presented in Table 5.4.

Figure 5.4 compares the composition of the pyrolysis gases at the final online GC, just prior to flaring, between average bioliq® results and the results obtained in this project. In a first glance, the experimental fraction of most relevant compounds except water varies negligibly with the moisture content of the biomass; the simulated results present a stronger variance with this parameter. Looking more specifically, the water fraction is well modeled during simulation, while the production of light hydrocarbonates (C₁-C₅) is mostly absent, indicating issues with either primary or secondary reaction modeling. The simulated productions of CO and CO₂ are almost symmetrical results of the experimental data, indicating further issues with reactor model; around 75% of the CO and 60% of the CO₂ appear to be produced during secondary pyrolysis. Simulation results also present relevant fractions of components assumed to condense, as around 10 wt.% of the simulated gas is comprised of acetic acid, formaldehyde and methylcyclopentenone; the presence of light oxygenates in the experimental pyrolysis gas cannot be ruled out, as the online instruments are not calibrated to account for this fraction.

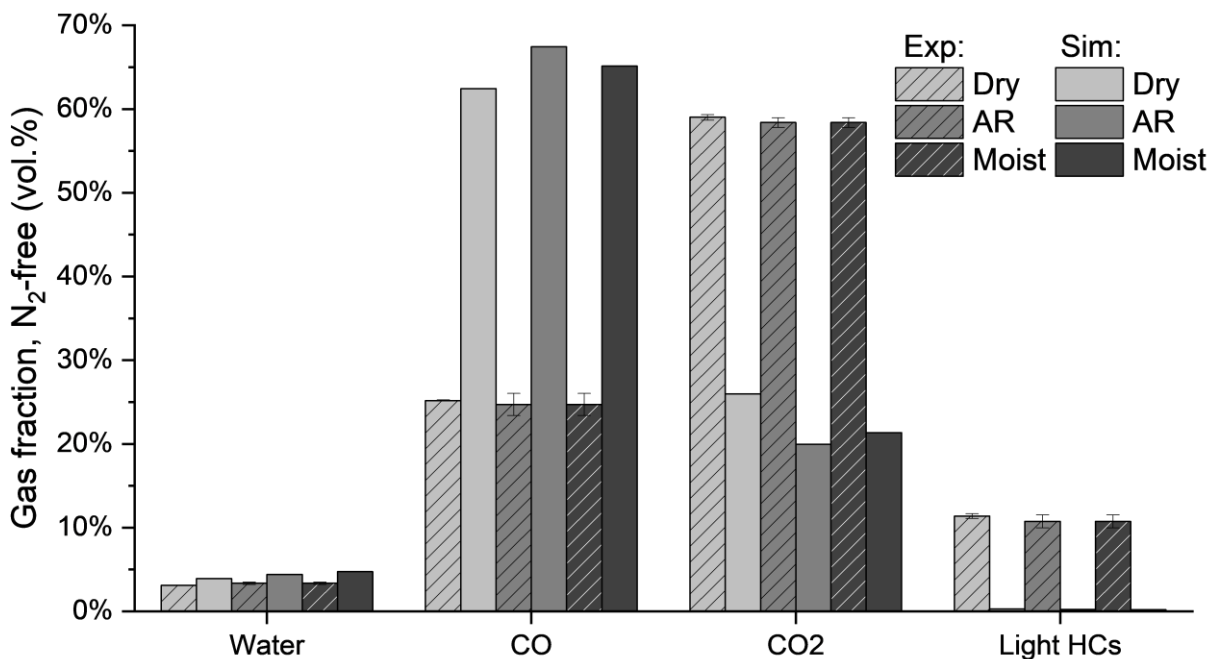


Figure 5.4: Comparison of the composition of the pyrolysis gas between campaign data and simulation results.

Table 5.4: Data estimated for the pyrolysis gas and coke products using Aspen Plus 12™.

		Unit	Dry	As Received	Moist
Gas	Mass Flow	kg·h ⁻¹	99.14	70.26	63.57
	Density	kg·m ⁻³	0.84	0.86	0.84
	Heat Capacity	J·kg ⁻¹ ·K ⁻¹	17.06	17.12	17.14
	Elemental composition (C/H/O) *	vol.%	25.77%/42.52%/31.71%	26.03%/43.13%/30.84%	24.50%/45.94%/29.56%
	Higher Heating Value **	MJ·kg ⁻¹	10.77	9.22	9.63
Coke	Condensate Produced	kg·h ⁻¹	86.37	67.78	61.93
	Density	kg·m ⁻³	2215	2265	2255
	Heat Capacity	kJ·kg ⁻¹ ·K ⁻¹	0.77	0.77	0.77
	Elemental composition (C/H/O)	wt.%	82.11%/3.50%/14.39%	85.56%/2.79%/11.65%	84.88%/2.98%/12.14%
	Higher Heating Value ***	MJ·kg ⁻¹	31.35	32.04	31.97

* Nitrogen-free

** Estimated by volume balance.

*** Estimated by mass balance, using the Channiwala and Parikh [360] method.

5.1.2. Energetic balance

It is possible to estimate the energetic demand of the reactor within the simulation, by summing the energy demand of the unit blocks within the hierarchy (section 4.3), and compare them with values estimated experimentally [5] or through energetics studies such as the ones conducted by Heinrich et al. [31], discussed in section 4.1.1. The simulated value considers two abstractions that may skew the value: 1. separating the biomass into its constitution (Table 5.1), 2. secondary pyrolysis and vaporization of feedstock moisture (3.39 MJ·kg⁻¹), which together total to an extra demand total of over 60 kW on top of the primary pyrolysis (section 4.3.1).

As stated in section 4.1.1, an HC ratio of 14.4:1 only supplies 55.6 kW, a value that pales in comparison with the estimated reactor demand using either estimation method. In that sense, the HC ratio necessary to cover the entire demand (assuming the same feedstock feed rate, temperature drop and heat capacity) was estimated; indicating that a ratio of 50:1 is more realistic to model the heat carrier demand, but not even this value suffices to model the simulated demand that considers feedstock splitting, volatilization and secondary pyrolysis. This indicates a relevant issue in the estimation of heat of reaction in the model, which may stem from human error, mass balance issues or even faults in the reaction network; the latter was design to fit the DSC behavior of a small biomass sample, thus not being an optimal representation of a real pyrolysis system.

Fonseca et al. [5] claimed it was theoretically possible to cover the reactor demand by combusting the pyrolysis gas. It is important to consider that the simulation results indicate an overproduction of gas for all cases, therefore values from the experimental mass balance were also include, using the same estimated heating value. These values are presented in Table 5.5, and the claim by Fonseca et al. [5] seems to hold true for all cases except when using the experimental pyrolysis gas with the simulated reactor demand during operation with moist wheat straw.

Table 5.5: Estimation of the reactor energy demand and comparison with the potential supply from combusting the pyrolysis gas, assuming a furnace efficiency of 80% [5]

	Reactor energy demand (kW)			Pyrolysis gas (kW)	
	Simulated	Heinrich et al. [269]	Fonseca et al. [5]	Simulated	Mass balance
Dry	403	128	138	237	227
As Received	192	145	133	144	171
Moist	186	175	161	136	154

* Refers to the value calculated based on the experimental mass balance estimated after trials in the Python-PDU.

Table 5.6 shows the estimation of the consumption of cooling water in the system, as well as its expected annual cost. Fonseca et al. [5] reported it was theoretically possible to cover the heating demand of a low-temperature dryer using the removed heat duty of the ORC loop, assuming a reduction in moisture content to 1.21 wt.% (AR → Dry: 18.73 kW, Moist → Dry: 50.56 kW), a result which still holds based on the results of the simulation, and would lead to relevant savings in utility costs.

Table 5.6: Estimation of cooling water consumption and cost in the system based on all cases.

		Flow (kg·h ⁻¹)	Duty (kW)	Cost (€/year) *
Dry	Coke	1576	7.3	192
	ORC	3361	97.5	419
	AC	13087	30.3	1594
	Total			2204
As Received	Coke	1595	7.4	194
	ORC	3084	89.5	384
	AC	13079	30.3	1593
	Total			2171
Moist	Coke	1593	7.4	194
	ORC	3537	102.7	441
	AC	13092	30.4	1594
	Total			2229

*: Cost of utility assumed to be 14.8 \$/1000 m³, yearly hours of operation: 8500 h/annum. Source: Turton [361]. Conversion USD\$ to € based on values on 18/11/2023, 12:38.

5.2. Comparison of lignocellulosic biomasses

The composition of the feedstocks is presented in Table 5.7.

Table 5.7: Composition of the feedstock as input to the model. Values in wt.%.

Lignocellulosic Analysis + Extractives				
	Wheat Straw	<i>Miscanthus</i>	Sugar Cane Bagasse	Beech Wood
Cellulose ^{a,b}	39.7%	43.0%	32.8%	39.1%
Hemicellulose ^{a,b}	28.3%	23.0%	31.5%	28.1%
Lignin-C ^{a,c}	4.6%	4.7%	4.5%	4.7%
Lignin-H ^{a,c}	8.2%	8.9%	8.4%	8.9%
Lignin-O ^{a,c}	6.6%	6.9%	6.6%	6.9%
Triglyceride ^{a,b}	1.7% [358]	0.4% [362]	0.1% [363]	0.1% [364]
Tannin ^{a,b}	3.1% [359]	0.2% [362]	0.7% [363]	0.8% [364]
Proximate Analysis				
Moisture	9.5%	9.4%	4.6%	10.2%
Ash	5.6%	3.5%	10.9%	1.1%
Fixed Carbon ^a	24.5%	15.8%	13.7%	16.4%
Volatile Matter ^a	60.5%	71.3%	70.8%	72.3%
Elemental Analysis				
Carbon	47.6%	48.6%	44.2%	48.3%
Hydrogen	5.1%	6.1%	5.3%	6.0%
Oxygen	40.9%	41.8%	39.5%	44.6%
HHV (MJ·kg⁻¹)	18.73	18.79	19.18	19.16

a: Adapted from the original values to sum to 100% with the ash and moisture content.

b: Values obtained from the Phyllis2 database (www.phyllis.eu).

c: Values obtained from the Phyllis2 database (www.phyllis.eu), and recalculated according to Peters et al. [4].

5.2.1. Product distribution

Figure 5.5 presents the product distribution for the four different biomasses, wheat straw (same as the *As Received* data, shown here for comparison purposes), *Miscanthus*, sugar cane bagasse and beech wood. The production of gas is slightly underestimated for all the newly-considered feedstocks, with a deviation never higher than 5 wt.%, while that of coke is very slightly overestimated for *Miscanthus* (if counting on the coke dragged to the ORC) but considerably higher for bagasse and beech, around 10 wt.%. Most of these contribute to a slight positive deviation for the *Miscanthus* case, and a starker negative deficit for the latter two, indicating a product sum that is higher than the material feed.

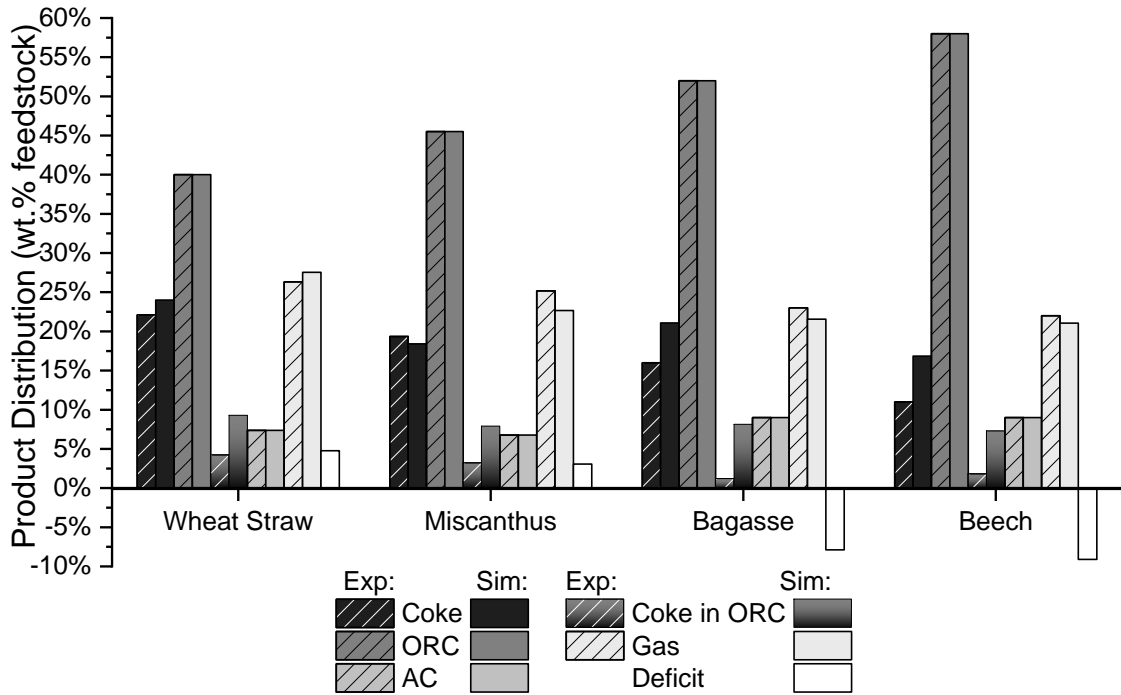


Figure 5.5: Product distribution comparison between experimental data (stripes) and simulation results. The coke in HTC metric does not sum to 100% with the others.

It must be kept in mind that all phenomena of biomass degradation were simulated using the same reaction network (section 4.3.1), which does not consider ash content. Figure 5.6 presents the composition of the simulated ORC and compares it with the experimental values obtained by GC/MS. The model visibly overestimates the water, ketones, and glycol/esters fractions, while underestimating the other species, with a particular impact in the aromatic and sugar contents, two-component groups more relevant in feedstocks other than wheat straw.

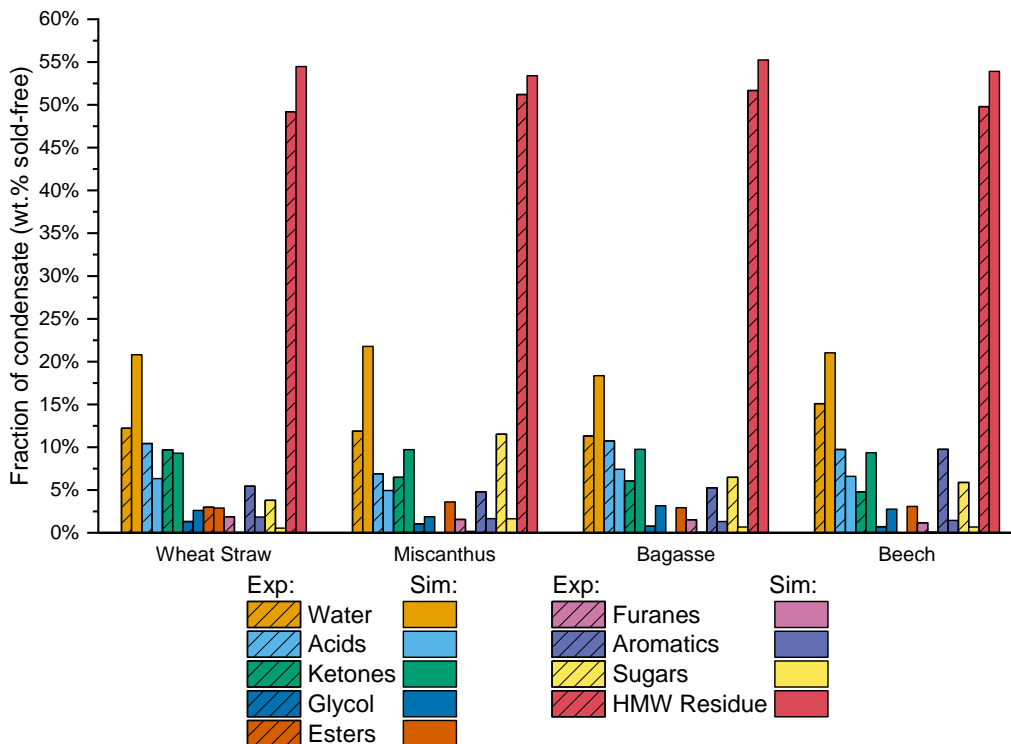


Figure 5.6: Comparison of the composition of the first condensate between experimental data (stripes) and simulation results.

These deviations are attributable to the reaction network, but also the loop pre-initialization method. The results of Table 5.8 indicate a very minor variation in the characteristics of the ORC when the feedstock is varied, hence only the results for water were presented. This fact indicates a shortcoming of the loop initialization method and was not so visible during section 5.1.1 due to more pronounced variances in feedstock moisture content between the different cases.

Table 5.8: Data estimated for the first condensate and K1 loop, using Aspen Plus 12™.

	Unit	Wheat Straw	Miscanthus	Sugar Cane Bagasse		Beech Wood
Condensate Produced	kg·h ⁻¹	151.58	163.79	187.20		208.80
Density	kg·m ⁻³	258.81	262.37	257.57		260.35
Heat Capacity	kJ·kg ⁻¹ ·K ⁻¹	2.54	2.61	2.47		2.56
Viscosity	cP	3.19	3.20	3.42		3.12
Loop Flow: Mass Balance Error *	kg·h ⁻¹ / kg·h ⁻¹	0.28%	0.36%	0.01%		0.04%
Elemental composition (C/H/O)	wt. %	47.14%/7.81%/45.05%	46.63%/7.85%/45.52%	48.17%/7.73%/44.10%		46.78%/7.83%/45.39%
	mol. %	27.11%/53.44%/19.45%	26.78%/53.59%/19.63%	27.82%/53.06%/19.12%		26.89%/53.53%/19.59%
Higher Heating Value **	MJ·kg ⁻¹	20.66	20.47	21.03		20.52
Water	Frac.	wt. %	20.8%	21.8%	18.4%	21.0%
		mol. %	73.7%	75.4%	69.7%	73.6%
	Act. coeff.	–	1.06	1.07	0.99	1.07

* Compared to the target mass flow of 85.37 times the feedstock mass flow (around 30733 kg·h⁻¹).

As shown in both Figure 5.6 and Table 5.8, the characteristics of the feedstock (Table 5.7). The model seems to overestimate the recovery of water and solids, and underestimate acetic acid, levoglucosan and high molecular weight for all biomasses, which may be attributed to the reaction network employed. The results reflect a very important dependence on the loop starter composition (e.g., in Table 4.2 for wheat straw). Neither transport parameters (density, heat capacity, viscosity) nor estimated activity coefficients (water, acetic acid, acetol, levoglucosan) vary appreciably between different estimated condensates, featuring the same issues discussed for the moisture content comparison.

Table 5.9: Data estimated for the second condensate and K2 loop, using Aspen Plus 12™.

	Unit	Wheat Straw	Miscanthus	Sugar Cane Bagasse	Beech Wood	
Condensate Produced	kg·h ⁻¹	41.68	24.39	32.40	32.40	
Density	kg·m ⁻³	937.79	937.81	937.81	937.81	
Heat Capacity	kJ·kg ⁻¹ ·K ⁻¹	3.57	3.57	3.57	3.57	
Viscosity	cP	0.85	0.85	0.85	0.85	
Loop Flow: Mass Balance Error *	kg·h ⁻¹ / kg·h ⁻¹	-0.37%	-0.48%	-0.37%	-0.43%	
Elemental composition (C/H/O)	wt.%	3.40%/11.07%/ 85.53%	3.40%/11.07%/ 85.53%	3.41%/11.07%/ 85.52%	3.40%/11.07%/ 85.53%	
	mol.%	1.71%/66.07%/ 32.22%	1.71%/66.07%/ 32.22%	1.71%/66.07%/ 32.22%	1.71%/66.07%/ 32.22%	
Higher Heating Value **	MJ·kg ⁻¹	4.57	4.57	4.57	4.57	
Water	Frac.	wt.%	91.8%	91.8%	91.8%	91.8%
		mol.%	96.8%	96.8%	96.8%	96.8%
	Act. coeff.	–	1.00	1.00	1.00	1.00

The characteristics of the AC (Table 5.9), gas and coke (Table 5.10) do not vary appreciably between the different feedstock. This can be attributed to aforementioned shortcomings associated with the decision of reaction network and loop pre-initialization issues, but also, at least for the former two, with the phase separation in the first condenser directly impacting the composition of the second one. The lack of variation between the biomasses in terms of lignocellulosic composition (Table 5.7) also leads to a higher similarity between the products.

Table 5.10: Data estimated for the pyrolysis gas and coke products using Aspen Plus 12™.

	Unit	Wheat Straw	Miscanthus	Sugar Cane Bagasse	Beech Wood	
Gas	Mass Flow	kg·h ⁻¹	70.26	81.62	77.66	75.77
	Density	kg·m ⁻³	0.86	0.92	0.85	0.87
	Heat Capacity	J·kg ⁻¹ ·K ⁻¹	17.12	16.94	17.10	17.09
	Elemental composition (C/H/O) *	vol.%	26.03%/43.13%/ 30.84%	29.40%/37.83%/ 32.77%	26.34%/42.34%/ 31.31%	26.91%/41.48%/ 31.60%
	Higher Heating Value **	MJ·kg ⁻¹	9.22	9.14	9.43	9.15
Coke	Condensate Produced	kg·h ⁻¹	67.78	66.26	75.90	60.61
	Density	kg·m ⁻³	2265	2205	2362	2147
	Heat Capacity	kJ·kg ⁻¹ ·K ⁻¹	0.77	0.77	0.77	0.77
	Elemental composition (C/H/O)	wt.%	85.56%/2.79%/ 11.65%	87.28%/2.66%/ 10.06%	83.07%/3.28%/ 13.65%	85.31%/2.87%/ 11.82%
	Higher Heating Value ***	MJ·kg ⁻¹	32.04	32.67	31.51	32.03

* Nitrogen-free

** Estimated by volume balance.

*** Estimated by mass balance, using the Channiwala and Parikh [360] method.

In the same way as Figure 5.4, Figure 5.7 compares the gas composition measured in the Python-PDU for *Miscanthus*, sugar cane bagasse and beech wood with bioliq® data for wheat straw, as well as estimated data from process simulations. Very similar behaviors to the ones observed in Figure 5.4 can be observed, with a different experimental behavior for each biomass, namely the fraction of CO, CO₂ and light hydrocarbons being highly variable, but very similar in the simulation results. Again, a relevant presence of light oxygenates in the simulated results whose detection is not accounted for in the experimental setup reveals that a non-negligible fraction of these gases may be volatilizing at K2 conditions.

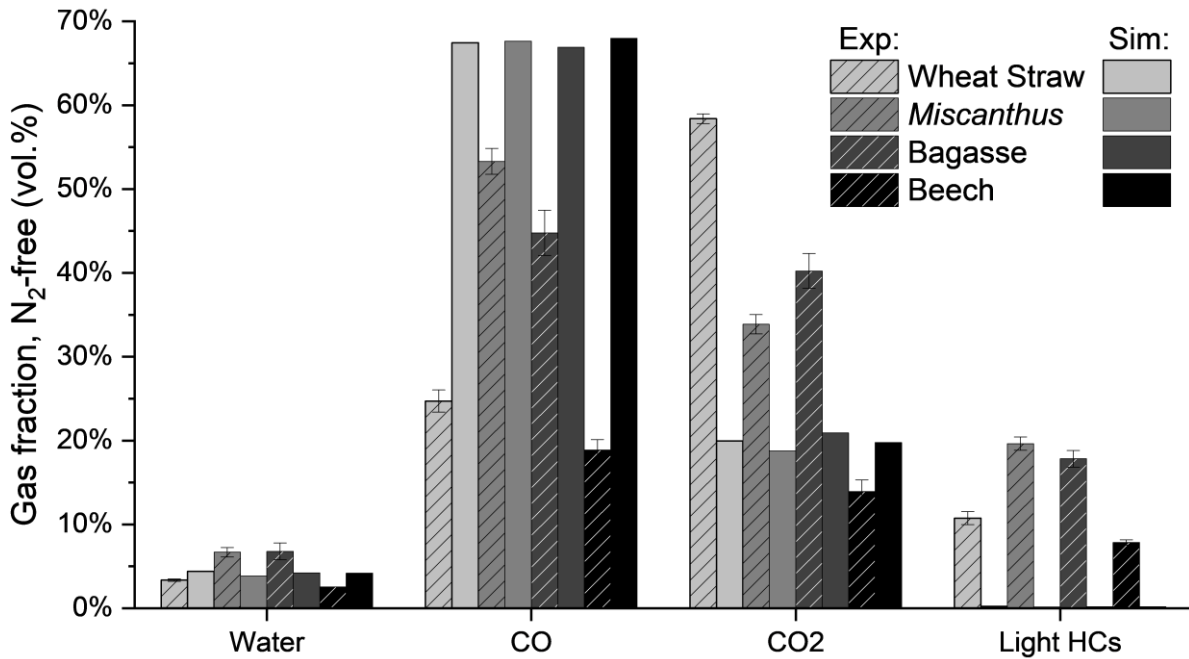


Figure 5.7: Comparison of the composition of the pyrolysis gas between campaign data and simulation results.

5.2.2. Energetic balance

As it was done in the comparison between the different moisture contents (section 5.1.2), the heat demand of the reactor was estimated by summing the demands of the individual unit blocks, with the same abstractions already mentioned. Heinrich et al. [31] did not propose coefficients for all the biomasses under study, hence not being used in this case.

The value estimated for the reactor demand for bagasse is considerably higher than those estimated for the other biomasses, as shown in Table 5.11. Due to the lack of considerable differences between feedstocks (Table 5.7), this difference can be attributed to issues like those discussed in section 5.1.2. Regarding the use of pyrolysis gas to cover the reactor demand [5], none of the pyrolysis gas heat supply estimates suffice to cover the simulated reactor demand, assuming as valid the heat demand estimated using Aspen Plus™.

Table 5.11: Estimation of the reactor demand and comparison with the potential supply from combusting the pyrolysis gas, assuming a furnace efficiency of 80% [5].

	Reactor energy demand (kW)	Pyrolysis gas (kW)	
	<i>Simulated</i>	<i>Simulated</i>	<i>Experimental</i> *
Wheat Straw	192	144	171
Miscanthus	207	166	184
Sugar Cane Bagasse	456	163	174
Beech	219	154	161

* Refers to the value calculated based on the experimental mass balance estimated after trials in the Python-PDU.

The estimated consumption of cooling water for the different cases is shown in Table 5.12. The values do not diverge appreciably between the different feedstocks for the two condensate loops, reinforcing the notion that the loop pre-initialization and lack of variability in composition between different biomasses lead to very similarly presenting simulation results. Regarding coke, higher yields and higher carbon contents lead to visibly higher cooling demands.

Table 5.12: Estimation of cooling water consumption and cost in the system based on all cases.

		Flow (kg·h ⁻¹)	Duty (kW)	Cost (€/year) *			Flow (kg·h ⁻¹)	Duty (kW)	Cost (€/year) *
Wheat Straw	<i>Coke</i>	1595	7.4	194	Sugar Cane Bagasse	<i>Coke</i>	5201	24.1	634
	<i>Loop 1</i>	3084	89.5	384		<i>Loop 1</i>	3868	112.3	482
	<i>Loop 2</i>	13079	30.3	1593		<i>Loop 2</i>	13074	30.3	1592
	<i>Total</i>			2171		<i>Total</i>			2708
Miscanthus	<i>Coke</i>	313	1.4	38	Beech Wood	<i>Coke</i>	1576	7.3	192
	<i>Loop 1</i>	2836	82.3	353		<i>Loop 1</i>	3361	97.5	419
	<i>Loop 2</i>	13086	30.3	1594		<i>Loop 2</i>	13074	30.3	1592
	<i>Total</i>			1985		<i>Total</i>			2203

*: Cost of utility assumed to be 14.8 \$/1000 m³, yearly hours of operation: 8500 h/annum. Source: Turton [361]. Conversion USD\$ to € based on values on 18/11/2023, 12:38.

6. Conclusions and Future Work

Societies and cultures require ever-expanding resource pools to ensure their sustenance, thrift, and expansion. Throughout the centuries, humanity has mastered ways to convert natural resources into goods and heat, and most recently into electricity. However, the approach to the consumption of these resources has seldom been holistic and sustainable, and the generation of waste and pollution was a non-factor until very recent times.

If until the age of discovery societies often made use of what was readily available, the arrival of steam power, as well as the subsequent discovery and taming of electricity, narrowed progress and resource-use in energy generation to carbon-rich materials such as coal, petroleum, and natural gas. Apart from the often-stated issues associated with the use of these commodities, such as air pollution and anthropogenic global warming, the worldwide distribution of these resources is uneven and of varying degrees of accessibility and environmental impact, making communities economically and politically dependent on external sources for their heat and energy.

Technology change is not instant. Older, less efficient technologies are shunned by developed countries but due to their seniority tend to be affordable and of inexpensive maintenance, therefore appealing to developing regions. Thus, instead of solving the political, economic and environmental problems associated with the use of fossil fuels, the trend in the latest decades has focused on moving them to societies with faster demographic expansion and with more permissive legislation. Pyrolysis and the downstream processing of its products are available in a series of technologies of different scales, bringing a potential source of heat, coke and bio-oil from renewable locally sourced materials, thus contributing to the economic valorization of rural areas, and lowering the economic dependency of communities worldwide.

A substantial fraction, if not the majority, of the electricity produced in Western Europe, stems from renewable non-biogenic resources (hydro, wind, solar, etc...). However, nuclear power is being discontinued or downscaled in countries such as Germany, and a direct substitution is likely to be made by fossil fuels. The use of fossil fuels is still a very relevant pillar in both electricity production and as a source of fuels and commodities, and the European continent as a whole has great petroleum and natural gas deficit, leading to economic dependency which can be used as diplomatic bargaining chips or used to foster conflict, thus impacting the local population. The present political and economic climate in the world is conducive to investment in alternative energy sources to reduce or dethrone the use of fossil fuels. While more established technologies can be used for the production of electricity avoiding the use of non-renewable and pollutant commodities, pyrolysis may assist in the production of fuels and chemicals akin to those currently produced from petroleum.

Returning to the use of biomass as a source of energy may be one solution amongst several to solve the external energetic dependency of communities without cheap access to these commodities while applying modern technology to ensure high energy and material yield from this biomass. Pyrolysis, a thermochemical process that employs heat to degrade solid materials into char, oil and gas, is a proven source of fuels, high-value chemicals and char; the combustion of the produced gas, of low heating value, may be used to partially or completely suppress the heat demand of the process.

The *bioliq*[®] concept stands on two premises: on one hand, the transportation of low-density solid biomass over long distances is logistically costly due to a very low energy density, and the fact that pyrolysis inherently produces two products of high energy density that are cheaper to transport (coke, oil). Therefore, the process decentralizes the pyrolysis step to small-scale local units closer to the production of biomass, either forestry or agricultural residues, and transports the product to a refining unit for the production of commodities. The use of residues ensures the further economic valorization of the crop or forest area, without competing with food production. The overarching objective of this work was, then, to develop a rigorous and versatile model of the first step of this concept, the decentralized fast pyrolysis unit (*bioliq*[®] I). Aspen Plus[™] was chosen as the process simulation software due to its ubiquity in academia and industry, ease of use, and access to both a powerful thermophysical database and a property estimation add-on (Aspen Properties[™]).

Several descriptive models are already available that connect a feedstock to a certain product distribution, but do not allow for variations in feedstock and operating conditions. To define a predictive model for fast pyrolysis that emulates the *bioliq*[®] I materialization not only is a flexible reactor model that specifically considers ash or alkali content required, but also the complete characterization of the feedstock and any chemical species considered in the model. Wheat straw was chosen as model lignocellulosic biomass due to being a non-optimal feedstock of high ash content, as well as being the prime feedstock used in the materialization of the *bioliq*[®] plant within the period 2015-2018.

Feedstock characterization has focused on its ultimate, proximate and lignocellulosic component analysis. While the former two are inexpensive, the latter is not only costly and cumbersome but also not standardized. Thermogravimetry is therefore employed, providing an inexpensive imperfect alternative to laboratory methods. The greatest challenge of TGA when characterizing biomasses like wheat straw is the presence of a single degradation peak that encompasses the entirety of the lignocellulosic degradation, in contrast to other biomasses that feature separate peaks for hemicellulose and cellulose. Detecting the peaks was achieved by mapping the zeros in the second derivative function to obtain inflection points (peaks) of the first derivative curve, based on heuristics proposed by Gaitán-Álvarez et al. [172] and Wu et al. [168]. This method is based on the ratio of areas of each component and thus can lead to underestimation of either hemicellulosic or cellulosic composition, explaining an average methodology error of 30.3 wt.%.

The TGA curves may also be used to calculate Arrhenius-type kinetics of the degradation assuming concurrent degradation of the different lignocellulosic components of the feedstocks. Two main types of methods

were employed: simultaneous curve-fitting to estimate kinetics and lignocellulosic composition, and isoconversional methods for the extrapolation to high decomposition rates. Unsurprisingly, due to being very close to the experimental curves, the curve-fitting methods led to the lowest deviations in terms of both lignocellulosic decomposition and biomass degradation modeling. Two sets of parameters were varied: ash content (contrasting beech wood with wheat straw) and particle size (contrasting wheat straw powder and hull, i.e., < 1 mm vs. 5 mm) the impact of the former is clear on the process, especially on the visual representation of the degradation speed at increasing temperature (by using the derivative of the mass loss), while the latter had a small but not negligible effect on the final values, with the results being presented in [159].

To ensure versatility in the biomass representation, the lignocellulosic composition, as well as moisture, ash, triglyceride, and tannin content of the biomass, was taken as characteristics of the different batches, ensuring the possibility of easy customization of the model even between different batches of the same biomass. This point was well achieved, by successfully employing a calculation scheme automatized by Peters et al. [4] to estimate the lignin fractions based on the lignin content. However, *a priori* estimation of these contents should be made for each batch used, which requires a series of morose and expensive analyses and/or the use of estimation methodologies based on deconvolution and heuristics (and possibly incurring systematic error), or the use of values available on the literature, which may not reflect the specific quality of the material in use.

Choosing how to correctly model the biomass decomposition in a way that is predictive and versatile should not make use of black-box models as frequently presented in other bodies of work (example [5]). Fortunately, a series of researchers have made advances in the modeling of the pyrolysis of lignocellulosic biomasses culminating in several reaction networks. The decision between these and the ultimate choice was focused on how well they estimated the biomass degradation based on thermogravimetry, and how well they estimate the product distribution and condensate composition using process simulation. However, transversal to all these networks is the fact that the presence of ash in the feedstock is not considered, nor is its catalytic effect on the degradation of biomass and the obtained final products. This subject has unfortunately not had sufficient research put into it, except for cellulose due to its ease of access and low cost; Trendewicz et al. [142], estimated the effect of potassium in the degradation of this material, in both kinetics and product distribution. In this work, the aforementioned pyrolysis reaction networks were adapted with this approach and tested at different potassium contents, for both thermogravimetry deviation and simulation performance. Based on these investigations, the decision ultimately fell on the RAC [119] network as the best match for the process, using wheat straw as model biomass. Further work should focus on the expanding the logic employed by Trendewicz et al. [142] into both other minerals, namely iron and calcium, or the other lignocellulosic feedstocks, to be able to account for the ash composition.

Not only are the kinetics important for the model, but also the selection of the reactor model to use. For complex kinetics in continuous steady-state, the choice often falls between variations of CSTR or PFR reactors. Henrich et al. [269] estimated that for a reactor of similar dimensions and operating conditions, a single PFR reactor would suffice. However, PFR reactors often present several modeling issues due to the modeling method

(integration over the length) when employing very complex reaction networks that often lead to mass imbalances. The tests mentioned in the last paragraph also considered this possibility, and ultimately it was decided to employ PFR models. Ultimately, both of these models are idealized concepts, and a third option may lay in the custom modeling of a reactor in a similar fashion to the work presented by Humbird et al. [113], for example, based on the dimensionless modeling by Funke et al. [365].

The final product composition obtained using the aforementioned reaction networks differed significantly from the experimental data, in terms of product distribution, and condensate composition (both species and their relative abundance). As a result, a series of secondary reactions have been devised to bridge this gap. It has to be kept in mind, that detailed oil characterization of made using GC/MS and a considerable amount of time can pass until the results are made available, thus requiring the consideration of aging mechanisms, which in this case were assumed to include esterification of alcohols (including ethylene glycol residua from the entrainment start-up phase of the real industrial process) and production of a high-molecular-weight residue.

The Aspen Tech™ software package, which includes Aspen Plus™ and Aspen Properties™, it is possible to develop custom models to represent unit operations that may be absent from the Aspen Plus™ repertoire. The process is, however, costly and was considered outside of the scope of this work. Nonetheless, more advanced hydrodynamic models may be able to produce results of better quality than PFR or CSTR unit block abstractions, due to considering all phases simultaneously.

In the *bioliq*® process materialization, downstream separation of the reaction product is made via two quenching loop steps, which were modeled assuming steady-state operation, thus assuming the start-up quenching medium had been totally or partially replaced by pyrolysis product. Due to the limitations of modeling the replacement of the quench entrainer by pyrolysis products, and the excess volume of entrainer in comparison to the removed material, it was necessary to consider surrogate entrainment mixtures, devised based on the GC/MS analysis of the condensates of several feedstocks. It must be stated, that this methodology indubitably influences the composition and characteristics of the simulated condensates, and alternative modeling strategies must be considered in further versions of the model.

Modeling of the heat carrier loop was done successfully assuming Gibbs energy minimization models at defined temperatures, including the intake of natural gas and air, and the consumption of the recycled coke that is not recovered with the reaction product. This allows possible future heat integration studies, such as those shown by Fonseca et al. [5] but with a more complete model, or variations in air quality and fuel consumption.

Very limited thermophysical data is available in the literature/databases for several of the compounds considered in the models. In that sense, a major focus of the work load was the definition of a possible chemical species present in the process and ensuring their characterization, by estimating properties using different methods and comparing the results with experimental data when available to choose the best method. The system includes 31 possible bio-oil components, 10 gases, and 20 solids (including bio-monomers and non-volatilized char). The bio-oil components were characterized by their normal boiling point, critical properties, acentric factor, saturated liquid molar volume, heat capacity, normal heat of formation, normal heat of vaporization, vapor

pressure, as well as vapor and liquid viscosity. Regarding the thermophysical property database, a notorious fault when using all of these methods is the lack of experimental data, notably on high-molecular-weight surrogates. The greatest issue with these surrogates, is the fact that they are hypothetical model compounds, designed to represent a heterogeneous and highly variable fraction. Prior to the development of standards that would represent this phase in thermodynamic, functional group and generation perspectives, simultaneously, it is difficult to obtain reliable experimental data. Manrique et al. [386] discussed the generation of properties via group contribution methods and DFT estimations, but provides no comparison to experimental data.

Testing of the final model focused on evaluating the product distribution and characteristics of the four pyrolysis products. The first round of tests focused on emulating the results found in [5], wherein the moisture content of wheat straw was varied; the results obtained fit those found in that manuscript, in that the moisture content leads to an overall higher condensate fraction, of a higher fraction of water in said condensate and lower gas and coke. The second round of tests considered a variety of species: wheat straw, *Miscanthus*, sugar cane biomass, and beech wood, leading to minor differences attributed to a small degree of variation in biomass characteristics. In addition, in both cases, the characteristics and composition of the estimated condensates have been skewed by the condensation loop initialization method. However, the trend observed in experiments was predicted correctly by the developed process model.

Both reactor heat demand and the pyrolysis gas heat potential have been estimated. For the case of wheat straw, heat demand estimations were higher than other estimations, and could not be suppressed by the combustion of the pyrolysis gas, contrasting with the conclusions reached by Fonseca et al. [5]. The heat demand for certain feedstocks was unusually high (around double the other values), a factor attributed to issues estimating reaction heat.

Improvements in future work should address the major shortcomings of this model, namely the modeling and initialization of the condensation loops and the estimation of the reactor heat demand. Solutions for the former may include simulation in dynamic state or making use of external software connections, such as those between Aspen Plus™ and Microsoft Excel™ and the ability of the latter to run macros in Visual Basic™ ([4,366]); this would also allow the user to run the simulations within a possibly more familiar Excel environment, requiring solely the input of the biomass characteristics. The latter demands adjustments of the reaction networks to better model the reaction heat, as well as the choice and details of the reactor models.

The major relevancy of this work lies in having a full-encompassing model that includes an entirely characterized set of compounds, a predictive model which allows the user to calculate the product distribution based on the biomass characterization, and a fully modeled system that may be modified to consider new process configurations, namely new reactors or condensation units. Modeled in Aspen Plus™, it may be integrated into other models, and integrated with other software to automatize complex routines or case studies. Directly or indirectly, it can be used for the development of future process units or valorization pathways for the different feedstocks and fast pyrolysis products, or even to optimize the selectivity and energy efficiency of existing units.

References

- [1] BP p.l.c., BP Statistical Review of World Energy 2018, London, UK, 2018.
- [2] IRENA, IEA Bioenergy, FAO, Bioenergy for Sustainable Development, 2017.
- [3] P. Basu, Biomass Gasification and Pyrolysis: Practical Design and Theory, Elsevier, 2010.
- [4] J.F. Peters, S.W. Banks, A. V. Bridgwater, J. Dufour, A kinetic reaction model for biomass pyrolysis processes in Aspen Plus, *Appl Energy*. 188 (2017) 595–603. <https://doi.org/10.1016/j.apenergy.2016.12.030>.
- [5] F.G. Fonseca, A. Funke, A. Niebel, A.P. Soares Dias, N. Dahmen, Moisture content as a design and operational parameter for fast pyrolysis, *J Anal Appl Pyrolysis*. 139 (2019) 73–86. <https://doi.org/10.1016/j.jaap.2019.01.012>.
- [6] P. Janoska, IEA - Energy Transitions Indicators, (2019). <https://www.iea.org/articles/energy-transitions-indicators> (accessed January 11, 2021).
- [7] H. Martín, S. Coronas, À. Alonso, J. de la Hoz, J. Matas, Renewable Energy Auction Prices: Near Subsidy-Free?, *Energies (Basel)*. 13 (2020) 3383. <https://doi.org/10.3390/en13133383>.
- [8] D.J.M. Hayes, Second-generation biofuels: why they are taking so long, *Wiley Interdiscip Rev Energy Environ*. 2 (2013) 304–334. <https://doi.org/10.1002/wene.59>.
- [9] M. Tripathi, J.N. Sahu, P. Ganesan, Effect of process parameters on production of biochar from biomass waste through pyrolysis: A review, *Renewable and Sustainable Energy Reviews*. 55 (2016) 467–481. <https://doi.org/10.1016/j.rser.2015.10.122>.
- [10] F. Alam, S. Mobin, H. Chowdhury, Third Generation Biofuel from Algae, *Procedia Eng*. 105 (2015) 763–768. <https://doi.org/10.1016/j.proeng.2015.05.068>.
- [11] H.B. Goyal, D. Seal, R.C. Saxena, Bio-fuels from thermochemical conversion of renewable resources: A review, *Renewable and Sustainable Energy Reviews*. 12 (2008) 504–517. <https://doi.org/10.1016/j.rser.2006.07.014>.
- [12] D. Hoornweg, P. Bhada-Tata, C. Kennedy, Environment: Waste production must peak this century, *Nature*. 502 (2013) 615–617. <https://doi.org/10.1038/502615a>.
- [13] B. Kamm, P.R. Gruber, M. Kamm, Biorefineries-Industrial Processes and Products, Wiley-VCH Verlag GmbH, Weinheim, Germany, 2005. <https://doi.org/10.1002/9783527619849>.
- [14] J.M. Suttie, Hay and straw conservation for small-scale farming and pastoral conditions, Food and Agriculture Organization of the United Nations, Rome, 2000.
- [15] World Food and Agriculture – Statistical Yearbook 2022, FAO, Rome, 2022. <https://doi.org/10.4060/cc2211en>.
- [16] Diercke Media, Ebenenkarte: Deutschland, (n.d.). <https://media.diercke.net/omeda/heimatundwelt/83201/> (accessed June 28, 2023).
- [17] M. Van de Velden, J. Baeyens, A. Brems, B. Janssens, R. Dewil, Fundamentals, kinetics and endothermicity of the biomass pyrolysis reaction, *Renew Energy*. 35 (2010) 232–242. <https://doi.org/10.1016/j.renene.2009.04.019>.
- [18] F.G. Fonseca, A. Funke, A. Niebel, A.P.S. Dias, N. Dahmen, Moisture content as a design and operational parameter for fast pyrolysis, in: 1. Deutsches Doktorandenkolloquium Bioenergie, DBFZ Deutsches Biomasseforschungszentrum gemeinnützige GmbH, 2018: p. 286.
- [19] A. Teella, G.W. Huber, D.M. Ford, Separation of acetic acid from the aqueous fraction of fast pyrolysis bio-oils using nanofiltration and reverse osmosis membranes, *J Memb Sci*. 378 (2011) 495–502. <https://doi.org/10.1016/j.memsci.2011.05.036>.
- [20] A.V. V. Bridgwater, Review of fast pyrolysis of biomass and product upgrading, *Biomass Bioenergy*. 38 (2012) 68–94. <https://doi.org/10.1016/j.biombioe.2011.01.048>.
- [21] A. Demirbas, G. Arin, An Overview of Biomass Pyrolysis, *Energy Sources*. 24 (2002) 471–482. <https://doi.org/10.1080/00908310252889979>.
- [22] A.V. Bridgwater, Renewable fuels and chemicals by thermal processing of biomass, *Chemical Engineering Journal*. 91 (2003) 87–102. [https://doi.org/10.1016/S1385-8947\(02\)00142-0](https://doi.org/10.1016/S1385-8947(02)00142-0).
- [23] A. Funke, N. Dahmen, Direct Thermochemical Liquefaction (DTL): Characteristics, processes and technologies, (2020).
- [24] J. Lédé, O. Authier, Temperature and heating rate of solid particles undergoing a thermal decomposition. Which criteria for characterizing fast pyrolysis?, *J Anal Appl Pyrolysis*. 113 (2015) 1–14. <https://doi.org/10.1016/j.jaap.2014.11.013>.
- [25] Z. Liu, V. Suntuo, S. Kuitunen, J. Roininen, V. Alopaues, Modeling of Mass Transfer and Reactions in Anisotropic Biomass Particles with Reduced Computational Load, *Ind Eng Chem Res*. 53 (2014) 4096–4103. <https://doi.org/10.1021/ie403400n>.
- [26] D. Meier, B. Van De Beld, A. V. Bridgwater, D.C. Elliott, A. Oasmaa, F. Preto, State-of-the-art of fast pyrolysis in IEA bioenergy member countries, *Renewable and Sustainable Energy Reviews*. 20 (2013) 619–641.

- <https://doi.org/10.1016/j.rser.2012.11.061>.
- [27] A.V. Bridgwater, The production of biofuels and renewable chemicals by fast pyrolysis of biomass, *International Journal of Global Energy Issues*. 27 (2007) 160. <https://doi.org/10.1504/IJGEI.2007.013654>.
- [28] C. Kornmeyer, Verfahrenstechnische Untersuchungen zur Schnellpyrolyse von Lignocellulose im Doppelschnecken-Mischreaktor, Dr.-Ing., Universität Fridericiana Karlsruhe, 2009.
- [29] A. Bridgwater, Fast pyrolysis processes for biomass, *Renewable and Sustainable Energy Reviews*. 4 (2000) 1–73. [https://doi.org/10.1016/S1364-0321\(99\)00007-6](https://doi.org/10.1016/S1364-0321(99)00007-6).
- [30] C.M. Lakshmanan, B. Gal-Or, H.E. Hoelscher, Production of Levoglucosan by Pyrolysis of Carbohydrates Pyrolysis, *Industrial & Engineering Chemistry Product Research and Development*. 8 (1969) 261–264. <https://doi.org/10.1002/star.19700220804>.
- [31] E. Henrich, N. Dahmen, F. Weirich, R. Reimert, C. Kornmeyer, Fast pyrolysis of lignocellulosics in a twin screw mixer reactor, *Fuel Processing Technology*. 143 (2016) 151–161. <https://doi.org/10.1016/j.fuproc.2015.11.003>.
- [32] P.C. Badger, P. Fransham, Use of mobile fast pyrolysis plants to densify biomass and reduce biomass handling costs—A preliminary assessment, *Biomass Bioenergy*. 30 (2006) 321–325. <https://doi.org/10.1016/j.biombioe.2005.07.011>.
- [33] M. Tomasi Morgano, H. Leibold, F. Richter, H. Seifert, Screw pyrolysis with integrated sequential hot gas filtration, *J Anal Appl Pyrolysis*. 113 (2015) 216–224. <https://doi.org/10.1016/j.jaap.2014.12.019>.
- [34] A. Funke, D. Richter, A. Niebel, N. Dahmen, J. Sauer, Fast Pyrolysis of Biomass Residues in a Twin-screw Mixing Reactor, *Journal of Visualized Experiments*. accepted f (2016) 1–8. <https://doi.org/10.3791/54395>.
- [35] T. Schulzke, S. Conrad, J. Westermeyer, Fractionation of flash pyrolysis condensates by staged condensation, *Biomass Bioenergy*. 95 (2016) 287–295. <https://doi.org/10.1016/j.biombioe.2016.05.022>.
- [36] B. Glaser, Prehistorically modified soils of central Amazonia: a model for sustainable agriculture in the twenty-first century, *Philosophical Transactions of the Royal Society B: Biological Sciences*. 362 (2007) 187–196. <https://doi.org/10.1098/rstb.2006.1978>.
- [37] P.S. Anderson, Introduction to the Rotatable Covered Cavity (RoCC) Kiln for Medium-size Production of Pyrolytic Biochar and Thermal Energy, *Green Carbon Webinar 25 June 2020*. (2020). <https://woodgas.com/resources/> (accessed July 15, 2020).
- [38] C.C. Schmitt, F.G. Fonseca, M.M.C. Fraga, A. Wisniewski, S. Karp, Á.H. Mello José, R.C.L.B. Rodrigues, R. Moreira, D.E. Hirayama, K. Raffelt, N. Dahmen, A.W. Jr, S. Karp, Á. Henrique, M. José, C. Rita, R. Moreira, D. Eiji, K. Raffelt, N. Dahmen, Thermochemical and Catalytic Conversion Technologies for the Development of Brazilian Biomass Utilization, *Catalysts*. 11 (2021) 1549. <https://doi.org/10.3390/catal11121549>.
- [39] R. Venderbosch, W. Prins, Fast pyrolysis technology development, *Biofuels, Bioproducts and Biorefining*. 4 (2010) 178–208. <https://doi.org/10.1002/bbb.205>.
- [40] D. Meier, B. Van De Beld, A. V. Bridgwater, D.C. Elliott, A. Oasmaa, F. Preto, State-of-the-art of fast pyrolysis in IEA bioenergy member countries, *Renewable and Sustainable Energy Reviews*. 20 (2013) 619–641. <https://doi.org/10.1016/j.rser.2012.11.061>.
- [41] A. Oasmaa, C. Peacocke, Properties and fuel use of biomass-derived fast pyrolysis liquids. A guide., VTT Publications, Espoo, 2010. <https://www.vttresearch.com/sites/default/files/pdf/publications/2010/P731.pdf>.
- [42] D. Rutz, R. Janssen, P. Reumerman, J. Spekreijse, D. Matschegg, D. Bacovsky, A. Gröngroft, S. Hauschild, N. Dögnitz, E. Karampinis, D.-S. Kourkoumpas, P. Grammelis, K. Melin, H. Saastamoinen, A.I.S. Torres, R. Iglesias, M. Ballesteros, G. Gustavsson, D. Johansson, A. Kazagić, A. Merzić, D. Trešnje, H. Dagevos, S.J. Sijtsema, M.J. Reinders, M. Meeusen, Technical options for retrofitting industries with bioenergy: A Handbook, Munich, Germany, 2020.
- [43] C. Wurzer, S. Sohi, O. Mašek, Synergies in sequential biochar systems, in: J.J. Manyà (Ed.), *Advanced Carbon Materials from Biomass: An Overview*, GreenCarbon Project and Consortium, 2019: pp. 147–159.
- [44] C. Wurzer, O. Mašek, Feedstock doping using iron rich waste increases the pyrolysis gas yield and adsorption performance of magnetic biochar for emerging contaminants, *Bioresour Technol*. 321 (2021) 124473. <https://doi.org/10.1016/j.biortech.2020.124473>.
- [45] C. del Pozo, F. Rego, Y. Yang, N. Puy, J. Bartrolí, E. Fàbregas, A. V. Bridgwater, Converting coffee silverskin to value-added products by a slow pyrolysis-based biorefinery process, *Fuel Processing Technology*. 214 (2021) 106708. <https://doi.org/10.1016/j.fuproc.2020.106708>.
- [46] A. Funke, A. Niebel, D. Richter, M.M. Abbas, A.K. Müller, S. Radloff, M. Paneru, J. Maier, N. Dahmen, J. Sauer, Fast pyrolysis char - Assessment of alternative uses within the bioliq® concept, *Bioresour Technol*. 200 (2016) 905–913. <https://doi.org/10.1016/j.biortech.2015.11.012>.
- [47] K. Raffelt, E. Henrich, A. Koegel, R. Stahl, J. Steinhart, F. Weirich, The BTL2 process of biomass utilization entrained-flow gasification of pyrolyzed biomass slurries, *Appl Biochem Biotechnol*. 129 (2006) 153–164. <https://doi.org/10.1385/ABAB:129:1:153>.
- [48] A. Funke, T. Demus, T. Willms, L. Schenke, T. Echterhof, A. Niebel, H. Pfeifer, N. Dahmen, Appli-

- cation of fast pyrolysis char in an electric arc furnace, *Fuel Processing Technology*. 174 (2018) 61–68. <https://doi.org/10.1016/j.fuproc.2018.02.013>.
- [49] A.U. Şen, H. Pereira, State-of-the-art char production with a focus on bark feedstocks: Processes, design, and applications, *Processes*. 9 (2021) 1–24. <https://doi.org/10.3390/pr9010087>.
- [50] J. Lehto, A. Oasmaa, Y. Solantausta, M. Kytö, D. Chiamonti, Fuel oil quality and combustion of fast pyrolysis bio-oils, VTT Publications. (2013) 79. <https://doi.org/http://dx.doi.org/10.1016/j.apenenergy.2013.11.040>.
- [51] A. Oasmaa, B. Van De Beld, P. Saari, D.C. Elliott, Y. Solantausta, Norms, standards, and legislation for fast pyrolysis bio-oils from lignocellulosic biomass, *Energy and Fuels*. 29 (2015) 2471–2484. <https://doi.org/10.1021/acs.energyfuels.5b00026>.
- [52] A. de R. Pinho, M.B.B. de Almeida, F.L. Mendes, L.C. Casavechia, M.S. Talmadge, C.M. Kinchin, H.L. Chum, Fast pyrolysis oil from pinewood chips co-processing with vacuum gas oil in an FCC unit for second generation fuel production, *Fuel*. 188 (2017) 462–473. <https://doi.org/10.1016/j.fuel.2016.10.032>.
- [53] A. Krutof, K. Hawboldt, Blends of pyrolysis oil, petroleum, and other bio-based fuels: A review, *Renewable and Sustainable Energy Reviews*. 59 (2016) 406–419. <https://doi.org/10.1016/j.rser.2015.12.304>.
- [54] A. Krutof, K.A. Hawboldt, Upgrading of biomass sourced pyrolysis oil review: focus on co-pyrolysis and vapour upgrading during pyrolysis, *Biomass Convers Biorefin*. 8 (2018) 775–787. <https://doi.org/10.1007/s13399-018-0326-6>.
- [55] C.C. Schmitt, C. Boscagli, M. Rapp, R. Raffelt, N. Dahmen, K. Raffelt, N. Dahmen, E.B. Conference, Characterization of light and heavy phase of pyrolysis-oil from distinct biomass for further upgrading reactions, *European Biomass Conference and Exhibition Proceedings*. 2017 (2017) 12–15. <https://doi.org/10.5071/25thEUBCE2017-3AV.3.15>.
- [56] K. Adolf, Entwicklung einer thermodynamischen Siedekurve von Schwelwasser, BSc, Karlsruher Institut für Technologie (KIT), 2021.
- [57] A. Krutof, K.A. Hawboldt, Thermodynamic model of fast pyrolysis bio-oil advanced distillation curves, *Fuel*. 261 (2020) 116446. <https://doi.org/10.1016/j.fuel.2019.116446>.
- [58] G.K. Parku, A. Krutof, A. Funke, D. Richter, N. Dahmen, Using fractional condensation to optimise aqueous pyrolysis condensates for downstream microbial conversion, (2022).
- [59] T. Nicoleit, N. Dahmen, J. Sauer, Production and Storage of Gasifiable Slurries Based on Flash-Pyrolyzed Straw, *Energy Technology*. 4 (2016) 221–229. <https://doi.org/10.1002/ente.201500273>.
- [60] N. Dahmen, J. Abeln, M. Eberhard, T. Kolb, H. Leibold, J. Sauer, D. Stapf, B. Zimmerlin, The bioliq process for producing synthetic transportation fuels, *Wiley Interdiscip Rev Energy Environ*. 6 (2017). <https://doi.org/10.1002/wene.236>.
- [61] S. Arnold, K. Moss, N. Dahmen, M. Henkel, R. Hausmann, Pretreatment strategies for microbial valorization of bio-oil fractions produced by fast pyrolysis of ash-rich lignocellulosic biomass, *GCB Bioenergy*. 11 (2019) 181–190. <https://doi.org/10.1111/gcbb.12544>.
- [62] T.M. Brueckner, P.G. Pickup, K.A. Hawboldt, Improvement of bark pyrolysis oil and value added chemical recovery by pervaporation, *Fuel Processing Technology*. 199 (2020) 106292. <https://doi.org/10.1016/j.fuproc.2019.106292>.
- [63] C. Pfitzer, N. Dahmen, N. Tröger, F. Weirich, J. Sauer, A. Günther, M. Müller-Hagedorn, Fast Pyrolysis of Wheat Straw in the Bioliq Pilot Plant, *Energy and Fuels*. 30 (2016) 8047–8054. <https://doi.org/10.1021/acs.energyfuels.6b01412>.
- [64] C.E. Pfitzer, N. Dahmen, N. Tröger, F. Weirich, J. Sauer, First Results of the Bioliq® Fast Pyrolysis Pilot Plant, in: *22nd European Biomass Conference and Exhibition*, 2014. <https://doi.org/10.5071/22ndEUBCE2014-3CV.2.70>.
- [65] F. Trippe, M. Fröhling, F. Schultmann, R. Stahl, E. Henrich, Techno-economic analysis of fast pyrolysis as a process step within biomass-to-liquid fuel production, *Waste Biomass Valorization*. 1 (2010) 415–430. <https://doi.org/10.1007/s12649-010-9039-1>.
- [66] N. Dahmen, E. Dinjus, T. Kolb, U. Arnold, H. Leibold, R. Stahl, State of the art of the bioliq process for synthetic biofuels production, *Environ Prog Sustain Energy*. 31 (2012) 176–181. <https://doi.org/10.1002/ep.10624>.
- [67] A. Niebel, A. Funke, C. Pfitzer, N. Dahmen, N. Weih, D. Richter, B. Zimmerlin, Fast Pyrolysis of Wheat Straw—Improvements of Operational Stability in 10 Years of Bioliq Pilot Plant Operation, *Energy & Fuels*. 35 (2021) 11333–11345. <https://doi.org/10.1021/acs.energyfuels.1c00851>.
- [68] R.P. Overend, T.A. Milne, L.K. Mudge, *Fundamentals of Thermochemical Biomass Conversion*, 1st ed., Springer Netherlands, Dordrecht, 1985. <https://doi.org/10.1007/978-94-009-4932-4>.
- [69] C. Di Blasi, Modeling chemical and physical processes of wood and biomass pyrolysis, *Prog Energy Combust Sci*. 34 (2008) 47–90. <https://doi.org/10.1016/j.pecs.2006.12.001>.
- [70] M. Garcia-Perez, T. Lewis, C.E. Kruger, *Methods for Producing Biochar and Advanced Biofuels in Washington State*, 2010. <https://doi.org/Ecology Publication Number 11-07-017>.
- [71] D. Radlein, A. Quignard, A Short Historical Review of Fast Pyrolysis of Biomass, *Oil & Gas Science and Technology – Revue d'IFP Energies Nouvelles*. 68 (2013) 765–783. <https://doi.org/10.2516/ogst/2013162>.
- [72] M.B. Pecha, J.I.M. Arbelaez, M. Garcia-Perez, F. Chejne, P.N. Ciesielski, Progress in understanding the four dominant intra-particle phenomena of lignocellulose pyrolysis: chemical reactions, heat

- transfer, mass transfer, and phase change, *Green Chemistry*. 21 (2019) 2868–2898. <https://doi.org/10.1039/C9GC00585D>.
- [73] A.S.N. Mahmood, J.G. Brammer, A. Hornung, A. Steele, S. Poulston, The intermediate pyrolysis and catalytic steam reforming of Brewers spent grain, *J Anal Appl Pyrolysis*. 103 (2013) 328–342. <https://doi.org/10.1016/j.jaap.2012.09.009>.
- [74] A. Jensen, K. Dam-Johansen, M.A. Wójtowicz, M.A. Serio, TG-FTIR Study of the Influence of Potassium Chloride on Wheat Straw Pyrolysis, *Energy & Fuels*. 12 (1998) 929–938. <https://doi.org/10.1021/ef980008i>.
- [75] J.E. White, W.J. Catalo, B.L. Legendre, Biomass pyrolysis kinetics: A comparative critical review with relevant agricultural residue case studies, *J Anal Appl Pyrolysis*. 91 (2011) 1–33. <https://doi.org/10.1016/j.jaap.2011.01.004>.
- [76] S.R.G. Oudenhoven, S.R.A. Kersten, Thermochemical Conversion: An Introduction to Fast Pyrolysis, in: W. de Jong, J.R. Ommen (Eds.), *Biomass as a Sustainable Energy Source for the Future: Fundamentals of Conversion Processes*, American Institute of Chemical Engineers, 2014: pp. 359–387. <https://doi.org/10.1002/9781118916643.ch11>.
- [77] S.W. Banks, D.J. Nowakowski, A. V. Bridgwater, Impact of Potassium and Phosphorus in Biomass on the Properties of Fast Pyrolysis Bio-oil, *Energy & Fuels*. 30 (2016) 8009–8018. <https://doi.org/10.1021/acs.energyfuels.6b01044>.
- [78] I.Y. Eom, K.H. Kim, J.Y. Kim, S.M. Lee, H.M. Yeo, I.G. Choi, J.W. Choi, Characterization of primary thermal degradation features of lignocellulosic biomass after removal of inorganic metals by diverse solvents, *Bioresour Technol*. 102 (2011) 3437–3444. <https://doi.org/10.1016/j.biortech.2010.10.056>.
- [79] R.J. Evans, T.A. Milne, Molecular characterization of the pyrolysis of biomass, *Energy & Fuels*. 1 (1987) 123–137. <https://doi.org/10.1021/ef00002a001>.
- [80] M. Carrier, M. Windt, B. Ziegler, J. Appelt, B. Saake, D. Meier, A. Bridgwater, Quantitative Insights into the Fast Pyrolysis of Extracted Cellulose, Hemicelluloses, and Lignin, *ChemSusChem*. 10 (2017) 3212–3224. <https://doi.org/10.1002/cssc.201700984>.
- [81] E. Ranzi, P.E.A. Debiagi, A. Frassoldati, Mathematical Modeling of Fast Biomass Pyrolysis and Bio-Oil Formation. Note II: Secondary Gas-Phase Reactions and Bio-Oil Formation, *ACS Sustain Chem Eng*. 5 (2017) 2882–2896. <https://doi.org/10.1021/acssuschemeng.6b03098>.
- [82] C. Dolu, L. Kuddusi, The effect of reactor height on coal gasification, *Thermal Science*. 21 (2017) 1937–1951. <https://doi.org/10.2298/TSCI150526112D>.
- [83] J. Navarro, M. Centeno, O. Laguna, J. Odriozola, Policies and Motivations for the CO₂ Valorization through the Sabatier Reaction Using Structured Catalysts. A Review of the Most Recent Advances, *Catalysts*. 8 (2018) 578. <https://doi.org/10.3390/catal8120578>.
- [84] A.G.W. Bradbury, Y. Sakai, F. Shafizadeh, A kinetic model for pyrolysis of cellulose, *J Appl Polym Sci*. 23 (1979) 3271–3280. <https://doi.org/10.1002/app.1979.070231112>.
- [85] J.P. Diebold, A unified, global model for the pyrolysis of cellulose, *Biomass Bioenergy*. 7 (1994) 75–85. [https://doi.org/10.1016/0961-9534\(94\)00039-V](https://doi.org/10.1016/0961-9534(94)00039-V).
- [86] Y.-C.C. Lin, J. Cho, G.A. Tompsett, P.R. Westmoreland, G.W. Huber, Kinetics and Mechanism of Cellulose Pyrolysis, *The Journal of Physical Chemistry C*. 113 (2009) 20097–20107. <https://doi.org/10.1021/jp906702p>.
- [87] X. Yang, Y. Zhao, W. Li, R. Li, Y. Wu, Unveiling the Pyrolysis Mechanisms of Hemicellulose: Experimental and Theoretical Studies, *Energy & Fuels*. 33 (2019) 4352–4360. <https://doi.org/10.1021/acs.energyfuels.9b00482>.
- [88] B. Saha, I. Klein, T. Parsell, M.M. Abu-Omar, Catalytic Hydrodeoxygenation of Lignin Model Compounds, in: M. Schlaf, Z.C. Zhang (Eds.), *Reaction Pathways and Mechanisms in Thermocatalytic Biomass Conversion II: Homogeneously Catalyzed Transformations, Acrylics from Biomass, Theoretical Aspects, Lignin Valorization and Pyrolysis Pathways*, Springer Singapore, Singapore, 2016: pp. 119–129. https://doi.org/10.1007/978-981-287-769-7_6.
- [89] W. Farhat, R. Venditti, A. Quick, M. Taha, N. Mignard, F. Becquart, A. Ayoub, Hemicellulose extraction and characterization for applications in paper coatings and adhesives, *Ind Crops Prod*. 107 (2017) 370–377. <https://doi.org/10.1016/j.indcrop.2017.05.055>.
- [90] P.E.A. Debiagi, C. Pecchi, G. Gentile, A. Frassoldati, A. Cuoci, T. Faravelli, E. Ranzi, Extractives Extend the Applicability of Multistep Kinetic Scheme of Biomass Pyrolysis, *Energy & Fuels*. 29 (2015) 6544–6555. <https://doi.org/10.1021/acs.energyfuels.5b01753>.
- [91] Y. Peng, S. Wu, The structural and thermal characteristics of wheat straw hemicellulose, *J Anal Appl Pyrolysis*. 88 (2010) 134–139. <https://doi.org/10.1016/j.jaap.2010.03.006>.
- [92] D.J. Robichaud, M.R. Nimlos, G.B. Ellison, Pyrolysis Mechanisms of Lignin Model Compounds Using a Heated Micro-Reactor, in: M. Schlaf, Z.C. Zhang (Eds.), *Reaction Pathways and Mechanisms in Thermocatalytic Biomass Conversion II*, Springer Science+Business Media, Singapore, 2016: pp. 145–171. https://doi.org/10.1007/978-981-287-769-7_8.
- [93] R. Houston, N. Abdoulmoumine, Kinetic Investigation of the Thermal Degradation of a β -O-4, α -O-4, and β -5 Model Lignin Tetramer, in: *2020 Thermal and Catalytic Sciences Virtual Symposium*, Cvent, Kennewick, USA, 2020.
- [94] S. Quideau, J. Ralph, A Biomimetic Route to Lignin Model Compounds via Silver (I) Oxide Oxidation: 1. Synthesis of Dilignols and Non-Cyclic Benzyl Aryl Ethers, *Holzforschung*. 48 (1994) 12–22. <https://doi.org/10.1515/hfsg.1994.48.1.12>.

- [95] T. Faravelli, A. Frassoldati, G. Migliavacca, E. Ranzi, Detailed kinetic modeling of the thermal degradation of lignins, *Biomass Bioenergy*. 34 (2010) 290–301. <https://doi.org/10.1016/j.biombioe.2009.10.018>.
- [96] E. Ranzi, A. Cuoci, T. Faravelli, A. Frassoldati, G. Migliavacca, S. Pierucci, S. Sommariva, Chemical Kinetics of Biomass Pyrolysis, *Energ Fuel*. 22 (2008) 4292–4300. <https://doi.org/10.1021/ef800551t>.
- [97] B. Scholze, C. Hanser, D. Meier, Characterization of the water-insoluble fraction from fast pyrolysis liquids (pyrolytic lignin): Part II. GPC, carbonyl groups, and ¹³C-NMR, *J Anal Appl Pyrolysis*. 58–59 (2001) 387–400. [https://doi.org/10.1016/S0165-2370\(00\)00173-X](https://doi.org/10.1016/S0165-2370(00)00173-X).
- [98] S. Ghysels, B. Dubuisson, M. Pala, L. Rohrbach, J. Van den Bulcke, H.J. Heeres, F. Ronsse, Improving fast pyrolysis of lignin using three additives with different modes of action, *Green Chemistry*. 22 (2020) 6471–6488. <https://doi.org/10.1039/D0GC02417A>.
- [99] J. Montoya, B. Pecha, F.C. Janna, M. Garcia-Perez, Single particle model for biomass pyrolysis with bubble formation dynamics inside the liquid intermediate and its contribution to aerosol formation by thermal ejection, *J Anal Appl Pyrolysis*. 124 (2017) 204–218. <https://doi.org/10.1016/j.jaap.2017.02.004>.
- [100] P.R. Patwardhan, J.A. Satrio, R.C. Brown, B.H. Shanks, Influence of inorganic salts on the primary pyrolysis products of cellulose, *Bioresour Technol*. 101 (2010) 4646–4655. <https://doi.org/10.1016/j.biortech.2010.01.112>.
- [101] C. Perez Locas, V.A. Yaylayan, Isotope Labeling Studies on the Formation of 5-(Hydroxymethyl)-2-furaldehyde (HMF) from Sucrose by Pyrolysis-GC/MS, *J Agric Food Chem*. 56 (2008) 6717–6723. <https://doi.org/10.1021/jf8010245>.
- [102] X. Zhang, W. Yang, W. Blasiak, Thermal decomposition mechanism of levoglucosan during cellulose pyrolysis, *J Anal Appl Pyrolysis*. 96 (2012) 110–119. <https://doi.org/10.1016/j.jaap.2012.03.012>.
- [103] A.D. Pouwels, G.B. Eijkel, J.J. Boon, Curie-point pyrolysis-capillary gas chromatography-high-resolution mass spectrometry of microcrystalline cellulose, *J Anal Appl Pyrolysis*. 14 (1989) 237–280. [https://doi.org/10.1016/0165-2370\(89\)80003-8](https://doi.org/10.1016/0165-2370(89)80003-8).
- [104] T. Hosoya, H. Kawamoto, S. Saka, Different pyrolytic pathways of levoglucosan in vapor- and liquid/solid-phases, *J Anal Appl Pyrolysis*. 83 (2008) 64–70. <https://doi.org/10.1016/j.jaap.2008.06.008>.
- [105] P.Y. Nikolov, V.A. Yaylayan, Thermal Decomposition of 5-(Hydroxymethyl)-2-furaldehyde (HMF) and Its Further Transformations in the Presence of Glycine, *J Agric Food Chem*. 59 (2011) 10104–10113. <https://doi.org/10.1021/jf202470u>.
- [106] E.-J. Shin, M.R. Nimlos, R.J. Evans, Kinetic analysis of the gas-phase pyrolysis of carbohydrates, *Fuel*. 80 (2001) 1697–1709. [https://doi.org/10.1016/S0016-2361\(01\)00056-4](https://doi.org/10.1016/S0016-2361(01)00056-4).
- [107] M.A. Grela, A.J. Colussi, Kinetics and mechanism of the thermal decomposition of unsaturated aldehydes: benzaldehyde, 2-butenal, and 2-furaldehyde, *J Phys Chem*. 90 (1986) 434–437. <https://doi.org/10.1021/j100275a016>.
- [108] A.K. Vasiliou, J.H. Kim, T.K. Ormond, K.M. Piech, K.N. Urness, A.M. Scheer, D.J. Robichaud, C. Mukarakate, M.R. Nimlos, J.W. Daily, Q. Guan, H.-H. Carstensen, G.B. Ellison, Biomass pyrolysis: Thermal decomposition mechanisms of furfural and benzaldehyde, *J Chem Phys*. 139 (2013) 104310. <https://doi.org/10.1063/1.4819788>.
- [109] F. Shafizadeh, G.D. McGinnis, C.W. Philpot, Thermal degradation of xylan and related model compounds, *Carbohydr Res*. 25 (1972) 23–33. [https://doi.org/10.1016/S0008-6215\(00\)82742-1](https://doi.org/10.1016/S0008-6215(00)82742-1).
- [110] S. Wang, B. Ru, H. Lin, Z. Luo, Degradation mechanism of monosaccharides and xylan under pyrolytic conditions with theoretic modeling on the energy profiles, *Bioresour Technol*. 143 (2013) 378–383. <https://doi.org/10.1016/j.biortech.2013.06.026>.
- [111] U. Räisänen, I. Pitkänen, H. Halttunen, M. Hurttä, Formation of the main degradation compounds from arabinose, xylose, mannose and arabinitol during pyrolysis, *J Therm Anal Calorim*. 72 (2003) 481–488. <https://doi.org/10.1023/A:1024557011975>.
- [112] R. Spielmann, C.A. Cramers, Cyclopentadienic compounds as intermediates in the thermal degradation of phenols. Kinetics of the thermal decomposition of cyclopentadiene, *Chromatographia*. 5 (1972) 295–300. <https://doi.org/10.1007/BF02310746>.
- [113] A.B. Lovell, K. Brezinsky, I. Glassman, The gas phase pyrolysis of phenol, *Int J Chem Kinet*. 21 (1989) 547–560. <https://doi.org/10.1002/kin.550210706>.
- [114] A.E. Harman-Ware, M. Crocker, A.P. Kaur, M.S. Meier, D. Kato, B. Lynn, Pyrolysis-GC/MS of sinapyl and coniferyl alcohol, *J Anal Appl Pyrolysis*. 99 (2013) 161–169. <https://doi.org/10.1016/j.jaap.2012.10.001>.
- [115] E. Ranzi, M. Dente, T. Faravelli, G. PENNATI, Prediction of Kinetic Parameters for Hydrogen Abstraction Reactions, *Combustion Science and Technology*. 95 (1993) 1–50. <https://doi.org/10.1080/00102209408935325>.
- [116] B. Husson, M. Ferrari, O. Herbinet, S.S. Ahmed, P.-A. Glaude, F. Battin-Leclerc, New experimental evidence and modeling study of the ethylbenzene oxidation, *Proceedings of the Combustion Institute*. 34 (2013) 325–333. <https://doi.org/10.1016/j.proci.2012.06.002>.
- [117] J.P.P. Diebold, A Review of the Chemical and Physical Mechanisms of the Storage Stability of Fast Pyrolysis Bio-Oils, Lakewood, CO, USA, 2000. <https://doi.org/NREL/SR-570-27613>.
- [118] J. Cai, Md.M. Rahman, S. Zhang, M. Sarker, X. Zhang, Y. Zhang, X. Yu, E.H. Fini, Review on Aging of Bio-Oil from Biomass Pyrolysis and Strategy to Slowing Aging, *Energy & Fuels*. 35 (2021) 11665–

11692. <https://doi.org/10.1021/acs.energyfuels.1c01214>.
- [119] A. Oasmaa, K. Sipilä, Y. Solantausta, E. Kuoppala, Quality Improvement of Pyrolysis Liquid: Effect of Light Volatiles on the Stability of Pyrolysis Liquids, *Energy & Fuels*. 19 (2005) 2556–2561. <https://doi.org/10.1021/ef0400924>.
- [120] C.D. Naske, P. Polk, P.Z. Wynne, J. Speed, W.E. Holmes, K.B. Walters, Postcondensation Filtration of Pine and Cottonwood Pyrolysis Oil and Impacts on Accelerated Aging Reactions, *Energy & Fuels*. 26 (2012) 1284–1297. <https://doi.org/10.1021/ef200541d>.
- [121] Q. Zhang, L. Zhang, T. Wang, Y. Xu, Q. Zhang, L. Ma, M. He, K. Li, Upgrading of Bio-oil by Removing Carboxylic Acids in Supercritical Ethanol, *Energy Procedia*. 61 (2014) 1033–1036. <https://doi.org/10.1016/j.egypro.2014.11.1018>.
- [122] R. Wang, H. Ben, Accelerated Aging Process of Bio-Oil Model Compounds: A Mechanism Study, *Front Energy Res*. 8 (2020). <https://doi.org/10.3389/fenrg.2020.00079>.
- [123] W. Xiong, Y. Fu, 郭庆祥, Q.& G. QingXiang Lu, Aging behavior and mechanism of bio-oil, *Chinese Science Bulletin*. 54 (2009) 2188–2195. <https://doi.org/10.1360/972009-50>.
- [124] E. Hoekstra, R.J.M. Westerhof, W. Brillman, W.P.M. Van Swaaij, S.R.A. Kersten, K.J.A. Hogendoorn, M. Windt, Heterogeneous and homogeneous reactions of pyrolysis vapors from pine wood, *AIChE Journal*. 58 (2012) 2830–2842. <https://doi.org/10.1002/aic.12799>.
- [125] S. Black, J.R. Ferrell, Accelerated aging of fast pyrolysis bio-oil: a new method based on carbonyl titration, *RSC Adv*. 10 (2020) 10046–10054. <https://doi.org/10.1039/D0RA00046A>.
- [126] M. Gupta, B. Bronson, D. Mazerolle, M. Ferguson, F. Preto, Evaluating stability of chemically quenched pyrolysis vapours using accelerated aging tests, in: 2020 Thermal and Catalytic Sciences Virtual Symposium, Cvent, Kennewick, USA, 2020.
- [127] C.C.C.C. Schmitt, R. Moreira, R.C.R.C. Neves, D. Richter, A. Funke, K. Raffelt, J.-D.J.-D.D. Grunwaldt, N. Dahmen, From agriculture residue to upgraded product: The thermochemical conversion of sugarcane bagasse for fuel and chemical products, *Fuel Processing Technology*. 197 (2020) 106199. <https://doi.org/10.1016/j.fuproc.2019.106199>.
- [128] R.S. Miller, J. Bellan, A generalized biomass pyrolysis model based on superimposed cellulose, hemicellulose and lignin kinetics, *Combustion Science and Technology*. 126 (1997) 97–137. <https://doi.org/10.1080/00102209708935670>.
- [129] D. Humbird, A. Trendewicz, R. Braun, A. Dutta, One-Dimensional Biomass Fast Pyrolysis Model with Reaction Kinetics Integrated in an Aspen Plus Biorefinery Process Model, *ACS Sustain Chem Eng*. 5 (2017) 2463–2470. <https://doi.org/10.1021/acssuschemeng.6b02809>.
- [130] M. Corbetta, S. Pierucci, E. Ranzi, H. Bennadji, E.M. Fisher, Multistep Kinetic Model of Biomass Pyrolysis, in: XXXVI Meeting of the Italian Section of the Combustion Institute, 2013: pp. 4–9.
- [131] E. Ranzi, M. Corbetta, F. Manenti, S. Pierucci, Kinetic modeling of the thermal degradation and combustion of biomass, *Chem Eng Sci*. 110 (2014) 2–12. <https://doi.org/10.1016/j.ces.2013.08.014>.
- [132] A. Trendewicz, R. Braun, A. Dutta, J. Ziegler, One dimensional steady-state circulating fluidized-bed reactor model for biomass fast pyrolysis, *Fuel*. 133 (2014) 253–262. <https://doi.org/10.1016/j.fuel.2014.05.009>.
- [133] E. Ranzi, P.E.A. Debiagi, A. Frassoldati, Mathematical Modeling of Fast Biomass Pyrolysis and Bio-Oil Formation. Note I: Kinetic Mechanism of Biomass Pyrolysis, *ACS Sustain Chem Eng*. 5 (2017) 2867–2881. <https://doi.org/10.1021/acssuschemeng.6b03096>.
- [134] A. Anca-Couce, R. Mehrabian, R. Scharler, I. Obernberger, Kinetic scheme of biomass pyrolysis considering secondary charring reactions, *Energy Convers Manag*. 87 (2014) 687–696. <https://doi.org/10.1016/j.enconman.2014.07.061>.
- [135] A. Anca-Couce, R. Scharler, Modelling heat of reaction in biomass pyrolysis with detailed reaction schemes, *Fuel*. 206 (2017) 572–579. <https://doi.org/10.1016/j.fuel.2017.06.011>.
- [136] M. Corbetta, A. Frassoldati, H. Bennadji, K. Smith, M.J. Serapiglia, G. Gauthier, T. Melkior, E. Ranzi, E.M. Fisher, Pyrolysis of Centimeter-Scale Woody Biomass Particles: Kinetic Modeling and Experimental Validation, *Energy & Fuels*. 28 (2014) 3884–3898. <https://doi.org/10.1021/ef500525v>.
- [137] R.J.M.M. Westerhof, H.S. Nygård, W.P.M.M. Van Swaaij, S.R.A.A. Kersten, D.W.F.F. Brillman, Effect of particle geometry and microstructure on fast pyrolysis of beech wood, *Energy and Fuels*. 26 (2012) 2274–2280. <https://doi.org/10.1021/ef201688n>.
- [138] D.S. Scott, J. Piskorz, The flash pyrolysis of aspen-poplar wood, *Can J Chem Eng*. 60 (1982) 666–674. <https://doi.org/10.1002/cjce.5450600514>.
- [139] A. Demirbas, Effects of temperature and particle size on bio-char yield from pyrolysis of agricultural residues, *J Anal Appl Pyrolysis*. 72 (2004) 243–248. <https://doi.org/10.1016/j.jaap.2004.07.003>.
- [140] P. Luangkiattikhun, C. Tangsathitkulchai, M. Tangsathitkulchai, Non-isothermal thermogravimetric analysis of oil-palm solid wastes, *Bioresour Technol*. 99 (2008) 986–997. <https://doi.org/10.1016/j.biortech.2007.03.001>.
- [141] J. Shen, X.-S. Wang, M. Garcia-Perez, D. Mourant, M.J. Rhodes, C.-Z. Li, Effects of particle size on the fast pyrolysis of oil mallee woody biomass, *Fuel*. 88 (2009) 1810–1817. <https://doi.org/10.1016/j.fuel.2009.05.001>.
- [142] E. Salehi, J. Abedi, T. Harding, Bio-oil from Sawdust: Effect of Operating Parameters on the Yield and Quality of Pyrolysis Products, *Energy & Fuels*. 25 (2011) 4145–4154. <https://doi.org/10.1021/ef200688y>.

- [143] S. Zhou, M. Garcia-Perez, B. Pecha, S.R.A. Kersten, A.G. McDonald, R.J.M. Westerhof, Effect of the fast pyrolysis temperature on the primary and secondary products of lignin, *Energy and Fuels*. 27 (2013) 5867–5877. <https://doi.org/10.1021/ef4001677>.
- [144] R.J.M. Westerhof, D.W.F. (Wim) Brillman, W.P.M. van Swaaij, S.R.A. Kersten, Effect of Temperature in Fluidized Bed Fast Pyrolysis of Biomass: Oil Quality Assessment in Test Units, *Ind Eng Chem Res*. 49 (2010) 1160–1168. <https://doi.org/10.1021/ie900885c>.
- [145] T.J. Haas, M.R. Nimlos, B.S. Donohoe, Real-time and post-reaction microscopic structural analysis of biomass undergoing pyrolysis, *Energy and Fuels*. 23 (2009) 3810–3817. <https://doi.org/10.1021/ef900201b>.
- [146] A.R. Teixeira, K.G. Mooney, J.S. Kruger, C.L. Williams, W.J. Suszynski, L.D. Schmidt, D.P. Schmidt, P.J. Dauenhauer, Aerosol generation by reactive boiling ejection of molten cellulose, *Energy Environ Sci*. 4 (2011) 4306. <https://doi.org/10.1039/c1ee01876k>.
- [147] S.R. a. Kersten, X. Wang, W. Prins, W.P.M. van Swaaij, Biomass Pyrolysis in a Fluidized Bed Reactor. Part 1: Literature Review and Model Simulations, *Ind Eng Chem Res*. 44 (2005) 8773–8785. <https://doi.org/10.1021/ie0504856>.
- [148] C. Di Blasi, C. Branca, Temperatures of wood particles in a hot sand bed fluidized by nitrogen, *Energy and Fuels*. 17 (2003) 247–254. <https://doi.org/10.1021/ef020146e>.
- [149] W. Chaiwat, I. Hasegawa, T. Tani, K. Sunagawa, K. Mae, Analysis of cross-linking behavior during pyrolysis of cellulose for elucidating reaction pathway, *Energy and Fuels*. 23 (2009) 5765–5772. <https://doi.org/10.1021/ef900674b>.
- [150] J.J. Manyà, J. Ruiz, J. Arauzo, Some peculiarities of conventional pyrolysis of several agricultural residues in a packed bed reactor, *Ind Eng Chem Res*. 46 (2007) 9061–9070. <https://doi.org/10.1021/ie070811c>.
- [151] R. Font, A. Marcilla, J. Devesa, E. Verdú, Gaseous hydrocarbons from flash pyrolysis of almond shells, *Ind Eng Chem Res*. 27 (1988) 1143–1149. <https://doi.org/10.1021/ie00079a009>.
- [152] H. Haykiri-Acma, The role of particle size in the non-isothermal pyrolysis of hazelnut shell, *J Anal Appl Pyrolysis*. 75 (2006) 211–216. <https://doi.org/10.1016/j.jaap.2005.06.002>.
- [153] S.A.A. Jayaweera, J.H. Moss, M.W. Thwaites, The effect of particle size on the combustion of wear-dale coal, *Thermochim Acta*. 152 (1989) 215–225. [https://doi.org/10.1016/0040-6031\(89\)85391-2](https://doi.org/10.1016/0040-6031(89)85391-2).
- [154] T. Funazukuri, R.R. Hudgins, P.L. Silveston, Product distribution in pyrolysis of cellulose in a microfluidized bed, *J Anal Appl Pyrolysis*. 9 (1986) 139–158. [https://doi.org/10.1016/0165-2370\(86\)85004-5](https://doi.org/10.1016/0165-2370(86)85004-5).
- [155] K. Raveendran, A. Ganesh, K.C. Khilar, Influence of mineral matter on biomass pyrolysis characteristics, *Fuel*. 74 (1995) 1812–1822. [https://doi.org/10.1016/0016-2361\(95\)80013-8](https://doi.org/10.1016/0016-2361(95)80013-8).
- [156] T.G. Bridgeman, L.I. Darvell, J.M. Jones, P.T. Williams, R. Fahmi, A. V. Bridgwater, T. Barraclough, I. Shield, N. Yates, S.C. Thain, I.S. Donnison, Influence of particle size on the analytical and chemical properties of two energy crops, *Fuel*. 86 (2007) 60–72. <https://doi.org/10.1016/j.fuel.2006.06.022>.
- [157] A. Marcilla, A.N. García, M. V. Pastor, M. León, A.J. Sánchez, D.M. Gómez, Thermal decomposition of the different particles size fractions of almond shells and olive stones. Thermal behaviour changes due to the milling processes, *Thermochim Acta*. 564 (2013) 24–33. <https://doi.org/10.1016/j.tca.2013.04.019>.
- [158] A. Trendewicz, R. Evans, A. Dutta, R. Sykes, D. Carpenter, R. Braun, Evaluating the effect of potassium on cellulose pyrolysis reaction kinetics, *Biomass Bioenergy*. 74 (2015) 15–25. <https://doi.org/10.1016/j.biombioe.2015.01.001>.
- [159] D. Zhao, Y. Dai, K.K. Chen, Y. Sun, F. Yang, K.K. Chen, Effect of potassium inorganic and organic salts on the pyrolysis kinetics of cigarette paper, *J Anal Appl Pyrolysis*. 102 (2013) 114–123. <https://doi.org/10.1016/j.jaap.2013.03.007>.
- [160] B. Peters, J. Smuła-Ostaszewska, Simultaneous prediction of potassium chloride and sulphur dioxide emissions during combustion of switchgrass, *Fuel*. 96 (2012) 29–42. <https://doi.org/10.1016/j.fuel.2011.12.073>.
- [161] K.A. Christensen, H. Livbjerg, A Field Study of Submicron Particles from the Combustion of Straw, *Aerosol Science and Technology*. 25 (1996) 185–199. <https://doi.org/10.1080/02786829608965390>.
- [162] Y. Sekiguchi, F. Shafizadeh, The effect of inorganic additives on the formation, composition, and combustion of cellulosic char, *J Appl Polym Sci*. 29 (1984) 1267–1286. <https://doi.org/10.1002/app.1984.070290421>.
- [163] L. Han, Q. Wang, Q. Ma, C. Yu, Z. Luo, K. Cen, Influence of CaO additives on wheat-straw pyrolysis as determined by TG-FTIR analysis, *J Anal Appl Pyrolysis*. 88 (2010) 199–206. <https://doi.org/10.1016/j.jaap.2010.04.007>.
- [164] M. Safar, B.-J. Lin, W.-H. Chen, D. Langauer, J.-S. Chang, H. Raclavska, A. Pétrissans, P. Rousset, M. Pétrissans, Catalytic effects of potassium on biomass pyrolysis, combustion and torrefaction, *Appl Energy*. 235 (2019) 346–355. <https://doi.org/10.1016/j.apenergy.2018.10.065>.
- [165] H.X. Wu, H. Bin Li, Y.P. Feng, X.B. Wang, Z.L. Zhao, F. He, Effects of potassium on the pyrolysis of biomass components by TG-FTIR analysis, *Ranliao Huaxue Xuebao/Journal of Fuel Chemistry and Technology*. 41 (2013) 950–957.
- [166] D.J. Nowakowski, J.M. Jones, Uncatalysed and potassium-catalysed pyrolysis of the cell-wall constituents of biomass and their model compounds, *J Anal Appl Pyrolysis*. 83 (2008) 12–25. <https://doi.org/10.1016/j.jaap.2008.05.007>.
- [167] H. Fan, J. Gu, Y. Wang, H. Yuan, Y. Chen, B. Luo, Ef-

- fect of potassium on the pyrolysis of biomass components: Pyrolysis behaviors, product distribution and kinetic characteristics, *Waste Management*. 121 (2021) 255–264. <https://doi.org/10.1016/j.wasman.2020.12.023>.
- [168] F. Guo, Y. Liu, Y. Wang, X. Li, T. Li, C. Guo, Pyrolysis kinetics and behavior of potassium-impregnated pine wood in TGA and a fixed-bed reactor, *Energy Convers Manag*. 130 (2016) 184–191. <https://doi.org/10.1016/j.enconman.2016.10.055>.
- [169] A. Saddawi, J.M. Jones, A. Williams, Influence of alkali metals on the kinetics of the thermal decomposition of biomass, *Fuel Processing Technology*. 104 (2012) 189–197. <https://doi.org/10.1016/j.fuproc.2012.05.014>.
- [170] A. Trubetskaya, P.A. Jensen, A.D. Jensen, M. Steibel, H. Spliethoff, P. Glarborg, F.H. Larsen, Comparison of high temperature chars of wheat straw and rice husk with respect to chemistry, morphology and reactivity, *Biomass Bioenergy*. 86 (2016) 76–87. <https://doi.org/10.1016/j.biombioe.2016.01.017>.
- [171] I.Y. Eom, J.Y. Kim, T.S. Kim, S.M. Lee, D. Choi, I.G. Choi, J.W. Choi, Effect of essential inorganic metals on primary thermal degradation of lignocellulosic biomass, *Bioresour Technol*. 104 (2012) 687–694. <https://doi.org/10.1016/j.biortech.2011.10.035>.
- [172] A. Singh, S. Nanda, F. Berruti, A Review of Thermochemical and Biochemical Conversion of Miscanthus to Biofuels, in: S. Nanda, D.-V. N. Vo, P.K. Sarangi (Eds.), *Biorefinery of Alternative Resources: Targeting Green Fuels and Platform Chemicals*, Springer Singapore, Singapore, 2020: pp. 195–220. https://doi.org/10.1007/978-981-15-1804-1_9.
- [173] S. Hu, L. Jiang, Y. Wang, S. Su, L. Sun, B. Xu, L. He, J. Xiang, Effects of inherent alkali and alkaline earth metallic species on biomass pyrolysis at different temperatures, *Bioresour Technol*. 192 (2015) 23–30. <https://doi.org/10.1016/j.biortech.2015.05.042>.
- [174] F.G. Fonseca, A. Anca-Couce, A. Funke, N. Dahmen, Kinetic parameter determination for wheat straw pyrolysis, in: *EPYRO2021*, Medicongress, Ghent, 2021.
- [175] F.G. Fonseca, A. Anca-Couce, A. Funke, N. Dahmen, Challenges in kinetic parameter determination for wheat straw pyrolysis, *Energies (Basel)*. 15 (2022) 7240. <https://doi.org/doi.org/10.3390/en15197240>.
- [176] F. Shafizadeh, G.D. McGinnis, Chemical composition and thermal analysis of cottonwood, *Carbohydr Res*. 16 (1971) 273–277. [https://doi.org/10.1016/S0008-6215\(00\)81161-1](https://doi.org/10.1016/S0008-6215(00)81161-1).
- [177] G. Maschio, A. Lucchesi, C. Koufopoulos, Study of Kinetic and Transfer Phenomena in the Pyrolysis of Biomass Particles, in: *Advances in Thermochemical Biomass Conversion*, Springer Netherlands, Dordrecht, 1993: pp. 746–759. https://doi.org/10.1007/978-94-011-1336-6_58.
- [178] J.A. Caballero, R. Font, A. Marcilla, Comparative study of the pyrolysis of almond shells and their fractions, holocellulose and lignin. Product yields and kinetics, *Thermochim Acta*. 276 (1996) 57–77. [https://doi.org/10.1016/0040-6031\(95\)02794-7](https://doi.org/10.1016/0040-6031(95)02794-7).
- [179] B. Alberts, A. Johnson, J. Lewis, M. Raff, K. Roberts, P. Walter, *Molecular Biology of the Cell*, 4th ed., Garland Science, New York, 2002.
- [180] J.I. Park, L. Liu, X. Philip Ye, M.K. Jeong, Y.S. Jeong, Improved prediction of biomass composition for switchgrass using reproducing kernel methods with wavelet compressed FT-NIR spectra, *Expert Syst Appl*. 39 (2012) 1555–1564. <https://doi.org/10.1016/j.eswa.2011.05.012>.
- [181] R.C. Pettersen, The Chemical Composition of Wood, in: *The Chemistry of Solid Wood*, American Chemical Society, Madison, WI 53705, 1984: pp. 57–126. <https://doi.org/10.1021/ba-1984-0207.ch002>.
- [182] F. Rego, A.P. Soares Dias, M. Casquilho, F.C. Rosa, A. Rodrigues, F. Rego, A.P.S. Dias, M. Casquilho, F.C. Rosa, A. Rodrigues, Fast determination of lignocellulosic composition of poplar biomass by Thermogravimetry, *Biomass Bioenergy*. 122 (2019) 375–380. <https://doi.org/10.1016/j.biombioe.2019.01.037>.
- [183] A. Anca-Couce, C. Tsekos, S. Retschitzegger, F. Zimbardi, A. Funke, S. Banks, T. Kraia, P. Marques, R. Scharler, W. de Jong, N. Kienzl, Biomass pyrolysis TGA assessment with an international round robin, *Fuel*. 276 (2020). <https://doi.org/10.1016/j.fuel.2020.118002>.
- [184] W. Wu, Y. Mei, L. Zhang, R. Liu, J. Cai, Kinetics and reaction chemistry of pyrolysis and combustion of tobacco waste, *Fuel*. 156 (2015) 71–80. <https://doi.org/10.1016/j.fuel.2015.04.016>.
- [185] V. Strezov, B. Moghtaderi, J.A. Lucas, Thermal study of decomposition of selected biomass samples, *J Therm Anal Calorim*. 72 (2003) 1041–1048. <https://doi.org/10.1023/A:1025003306775>.
- [186] H. Yang, R. Yan, H. Chen, D.H. Lee, C. Zheng, Characteristics of hemicellulose, cellulose and lignin pyrolysis, *Fuel*. 86 (2007) 1781–1788. <https://doi.org/10.1016/j.fuel.2006.12.013>.
- [187] I. Šimkovic, K. Csomorová, Thermogravimetric analysis of agricultural residues: Oxygen effect and environmental impact, *J Appl Polym Sci*. 100 (2006) 1318–1322. <https://doi.org/10.1002/app.23818>.
- [188] J. Gaitán-Álvarez, R. Moya, A. Puente-Urbina, A. Rodríguez-Zúñiga, Thermogravimetric, devolatilization rate, and differential scanning calorimetry analyses of biomass of tropical plantation species of Costa Rica torrefied at different temperatures and times, *Energies (Basel)*. 11 (2018). <https://doi.org/10.3390/en11040696>.
- [189] A.C. Yew, *Numerical differentiation: finite differences*, Providence, RI, USA, 2011.
- [190] M. Carrier, A. Loppinet-Serani, D. Denux, J.-M.M. Lasnier, F. Ham-Pichavant, F. Cansell, C. Aymonier, Thermogravimetric analysis as a new method to determine the lignocellulosic composition of biomass, *Biomass Bioenergy*. 35 (2011) 298–307. <https://doi.org/10.1016/j.biombioe.2010.08.067>.

- [191] H. Zhou, Y. Long, A. Meng, Q. Li, Y. Zhang, The pyrolysis simulation of five biomass species by hemi-cellulose, cellulose and lignin based on thermogravimetric curves, *Thermochim Acta*. 566 (2013) 36–43. <https://doi.org/10.1016/j.tca.2013.04.040>.
- [192] T. Hatakeyama, F.X. Quinn, *Thermal analysis: fundamentals and applications to polymer science*, 2nd ed., John Wiley & Sons Ltd., Chichester, 1999.
- [193] I. Tubby, a Armstrong, Establishment and management of short rotation coppice, Practice Note-Forestry Commission. 7 (2002) 1–12.
- [194] N. Manić, B. Jankovic, D. Stojiljkovic, V. Jovanovic, M. Radojevic, TGA-DSC-MS analysis of pyrolysis process of various agricultural residues, *Thermal Science*. 23 (2019) 1457–1472. <https://doi.org/10.2298/TSCI180118182M>.
- [195] G. Maschio, V. Cozzani, A. Lucchesi, G. Stoppato, G. Maschio, A New Method to Determine the Composition of Biomass by Thermogravimetric Analysis, *Canadian Journal of Chemical Engineering*. 75 (1997) 127–133. <https://doi.org/10.1002/cjce.5450750120>.
- [196] A. Anca-Couce, A. Berger, N. Zobel, How to determine consistent biomass pyrolysis kinetics in a parallel reaction scheme, *Fuel*. 123 (2014) 230–240. <https://doi.org/10.1016/j.fuel.2014.01.014>.
- [197] J. Cai, D. Xu, Z. Dong, X. Yu, Y. Yang, S.W. Banks, A. V. Bridgwater, Processing thermogravimetric analysis data for isoconversional kinetic analysis of lignocellulosic biomass pyrolysis: Case study of corn stalk, *Renewable and Sustainable Energy Reviews*. 82 (2018) 2705–2715. <https://doi.org/10.1016/j.rser.2017.09.113>.
- [198] S. Vyazovkin, A time to search: finding the meaning of variable activation energy, *Phys. Chem. Chem. Phys.*, 18 (2016) 18643–18656. <https://doi.org/10.1039/C6CP02491B>.
- [199] J. Cai, W. Wu, R. Liu, G.W. Huber, A distributed activation energy model for the pyrolysis of lignocellulosic biomass, *Green Chemistry*. 15 (2013) 1331–1340. <https://doi.org/10.1039/c3gc36958g>.
- [200] E. Grieco, G. Baldi, Analysis and modelling of wood pyrolysis, *Chem Eng Sci*. 66 (2011) 650–660. <https://doi.org/10.1016/j.ces.2010.11.018>.
- [201] R. Font, A. Marcilla, E. Verdú, J. Devesa, Thermogravimetric kinetic study of the pyrolysis of almond shells and almond shells impregnated with CoCl₂, *J Anal Appl Pyrolysis*. 21 (1991) 249–264. [https://doi.org/10.1016/0165-2370\(91\)80001-O](https://doi.org/10.1016/0165-2370(91)80001-O).
- [202] J.A. Caballero, J.A. Conesa, R. Font, A. Marcilla, Pyrolysis kinetics of almond shells and olive stones considering their organic fractions, *J Anal Appl Pyrolysis*. 42 (1997) 159–175. [https://doi.org/10.1016/S0165-2370\(97\)00015-6](https://doi.org/10.1016/S0165-2370(97)00015-6).
- [203] J. Šesták, G. Berggren, Study of the kinetics of the mechanism of solid-state reactions at increasing temperatures, *Thermochim Acta*. 3 (1971) 1–12. [https://doi.org/10.1016/0040-6031\(71\)85051-7](https://doi.org/10.1016/0040-6031(71)85051-7).
- [204] C.J. Gómez, J.J. Manyà, E. Velo, L. Puigjaner, Further Applications of a Revisited Summative Model for Kinetics of Biomass Pyrolysis, *Ind Eng Chem Res*. 43 (2004) 901–906. <https://doi.org/10.1021/ie030621b>.
- [205] J.J. Manyà, E. Velo, L. Puigjaner, Kinetics of biomass pyrolysis: A reformulated three-parallel-reactions model, *Ind Eng Chem Res*. 42 (2003) 434–441. <https://doi.org/10.1021/ie020218p>.
- [206] A.U. Şen, F.G. Fonseca, A. Funke, H. Pereira, F. Lemos, Pyrolysis kinetics and estimation of chemical composition of *Quercus cerris* cork, *Biomass Convers Biorefin.* (2020). <https://doi.org/10.1007/s13399-020-00964-y>.
- [207] M. Carrier, L. Auret, A. Bridgwater, J.H. Knoetze, Using apparent activation energy as a reactivity criterion for biomass pyrolysis, *Energy & Fuels*. 30 (2016) 7834–7841.
- [208] S. Vyazovkin, A.K. Burnham, J.M. Criado, L.A. Pérez-Maqueda, C. Popescu, N. Sbirrazzuoli, ICTAC Kinetics Committee recommendations for performing kinetic computations on thermal analysis data, *Thermochim Acta*. 520 (2011) 1–19. <https://doi.org/10.1016/j.tca.2011.03.034>.
- [209] M.E. Brown, *Introduction to Thermal Analysis: Techniques and Applications*, Springer Science & Business Media, 2004.
- [210] F. Xu, B. Wang, D. Yang, J. Hao, Y. Qiao, Y. Tian, Thermal degradation of typical plastics under high heating rate conditions by TG-FTIR: Pyrolysis behaviors and kinetic analysis, *Energy Convers Manag.* 171 (2018) 1106–1115. <https://doi.org/10.1016/j.enconman.2018.06.047>.
- [211] R.J. Wooley, V. Putsche, *Development of an ASPEN PLUS physical property database for biofuels components*, Golden, Colorado, 1996. <https://doi.org/10.2172/257362>.
- [212] A. Visconti, M. Miccio, C. Republic, D. Juchelková, Equilibrium-based simulation of lignocellulosic biomass pyrolysis via Aspen Plus®, in: *Recent Advances in Applied Mathematics, Modelling and Simulation*, 2014.
- [213] A.M.A.M.A. Ahmed, A. Salmiaton, T.S.Y.S.Y. Choong, W.A.K.G. Wan Azlina, Review of kinetic and equilibrium concepts for biomass tar modeling by using Aspen Plus, *Renewable and Sustainable Energy Reviews*. 52 (2015) 1623–1644. <https://doi.org/10.1016/j.rser.2015.07.125>.
- [214] M. Gupta, M. Ferguson, A. McFarlan, An Equilibrium Reactor Based Modelling of Biomass Torrefaction for Integrated Processes, in: *2020 Thermal and Catalytic Sciences Virtual Symposium*, Cvent, Kennewick, USA, 2020.
- [215] H.M. Yan, D.K. Zhang, Modeling of a Low Temperature Pyrolysis Process Using ASPEN PLUS, *Developments in Chemical Engineering and Mineral Processing*. 7 (1999) 577–591. <https://doi.org/10.1002/apj.5500070511>.
- [216] X. Xianjun, S. Zongkang, M. Peiyong, Y. Jin, W. zhaobin, Establishment of Three Components of Biomass Pyrolysis Yield Model, *Energy Procedia*. 66 (2015) 293–296. <https://doi.org/10.1016/j.egypro.2015.02.061>.

- [217] P. Lestinsky, A. Palit, Wood Pyrolysis Using Aspen Plus Simulation and Industrially Applicable Model, *GeoScience Engineering*. 62 (2016) 11–16. <https://doi.org/10.1515/gse-2016-0003>.
- [218] J.O. Ighalo, A.G. Adeniyi, Thermodynamic modeling and temperature sensitivity analysis of banana (*Musa spp.*) waste pyrolysis, *SN Appl Sci*. 1 (2019) 1086. <https://doi.org/10.1007/s42452-019-1147-3>.
- [219] A.G. Adeniyi, T.E. Odetoye, J. Titiloye, J.O. Ighalo, A Thermodynamic Study of Rice Husk (*Oryza Sativa*) Pyrolysis, *European Journal of Sustainable Development Research*. 3 (2019). <https://doi.org/10.29333/ejosdr/5830>.
- [220] M. Shahbaz, A. AlNouss, P. Parthasarathy, A.H. Abdelaal, H. Mackey, G. McKay, T. Al-Ansari, Investigation of biomass components on the slow pyrolysis products yield using Aspen Plus for techno-economic analysis, *Biomass Convers Biorefin*. (2020). <https://doi.org/10.1007/s13399-020-01040-1>.
- [221] R.C. Neves, A. Funke, E. Olivarez-Gómez, A. Bonomia, N. Dahmen, R. Maciel Filho, Process simulation of fast pyrolysis to produce bioslurry from lignocellulosic biomass residues combining first and second generation biofuels, in: 6th International Symposium on Energy from Biomass and Waste, Venice, Italy, 2016.
- [222] N.L. Hammer, A. a Boateng, C. a Mullen, M.C. Wheeler, Aspen Plus® and economic modeling of equine waste utilization for localized hot water heating via fast pyrolysis., *J Environ Manage*. 128 (2013) 594–601. <https://doi.org/10.1016/j.jenvman.2013.06.008>.
- [223] K. Onarheim, Y.Y. Solantausta, J. Lehto, Process Simulation Development of Fast Pyrolysis of Wood Using Aspen Plus, *Energy & Fuels*. 29 (2015) 205–217. <https://doi.org/10.1021/ef502023y>.
- [224] G. Kabir, B.H. Hameed, Recent progress on catalytic pyrolysis of lignocellulosic biomass to high-grade bio-oil and bio-chemicals, *Renewable and Sustainable Energy Reviews*. 70 (2017) 945–967. <https://doi.org/10.1016/j.rser.2016.12.001>.
- [225] J. Ward, M.G.G. Rasul, M.M.K.M.K. Bhuiya, Energy Recovery from Biomass by Fast Pyrolysis, *Procedia Eng*. 90 (2014) 669–674. <https://doi.org/10.1016/j.proeng.2014.11.791>.
- [226] M.B. Gorenssek, R. Shukre, C.-C.C. Chen, Development of a Thermophysical Properties Model for Flowsheet Simulation of Biomass Pyrolysis Processes, *ACS Sustain Chem Eng*. 7 (2019) 9017–9027. <https://doi.org/10.1021/acsschemeng.9b01278>.
- [227] B.H. Caudle, M.B. Gorenssek, C. Chen, A rigorous process modeling methodology for biomass fast pyrolysis with an entrained-flow reactor, *J Adv Manuf Process*. 2 (2020) 1–13. <https://doi.org/10.1002/amp2.10031>.
- [228] J.F. Peters, D. Iribarren, J. Dufour, Predictive pyrolysis process modelling in Aspen Plus, 22nd European Biomass Conference and Exhibition. 1 (2014) 352–368. <https://doi.org/10.5071/21stEUBCE2013-2CV.4.8>.
- [229] J.F. Peters, S.W. Banks, A. Susmozas, J. Dufour, Experimental validation of a predictive pyrolysis model in Aspen Plus, 21st European Biomass Conference and Exhibition. (2014) 1160–1163. <https://doi.org/10.5071/22ndEUBCE2014-3CV.2.27>.
- [230] M.B. Shemfe, S. Gu, P. Ranganathan, Techno-economic performance analysis of biofuel production and miniature electric power generation from biomass fast pyrolysis and bio-oil upgrading, *Fuel*. 143 (2015) 361–372. <https://doi.org/10.1016/j.fuel.2014.11.078>.
- [231] I.Y. Mohammed, Y.A. Abakr, R. Mokaya, Integrated biomass thermochemical conversion for clean energy production: Process design and economic analysis, *J Environ Chem Eng*. 7 (2019) 103093. <https://doi.org/10.1016/j.jece.2019.103093>.
- [232] Y.C. Ardila, Gaseificação da biomassa para a produção de gás de síntese e posterior fermentação para bioetanol : modelagem e simulação do processo, Universidade Estadual de Campinas, 2015.
- [233] R.C. Neves, Techno-economic investigation of first-generation sugarcane biorefinery integrated with second generation thermochemical route to produce biojet fuel, Universidade Estadual de Campinas, 2019.
- [234] H.Y. Ismail, A. Abbas, F. Azizi, J. Zeaiter, Pyrolysis of waste tires: A modeling and parameter estimation study using Aspen Plus®, *Waste Management*. 60 (2017) 482–493. <https://doi.org/10.1016/j.wasman.2016.10.024>.
- [235] L. Gura, Development of pyrolysis process models for the production of lignin based phenols using Aspen Plus, Stellenbosch University, 2017.
- [236] R. Demol, A. Dufour, Y. Rogaume, G. Mauviel, Production of Purified H₂, Heat, and Biochar from Wood: Comparison between Gasification and Autothermal Pyrolysis Based on Advanced Process Modeling, *Energy & Fuels*. 36 (2022) 488–501. <https://doi.org/10.1021/acs.energyfuels.1c03528>.
- [237] G.M. Wilson, Vapor-Liquid Equilibrium. XI. A New Expression for the Excess Free Energy of Mixing, *J Am Chem Soc*. 86 (1964) 127–130. <https://doi.org/10.1021/ja01056a002>.
- [238] C. Gustavsson, L. Nilsson, Co-production of pyrolysis oil in district heating plants: Systems analysis of dual fluidized-bed pyrolysis with sequential vapor condensation, *Energy and Fuels*. 27 (2013) 5313–5319. <https://doi.org/10.1021/ef401143v>.
- [239] A. Funke, M. Tomasi Morgano, H. Leibold, N. Dahmen, H. Leibold, Experimental comparison of two bench scale units for fast and intermediate pyrolysis, *J Anal Appl Pyrolysis*. 124 (2017) 504–514. <https://doi.org/10.1016/j.jaap.2016.12.033>.
- [240] N. Tröger, D. Richter, R. Stahl, Effect of feedstock composition on product yields and energy recovery rates of fast pyrolysis products from different straw types, *J Anal Appl Pyrolysis*. 100 (2013) 158–165. <https://doi.org/10.1016/j.jaap.2012.12.012>.
- [241] G.V. Brigagão, O. de Queiroz Fernandes Araújo, J.L.

- de Medeiros, H. Mikulcic, N. Duic, A techno-economic analysis of thermochemical pathways for corncob-to-energy: Fast pyrolysis to bio-oil, gasification to methanol and combustion to electricity, *Fuel Processing Technology*. 193 (2019) 102–113. <https://doi.org/10.1016/j.fuproc.2019.05.011>.
- [242] P. Kim, S. Weaver, N. Labbé, Effect of sweeping gas flow rates on temperature-controlled multistage condensation of pyrolysis vapors in an auger intermediate pyrolysis system, *J Anal Appl Pyrolysis*. 118 (2016) 325–334. <https://doi.org/10.1016/j.jaap.2016.02.017>.
- [243] Aspen Technology Inc., *Aspen Physical Property System: Physical Property Methods*, (2016).
- [244] E. Carlson, Don't Gamble With Physical Properties For Simulations, *Chem Eng Prog.* (1996) 35–46. <http://www.cchem.berkeley.edu/cbe150b/docs/VLE/Guidelines.pdf>.
- [245] H. Li, S. Xia, M. Wu, P. Ma, Isobaric (vapour+liquid) equilibria of binary systems containing butyl acetate for the separation of methoxy aromatic compounds (anisole and guaiacol) from biomass fast pyrolysis oil, *J Chem Thermodyn.* 87 (2015) 141–146. <https://doi.org/10.1016/j.jct.2015.04.003>.
- [246] Y. Ille, F.A. Sánchez, N. Dahmen, S. Pereda, Multi-phase Equilibria Modeling of Fast Pyrolysis Bio-Oils. Group Contribution Associating Equation of State Extension to Lignin Monomers and Derivatives, *Ind Eng Chem Res.* 58 (2019) 7318–7331. <https://doi.org/10.1021/acs.iecr.9b00227>.
- [247] F.A. Sánchez, Y. Ille, N. Dahmen, S. Pereda, GCA-EOS extension to mixtures of phenol ethers and derivatives with hydrocarbons and water, *Fluid Phase Equilib.* 490 (2019) 13–21. <https://doi.org/10.1016/j.fluid.2019.02.017>.
- [248] Y. Ille, F. Kröhl, A. Velez, A. Funke, S. Pereda, K. Schaber, N. Dahmen, Activity of water in pyrolysis oil—Experiments and modelling, *J Anal Appl Pyrolysis*. 135 (2018) 260–270. <https://doi.org/10.1016/j.jaap.2018.08.027>.
- [249] M.I. Campos-Franzani, N.F. Gajardo-Parra, C. Pazo-Carballo, P. Aravena, R. Santiago, J. Palomar, N. Escalona, R.I. Canales, Extraction of guaiacol from hydrocarbons as an alternative for the upgraded bio-oil purification: Experimental and computational thermodynamic study, *Fuel*. 280 (2020) 118405. <https://doi.org/10.1016/j.fuel.2020.118405>.
- [250] L. Cesari, S. Namysl, L. Canabady-Rochelle, F. Mutelet, Phase equilibria of phenolic compounds in water or ethanol, *Fluid Phase Equilib.* 453 (2017) 58–66. <https://doi.org/10.1016/j.fluid.2017.09.008>.
- [251] L. V. Jaspersen, R.J. McDougal, V. Diky, E. Paulechka, R.D. Chirico, K. Kroenlein, K. Lisa, A. Dutta, Liquid–Liquid Equilibrium Measurements for Model Systems Related to Catalytic Fast Pyrolysis of Biomass, *J Chem Eng Data*. 62 (2017) 243–252. <https://doi.org/10.1021/acs.jced.6b00625>.
- [252] A. Dutta, A. Sahir, E. Tan, D. Humbird, L.J. Snowden-Swan, P. Meyer, J. Ross, D. Sexton, R. Yap, J.L. Lukas, *Process Design and Economics for the Conversion of Lignocellulosic Biomass to Hydrocarbon Fuels. Thermochemical Research Pathways with In Situ and Ex Situ Upgrading of Fast Pyrolysis Vapors*, Golden, CO (United States), 2015. <https://doi.org/10.2172/1215007>.
- [253] W. Feng, H.J. Van Der Kooij, J. De Swaan Arons, Application of the SAFT equation of state to biomass fast pyrolysis liquid, *Chem Eng Sci.* 60 (2005) 617–624. <https://doi.org/10.1016/j.ces.2004.08.023>.
- [254] D.S. Fardhyanti, B. Triwibowo, H. Istanto, M.K. Anajib, A. Larasati, W. Oktaviani, Liquid phase equilibrium of phenol extraction from bio-oil produced by biomass pyrolysis using thermodynamic models, *Chin J Chem Eng.* 27 (2019) 391–399. <https://doi.org/10.1016/j.cjche.2018.08.011>.
- [255] M. Gupta, A. McFarlan, F. Preto, M. Ferguson, Comparative Evaluation of a Predictive Process Model for Multistage Condensation in Fast Pyrolysis Systems, in: *2020 Thermal and Catalytic Sciences Virtual Symposium*, Cvent, Kennewick, USA, 2020.
- [256] C. Stephan, M. Dicko, P. Stringari, C. Coquelet, Liquid-liquid equilibria of water + solutes (acetic acid/acetol/furfural/guaiacol/methanol/phenol/propanal) + solvents (isopropyl acetate/toluene) ternary systems for pyrolysis oil fractionation, *Fluid Phase Equilib.* 468 (2018) 49–57. <https://doi.org/10.1016/j.fluid.2018.04.016>.
- [257] L. Fele Žilnik, A. Jazbinšek, Recovery of renewable phenolic fraction from pyrolysis oil, *Sep Purif Technol.* 86 (2012) 157–170. <https://doi.org/10.1016/j.seppur.2011.10.040>.
- [258] Y.H. Stark, Modellierung der Kondensation von Schnellpyrolysedämpfen unter Berücksichtigung von Aerosolbildung, *Karlsruher Instituts für Technologie*, 2020.
- [259] R.J.M. Westerhof, N.J.M. Kuipers, S.R.A. Kersten, W.P.M. van Swaaij, Controlling the water content of biomass fast pyrolysis oil, *Ind Eng Chem Res.* 46 (2007) 9238–9247. <https://doi.org/10.1021/ie070684k>.
- [260] M.R. Fenske, Fractionation of Straight-Run Pennsylvania Gasoline, *Ind Eng Chem.* 24 (1932) 482–485. <https://doi.org/10.1021/ie50269a003>.
- [261] E.U. Hartge, M. Pogodda, C. Reimers, D. Schwier, G. Gruhn, J. Werther, Flowsheet simulation of solids processes, *KONA Powder and Particle Journal.* 24 (2006) 146–158. <https://doi.org/10.14356/kona.2006017>.
- [262] Honeywell UOP, *RTP Biomass Conversion - Renewable Fuels*, (n.d.). <https://uop.honeywell.com/en/industry-solutions/renewable-fuels/rtp-biomass-conversion> (accessed May 19, 2021).
- [263] K. Sipilä, E. Kuoppala, L. Fagernäs, A. Oasmaa, Characterization of biomass-based flash pyrolysis oils, *Biomass Bioenergy.* 14 (1998) 103–113. [https://doi.org/10.1016/S0961-9534\(97\)10024-1](https://doi.org/10.1016/S0961-9534(97)10024-1).
- [264] D.C. Elliott, D. Meier, A. Oasmaa, B. Van De Beld, A.

- V. Bridgwater, M. Marklund, Results of the International Energy Agency Round Robin on Fast Pyrolysis Bio-oil Production, *Energy and Fuels*. 31 (2017) 5111–5119. <https://doi.org/10.1021/acs.energyfuels.6b03502>.
- [265] M. V. Olarte, J. Taylor, M. Swita, T. Lemmon, R. Ma, D. Auberry, S. Burton, D. Howe, A. Padmaperuma, Revisiting Quantification of Phenolics in Bio-oils and Biocrudes, in: 2020 Thermal and Catalytic Sciences Virtual Symposium, Cvent, Kennewick, USA, 2020.
- [266] F.J.F. Lopes, F.O. Silvério, D.C.F. Baffa, M.E. Loureiro, M.H.P. Barbosa, Determination of Sugarcane Bagasse Lignin S/G/H Ratio by Pyrolysis GC/MS, *Journal of Wood Chemistry and Technology*. 31 (2011) 309–323. <https://doi.org/10.1080/02773813.2010.550379>.
- [267] G. Pereira da Silva Maciel, M.E. Machado, J.A. Barabará, D.D. Molin, E.B. Caramão, R.A. Jacques, GC × GC/TOFMS analysis concerning the identification of organic compounds extracted from the aqueous phase of sugarcane straw fast pyrolysis oil, *Biomass Bioenergy*. 85 (2016) 198–206. <https://doi.org/10.1016/j.biombioe.2015.11.009>.
- [268] M. Al-Owaisi, N. Al-Hadiwi, S.A. Khan, GC-MS analysis, determination of total phenolics, flavonoid content and free radical scavenging activities of various crude extracts of *Moringa peregrina* (Forssk.) Fiori leaves, *Asian Pac J Trop Biomed*. 4 (2014) 964–970. <https://doi.org/10.12980/APJTB.4.201414B295>.
- [269] D. Meier, Summary of the Analytical Methods Available for Chemical Analysis of Pyrolysis Liquids, in: *Fast Pyrolysis of Biomass: A Handbook*, Aston University, Birmingham, 2002: pp. 59–68.
- [270] R.J.M. Westerhof, D.W.F. Brilman, M. Garcia-Perez, Z. Wang, S.R.G. Oudenhoven, W.P.M. Van Swaaij, S.R.A. Kersten, Fractional condensation of biomass pyrolysis vapors, *Energy and Fuels*. 25 (2011) 1817–1829. <https://doi.org/10.1021/ef2000322>.
- [271] S. Jones, P. Meyer, L. Snowden-Swan, K.J. Susanne, M. Pimphan, Snowden-SwanLesley, P. Asanga, T. Eric, D. Abhijit, J. Jacob, Cafferty, S. Jones, P. Meyer, L. Snowden-Swan, Process design and economics for the conversion of lignocellulosic biomass to hydrocarbon fuels: Fast pyrolysis and hydrotreating bio-oil pathway, *Energy*. (2013) 97. <https://doi.org/PNNL-23053-NREL/TP-5100-61178>.
- [272] A.P. Pinheiro Pires, J. Arauzo, I. Fonts, M.E. Domine, A. Fernández Arroyo, M.E.M.M.E. Garcia-Perez, J. Montoya, F. Chejne, P. Pfromm, M.E.M.M.E. Garcia-Perez, Challenges and opportunities for bio-oil refining: A review, *Energy and Fuels*. 33 (2019) 4683–4720. <https://doi.org/10.1021/acs.energyfuels.9b00039>.
- [273] I. Fonts, M. Atienza-Martínez, H.-H.H. Carstensen, M. Benés, A.P. Pinheiro Pires, M. Garcia-Perez, R. Bilbao, Thermodynamic and Physical Property Estimation of Compounds Derived from the Fast Pyrolysis of Lignocellulosic Materials, *Energy & Fuels*. 35 (2021) 17114–17137. <https://doi.org/10.1021/acs.energyfuels.1c01709>.
- [274] A. Alves, M. Schwanninger, H. Pereira, J. Rodrigues, Analytical pyrolysis as a direct method to determine the lignin content in wood: Part 1: Comparison of pyrolysis lignin with Klason lignin, *J Anal Appl Pyrolysis*. 76 (2006) 209–213. <https://doi.org/10.1016/j.jaap.2005.11.004>.
- [275] L. Wu, X. Hu, S. Wang, D. Mourant, Y. Song, T. Li, C.-Z. Li, Formation of coke during the esterification of pyrolysis bio-oil, *RSC Adv*. 6 (2016) 86485–86493. <https://doi.org/10.1039/C6RA14939A>.
- [276] J.L. Banyasz, S. Li, J.L. Lyons-Hart, K.H. Shafer, Cellulose pyrolysis: the kinetics of hydroxyacetaldehyde evolution, *J Anal Appl Pyrolysis*. 57 (2001) 223–248. [https://doi.org/10.1016/S0165-2370\(00\)00135-2](https://doi.org/10.1016/S0165-2370(00)00135-2).
- [277] S.-J. Oh, G.-G. Choi, J.-S. Kim, Production of acetic acid-rich bio-oils from the fast pyrolysis of biomass and synthesis of calcium magnesium acetate deicer, *J Anal Appl Pyrolysis*. 124 (2017) 122–129. <https://doi.org/10.1016/j.jaap.2017.01.032>.
- [278] K. Routray, K.J. Barnett, G.W. Huber, Hydrodeoxygenation of Pyrolysis Oils, *Energy Technology*. 5 (2017) 80–93. <https://doi.org/10.1002/ente.201600084>.
- [279] T. Shoji, H. Kawamoto, S. Saka, Boiling point of levoglucosan and devolatilization temperatures in cellulose pyrolysis measured at different heating area temperatures, *J Anal Appl Pyrolysis*. 109 (2014) 185–195. <https://doi.org/10.1016/j.jaap.2014.06.014>.
- [280] A. Anca-Couce, P. Sommersacher, R. Scharler, Online experiments and modelling with a detailed reaction scheme of single particle biomass pyrolysis, *J Anal Appl Pyrolysis*. 127 (2017) 411–425. <https://doi.org/10.1016/j.jaap.2017.07.008>.
- [281] P. Debiagi, G. Gentile, A. Cuoci, A. Frassoldati, E. Ranzi, T. Faravelli, A predictive model of biochar formation and characterization, *J Anal Appl Pyrolysis*. 134 (2018) 326–335. <https://doi.org/10.1016/j.jaap.2018.06.022>.
- [282] R. Bayerbach, D. Meier, Characterization of the water-insoluble fraction from fast pyrolysis liquids (pyrolytic lignin). Part IV: Structure elucidation of oligomeric molecules, *J Anal Appl Pyrolysis*. 85 (2009) 98–107. <https://doi.org/10.1016/j.jaap.2008.10.021>.
- [283] J.C. del Río, J. Rencoret, P. Prinsen, Á.T. Martínez, J. Ralph, A. Gutiérrez, Structural Characterization of Wheat Straw Lignin as Revealed by Analytical Pyrolysis, 2D-NMR, and Reductive Cleavage Methods, *J Agric Food Chem*. 60 (2012) 5922–5935. <https://doi.org/10.1021/jf301002n>.
- [284] M. Fortin, M. Mohadjer Beromi, A. Lai, P.C. Tarves, C.A. Mullen, A.A. Boateng, N.M. West, Structural Analysis of Pyrolytic Lignins Isolated from Switchgrass Fast-Pyrolysis Oil, *Energy & Fuels*. 29 (2015) 8017–8026. <https://doi.org/10.1021/acs.energyfuels.5b01726>.
- [285] N. Charon, J. Ponthus, D. Espinat, F. Broust, G.

- Volle, J. Valette, D. Meier, Multi-technique characterization of fast pyrolysis oils, *J Anal Appl Pyrolysis*. 116 (2015) 18–26. <https://doi.org/http://dx.doi.org/10.1016/j.jaap.2015.10.012>.
- [286] A. Funke, D. Richter, A. Niebel, N. Dahmen, J. Sauer, Fast Pyrolysis of Biomass Residues in a Twin-screw Mixing Reactor, *Journal of Visualized Experiments*. accepted f (2016) 1–8. <https://doi.org/10.3791/54395>.
- [287] C. Kornmayer, Verfahrenstechnik Untersuchungen zur Schnellpyrolyse von Lignocellulose im Doppenschnecken-Mischreaktor, Universität Fridericiana Karlsruhe, 2009.
- [288] J. Wang, E. Minami, H. Kawamoto, Thermal reactivity of hemicellulose and cellulose in cedar and beech wood cell walls, *Journal of Wood Science*. 66 (2020) 41. <https://doi.org/10.1186/s10086-020-01888-x>.
- [289] F. Trippe, M. Fröhling, F. Schultmann, R. Stahl, E. Henrich, Techno-economic assessment of gasification as a process step within biomass-to-liquid (BtL) fuel and chemicals production, *Fuel Processing Technology*. 92 (2011) 2169–2184. <https://doi.org/10.1016/j.fuproc.2011.06.026>.
- [290] F.G. Fonseca, Moisture Content as a design and operational parameter for fast pyrolysis, *Lisbon Tech*, 2015.
- [291] P.E. Liley, G.H. Thomson, D.G. Friend, T.E. Daubert, E. Buck, Physical and Chemical Data, in: D.W. Green, J.O. Maloney (Eds.), *Perry's Chemical Engineers' Handbook*, 7th ed., McGraw-Hill, 1997.
- [292] H. Yang, S. Kudo, H.-P. Kuo, K. Norinaga, A. Mori, O. Mašek, J. Hayashi, Estimation of Enthalpy of Bio-Oil Vapor and Heat Required for Pyrolysis of Biomass, *Energy & Fuels*. 27 (2013) 2675–2686. <https://doi.org/10.1021/ef400199z>.
- [293] J.P. Polin, C.A. Peterson, L.E. Whitmer, R.G. Smith, R.C. Brown, Process intensification of biomass fast pyrolysis through autothermal operation of a fluidized bed reactor, *Appl Energy*. 249 (2019) 276–285. <https://doi.org/10.1016/j.apenergy.2019.04.154>.
- [294] X. Zheng, Z. Zhong, B. Zhang, H. Du, W. Wang, Q. Li, Environmental impact comparison of wheat straw fast pyrolysis systems with different hydrogen production processes based on life cycle assessment, *Waste Management & Research: The Journal for a Sustainable Circular Economy*. 40 (2022) 654–664. <https://doi.org/10.1177/0734242X211045004>.
- [295] F. Liotta, P. Chatellier, G. Esposito, M. Fabbricino, E.D. Van Hullebusch, P.N.L. Lens, Hydrodynamic Mathematical Modelling of Aerobic Plug Flow and Nonideal Flow Reactors: A Critical and Historical Review, *Crit Rev Environ Sci Technol*. 44 (2014) 2642–2673. <https://doi.org/10.1080/10643389.2013.829768>.
- [296] J.M. St. Clair, K.M. Spencer, M.R. Beaver, J.D. Crouse, F. Paulot, P.O. Wennberg, Quantification of hydroxyacetone and glycolaldehyde using chemical ionization mass spectrometry, *Atmos Chem Phys*. 14 (2014) 4251–4262. <https://doi.org/10.5194/acp-14-4251-2014>.
- [297] F.G. Fonseca, A. Funke, N. Dahmen, Aspen Plus™ modeling of Fractional Condensation schemes for production of Fast Pyrolysis bio-oil, in: 27th European Biomass Conference and Exhibition, ETA-Flourance Renewable Energies, Lisbon, 2019: pp. 681–683. <https://doi.org/10.5071/27thEUBCE2019-3BV.7.9>.
- [298] H. Sui, H. Yang, J. Shao, X. Wang, Y. Li, H. Chen, Fractional condensation of multicomponent vapors from pyrolysis of cotton stalk, *Energy and Fuels*. 28 (2014) 5095–5102. <https://doi.org/10.1021/ef5006012>.
- [299] A.N. Huang, C.P. Hsu, B.R. Hou, H.P. Kuo, Production and separation of rice husk pyrolysis bio-oils from a fractional distillation column connected fluidized bed reactor, *Powder Technol*. 323 (2018) 588–593. <https://doi.org/10.1016/j.powtec.2016.03.052>.
- [300] R. Yin, R. Liu, Y. Mei, W. Fei, X. Sun, Characterization of bio-oil and bio-char obtained from sweet sorghum bagasse fast pyrolysis with fractional condensers, *Fuel*. 112 (2013) 96–104. <https://doi.org/10.1016/j.fuel.2013.04.090>.
- [301] A. Fredenslund, R.L. Jones, J.M. Prausnitz, Group-contribution estimation of activity coefficients in nonideal liquid mixtures, *AIChE Journal*. 21 (1975) 1086–1099. <https://doi.org/10.1002/aic.690210607>.
- [302] A. Fredenslund, J. Gmehling, P. Rasmussen, Vapor-Liquid equilibria using UNIFAC a group-contribution method, Wiley-VCH Verlag GmbH & Co, Weinheim, Germany, 1977.
- [303] G. Maurer, J.M. Prausnitz, On the derivation and extension of the uniquac equation, *Fluid Phase Equilib*. 2 (1978) 91–99. [https://doi.org/10.1016/0378-3812\(78\)85002-X](https://doi.org/10.1016/0378-3812(78)85002-X).
- [304] D.S. Abrams, J.M. Prausnitz, Statistical thermodynamics of liquid mixtures: A new expression for the excess Gibbs energy of partly or completely miscible systems, *AIChE Journal*. 21 (1975) 116–128. <https://doi.org/10.1002/aic.690210115>.
- [305] H. Renon, J.M. Prausnitz, Local compositions in thermodynamic excess functions for liquid mixtures, *AIChE Journal*. 14 (1968) 135–144. <https://doi.org/10.1002/aic.690140124>.
- [306] J.M. Prausnitz, R.N. Lichtenthaler, E.G. de Azevedo, Fugacities in Liquid Mixtures: Excess Functions, in: *Molecular Thermodynamics of Fluid-Phase Equilibria*, Prentice-Hall, Englewood Cliffs, N.J., USA, 1986.
- [307] Otto. Redlich, J.N.S. Kwong, On the Thermodynamics of Solutions. V. An Equation of State. Fugacities of Gaseous Solutions., *Chem Rev*. 44 (1949) 233–244. <https://doi.org/10.1021/cr60137a013>.
- [308] D.S.H. Wong, S.I. Sandler, A theoretically correct mixing rule for cubic equations of state, *AIChE Journal*. 38 (1992) 671–680. <https://doi.org/10.1002/aic.690380505>.
- [309] M.-J. Huron, J. Vidal, New mixing rules in simple equations of state for representing vapour-liquid

- equilibria of strongly non-ideal mixtures, *Fluid Phase Equilib.* 3 (1979) 255–271. [https://doi.org/10.1016/0378-3812\(79\)80001-1](https://doi.org/10.1016/0378-3812(79)80001-1).
- [310] T. Holderbaum, J. Gmehling, PSRK: A Group Contribution Equation of State Based on UNIFAC, *Fluid Phase Equilib.* 70 (1991) 251–265. [https://doi.org/10.1016/0378-3812\(91\)85038-V](https://doi.org/10.1016/0378-3812(91)85038-V).
- [311] D.F. Othmer, S.J. Silvis, A. Spiel, Composition of Vapors from Boiling Binary Solutions: Pressure Equilibrium Still for Studying Water–Acetic Acid System, *Ind Eng Chem.* 44 (1952) 1864–1872. <https://doi.org/10.1021/ie50512a041>.
- [312] Q. Xie, H. Wan, M. Han, G. Guan, Investigation on isobaric vapor–liquid equilibrium for acetic acid+water+methyl ethyl ketone+isopropyl acetate, *Fluid Phase Equilib.* 280 (2009) 120–128. <https://doi.org/10.1016/j.fluid.2009.03.008>.
- [313] V.N. Kabadi, R.P. Danner, A modified Soave-Redlich-Kwong equation of state for water-hydrocarbon phase equilibria, *Industrial & Engineering Chemistry Process Design and Development.* 24 (1985) 537–541. <https://doi.org/10.1021/i200030a004>.
- [314] J.S. Lopez-Echeverry, S. Reif-Acherman, E. Araujo-Lopez, Peng-Robinson equation of state: 40 years through cubics, *Fluid Phase Equilib.* 447 (2017) 39–71. <https://doi.org/10.1016/j.fluid.2017.05.007>.
- [315] W. Reinders, C.H. de Minjer, Vapour-liquid equilibria in ternary systems. VI. The system water-acetone-chloroform, *Recueil Des Travaux Chimiques Des Pays-Bas.* 66 (2010) 573–604. <https://doi.org/10.1002/recl.19470660906>.
- [316] D.F. Othmer, M.M. Chudgar, S.L. Levy, Binary and Ternary Systems of Acetone, Methyl Ethyl Ketone, and Water, *Ind Eng Chem.* 44 (1952) 1872–1881. <https://doi.org/10.1021/ie50512a042>.
- [317] G. Bredig, R. Bayer, I. Die Dampfdrücke des binären Systems Methylalkohol-Wasser, *Zeitschrift Für Physikalische Chemie.* 130U (1927) 1–28. <https://doi.org/10.1515/zpch-1927-13002>.
- [318] G.W. Bennett, A laboratory experiment on the boiling-point curves of non-azeotropic binary mixtures, *J Chem Educ.* 6 (1929) 1544. <https://doi.org/10.1021/ed006p1544>.
- [319] R. Weller, H. Schuberth, E. Leibnitz, Phasengleichgewichtsmessungen. IV. Die Phasengleichgewichte dampfförmig/flüssig des Systems Phenol/n-Butylacetat/Wasser bei 44,4°C, *Journal Für Praktische Chemie.* 21 (1963) 234–249. <https://doi.org/10.1002/prac.19630210502>.
- [320] C.H. Chou, J.L. Perng, M.D. Lee, Y.P. Chen, Vapor-liquid equilibrium measurements of the ternary system of ethanol, water and phenol at 760 mmHg, *Journal of the Chinese Institute of Chemical Engineers.* 18 (1987) 393–399.
- [321] N.M. Morozov, M.Ya. Kagan, E.S. Grossblyat, Dampfdruck der binären Mischungen Acetaldehyd - Wasser und Acetaldehyd - Essigsäure, *Zh.Obshch.Khim.* (1934) 1322–1326.
- [322] J. Suška, Phase equilibria in binary systems containing acetaldehyde, *Collect Czechoslov Chem Commun.* 44 (1979) 1852–1856. <https://doi.org/10.1135/cccc19791852>.
- [323] S.-H. Chang, Measurement of Vapor-Liquid Equilibrium for the Systems in the Industrial Preparation of Acetic Acid (I), *Huaxue-Gongcheng.* (1978) 75–85.
- [324] A. Rius, J.L. Otero, A. Macarron, Equilibres liquide—vapeur de mélanges binaires donnant une réaction chimique: systèmes méthanol—acide acétique ; éthanol—acide acétique ; n-propanol—acide acétique ; n-butanol—acide acétique, *Chem Eng Sci.* 10 (1959) 105–111. [https://doi.org/10.1016/0009-2509\(59\)80029-4](https://doi.org/10.1016/0009-2509(59)80029-4).
- [325] S. Amer Amezaga, J. Fernández Biarge, Comportamiento Termodinámico de Agunos Sistemas Binarios Acido Acetico-Alcohol en Equilibrio Liquido Vapor, *Anal.Quim.* 69 (1973) 569–586.
- [326] N.V. Chalov, E.F. Goryachikh, L.Kh. Vodolazova, Untersuchung der Dampf-Flüssig-Zusammensetzungen in binären Phenol-Lösungen, *Gidroliz.Lesokhim.Prom.* 8 (1955) 11.12.
- [327] I.I. Vasileva, A.K. Gryaznov, V.M. Zakoshanskii, A.A. Naumova, A.A. Polyakov, Liquid-Vapor Equilibrium in the Acetone-Phenol-System, *J.Appl.Chem.USSR.* 64 (1991) 410–413.
- [328] K. Ochi, B.C.-Y. Lu, Determination and correlation of binary vapor-liquid equilibrium data, *Fluid Phase Equilib.* 1 (1977) 185–200. [https://doi.org/10.1016/0378-3812\(77\)80002-2](https://doi.org/10.1016/0378-3812(77)80002-2).
- [329] C.R. Fordyce, D.R. Simonsen, Cellulose Ester Solutions - Evaporation in Binary Solvent Mixtures, *Ind Eng Chem.* 41 (1949) 104–111. <https://doi.org/10.1021/ie50469a027>.
- [330] V. Bekárek, Liquid-vapour equilibrium. XL. Liquid-vapour equilibrium in the systems SO₂-CH₃COOH₃-CH₃OH and SO₂-CH₃COH₃-CH₃OH, *Collect Czechoslov Chem Commun.* 33 (1968) 2608–2619. <https://doi.org/10.1135/cccc19682608>.
- [331] R.A. Wilsak, S.W. Campbell, G. Thodos, Vapor—liquid equilibrium measurements for the methanol—acetone system at 372.8, 397.7 and 422.6 K, *Fluid Phase Equilib.* 28 (1986) 13–37. [https://doi.org/10.1016/0378-3812\(86\)85066-X](https://doi.org/10.1016/0378-3812(86)85066-X).
- [332] N.K. Tikhonova, V.S. Timofeev, L.A. Serafimov, Z.N. Kupriyanova, Dampf-Flüssig-Gleichgewicht im ternären System Acetaldehyd-Aceton-Vinylacetat bei Atmosphärendruck, *Izv.Vyssh.Uchebn.Zaved.Khim.Khim.Tekhnol.* 13 (1970) 349–351.
- [333] A.D. Leu, C.J. Chen, D.B. Robinson, Vapor-liquid equilibrium in selected binary systems, *AIChE Symposium Series.* 85 (1989) 11–16.
- [334] L. Fele, V. Grilc, Separation of Furfural from Ternary Mixtures, *J Chem Eng Data.* 48 (2003) 564–570. <https://doi.org/10.1021/je020117y>.
- [335] H. Zheng, X. Luo, G. Yin, J. Chen, S. Zhao, Vapor Pressure and Isobaric Vapor–Liquid Equilibrium for

- Binary Systems of Furfural, 2-Acetylfuran, and 5-Methylfurfural at 3.60 and 5.18 kPa, *J Chem Eng Data*. 63 (2018) 49–56. <https://doi.org/10.1021/acs.jced.7b00574>.
- [336] H. Li, S. Xia, P. Ma, F. Yan, Z. Yang, Y. Li, Isobaric (vapour+liquid) equilibria for three binary systems (toluene+anisole, n-butylbenzene+anisole, and guaiacol+anisole) at 101.33kPa, *Fluid Phase Equilib.* 369 (2014) 109–114. <https://doi.org/10.1016/j.fluid.2014.02.025>.
- [337] L. Cesari, S. Namysl, L. Canabady-Rochelle, F. Mutelet, Phase equilibria of phenolic compounds in water or ethanol, *Fluid Phase Equilib.* 453 (2017) 58–66. <https://doi.org/10.1016/j.fluid.2017.09.008>.
- [338] J.C. Dearden, Quantitative structure-property relationships for prediction of boiling point, vapor pressure, and melting point, *Environ Toxicol Chem.* 22 (2003) 1696. <https://doi.org/10.1897/01-363>.
- [339] D. Mackay, W.-Y. Shiu, K.-C. Ma, S.C. Lee, W.-Y. Shiu, S.C. Lee, *Handbook of Physical-Chemical Properties and Environmental Fate for Organic Chemicals*, CRC Press, 2006. <https://doi.org/10.1201/9781420044393>.
- [340] M. Leistra, Methods for estimating the vapour pressure of organic chemicals: application to five pesticides, *Alterrareport* 2215. (2011) 60.
- [341] K.G. Joback, Obtain the best physical property data, *Chem Eng Prog.* 105 (2009) 30–39.
- [342] D.J. Marino, Variability in Physical Constant Parameter Values from Standard Data Sources and the Implication of This Variability for Risk Analysis, *Risk Analysis.* 26 (2006) 555–572. <https://doi.org/10.1111/j.1539-6924.2006.00752.x>.
- [343] K.G. Joback, R.C. Reid, Estimation of pure-component properties from group-contributions, *Chem Eng Commun.* 57 (1987) 233–243. <https://doi.org/10.1080/00986448708960487>.
- [344] L. Constantinou, R. Gani, New group contribution method for estimating properties of pure compounds, *AIChE Journal.* 40 (1994) 1697–1710. <https://doi.org/10.1002/aic.690401011>.
- [345] W. Cordes, J. Rarey, A new method for the estimation of the normal boiling point of non-electrolyte organic compounds, *Fluid Phase Equilib.* 201 (2002) 409–433. [https://doi.org/10.1016/S0378-3812\(02\)00050-X](https://doi.org/10.1016/S0378-3812(02)00050-X).
- [346] A.L. Lydersen, *Estimation of Critical Properties of Organic Compounds*, Madison, Wisconsin, 1955.
- [347] R.F. Fedors, A relationship between chemical structure and the critical temperature, *Chem Eng Commun.* 16 (1982) 149–151. <https://doi.org/10.1080/00986448208911092>.
- [348] D. Ambrose, *Correlation and Estimation of Vapor-Liquid Critical Properties: I. Critical Temperatures of Organic Compounds*, Teddington, 1978.
- [349] K.M. Klincewicz, R.C. Reid, Estimation of critical properties with group contribution methods, *AIChE Journal.* 30 (1984) 137–142. <https://doi.org/10.1002/aic.690300119>.
- [350] Y. Nannoolal, J. Rarey, D. Ramjugernath, Estimation of pure component properties: Part 2. Estimation of critical property data by group contribution, *Fluid Phase Equilib.* 252 (2007) 1–27. <https://doi.org/10.1016/j.fluid.2006.11.014>.
- [351] J.W. Hogge, N.F. Giles, T.A. Knotts, R.L. Rowley, W.V. Wilding, The Riedel vapor pressure correlation and multi-property optimization, *Fluid Phase Equilib.* 429 (2016) 149–165. <https://doi.org/10.1016/j.fluid.2016.08.032>.
- [352] B.I. Lee, M.G. Kesler, A generalized thermodynamic correlation based on three-parameter corresponding states, *AIChE Journal.* 21 (1975) 510–527. <https://doi.org/10.1002/aic.690210313>.
- [353] S.W. Benson, New Methods for Estimating the Heats of Formation, Heat Capacities, and Entropies of Liquids and Gases, *J Phys Chem A.* 103 (1999) 11481–11485. <https://doi.org/10.1021/jp992971a>.
- [354] V. Růžička, E.S. Domalski, Estimation of the Heat Capacities of Organic Liquids as a Function of Temperature using Group Additivity. II. Compounds of Carbon, Hydrogen, Halogens, Nitrogen, Oxygen, and Sulfur, *J Phys Chem Ref Data.* 22 (1993) 619–657. <https://doi.org/10.1063/1.555924>.
- [355] V. Růžička, E.S. Domalski, Estimation of the Heat Capacities of Organic Liquids as a Function of Temperature using Group Additivity. I. Hydrocarbon Compounds, *J Phys Chem Ref Data.* 22 (1993) 597–618. <https://doi.org/10.1063/1.555923>.
- [356] M. Zábanský, V. Růžička, Estimation of the Heat Capacities of Organic Liquids as a Function of Temperature Using Group Additivity: An Amendment, *J Phys Chem Ref Data.* 33 (2004) 1071–1081. <https://doi.org/10.1063/1.1797811>.
- [357] L. Riedel, Eine Neue Dampfdruckformel, *Chem. Ing. Tech.* (1954) 83.89.
- [358] P. Li, P.-S. Ma, S.-Z. Yi, Z.-G. Zhao, L.-Z. Cong, A new Corresponding-States Group-Contribution method (CSGC) for estimating vapor pressures of pure compounds, *Fluid Phase Equilib.* 101 (1994) 101–119. [https://doi.org/10.1016/0378-3812\(94\)02607-6](https://doi.org/10.1016/0378-3812(94)02607-6).
- [359] Y. Nannoolal, J. Rarey, D. Ramjugernath, Estimation of pure component properties: Part 3. Estimation of the vapor pressure of non-electrolyte organic compounds via group contributions and group interactions, *Fluid Phase Equilib.* 269 (2008) 117–133. <https://doi.org/10.1016/j.fluid.2008.04.020>.
- [360] A. Vetere, New correlations for predicting vaporization enthalpies of pure compounds, *The Chemical Engineering Journal.* 17 (1979) 157–162. [https://doi.org/10.1016/0300-9467\(79\)85008-X](https://doi.org/10.1016/0300-9467(79)85008-X).
- [361] I. Kikic, A. Vetere, Evaluation of several literature equations to predict the vaporization enthalpies at the normal boiling point, *Fluid Phase Equilib.* (2011). <https://doi.org/10.1016/j.fluid.2011.06.026>.
- [362] M. Ducros, J.F. Gruson, H. Sannier, Estimation des

- enthalpies de vaporisation des composés organiques liquides. Partie 1. Applications aux alcanes, cycloalcanes, alcènes, hydrocarbures benzeniques, alcools, alcanes thiols, chloro et bromoalcanes, nitriles, esters, acides et aldéhydes, *Thermochim Acta*. 36 (1980) 39–65.
[https://doi.org/10.1016/0040-6031\(80\)80109-2](https://doi.org/10.1016/0040-6031(80)80109-2).
- [363] M. Ducros, J.F. Gruson, H. Sannier, I. Velasco, Estimation des enthalpies de vaporisation des composés organiques liquides. Partie 2. Applications aux éthersoxydes, thioalcanes, cétones et amines, *Thermochim Acta*. 44 (1981) 131–140.
[https://doi.org/10.1016/0040-6031\(81\)80035-4](https://doi.org/10.1016/0040-6031(81)80035-4).
- [364] M. Ducros, H. Sannier, Estimation des enthalpies de vaporisation des composés organiques liquides, partie 3. Application aux hydrocarbures insaturés, *Thermochim Acta*. 54 (1982) 153–157.
[https://doi.org/10.1016/0040-6031\(82\)85074-0](https://doi.org/10.1016/0040-6031(82)85074-0).
- [365] T. Yamada, R.D. Gunn, Saturated liquid molar volumes. The Rackett equation, *J Chem Eng Data*. 18 (1973) 234–236.
<https://doi.org/10.1021/je60057a006>.
- [366] R.C. Reid, J.M. Prausnitz, T.K. Sherwood, *The Properties of Gases and Liquids*, McGraw-Hill, New York, 1977.
- [367] D. Reichenberg, New methods for the estimation of the viscosity coefficients of pure gases at moderate pressures (with particular reference to organic vapors), *AIChE Journal*. 21 (1975) 181–183.
<https://doi.org/10.1002/aic.690210130>.
- [368] A. Letsou, L.I. Stiel, Viscosity of saturated nonpolar liquids at elevated pressures, *AIChE Journal*. 19 (1973) 409–411.
<https://doi.org/10.1002/aic.690190241>.
- [369] B.E. Poling, J.M. Prausnitz, J.P. O'Connell, Viscosity, in: *The Properties of Gases and Liquids*, 5th ed., McGraw-Hill, 2001.
<https://doi.org/10.1036/0070116822>.
- [370] Y. Nannoolal, J. Rarey, D. Ramjugernath, Estimation of pure component properties. Part 4: Estimation of the saturated liquid viscosity of non-electrolyte organic compounds via group contributions and group interactions, *Fluid Phase Equilib*. 281 (2009) 97–119.
<https://doi.org/10.1016/j.fluid.2009.02.016>.
- [371] C. Dupont, R. Chiriac, G. Gauthier, F. Toche, Heat capacity measurements of various biomass types and pyrolysis residues, *Fuel*. 115 (2014) 644–651.
<https://doi.org/10.1016/j.fuel.2013.07.086>.
- [372] E. Barteková, M. Bajus, Pyrolysis of Hexadecane, *Collect Czechoslov Chem Commun*. 62 (1997) 1057–1069.
<https://doi.org/10.1135/cccc19971057>.
- [373] F. Fantozzi, A. Frassoldati, P. Bartocci, G. Cinti, F. Quagliarini, G. Bidini, E.M. Ranzi, An experimental and kinetic modeling study of glycerol pyrolysis, *Appl Energy*. 184 (2016) 68–76.
<https://doi.org/10.1016/j.apenergy.2016.10.018>.
- [374] F.O. Rice, R.E. Vollrath, The thermal decomposition of acetone in the gaseous state, *Proceedings of the National Academy of Sciences*. 15 (1929) 702–705.
<https://doi.org/10.1073/pnas.15.9.702>.
- [375] J. López-Beceiro, A.M. Díaz-Díaz, A. Álvarez-García, J. Tarrío-Saavedra, S. Naya, R. Artiaga, The Complexity of Lignin Thermal Degradation in the Isothermal Context, *Processes*. 9 (2021) 1154.
<https://doi.org/10.3390/pr9071154>.
- [376] Y. Qiao, B. Wang, P. Zong, Y. Tian, F. Xu, D. Li, F. Li, Y. Tian, Thermal behavior, kinetics and fast pyrolysis characteristics of palm oil: Analytical TG-FTIR and Py-GC/MS study, *Energy Convers Manag*. 199 (2019) 111964. <https://doi.org/10.1016/j.enconman.2019.111964>.
- [377] J. Asomaning, P. Mussone, D.C. Bressler, Pyrolysis of polyunsaturated fatty acids, *Fuel Processing Technology*. 120 (2014) 89–95.
<https://doi.org/10.1016/j.fuproc.2013.12.007>.
- [378] E.-J. Shin, M.R. Nimlos, R.J. Evans, Kinetic analysis of the gas-phase pyrolysis of carbohydrates, *Fuel*. 80 (2001) 1697–1709.
[https://doi.org/10.1016/S0016-2361\(01\)00056-4](https://doi.org/10.1016/S0016-2361(01)00056-4).
- [379] A.T. Williamson, The Polymerization and Thermal Decomposition of Ketene, *J Am Chem Soc*. 56 (1934) 2216–2218.
<https://doi.org/10.1021/ja01326a003>.
- [380] B. Chen, Z. Shi, S. Jiang, H. Tian, Mechanism studies of 5-HMF pyrolysis by quantum chemistry, *J Cent South Univ*. 24 (2017) 2565–2571.
<https://doi.org/10.1007/s11771-017-3670-y>.
- [381] N. Weih, A. Funke, Y. Ille, C. Pfitzer, A. Niebel, N. Dahmen, Online Balancing of a Pilot Scale Fast Pyrolysis Plant, in: *European Biomass Conference and Exhibition Proceedings*, 2017.
- [382] S.A. Channiwala, P.P. Parikh, A unified correlation for estimating HHV of solid, liquid and gaseous fuels, *Fuel*. 81 (2002) 1051–1063.
[https://doi.org/10.1016/S0016-2361\(01\)00131-4](https://doi.org/10.1016/S0016-2361(01)00131-4).
- [383] R. Turton, R.C. Bailie, B.W. Wallace, J.A. Shaelwitz, *Analysis, synthesis, and design of chemical processes*, 2009.
- [384] M.W. Nolte, M.W. Liberatore, Viscosity of Biomass Pyrolysis Oils from Various Feedstocks, *Energy & Fuels*. 24 (2010) 6601–6608.
<https://doi.org/10.1021/ef101173r>.
- [385] J. Kestin, M. Sokolov, W.A. Wakeham, Viscosity of liquid water in the range –8 °C to 150 °C, *J Phys Chem Ref Data*. 7 (1978) 941–948.
<https://doi.org/10.1063/1.555581>.
- [386] R. Manrique, E. Terrell, P. Kostetskyy, F. Chejne, M. Olarte, L. Broadbelt, M. García-Pérez, Elucidating Biomass-Derived Pyrolytic Lignin Structures from Demethylation Reactions through Density Functional Theory Calculations, *Energy and Fuels*. 37 (2023) 5189–5205.
<https://doi.org/10.1021/acs.energyfuels.2c04292>.

Appendix

Appendix: Table of Contents

Appendix	<i>i</i>
Appendix: Table of Contents	<i>i</i>
Appendix: List of Figures	<i>iii</i>
Appendix: List of Tables	<i>v</i>
Appendix A: bioliq® data	<i>vii</i>
Appendix B	<i>ix</i>
Thermogravimetric data	<i>ix</i>
Deconvolution	<i>xi</i>
Model-fitting	<i>xv</i>
Isoconversional Methods	<i>xxxix</i>
Numerical values	<i>xxxix</i>
Arrhenius Plots	<i>xxxiv</i>
Appendix C	<i>xxxvii</i>
Primary reaction networks	<i>xxxvii</i>
Appendix D	<i>liii</i>
List of components	<i>liii</i>
Decision on heavy fraction surrogate	<i>liv</i>
Thermophysical property values	<i>lvii</i>
Vapor pressure	<i>lxvii</i>
Group contribution assignment	<i>lxxv</i>
Property estimation parameters	<i>xc</i>

Appendix: List of Figures

- Fig. 1: Comparison of the behavior of the mass loss profiles for the different samples at the different heating rates tested. Source: [159]. x
- Fig. 2: DTG Deconvolution for Beech. Source: [159]. xi
- Fig. 3: DTG Deconvolution for WS-P. Source: [159]. xii
- Fig. 4: DTG Deconvolution for WS-H. Source: [159]. xiii
- Fig. 5: Model-fitting graphs for Beech, model first-order. Source: [159]. xviii
- Fig. 6: Model-fitting graphs for Beech, model third order to lignin. Source: [159]. xix
- Fig. 7: Model-fitting graphs for Beech, model free-order. Source: [159]. xx
- Fig. 8: Model-fitting graphs for Wheat straw powder (WS-P), model first-order. Part 1 of 2. Source: [159]. ... xxii
- Fig. 9: Model-fitting graphs for Wheat straw powder (WS-P), model first-order. Part 2 of 2. Source: [159]. .. xxiii
- Fig. 10: Model-fitting graphs for Wheat straw powder (WS-P), model third-order to lignin. Part 1 of 2. Source: [159]. xxiv
- Fig. 11: Model-fitting graphs for Wheat straw powder (WS-P), model third-order to lignin. Part 2 of 2. Source: [159]. xxv
- Fig. 12: Model-fitting graphs for Wheat straw powder (WS-P), model free-order. Part 1 of 2. Source: [159]. ... xxv
- Fig. 13: Model-fitting graphs for Wheat straw powder (WS-P), model free-order. Part 2 of 2. Source: [159]. . xxvi
- Fig. 14: Model-fitting graphs for Wheat straw hull (WS-W), model first-order. Source: [159]. xxvii
- Fig. 15: Model-fitting graphs for Wheat straw hull (WS-W), model third-order to lignin. Source: [159]. . xxviii
- Fig. 16: Model-fitting graphs for Wheat straw hull (WS-W), model free-order. Source: [159]. xxix
- Fig. 17: Arrhenius plots for the isoconversional methods for Beech. Source: [159]. xxxiv
- Fig. 18: Arrhenius plots for the isoconversional methods for WS-P. Source: [159]. xxxv
- Fig. 19: Arrhenius plots for the isoconversional methods for WS-H. Source: [159]. xxxvi
- Fig. 20: Comparison of the degradation profiles of the feedstocks (10 K/min) with the decomposition patterns by Ranzi et al. (2008) [80]: mass loss (left) and derivative mass loss (right). Source: [159]. xlvi
- Fig. 21: Comparison of the degradation profiles of the feedstocks (10 K/min) with the holocellulosic decomposition patterns by Ranzi et al. (2008) [80], and the lignin degradation patterns by Faravelli et al. [79], modified by Peters et al. [82]: mass loss (left) and derivative mass loss (right). Source: [159]. xlvi
- Fig. 22: Comparison of the degradation profiles of the feedstocks (10 K/min) with the decomposition patterns by Corbetta et al. [114]: mass loss (left) and derivative mass loss (right). Source: [159]. xlvi
- Fig. 23: Comparison of the degradation profiles of the feedstocks (10 K/min) with the decomposition patterns by Anca-Couce and Scharler [119]: mass loss (left) and derivative mass loss (right). Source: [159]. xlviii
- Fig. 24: Comparison of the degradation profiles of the feedstocks (10 K/min) with the decomposition patterns by Ranzi et al. (2017a) [117]: mass loss (left) and derivative mass loss (right). Hemicellulose assumed to be xylan-rich based on the conclusions of Peng and Wu [74]. Source: [159]. xlix
- Fig. 25: Comparison of the degradation profiles of the feedstocks (10 K/min) with the decomposition patterns by Ranzi et al. (2017b) [65]: mass loss (left) and derivative mass loss (right). Hemicellulose assumed to be xylan-rich based on the conclusions of Peng and Wu [74]. Source: [159]. l
- Fig. 26: Comparison of the degradation profiles of the feedstocks (10 K/min) with the decomposition patterns by Debiagi et al. [265]: mass loss (left) and derivative mass loss (right). Hemicellulose assumed to be xylan-rich based on the conclusions of Peng and Wu [74]. Source: [159]. . li
- Fig. 27: Comparison of the degradation profiles of the feedstocks (10 K/min) with the decomposition patterns by Debiagi et al. [265] : mass loss (left) and derivative mass loss (right). Hemicellulose assumed to be cereal-type. Source: [159]. lii
- Fig. 28: Visual comparison of the p-T curves for several bio-oil components focused on the range of 0-150 °C. Dotted curves represent values outside the range of validity of the parameters. Components: ACETALDY, ACETICAC, ACETOL, ACETONE. lxix
- Fig. 29: Visual comparison of the p-T curves for several bio-oil components focused on the range of 0-150 °C. Dotted curves represent values outside the range of validity of the parameters. Components: ACROLEIN, ANISOLE, CRESOL, EG. lxx
- Fig. 30: Visual comparison of the p-T curves for several bio-oil components focused on the range of 0-150 °C. Dotted curves represent values outside the range of validity of the parameters. Components: EGACET, ETHANOL, FORMALDY, FORMICAC. lxxi
- Fig. 31: Visual comparison of the p-T curves for several bio-oil components focused on the range of 0-150 °C. Dotted curves represent values outside the range of validity of the parameters. Components: FURFURAL, GLYOXAL, GUAIACOL, HAA. lxxii
- Fig. 32: Visual comparison of the p-T curves for several bio-oil components focused on the range of 0-150 °C. Dotted curves represent values outside the range of validity of the parameters. Components: HEXADEC, HMF, KETENE, LEVOGLUC. lxxiii
- Fig. 33: Visual comparison of the p-T curves for several bio-oil components focused on the range of 0-150 °C. Dotted curves represent values outside the range of validity of the parameters. Components: METHANOL, PHENOL, SYRINGOL. lxxiv

Appendix: List of Tables

Tab. 1: Flow rates of relevant streams included in the furnace/liftpipe system.	vii
Tab. 2: Operating conditions of different parts of the furnace/liftpipe system.	vii
Tab. 3: Distribution of coke in the system. All values as a fraction of the formed coke.....	vii
Tab. 4: Operating conditions of the reactor and cyclone	viii
Tab. 5: Flow rates of relevant streams included in the condensation loops system.	viii
Tab. 6: Operating conditions of the condensation loops system.....	viii
Tab. 7: TGA instrument characteristics (Netzsch STA-409). Source: #3, Table 3 at [167].....	ix
Tab. 8: Fundamentals of the thermogravimetric data (TGA/DTG) for the Beech wood powder samples. Source: [159].	ix
Tab. 9: Fundamentals of the thermogravimetric data (TGA/DTG) for the wheat straw powder (WS-P) samples. Source: [159].	ix
Tab. 10: Fundamentals of the thermogravimetric data (TGA/DTG) for the wheat straw hull (WS-H) samples. Source: [159].	x
Tab. 11: Results from the second-derivative study. CI 95%. Source: [69].	xi
Tab. 12: Lignocellulosic composition of the different materials, obtained using Gaussian deconvolution procedures (wt.%, dab., extractives-free). Values disregarded to estimate the total average are in italic. Source: [159].	xiv
Tab. 13: Comparison of replicas (WS-P, 10 K/min), obtained using Gaussian deconvolution procedures (wt.%, dab., extractives-free). Source: [159].....	xiv
Tab. 14: Results of the model fitting for Beech, obtained by simultaneous fitting to all thermograms. Source: [159].	xv
Tab. 15: Results of the model fitting for WS-P, averaged from all 5 heating rates, obtained by simultaneous fitting to all thermograms. Source: [159].	xvi
Tab. 16: Results of the model fitting for WS-H, obtained by simultaneous fitting to all thermograms. Source: [159].	xvii
Tab. 17: Kinetic parameters obtained for Beech using the isoconversional methods. Source: [159].	xxxi
Tab. 18: Kinetic parameters obtained for WS-P using the isoconversional methods. Source: [159].	xxxii
Tab. 19: Kinetic parameters obtained for WS-H using the isoconversional methods. Source: [159].	xxxiii
Tab. 20: Reaction network from Ranzi et al. [80]. Source: [159].	xxxvii
Tab. 21: Reaction network from Ranzi et al. [80] and Faravelli et al. [79], and modified by Peters et al. [82]. Source: [159].	xxxviii
Tab. 22: Reaction network from Corbetta et al. [114]. Hemicellulose assumed to be xylan-rich based on the conclusions of Peng and Wu [74]. Source: [159].	xxxix
Tab. 23: Reaction network from Anca-Couce and Scharler [119], assuming low charring conditions as reported by Pecha et al. [56]. Source: [159].	xl
Tab. 24: Reaction network from Anca-Couce and Scharler [119], assuming high charring conditions as reported by Pecha et al. [56]. Source: [159].	xli
Tab. 25: Reaction network from Ranzi et al. [117]. Hemicellulose assumed to be xylan-rich based on the conclusions of Peng and Wu [74]. Source: [159].	xlii
Tab. 26: Reaction network from Ranzi et al. [65]. Hemicellulose assumed to be xylan-rich based on the conclusions of Peng and Wu [74]. Source: [159].	xliiii
Tab. 27: Reaction network from Debiagi et al. [265]. In reaction 1 of hemicellulose, first set of values assumes xylan-rich hemicellulose, based on the conclusions of Peng and Wu [74], while second set assumes cereal structure. Source: [159].	xliv
Tab. 29: List of solid components included in the simulation.	liiii
Tab. 30: List of gaseous components included in the simulation.	liiii
Tab. 31: Flash modelling of the separation of ORC/AC/gas surrogates. Test using 3,4,4'-biphenyltriol as heavy fraction in ORC.....	liv
Tab. 32: Flash modelling of the separation of ORC/AC/gas surrogates. Test using HMWL as heavy fraction in ORC.	lv
Tab. 33: Flash modelling of the separation of ORC/AC/gas surrogates. Test using 3,4,4'-biphenyltriol as heavy fraction in ORC.....	lvi
Tab. 34: Comparison of normal boiling point estimation methods for the components in the simulation. Values in °C.....	lvii
Tab. 35: Comparison of critical temperature estimation methods for the components in the simulation. Values in °C.....	lviii
Tab. 36: Comparison of critical pressure estimation methods for the components in the simulation. Values in bar.....	lix
Tab. 37: Comparison of critical volume estimation methods for the components in the simulation. Values in $\text{cm}^3 \cdot \text{mol}^{-1}$	lx
Tab. 38: Comparison of acentric volume and saturated molar volume estimation methods for the components in the simulation.	lxi
Tab. 39: Comparison of heat capacity (ideal gas, liquid-phase) estimation methods for the components in the simulation. Values in $\text{J} \cdot \text{mol}^{-1} \cdot \text{K}^{-1}$. Temperature of 25 °C.....	lxii
Tab. 40: Comparison of estimation methods for the standard enthalpy of ideal gas formation for the components in the simulation. Values in $\text{kJ} \cdot \text{mol}^{-1}$	lxiii
Tab. 41: Comparison of estimation methods for the standard Gibbs energy of ideal gas formation for the components in the simulation. Values in $\text{kJ} \cdot \text{mol}^{-1}$	lxiv
Tab. 42: Comparison of estimation methods for the enthalpy of vaporization at boiling point for the components in the simulation. Values in $\text{kJ} \cdot \text{mol}^{-1}$	lxv

Tab. 43: Comparison of estimation methods for the viscosity at 90 °C for the components in the simulation.	lxvi
Tab. 44: Vapor pressure estimations using different methods at 25 °C. Values in kPa.	lxvii
Tab. 45: Vapor pressure estimations using different methods at 90 °C. Values in kPa.	lxviii
Tab. 46: Group contribution list for the Cordes et al. [327] method for the normal boiling point, as well as the Nannoolal et al. methods for the critical properties [332], vapor pressure [341], and saturated liquid viscosity [352]. Numbering follows according to the source. Part 1 of 2.	lxv
Tab. 47: Group contribution list for the Růžička et al. [336–338] method for the liquid heat capacity. Part 1 of 2.	lxvii
Tab. 48: Group contribution list for the Růžička et al. [336–338] method for the liquid heat capacity. Part 2 of 2.	lxvii
Tab. 49: Group contribution list for the Ambrose [330] group contribution method.	lxviii
Tab. 50: Group contribution list for the Benson [335] group contribution method. Part 1 of 2.	lxix
Tab. 51: Group contribution list for the Benson [335] group contribution method. Part 2 of 2.	lxxx
Tab. 52: Group contribution list for the Ducros [344–346] group contribution method. Part 1 of 2.	lxxxi
Tab. 53: Group contribution list for the Ducros [344–346] group contribution method. Part 2 of 2.	lxxxii
Tab. 54: Group contribution list for the Fedors [329] group contribution method.	lxxxiii
Tab. 55: Group contribution list for the Gani [326] group contribution method.	lxxxiv
Tab. 56: Group contribution list for the Joback [325] group contribution method.	lxxxv
Tab. 57: Group contribution list for the Le Bas [348] group contribution method.	lxxxvi
Tab. 58: Group contribution list for the Li-Ma [340] group contribution method.	lxxxvii
Tab. 59: Group contribution list for the Lydersen [328] group contribution method.	lxxxviii
Tab. 60: Group contribution list for the UNIFAC [225,284,285] group contribution method.	lxxxix
Tab. 61: Parameters for the estimation of the ideal gas heat capacity (C_p^*, i_g) using the Benson and the Joback methods. Values in $J \cdot mol^{-1} \cdot K^{-1}$, temperature in K. Estimated using Aspen Plus™ V12.	xc
Tab. 62: Parameters for the estimation of the ideal gas heat capacity (C_p^*, i_g) using sourced data from the TDE. Estimated using Aspen Plus™ V12. Validity region: 200-1000 K.	xcii
Tab. 63: Parameters for the estimation of the liquid heat capacity (C_p, i^*, l) using sourced data from the TDE. Estimated using Aspen Plus™ V12.	xcii
Tab. 64: Parameters for the estimation of the liquid heat capacity (C_p, i^*, l) using the Růžička method. Temperature in K. Estimated using Aspen Plus™ V12.	xciii
Tab. 65: Parameters for the estimation of the vapor pressure (p_i^*, l) calculated from experimental data and Nannoolal-Rarey estimates. Values in Pa, temperature in K. Estimated using Aspen Plus™ V12, and using the method described in [341].	xciii
Tab. 66: Parameters for the estimation of the vapor pressure (p_i^*, l) using the Riedel and Li-Ma methods. Values in Pa, temperature in K. Estimated using Aspen Plus™ V12.	xciv
Tab. 67: Parameters for the estimation of the vapor pressure (p_i^*, l) using the Mani method. Values in Pa, temperature in K. Estimated using Aspen Plus™ V12.	xcv
Tab. 68: Parameters for the estimation of the vapor pressure (p_i^*, l) using sourced data from the TDE. Estimated using Aspen Plus™ V12.	xcv
Tab. 69: Parameters for the estimation of the standard enthalpy of vaporization ($\Delta vap H_i^*$) using the presented methods. Values in $J \cdot mol^{-1} \cdot K^{-1}$, temperature in K. Estimated using Aspen Plus™ V12.	xcvi
Tab. 70: Parameters for the estimation of the standard enthalpy of vaporization ($\Delta vap H_i^*$) using sourced data from the TDE. Temperature in K. Estimated using Aspen Plus™ V12.	xcvii
Tab. 71: Parameters for the estimation of the gas-phase viscosity (η_i^*, v) using sourced data from the TDE. Temperature in K. Estimated using Aspen Plus™ V12.	xcviii
Tab. 72: Parameters for the estimation of the liquid-phase viscosity (η_i^*, l) using sourced data from the TDE. Values in cP, temperature in °C. Estimated using Aspen Plus™ V12.	xcviii
Tab. 73: Parameters for the estimation of the liquid viscosity (η_i^*, l) using the shown methods. Values in $N \cdot s \cdot m^{-2}$, temperature in K. Estimated using Aspen Plus™ V12.	xcix

Appendix A: *bioliq*[®] data

Data for 2016 was considered unviable, was not considered for the calculations, and is not shown.

Tab. 1: Flow rates of relevant streams included in the furnace/liftpipe system.

	Feedstock Feed (kg/h)	Natural Gas – Furnace (Nm ³ /h)	Natural Gas – Steam Production (Nm ³ /h)	Primary Air (Nm ³ /h)	Secondary Air (Nm ³ /h)	Vapor injection furnace (kg/h)	Vapor injection liftpipe (kg/h)	Water injection furnace (kg/h)
2015	365	15.8	23.4	170	105.0	30	34.8	34.5
2017	349	16.8	18.2	171	85.8	30	30.4	53.0
2018	350	14.9	18.6	158	95.9	30	27.8	60.2
Average	355 ± 8	15.8 ± 0.9	20.1 ± 2.7	166 ± 6	95.6 ± 8.9	30 ± 0	31.0 ± 3.3	49.2 ± 12.2

Tab. 2: Operating conditions of different parts of the furnace/liftpipe system.

	Air (°C)	Furnace (°C)	Furnace Flue (°C)	Midpoint liftpipe (°C)	HC Silo exhaust (°C)	HC Silo solid (°C)	HC liftpipe recycle (°C)	ΔP Liftpipe (mbar)
2015	224	951	895	568	586	559	479	33.0
2017	295	925	854	555	568	549	476	36.4
2018	251	820	753	548	578	553	548	31.2
Average	257 ± 33	898 ± 64	834 ± 68	557 ± 9	577 ± 8	554 ± 5	501 ± 38	33.5 ± 2.5

Tab. 3: Distribution of coke in the system. All values as a fraction of the formed coke.

	Coke furnace (% coke)	Coke dragged with HC (% coke)	Coke flue filter (% coke)	Coke HTC (% coke)	Main Coke Recovery (% coke)
2015	22.8%	9.1%	5.9%	10.1%	52.1%
2017	12.7%	6.2%	18.0%	11.7%	51.5%
2018	21.8%	4.0%	5.3%	25.1%	43.8%
Average	19.1% ± 5.2%	6.4% ± 2.4%	9.7% ± 6.6%	15.6% ± 7.6%	49.1% ± 4.3%

Tab. 4: Operating conditions of the reactor and cyclone

	Sweeping gas (Nm ³ /h)	Spent HC (°C)	Aerosol (°C)	Pre-Cyclone (°C)	Cyclone (°C)	ΔP reactor (mbar)	ΔP cyclone (mbar)	CW coke (°C) in	CW coke (°C) out
2015	12.0	505	500	470	470	0.0	32.5	24	27
2017	13.7	504	500	437	437	0.1	16.6	28	31
2018	15.0	505	500	444	444	0.1	17.0	27	31
Average	13.6 ± 1.4	505 ± 0	500 ± 0	450 ± 16	450 ± 16	0.1 ± 0.0	22.0 ± 8.4	26 ± 2	30 ± 2

Tab. 5: Flow rates of relevant streams included in the condensation loops system.

	Bypass K1 (kg/h)	Shower K1 (kg/h)	Quench K1 (kg/h)	Bypass K2 (kg/h)	Shower K2 (kg/h)	Water K1 (m ³ /h)	Water K2 (m ³ /h)	Sweeping K1 (Nm ³ /h)
2015	7250	13000	11090	15000	15000	3.0	28.6	12.8
2017	6952	11833	14343	14987	15002	2.7	24.1	7.8
2018	7536	10086	8809	14965	15005	3.6	23.3	9.2
Average	7246 ± 270	11640 ± 1355	11414 ± 2570	14984 ± 16	15002 ± 2	3.1 ± 0.4	25.3 ± 2.7	9.9 ± 2.4

Tab. 6: Operating conditions of the condensation loops system.

	LVE after Quench (°C)	K1 bottoms (°C)	K1 bottoms cooled (°C)	K1 CW in (°C)	K1 CW out (°C)	K2 bottoms (°C)	K2 bottoms cooled (°C)	K2 gas intake (°C)	K2 CW in (°C)	K2 CW out (°C)	K2 gas exhaust (°C)
2015	96	89	84	50	75	29	27	90	24	24	22
2017	96	93	88	52	77	33	32	92	28	28	30
2018	98	93	86	52	76	32	31	82	27	27	30
Average	97 ± 1	91 ± 2	86 ± 2	51 ± 1	76 ± 1	31 ± 2	30 ± 2	88 ± 5	26 ± 2	26 ± 2	27 ± 4

Appendix B

Thermogravimetric data

Tab. 7: TGA instrument characteristics (Netzsch STA-409). Source: #3, Table 3 at [167]

Sensitivity (μg)	Temperature accuracy (K)	Sample mass (mg)	Type	N ₂ purge flow (ml/min)	Sample holder	Calibration
1	1	≈ 200	Vertical	70	Alumina	Melting point

Tab. 8: Fundamentals of the thermogravimetric data (TGA/DTG) for the Beech wood powder samples. Source: [159].

β (K/min)	T peak DTG ($^{\circ}\text{C}$)	T shoulder DTG ($^{\circ}\text{C}$)	Initial mass (mg)	Char yield @ 900 $^{\circ}\text{C}$ (wt. %)	$\Delta m/\Delta T_{\text{max}}$ (K^{-1})	Kissinger Kinetics $R^2 = 0.99$		# Curves
						E_a (kJ/mol)	$\log_{10}(A)$ [s^{-1})]	
1	322.9 ± 0.1	260.6 ± 0.5	99.7 ± 0.0	25.8 ± 1.1	1.12 ± 0.00	218.48 ± 12.63	16.15 ± 2.47	2
5	345.1 ± 0.7	294.3 ± 0.9	99.9 ± 1.3	25.1 ± 0.1	5.12 ± 0.00			2
10	354.9 ± 0.2	299.1 ± 0.6	99.9 ± 0.9	25.1 ± 0.1	10.17 ± 0.05			2
20	368.3	312.2	108.3	24.8	22.85			1

Tab. 9: Fundamentals of the thermogravimetric data (TGA/DTG) for the wheat straw powder (WS-P) samples. Source: [159].

β (K/min)	T peak DTG ($^{\circ}\text{C}$)	Initial mass (mg)	Char yield @ 900 $^{\circ}\text{C}$ (wt. %)	$\Delta m/\Delta T_{\text{max}}$ (K^{-1})	Kissinger Kinetics $R^2 = 0.93$ *		# Curves
					E_a (kJ/mol)	$\log_{10}(A)$ [s^{-1})]	
1	288.6 ± 0.5	211.9 ± 33.3	25.6 ± 0.5	0.75 ± 0.00	220.21 ± 43.57	17.41 ± 5.73	2
5	310.9 ± 1.9	182.7 ± 1.0	26.9 ± 0.0	3.84 ± 0.02			2
10	321.4 ± 1.0	224.2 ± 11.0	26.9 ± 0.0	8.08 ± 0.02			5
20	334.6 ± 0.1	200.1 ± 14.3	26.3 ± 0.0	17.83 ± 0.15			2
50	338.5 ± 0.2	180.2 ± 4.0	25.2 ± 0.0	72.34 ± 0.31			2

* The values from the 1 K/min curve were not considered to improve fit. Removing the 50 K/min curve (while keeping the 1 K/min curve), the values obtained are E_a 121.78 ± 19.27 , $\log_{10}A$: 8.51 ± 3.30 , R^2 : 0.95.

Tab. 10: Fundamentals of the thermogravimetric data (TGA/DTG) for the wheat straw hull (WS-H) samples. Source: [159].

β (K/min)	T peak DTG (°C)	Initial mass (mg)	Char yield @ 900 °C (wt. %)	$\Delta m/\Delta T_{\max}$ (K ⁻¹)	Kissinger Kinetics R ² = 0.85 *		# Curves
					Ea (kJ/mol)	log ₁₀ (A [s ⁻¹])	
1	287.9	195.6	25.7	0.70	222.04 ± 53.83	17.90 ± 6.85	1
5	300.7	216.8	26.7	2.63			1
10	319.5	183.7	26.7	7.62			1
20	326.7 ± 1.4	169.2 ± 5.4	25.8 ± 0.0	15.59 ± 0.14			2
50	321.5 ± 2.5	191.4 ± 4.9	24.7 ± 0.1	67.51 ± 2.36			2

* Removing the 50 K/min curve, the values obtained are Ea 187.81 ± 34.00, log₁₀A: 14.67 ± 4.89, R²: 0.94.

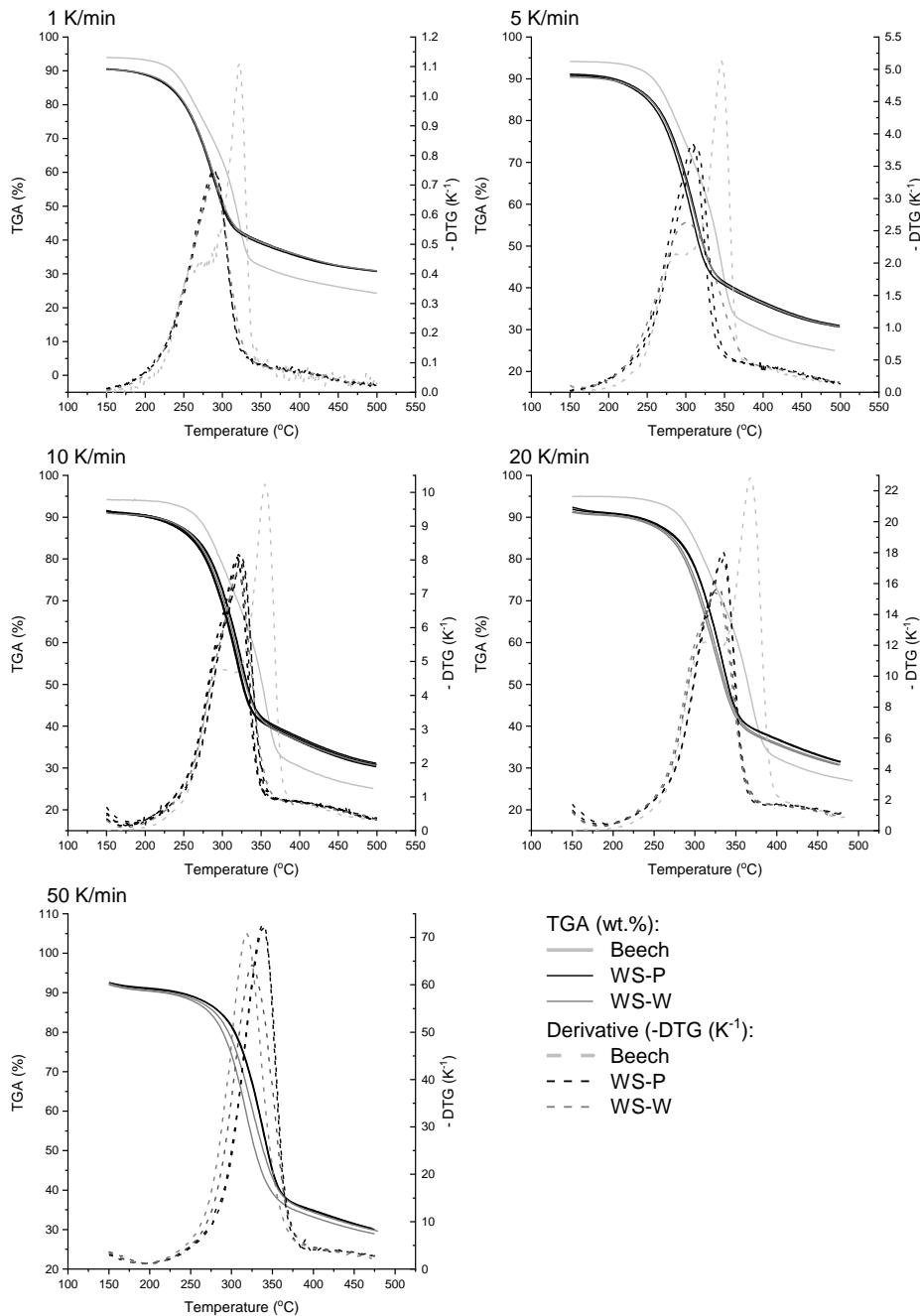


Fig. 1: Comparison of the behavior of the mass loss profiles for the different samples at the different heating rates tested. Source: [159].

Deconvolution

Tab. 11: Results from the second-derivative study. CI 95%. Source: [69].

Heating rate (K min ⁻¹)	Hemicellulose	Cellulose	Lignin
Beech			
1	T = 260.6 ± 0.5; α = 0.17 ± 0.01	T = 322.9 ± 0.1; α = 0.71 ± 0.00	T = 344.8 ± 0.4; α = 0.88 ± 0.00
5	T = 294.3 ± 0.9; α = 0.25 ± 0.00	T = 345.1 ± 0.7; α = 0.69 ± 0.00	T = 370.0 ± 1.1; α = 0.89 ± 0.00
10	T = 299.1 ± 0.6; α = 0.22 ± 0.01	T = 354.9 ± 0.2; α = 0.69 ± 0.00	T = 391.3 ± 0.8; α = 0.91 ± 0.00
20	T = 312.2; α = 0.23	T = 368.3; α = 0.71	T = 400.3; α = 0.92
WS-P			
1	T = 263.3 ± 2.5; α = 0.26 ± 0.03	T = 288.6 ± 0.5; α = 0.53 ± 0.00	T = 330.6 ± 5.4; α = 0.82 ± 0.01
5	T = 275.5 ± 3.4; α = 0.21 ± 0.01	T = 310.9 ± 1.9; α = 0.57 ± 0.00	T = 353.5 ± 2.4; α = 0.84 ± 0.00
10	T = 283.5 ± 1.6; α = 0.21 ± 0.00	T = 321.4 ± 1.0; α = 0.59 ± 0.00	T = 369.6 ± 1.5; α = 0.86 ± 0.00
20	T = 299.6 ± 0.2; α = 0.23 ± 0.00	T = 334.6 ± 0.1; α = 0.62 ± 0.00	T = 379.1 ± 0.2; α = 0.88 ± 0.00
50	T = 316.6 ± 0.8; α = 0.31 ± 0.01	T = 338.5 ± 0.2; α = 0.60 ± 0.00	T = 393.5 ± 4.0; α = 0.92 ± 0.00
WS-H			
1	T = 257.1; α = 0.21	T = 287.9; α = 0.52	T = 349.7; α = 0.86
5	T = 256.1; α = 0.10	T = 300.7; α = 0.42	T = 352.3; α = 0.83
10	T = 279.8; α = 0.17	T = 319.5; α = 0.55	T = 375.9; α = 0.89
20	T = 289.9 ± 0.9; α = 0.20 ± 0.01	T = 326.7 ± 1.4; α = 0.57 ± 0.01	T = 400.4 ± 1.7; α = 0.92 ± 0.00
50	T = 302.7 ± 1.9; α = 0.27 ± 0.00	T = 321.5 ± 2.5; α = 0.51 ± 0.00	T = 420.5 ± 3.3; α = 0.95 ± 0.00

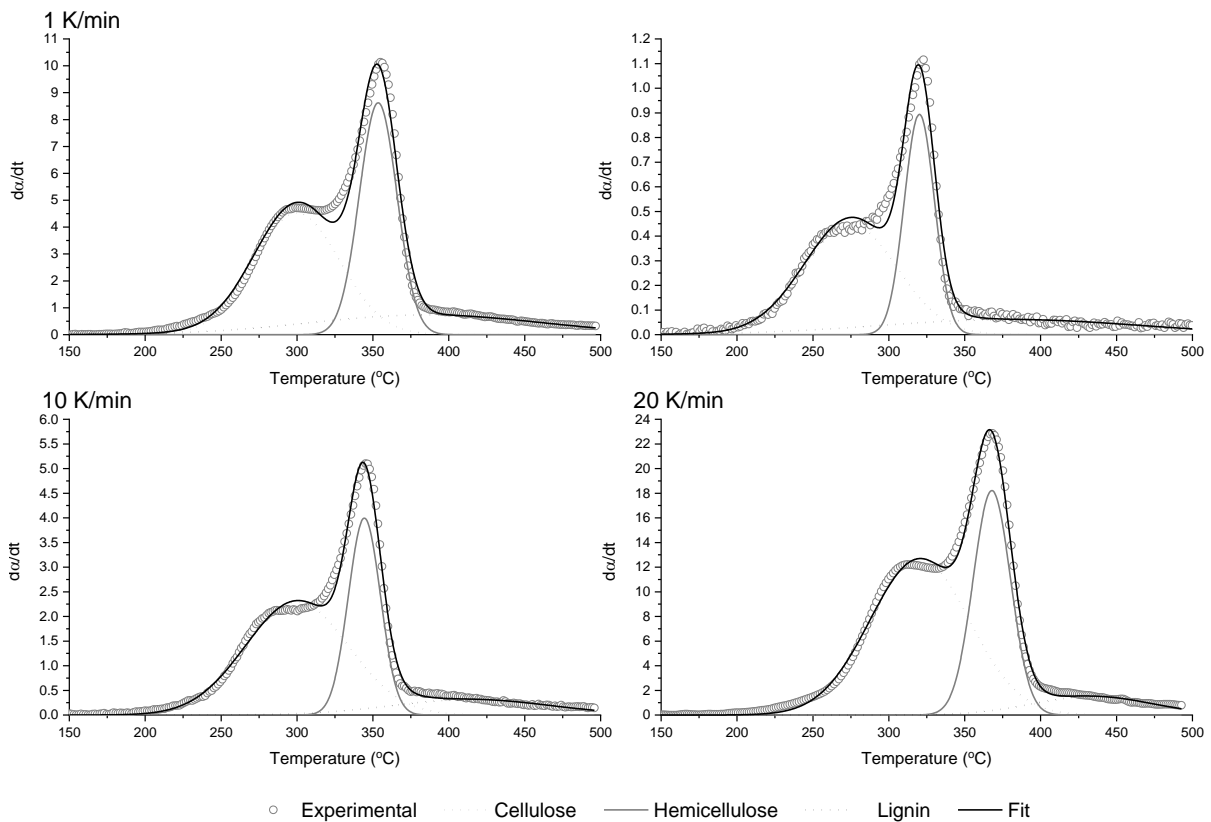


Fig. 2: DTG Deconvolution for Beech. Source: [159].

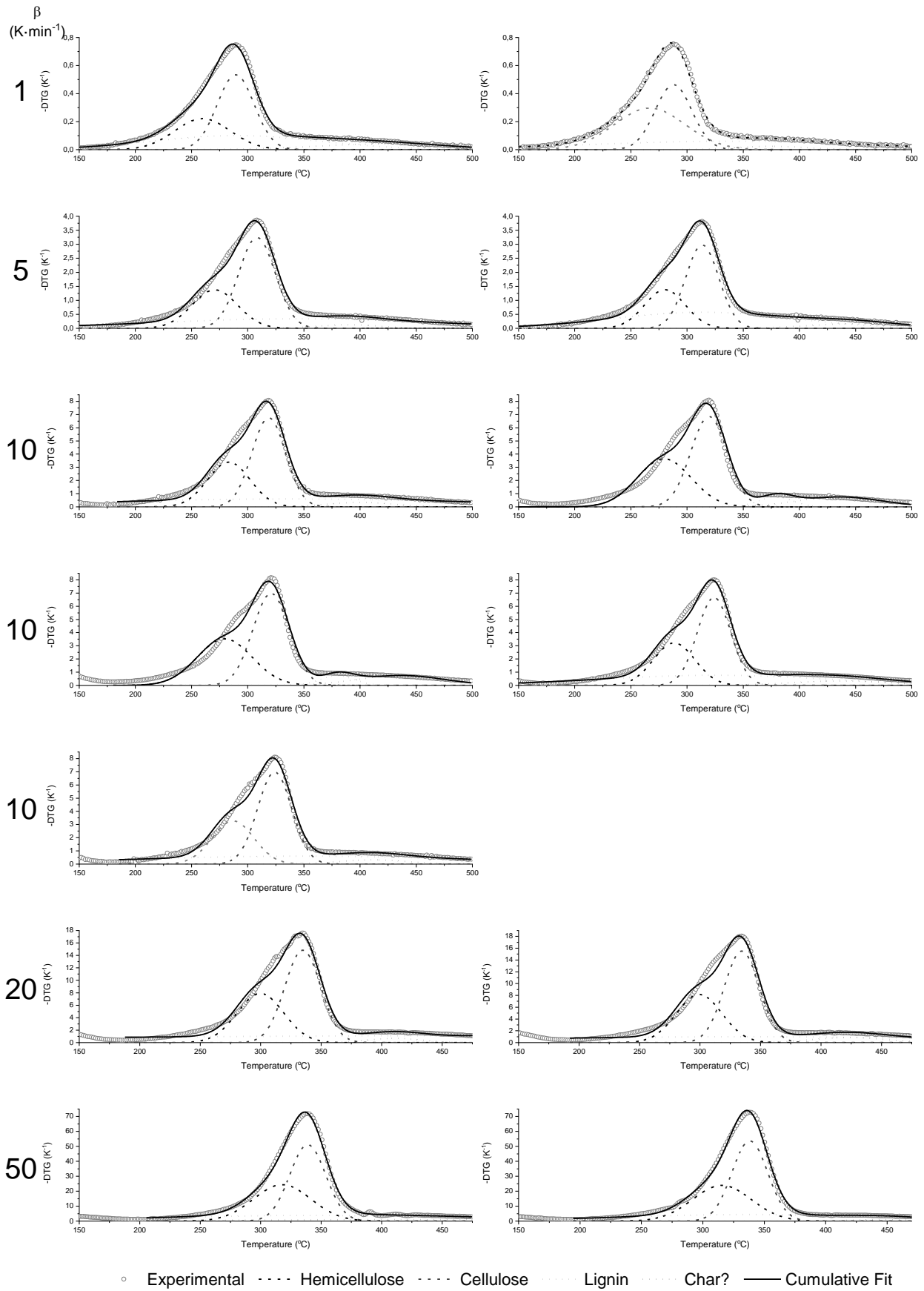


Fig. 3: DTG Deconvolution for WS-P. Source: [159].

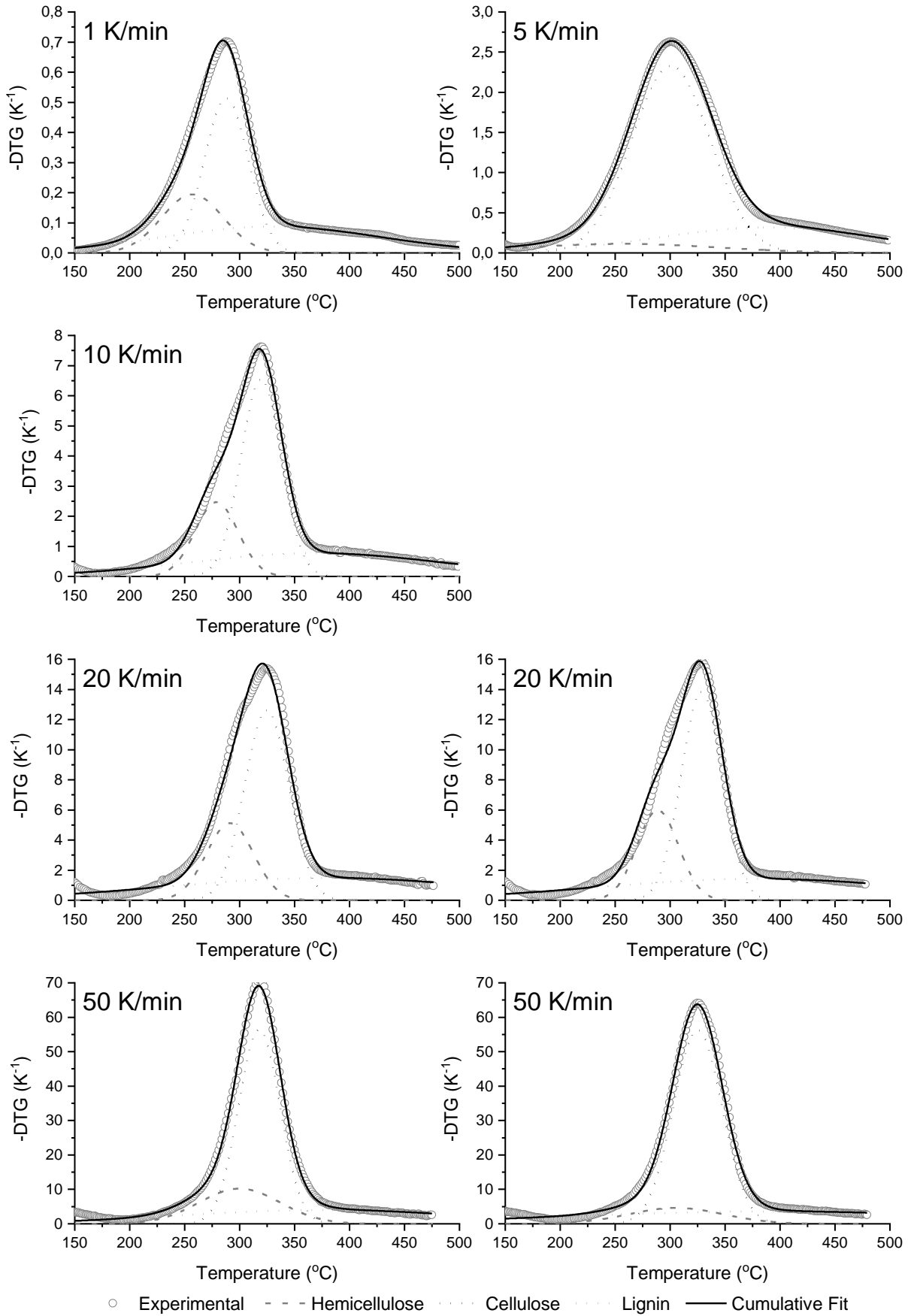


Fig. 4: DTG Deconvolution for WS-H. Source: [159].

Tab. 12: Lignocellulosic composition of the different materials, obtained using Gaussian deconvolution procedures (wt.%, dab., extractives-free). Values disregarded to estimate the total average are in italic. Source: [159].

β (K·min ⁻¹)	Beech				WS-P				WS-H				
	Hemicellulose	Cellulose	Lignin	R ²	Hemicellulose	Cellulose	Lignin	R ²	Hemicellulose	Cellulose	Lignin	R ²	
1	44.7 ± 17.1	34.1 ± 2.2	21.2 ± 19.4	0.92	31.0 ± 0.6	33.0 ± 0.5	36.0 ± 0.5	1.00 ± 0.00	22.4 ± 0.4	42.2 ± 0.4	35.0 ± 0.6	1.00	
5	45.6 ± 2.5	33.3 ± 0.9	21.1 ± 2.5	0.99	23.5 ± 1.1	38.5 ± 1.7	38.0 ± 0.5	0.99 ± 0.00	7.9 ± 0.8	67.0 ± 0.6	25.2 ± 0.8	1.00	
10	47.0 ± 3.9	36.0 ± 0.9	17.0 ± 4.7	0.99	24.1 ± 0.7	37.8 ± 0.6	38.1 ± 2.3	0.98 ± 0.00	18.9 ± 0.4	46.8 ± 0.4	34.3 ± 1.0	1.00	
20	48.9 ± 1.3	36.4 ± 0.8	14.7 ± 1.8	0.99	24.0 ± 0.6	35.6 ± 0.5	40.4 ± 0.4	0.99 ± 0.00	19.3 ± 0.5	44.0 ± 0.5	36.8 ± 1.7	0.99 ± 0.00	
50					29.3 ± 0.5	37.1 ± 0.4	33.6 ± 1.6	1.00 ± 0.00	14.3 ± 0.8	56.6 ± 0.6	29.0 ± 1.5	1.00 ± 0.00	
Average					47.1 ± 2.8	35.3 ± 0.9	17.6 ± 3.3	26.4 ± 1.1	36.4 ± 1.3	37.2 ± 0.4	20.2 ± 0.4	44.3 ± 0.4	35.5 ± 0.7
Reference ^a					34.3 ± 1.9	45.0 ± 5.4	20.7 ± 2.7	32.6 ± 0.7	45.5 ± 1.4	21.9 ± 1.0	32.6 ± 0.7	45.5 ± 1.4	21.9 ± 1.0

a: Based on data obtained in the Phyllis2 database (www.phyllis.nl). Using 14 sources for wheat straw data and 3 for beech wood data.

Tab. 13: Comparison of replicas (WS-P, 10 K/min), obtained using Gaussian deconvolution procedures (wt.%, dab., extractives-free). Source: [159].

Replicas	Hemicellulose	Cellulose	Lignin	R ²
R1	24.4 ± 0.6	37.1 ± 0.5	38.4 ± 1.6	0.99
R2	26.1 ± 0.9	38.1 ± 0.8	35.7 ± 2.8	0.98
R3	23.9 ± 0.8	38.0 ± 0.7	38.1 ± 2.9	0.98
R4	23.7 ± 0.5	37.2 ± 0.5	39.2 ± 1.5	0.99
R5	22.5 ± 0.6	38.7 ± 0.6	38.8 ± 2.0	0.99
Average	24.1 ± 0.7	37.8 ± 0.6	38.1 ± 2.3	

Model-fitting

Tab. 14: Results of the model fitting for Beech, obtained by simultaneous fitting to all thermograms. Source: [159].

	First-order			fit % *
	Cellulose	Hemicellulose	Lignin	3.9% ± 1.9%
$\log_{10}(A [s^{-1}])$	14.68	10.50	1.04	
$E_a [kJ \cdot mol^{-1}]$	199.76	137.24	51.93	
c_i	53.5%	27.6%	18.9%	
T_p	318.70 - 366.20	257.07 - 314.69	320.10 – 500**	
	$n_{Lig}=3$			
	Cellulose	Hemicellulose	Lignin	3.6% ± 1.4%
$\log_{10}(A [s^{-1}])$	15.31	10.73	6.21	
$E_a [kJ \cdot mol^{-1}]$	207.01	139.51	91.32	
c_i	48.4%	25.7%	25.9%	
T_p	320.10 - 364.59	257.07 - 314.69	297.78 - 388.63	
	Free-order			
	Cellulose	Hemicellulose	Lignin	2.7% ± 0.7%
$\log_{10}(A [s^{-1}])$	15.57	14.66	28.55	
$E_a [kJ \cdot mol^{-1}]$	210.39	173.67	313.17	
c_i	49.1%	37.2%	13.7%	
n_i	1.00	2.44	8.22	
T_p	320.10 - 366.20	259.89 - 306.77	374.91 - 406.75	

*: Confidence interval of 95%.

** : Peak of curve outside of the temperature interval considered for this work.

Tab. 15: Results of the model fitting for WS-P, averaged from all 5 heating rates, obtained by simultaneous fitting to all thermograms. Source: [159].

	First-order			fit % *
	Cellulose	Hemicellulose	Lignin	6.4% ± 6.7%
log₁₀ (A [s⁻¹])	14.14	8.68	2.66	
E_a [kJ·mol⁻¹]	184.40	116.58	69.08	
c_i	46.1%	30.7%	23.2%	
T_p	290.70 - 356.71	245.81 - 336.68	320.07 - 500 **	
	n_{Lig}=3			
	Cellulose	Hemicellulose	Lignin	5.9% ± 6.7%
log₁₀ (A [s⁻¹])	14.88	8.83	7.86	
E_a [kJ·mol⁻¹]	192.74	118.89	113.25	
c_i	40.8%	33.3%	25.8%	
T_p	289.29 - 348.11	248.64 - 326.60	294.95 - 438.61	
	Free-order			
	Cellulose	Hemicellulose	Lignin	4.6% ± 3.4%
log₁₀ (A [s⁻¹])	12.34	17.84	11.41	
E_a [kJ·mol⁻¹]	148.46	222.33	149.93	
c_i	45.4%	37.9%	16.6%	
n_i	2.88	1.41	4.06	
T_p	252.84 - 326.73	292.12 - 347.33	365.07 - 461.70	

*: Confidence interval of 95%.

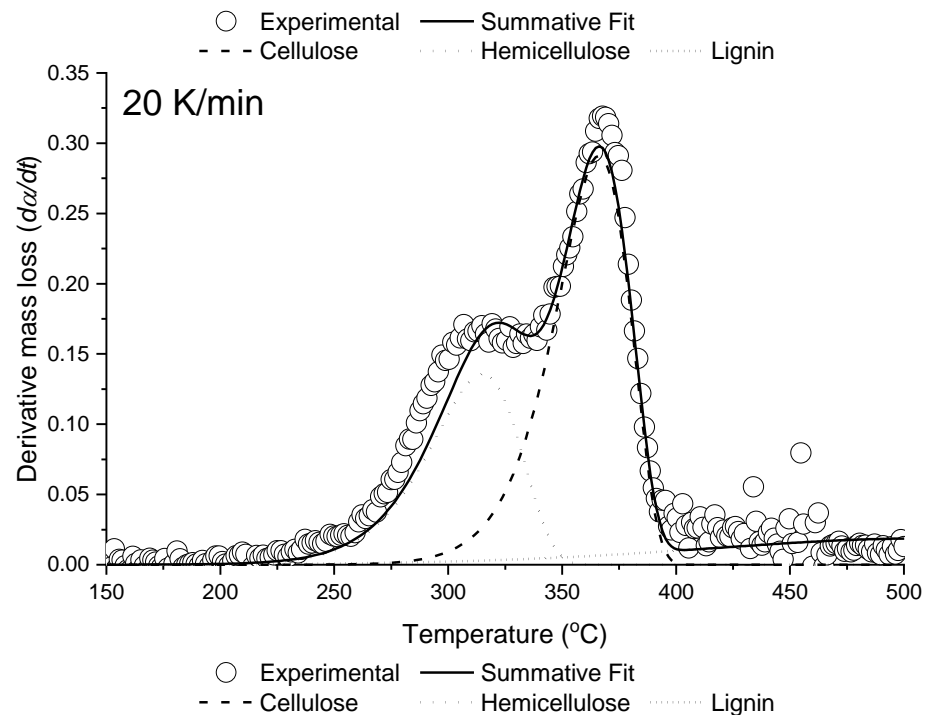
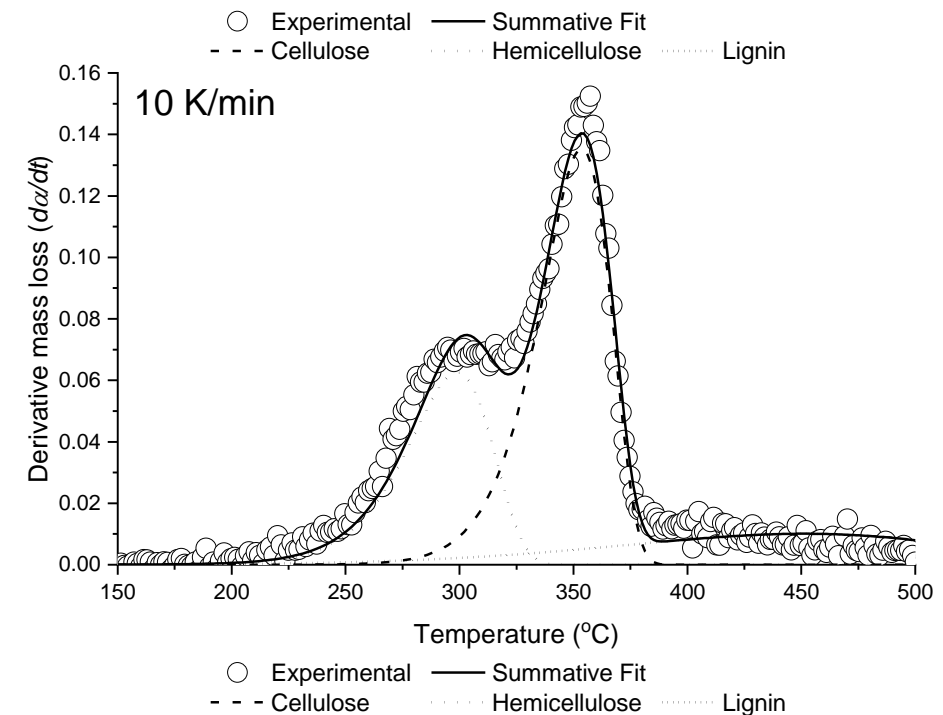
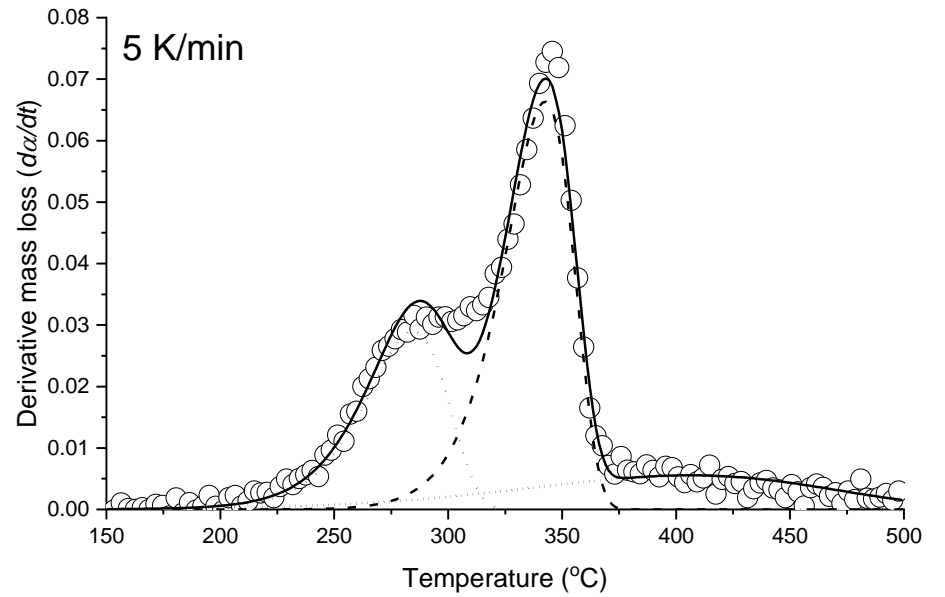
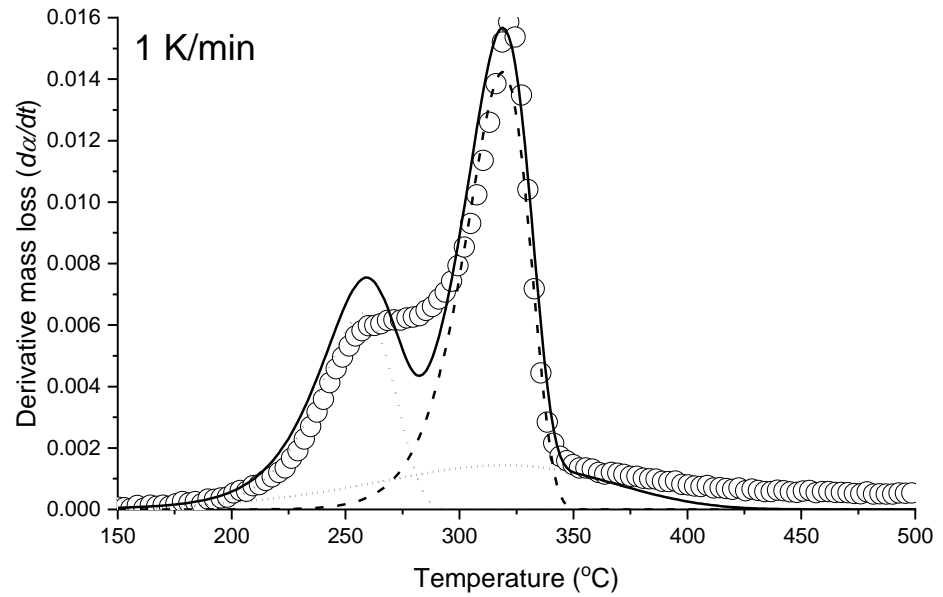
** : Peak of curve outside of the temperature interval considered for this work.

Tab. 16: Results of the model fitting for WS-H, obtained by simultaneous fitting to all thermograms. Source: [159].

	First-order			fit % *
	Cellulose	Hemicellulose	Lignin	10.4% ± 9.1%
log₁₀ (A [s⁻¹])	11.56	15.98	2.30	
E_a [kJ·mol⁻¹]	147.67	206.28	63.84	
c_i	40.8%	33.3%	25.8%	
T_p	257.08 - 332.06	297.77 - 357.24	310.31 - 500**	
	n_{Lig}=3			
	Cellulose	Hemicellulose	Lignin	8.8% ± 8.9%
log₁₀ (A [s⁻¹])	15.81	11.83	8.92	
E_a [kJ·mol⁻¹]	202.83	149.01	123.52	
c_i	38.3%	33.3%	28.3%	
T_p	293.53 - 352.93	252.88 - 325.06	311.71 - 410.45	
	Free-order			
	Cellulose	Hemicellulose	Lignin	6.1% ± 7.2%
log₁₀ (A [s⁻¹])	21.48	16.96	20.19	
E_a [kJ·mol⁻¹]	258.30	192.48	238.81	
c_i	47.8%	36.8%	15.4%	
n_i	2.50	2.84	6.24	
T_p	293.53 - 340.23	254.28 - 309.66	383.20 - 447.19	

*: Confidence interval of 95%.

** : Peak of curve outside of the temperature interval considered for this work.



ii/xx

Fig. 5: Model-fitting graphs for Beech, model first-order. Source: [159].

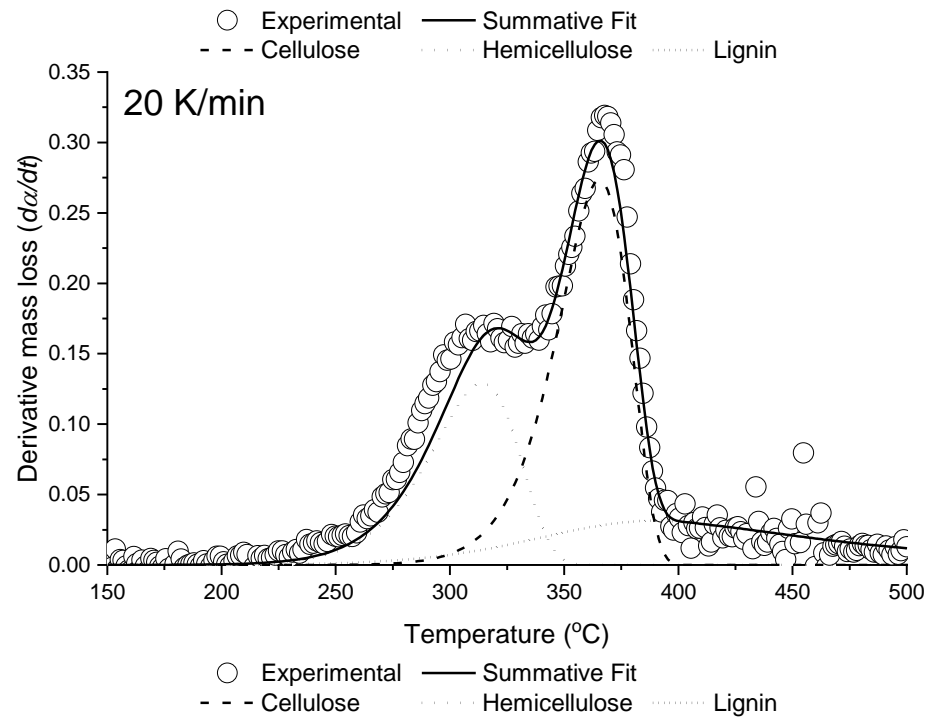
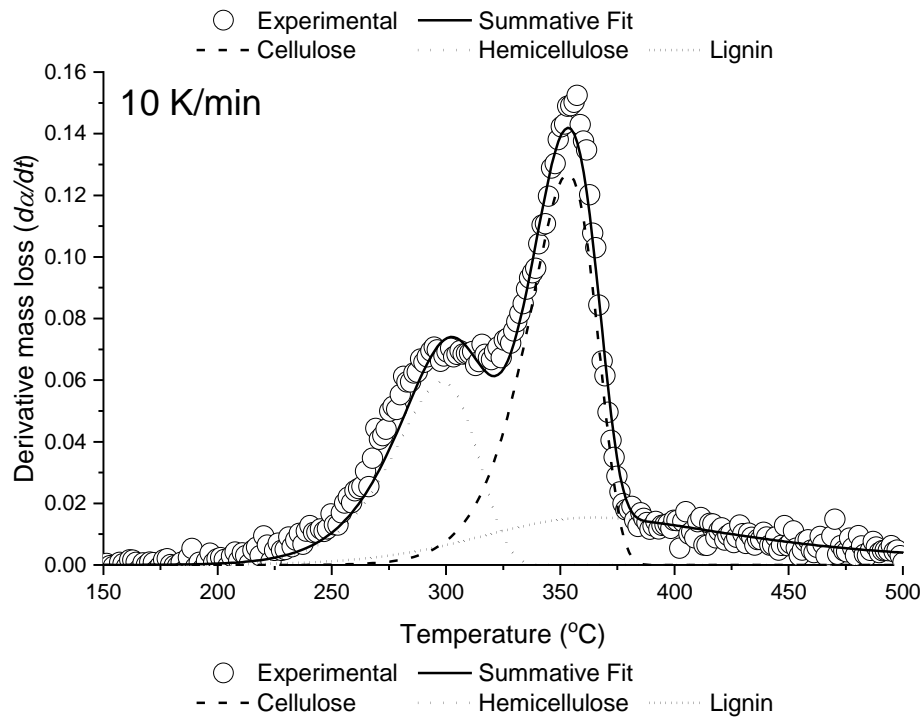
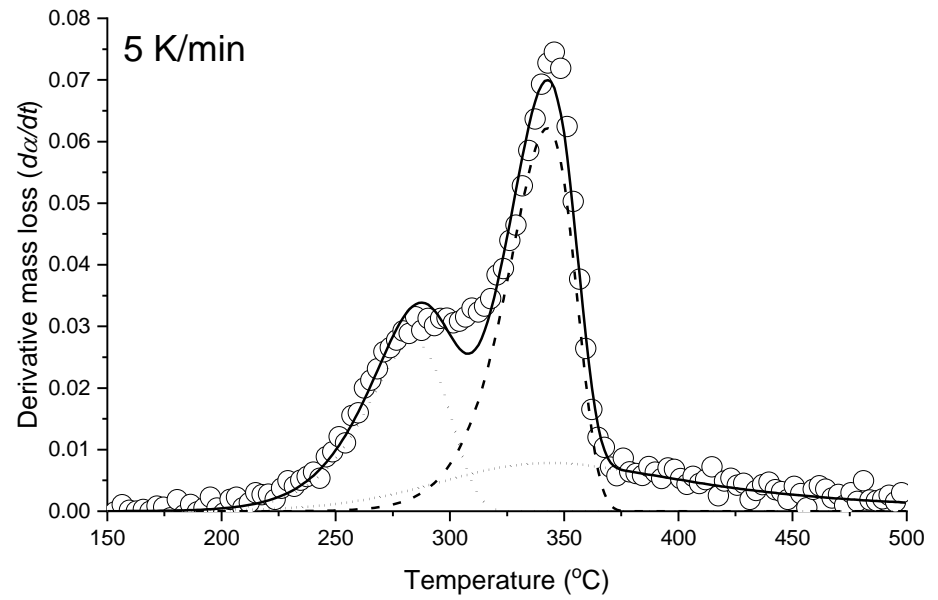
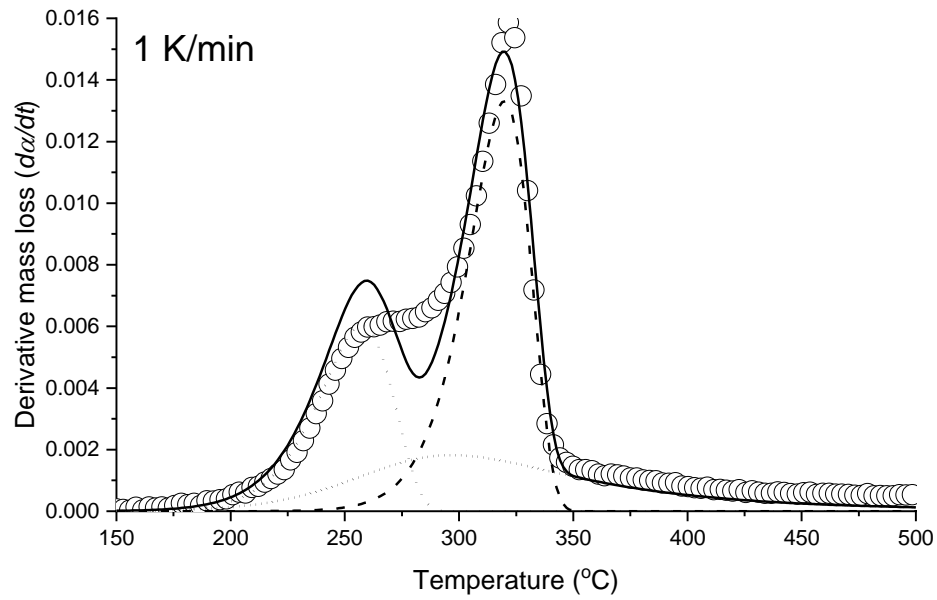


Fig. 6: Model-fitting graphs for Beech, model third order to lignin. Source: [159].

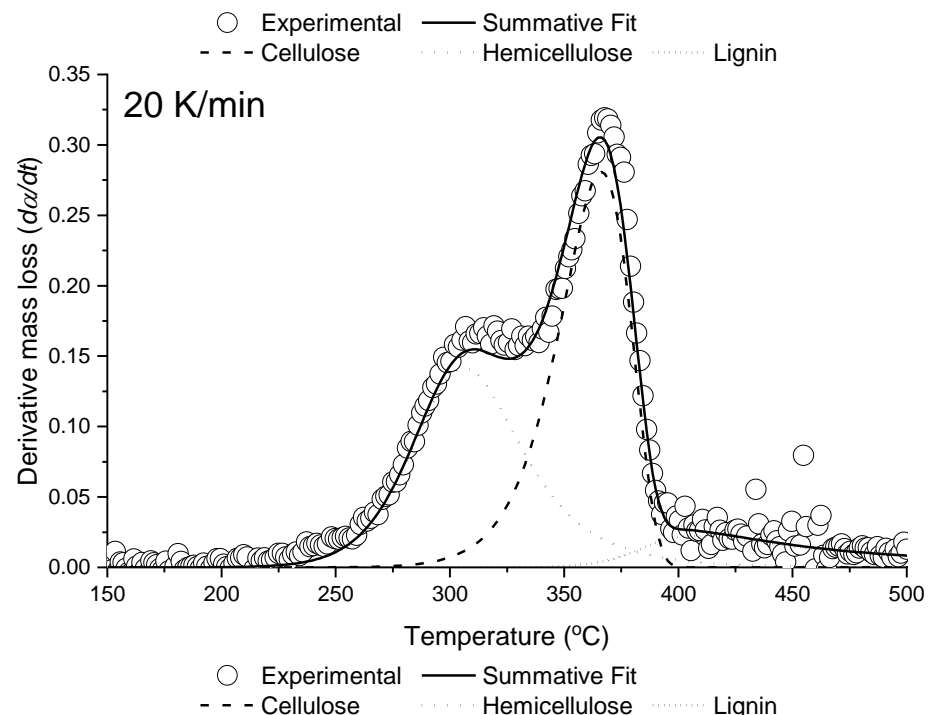
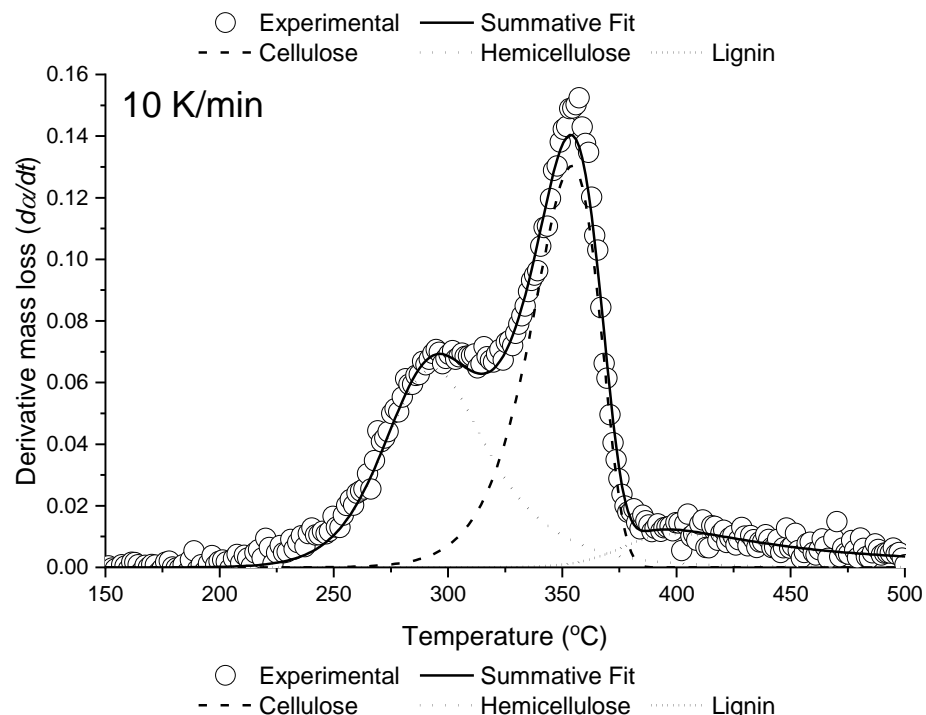
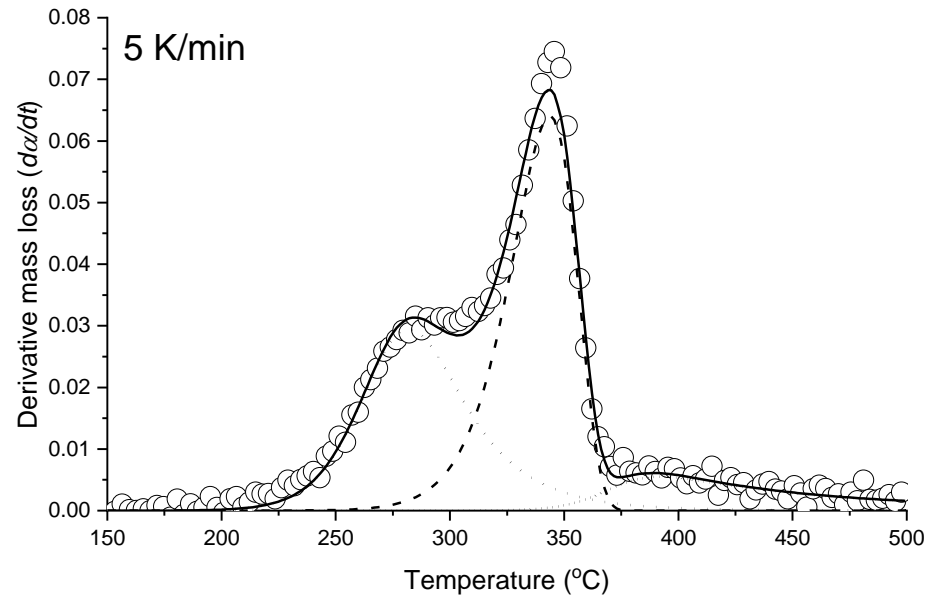
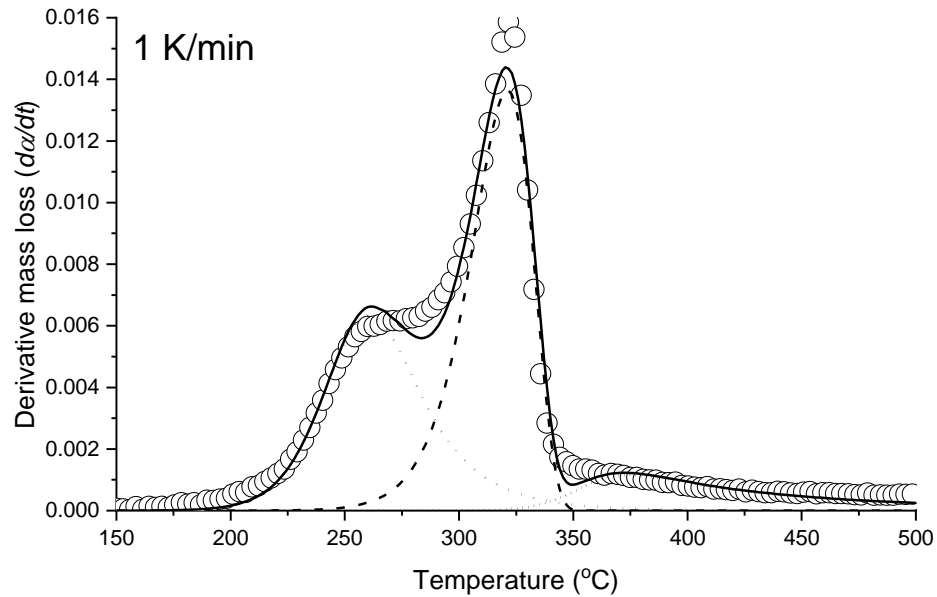


Fig. 7: Model-fitting graphs for Beech, model free-order. Source: [159].

xx

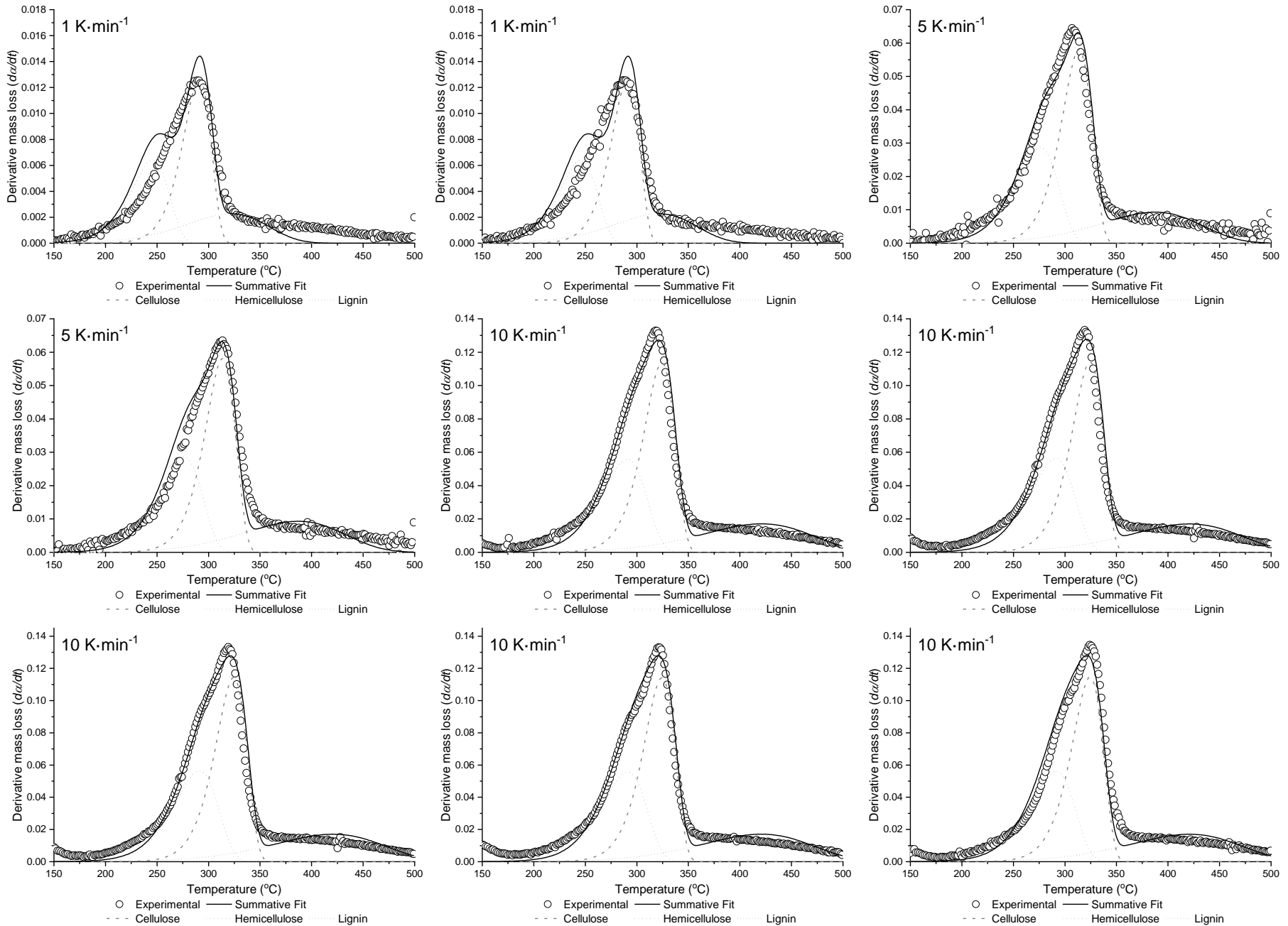


Fig. 8: Model-fitting graphs for Wheat straw powder (WS-P), model first-order. Part 1 of 2. Source: [159].

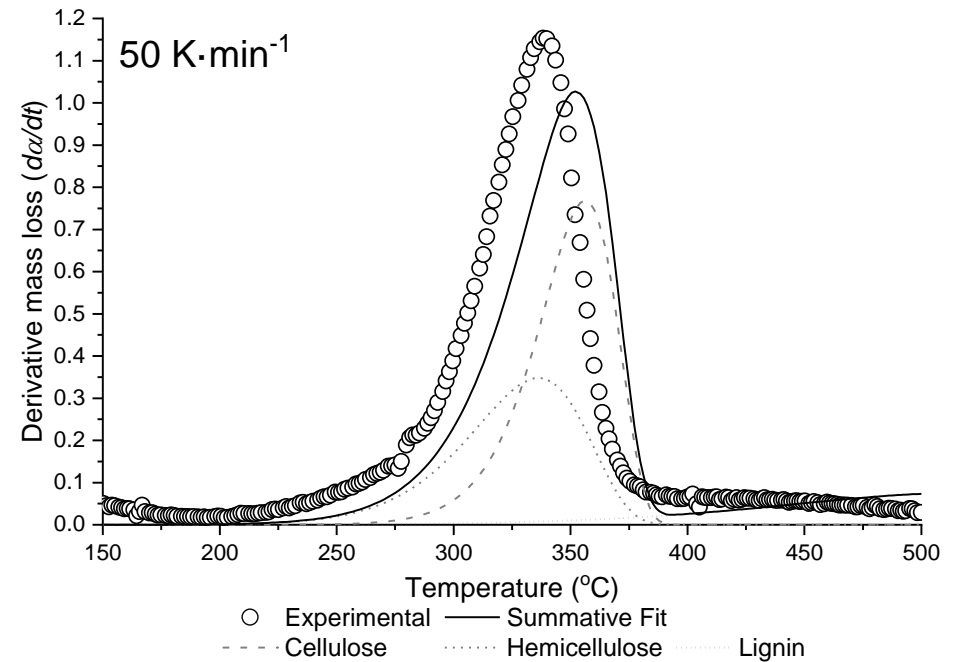
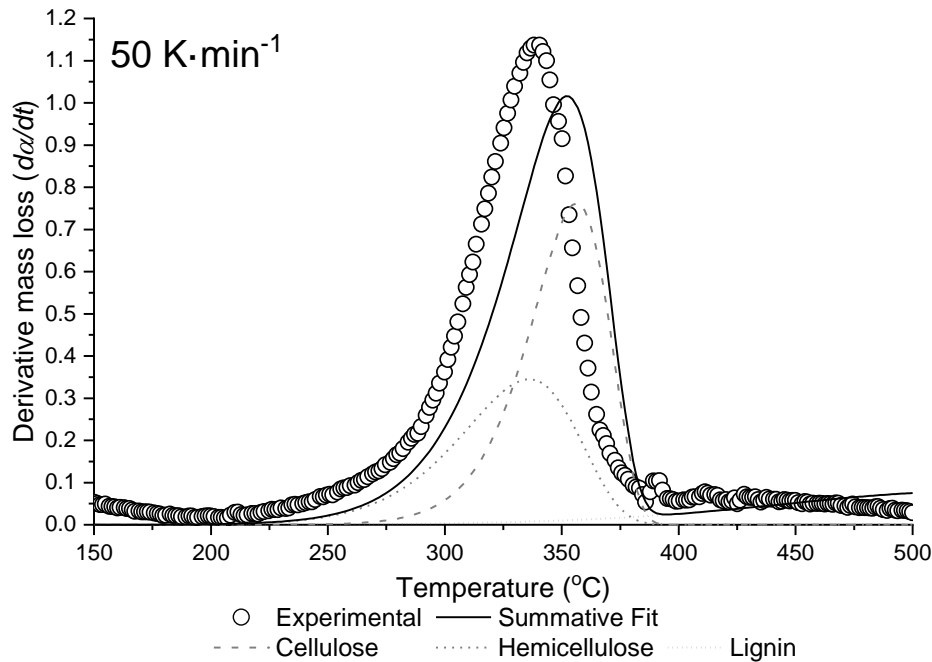
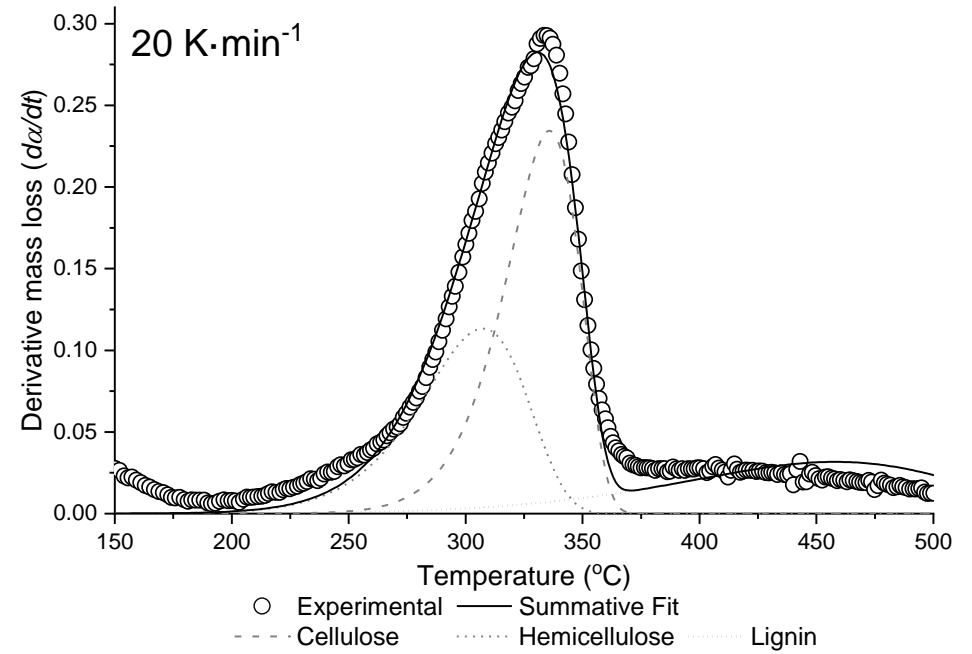
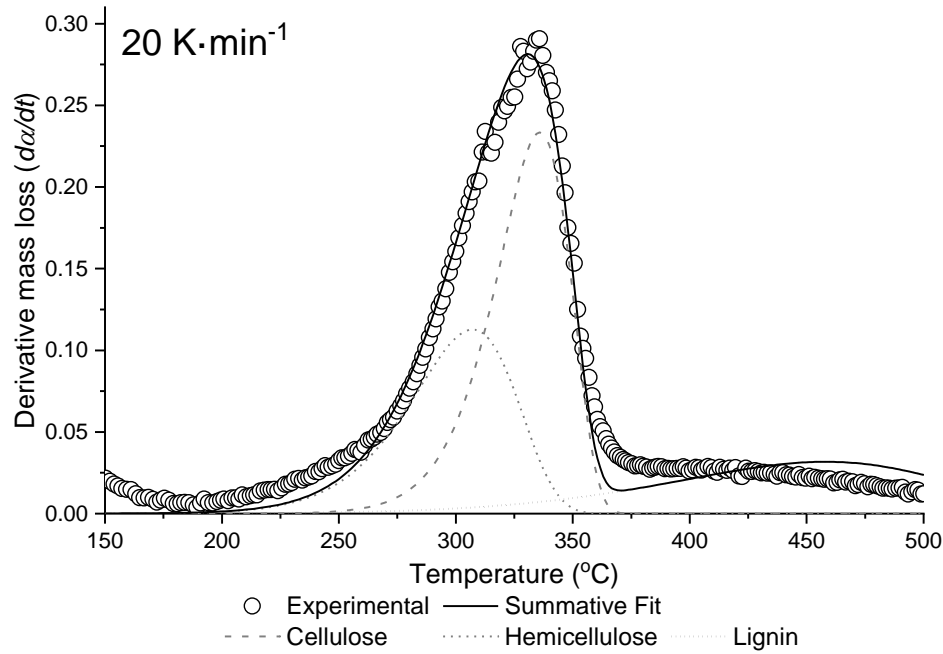


Fig. 9: Model-fitting graphs for Wheat straw powder (WS-P), model first-order. Part 2 of 2. Source: [159].

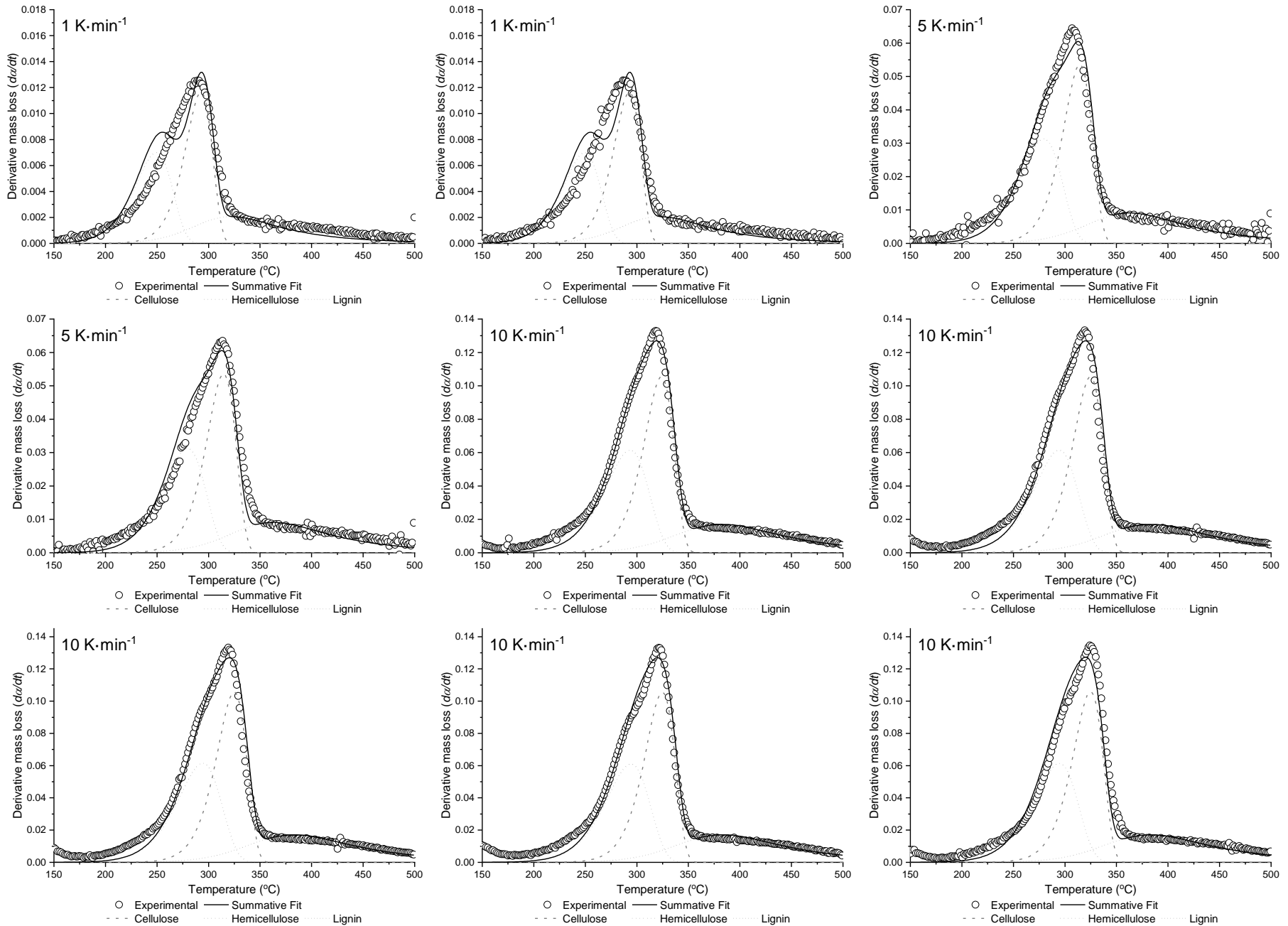


Fig. 10: Model-fitting graphs for Wheat straw powder (WS-P), model third-order to lignin. Part 1 of 2. Source: [159].

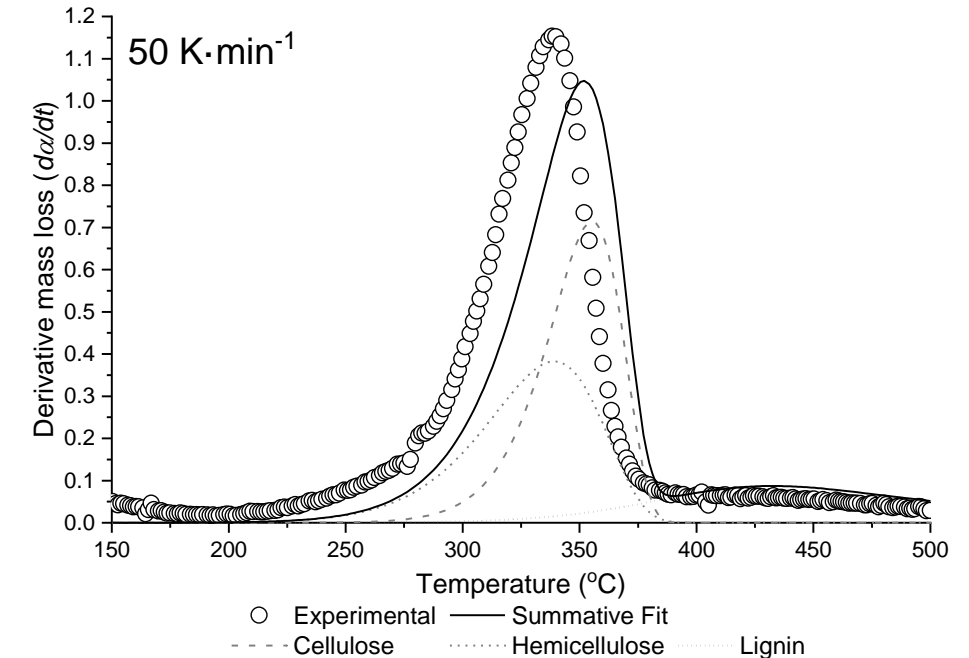
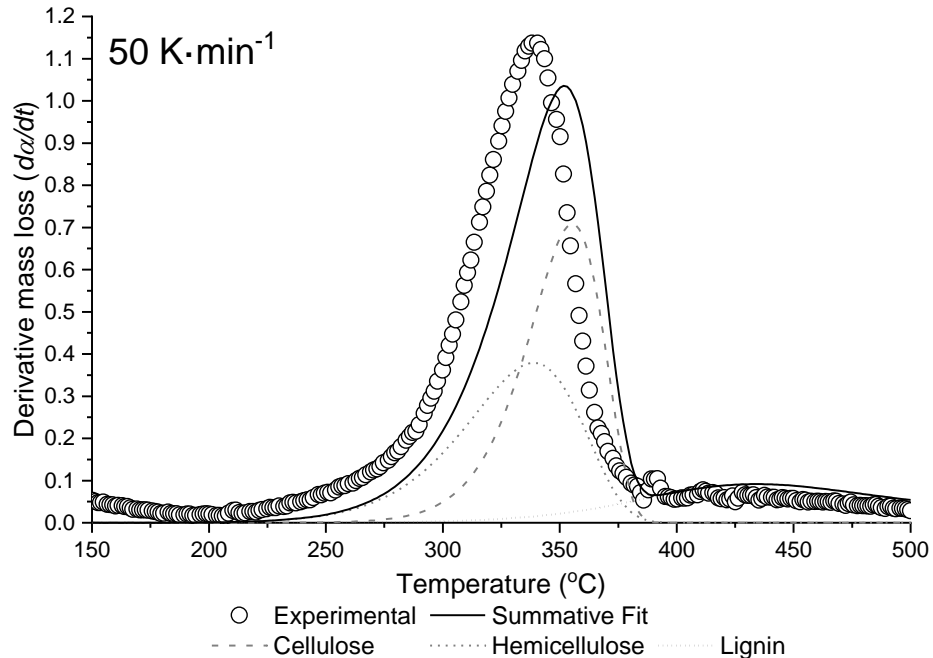
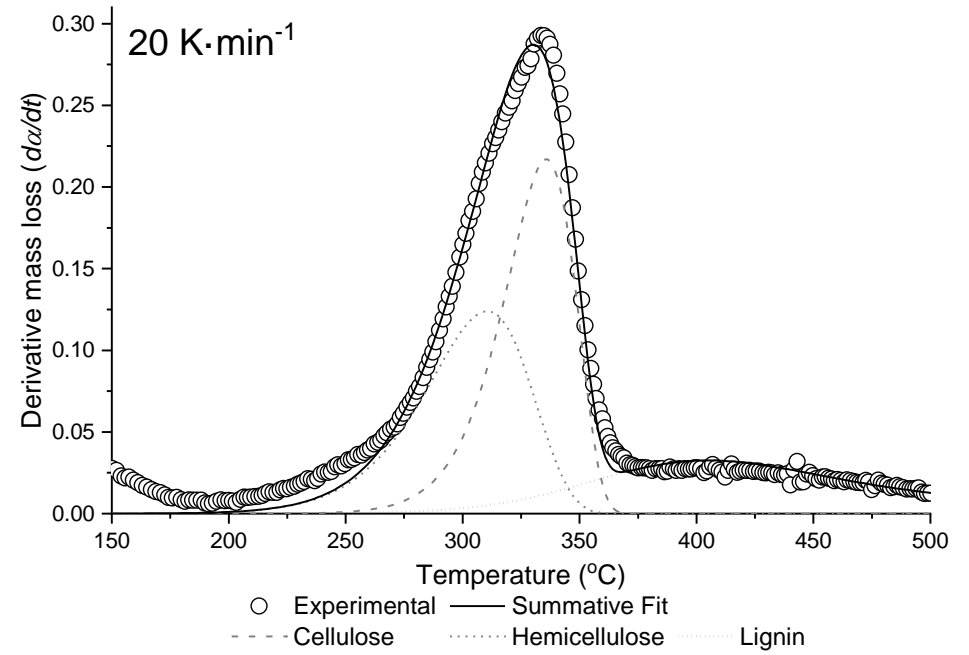
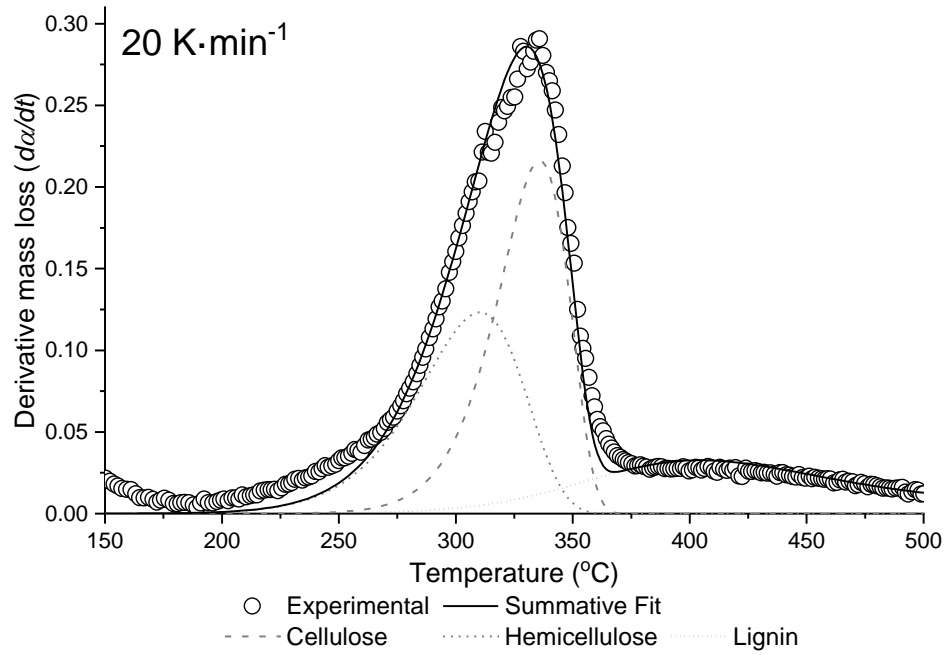


Fig. 11: Model-fitting graphs for Wheat straw powder (WS-P), model third-order to lignin. Part 2 of 2. Source: [159].

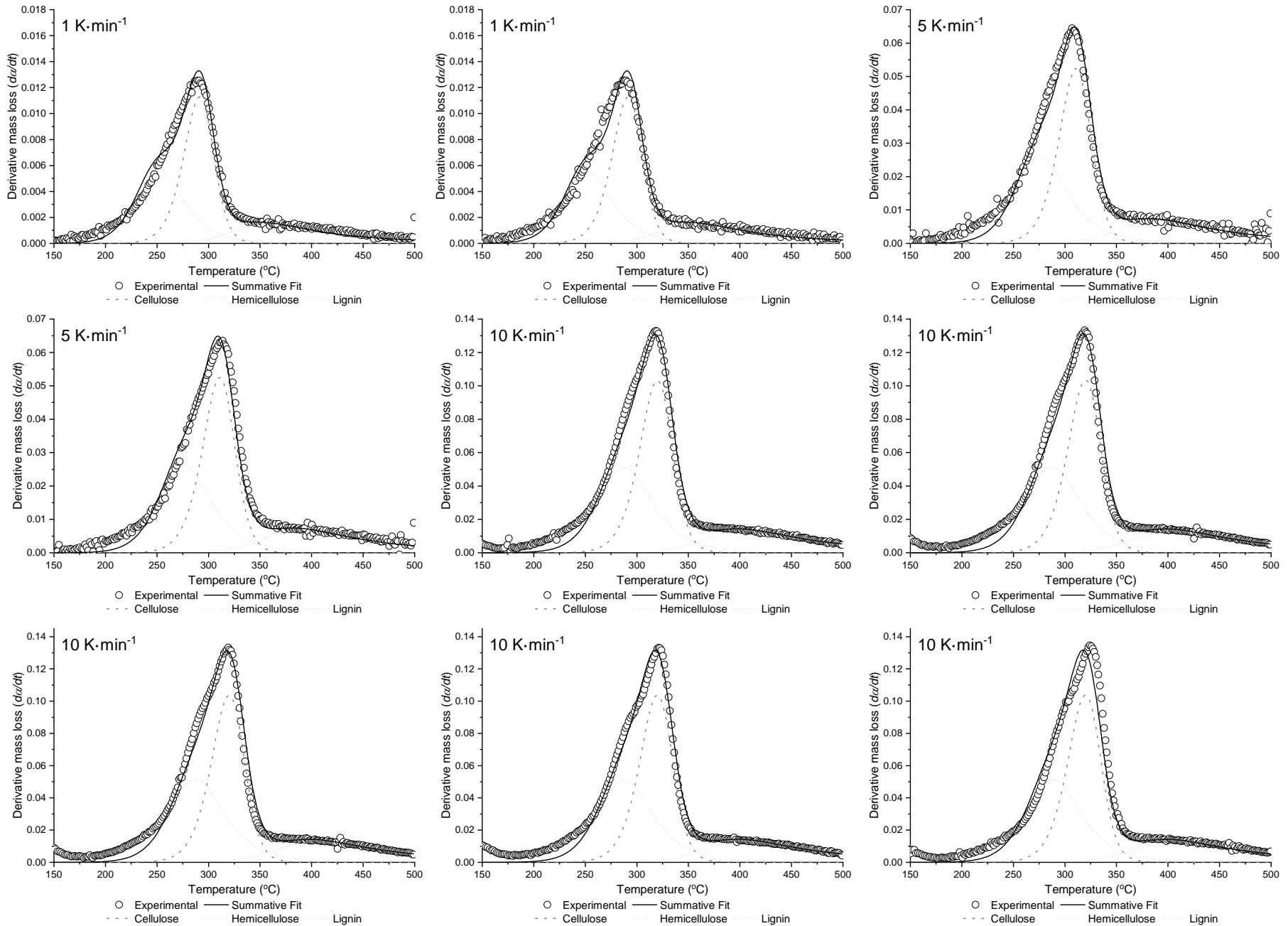


Fig. 12: Model-fitting graphs for Wheat straw powder (WS-P), model free-order. Part 1 of 2. Source: [159].

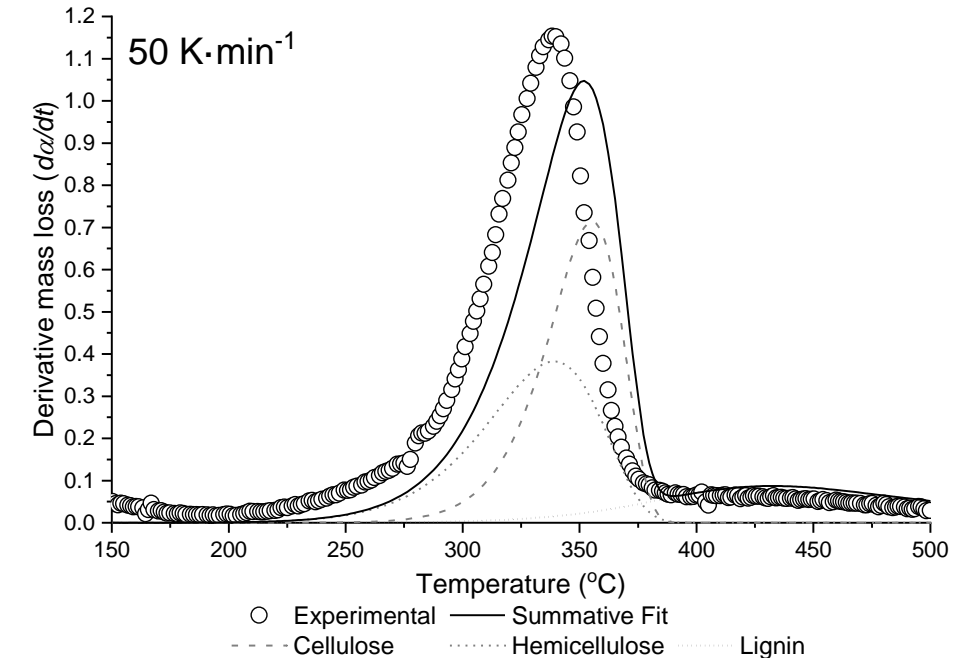
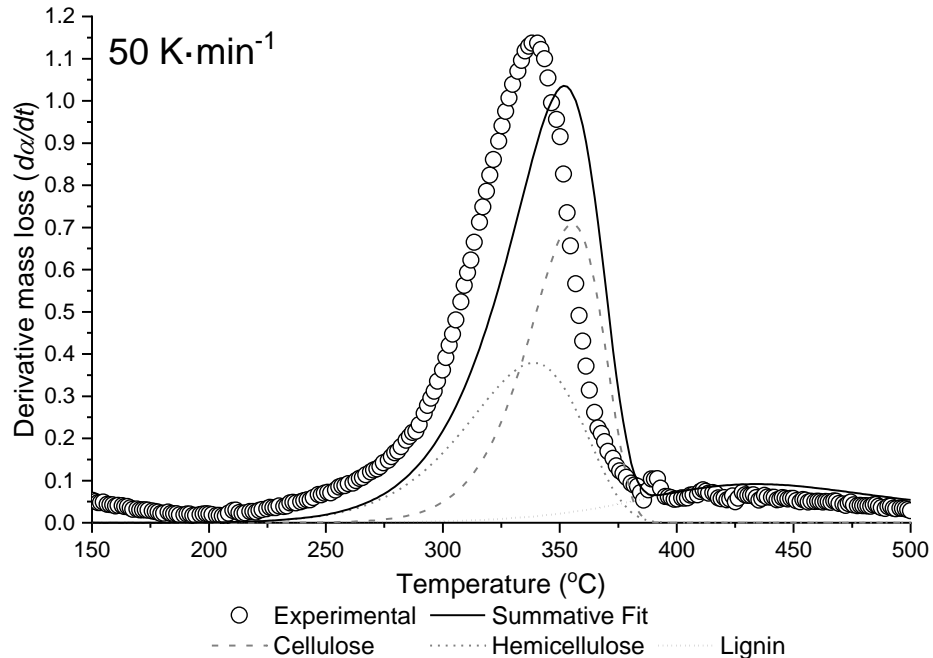
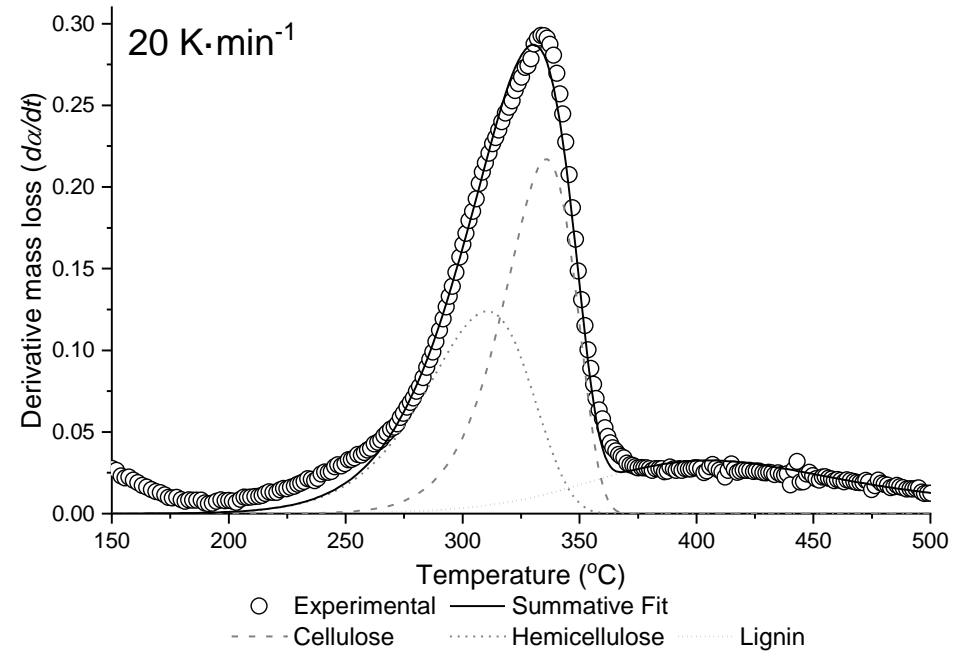
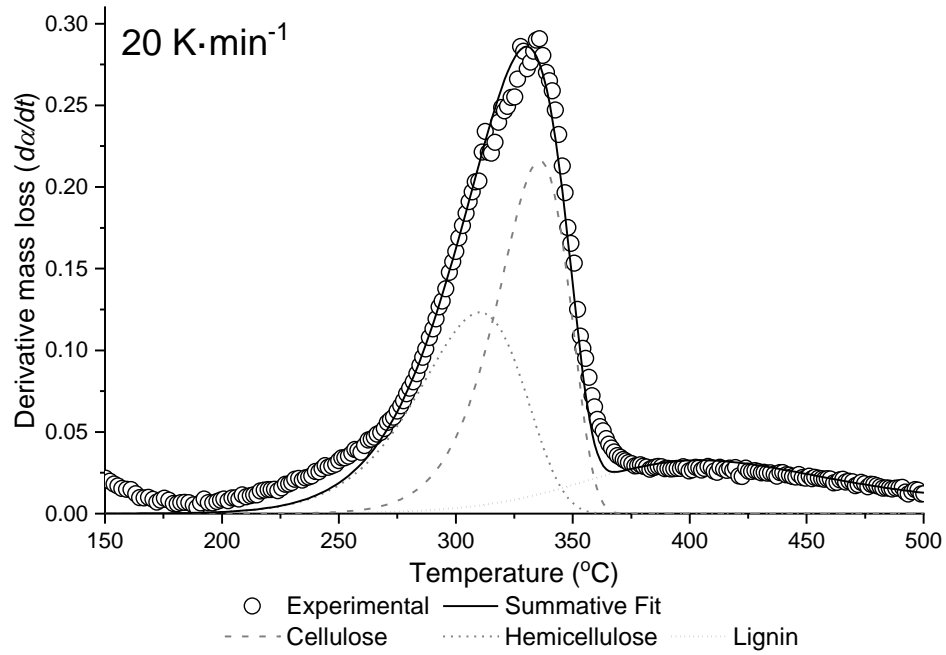


Fig. 13: Model-fitting graphs for Wheat straw powder (WS-P), model free-order. Part 2 of 2. Source: [159].

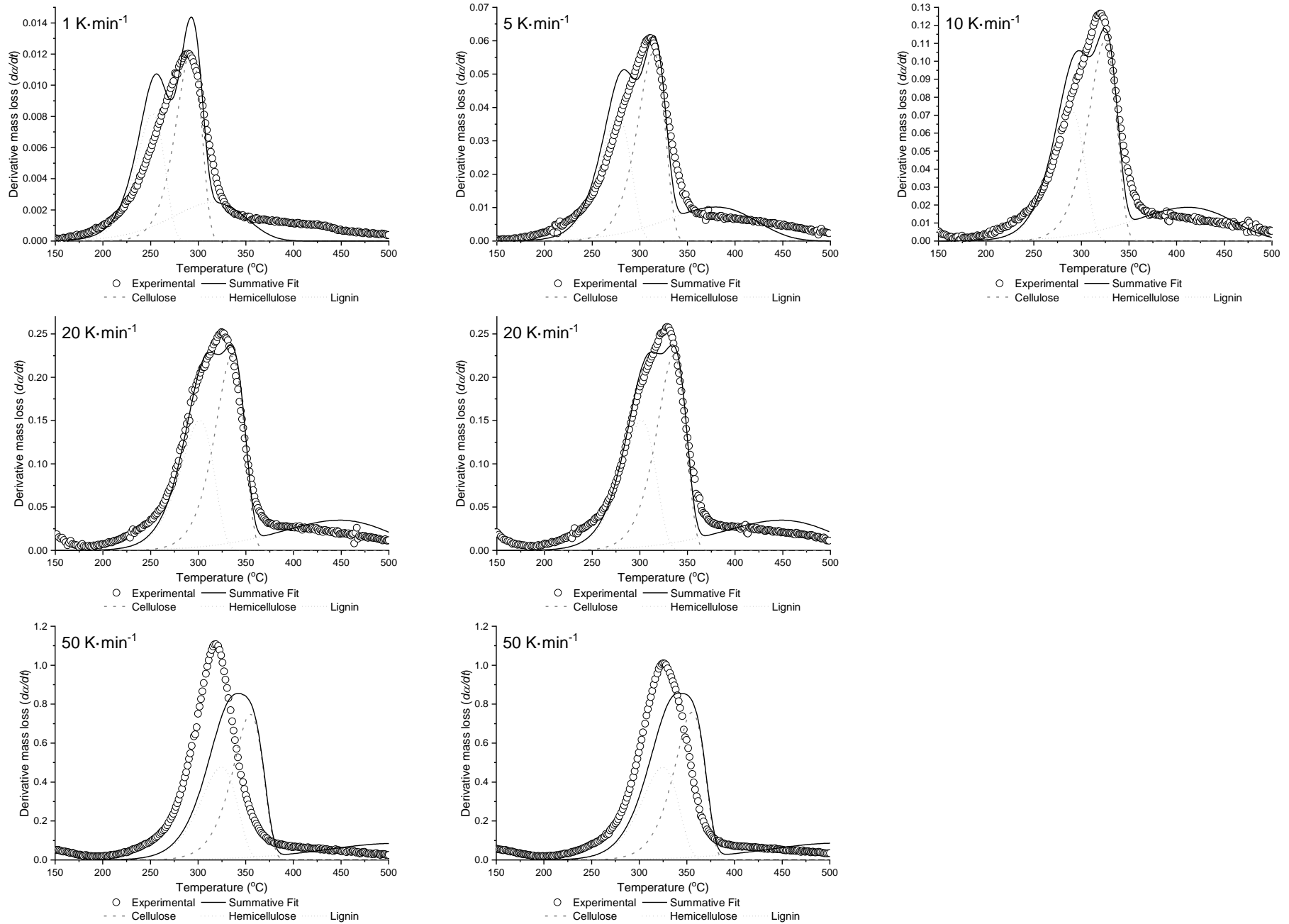


Fig. 14: Model-fitting graphs for Wheat straw hull (WS-W), model first-order. Source: [159].

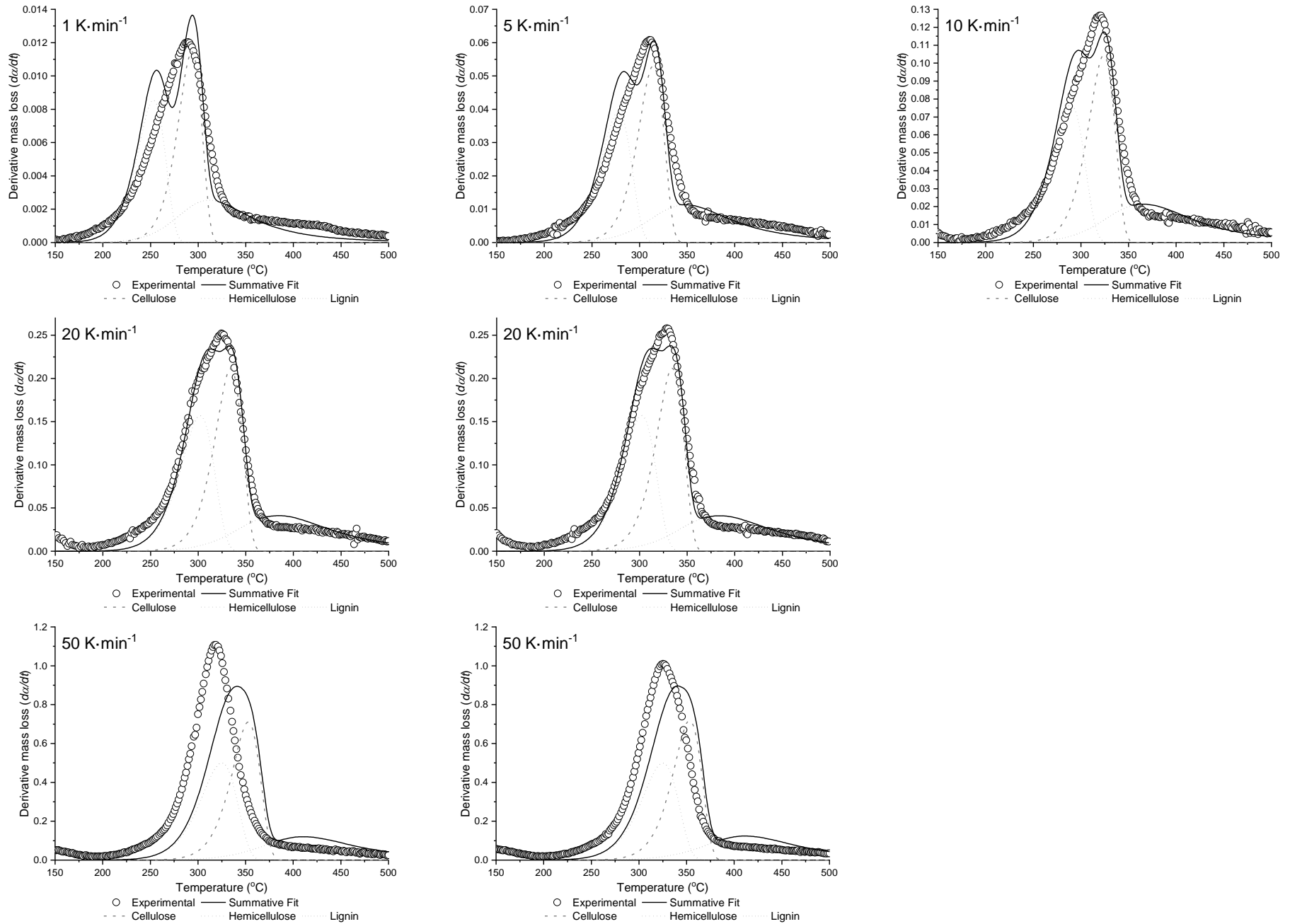


Fig. 15: Model-fitting graphs for Wheat straw hull (WS-W), model third-order lignin. Source: [159].

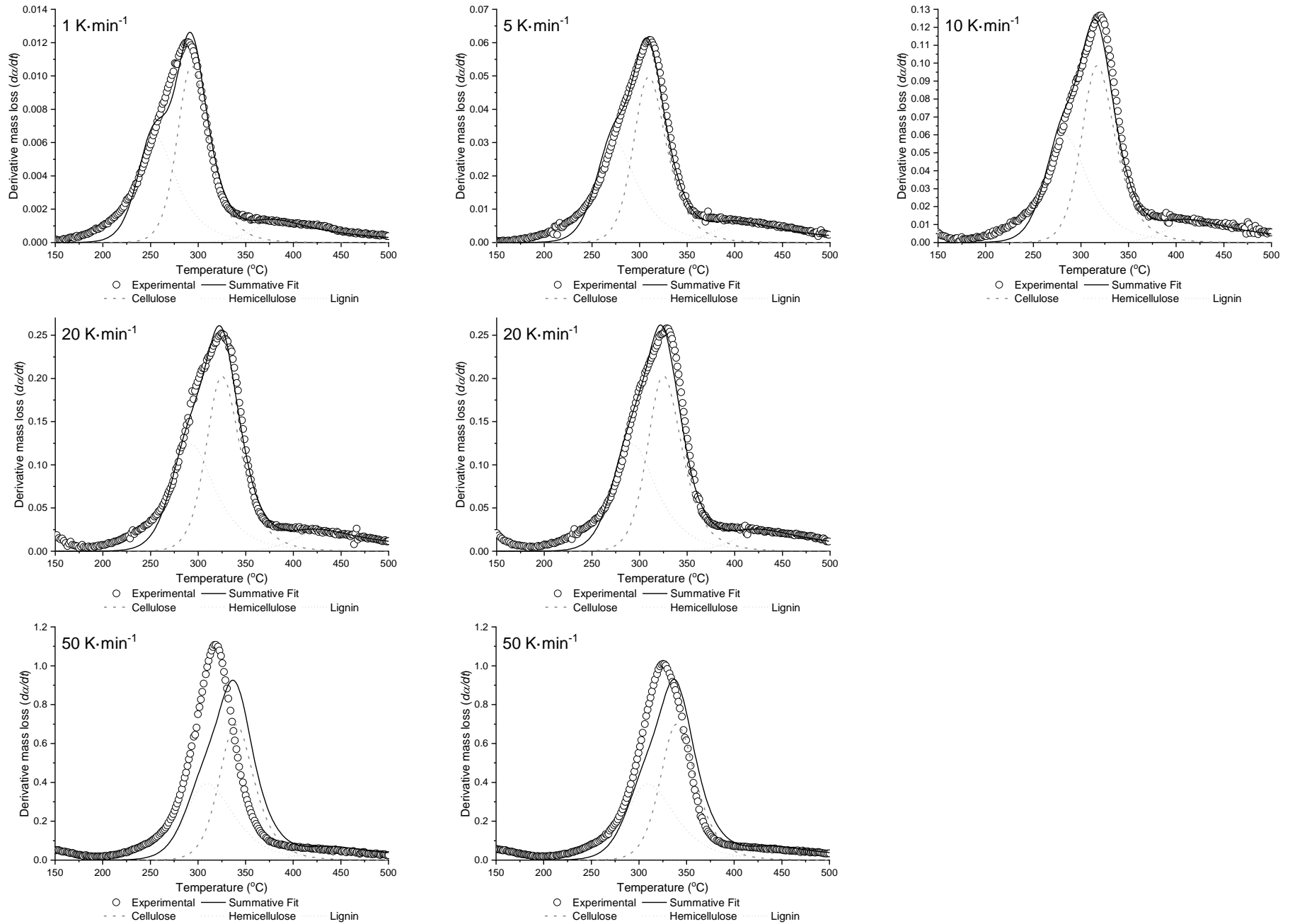


Fig. 16: Model-fitting graphs for Wheat straw hull (WS-W), model free-order. Source: [159].

Isoconversional Methods

Numerical values

Tab. 17: Kinetic parameters obtained for Beech using the isoconversional methods. Source: [159].

α	KAS		FWO		Friedman	
	E_a (kJ/mol)	$\log_{10}(A [s^{-1}])$	E_a (kJ/mol)	$\log_{10}(A [s^{-1}])$	E_a (kJ/mol)	$\log_{10}(A [s^{-1}])$
0.05	164.21 ± 6.71	12.68 ± 0.50	164.44 ± 6.31	10.41 ± 5.29	162.65 ± 3.56	12.42 ± 1.41
0.10	164.91 ± 4.50	12.61 ± 0.41	165.33 ± 4.21	10.35 ± 5.04	169.75 ± 3.38	12.95 ± 1.41
0.15	170.44 ± 5.65	13.05 ± 0.80	170.73 ± 5.32	10.78 ± 4.85	179.13 ± 5.41	13.67 ± 1.20
0.20	177.45 ± 3.64	13.61 ± 0.55	177.53 ± 3.40	11.31 ± 4.71	188.90 ± 1.56	14.38 ± 1.54
0.25	177.52 ± 5.11	13.47 ± 0.94	177.72 ± 4.79	11.19 ± 4.62	190.76 ± 5.54	14.34 ± 1.15
0.30	187.77 ± 8.19	14.28 ± 1.51	187.60 ± 7.73	11.97 ± 4.46	197.45 ± 6.64	14.74 ± 1.02
0.35	193.60 ± 6.30	14.67 ± 1.30	193.25 ± 5.93	12.33 ± 4.44	199.26 ± 4.42	14.72 ± 1.20
0.40	196.12 ± 3.23	14.74 ± 0.80	195.76 ± 3.00	12.41 ± 4.35	199.80 ± 2.53	14.62 ± 1.33
0.45	196.71 ± 3.54	14.66 ± 0.94	196.43 ± 3.30	12.33 ± 4.30	200.80 ± 2.37	14.62 ± 1.31
0.50	201.05 ± 3.93	14.94 ± 1.08	200.64 ± 3.70	12.60 ± 4.25	200.56 ± 0.81	14.55 ± 1.41
0.55	202.88 ± 1.61	15.03 ± 0.55	202.45 ± 1.48	12.69 ± 3.99	201.08 ± 1.03	14.58 ± 1.34
0.60	199.93 ± 4.02	14.70 ± 1.21	199.72 ± 3.75	12.38 ± 4.14	198.90 ± 4.25	14.38 ± 1.02
0.65	202.65 ± 4.59	14.90 ± 1.37	202.35 ± 4.36	12.58 ± 4.09	200.60 ± 6.70	14.53 ± 0.76
0.70	201.77 ± 3.63	14.78 ± 1.25	201.57 ± 3.39	12.46 ± 4.01	201.44 ± 4.93	14.56 ± 0.84
0.75	198.78 ± 5.00	14.49 ± 1.56	198.79 ± 4.71	12.19 ± 3.98	202.19 ± 6.36	14.56 ± 0.65
0.80	198.05 ± 4.67	14.39 ± 1.57	198.16 ± 4.38	12.09 ± 3.91	210.60 ± 6.68	15.14 ± 0.53
0.85	212.14 ± 5.77	15.51 ± 1.82	211.63 ± 5.43	13.16 ± 3.84	275.01 ± 6.18	20.15 ± 0.45
0.90	354.51 ± 23.26	26.72 ± 3.89	347.28 ± 22.06	23.97 ± 2.98	443.27 ± 11.50	32.66 ± 0.14
0.95	1006.56 ± 234.32	74.53 ± 20.77	967.78 ± 222.73	70.93 ± 11.89	1101.33 ± 338.10	80.00 ± 24.94

Tab. 18: Kinetic parameters obtained for WS-P using the isoconversional methods. Source: [159].

α	KAS		FWO		Friedman	
	E_a (kJ/mol)	$\log_{10}(A [s^{-1}])$	E_a (kJ/mol)	$\log_{10}(A [s^{-1}])$	E_a (kJ/mol)	$\log_{10}(A [s^{-1}])$
0.05	222.51 ± 16.03	19.67 ± 1.87	241.08 ± 21.28	19.43 ± 4.18	195.54 ± 10.33	16.38 ± 0.70
0.10	186.63 ± 8.20	15.31 ± 1.05	193.57 ± 7.56	13.73 ± 4.94	168.14 ± 8.85	13.10 ± 0.87
0.15	176.54 ± 8.19	14.04 ± 1.21	185.59 ± 8.52	12.65 ± 4.72	170.23 ± 9.32	13.13 ± 0.82
0.20	182.34 ± 7.72	14.44 ± 1.27	190.19 ± 7.60	12.92 ± 4.64	181.17 ± 7.93	14.05 ± 0.94
0.25	181.98 ± 8.18	14.30 ± 1.44	190.24 ± 7.96	12.81 ± 4.52	186.86 ± 6.66	14.49 ± 1.04
0.30	184.47 ± 7.04	14.44 ± 1.35	193.45 ± 8.08	13.01 ± 4.43	192.84 ± 4.40	14.95 ± 1.22
0.35	193.29 ± 8.86	15.20 ± 1.70	201.51 ± 8.40	13.68 ± 4.34	200.59 ± 4.98	15.58 ± 1.14
0.40	197.54 ± 6.76	15.51 ± 1.45	210.33 ± 11.40	14.43 ± 4.12	209.08 ± 3.28	16.27 ± 1.26
0.45	205.68 ± 6.87	16.19 ± 1.54	216.54 ± 9.99	14.91 ± 4.14	216.00 ± 3.75	16.81 ± 1.18
0.50	200.96 ± 7.03	15.67 ± 1.62	217.55 ± 15.07	14.93 ± 3.79	219.58 ± 5.02	17.06 ± 1.03
0.55	201.21 ± 5.78	15.63 ± 1.48	220.11 ± 17.34	15.10 ± 3.58	224.17 ± 6.82	17.40 ± 0.83
0.60	210.75 ± 8.13	16.44 ± 1.89	225.84 ± 14.01	15.55 ± 3.75	233.26 ± 5.10	18.12 ± 0.93
0.65	218.34 ± 5.78	17.06 ± 1.59	234.34 ± 14.65	16.24 ± 3.66	246.28 ± 2.83	19.16 ± 1.08
0.70	233.13 ± 6.32	18.28 ± 1.73	251.05 ± 17.10	17.64 ± 3.45	276.96 ± 4.28	21.65 ± 0.88
0.75	244.29 ± 4.69	19.14 ± 1.52	266.04 ± 21.47	18.84 ± 3.11	308.74 ± 17.27	24.12 ± 0.31
0.80	293.39 ± 13.69	23.15 ± 2.81	323.86 ± 34.95	23.66 ± 2.08	410.51 ± 47.73	32.25 ± 2.97
0.85	399.75 ± 151.71	31.30 ± 15.28	389.93 ± 144.20	28.41 ± 6.77	509.70 ± 290.93	39.17 ± 23.13
0.90	499.99 ± 334.65	37.73 ± 29.53	485.73 ± 318.10	34.70 ± 20.34	495.08 ± 345.33	35.97 ± 26.40
0.95	656.71 ± 600.22	47.35 ± 48.14	635.34 ± 570.53	44.13 ± 38.44	723.02 ± 653.27	50.93 ± 48.05

Tab. 19: Kinetic parameters obtained for WS-H using the isoconversional methods. Source: [159].

α	KAS		FWO		Friedman	
	E_a (kJ/mol)	$\log_{10}(A [s^{-1}])$	E_a (kJ/mol)	$\log_{10}(A [s^{-1}])$	E_a (kJ/mol)	$\log_{10}(A [s^{-1}])$
0.05	219.08 ± 23.28	19.04 ± 2.76	216.27 ± 22.16	16.49 ± 4.11	191.55 ± 9.25	15.78 ± 0.81
0.10	192.54 ± 14.15	15.81 ± 1.86	191.36 ± 13.49	13.40 ± 4.57	189.51 ± 11.80	15.20 ± 0.57
0.15	198.97 ± 13.35	16.21 ± 1.92	197.65 ± 12.74	13.79 ± 4.46	205.13 ± 13.57	16.52 ± 0.40
0.20	204.35 ± 13.73	16.57 ± 2.09	202.90 ± 13.09	14.13 ± 4.32	212.06 ± 13.83	17.01 ± 0.37
0.25	204.04 ± 14.73	16.42 ± 2.31	202.71 ± 14.05	14.00 ± 4.16	215.23 ± 15.96	17.17 ± 0.16
0.30	209.52 ± 16.45	16.84 ± 2.60	208.00 ± 15.69	14.40 ± 3.97	219.03 ± 18.29	17.40 ± 0.07
0.35	215.63 ± 18.45	17.30 ± 2.90	213.89 ± 17.58	14.84 ± 3.77	221.32 ± 18.50	17.49 ± 0.11
0.40	215.69 ± 14.95	17.22 ± 2.55	214.02 ± 14.26	14.77 ± 3.94	224.49 ± 14.02	17.69 ± 0.28
0.45	226.86 ± 18.57	18.15 ± 3.02	224.72 ± 17.69	15.67 ± 3.65	235.21 ± 16.02	18.55 ± 0.07
0.50	229.45 ± 17.59	18.29 ± 2.97	227.25 ± 16.76	15.81 ± 3.66	240.52 ± 15.75	18.92 ± 0.06
0.55	225.04 ± 14.68	17.82 ± 2.68	223.11 ± 14.01	15.36 ± 3.79	238.31 ± 14.34	18.64 ± 0.15
0.60	230.22 ± 16.60	18.20 ± 2.95	228.10 ± 15.83	15.73 ± 3.62	246.08 ± 17.82	19.21 ± 0.20
0.65	244.68 ± 13.63	19.40 ± 2.65	241.92 ± 13.01	16.87 ± 3.75	269.20 ± 16.42	21.08 ± 0.12
0.70	241.81 ± 21.62	19.02 ± 3.60	239.26 ± 20.60	16.51 ± 3.20	267.03 ± 29.81	20.69 ± 1.34
0.75	262.39 ± 23.47	20.68 ± 3.84	258.92 ± 22.35	18.11 ± 3.04	300.05 ± 35.25	23.28 ± 1.86
0.80	275.57 ± 15.46	21.48 ± 3.02	271.57 ± 14.73	18.89 ± 3.50	326.19 ± 20.22	24.89 ± 0.65
0.85	363.52 ± 79.40	28.17 ± 9.05	355.49 ± 75.49	25.37 ± 1.11	375.81 ± 88.40	27.92 ± 6.36
0.90	435.08 ± 75.05	32.36 ± 8.43	424.06 ± 71.36	31.76 ± 0.54	455.00 ± 76.93	32.61 ± 5.26
0.95	600.73 ± 67.29	42.79 ± 7.58	582.18 ± 63.98	41.97 ± 0.22	605.02 ± 58.80	41.80 ± 3.87

Arrhenius Plots

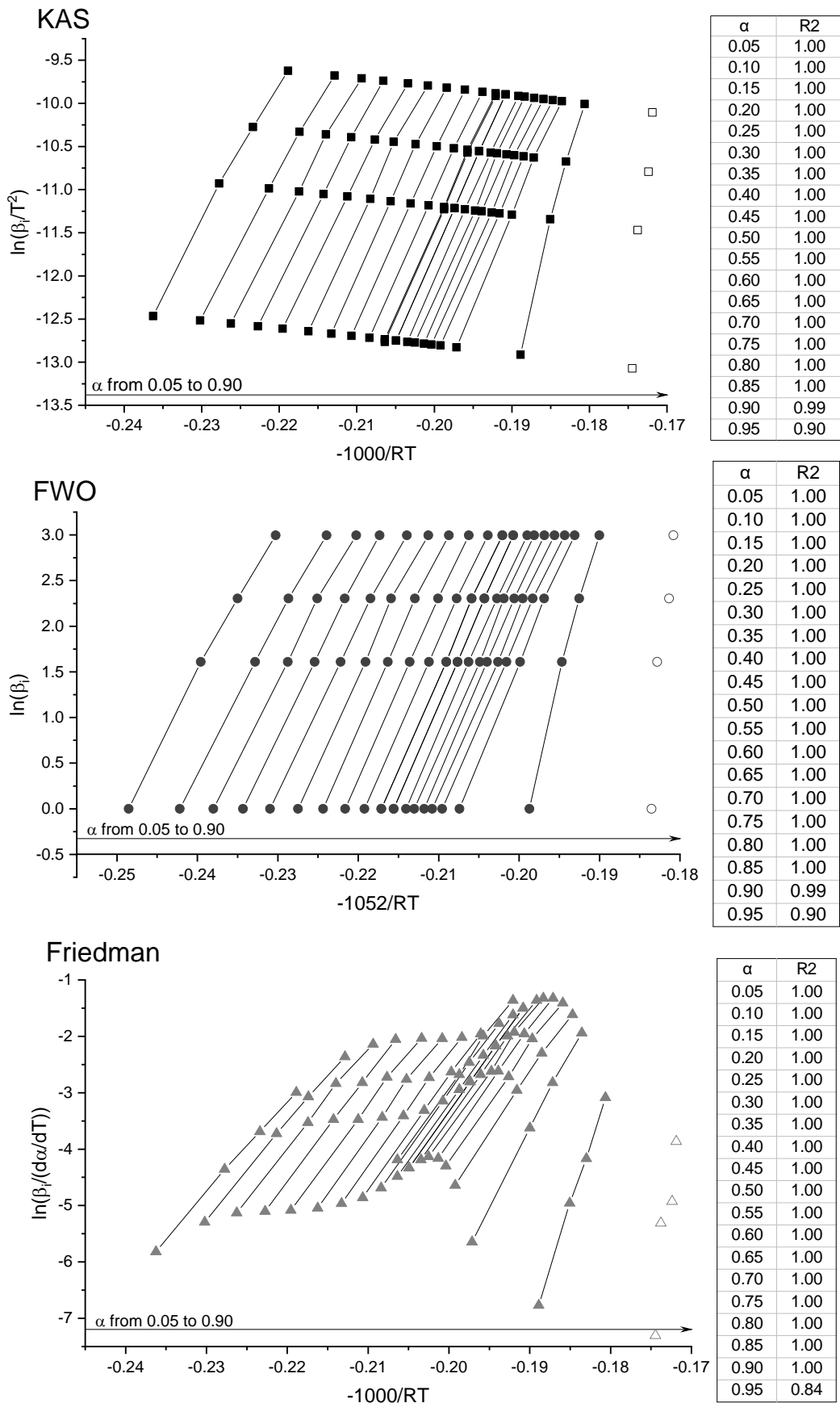


Fig. 17: Arrhenius plots for the isoconversional methods for Beech. Source: [159].

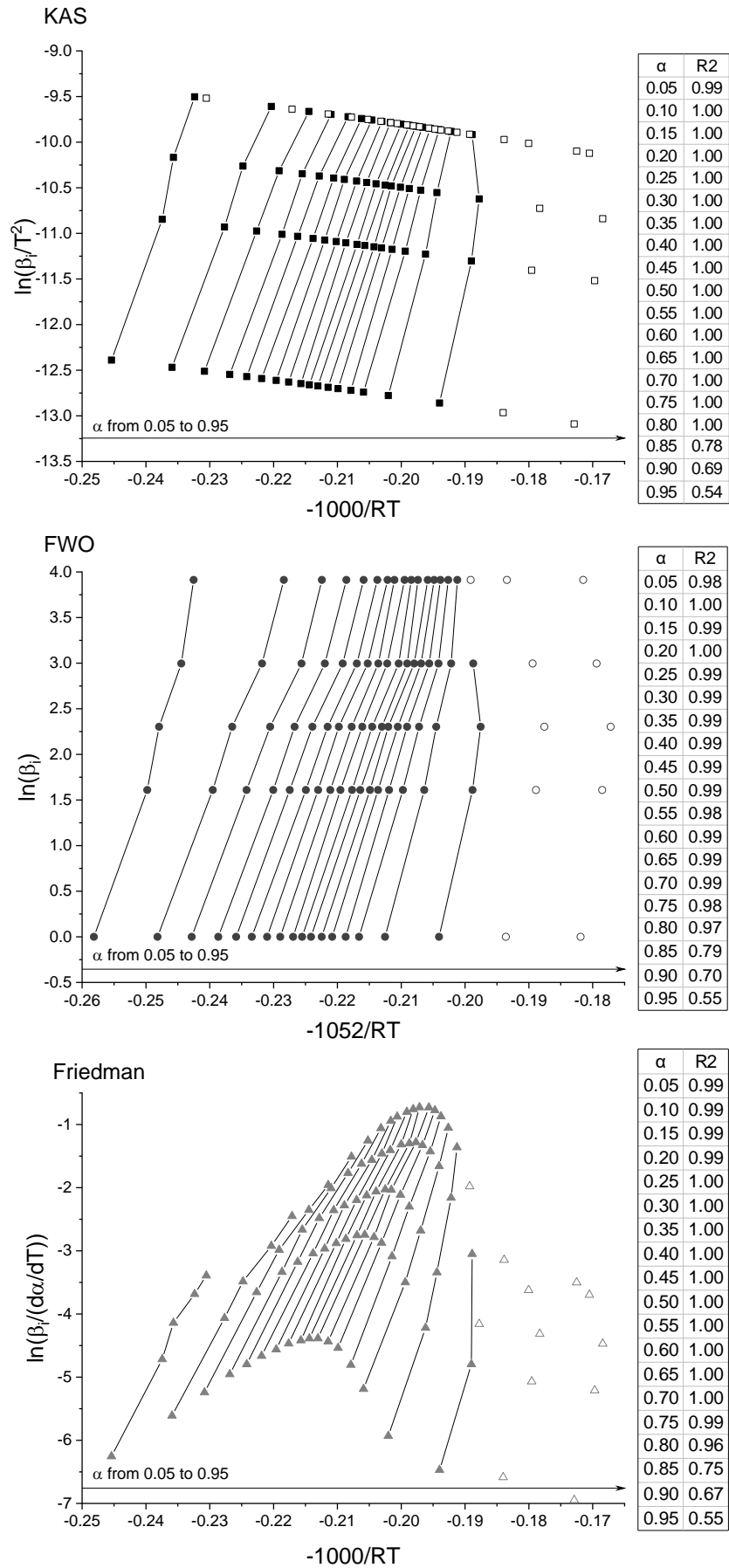


Fig. 18: Arrhenius plots for the isoconversional methods for WS-P. Source: [159].

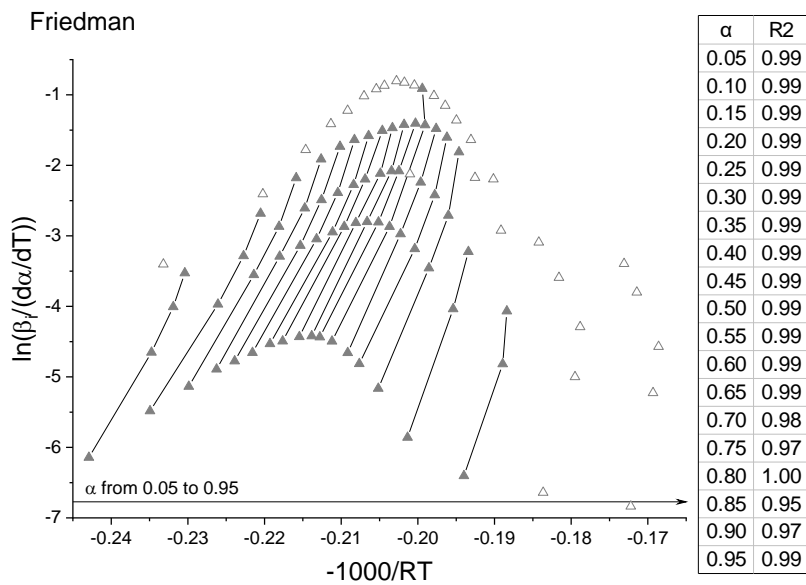
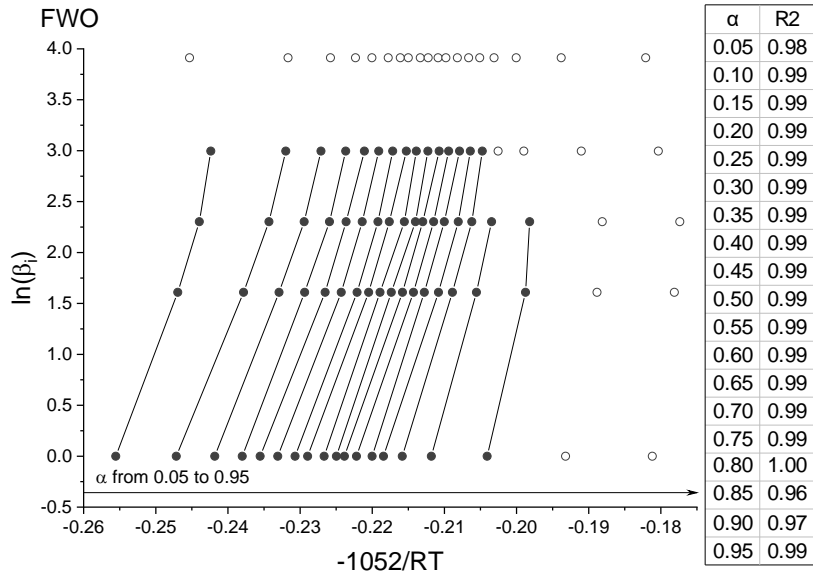
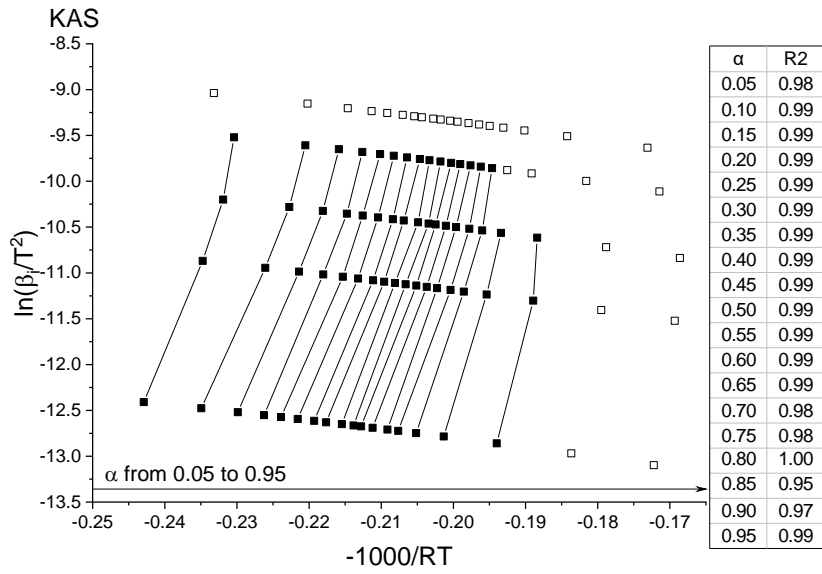


Fig. 19: Arrhenius plots for the isoconversional methods for WS-H. Source: [159].

Appendix C

Primary reaction networks

All the kinetics assume first-order (also called power law), which can vary with the operational temperature:

$$r = AT^n \exp\left(\frac{E_a}{RT}\right)$$

Tab. 20: Reaction network from Ranzi et al. [80]. Source: [159].

Group	#		E _a (kJ/mol)	log ₁₀ [A (s ⁻¹)]	T ⁿ
Cellulose	1	CELLULOS → CELL-ACT	192.28	13.90	0
	2	CELL-ACT → 0.95 HAA + 0.25 GLYOxAL + 0.2 ACETALDY + 0.25 HMF + 0.2 CO ₂ + 0.15 CO + 0.9 WATER + 0.65 C + 0.2 ACETONE + 0.1 H ₂ + 0.1 CH ₄	125.40	9.00	0
	3	CELL-ACT → LEVOGLUC	41.80	0.60	1
	4	CELLULOS → 5 WATER + 6 C	133.76	7.90	0
Hemicellulose	1	HEMICELL → 0.4 HEMCELL1 + 0.6 HEMCELL2	129.58	10.00	0
	2	HEMCELL1 → 2.5 H ₂ + 0.775 CO ₂ + CO + 0.5 FORMALDY + 0.25 METHANOL + 0.125 ETHANOL + 0.125 WATER + 2 C	112.86	9.48	0
	3	HEMCELL1 → xYLOSE	45.98	0.48	1
	4	HEMCELL2 → 0.2 CO ₂ + 1.5 H ₂ + 0.7 FORMALDY + 0.25 METHANOL + 0.125 ETHANOL + 0.125 WATER + 2 C + 0.8 GCO ₂ + 0.8 GCOH ₂	137.94	10.00	0
Lignin	1	LIGNIN-C → 0.35 LIGN-CC + 0.1 CMRYLALC + 0.08 PHENOL + 1.49 H ₂ + WATER + 7.05 C + 1.32 GCOH ₂	202.73	15.60	0
	2	LIGNIN-H → LIGN-OH + ACETONE	156.75	13.30	0
	3	LIGNIN-O → LIGN-OH + CO ₂	106.59	9.00	0
	4	LIGN-CC → 0.3 CMRYLALC + 0.2 PHENOL + 0.35 PROPDIAL + 1.2 H ₂ + 0.7 WATER + 0.25 CH ₄ + 0.25 ETHENE + 7.5 C + 0.5 GCO + 1.3 GCOH ₂	131.67	6.70	0
	5	LIGN-OH → LIG + 0.5 H ₂ + WATER + METHANOL + 5 C + GCO + GCOH ₂	206.91	13.00	0
	6	LIG → SYNAPALD	50.16	1.90	1
	7	LIG → WATER + 0.5 CO + 0.4 CH ₄ + 0.4 FORMALDY + 0.5 ETHENE + 6 C + 0.7 H ₂ + 0.4 METHANOL + 0.2 ACETALDY + 0.2 PROPDIAL + GCO + 0.5 GCOH ₂	125.40	9.08	0

Tab. 21: Reaction network from Ranzi et al. [80] and Faravelli et al. [79], and modified by Peters et al. [82]. Source: [159].

Group	#		E _a (kJ/mol)	log ₁₀ [A (s ⁻¹)]	T ⁿ
Cellulose	1	CELLULOS → CELL-ACT	221.12	13.90	0
	2	CELL-ACT → 0.95 HAA + 0.25 GLYOxAL + 0.2 ACETALDY + 0.25 HMF + 0.2 CO ₂ + 0.15 CO + 0.9 WATER + 0.65 C + 0.2 ACETONE + 0.1 H ₂ + 0.1 CH ₄	125.40	9.00	0
	3	CELL-ACT → LEVOGLUC	41.80	0.60	1
	4	CELLULOS → 5 WATER + 6 C	153.82	7.90	0
Hemicellulose	1	HEMICELL → 0.4 HEMCELL1 + 0.6 HEMCELL2	129.58	10.00	0
	2	HEMCELL1 → 2.5 H ₂ + 0.775 CO ₂ + CO + 0.5 FORMALDY + 0.25 METHANOL + 0.125 ETHANOL + 0.125 WATER + 2 C	11.29	9.48	0
	3	HEMCELL1 → xYLOSE	45.98	0.48	1
	4	HEMCELL2 → 0.2 CO ₂ + 1.5 H ₂ + 0.7 FORMALDY + 0.25 METHANOL + 0.125 ETHANOL + 0.125 WATER + 2 C + 0.8 GCO ₂ + 0.8 GCOH ₂	137.94	9.90	0
Lignin	1	1LIGH → PROPENE + 1ROH + 1RLIGM2A	163.25	13.00	0
	2	LIGNIN-H → 1PRLIGH + 1RH	163.25	13.00	0
	3	1LIGM2 → 1RPHOxM2 + 1RADIOM2	163.25	13.00	0
	4	LIGN-OH → 1PRLGM2A + 1RH	163.25	13.00	0
	5	LIGN-OH + 1RH → 1RPHOxM2 + 1RADIOM2	163.25	13.00	0
	6	1LIG → 1RPHENOx + 1RADIO	184.18	13.00	0
	7	LIGNIN-C → 1PRLIG-A + 1RH	184.18	13.00	0
	8	LIGNIN-C → 1RPHENOx + 1PRADIO	188.37	13.00	0
	9	1PADIOM2 → 1RADIOM2	171.63	13.00	0
	10	1PADIO → 1PRADIO + 1RH	180.00	13.00	0
	11	1PKETM2 → 1PRKETM2 + 1RH	167.44	13.00	0
	12	1PLIGC → LIGNIN-C + KETEN-01	121.39	8.00	0
	13	LIGNIN-O → LIGN-OH + CO ₂	108.84	9.00	0

Tab. 22: Reaction network from Corbetta et al. [114]. Hemicellulose assumed to be xylan-rich based on the conclusions of Peng and Wu [74]. Source: [159].

Group	#		E _a (kJ/mol)	log ₁₀ [A (s ⁻¹)]	T ⁿ
Cellulose	1	CELL → CELLA	188.10	13.60	0
	2	CELLA → 0.8 HAA + 0.2 GLYOxAL + 0.1 ACETALDY + 0.25 HMF + 0.3 ACETONE + 0.21 CO ₂ + 0.1 H ₂ + 0.4 FORMALDY + 0.16 CO + 0.1 CH ₄ + 0.83 WATER + 0.02 FORMICAC + 0.61 C	121.22	8.70	0
	3	CELLA → LEVOGLUC	41.80	0.26	1
	4	CELL → 5 WATER + 6 C	163.02	7.60	0
Hemicellulose	1	xyHW → 0.4 HEM1 + 0.6 HEM2	129.58	9.52	0
	2	HEM1 → 0.025 WATER + 0.5 CO ₂ + 0.025 FORMICAC + 0.5 CO + 0.8 FORMALDY + 0.125 ETHANOL + 0.1 METHANOL + 0.25 C ₂ H ₄ + 0.125 GH ₂ + 0.275 GCO ₂ + 0.4 GCOH ₂ + 0.45 GCH ₃ OH + 0.325 GCH ₄ + 0.875 C	133.76	9.00	0
	3	HEM1 → 0.25 WATER + 0.5 CO ₂ + 0.05 FORMICAC + 0.3 CO + 0.15 GCO + 0.25 GCO ₂ + 1.7 GCOH ₂ + 0.625 GCH ₄ + 0.375 GC ₂ H ₄ + 0.875 C	45.98	-0.05	1
	4	HEM1 → xyLOSAN	33.44	-1.30	1
	5	HEM2 → 0.2 WATER + 0.175 CO + 0.275 CO ₂ + 0.5 FORMALDY + 0.1 ETHANOL + 0.2 HAA + 0.025 FORMICAC + 0.25 GCH ₄ + 0.3 GCH ₃ OH + 0.275 GC ₂ H ₄ + 0.4 GCO ₂ + 0.925 GCOH ₂ + C	137.94	9.52	0
Lignin	1	LIGC → 0.35 LIGCC + 0.1 CMRYLALC + 0.08 PHENOL + 0.41 C ₂ H ₄ + WATER + 0.3 FORMALDY + 0.32 CO + 0.7 GCOH ₂ + 0.495 GCH ₄ + 5.735 C	202.73	15.12	0
	2	LIGH → LIGOH + ACETONE	156.75	12.83	0
	3	LIGO → LIGOH + GCO ₂	106.59	8.52	0
	4	LIGCC → 0.3 CMRYLALC + 0.2 PHENOL + 0.35 HAA + 0.7 WATER + 0.4 CO + 0.65 GCH ₄ + 0.6 GC ₂ H ₄ + GCOH ₂ + 0.4 GCO + 6.75 C	131.67	6.20	0
	5	LIGOH → LIG + 0.15 GH ₂ + 0.9 WATER + 0.1 CH ₄ + 0.5 METHANOL + 0.5 GCH ₃ OH + 0.05 CO ₂ + 0.3 CO + GCO + 0.05 FORMICAC + 0.6 GCOH ₂ + 0.35 GCH ₄ + 0.2 GC ₂ H ₄ + 4.15 C	125.40	7.70	0
	6	LIGOH → 1.5 WATER + 0.5 CO + 0.1 CH ₄ + 0.5 GH ₂ + 1.6 GCO + 3.9 GCOH ₂ + 1.65 GCH ₄ + 0.3 GC ₂ H ₄ + 0.5 GCH ₃ OH + 10.15 C	62.70	1.52	1
	7	LIG → SYNAPALD	50.16	0.38	1
	8	LIG → 0.95 WATER + 0.2 FORMALDY + 0.4 METHANOL + CO + 0.2 CH ₄ + 0.05 FORMICAC + 0.45 GCO + 0.5 GCOH ₂ + 0.4 GCH ₄ + 0.65 GC ₂ H ₄ + 0.2 ACETALDY + 0.2 ACETONE + 5.5 C	125.40	8.60	0
	9	LIG → 0.6 WATER + 0.4 CO + 0.2 CH ₄ + 0.4 FORMALDY + 0.2 GCO + 0.4 GCH ₄ + 0.5 GC ₂ H ₄ + 0.4 GCH ₃ OH + 2 GCOH ₂ + 6 C	33.44	-1.08	1

Tab. 23: Reaction network from Anca-Couce and Scharler [119], assuming low charring conditions as reported by Pecha et al. [56]. Source: [159].

Group	#		E _a (kJ/mol)	log ₁₀ [A (s ⁻¹)]	T ⁿ
Cellulose	1	CELLULOS → CELL-ACT	188.37	13.60	0
	2	CELL-ACT → 0.43875 HAA + 0.195 GLYOxAL + 0.2925 ACETONE + 0.24375 HMF + 0.07375 H ₂ + 0.30225 CO + 0.41225 CO ₂ + 0.39 FORMALDY + 0.14625 METHANOL + 0.0975 ACETALDY + 0.90925 WATER + 0.0195 FORMICAC + 0.04875 GH ₂ + 0.195 GCH ₄ + 0.73225 C	80.00	6.30	0
	3	CELL-ACT → 0.975 LEVOGLUC + 0.1375 C + 0.1 WATER + 0.0125 CO ₂ + 0.025 H ₂	41.86	0.60	1
Hemicellulose	1	HEMICELL → 0.58 HEMCELL1 + 0.42 HEMCELL2 + 0.4 ACETICAC	129.77	10.00	0
	2	HEMICELL1 → 0.475 CO + 0.5 CO ₂ + 0.30875 CH ₄ + 0.76 FORMALDY + 0.095 METHANOL + 0.2375 C ₂ H ₄ + 0.11875 ETHANOL + 0.17375 WATER + 0.02375 FORMICAC + 0.26125 GCO ₂ + 0.38 GCOH ₂ + 0.11875 GH ₂ + 0.4275 GCH ₃ OH + 1.05625 C + 0.05 H ₂	125.58	9.08	0
	3	HEMICELL1 → 0.095 CO + 0.785 CO ₂ + 0.285 FORMALDY + 0.3875 WATER + 0.0475 FORMICAC + 0.1425 GCO ₂ + 0.1425 GCO + 1.14 GCOH ₂ + 0.19 GH ₂ + 0.59375 GCH ₄ + 0.35625 GC ₂ H ₄ + 1.05625 C + 0.05 H ₂	33.50	-0.82	1
	4	HEMICELL1 → 0.95 xYLOSAN + 0.225 C + 0.15 WATER + 0.025 CO ₂ + 0.05 H ₂	46.05	0.48	1
	5	HEMICELL2 → 0.19 HAA + 0.16625 CO + 0.29 CO ₂ + 0.475 FORMALDY + 0.095 ETHANOL + 0.34 WATER + 0.02375 FORMICAC + 0.38 GCO ₂ + 0.87875 GCOH ₂ + 0.2375 GCH ₄ + 0.285 GCH ₃ OH + 0.26125 GC ₂ H ₄ + 1.18 C + 0.05 H ₂	138.14	9.70	0
Lignin	1	LIGNIN-C → 0.35 LIGN-CC + 0.1 CMRYLALC + 0.08 PHENOL + 0.32 CO + 0.3 FORMALDY + WATER + 0.7 GCOH ₂ + 0.495 GCH ₄ + 0.41 GC ₂ H ₄ + 5.735 C	203.02	15.12	0
	2	LIGNIN-H → LIGN-OH + 0.25 HAA + 0.5 ACETONE + 5 GC ₂ H ₄	156.97	12.83	0
	3	LIGNIN-O → LIGN-OH + CO ₂	106.74	8.52	0
	4	LIGN-CC → 0.315 HAA + 0.27 CMRYLALC + 0.18 PHENOL + 0.36 CO + 0.585 CH ₄ + 0.54 C ₂ H ₄ + 1.03 WATER + 0.36 GCO + 0.9 GCOH ₂ + 7.575 C + 0.3 H ₂	131.86	7.48	0
	5	LIGN-OH → LIG + 0.55 CO + 0.05 CO ₂ + 0.1 CH ₄ + 0.6 METHANOL + 0.9 WATER + 0.05 FORMICAC + 0.6 GCO + 0.85 GCOH ₂ + 0.1 GH ₂ + 0.35 GCH ₄ + 0.3 GCH ₃ OH + 0.2 GC ₂ H ₄ + 4.15 C	125.58	8.00	0
	6	LIG → 0.9 SYNAPALD + 1.1 C + 0.3 WATER + 0.1 CO ₂ + 0.3 H ₂	50.20	0.60	1
	7	LIG → 0.18 ACETONE + 0.9 CO + 0.18 CH ₄ + 0.18 FORMALDY + 0.36 METHANOL + 0.18 ACETALDY + 1.155 WATER + 0.045 FORMICAC + 0.405 GCO + 0.45 GCOH ₂ + 0.36 GCH ₄ + 0.585 GC ₂ H ₄ + 6 C + 0.05 CO ₂ + 0.3 H ₂	125.58	8.60	0
	8	LIG → 0.36 CO + 0.18 CH ₄ + 0.36 FORMALDY + 0.84 WATER + 0.18 GCO + 1.8 GCOH ₂ + 0.36 GCH ₄ + 0.36 GCH ₃ OH + 0.45 GC ₂ H ₄ + 6.45 C + 0.05 CO ₂ + 0.3 H ₂	33.50	-1.08	1
Extractives	1	TANN → PHENOL + ITANN	46.02	1.70	0
	2	ITANN → 5 C + 3 CO + GCOH ₂ + 2 WATER	25.52	3.79	0
	3	TGL → ACROLEIN + 3 FFA	191.20	12.85	0

Tab. 24: Reaction network from Anca-Couce and Scharler [119], assuming high charring conditions as reported by Pecha et al. [56]. Source: [159].

Group	#		E _a (kJ/mol)	log ₁₀ [A (s ⁻¹)]	T ⁿ
Cellulose	1	CELLULOS → CELL-ACT	188.37	13.60	0
	2	CELL-ACT → 0.405 HAA + 0.18 GLYOxAL + 0.27 ACETONE + 0.225 HMF + 0.145 H ₂ + 0.279 CO + 0.419 CO ₂ + 0.36 FORMALDY + 0.135 METHANOL + 0.09 ACETALDY + 1.147 WATER + 0.018 FORMICAC + 0.045 GH ₂ + 0.18 GCH ₄ + 1.099 C	80.00	6.30	0
	3	CELL-ACT → 0.405 HAA + 0.18 GLYOxAL + 0.27 ACETONE + 0.225 HMF + 0.145 H ₂ + 0.279 CO + 0.419 CO ₂ + 0.36 FORMALDY + 0.135 METHANOL + 0.09 ACETALDY + 1.147 WATER + 0.018 FORMICAC + 0.045 GH ₂ + 0.18 GCH ₄ + 1.099 C	41.86	0.60	1
Hemicellulose	1	HEMICELL → 0.58 HEMCELL1 + 0.42 HEMCELL2 + 0.4 ACETICAC	129.77	10.00	0
	2	HEMICELL1 → 0.4 CO + 0.5 CO ₂ + 0.26 CH ₄ + 0.64 FORMALDY + 0.08 METHANOL + 0.2 C ₂ H ₄ + 0.1 ETHANOL + 0.62 WATER + 0.02 FORMICAC + 0.22 GCO ₂ + 0.32 GCOH ₂ + 0.1 GH ₂ + 0.36 GCH ₃ OH + 1.6 C + 0.2 H ₂	125.58	9.08	0
	3	HEMICELL1 → 0.08 CO + 0.74 CO ₂ + 0.24 FORMALDY + 0.8 WATER + 0.04 FORMICAC + 0.12 GCO ₂ + 0.12 GCO + 0.96 GCOH ₂ + 0.16 GH ₂ + 0.5 GCH ₄ + 0.3 GC ₂ H ₄ + 1.6 C + 0.2 H ₂	33.50	-0.82	1
	4	HEMICELL1 → 0.08 CO + 0.74 CO ₂ + 0.24 FORMALDY + 0.8 WATER + 0.04 FORMICAC + 0.12 GCO ₂ + 0.12 GCO + 0.96 GCOH ₂ + 0.16 GH ₂ + 0.5 GCH ₄ + 0.3 GC ₂ H ₄ + 1.6 C + 0.2 H ₂	46.05	0.48	1
	5	HEMICELL2 → 0.16 HAA + 0.14 CO + 0.32 CO ₂ + 0.4 FORMALDY + 0.08 ETHANOL + 0.76 WATER + 0.02 FORMICAC + 0.32 GCO ₂ + 0.74 GCOH ₂ + 0.2 GCH ₄ + 0.24 GCH ₃ OH + 0.22 GC ₂ H ₄ + 1.7 C + 0.2 H ₂	138.14	9.70	0
Lignin	1	LIGNIN-C → 0.35 LIGN-CC + 0.1 CMRYLALC + 0.08 PHENOL + 0.32 CO + 0.3 FORMALDY + WATER + 0.7 GCOH ₂ + 0.495 GCH ₄ + 0.41 GC ₂ H ₄ + 5.735 C	203.02	15.12	0
	2	LIGNIN-H → LIGN-OH + 0.25 HAA + 0.5 ACETONE + 5 GC ₂ H ₄	156.97	12.83	0
	3	LIGNIN-O → LIGN-OH + CO ₂	106.74	8.52	0
	4	LIGN-CC → 0.21 HAA + 0.18 CMRYLALC + 0.12 PHENOL + 0.24 CO + 0.39 CH ₄ + 0.36 C ₂ H ₄ + 2.02 WATER + 0.24 GCO + 0.6 GCOH ₂ + 10.05 C + 1.2 H ₂	131.86	7.48	0
	5	LIGN-OH → LIG + 0.55 CO + 0.05 CO ₂ + 0.1 CH ₄ + 0.6 METHANOL + 0.9 WATER + 0.05 FORMICAC + 0.6 GCO + 0.85 GCOH ₂ + 0.1 GH ₂ + 0.35 GCH ₄ + 0.3 GCH ₃ OH + 0.2 GC ₂ H ₄ + 4.15 C	125.58	8.00	0
	6	LIG → 0.6 SYNAPALD + 4.2 C + 1.2 WATER + 0.2 CO ₂ + 1.2 H ₂	50.20	0.60	1
	7	LIG → 0.12 ACETONE + 0.6 CO + 0.12 CH ₄ + 0.12 FORMALDY + 0.24 METHANOL + 0.12 ACETALDY + 1.77 WATER + 0.03 FORMICAC + 0.27 GCO + 0.3 GCOH ₂ + 0.24 GCH ₄ + 0.39 GC ₂ H ₄ + 8 C + 0.2 CO ₂ + 1.2 H ₂	125.58	8.60	0
	8	LIG → 0.24 CO + 0.12 CH ₄ + 0.24 FORMALDY + 1.56 WATER + 0.12 GCO + 1.2 GCOH ₂ + 0.24 GCH ₄ + 0.24 GCH ₃ OH + 0.3 GC ₂ H ₄ + 7.8 C + 0.2 CO ₂ + 1.2 H ₂	33.50	-1.08	1
Extractives	1	TANN → PHENOL + ITANN	46.02	1.70	0
	2	ITANN → 5 C + 3 CO + GCOH ₂ + 2 WATER	25.52	3.79	0
	3	TGL → ACROLEIN + 3 FFA	191.20	12.85	0

Tab. 25: Reaction network from Ranzi et al. [117]. Hemicellulose assumed to be xylan-rich based on the conclusions of Peng and Wu [74]. Source: [159].

Group	#		E _a (kJ/mol)	log ₁₀ [A (s ⁻¹)]	T ⁿ
Cellulose	1	CELL → CELLA	196.46	14.18	0
	2	CELLA → 0.45 HAA + 0.2 GLYOxAL + 0.1 ACETALDY + 0.25 HMF + 0.3 NPROPALD + 0.15 METHANOL + 0.4 FORMALDY + 0.31 CO + 0.41 CO ₂ + 0.05 H ₂ + 0.83 WATER + 0.02 FORMICAC + 0.2 GCH ₄ + 0.05 GH ₂ + 0.61 C	79.84	6.30	0
	3	CELLA → LEVOGLUC	41.80	0.60	1
	4	CELL → 5 WATER + 6 C	129.58	7.81	0
Hemicellulose	1	xYHW → 0.58 HEM1 + 0.42 HEM2	129.58	10.00	0
	2	HEM1 → 0.025 WATER + 0.5 CO ₂ + 0.025 FORMICAC + 0.5 CO + 0.8 FORMALDY + 0.125 ETHANOL + 0.1 METHANOL + 0.25 C ₂ H ₄ + 0.125 GH ₂ + 0.275 GCO ₂ + 0.4 GCOH ₂ + 0.45 GCH ₃ OH + 0.325 GCH ₄ + 0.875 C	125.40	9.08	0
	3	HEM1 → 0.25 WATER + 0.8 CO ₂ + 0.05 FORMICAC + 0.1 CO + 0.15 GCO + 0.15 GCO ₂ + 0.2 GH ₂ + 0.3 FORMALDY + 1.2 GCOH ₂ + 0.625 GCH ₄ + 0.375 GC ₂ H ₄ + 0.875 C	33.44	-0.82	1
	4	HEM1 → xYLOSAN	45.98	0.48	1
	5	HEM2 → 0.2 WATER + 0.175 CO + 0.275 CO ₂ + 0.5 FORMALDY + 0.1 ETHANOL + 0.2 HAA + 0.025 FORMICAC + 0.25 GCH ₄ + 0.3 GCH ₃ OH + 0.275 GC ₂ H ₄ + 0.4 GCO ₂ + 0.925 GCOH ₂ + C	137.94	9.70	0
Lignin	1	LIGC → 0.35 LIGCC + 0.1 CMRYLALC + 0.08 PHENOL + 0.41 C ₂ H ₄ + WATER + 0.7 GCOH ₂ + 0.3 FORMALDY + 0.32 CO + 0.495 GCH ₄ + 5.735 C	202.73	15.12	0
	2	LIGH → LIGOH + 0.5 NPROPALD + 0.5 C ₂ H ₄ + 0.25 HAA	156.75	12.83	0
	3	LIGO → LIGOH + CO ₂	106.59	8.52	0
	4	LIGCC → 0.3 CMRYLALC + 0.2 PHENOL + 0.35 HAA + 0.7 WATER + 0.65 GCH ₄ + 0.6 GC ₂ H ₄ + GCOH ₂ + 0.4 CO + 0.4 GCO + 6.75 C	131.67	6.22	0
	5	LIGOH → LIG + 0.9 WATER + 0.1 CH ₄ + 0.6 METHANOL + 0.1 GH ₂ + 0.3 GCH ₃ OH + 0.05 CO ₂ + 0.55 CO + 0.6 GCO + 0.05 FORMICAC + 0.85 GCOH ₂ + 0.35 GCH ₄ + 0.2 GC ₂ H ₄ + 4.15 C	125.40	8.00	0
	6	LIG → 0.7 SYNAPALD + 0.3 ANISOLE + 0.3 CO + 0.3 GCO + 0.3 ACETALDY	50.16	0.60	1
	7	LIG → 0.95 WATER + 0.2 FORMALDY + 0.4 METHANOL + CO + 0.2 CH ₄ + 0.05 FORMICAC + 0.45 GCO + 0.5 GCOH ₂ + 0.4 GCH ₄ + 0.65 GC ₂ H ₄ + 0.2 ACETALDY + 0.2 NPROPALD + 5.5 C	125.40	8.60	0
	8	LIG → 0.6 WATER + 0.4 CO + 0.2 CH ₄ + 0.4 FORMALDY + 0.2 GCO + 0.4 GCH ₄ + 0.5 GC ₂ H ₄ + 0.4 GCH ₃ OH + 2 GCOH ₂ + 6 C	33.44	-1.08	1
Extractives	1	TGL → ACROLEIN + 3 FFA	191.03	12.85	0
	2	TANN → PHENOL + ITANN	45.98	1.70	0
	3	ITANN → 6 C + 3 CO + 3 WATER	25.50	-1.82	0

Tab. 26: Reaction network from Ranzi et al. [65]. Hemicellulose assumed to be xylan-rich based on the conclusions of Peng and Wu [74]. Source: [159].

Group	#		E _a (kJ/mol)	log ₁₀ [A (s ⁻¹)]	T ⁿ
Cellulose	1	CELL → CELLA	196.46	14.18	0
	2	CELLA → 0.4 HAA + 0.05 GLYOxAL + 0.15 ACETALDY + 0.25 HMF + 0.35 NPROPALD + 0.15 METHANOL + 0.3 FORMALDY + 0.61 CO + 0.36 CO ₂ + 0.05 H ₂ + 0.93 WATER + 0.02 FORMICAC + 0.05 GCH ₄ + 0.05 GH ₂ + 0.61 C	79.84	6.41	0
	3	CELLA → LEVOGLUC	41.80	0.52	1
	4	CELL → 5 WATER + 6 C	129.58	7.78	0
Hemicellulose	1	xYHW → 0.35 HEM1 + 0.65 HEM2	119.13	10.00	0
	2	HEM1 → 0.6 xYLOSAN + 0.2 ACETOL + 0.12 GLYOxAL + 0.2 FURFURAL + 0.4 WATER + 0.08 GH ₂ + 0.16 CO	45.98	0.48	1
	3	HEM1 → 0.4 WATER + 0.79 CO ₂ + 0.05 FORMICAC + 0.69 CO + 0.01 GCO + 0.01 GCO ₂ + 0.35 GH ₂ + 0.3 FORMALDY + 0.9 GCOH ₂ + 0.625 GCH ₄ + 0.375 GC ₂ H ₄ + 0.875 C	12.54	-2.74	1
	4	HEM2 → 0.2 WATER + 0.275 CO + 0.275 CO ₂ + 0.5 FORMALDY + 0.1 ETHANOL + 0.05 HAA + 0.35 ACETICAC + 0.025 FORMICAC + 0.25 GCH ₄ + 0.3 GCH ₃ OH + 0.225 GC ₂ H ₄ + 0.4 GCO ₂ + 0.725 GCOH ₂ + C	131.67	9.70	0
Lignin	1	LIGNIN-C → 0.35 LIGN-CC + 0.1 CMRYLALC + 0.08 PHENOL + 0.41 C ₂ H ₄ + WATER + 0.7 GCOH ₂ + 0.3 FORMALDY + 0.32 CO + 0.495 GCH ₄ + 5.735 C	155.50	11.00	0
	2	LIGNIN-H → LIGN-OH + 0.5 NPROPALD + 0.5 C ₂ H ₄ + 0.25 HAA	156.75	12.83	0
	3	LIGNIN-O → LIGN-OH + CO ₂	106.59	8.52	0
	4	LIGN-CC → 0.3 CMRYLALC + 0.2 PHENOL + 0.35 HAA + 0.7 WATER + 0.65 GCH ₄ + 0.6 GC ₂ H ₄ + GCOH ₂ + 0.4 CO + 0.4 GCO + 6.75 C	103.66	4.00	0
	5	LIGN-OH → LIG + 0.9 WATER + 0.1 CH ₄ + 0.6 METHANOL + 0.1 GH ₂ + 0.3 GCH ₃ OH + 0.05 CO ₂ + 0.55 CO + 0.6 GCO + 0.05 FORMICAC + 0.85 GCOH ₂ + 0.35 GCH ₄ + 0.2 GC ₂ H ₄ + 4.15 C	125.40	8.00	0
	6	LIG → 0.7 SYNAPALD + 0.3 ANISOLE + 0.3 CO + 0.3 GCO + 0.3 ACETALDY	50.16	0.60	1
	7	LIG → 0.6 WATER + 0.4 CO + 0.2 CH ₄ + 0.4 FORMALDY + 0.2 GCO + 0.4 GCH ₄ + 0.5 GC ₂ H ₄ + 0.4 GCH ₃ OH + 2 GCOH ₂ + 6 C	33.44	-1.08	1
	8	LIG → 0.6 WATER + 2.6 CO + 1.1 CH ₄ + 0.4 FORMALDY + C ₂ H ₄ + 0.4 METHANOL	101.57	7.00	0
Extractives	1	TGL → ACROLEIN + 3 FFA	191.03	12.85	0
	2	TANN → PHENOL + ITANN	41.80	1.30	0
	3	ITANN → 6 C + 3 CO + 3 WATER	104.50	3.00	0

Tab. 27: Reaction network from Debiagi et al. [265]. In reaction 1 of hemicellulose, first set of values assumes xylan-rich hemicellulose, based on the conclusions of Peng and Wu [74], while second set assumes cereal structure. Source: [159].

Group	#		E _a (kJ/mol)	log ₁₀ [A (s ⁻¹)]	T ⁿ
Cellulose	1	CELL → CELLA	196.46	14.18	0
	2	CELLA → 0.05 3HYDPROP + 0.4 HAA + 0.03 GLYOxAL + 0.17 ACETALDY + 0.25 HMF + 0.35 NPROPALD + 0.2 METHANOL + 0.15 FORMALDY + 0.49CO + 0.43CO ₂ + 0.13H ₂ + 0.93 WATER + 0.02 FORMICAC + 0.05 CH ₄ + 0.66 C + 0.05 GCO + 0.05 GCOH ₂ L + 0.1 GH ₂	79.84	6.40	0
	3	CELLA → LEVOGLUC	41.80	0.52	1
	4	CELL → 0.125 H ₂ + 4.45 WATER + 5.45 C + 0.12 GCOH ₂ S + 0.25 GCO + 0.18 GCOH ₂ L + 0.125 GH ₂	129.58	7.95	0
Hemicellulose	1	xYHW → 0.35/0.12 HEM1 + 0.65/0.88 HEM2	131.25	11.10	0
	2	HEM1 → 0.06 3HYDPROP + 0.16 FURFURAL + 0.1 GLYOxAL + 0.13 HMF + 0.09 CO ₂ + 0.02 H ₂ + 0.54 WATER + 0.25 LEVOGLUC + 0.1 CH ₄ + 0.25 xyLOSAN + 0.1 C	53.92	1.20	1
	3	HEM1 → 0.4 FORMALDY + 0.49 CO + 0.39 CO ₂ + 0.1 H ₂ + 0.4 WATER + 0.05 FORMICAC + 0.1 C ₂ H ₄ + 0.3 CH ₄ + 0.975 C + 0.37GCOH ₂ S + 0.51 GCO ₂ + 0.01 GCO + 0.325 GCH ₄ + 0.075 GC ₂ H ₄ + 0.43 GCOH ₂ L + 0.05 GH ₂ + 0.2 GC ₂ H ₆	15.05	-2.52	1
	4	HEM2 → 0.145 FURFURAL + 0.105 ACETICAC + 0.035 HAA + 0.3 CO + 0.5125 CO ₂ + 0.5505 H ₂ + 0.056 WATER + 0.0175 FORMICAC + 0.049 ETHANOL + 0.1895 CH ₄ + 0.7125 C + 0.78 GCOH ₂ S + 0.45 GCO ₂ + 0.105 GCH ₃ OH + 0.05 GCH ₄ + 0.1GC ₂ H ₄ + 0.18 GCOH ₂ L + 0.21 GH ₂ + 0.2 GC ₂ H ₆	127.49	9.85	0
Lignin	1	LIGC → 0.1 ANISOLE + 0.22 FORMALDY + 0.21 CO + 0.1 CO ₂ + WATER + 0.27 C ₂ H ₄ + 0.1 VANILLIN + 0.35 LIGCC + 5.85 C + 0.4 GCOH ₂ S + 0.36 GCH ₄ + 0.17 GCOH ₂ L + 0.1 GH ₂ + 0.2 GC ₂ H ₆	155.50	11.00	0
	2	LIGH → 0.2 HAA + 0.5 NPROPALD + 0.1 CO + 0.4 C ₂ H ₄ + 0.1 C ₂ H ₆ + LIGOH	156.75	12.83	0
	3	LIGO → LIGOH + CO ₂	106.59	8.52	0
	4	LIGCC → 0.15 ANISOLE + 0.35 HAA + 1.15 CO + 0.7 H ₂ + 0.7 WATER + 0.3 C ₂ H ₄ + 0.45 CH ₄ + 0.25 VANILLIN + 0.15 CRESOL + 0.4 C ₂ H ₆ + 6.8 C + 0.4 GCO	103.66	4.00	0
	5	LIGOH → 0.025 HMWL + 0.1 ACROLEIN + 0.6 CH ₃ OH + 0.65 CO + 0.05 CO ₂ + WATER + 0.05 FORMICAC + 0.1 CH ₄ + 0.9 LIG + 4.25 C + 0.4 GCOH ₂ S + 0.6 GCO + 0.3 GCH ₃ OH + 0.25 GCH ₄ + 0.1 GC ₂ H ₄ + 0.45 GCOH ₂ L + 0.15 GC ₂ H ₆	125.40	8.00	0
	6	LIG → 0.1 ANISOLE + 0.3 ACETALDY + 0.6 CO + 0.5 C ₂ H ₄ + VANILLIN + 0.1 C	50.16	0.60	1
	7	LIG → 0.4 METHANOL + 0.4 FORMALDY + 2.6 CO + 0.6 WATER + 0.75 C ₂ H ₄ + 0.6 CH ₄ + 0.5 C ₂ H ₆ + 4.5 C	131.67	9.18	0
	8	LIG → 0.4 FORMALDY + 0.3 CO + 0.1 CO ₂ + 0.6 WATER + 0.2 CH ₄ + 6.1 C + 0.65 GCOH ₂ L + 0.2 GCO + 0.4 GCH ₃ OH + 0.4 GCH ₄ + 0.5 GC ₂ H ₄ + 1.25 GCOH ₂ L + 0.1 GH ₂	33.44	-1.08	1
Extractives	1	TGL → ACROLEIN + 0.5 U ₂ ME ₁₂ + 2.5 MLINO	191.03	12.85	0
	2	TANN → WATER + 0.85 PHENOL + ITANN + GCO + 0.15 GC ₆ H ₅ OH	41.80	1.30	0
	3	ITANN → 2 CO + WATER + 5 C + 0.45 GCOH ₂ S + 0.55 GCOH ₂ L	104.50	3.00	0

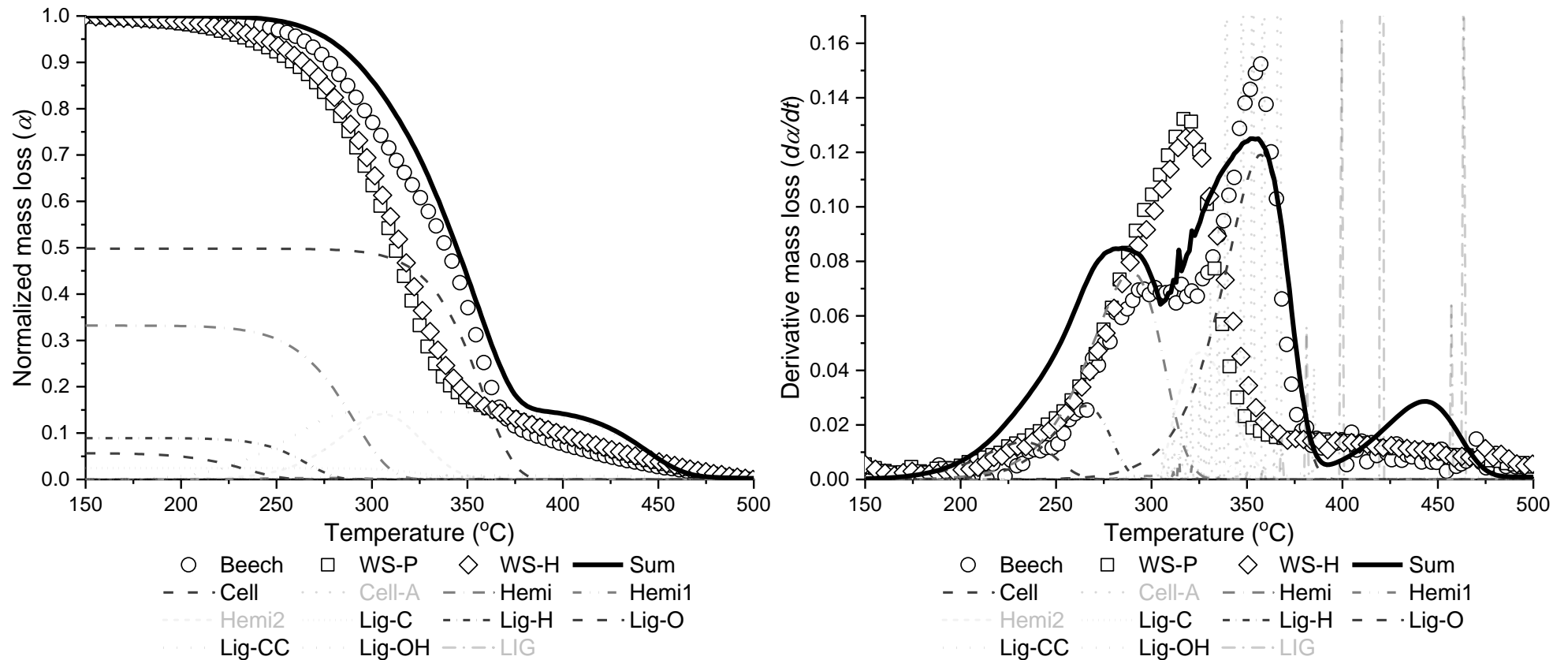


Fig. 20: Comparison of the degradation profiles of the feedstocks (10 K/min) with the decomposition patterns by Ranzi et al. (2008) [80]: mass loss (left) and derivative mass loss (right). Source: [159].

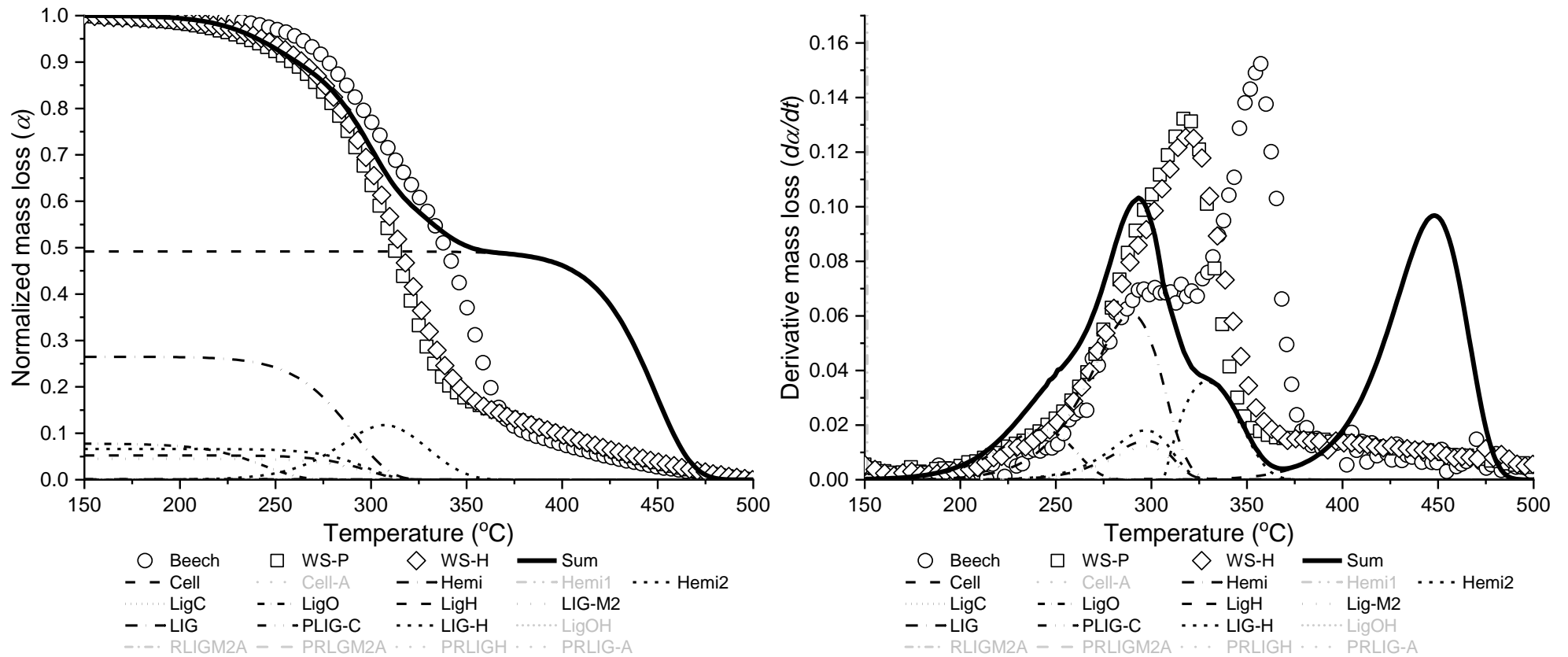


Fig. 21: Comparison of the degradation profiles of the feedstocks (10 K/min) with the holocellulosic decomposition patterns by Ranzi et al. (2008) [80], and the lignin degradation patterns by Faravelli et al. [79], modified by Peters et al. [82]: mass loss (left) and derivative mass loss (right). Source: [159].

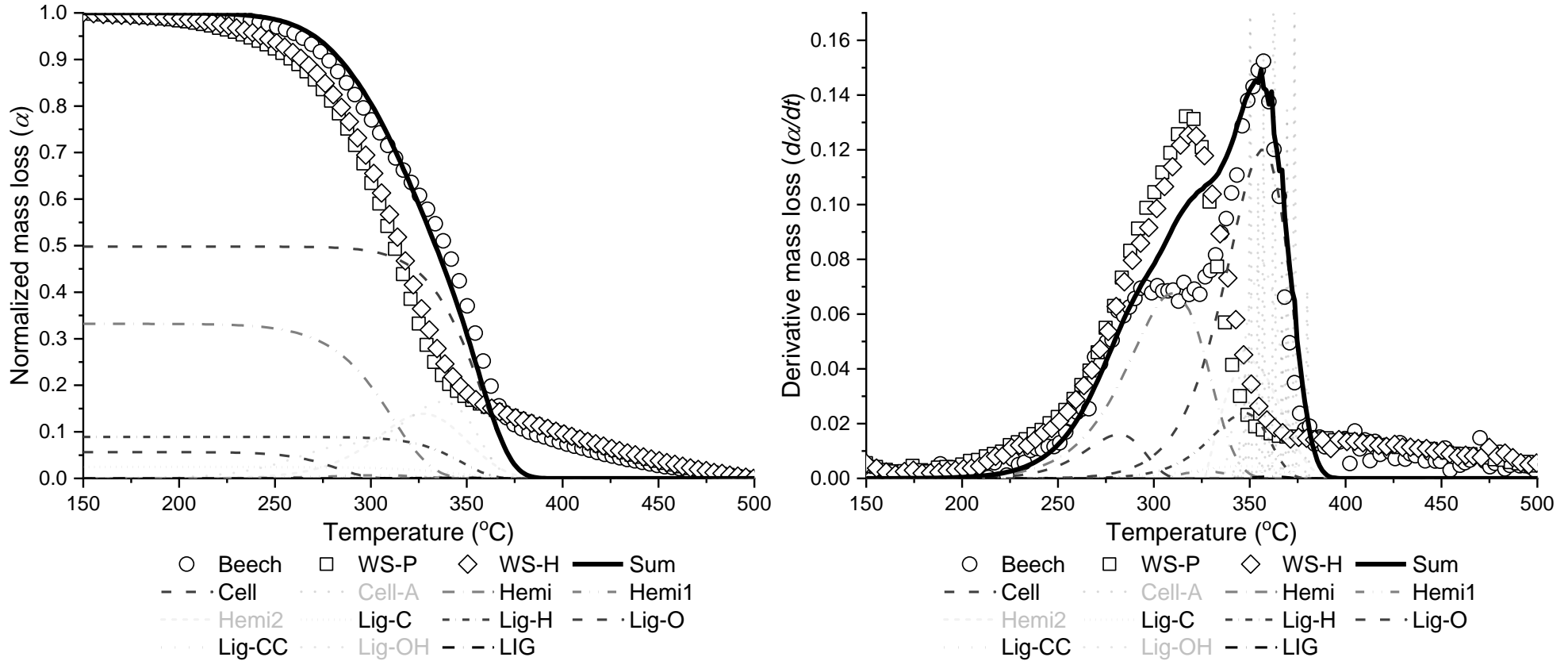


Fig. 22: Comparison of the degradation profiles of the feedstocks (10 K/min) with the decomposition patterns by Corbetta et al. [114]: mass loss (left) and derivative mass loss (right). Source: [159].

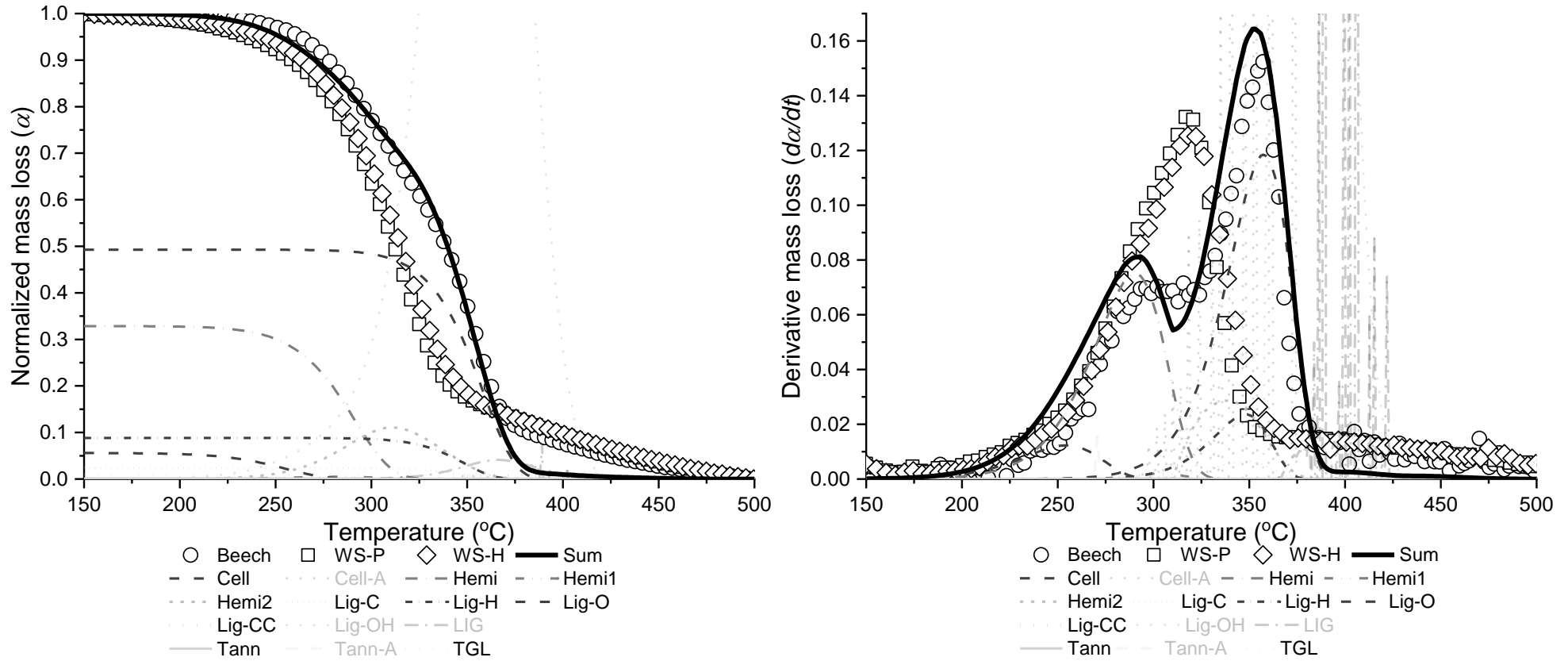


Fig. 23: Comparison of the degradation profiles of the feedstocks (10 K/min) with the decomposition patterns by Anca-Couce and Scharler [119]: mass loss (left) and derivative mass loss (right). Source: [159].

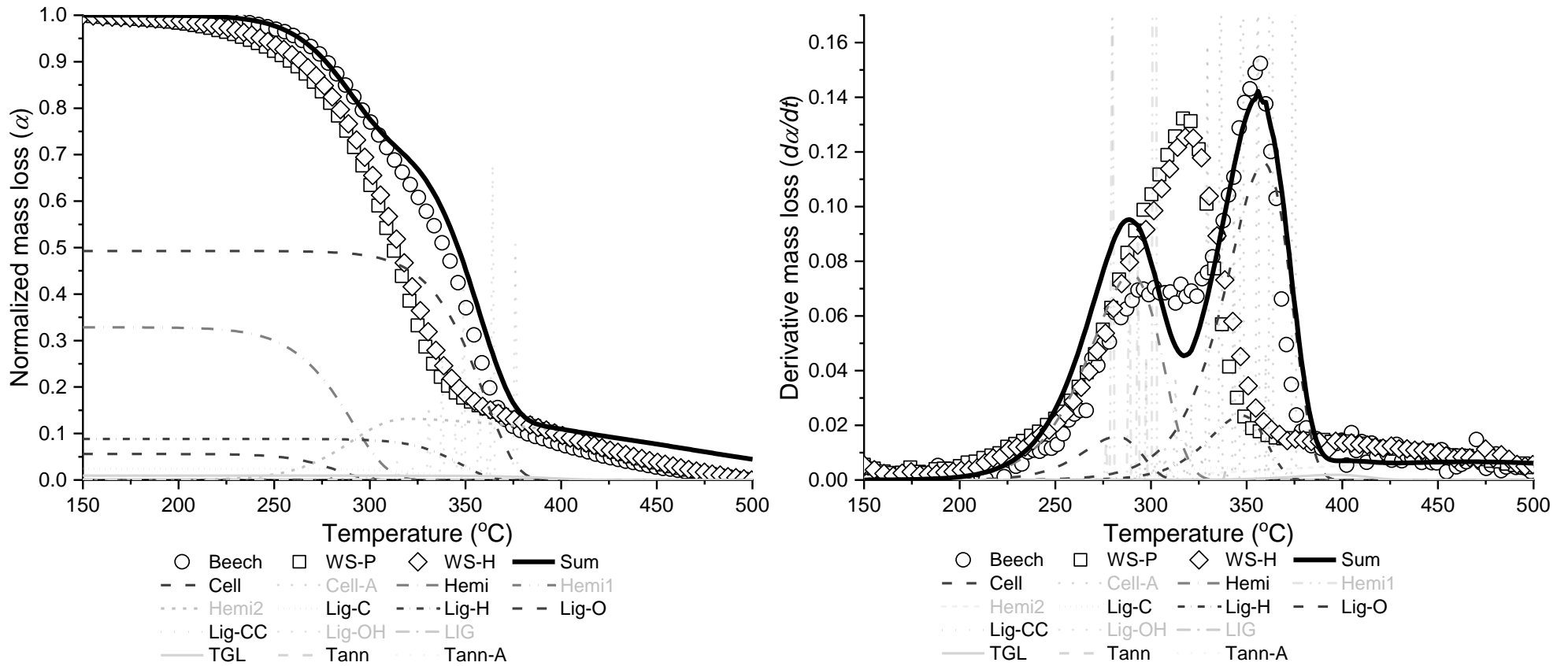


Fig. 24: Comparison of the degradation profiles of the feedstocks (10 K/min) with the decomposition patterns by Ranzi et al. (2017a) [117]: mass loss (left) and derivative mass loss (right). Hemicellulose assumed to be xylan-rich based on the conclusions of Peng and Wu [74]. Source: [159].

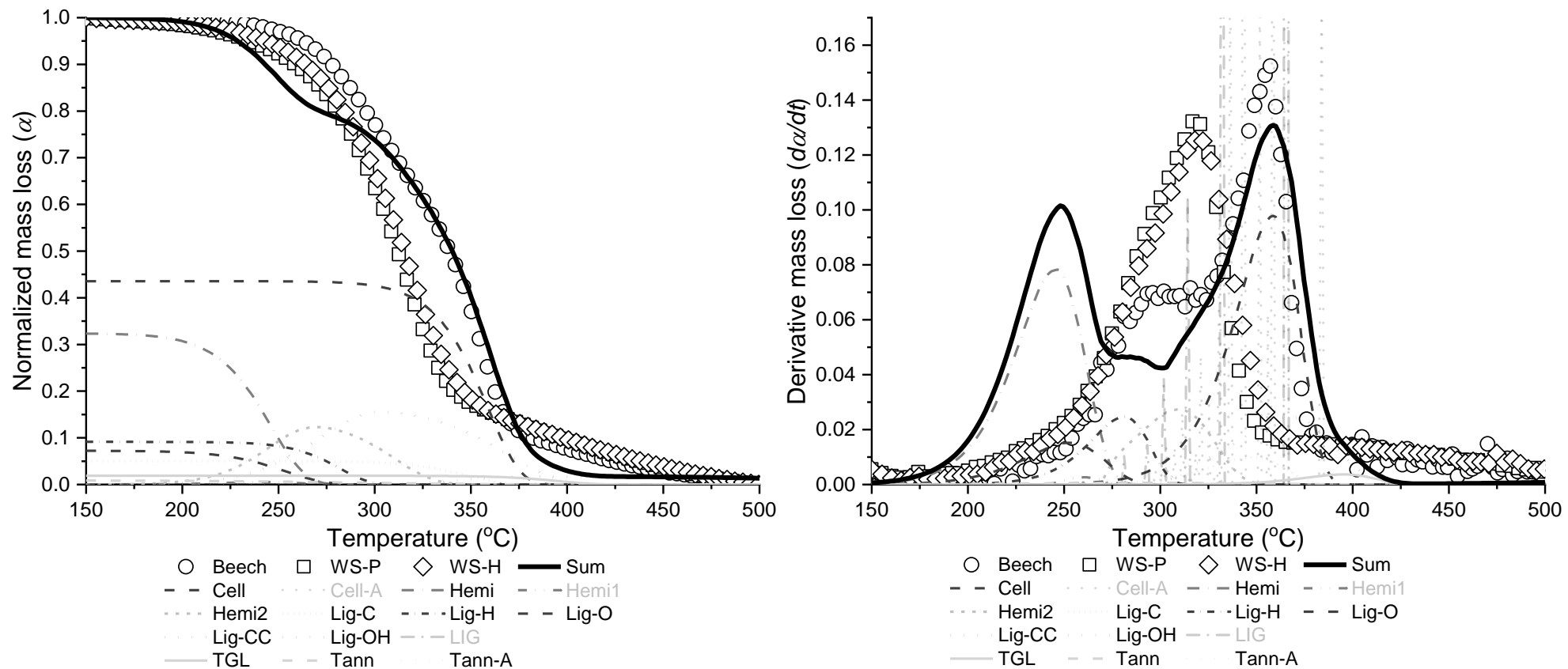


Fig. 25: Comparison of the degradation profiles of the feedstocks (10 K/min) with the decomposition patterns by Ranzi et al. (2017b) [65]: mass loss (left) and derivative mass loss (right). Hemicellulose assumed to be xylan-rich based on the conclusions of Peng and Wu [74]. Source: [159].

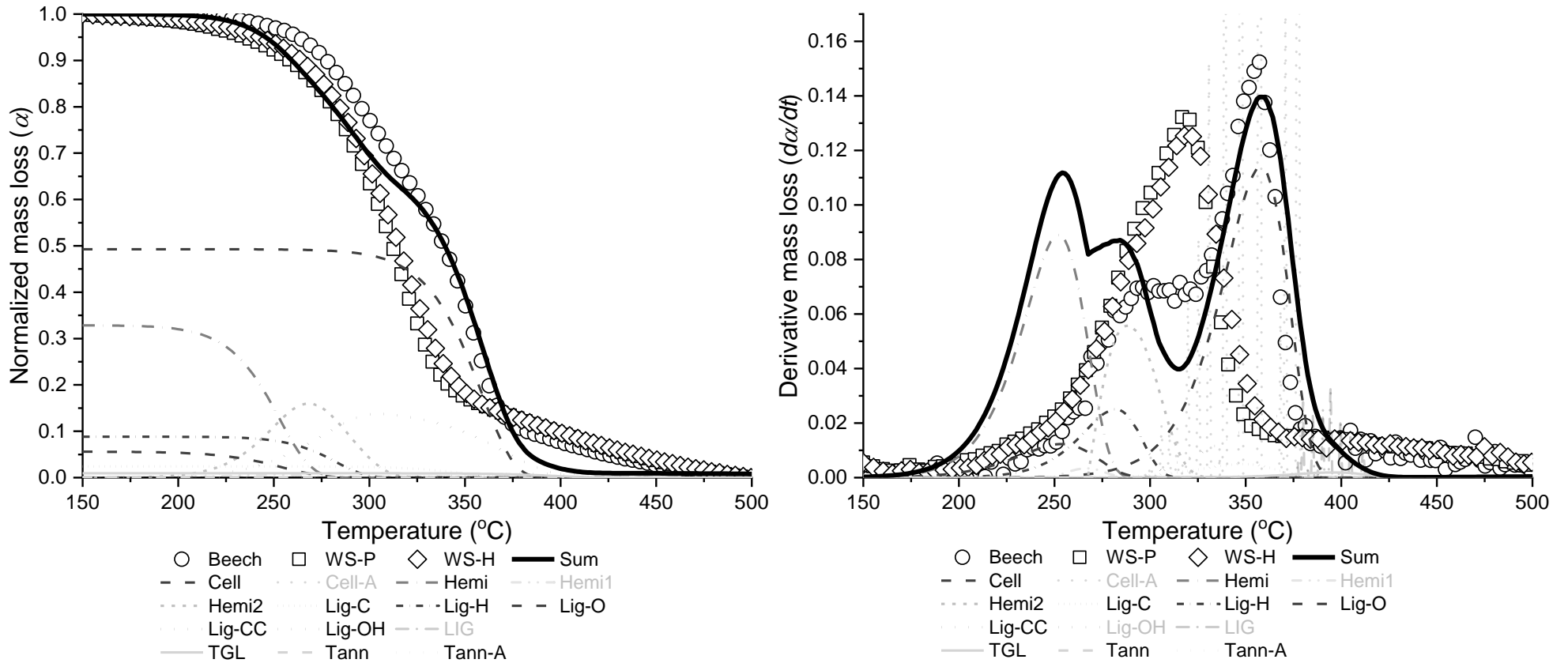


Fig. 26: Comparison of the degradation profiles of the feedstocks (10 K/min) with the decomposition patterns by Debiagi et al. [265]: mass loss (left) and derivative mass loss (right). Hemicellulose assumed to be xylan-rich based on the conclusions of Peng and Wu [74]. Source: [159].

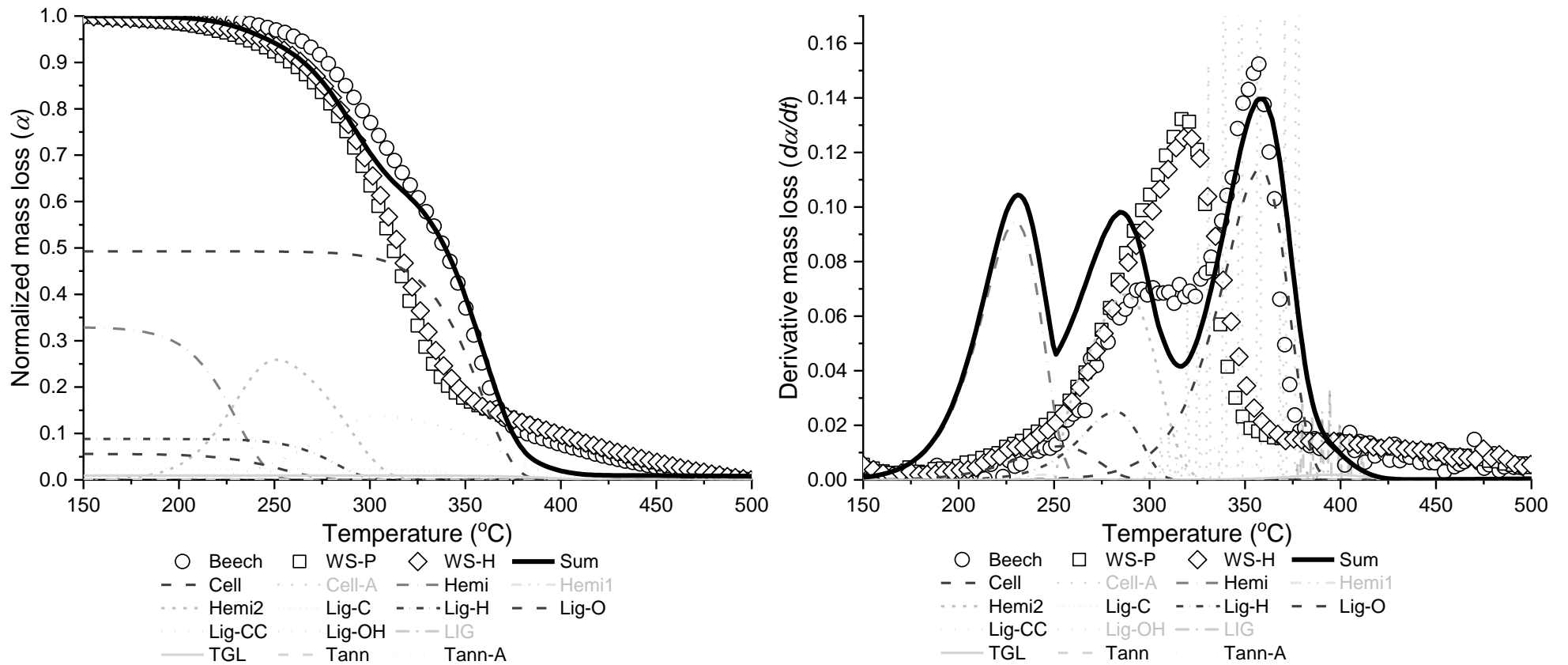


Fig. 27: Comparison of the degradation profiles of the feedstocks (10 K/min) with the decomposition patterns by Debiagi et al. [265]: mass loss (left) and derivative mass loss (right). Hemicellulose assumed to be cereal-type. Source: [159].

Appendix D

List of components

Tab. 28: List of solid components included in the simulation.

	ID	Name	Formula
Heat Carrier	SAND	Sand	SiO ₂
	ASH	Ash	-
	C	Carbon (coke)	C
Bio-Macromolecules	CELLULOS	Cellulose	C ₆ H ₁₀ O ₅
	CELL-ACT	Active Cellulose	C ₆ H ₁₀ O ₅
	HEMICELL	Hemicellulose	C ₅ H ₁₀ O ₄
	HEMCELL1	Active Hemicellulose 1	C ₅ H ₁₀ O ₄
	HEMCELL2	Active Hemicellulose 1	C ₅ H ₁₀ O ₄
	LIGNIN-C	Active Lignin C	C ₁₅ H ₁₄ O ₄
	LIGNIN-H	Active Lignin H	C ₂₂ H ₂₈ O ₉
	LIGNIN-O	Active Lignin O	C ₂₀ H ₂₂ O ₁₀
	LIG	Active Lignin	C ₁₅ H ₁₅ O ₄
	LIGN-CC	Active Lignin CC	C ₁₅ H ₁₄ O ₄
	LIGN-OH	Active Lignin OH	C ₁₉ H ₂₂ O ₈
	TANN	Tannin	C ₁₅ H ₁₂ O ₇
	ITANN	Active Tannin	C ₈ H ₄ O ₄
	TGL	Triglyceride (Trilinolein)	C ₅₇ H ₉₈ O ₆
Delayed Gasification	GCO	Carbon Monoxide	CO
	GCO2	Carbon Dioxide	CO ₂
	GCOH2	Formaldehyde	CH ₂ O
	GH2	Hydrogen	H ₂
	GCH4	Methane	CH ₄
	GC2H4	Ethylene	C ₂ H ₄
	GCH3OH	Methanol	CH ₄ O

Tab. 29: List of gaseous components included in the simulation.

ID	Name	Formula	CAS Number
N2	Nitrogen	N ₂	7727-37-9
H2	Hydrogen	H ₂	1333-74-0
CO	Carbon-Monoxide	CO	630-08-0
CO2	Carbon-Dioxide	CO ₂	124-38-9
CH4	Methane	CH ₄	74-82-8
C2H2	Acetylene	C ₂ H ₂	74-86-2
C2H4	Ethylene	C ₂ H ₄	74-85-1
C2H6	Ethane	C ₂ H ₆	74-84-0
C3H6	Propylene	C ₃ H ₆	115-07-1
C4H6	Cyclobutene	C ₄ H ₆	822-35-5
C5H8	Cis-1,3-Pentadiene	C ₅ H ₈	1574-41-0

Decision on heavy fraction surrogate

Tab. 30: Flash modelling of the separation of ORC/AC/gas surrogates. Test using 3,4,4'-biphenyltriol as heavy fraction in ORC.

Liquid	Vapor	Dev ORC (m/m)	x _{ORC} Water (wt.%)	y _{ORC} Water	x _{ORC} Oxygenates (wt.%)	x _{ORC} Levoglucosan (wt.%)	x _{ORC} Aromatics (wt.%)	x _{ORC} Heavy (wt.%)	Dev AC (m/m)	x _{ORC} AC (wt.%)	y _{AC} Water
NRTL	Ideal	34.6%	0.0%	6.01	2.9%	1.1%	0.0%	93.6%	Absent condensate		0.00
NRTL	Hayden O'Connell	34.1%	0.0%	7.83	3.1%	1.1%	0.1%	93.0%			0.00
NRTL	Redlich-Kwong	34.1%	0.0%	7.83	3.1%	1.1%	0.1%	93.0%			0.00
Modified UNIFAC	Predictive SRK	20.4%	27.4%	1.19	14.4%	2.3%	3.9%	50.9%	24.4%	85.1%	1.01
PR-Boston Mathias	PR-Boston Mathias	18.5%	3.9%	4.30	10.8%	3.4%	5.3%	75.2%	33.1%	96.4%	1.00
UNIFAC	PR-Huron Vidal	24.9%	29.5%	1.12	14.2%	2.2%	3.8%	49.0%	23.6%	84.3%	1.01
UNIFAC-Dortmund	PR-Huron Vidal	17.2%	26.6%	1.21	13.5%	2.4%	4.0%	52.3%	23.4%	84.1%	1.01
UNIFAC	PR-Wong Sandler	47.7%	38.7%	0.74	13.6%	1.9%	3.2%	41.5%	23.6%	84.3%	1.00
UNIFAC-Dortmund	PR-Wong Sandler	45.3%	38.5%	0.76	13.0%	1.9%	3.3%	42.1%	23.5%	84.2%	1.00
Modified UNIFAC	RKS-Huron Vidal mod	12.7%	23.8%	1.31	14.1%	2.5%	4.1%	54.4%	24.1%	84.9%	1.01
UNIFAC-Dortmund	RKS-Huron Vidal mod	10.1%	22.5%	1.35	13.9%	2.5%	4.2%	55.6%	23.8%	84.5%	1.01
Modified UNIFAC	RKS-Wong Sandler mod	47.7%	38.7%	0.74	13.6%	1.9%	3.2%	41.5%	23.6%	84.3%	1.00
UNIFAC-Dortmund	RKS-Wong Sandler mod	45.9%	38.6%	0.75	13.1%	1.9%	3.3%	42.0%	23.6%	84.3%	1.00
SRK	SRK	32.2%	33.9%	1.03	12.9%	2.1%	3.6%	46.3%	24.5%	85.7%	1.01
SRK	SRK-Kabadi Danner	34.7%	33.9%	0.99	12.5%	2.1%	3.6%	45.5%	21.2%	82.0%	0.95
Raoult Law	Ideal Gas	37.9%	0.0%	1.00	0.9%	0.3%	0.0%	98.7%	Absent condensate		0.00
UNIFAC-Dortmund	Redlich-Kwong-Soave BM	34.5%	0.0%	1.32	2.3%	3.8%	0.1%	93.5%			0.00
UNIFAC-Dortmund	Hayden O'Connell	34.5%	0.0%	1.32	2.3%	3.8%	0.1%	93.5%			0.00
UNIFAC	Hayden O'Connell	33.9%	0.0%	0.20	2.5%	4.1%	0.3%	92.7%			0.00
UNIFAC-Lyngby	Ideal	38.2%	0.0%	0.37	0.6%	0.3%	0.0%	99.1%			0.00
UNIFAC	Redlich-Kwong	34.7%	0.0%	0.22	1.6%	4.2%	0.1%	93.8%			0.00
UNIFAC	SRK	34.7%	0.0%	0.22	1.6%	4.2%	0.1%	93.8%			0.00
UNIQUAC	Hayden O'Connell	Absent condensates									
UNIQUAC	Redlich-Kwong										
UNIQUAC	Ideal Gas										
WILSON	Hayden O'Connell	33.9%	0.2%	0.14	2.6%	3.8%	0.3%	92.7%	Absent condensate		0.00
WILSON	Redlich-Kwong	34.7%	0.1%	0.12	1.7%	3.9%	0.1%	93.7%			0.00
WILSON	Ideal Gas	34.8%	0.1%	0.12	1.7%	4.0%	0.1%	93.9%			0.00
Modified UNIFAC	Volume Translated PR	25.0%	30.0%	1.10	14.0%	2.2%	3.8%	49.0%	24.0%	84.8%	1.01

Tab. 31: Flash modelling of the separation of ORC/AC/gas surrogates. Test using HMWL as heavy fraction in ORC.

Liquid	Vapor	Dev ORC (m/m)	x _{ORC} Water (wt.%)	Y _{ORC} Water	x _{ORC} Oxygenates (wt.%)	x _{ORC} Levoglucosan (wt.%)	x _{ORC} Aromatics (wt.%)	x _{ORC} Heavy (wt.%)	Dev AC (m/m)	x _{ORC} AC (wt.%)	Y _{AC} Water
NRTL	Ideal	35.6%	0.0%	1.30	0.5%	2.9%	1.6%	95.0%	Absent condensate		0.00
NRTL	Hayden O'Connell	35.6%	0.0%	1.30	0.5%	2.9%	1.6%	95.0%			0.00
NRTL	Redlich-Kwong	35.5%	0.0%	1.32	0.5%	3.0%	1.6%	94.9%			0.00
Modified UNIFAC	Predictive SRK	11.4%	22.9%	1.20	14.2%	2.5%	4.3%	55.0%	24.4%	85.1%	1.01
PR-Boston Mathias	PR-Boston Mathias	34.5%	0.1%	26.03	0.6%	4.1%	1.6%	93.5%	33.1%	96.4%	1.00
UNIFAC	PR-Huron Vidal	17.7%	26.5%	1.11	13.8%	2.4%	4.0%	52.0%	23.6%	84.3%	1.01
UNIFAC-Dortmund	PR-Huron Vidal	12.0%	9.5%	1.70	10.9%	3.2%	5.3%	69.6%	23.4%	84.1%	1.01
UNIFAC	PR-Wong Sandler	66.9%	43.6%	0.32	13.7%	1.7%	2.9%	36.7%	23.6%	84.3%	1.00
UNIFAC-Dortmund	PR-Wong Sandler	66.0%	43.5%	0.34	13.4%	1.7%	2.9%	36.9%	23.5%	84.2%	1.00
Modified UNIFAC	RKS-Huron Vidal mod	2.3%	15.9%	1.39	12.6%	2.9%	4.6%	62.7%	24.1%	84.9%	1.01
UNIFAC-Dortmund	RKS-Huron Vidal mod	16.3%	5.7%	2.20	10.9%	3.3%	5.5%	73.1%	23.8%	84.5%	1.01
Modified UNIFAC	RKS-Wong Sandler mod	66.8%	43.6%	0.32	13.5%	1.7%	2.9%	36.7%	23.6%	84.3%	1.00
UNIFAC-Dortmund	RKS-Wong Sandler mod	66.8%	43.6%	0.32	13.5%	1.7%	2.9%	36.7%	23.6%	84.3%	1.00
SRK	SRK	40.4%	35.8%	0.88	13.8%	2.0%	3.5%	43.6%	24.5%	85.7%	1.01
SRK	SRK-Kabadi Danner	41.3%	35.5%	0.86	13.7%	2.0%	3.5%	43.4%	21.2%	82.0%	0.95
Raoult Law	Ideal Gas	Absent condensates									
UNIFAC-Dortmund	Redlich-Kwong-Soave BM										
UNIFAC-Dortmund	Hayden O'Connell										
UNIFAC	Hayden O'Connell										
UNIFAC-Lyngby	Ideal										
UNIFAC	Redlich-Kwong										
UNIFAC	SRK										
UNIQUAC	Hayden O'Connell										
UNIQUAC	Redlich-Kwong										
UNIQUAC	Ideal Gas										
WILSON	Hayden O'Connell	37.1%	0.0%	0.45	0.5%	0.6%	1.4%	97.4%	Absent condensate		0.00
WILSON	Redlich-Kwong	37.2%	0.0%	0.45	0.5%	0.6%	1.3%	97.6%			0.00
WILSON	Ideal Gas	38.4%	0.0%	0.41	0.3%	0.1%	0.1%	99.5%			0.00
Modified UNIFAC	Vol Trans PR	38.8%	37.5%	0.77	12.0%	2.0%	3.4%	44.1%	24.0%	84.8%	1.01

Tab. 32: Flash modelling of the separation of ORC/AC/gas surrogates. Test using 3,4,4'-biphenyltriol as heavy fraction in ORC.

Liquid	Vapor	Dev ORC (m/m)	x _{ORC} Water (wt.%)	y _{ORC} Water	x _{ORC} Oxygenates (wt.%)	x _{ORC} Levoglucosan (wt.%)	x _{ORC} Aromatics (wt.%)	x _{ORC} Heavy (wt.%)	Dev AC (m/m)	x _{ORC} AC (wt.%)	y _{AC} Water	
NRTL	Ideal	70.3%	0.0%	0.29	0.3%	0.1%	0.1%	99.5%	Absent condensate		0.00	
NRTL	Hayden O'Connell	70.2%	0.0%	0.31	0.3%	0.5%	0.2%	99.0%			0.00	
NRTL	Redlich-Kwong	70.2%	0.0%	0.31	0.3%	0.5%	0.2%	99.0%			0.00	
Modified UNIFAC	Predictive SRK	28.4%	31.3%	0.96	14.0%	2.2%	3.7%	47.7%	24.4%	85.1%	1.01	
PR-Boston Mathias	PR-Boston Mathias	38.5%	0.2%	12.26	0.1%	0.0%	0.0%	99.6%	33.1%	96.4%	1.00	
UNIFAC	PR-Huron Vidal	62.9%	41.8%	0.46	14.3%	1.7%	3.0%	37.6%	23.6%	84.3%	1.01	
UNIFAC-Dortmund	PR-Huron Vidal	60.8%	41.5%	0.49	14.1%	1.7%	3.0%	38.1%	23.4%	84.1%	1.01	
UNIFAC	PR-Wong Sandler	86.6%	43.3%	0.00	14.3%	1.5%	2.6%	32.8%	23.6%	84.3%	1.00	
UNIFAC-Dortmund	PR-Wong Sandler	86.4%	43.3%	0.00	14.3%	1.5%	2.6%	32.9%	23.5%	84.2%	1.00	
Modified UNIFAC	RKS-Huron Vidal mod	84.3%	42.9%	0.11	14.4%	1.5%	2.7%	33.2%	24.1%	84.9%	1.01	
UNIFAC-Dortmund	RKS-Huron Vidal mod	89.0%	41.6%	0.14	14.0%	1.5%	2.6%	32.4%	23.8%	84.5%	1.01	
Modified UNIFAC	RKS-Wong Sandler mod	72.5%	44.7%	0.00	13.4%	1.6%	2.8%	35.5%	23.6%	84.3%	1.00	
UNIFAC-Dortmund	RKS-Wong Sandler mod	72.5%	44.7%	0.00	13.4%	1.6%	2.8%	35.5%	23.6%	84.3%	1.00	
SRK	SRK	82.2%	43.1%	0.14	14.4%	1.5%	2.7%	33.6%	24.5%	85.7%	1.01	
SRK	SRK-Kabadi Danner	82.3%	43.1%	0.13	14.4%	1.5%	2.7%	33.6%	21.2%	82.0%	0.95	
Raoult Law	Ideal Gas	77.3%	0.0%	1.00	0.3%	0.1%	0.0%	99.5%	Absent condensate			
UNIFAC-Dortmund	Redlich-Kwong-Soave BM	70.3%	0.0%	1.32	0.4%	0.1%	0.0%	99.4%				
UNIFAC-Dortmund	Hayden O'Connell	70.3%	0.0%	1.32	0.4%	0.1%	0.0%	99.4%				
UNIFAC	Hayden O'Connell	70.1%	0.0%	0.20	1.0%	0.1%	0.2%	98.6%				
UNIFAC-Lyngby	Ideal	71.7%	0.0%	0.37	0.4%	0.1%	0.0%	99.5%				
UNIFAC	Redlich-Kwong	69.7%	0.0%	0.22	1.6%	0.2%	0.2%	97.5%				
UNIFAC	SRK	69.7%	0.0%	0.22	1.6%	0.2%	0.2%	97.5%				
UNIQUAC	Hayden O'Connell	70.1%	0.0%	0.32	0.9%	0.2%	0.1%	98.7%				
UNIQUAC	Redlich-Kwong	69.7%	0.0%	0.35	1.5%	0.6%	0.1%	97.4%				
UNIQUAC	Ideal Gas	77.1%	0.0%	0.33	0.7%	0.2%	0.0%	99.0%				
WILSON	Hayden O'Connell	70.3%	0.0%	0.29	0.3%	0.1%	0.1%	99.5%				
WILSON	Redlich-Kwong	70.1%	0.0%	0.31	0.6%	0.3%	0.1%	98.8%				
WILSON	Ideal Gas	38.5%	0.0%	0.20	0.2%	0.1%	0.0%	99.7%				
Modified UNIFAC	Vol Trans PR	Absent condensate								24.0%	84.8%	1.01

Thermophysical property values

Tab. 33: Comparison of normal boiling point estimation methods for the components in the simulation. Values in °C.

ID	Experimental	ACD/Labs ^a	Stein & Brown [372]		Joback [325]		Mani	Gani [326]	Cordes et al. [327]	TDE
			This work ^b	Fonts [264]	This work	Fonts [264]				
ACETALDY	20.2 [276]	18.6	33.8	n.a.	20.7	n.a.	19.7	-9.4	16.7	20.6
ACETICAC	118.1 [276]	117.1	145.0	122.4	117.5	117.7	120.5	116.3	116.1	117.8
ACETOL	145.5 [264]	145.5	n.a.	136.0	140.9	141.1	128.8	151.8	158.9	151.3
ACETONE	56.2 ^c	46.5	44.8	n.a.	48.8	n.a.	n.a.	32.2	45.3	56.1
ACROLEIN	52.6 [373]	52.8	57.9	n.a.	40.2	n.a.	n.a.	35.5	53.4	52.3
ANISOLE	154.1 [374]	153.6	149.2	n.a.	135.5	n.a.	n.a.	158.5	159.4	153.6
CMRYLALC	323.5 ^d	323.5	389.2	n.a.	335.8	n.a.	n.a.	277.9	313.8	335.8
CRESOL	190.8 [276]	202.0	190.8	n.a.	162.7	n.a.	n.a.	199.2	131.1	202.0
EG	197.3 [276]	197.5	153.5	n.a.	156.4	n.a.	164.8	158.7	185.0	197.4
EGACET	181.7 [375]	183.0	n.a.	n.a.	151.6	n.a.	174.8	168.9	167.3	187.7
ETHANOL	78.3 [276]	72.6	65.1	n.a.	64.2	n.a.	n.a.	56.9	64.1	78.3
FFA	229.5 [276]	360.6	389.2	n.a.	491.9	n.a.	n.a.	353.6	417.6	348.0
FORMALDY	-19.3 [376]	-19.5	9.5	n.a.	-2.9	n.a.	n.a.	-58.9	-7.6	-19.2
FORMICAC	100.8 [276]	100.6	100.9	101.0	93.9	94.2	n.a.	87.3	104.3	101.2
FURFURAL	161.8 [276]	161.8	143.8	156.6	139.5	139.7	492.5	138.4	166.3	161.6
GLYOXAL	50.5 [373]	50.0	97.9	n.a.	69.3	n.a.	n.a.	82.7	100.9	n.a.
GUAIACOL	205.1 [373]	205.0	211.4	211.5	216.1	216.4	212.7	234.6	221.8	204.3
HAA	n.a.	131.3	126.4	126.4	112.9	113.1	161.0	124.2	142.9	n.a.
HEXADEC	287.5 [276]	286.6	277.1	n.a.	292.3	n.a.	288.9	276.0	278.7	286.9
HMF	199.0 [373]	270.1	n.a.	n.a.	220.1	n.a.	254.1	211.4	405.8	253.6
HMWL	n.a.	n.a.	n.a.	n.a.	1526.4	n.a.	n.a.	568.9	703.4	1909.6
KETENE	-56.0 [276]	-56.0	-50.2	n.a.	19.8	n.a.	-59.2	4.8	94.9	-49.8
LEVOGLUC	385.0 [261]	383.8	313.8	313.8	402.0	402.2	353.5	278.1	291.8	n.a.
METCSONE	157.6 [373]	157.5	154.0	n.a.	155.4	n.a.	166.2	158.2	145.2	142.9
METHANOL	64.7 [276]	48.1	39.4	n.a.	41.3	n.a.	59.5	15.4	48.8	64.5
MF	187.1 [373]	187.0	165.7	n.a.	167.4	n.a.	n.a.	154.3	176.7	167.4
PHENOL	181.9 [276]	165.9	170.0	170.1	134.8	166.1	175.3	177.0	167.7	181.8
SYNAPALD	n.a.	372.3	336.1	n.a.	370.4	n.a.	n.a.	346.9	367.2	346.9
SYRINGOL	261.9 [377] ^e	264.5	249.1	249.1	266.4	266.6	251.6	279.6	320.3	261.4
VANILLIN	285.0 [276]	282.6	274.3	268.4	292.7	292.9	297.6	299.5	288.3	290.5
VINYLKET	n.a.	38.9	14.7	n.a.	73.0	n.a.	n.a.	62.2	252.4	58.7
XYLOSAN	n.a.	318.8	247.4	n.a.	282.9	n.a.	n.a.	218.3	230.3	282.9
Average deviation		10.5 ± 11.7	26.5 ± 17.0		27.9 ± 22.3		34.8 ± 45.9	29.5 ± 16.3	34.6 ± 25.8	10.8 ± 11.2
Av. Dev. Non-Aromatics		8.1 ± 12.7	24.0 ± 18.7		26.6 ± 27.0		5.2 ± 4.8	29.7 ± 19.3	27.6 ± 24.4	8.2 ± 11.6
Av. Dev. Aromatics		9.2 ± 13.8	14.4 ± 15.2		15.3 ± 12.7		37.5 ± 62.7	13.0 ± 11.8	29.1 ± 40.5	7.7 ± 10.7

n.a.: not available/not estimated/value considered unviable.

a: Commercial property estimation software that uses undisclosed methods. Values obtained from the database www.chemspider.com.

b: Values obtained from the database www.chemspider.com using a modified Stein & Brown method.

c: Sourced from the NIST database, averaged from several literature sources.

d: Data from the supplier.

e: Estimation using PC-SAFT based on vapor pressure.

Tab. 34: Comparison of critical temperature estimation methods for the components in the simulation. Values in °C.

ID	Experimental	Joback [325]		Gani [326]	Lydersen [328]		Fedors [329]	Ambrose [330]	Klincewicz and Reid [331]	Mani	Nannoolal et al. [332]	Gorenssek	TDE
		This work	Fonts [264]		This work	Fonts [264]							
ACETALDY	192.9 [276]	192.1	n.a.	149.2	193.0	n.a.	188.1	304.4	184.3	n.a.	190.6	n.a.	191.0
ACETICAC	318.8 [276]	314.1	314.7	313.0	317.9	318.5	313.9	317.0	318.3	286.9	302.2	n.a.	321.6
ACETOL	n.a.	315.9	322.4	317.2	316.1	322.6	342.0	343.0	349.1	456.9	355.1	n.a.	342.9
ACETONE	234.9 ^a	227.1	n.a.	217.0	229.4	n.a.	235.8	220.4	221.7	n.a.	220.9	n.a.	234.9
ACROLEIN	n.a.	216.5	n.a.	200.0	213.5	n.a.	223.5	211.9	209.9	n.a.	260.3	n.a.	254.9
ANISOLE	373.0 [378]	346.3	n.a.	368.0	357.4	n.a.	356.7	343.4	336.0	n.a.	380.0	n.a.	373.0
CMRYLALC	n.a.	550.5	n.a.	510.5	542.3	n.a.	517.6	606.2	611.7	n.a.	568.3	518.3	606.2
CRESOL	431.5 [276]	388.3	n.a.	432.0	372.7	n.a.	385.7	377.8	374.3	n.a.	352.1	n.a.	431.4
EG	446.6 [276]	316.1	n.a.	320.0	315.7	n.a.	339.0	390.4	372.7	439.6	344.1	n.a.	446.3
EGACET	n.a.	344.0	n.a.	338.7	316.6	n.a.	362.5	334.6	359.3	372.7	349.9	n.a.	386.9
ETHANOL	240.8 [378]	226.0	n.a.	216.1	227.3	n.a.	231.1	213.5	245.3	n.a.	229.0	n.a.	241.4
FFA	522.9 [379]	677.8	n.a.	525.2	671.3	n.a.	547.5	673.9	810.9	n.a.	729.5	n.a.	513.9
FORMALDY	134.9 [276]	137.1	n.a.	147.5	141.4	n.a.	122.5	139.6	130.4	n.a.	163.7	n.a.	145.0
FORMICAC	314.9 [276]	288.1	298.9	300.7	296.2	307.2	278.0	281.4	287.3	n.a.	295.3	n.a.	314.9
FURFURAL	397.0 [264]	352.0	385.7	382.7	350.4	384.0	353.3	428.3	343.5	242.0	392.6	n.a.	384.9
GLYOXAL	n.a.	252.6	n.a.	273.0	250.7	n.a.	283.6	257.5	250.7	n.a.	324.4	n.a.	n.a.
GUAIACOL	n.a.	443.5	427.3	474.3	440.1	424.0	467.4	432.4	447.1	420.9	452.2	n.a.	420.9
HAA	n.a.	283.7	303.3	298.1	282.6	302.2	313.0	285.3	311.7	408.0	356.0	n.a.	n.a.
HEXADDEC	449.9 [276]	451.1	n.a.	443.4	447.6	n.a.	448.6	456.2	538.1	445.6	553.7	n.a.	449.2
HMF	n.a.	449.1	n.a.	424.6	446.7	n.a.	469.8	541.7	452.4	521.3	295.9	n.a.	452.9
HMWL	n.a.	2495.7	n.a.	750.6	2095.0	n.a.	839.5	1828.3	2205.5	n.a.	677.6	n.a.	4738.1
KETENE	n.a.	192.5	n.a.	212.8	198.1	n.a.	177.3	217.7	183.4	270.3	337.3	n.a.	127.9
LEVOGLUC	n.a.	583.6	562.1	457.4	577.6	556.2	470.1	741.8	703.0	532.7	291.3	n.a.	n.a.
METC5ONE	n.a.	358.3	n.a.	349.0	350.7	n.a.	345.8	359.5	340.3	n.a.	370.4	n.a.	413.9
METHANOL	239.5 [276]	202.3	n.a.	167.8	204.3	n.a.	192.5	181.2	215.3	252.5	220.4	n.a.	239.5
MF	n.a.	378.8	n.a.	351.4	377.4	n.a.	374.4	416.5	380.6	n.a.	395.3	n.a.	378.8
PHENOL	421.1 [276]	422.3	422.4	414.7	350.1	422.0	425.4	350.9	337.3	409.0	402.8	n.a.	421.1
SYNAPALD	n.a.	595.9	n.a.	572.0	618.8	n.a.	573.5	592.0	651.2	n.a.	537.4	564.8	572.0
SYRINGOL	n.a.	481.3	480.9	519.1	475.5	475.1	502.9	456.5	469.4	471.4	488.8	n.a.	483.9
VANILLIN	n.a.	520.4	509.7	535.3	514.4	503.8	514.9	520.3	550.5	494.2	530.6	n.a.	508.9
VINYLKET	n.a.	253.0	n.a.	248.5	255.0	n.a.	259.3	260.7	253.9	n.a.	539.4	n.a.	266.9
XYLOSAN	n.a.	454.8	n.a.	413.1	462.4	n.a.	392.1	556.0	n.a.	n.a.	358.0	471.2	454.8
Average deviation		35.5 ± 31.8		25.1 ± 22.8	39.6 ± 33.1		25.7 ± 20.7	46.4 ± 33.6	54.6 ± 48.7	37.2 ± 57.1	85.7 ± 71.6		2.7 ± 2.7
Av. Dev. Non-Aromatics		18.1 ± 19.9		15.5 ± 14.9	17.2 ± 19.4		11.9 ± 12.1	22.1 ± 20.0	25.4 ± 29.9	2.7 ± 3.4	33.3 ± 31.9		1.2 ± 1.3
Av. Dev. Aromatics		10.6 ± 12.7		2.4 ± 3.1	17.4 ± 19.5		10.0 ± 12.2	16.8 ± 18.4	21.0 ± 22.5	15.2 ± 29.1	45.5 ± 67.8		1.1 ± 2.3

n.a.: not available/not estimated/value considered unviable.

a: Sourced from the NIST database, averaged from several literature sources.

Tab. 35: Comparison of critical pressure estimation methods for the components in the simulation. Values in bar.

ID	Experimental	Joback [325]		Gani [326]	Lydersen [328]		Ambrose [330]	Nannoolal et al. [332]	Gorenssek	TDE
		This work	Fonts [264]		This work	Fonts [264]				
ACETALDY	55.70 [276]	56.03	n.a.	53.98	55.48	n.a.	38.99	59.13	n.a.	60.08
ACETICAC	57.40 [276]	57.31	57.50	59.08	65.07	65.10	58.29	50.03	n.a.	56.32
ACETOL	n.a.	54.79	54.80	50.20	57.35	57.40	42.24	56.07	n.a.	55.31
ACETONE	48.00 ^a	48.02	n.a.	48.80	50.08	n.a.	34.42	46.43	n.a.	47.04
ACROLEIN	n.a.	51.76	n.a.	50.28	49.99	n.a.	40.82	54.32	n.a.	62.98
ANISOLE	42.22 [378]	40.26	n.a.	41.29	40.20	n.a.	39.77	38.79	n.a.	42.09
CMRYLALC	n.a.	47.04	n.a.	38.40	40.98	n.a.	43.83	49.97	56.90	43.83
CRESOL	51.50 [276]	52.06	n.a.	50.75	36.40	n.a.	50.46	54.08	n.a.	40.78
EG	77.10 [276]	66.53	n.a.	59.08	75.28	n.a.	93.94	96.31	n.a.	82.31
EGACET	n.a.	48.70	n.a.	42.72	43.85	n.a.	45.54	46.02	n.a.	44.31
ETHANOL	61.70 [380]	57.57	n.a.	55.57	64.00	n.a.	60.13	60.08	n.a.	62.26
FFA	124.00 [379]	13.19	n.a.	12.94	14.14	n.a.	12.55	63.54	n.a.	15.46
FORMALDY	65.90 [276]	69.91	n.a.	77.90	67.77	n.a.	48.73	74.02	n.a.	69.34
FORMICAC	58.10 [276]	71.70	53.80	81.48	85.16	49.20	44.68	60.96	n.a.	120.96
FURFURAL	56.60 [264]	53.83	53.80	51.39	49.25	49.20	144.66	49.26	n.a.	46.17
GLYOXAL	n.a.	62.79	n.a.	62.02	58.81	n.a.	57.46	71.10	n.a.	n.a.
GUAIACOL	n.a.	49.11	49.10	48.59	47.28	47.30	50.11	45.61	n.a.	40.94
HAA	n.a.	64.62	64.60	60.53	66.44	66.40	53.21	70.78	n.a.	n.a.
HEXADEC	14.10 [276]	13.18	n.a.	13.44	14.54	n.a.	14.48	13.81	n.a.	14.48
HMF	n.a.	67.85	n.a.	47.94	66.52	n.a.	202.07	3473.49	n.a.	52.36
HMWL	n.a.	9.78	n.a.	7.87	10.27	n.a.	11.01	1.29	n.a.	11.59
KETENE	n.a.	60.37	n.a.	73.11	62.13	n.a.	62.98	55.05	n.a.	52.23
LEVOGLUC	n.a.	56.96	57.00	48.34	45.32	45.30	43.04	36.68	n.a.	n.a.
METC5ONE	n.a.	43.00	n.a.	46.78	63.13	n.a.	n.a.	40.78	n.a.	44.83
METHANOL	61.20 [276]	66.97	n.a.	65.09	82.58	n.a.	72.51	71.79	n.a.	80.56
MF	n.a.	46.03	n.a.	42.17	41.84	n.a.	101.61	41.52	n.a.	46.03
PHENOL	60.60 [276]	59.26	59.30	60.10	61.62	61.60	61.41	57.55	n.a.	53.86
SYNAPALD	n.a.	34.00	n.a.	25.92	28.02	n.a.	27.27	32.73	29.25	25.92
SYRINGOL	n.a.	41.36	41.40	40.16	38.36	38.40	42.26	34.55	n.a.	35.91
VANILLIN	n.a.	46.66	46.70	39.59	40.09	40.10	37.29	44.24	n.a.	27.61
VINYLKET	n.a.	46.34	n.a.	45.97	43.21	n.a.	34.28	45.02	n.a.	53.91
XYLOSAN	n.a.	61.61	n.a.	42.70	49.05	n.a.	42.41	32.97	2.13	61.61
Average deviation		11.2 ± 16.3		13.3 ± 16.8	14.3 ± 17.0		21.1 ± 21.3	11.3 ± 16.2		16.8 ± 18.6
Av. Dev. Non-Aromatics		7.2 ± 10.8		8.5 ± 11.1	8.3 ± 11.0		9.7 ± 11.2	6.7 ± 10.6		9.8 ± 12.2
Av. Dev. Aromatics		0.6 ± 0.7		0.7 ± 1.0	2.3 ± 3.2		8.4 ± 16.5	1.7 ± 2.0		2.5 ± 3.1

n.a.: not available/not estimated/value considered unviable.

a: Sourced from the NIST database, averaged from several literature sources.

Tab. 36: Comparison of critical volume estimation methods for the components in the simulation. Values in $\text{cm}^3\text{-mol}^{-1}$.

ID	Experimental	Joback [325]		Gani [326]	Lydersen [328]		Ambrose [330]	Riedel [333]	Fedors [381]	Nannoolal et al. [332]	TDE
		This work	Fonts [264]		This work	Fonts [264]					
ACETALDY	154.0 [276]	164.5	n.a.	168.0	150.4	n.a.	230.2	169.1	157.5	155.8	158.6
ACETICAC	179.0 [276]	171.5	171.5	175.0	172.6	175.0	175.1	215.7	177.8	180.9	171.1
ACETOL	n.a.	228.5	228.5	228.0	221.6	228.0	280.3	202.6	228.2	226.2	233.3
ACETONE	216.0 [382]	209.5	n.a.	210.0	204.7	n.a.	265.3	240.7	210.2	207.3	215.2
ACROLEIN	n.a.	201.5	n.a.	203.0	191.8	n.a.	240.3	211.4	196.9	191.0	188.7
ANISOLE	341.3 [378]	337.5	n.a.	331.0	333.3	n.a.	385.7	331.8	336.8	315.5	343.0
CMRYLALC	n.a.	396.5	n.a.	426.0	434.1	n.a.	485.9	448.4	444.8	378.6	485.9
CRESOL	277.0 [276]	253.5	n.a.	299.5	350.0	n.a.	380.7	278.2	300.2	303.5	350.7
EG	191.0 [276]	185.5	n.a.	186.0	185.1	n.a.	180.2	120.8	186.5	189.6	180.1
EGACET	n.a.	251.5	n.a.	303.0	305.0	n.a.	300.3	282.1	301.3	308.0	310.6
ETHANOL	168.0 [377]	166.5	n.a.	168.0	165.4	n.a.	165.2	145.5	168.5	171.2	166.8
FFA	n.a.	1027.5	n.a.	1032.5	1015.0	n.a.	1071.8	2017.1	995.4	886.3	1038.2
FORMALDY	115.0 [276]	99.5	n.a.	113.0	82.0	n.a.	150.1	136.3	95.5	116.0	102.1
FORMICAC	125.0 [276]	106.5	106.5	120.0	97.5	120.0	175.1	129.4	115.8	138.0	114.2
FURFURAL	n.a.	267.5	267.5	268.0	264.8	268.0	130.1	289.7	252.0	215.6	273.2
GLYOXAL	n.a.	181.5	n.a.	186.0	168.4	n.a.	205.1	206.0	164.4	156.0	n.a.
GUAIACOL	n.a.	303.5	303.5	338.0	323.2	338.0	400.7	362.6	354.8	335.4	361.3
HAA	n.a.	183.5	183.5	186.0	176.7	186.0	220.2	164.7	175.5	176.4	183.5
HEXADEC	943.0 [276]	931.5	n.a.	926.4	920.0	n.a.	921.6	946.2	889.3	1035.1	1026.6
HMF	n.a.	233.5	n.a.	270.0	303.8	n.a.	145.1	276.9	279.1	285.1	328.0
HMWL	n.a.	1837.5	n.a.	1759.0	1946.0	n.a.	2029.7	7518.6	1900.2	1318.0	n.a.
KETENE	n.a.	135.5	n.a.	107.6	145.0	n.a.	138.1	164.7	141.6	187.6	135.7
LEVOGLUC	n.a.	365.5	365.5	384.5	370.2	384.5	385.0	220.5	419.5	535.8	365.5
METCSONE	n.a.	306.5	n.a.	289.7	250.3	n.a.	368.0	297.8	239.1	303.8	304.6
METHANOL	117.0 [276]	110.5	n.a.	113.0	109.7	n.a.	110.1	118.2	115.7	124.4	117.6
MF	n.a.	323.5	n.a.	322.0	326.6	n.a.	185.2	371.6	304.7	265.7	323.5
PHENOL	229.0 [276]	229.5	229.5	264.0	238.0	264.0	325.6	256.6	281.8	285.6	277.1
SYNAPALD	n.a.	524.5	n.a.	554.0	722.5	n.a.	676.1	582.1	579.9	397.9	635.0
SYRINGOL	n.a.	377.5	377.5	392.0	412.0	412.0	475.8	412.0	427.9	308.0	440.1
VANILLIN	n.a.	376.5	376.5	410.0	449.4	410.0	510.8	586.7	423.8	411.8	430.0
VINYLKET	n.a.	246.5	n.a.	255.0	237.7	n.a.	283.4	272.6	247.2	200.1	213.1
XYLOSAN	n.a.	319.5	n.a.	320.5	270.1	n.a.	353.5	165.9	348.7	392.8	319.5
Average deviation		9.3 ± 6.7		10.4 ± 8.4	17.6 ± 15.4		41.8 ± 31.8	19.8 ± 16.1	15.0 ± 14.0	23.3 ± 22.3	21.4 ± 21.0
Av. Dev. Non-Aromatics		4.0 ± 3.0		2.7 ± 2.3	5.7 ± 4.9		12.2 ± 10.7	9.5 ± 8.6	4.7 ± 5.6	6.2 ± 9.0	6.3 ± 8.3
Av. Dev. Aromatics		2.5 ± 4.4		6.2 ± 8.0	8.2 ± 13.8		22.2 ± 27.8	3.5 ± 5.5	7.3 ± 10.8	13.5 ± 17.0	11.2 ± 16.4

n.a.: not available/not estimated/value considered unviable.

Tab. 37: Comparison of acentric volume and saturated molar volume estimation methods for the components in the simulation.

ID	Acentric factor				Saturated molar volume (cm ³ ·mol ⁻¹)					
	Experimental	Definition	Lee-Kesler [334]	TDE	Experimental	ACD/Labs ^a	Gunn-Yamada [347]	Le Bas [348]	TDE	Fonts et al. [264]
ACETALDY	0.29 [276]	0.31	0.29	0.43	73.3 [276]	58.8	37.0	42.1	56.1	n.a.
ACETICAC	0.46 [276]	0.47	0.47	0.23	63.9 [276]	56.1	39.8	43.4	n.a.	46.1
ACETOL	n.a.	0.82	0.76	0.65	70.0 [383]	72.6	43.5	40.8	71.3	59.1
ACETONE	0.31 [276]	0.15	0.15	0.31	77.4 [276]	75.2	36.1	41.0	73.0	n.a.
ACROLEIN	n.a.	0.31	0.31	0.22	n.a.	70.5	38.1	41.1	66.3	n.a.
ANISOLE	n.a.	0.34	0.34	0.34	n.a.	113.4	38.5	38.1	108.4	n.a.
CMRYLALC	n.a.	0.49	0.49	0.49	n.a.	126.3	40.7	34.4	126.6	n.a.
CRESOL	0.51 [276]	0.39	0.39	0.41	106.1 [276]	104.1	98.7	127.5	n.a.	n.a.
EG	0.49 [276]	1.40	1.23	0.52	63.9 [276]	56.5	41.3	37.3	55.6	n.a.
EGACET	n.a.	0.53	0.55	0.63	n.a.	95.5	43.0	31.9	93.5	n.a.
ETHANOL	0.64 [276]	0.74	0.74	0.64	62.7 [276]	59.1	45.0	40.1	58.1	n.a.
FFA	0.78 [379]	n.a.	0.12	0.95		307.5	755.6	408.8	285.7	n.a.
FORMALDY	0.28 [276]	0.21	0.20	0.21	36.9 [276]	43.8	36.7	49.7	39.2	n.a.
FORMICAC	0.32 [276]	0.60	0.59	0.63	41.3 [276]	39.9	42.5	41.4	37.6	31.6
FURFURAL	n.a.	0.25	0.37	0.37	82.8 [384]	83.8	39.0	38.4	82.5	76.6
GLYOXAL	n.a.	0.26	0.25	n.a.	n.a.	56.3	37.4	44.5	n.a.	n.a.
GUAIACOL	n.a.	0.42	0.47	0.51	110.0 [385]	111.8	41.1	40.5	n.a.	101.4
HAA	n.a.	1.18	0.74	n.a.	n.a.	56.3	55.0	43.3	n.a.	46.2
HEXADEC	0.72 [276]	0.77	0.81	n.a.	397.8 [276]	292.6	363.5	390.0	n.a.	
HMF	n.a.	0.34	0.57	0.96	104.6 [385]	116.1	49.6	41.9	n.a.	n.a.
HMWL	n.a.	-0.12	-0.20	0.00	n.a.	530.2	33.0	72.4	n.a.	n.a.
KETENE	n.a.	0.33	0.28	n.a.	n.a.	59.0	50.3	37.1	57.5	
LEVOGLUC	n.a.	2.46	1.91	n.a.	n.a.	95.9	153.1	35.0	n.a.	108.2
METCSONE	n.a.	0.14	0.05	0.08	n.a.	96.4	35.2	41.2	99.1	n.a.
METHANOL	0.57 [276]	0.95	0.57	0.56	46.6 [276]	42.5	41.9	44.4	40.3	n.a.
MF	n.a.	0.21	0.21	0.21	n.a.	100.2	36.9	38.7	93.9	n.a.
PHENOL	0.44 [276]	0.68	0.31	0.38	101.6 [276]	87.8	39.2	36.6	n.a.	78.5
SYNAPALD	n.a.	0.81	0.82	0.81	n.a.	174.2	46.6	36.1	157.9	n.a.
SYRINGOL	n.a.	0.52	0.54	0.60	133.1 [384]	135.8	42.5	39.5	n.a.	118.0
VANILLIN	n.a.	0.51	0.53	0.60	n.a.	123.5	42.5	50.0	n.a.	112.2
VINYLKET	n.a.	0.28	0.28	0.17	n.a.	85.6	37.7	39.0	73.8	n.a.
XYLOSAN	n.a.	2.74	2.94	2.74	n.a.	81.3	253.0	30.6	84.4	n.a.
Average deviation		0.21 ± 0.20	0.20 ± 0.18	0.10 ± 0.09	Av. Dev.	12.5 ± 13.8	37.9 ± 23.4	38.0 ± 23.9	5.4 ± 5.0	
Av. Dev. Non-Aromatics		0.09 ± 0.10	0.10 ± 0.10	0.05 ± 0.04	Av. Dev. NA	7.4 ± 10.2	9.9 ± 7.6	9.0 ± 6.8	2.3 ± 2.1	
Av. Dev. Aromatics		0.03 ± 0.05	0.02 ± 0.03	0.01 ± 0.02	Av. Dev. A	4.0 ± 4.2	36.2 ± 31.2	38.0 ± 32.7	0.0 ± 0.1	

n.a.: not available/not estimated/value considered unviable.

a: Commercial property estimation software that uses undisclosed methods. Values obtained from the database www.chemspider.com.

Tab. 38: Comparison of heat capacity (ideal gas, liquid-phase) estimation methods for the components in the simulation. Values in J·mol⁻¹·K⁻¹. Temperature of 25 °C.

ID	Ideal gas heat capacity						Liquid heat capacity					
	Experimental	Benson [335]	Joback [325]		Harrison-Seaton [386]	<i>ab initio</i>	TDE	Gorensek	Experimental	Růžička [336–338]	TDE	Chueh-Swanson [387]
			This work	Fonts et al. [264]	Fonts et al. [264]	Fonts et al. [264]						Fonts et al. [264]
ACETALDY	55.3 [276]	55.0	56.0	n.a.	n.a.	n.a.	n.a.	n.a.	112.7 [276]	102.8	n.a.	n.a.
ACETICAC	63.7 [276]	68.7	65.7	68.6	68.5	70.7	n.a.	n.a.	123.9 [276]	124.5	170.0	116.7
ACETOL	n.a.	89.5	87.9	87.7	88.9	90.3	97.0	n.a.	n.a.	155.8	n.a.	163.0
ACETONE	40.5 [276]	74.7	75.0	n.a.	n.a.	n.a.	n.a.	n.a.	126.3 [276]	130.7	180.9	n.a.
ACROLEIN	n.a.	66.3	68.4	n.a.	n.a.	n.a.	n.a.	n.a.	n.a.	127.2	128.0	n.a.
ANISOLE	n.a.	123.7	121.7	n.a.	n.a.	n.a.	126.0	n.a.	n.a.	211.3	183.4	n.a.
CMRYLALC	n.a.	157.8	168.9	n.a.	n.a.	n.a.	n.a.	344.0	n.a.	332.2	n.a.	n.a.
CRESOL	124.9 [276]	124.9	113.5	n.a.	n.a.	n.a.	n.a.	n.a.	223.6 [276]	229.1	n.a.	n.a.
EG	97.1 [276]	56.9	77.6	n.a.	n.a.	n.a.	n.a.	n.a.	149.3 [276]	133.1	n.a.	n.a.
EGACET	n.a.	129.4	129.4	n.a.	n.a.	n.a.	124.6	n.a.	203.0 [388]	232.1	n.a.	n.a.
ETHANOL	65.1 [276]	64.5	64.6	n.a.	n.a.	n.a.	n.a.	n.a.	112.3 [276]	119.6	n.a.	n.a.
FFA	n.a.	406.7	403.2	n.a.	n.a.	n.a.	413.1	n.a.	n.a.	465.2	453.8	n.a.
FORMALDY	35.4 [276]	35.3	27.9	n.a.	n.a.	n.a.	n.a.	n.a.	70.3 [276]	61.7	128.2	n.a.
FORMICAC	45.7 [276]	45.2	37.5	37.3	48.1	44.5	n.a.	n.a.	99.4 [276]	100.3	n.a.	94.6
FURFURAL	98.1 [389]	89.4	94.9	83.3	95.6	91.2	n.a.	n.a.	n.a.	158.0	333.0	185.6
GLYOXAL	n.a.	56.1	60.4	n.a.	n.a.	n.a.	n.a.	n.a.	n.a.	123.3	n.a.	n.a.
GUAIACOL	242.3[390]	149.3	139.6	124.6	136.5	144.5	146.1	n.a.	n.a.	242.2	n.a.	229.7
HAA	n.a.	73.1	69.0	68.6	68.5	70.7	71.9	n.a.	n.a.	152.5	n.a.	n.a.
HEXADEC	368.7 [276]	365.4	372.2	n.a.	n.a.	n.a.	n.a.	n.a.	500.4 [276]	351.3	368.2	n.a.
HMF	77.8 [391]	113.0	112.8	n.a.	n.a.	n.a.	135.5	n.a.	n.a.	241.7	n.a.	n.a.
HMWL	n.a.	843.7	833.8	n.a.	n.a.	n.a.	n.a.	n.a.	n.a.	1355.4	n.a.	n.a.
KETENE	n.a.	44.5	43.5	n.a.	n.a.	n.a.	n.a.	n.a.	n.a.	85.2	n.a.	n.a.
LEVOGLUC	187.2 [264]	176.2	170.0	168.8	173.0	176.4	171.2	n.a.	n.a.	390.4	n.a.	n.a.
METCSONE	n.a.	95.8	108.8	n.a.	n.a.	n.a.	111.2	n.a.	n.a.	169.0	143.2	n.a.
METHANOL	44.0 [276]	43.8	41.7	n.a.	n.a.	n.a.	n.a.	n.a.	81.2 [276]	90.9	n.a.	n.a.
MF	n.a.	85.9	119.7	n.a.	n.a.	n.a.	n.a.	n.a.	n.a.	156.0	179.3	n.a.
PHENOL	104.4 [276]	101.5	99.7	80.8	104.6	102.1	n.a.	n.a.	196.4 [276]	209.9	n.a.	167.8
SYNAPALD	n.a.	175.8	224.8	n.a.	n.a.	n.a.	n.a.	452.1	n.a.	443.5	n.a.	n.a.
SYRINGOL	n.a.	197.0	179.4	168.4	168.3	187.0	186.7	n.a.	n.a.	290.9	n.a.	291.6
VANILLIN	n.a.	202.0	168.7	157.5	156.9	170.2	175.1	n.a.	276.2 [392]	312.7	n.a.	291.5
VINYLKET	n.a.	87.7	85.4	n.a.	n.a.	n.a.	n.a.	n.a.	n.a.	145.5	99.2	n.a.
XYLOSAN	n.a.	123.1	150.1	n.a.	n.a.	n.a.	n.a.	240.0	n.a.	286.4	n.a.	n.a.
Average deviation		15.7 ± 15.4	16.9 ± 16.0				56.7 ± 90.7		Av. Dev.	22.4 ± 24.9	72.7 ± 91.1	
Av. Dev. Non-Aromatics		4.5 ± 5.2	4.6 ± 4.3				0.8 ± 1.5		Av. Dev. NA	11.2 ± 14.7	13.8 ± 15.4	
Av. Dev. Aromatics		12.7 ± 18.7	14.3 ± 20.4				14.0 ± 21.0		Av. Dev. A	5.0 ± 7.3	0.0 ± 0.0	

n.a.: not available/not estimated/value considered unviable.

Tab. 39: Comparison of estimation methods for the standard enthalpy of ideal gas formation for the components in the simulation. Values in $\text{kJ}\cdot\text{mol}^{-1}$.

ID	Experimental	Joback [325]		Gani [326]	Benson [335]	<i>ab initio</i>	Gorenssek	TDE
		This work	Fonts [264]			Fonts [264]		
ACETALDY	-166.2 [276]	-170.2	n.a.	-166.4	-164.1	n.a.	n.a.	n.a.
ACETICAC	-432.8 [276]	-434.9	-434.6	-431.4	-347.8	-431.9	n.a.	n.a.
ACETOL	-414.2 [393]	-370.1	-369.8	-380.9	-352.3	-373.9	n.a.	n.a.
ACETONE	-215.7 [276]	-217.8	n.a.	-217.4	-216.1	n.a.	n.a.	-216.6
ACROLEIN	n.a.	-65.4	n.a.	-66.7	-60.0	n.a.	n.a.	n.a.
ANISOLE	-76.7 [394]	-83.5	n.a.	-68.2	-71.6	n.a.	n.a.	n.a.
CMRYLALC	n.a.	-204.9	n.a.	-209.7	-235.0	n.a.	-193.5	n.a.
CRESOL	-125.4 [276]	-175.0	n.a.	-128.3	-126.3	n.a.	n.a.	n.a.
EG	-387.5 [276]	-389.1	n.a.	-393.5	-351.3	n.a.	n.a.	n.a.
EGACET	-595.7 [395] ^a	-609.0	n.a.	-601.9	-568.2	n.a.	n.a.	n.a.
ETHANOL	-235.0 [276]	-170.9	n.a.	-173.2	-170.4	n.a.	n.a.	-234.6
FFA	-63.8 [396] ^b	-530.7	n.a.	-540.6	-529.2	n.a.	n.a.	n.a.
FORMALDY	-108.6 [276]	-93.7	n.a.	-118.3	-108.9	n.a.	n.a.	-108.7
FORMICAC	-378.6 [276]	-358.4	-358.2	-385.4	-377.7	-378.5	n.a.	n.a.
FURFURAL	-152.0 [389]	-179.2	-179.1	-198.4	-191.4	-153.1	n.a.	n.a.
GLYOXAL	n.a.	-255.8	n.a.	-247.5	-211.9	n.a.	n.a.	-212.1
GUAIACOL	-246.1 [397]	-260.8	-260.6	-245.6	-247.9	-244.3	n.a.	n.a.
HAA	n.a.	-322.4	-322.2	-320.5	-322.8	-318.3	n.a.	n.a.
HEXADEC	-374.2 [276]	-373.6	n.a.	-371.7	-363.4	n.a.	n.a.	n.a.
HMF	n.a.	-356.5	n.a.	-379.8	-274.5	n.a.	n.a.	n.a.
HMWL	n.a.	-1758.9	n.a.	-1835.5	-1666.2	n.a.	n.a.	n.a.
KETENE	-87.3 [276]	-74.6	n.a.	-153.6	-105.3	n.a.	n.a.	-47.7
LEVOGLUC	-824.5 [264]	-815.6	-815.1	-829.1	-801.7	-819.2	n.a.	n.a.
METCSONE	n.a.	-177.7	n.a.	-121.7	-52.6	n.a.	n.a.	n.a.
METHANOL	-200.9 [276]	-216.2	n.a.	-216.5	-201.0	n.a.	n.a.	-201.7
MF	n.a.	-211.3	n.a.	-234.1	-270.1	n.a.	n.a.	n.a.
PHENOL	-96.4 [276]	-96.5	-96.4	-97.8	-93.4	-88.3	n.a.	n.a.
SYNAPALD	n.a.	-334.7	n.a.	-426.5	-428.8	n.a.	-483.8	n.a.
SYRINGOL	-381.7 [397]	-425.1	-424.8	-393.3	-402.4	-377.6	n.a.	n.a.
VANILLIN	-463.6 [398] ^c	-378.5	-378.2	-347.7	-410.3	-376.0	n.a.	n.a.
VINYLKET	n.a.	-124.1	n.a.	-190.9	-158.8	n.a.	n.a.	n.a.
XYLOSAN	n.a.	-525.2	n.a.	-686.3	-677.4	n.a.	-642.3	n.a.
Average deviation		42.7 ± 46.7		41.9 ± 48.1	43.8 ± 46.8			8.3 ± 17.4
Av. Dev. Non-Aromatics		31.9 ± 45.4		33.0 ± 46.6	37.9 ± 46.3			2.0 ± 3.8
Av. Dev. Aromatics		20.6 ± 21.0		17.0 ± 23.5	11.3 ± 13.0			0.0 ± 0.0

n.a.: not available/not estimated/value considered unviable.
a: Based on gas-phase simulations conducted by the authors.
b: Heat of liquid formation.
c: Based on heat of combustion calculations.

Tab. 40: Comparison of estimation methods for the standard Gibbs energy of ideal gas formation for the components in the simulation. Values in $\text{kJ}\cdot\text{mol}^{-1}$.

ID	Experimental	Joback [325]		Gani [326]	Benson [335]	TDE
		This work	Fonts [264]			
ACETALDY	-133.1 [276]	-133.6	n.a.	-132.1	-133.8	n.a.
ACETICAC	-374.6 [276]	-378.0	-377.7	-372.3	-298.1	n.a.
ACETOL	n.a.	-291.4	-291.2	-313.8	-274.3	n.a.
ACETONE	-151.3 [276]	-154.5	n.a.	-154.2	-158.1	-64.0
ACROLEIN	n.a.	-37.3	n.a.	-39.1	-24.5	n.a.
ANISOLE	n.a.	15.5	n.a.	21.9	14.8	n.a.
CMRYLALC	n.a.	-73.9	n.a.	-82.8	-92.4	n.a.
CRESOL	-31.7 [276]	-88.2	n.a.	-34.3	-37.4	n.a.
EG	-302.6 [276]	-307.7	n.a.	-315.5	-254.6	n.a.
EGACET	n.a.	-472.6	n.a.	-475.6	-441.4	n.a.
ETHANOL	-167.9 [276]	-236.8	n.a.	-237.3	-234.8	-83.7
FFA	n.a.	-82.8	n.a.	-87.7	-86.8	n.a.
FORMALDY	-102.6 [276]	-89.6	n.a.	-122.7	-104.6	-37.4
FORMICAC	-351.0 [276]	-334.0	-333.8	-364.3	-350.0	n.a.
FURFURAL	n.a.	-99.9	-99.8	-139.2	-130.4	n.a.
GLYOXAL	n.a.	-233.1	n.a.	-230.5	-161.5	-108.5
GUAIACOL	n.a.	-139.2	-139.0	-132.1	-134.1	n.a.
HAA	n.a.	-270.4	-270.2	-273.0	-298.1	n.a.
HEXADEC	82.2 [276]	83.8	n.a.	84.3	79.1	n.a.
HMF	n.a.	-254.5	n.a.	-297.8	-255.6	n.a.
HMWL	n.a.	-853.5	n.a.	-999.5	-869.5	n.a.
KETENE	n.a.	-62.9	n.a.	-85.5	-147.2	25.3
LEVOGLUC	n.a.	-508.9	-508.6	-604.9	-571.8	n.a.
METCSONE	n.a.	-58.4	n.a.	-97.1	-121.7	n.a.
METHANOL	-162.3 [276]	-179.3	n.a.	-181.4	-165.0	-91.5
MF	n.a.	-101.1	n.a.	-144.1	-225.3	n.a.
PHENOL	-32.6 [276]	-32.9	-32.9	-34.3	-31.1	n.a.
SYNAPALD	n.a.	-144.0	n.a.	-232.9	-208.4	n.a.
SYRINGOL	n.a.	-245.4	-245.2	-229.9	-237.0	n.a.
VANILLIN	n.a.	-239.9	-239.7	-209.4	-321.7	n.a.
VINYLKET	n.a.	-53.6	n.a.	-104.0	-72.9	n.a.
XYLOSAN	n.a.	-279.1	n.a.	-485.3	-496.5	n.a.
Average deviation		99.6 ± 17.5		94.6 ± 14.4	103.5 ± 21.1	119.2 ± 87.6
Av. Dev. Non-Aromatics		65.6 ± 7.1		57.3 ± 7.4	71.9 ± 10.8	28.4 ± 14.8
Av. Dev. Aromatics		64.7 ± 10.6		71.3 ± 0.6	60.4 ± 1.1	0.0 ± 0.0

n.a.: not available/not estimated/value considered unviable.
a: Based on gas-phase simulations conducted by the authors.
b: Heat of liquid formation.
c: Based on heat of combustion calculations..

Tab. 41: Comparison of estimation methods for the enthalpy of vaporization at boiling point for the components in the simulation. Values in $\text{kJ}\cdot\text{mol}^{-1}$.

ID	Experimental	ACD/Labs ^a	Clausius-Clayperon ^b	Gani [398]	Ducros [344–346]	Vetere [342,343]	Li-Ma [399]	TDE	Joback [325]	Riedel [398]	Mod. Watson [399–401]
									Fonts [264]	Fonts [264]	Fonts [264]
ACETALDY	24.9 [276]	25.8	26.2	24.3	25.7	27.0	26.1	1.7	n.a.	n.a.	n.a.
ACETICAC	23.9 [276]	23.7	41.4	46.5	45.9	37.9	n.a.	n.a.	37.2	40.4	42.9
ACETOL	42.0 [264]	44.6	50.2	47.8	22.1	40.1	53.3	1.8	45.7	50.1	56.4
ACETONE	27.8 [276]	29.1	28.3	28.2	28.3	29.0	n.a.	1.7	n.a.	n.a.	n.a.
ACROLEIN	n.a.	29.6	27.2	25.4	27.0	23.8	27.0	1.8	n.a.	n.a.	n.a.
ANISOLE	39.0 [402]	39.0	34.7	42.6	36.4	34.3	36.4	1.9	n.a.	n.a.	n.a.
CMRYLALC	n.a.	59.7	61.0	84.4	77.2	58.1	n.a.	1.8	n.a.	n.a.	n.a.
CRESOL	49.5 [276]	n.a.	49.3	58.9	50.2	36.7	45.7	n.a.	n.a.	n.a.	n.a.
EG	52.7 [276]	50.5	68.9	55.9	0.6	43.1	69.8	1.8	n.a.	n.a.	n.a.
EGACET	63.9 [395]	48.8	41.3	51.7	25.4	36.4	54.7	1.8	n.a.	n.a.	n.a.
ETHANOL	38.6 [276]	38.6	37.8	36.0	35.3	32.0	37.8	1.8	n.a.	n.a.	n.a.
FFA	n.a.	n.a.	116.9	83.7	88.7	139.3	85.0	1.9	n.a.	n.a.	n.a.
FORMALDY	23.1 [276]	22.3	21.7	22.4	22.5	24.4	23.7	1.7	n.a.	n.a.	n.a.
FORMICAC	31.4 [276]	22.7	38.4	44.4	42.5	37.4	n.a.	1.7	34.8	37.1	38.8
FURFURAL	50.7 [403]	39.8	44.7	38.8	38.1	35.7	n.a.	1.9	39.8	42.5	51.0
GLYOXAL	n.a.	29.3	32.3	30.4	36.8	31.5	32.5	n.a.	n.a.	n.a.	n.a.
GUAIACOL	62.6 [397]	45.9	45.4	69.1	63.7	45.6	n.a.	1.8	48.9	50.0	61.6
HAA	70.0 [264]	43.0	37.7	41.4	19.2	34.9	44.1	n.a.	43.4	48.6	52.1
HEXADEC	51.1 [276]	50.5	54.2	55.4	56.0	51.6	53.6	1.9	n.a.	n.a.	n.a.
HMF	83.4 [397]	53.7	41.4	52.9	54.9	42.4	n.a.	1.9	n.a.	n.a.	n.a.
HMWL	n.a.	n.a.	n.a.	337.8	339.1	180.4	n.a.	n.a.	n.a.	n.a.	n.a.
KETENE	20.4 [404]	20.2	35.7	33.7	30.8	33.6	33.3	n.a.	n.a.	n.a.	n.a.
LEVOGLUC	97.0 [405] ^c	73.1	101.0	70.5	66.4	74.2	n.a.	n.a.	87.2	132.8	138.8
METCSONE	n.a.	39.4	40.0	37.0	39.0	35.1	n.a.	1.8	n.a.	n.a.	n.a.
METHANOL	35.3 [276]	35.2	39.7	33.2	35.0	33.0	41.6	1.8	n.a.	n.a.	n.a.
MF	n.a.	42.3	42.2	29.2	30.8	28.6	34.6	1.8	n.a.	n.a.	n.a.
PHENOL	46.5 [276]	43.5	36.7	55.8	54.2	34.0	n.a.	1.8	43.6	46.7	55.0
SYNAPALD	n.a.	64.4	30.3	94.1	72.5	62.3	n.a.	1.9	62.8	54.3	84.7
SYRINGOL	76.7 [405] ^d	52.3	50.0	80.7	71.8	43.8	n.a.	1.8	54.2	57.7	73.0
VANILLIN	66.9 [397]	54.2	53.3	83.1	67.8	52.7	n.a.	1.8	58.5	62.6	80.1
VINYLKET	n.a.	28.4	33.1	29.7	29.0	31.4	32.5	1.8	n.a.	n.a.	n.a.
XYLOSAN	n.a.	65.0	56.5	60.5	63.0	52.5	n.a.	1.9	n.a.	n.a.	n.a.
Average deviation		7.1 ± 5.3	11.1 ± 7.0	9.8 ± 5.9	13.7 ± 9.7	12.0 ± 7.3	7.5 ± 6.2	44.6 ± 24.1			
Av. Dev. Non-Aromatics		3.0 ± 3.1	6.1 ± 4.7	5.1 ± 4.2	10.4 ± 8.7	5.9 ± 4.9	4.0 ± 3.4	17.9 ± 12.0			
Av. Dev. Aromatics		6.6 ± 7.1	8.5 ± 9.1	8.1 ± 7.4	5.0 ± 6.0	10.5 ± 9.7	0.5 ± 0.7	30.7 ± 26.6			

n.a.: not available/not estimated/value considered unviable.

a: Commercial property estimation software that uses undisclosed methods. Values obtained from the database www.chemspider.com; b: Obtained using the Clausius-Clayperon equation based on vapor pressure data; c: Estimation; d: Value assuming 25 °C. Value assumed valid as enthalpy of vaporization tends to vary little with temperature

Tab. 42: Comparison of estimation methods for the viscosity at 90 °C for the components in the simulation.

ID	Gas (kPa·s)			Liquid (cP)				
	Experimental	Reichenberg[349]	TDE	Experimental	Letsou-Stiel [350]	Orrick-Erbar [351]	Nannoolal-Rarey [352]	TDE
ACETALDY	n.a.	1.060	1.391	0.15 [276]	0.14	0.14	0.17	0.13
ACETICAC	1.000 [276]	1.035	0.552	0.51 [276]	0.29	0.38	0.79	0.51
ACETOL	n.a.	0.897	1.008	n.a.	0.33	1.40	1.21	1.12
ACETONE	0.925 [276]	0.934	0.537	0.19 [276]	0.16	0.15	0.18	n.a.
ACROLEIN	n.a.	1.014	1.044	n.a.	0.17	0.18	0.20	n.a.
ANISOLE	n.a.	0.841	0.831	0.45 [276]	0.36	0.29	0.49	n.a.
CMRYLALC	n.a.	0.805	0.734	n.a.	0.05	n.a.	9.38	n.a.
CRESOL	n.a.	0.805	0.731	0.70 [276]	0.34	1.84	0.61	1.52
EG	n.a.	1.010	0.989	2.50 [276]	0.33	3.30	1.11	n.a.
EGACET	n.a.	0.871	0.820	n.a.	0.33	1.62	1.23	n.a.
ETHANOL	1.075 [276]	1.067	1.423	0.37 [276]	0.26	0.40	0.44	0.37
FFA	n.a.	0.485	0.532	n.a.	0.01	3.10	5.38	4.60
FORMALDY	n.a.	1.434	1.579	n.a.	0.09	0.08	0.15	n.a.
FORMICAC	n.a.	1.344	1.201	0.60 [276]	0.37	0.39	0.76	n.a.
FURFURAL	n.a.	0.932	0.819	0.66 [406]	0.31	0.40	0.50	0.64
GLYOXAL	n.a.	1.003	n.a.	n.a.	0.23	0.30	n.a.	n.a.
GUAIACOL	n.a.	0.802	0.800	5.65 [407]	1.07	1.52	2.23	1.09
HAA	n.a.	1.007	n.a.	n.a.	0.45	1.65	1.19	n.a.
HEXADEC	n.a.	0.512	-0.444	n.a.	0.03	1.17	0.94	1.00
HMF	n.a.	0.933	0.896	n.a.	0.21	4.96	n.a.	5.78
HMWL	n.a.	0.364	n.a.	n.a.	0.00	n.a.	n.a.	n.a.
KETENE	n.a.	1.212	1.496	n.a.	0.15	0.11	0.25	n.a.
LEVOGLUC	n.a.	1.075	n.a.	n.a.	0.00	n.a.	0.13	n.a.
METGLYCO	n.a.	0.818	0.762	n.a.	0.25	0.33	0.36	n.a.
METHANOL	1.175 [276]	1.227	2.295	0.26 [276]	0.22	0.23	0.55	n.a.
MF	n.a.	0.851	0.810	n.a.	0.27	0.64	0.57	n.a.
PHENOL	n.a.	0.874	0.894	1.30 [276]	0.35	1.42	1.14	n.a.
SYNAPALD	n.a.	0.676	0.602	n.a.	0.01	n.a.	n.a.	n.a.
SYRINGOL	n.a.	0.791	0.732	n.a.	0.17	3.08	n.a.	n.a.
VANILLIN	n.a.	0.723	0.586	1.43 [392]	0.06	3.20	6.81	n.a.
VINYLKET	n.a.	0.935	1.095	n.a.	0.21	0.23	0.62	n.a.
XYLOSAN	n.a.	1.227	0.988	n.a.	0.00	n.a.	0.61	n.a.
Average deviation		0.026 ± 0.036	0.576 ± 0.743	Average deviation	0.81 ± 0.84	0.68 ± 0.74	0.88 ± 1.03	0.90 ± 1.66
Av. Dev. Non-Aromatics		0.005 ± 0.006	0.110 ± 0.126	Av. Dev. Non-Aromatics	0.13 ± 0.21	0.06 ± 0.08	0.11 ± 0.14	0.00 ± 0.00
Av. Dev. Aromatics		0.000 ± 0.000	0.000 ± 0.000	Av. Dev. Aromatics	0.70 ± 0.92	0.69 ± 0.87	0.84 ± 1.19	0.49 ± 0.87

n.a.: not available/not estimated/value considered unviable.

Tab. 43: Vapor pressure estimations using different methods at 25 °C. Values in kPa.

ID	Exp.	ACD/Labs ^a	EPISuite ^b	Riedel [339]	Li-Ma [340]	Mani	Nannoolal-Rarey [341]	TDE	Fonts [264]	Gorensek
ACETALDY	116.0 [276]	128.6	121.3	124.0	117.9	120.5	136.0	118.0	n.a.	n.a.
ACETICAC	2.1 [276]	1.9	2.3	1.0	2.1	1.2	3.2	2.1	1.4	n.a.
ACETOL	0.6 [408]	0.3	n.a.	0.5	0.1	0.6	0.6	0.6	0.2	n.a.
ACETONE	30.6 [276]	46.4	33.2	40.2	42.0	29.5	48.0	30.6	n.a.	n.a.
ACROLEIN	34.6 [409]	34.8	35.2	55.7	57.5	37.8	35.5	35.3	n.a.	n.a.
ANISOLE	0.5 [410]	0.6	0.5	1.2	1.1	0.3	0.6	0.5	n.a.	n.a.
CMRYLALC	0.0 [210] ^c	0.0	0.0	0.0	0.0	n.a.	0.0	0.0	n.a.	0.0
CRESOL	0.0 [276]	0.0	0.0	0.2	0.1	372.6	1.8	0.0	n.a.	n.a.
EG	0.0 [276]	0.0	0.0	0.0	0.0	0.0	0.2	0.0	n.a.	n.a.
EGACET	0.0 [395]	0.0	0.0	0.0	0.2	0.0	0.4	0.0	n.a.	n.a.
ETHANOL	7.9 [276]	11.0	8.1	16.5	15.6	9.6	23.8	7.8	n.a.	n.a.
FFA	n.a.	0.0	0.0	0.0	0.2	0.0	0.0	0.0	n.a.	n.a.
FORMALDY	516.1 [276]	461.8	465.3	515.9	470.6	514.5	322.2	509.5	n.a.	n.a.
FORMICAC	5.6 [276]	4.9	4.8	3.2	45.1	5.2	5.1	5.6	3.7	n.a.
FURFURAL	0.3 [403]	0.3	0.3	0.0	0.0	n.a.	0.4	0.3	0.3	n.a.
GLYOXAL	7.6 [411]	38.9	38.4	14.6	17.5	7.6	5.8	n.a.	n.a.	n.a.
GUAIACOL	0.0 [412]	0.0	0.0	0.0	0.0	0.0	0.0	0.0	0.0	n.a.
HAA	0.0 [408]	0.5	0.1	0.0	1.6	0.0	1.1	n.a.	n.a.	n.a.
HEXADEC	0.0 [276]	0.0	0.0	0.0	0.0	0.0	0.0	0.0	n.a.	n.a.
HMF	0.0 [391]	0.0	0.0	0.0	0.0	0.0	0.0	0.0	n.a.	n.a.
HMWL	n.a.	n.a.	n.a.	0.0	n.a.	n.a.	0.0	n.a.	n.a.	n.a.
LEVOGLUC	0.0 [413]	1678.5	1102.6	123.6	121.5	729.9	7.3	1471.0	n.a.	n.a.
KETENE	303.4 [404]	0.0	0.0	0.0	9164.5	0.0	0.0	n.a.	n.a.	n.a.
METCSONE	n.a.	0.4	0.5	0.7	0.5	0.4	1.0	1.9	0.0	n.a.
METHANOL	16.7 [276]	35.4	15.9	16.9	17.5	15.3	42.1	16.8	n.a.	n.a.
MF	n.a.	0.1	0.1	0.1	0.2	0.0	0.3	0.1	n.a.	n.a.
PHENOL	0.1 [276]	0.1	0.0	156.2	234.8	0.0	0.4	0.1	0.2	n.a.
SYNAPALD	0.0 [210] ^c	0.0	0.0	0.0	0.5	0.0	0.0	0.0	n.a.	0.0
SYRINGOL	n.a.	0.0	0.0	0.0	2.0	0.0	0.0	0.0	0.0	n.a.
VANILLIN	n.a.	0.0	0.0	0.0	1.4	0.0	0.0	0.0	0.0	n.a.
VINYLKET	n.a.	59.9	148.0	14.2	15.7	n.a.	0.0	29.8	n.a.	n.a.
XYLOSAN	0.0 [210] ^c	0.0	0.0	0.0	0.0	0.0	0.0	0.0	n.a.	0.0
Average		65.8 ± 120.0	40.5 ± 73.1	17.2 ± 20.9	422.9 ± 799.0	37.0 ± 51.6	25.1 ± 31.0	58.9 ± 117.4		
Average Non-Aromatics		72.0 ± 131.7	42.5 ± 76.6	11.3 ± 17.4	451.8 ± 876.7	21.0 ± 40.8	27.4 ± 34.1	56.1 ± 111.7		
Average Aromatics		0.0 ± 0.0	0.0 ± 0.0	14.3 ± 29.2	21.6 ± 43.9	33.9 ± 69.6	0.2 ± 0.3	0.0 ± 0.0		

Exp.: experimental value; n.a.: not available/not estimated/value considered unviable.; a: Commercial property estimation software that uses undisclosed methods. Values obtained from the database www.chemspider.com.; b: Mean value calculated from both Antoine and Grain methods. Values obtained from the database www.chemspider.com.; c: Estimated from the vapor pressure of other bio-molecules.

Tab. 44: Vapor pressure estimations using different methods at 90 °C. Values in kPa.

ID	Experimental	Riedel [339]	Li-Ma [340]	Mani	Nannoolal-Rarey [341]	TDE	Fonts [264]	Gorenssek
ACETALDY	738.4 [276]	894.8	732.8	875.2	842.2	751.8	n.a.	n.a.
ACETICAC	39.8 [276]	35.6	40.3	33.2	46.3	40.2	39.9	n.a.
ACETOL	11.8 [408]	13.2	9.2	23.2	12.3	12.7	10.5	n.a.
ACETONE	285.8 [276]	358.4	335.3	272.4	374.4	285.5	n.a.	n.a.
ACROLEIN	349.8 [409]	470.3	430.0	391.0	296.0	320.9	n.a.	n.a.
ANISOLE	0.0 [410]	23.6	23.2	11.2	12.1	12.7	n.a.	n.a.
CMRYLALC	0.1 [210]	0.0	0.0	n.a.	0.1	0.0	n.a.	0.0
CRESOL	1.8 [276]	7.9	5.1	678.0	29.3	1.5	n.a.	n.a.
EG	1.2 [276]	1.3	1.9	1.7	5.4	1.2	n.a.	n.a.
EGACET	2.3 [395]	3.5	5.8	2.6	9.5	2.2	n.a.	n.a.
ETHANOL	157.8 [276]	256.5	269.0	196.9	217.4	158.1	n.a.	n.a.
FFA	n.a.	0.0	0.9	0.0	0.0	0.0	n.a.	n.a.
FORMALDY	2752.5 [276]	2592.0	2221.3	2589.6	1654.8	2543.8	n.a.	n.a.
FORMICAC	72.8 [276]	86.9	95.7	100.1	66.1	71.9	74.3	n.a.
FURFURAL	8.6 [403]	0.0	0.0	n.a.	9.8	9.0	8.5	n.a.
GLYOXAL	107.2 [411]	205.7	191.7	135.6	73.3	n.a.	n.a.	n.a.
GUAIACOL	1.2 [412]	1.2	0.8	1.3	1.6	1.5	1.3	n.a.
HAA	0.7 [408]	2.9	45.2	1.5	20.3	n.a.	n.a.	n.a.
HEXADEC	0.1 [276]	0.0	0.0	0.0	0.2	0.1	n.a.	n.a.
HMF	0.0 [391]	0.0	0.2	0.0	0.0	0.0	n.a.	n.a.
HMWL	n.a.	0.0	n.a.	n.a.	0.0	n.a.	n.a.	n.a.
LEVOGLUC	0.0 [413]	899.5	743.4	1985.2	87.4	5262.6	n.a.	n.a.
KETENE	523.1 [404]	0.0	n.a.	0.0	0.0	n.a.	n.a.	n.a.
METCSONE	n.a.	27.0	20.5	9.4	18.9	24.2	1.6	n.a.
METHANOL	255.6 [276]	396.0	261.2	366.7	337.8	255.3	n.a.	n.a.
MF	n.a.	6.3	7.1	3.2	7.0	3.1	n.a.	n.a.
PHENOL	3.4 [276]	8.6	8.7	2.7	9.4	3.5	10.5	n.a.
SYNAPALD	0.1 [210]	0.0	2.2	0.0	0.0	0.0	n.a.	0.0
SYRINGOL	n.a.	0.1	8.4	0.1	0.1	0.1	0.1	n.a.
VANILLIN	n.a.	0.0	5.8	0.0	0.2	0.0	0.0	n.a.
VINYLKET	n.a.	174.8	169.6	n.a.	0.6	250.5	n.a.	n.a.
XYLOSAN	0.0 [210]	0.0	0.2	0.0	1.0	0.4	n.a.	0.0
Average		55.8 ± 43.1	671.8 ± 1242.8	123.8 ± 147.9	89.5 ± 104.5	250.0 ± 476.1		
Average Non-Aromatics		59.0 ± 47.3	733.6 ± 1364.1	96.8 ± 141.0	95.7 ± 114.6	237.4 ± 452.9		
Average Aromatics		4.2 ± 5.0	4.3 ± 4.9	62.8 ± 126.4	4.5 ± 5.8	1.4 ± 2.4		

n.a.: not available/not estimated/value considered unviable.

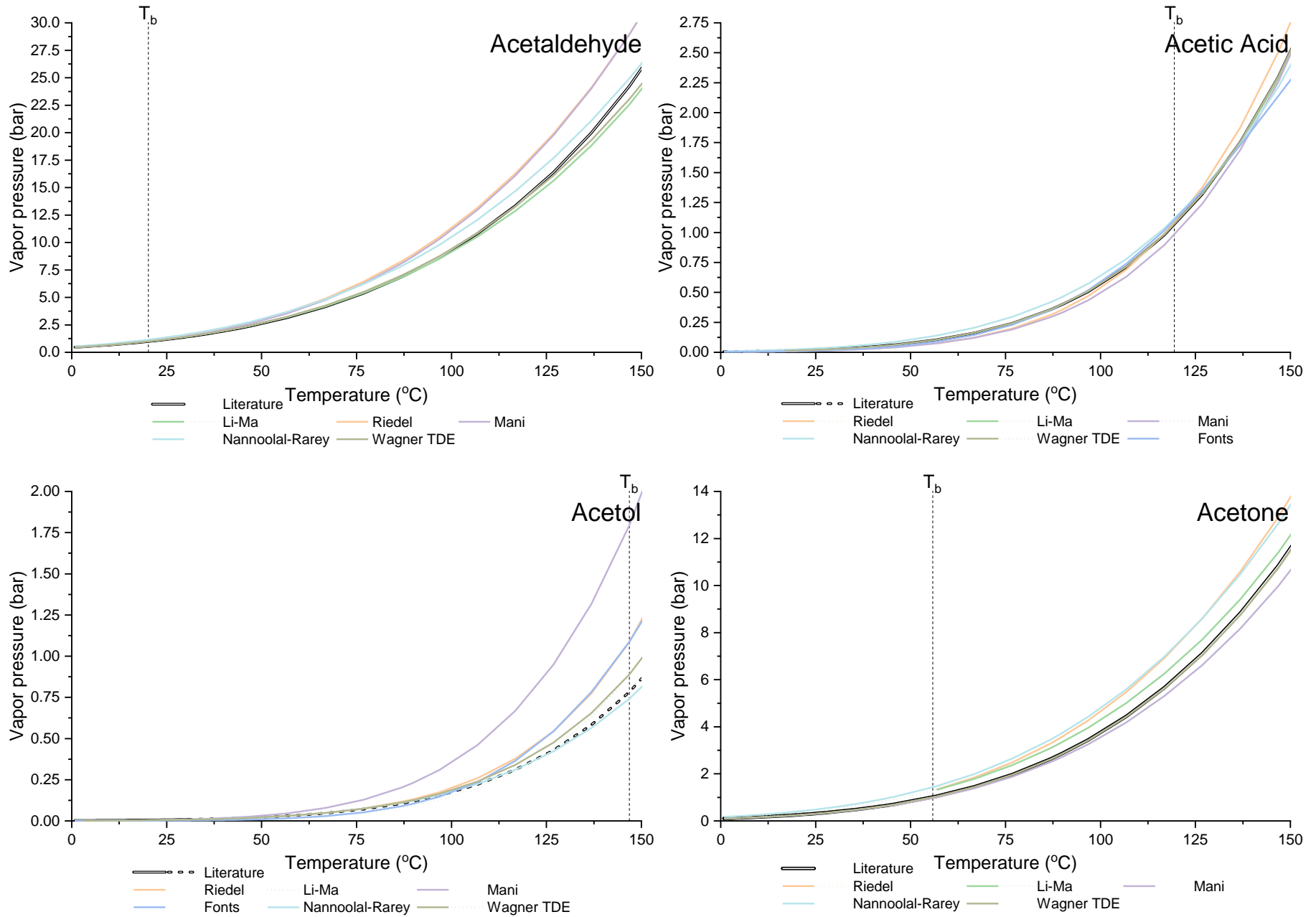


Fig. 28: Visual comparison of the p - T curves for several bio-oil components focused on the range of 0-150 °C. Dotted curves represent values outside the range of validity of the parameters. Components: ACETALDY, ACETICAC, ACETOL, ACETONE.

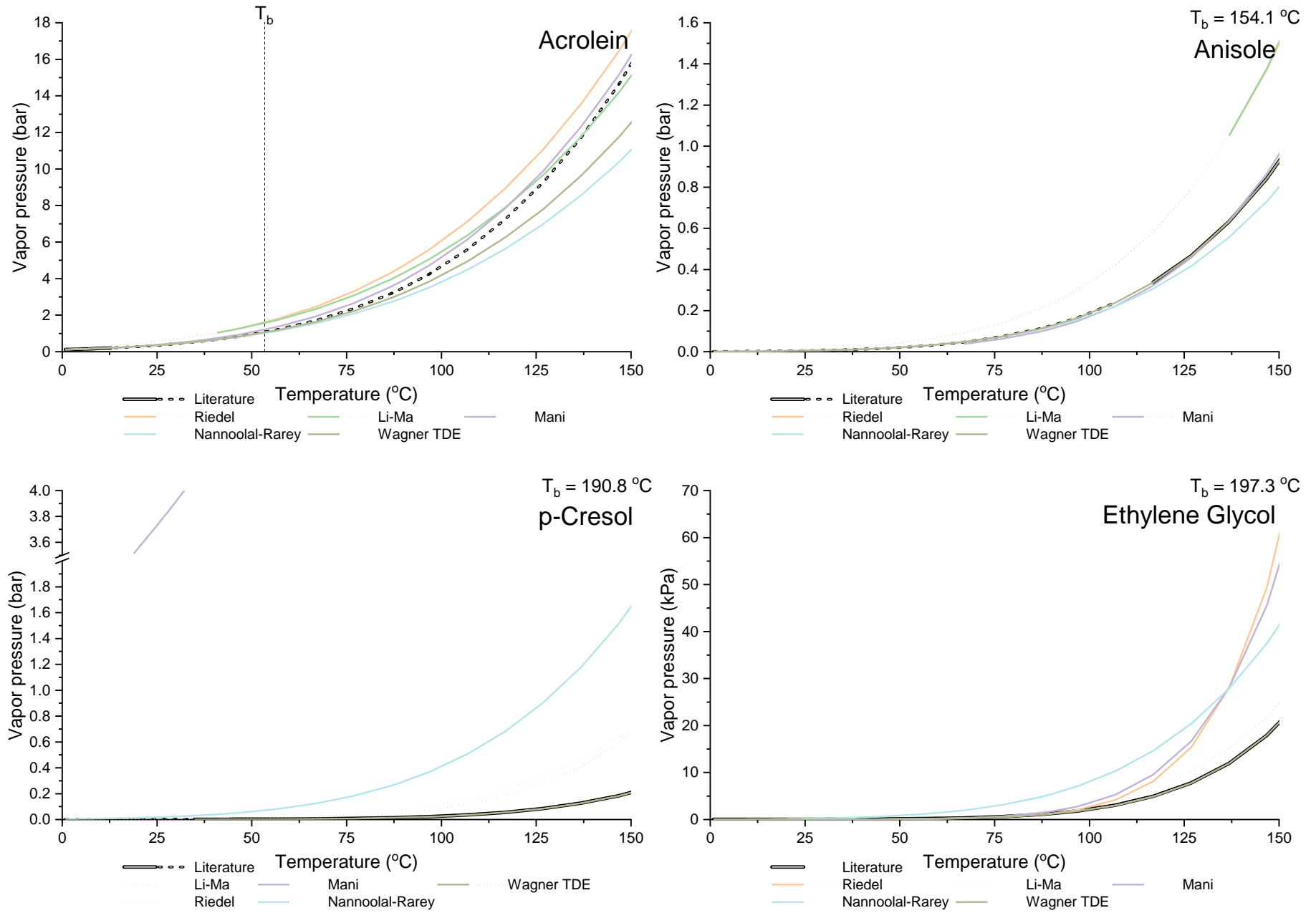


Fig. 29: Visual comparison of the p - T curves for several bio-oil components focused on the range of 0-150 °C. Dotted curves represent values outside the range of validity of the parameters. Components: ACROLEIN, ANISOLE, CRESOL, EG.

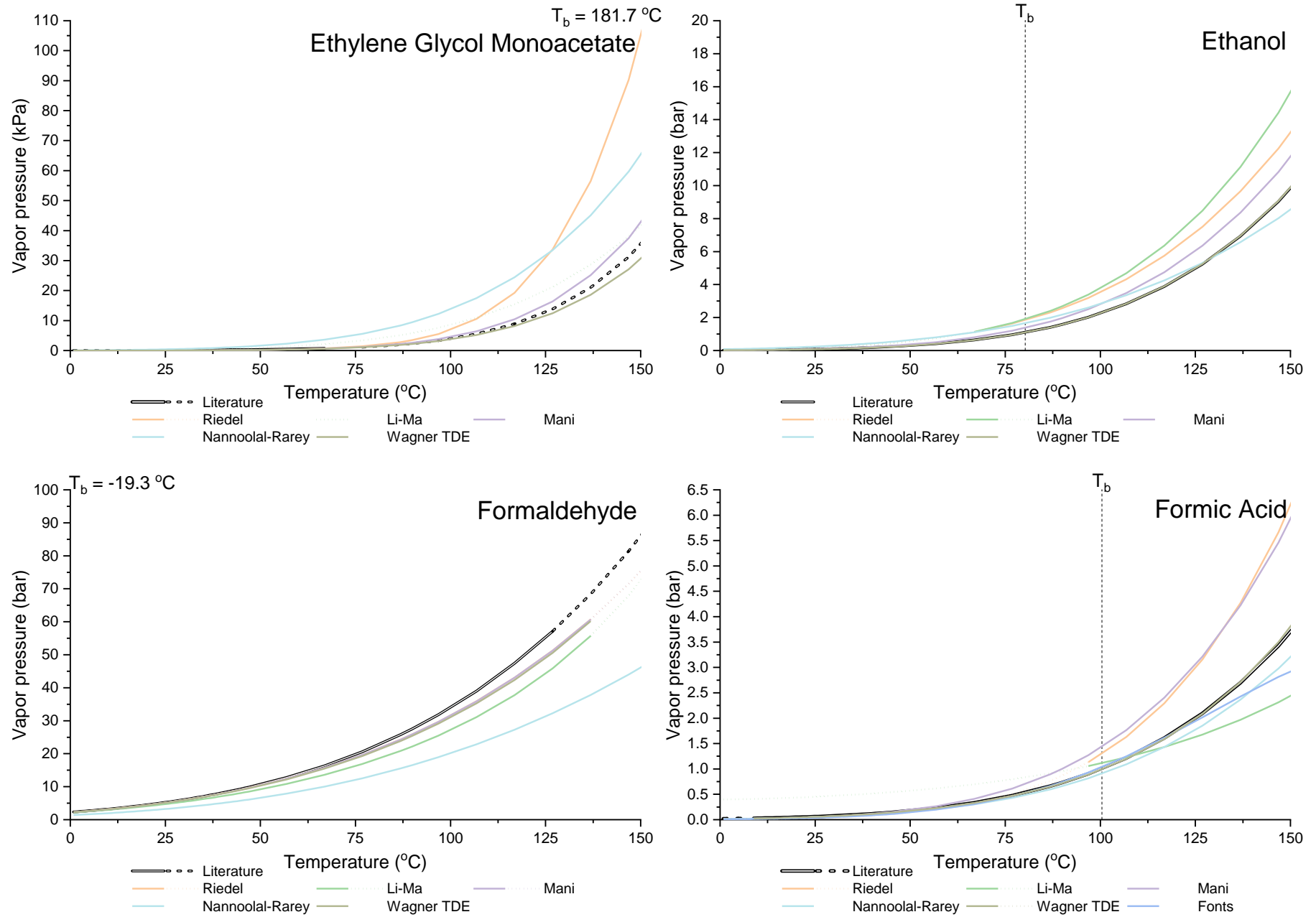


Fig. 30: Visual comparison of the p-T curves for several bio-oil components focused on the range of 0-150 °C. Dotted curves represent values outside the range of validity of the parameters. Components: EGACET, ETHANOL, FORMALDY, FORMICAC.

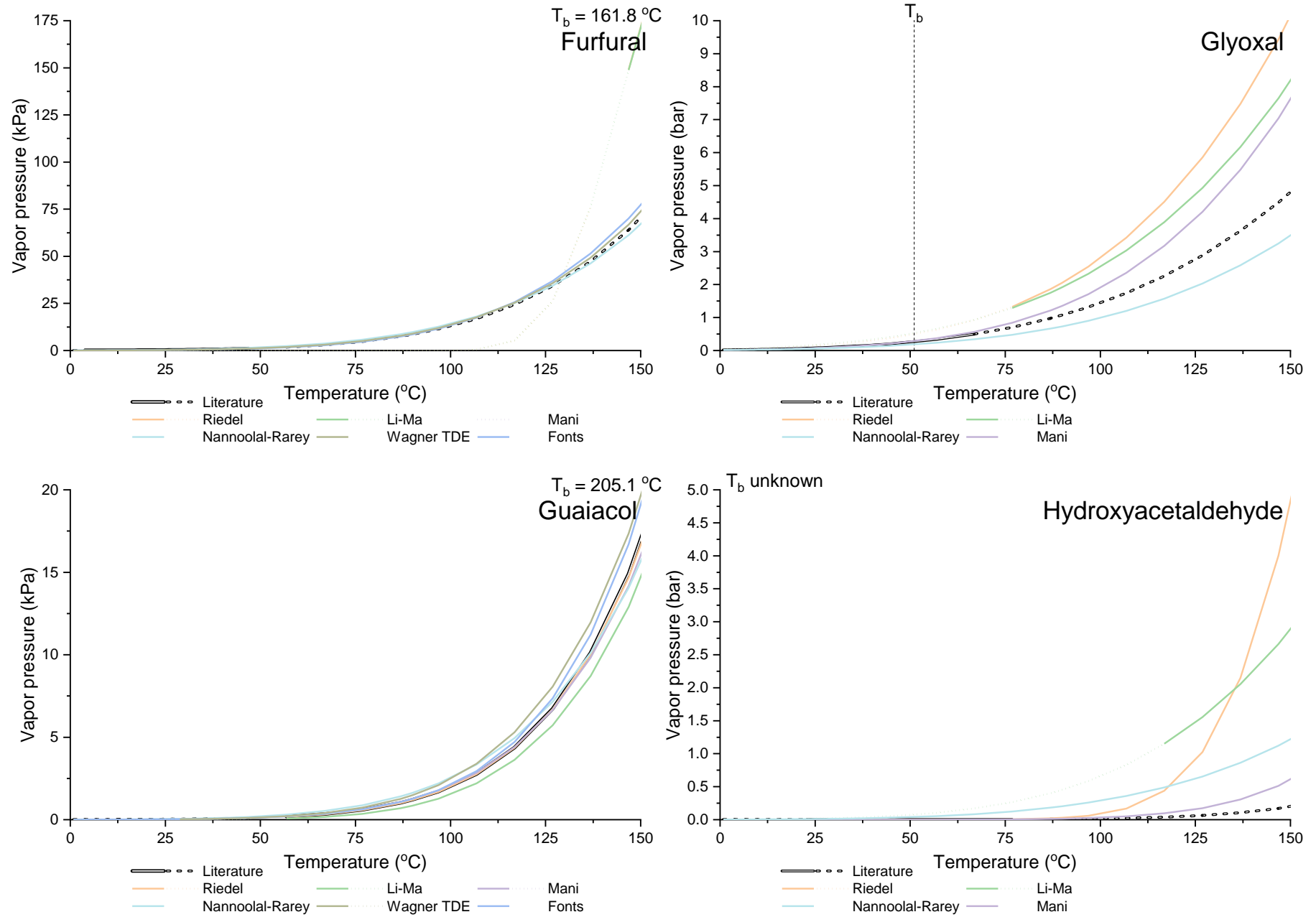


Fig. 31: Visual comparison of the p - T curves for several bio-oil components focused on the range of 0-150 °C. Dotted curves represent values outside the range of validity of the parameters. Components: FURFURAL, GLYOXAL, GUAIACOL, HAA.

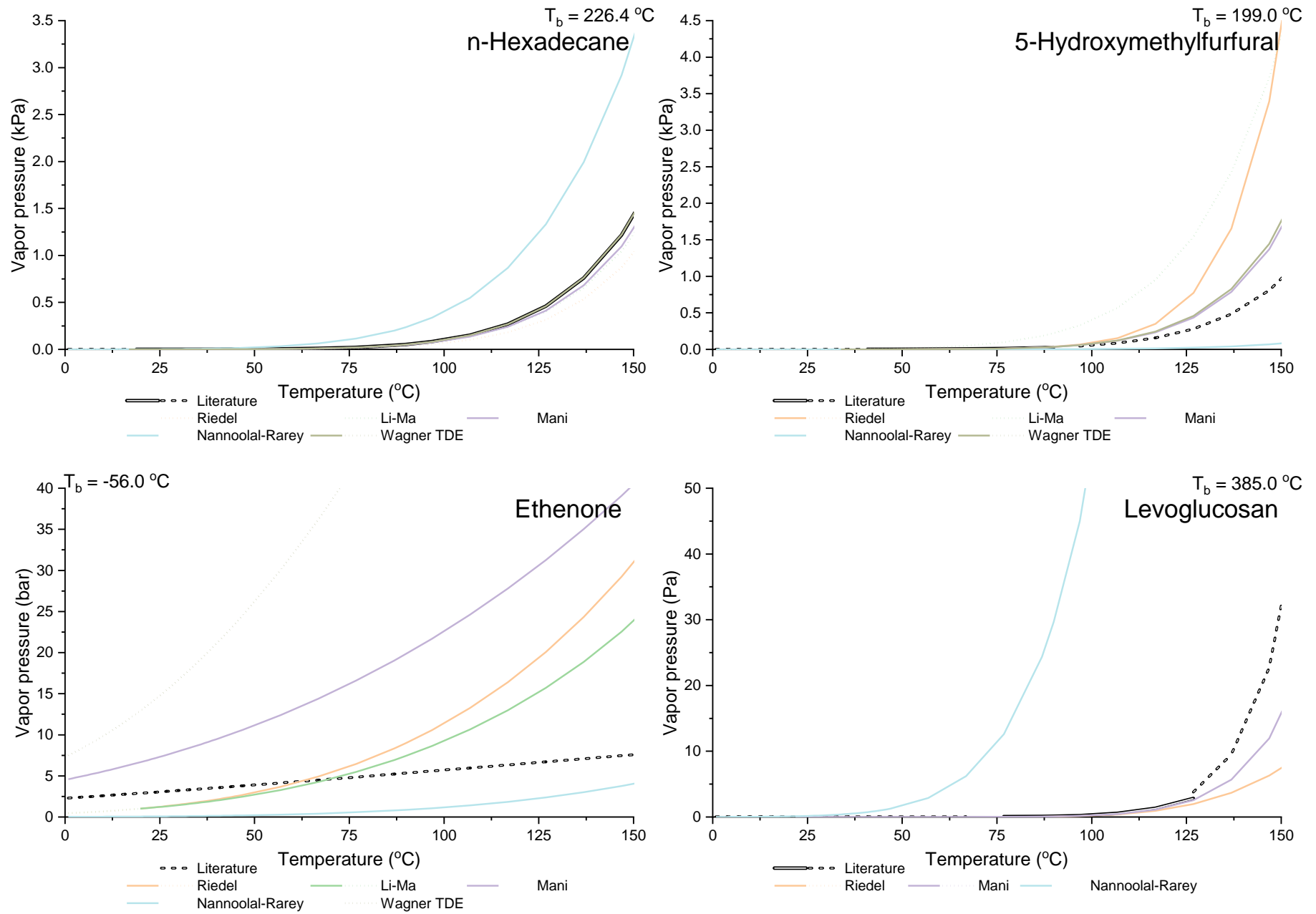


Fig. 32: Visual comparison of the p - T curves for several bio-oil components focused on the range of 0-150 °C. Dotted curves represent values outside the range of validity of the parameters. Components: HEXADEC, HMF, KETENE, LEVOGLUC.

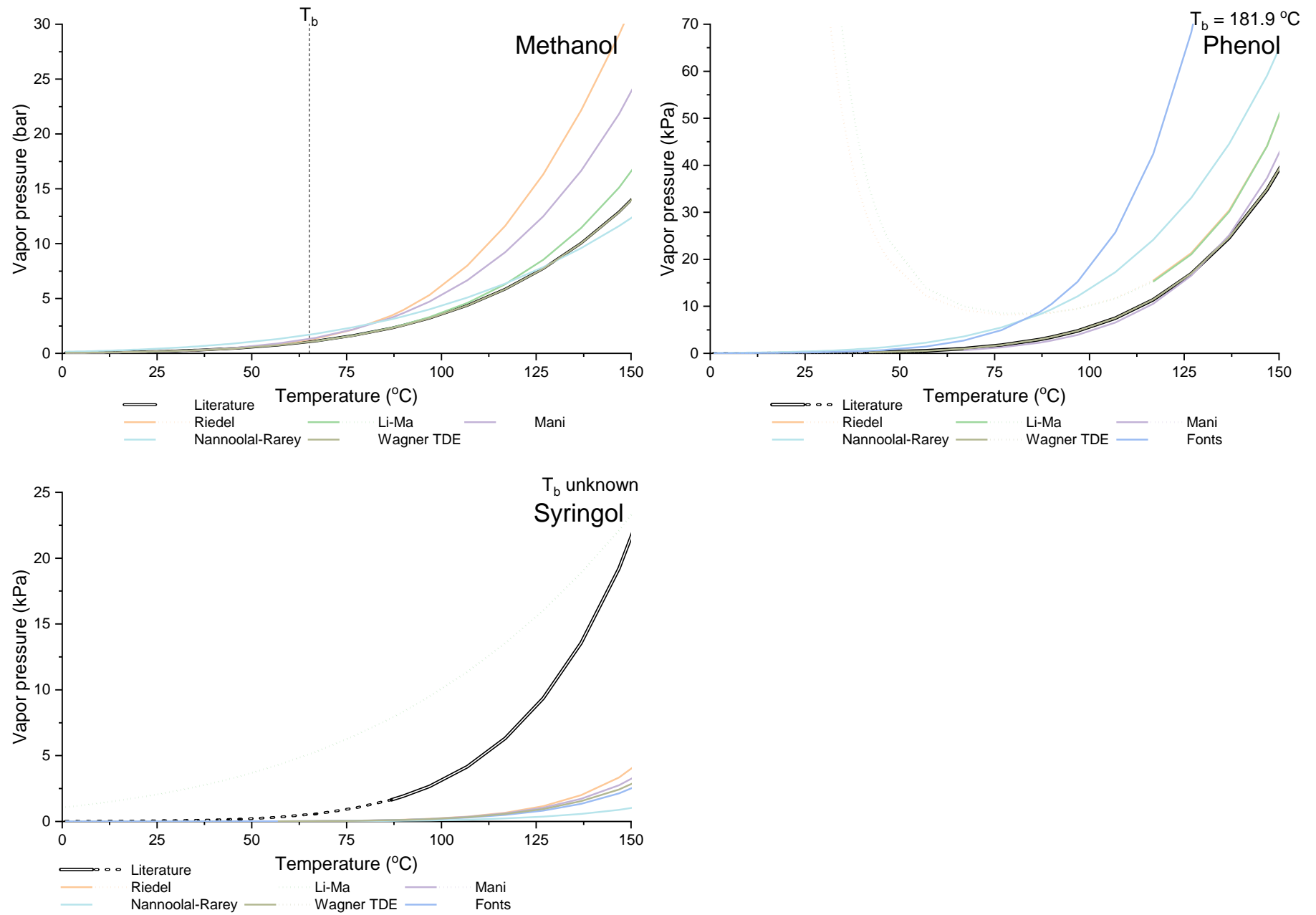


Fig. 33: Visual comparison of the p - T curves for several bio-oil components focused on the range of 0-150 °C. Dotted curves represent values outside the range of validity of the parameters. Components: METHANOL, PHENOL, SYRINGOL.

Group contribution assignment

Tab. 45: Group contribution list for the Cordes et al. [327] method for the normal boiling point, as well as the Nannoolal et al. methods for the critical properties [332], vapor pressure [341], and saturated liquid viscosity [352]. Numbering follows according to the source. Part 1 of 2.

ID	1	2	3	4	7	9	10	12	13	15	16	17	34	36	37	38	39	44	45	51	52	58	59	60	61	62	65	90	126	129	134	135	140	148	178	194		
ACETALDY	1																				1																	
ACETICAC	1																	1																				
ACETOL	1				1									1							1																	
ACETONE	2																				1																	
ACROLEIN																						1				1												
ANISOLE		1								5		1				1																						
CMRYLALC					1					4	1	1		1	1									1						1		1						
CRESOL			1							4	1	1				1															1							
EG					2											2																			1			
EGACET	1				2									1					1																			
ETHANOL	1				1									1																								
FFA	1			12															1				2															
FORMALDY																						1																
FORMICAC																		1																				
FURFURAL										2		2																1	1	1								
GLYOXAL																						2															1	
GUAIACOL		1								4		2				1	1																					1
HAA					1									1								1																
HEXADEC	2			14																																		
HMF					1					2		2		1														1	1	1								
HMWL		4		3	6					12				3	2	7																2	21	1	6			
KETENE																					1					1												
LEVOGLUC								3	3				3				2																	2	6		1	
METCSONE	1					1	1														1					1			1		1							
METHANOL		1												1																								
MF			1							2		2																1	1	1								
PHENOL										5		1				1																						
SYNAPALD		2								2	1	3				1	2					1		1						1							1	
SYRINGOL		2								3		3				1	2																					1
VANILLIN		1								3	1	2				1	1													1								
VINYLKET																					1		1		1													
XYLOSAN								2	3					2				2													1				1	4		1

Tab. 46: Group contribution list for the Růžička et al. [336–338] method for the liquid heat capacity. Part 1 of 2.

ID	C-(C)(H)3	C-(C)2(H)2	CD-(H)2	CD-(C)(H)	CD-(C)2	CD-(CD)(H)	CD-(CB)(H)	C-(CD)2(H)2	C-(CD)(C)(H)2	C-(CB)(H)3	CB-(H)	CB-(C)	CB-(CD)	Cyclopentene	CO-(O)(C)	CO-(O)(H)	CO-(CD)(H)	CO-(C)2	CO-(C)(H)	O-(CO)(C)	O-(CO)(H)
ACETALDY																			1		
ACETICAC															1						1
ACETOL	1	1																1			
ACETONE																		1			
ACROLEIN			1																1		
ANISOLE											5										
CMRYLALC				1							4		1								
CRESOL										1	4	1									
EG		2																			
EGACET	1														1					1	
ETHANOL	1																				
FFA	1	8		4				1	2						1						1
FORMALDY																			1		
FORMICAC																1					1
FURFURAL											2						1				
GLYOXAL																			2		
GUAIACOL	1										5										
HAA																			1		
HEXADEC	2	16																			
HMF							4										1				
HMWL				5	5		2				4	4						8	1		
KETENE			1															1			
LEVOGLUC																					
METCSONE	1	2		1										1				1			
METHANOL																					
MF	1						2														
PHENOL											5										
SYNAPALD							1				2		1				1				
SYRINGOL	2										4										
VANILLIN	1										5	1							1		
VINYLKET	1								1									1			
XYLOSAN																					

Tab. 47: Group contribution list for the Růžička et al. [336–338] method for the liquid heat capacity. Part 2 of 2.

ID	O-(CB)2	O-(CB)(C)	O-(CB)(H)	O-(C)2	O-(C)(H)	CD-(CO)(H)	CB-(O)	C-(CO)(C)2(H)	C-(CO)(C)(H)2	C-(CO)(H)3	C-(O)2(C)2	C-(O)(C)3 (Ester, ether)	C-(O)(CD)(H)2	C-(O)(C)3 (Alcohol)	C-(O)(C)2(H) (Alcohol)	C-(O)(C)(H)2	C-(O)(H)3	Tetrahydrofuran	Tetrahydropyran	Furan
ACETALDY										1										
ACETICAC										1										
ACETOL					1															
ACETONE										2										
ACROLEIN						1														
ANISOLE		1					1										1			
CMRYLALC			1		1		1						1			1				
CRESOL			1				1													
EG					2															
EGACET					1											2				
ETHANOL					1											1				
FFA									1											
FORMALDY																				
FORMICAC																				
FURFURAL				1								2								1
GLYOXAL																				
GUAIACOL		1	1									1								
HAA					1					1										
HEXADEC																				
HMF					1															1
HMWL	2				5			4	3	1					2	3				
KETENE																				
LEVOGLUC				2	3										3	3				
METCSONE						1														
METHANOL					1												1			
MF				1								3								1
PHENOL					1									1						
SYNAPALD		2			1	1	3										2			
SYRINGOL		2	1									2								
VANILLIN		1	1									1								
VINYLKET						1														
XYLOSAN				2	2						1				3	1		1	1	

Tab. 48: Group contribution list for the Ambrose [330] group contribution method.

ID	C (alkyl)	>CH- corr. (alkyl)	>C< corr. (alkyl)	Double bond corr. (alkyl)	-O-	>C=O	O=CH-	COOH	-COO-	-OH (aliph)	>CH ₂ (ring)	>CH- (fused-ring)	Double bond corr. (ring)	-O- (ring)	Benzene	-OH (arom)	1st nonhalo sub. (arom)	Other nonhalo sub. (arom)	Ortho pair w/ -OH	Ortho pair wo/ -OH
ACETALDY	2						1													
ACETICAC	2							1												
ACETOL	3					1				1										
ACETONE	3					1														
ACROLEIN	3			1			1													
ANISOLE	1				1										1					
CMRYLALC	3			1						1					1	1				
CRESOL	1														1	1				
EG	2									2										
EGACET	4								1	1										
ETHANOL	2									1										
FFA	18			2				1												
FORMALDY	1						1													
FORMICAC	1							1												
FURFURAL	1						1						2	1						
GLYOXAL	1						2													
GUAIACOL	1				1										1	1	1		1	
HAA	2						1			1										
HEXADEC	16																			
HMF	1						1						2	1		1				
HMWL	13	3			7					3					4	2	4	2	1	3
KETENE	2		1			1														
LEVOGLUC	5	5								3	1			2						
METCSONE	3					1							1							
METHANOL	1									1										
MF	2						1						2	1						
PHENOL															1	1				
SYNAPALD	5			1	2		1								1	1	1	1	2	
VANILLIN	2				1		1								1	1	1		1	
VINYLKET	4		1	1		1														
XYLOSAN	5	4			2					2										

Tab. 49: Group contribution list for the Benson [335] group contribution method. Part 1 of 2.

ID	C-(C)(H)3	C-(C)2(H)2	CD-(H)2	CD-(C)(H)	CD-(CD)(H)	C-(CD)(H)3	C-(CD)2(H)2	C-(CD)(C)(H)2	C-(CB)(H)3	CB-(H)	CB-(C)	CB-(CD)	Ortho corr.	5-ring corr.	6-ring corr.	CO-(CO)(H)	CO-(O)(C)	CO-(O)(H)	CO-(CD)(H)	CO-(CB)(H)	CO-(C)2	CO-(C)(H)	CO-(H)2
ACETALDY																						1	
ACETICAC	1																1						
ACETOL	1	1																			1		
ACETONE																					1		
ACROLEIN			1																			1	
ANISOLE										5													
CMRYLALC				1						4		1											
CRESOL									1	4	1												
EG																							
EGACET	1	2															1						
ETHANOL	1																						
FFA	1	8		4			1	2									1						
FORMALDY																							1
FORMICAC																		1					
FURFURAL				2																1			
GLYOXAL																2							
GUAIACOL	1									4			1										
HAA																						1	
HEXADEC	2	14																					
HMF				2	2																	1	
HMWL		3								12	3		4										
KETENE			1																		1		
LEVOGLUC														1	1								
METCSONE	1	1		2																	1		
METHANOL																							
MF				2		1													1				
PHENOL										5													
SYNAPALD										2		1							1				
SYRINGOL	2									3			2										
VANILLIN	2									3			1									1	
VINYLKET	1							1													1		
XYLOSAN																							

Tab. 50: Group contribution list for the Benson [335] group contribution method. Part 2 of 2.

ID	O-(CO)(C)	O-(CO)(H)	O-(CD)2	O-(CD)(C)	O-(CB)(C)	O-(CB)(H)	O-(C)2	O-(C)(H)	CD-(CO)(H)	CB-(CO)	CB-(O)	C-(CO)(C)(H)2	C-(CO)(H)3	C-(O)2(C)(H)	C-(O)(CD)(H)2	C-(O)(C)2(H)	C-(O)(C)(H)2	C-(O)(H)3	Tetrahydro furan corr.	Tetrahydro pyran corr.	Furan corr.	Cyclopentanone corr.
ACETALDY													1									
ACETICAC								1														
ACETOL								1														
ACETONE													2									
ACROLEIN									1													
ANISOLE					1						1							1				
CMRYLALC						1		1			1				1							
CRESOL						1					1											
EG								2										2				
EGACET	1							1														
ETHANOL								1										1				
FFA		1										1										
FORMALDY																						
FORMICAC		1																				
FURFURAL				1						1	1											1
GLYOXAL																						
GUAIACOL							1	1			1											
HAA								1					1									
HEXADEC																						
HMF							1	1														1
HMWL					7	2		3			9						3	3	4			
KETENE																						
LEVOGLUC							2	3									5	1				
METCSONE												1										1
METHANOL								1											1			
MF			1																			1
PHENOL								1			1											
SYNAPALD					2	1			1		1								1			
SYRINGOL							2	1			3											
VANILLIN							1	1		1	2											
VINYLKET									1													
XYLOSAN							2	2						1		3	1		1	1		

Tab. 51: Group contribution list for the Ducros [344–346] group contribution method. Part 1 of 2.

ID	C-(C)(H)3	C-(C)2(H)2	C-(C)3(H)	CD-(H)2	CD-(C)(H)	CD-(CD)(H)	C-(CD)2(H)2	C-(CD)(C)(H)2	C-(CB)(H)3	CB-(H)	CB-(C)	5-ring-ene corr.	5-ring-diene corr.	6-ring-ane corr.	CO-(O)(C)	CO-(C)2	CO-(C)(H)	O-(CO)(C)
ACETALDY																	1	
ACETICAC	1														1			
ACETOL																	1	
ACETONE																		
ACROLEIN				1													1	
ANISOLE										5								
CMRYLALC					2					4	1							
CRESOL									1	4	1							
EG			2															
EGACET	1	2													1			1
ETHANOL	1																	
FFA	1	8			4		1	2							1			
FORMALDY																	1	
FORMICAC															1			
FURFURAL					2												1	
GLYOXAL																	2	
GUAIACOL	1									6								
HAA																	1	
HEXADEC	2	14																
HMF					2	2											1	
HMWL		3								12	12							
KETENE				1												1		
LEVOGLUC																		
METCSONE	1	1			2							1						
METHANOL																		
MF	1					2							1				1	
PHENOL										6								
SYNAPALD					1					2	1						1	
SYRINGOL	2									6								
VANILLIN	1									5							1	
VINYLKET	1							1										
XYLOSAN														1				

Tab. 52: Group contribution list for the Ducros [344–346] group contribution method. Part 2 of 2.

ID	O-(CO)(H)	C-(CO)(C)2(H)	C-(CO)(C)(H)2	C-(CO)(C)3	C-(CO)(H)3	C-(O)2(C)(H)	C-(O)(C)3	C-(O)(C)2(H)	C-(O)(C)(H)2	C-(O)(H)3	O-(C)(H)	O-(C)(H) (Primary)	O-(C)2 (Non-ring)	CO-(C)2	O-(C)2 (Ring)	O-(C)2 (Ring -C-O-C-O-C-)	O-(C)(H) (Secondary)
ACETALDY					1												
ACETICAC	1																
ACETOL			1		1							1					
ACETONE					2									1			
ACROLEIN		1															
ANISOLE							1			1			1				
CMRYLALC							1		1		2						
CRESOL							1				1						
EG												2					
EGACET												1					
ETHANOL									1		1	1					
FFA	1		1														
FORMALDY																	
FORMICAC	1																
FURFURAL								1	1						1		
GLYOXAL																	
GUAIACOL											1		1				
HAA					1							1					
HEXADEC																	
HMF											1				1		1
HMWL								3	3	7	5		7				
KETENE																	
LEVOGLUC								5	1		3				2		3
METC5ONE			1											1			
METHANOL										1	1						
MF							3								1		
PHENOL											1						
SYNAPALD		1					3			3	1		2				
SYRINGOL											1		2				
VANILLIN				1							1		1				
VINYLKET		1												1			
XYLOSAN						1		3	1		2	2	2			1	

Tab. 53: Group contribution list for the Fedors [329] group contribution method.

ID	-CH3	>CH2	>CH-	=CH2	=CH-	=C<	-COOH	-COO-	>C=O	-O- (alkyl)	-O- (arom)	-OH (alkyl)	-OH (arom)	O=CH-	5-ring corr.	6-ring corr.	Corr. hetero atom (ring)	Subst in double bond (non- ring)	Ortho corr.	Double bond conj.	C- (O)(C)2 (H)	C- (O)(C)(H)2	C- (O)(H)3	O- (C)(H)	O-(C)2 (Non- ring)
ACETALDY	1													1											
ACETICAC	1						1																		
ACETOL	1	1							1			1													
ACETONE	1								1																
ACROLEIN				1	1									1											
ANISOLE	1				5	1					1														
CMRYLALC		1			6	2						1	1												
CRESOL	1				4								1												
EG		2											2												
EGACET	1	2						1				1													
ETHANOL	1	1										1													
FFA	1	12			4		1																		
FORMALDY														1											
FORMICAC							1																		
FURFURAL					3	1				1				1	1			1							
GLYOXAL														2											
GUAIACOL	1				4	2				1			1							1					
HAA		1										1		1											
HEXADEC	2	14																							
HMF					3	1				1			1	1	1			1							
HMWL		3			12	12															3	3	7	5	7
KETENE				1					1																
LEVOGLUC		1	5							2		3						2							
METCSONE	1	2			1	1			1						1										
METHANOL	1											1													
MF	1				2	2				1				1	1			1			1				
PHENOL					5	1							1												
SYNAPALD	2				4	4					2		1	1									2		
SYRINGOL	2				3	3				2		3	1										2		
VANILLIN	1				4	2				1			1	1									1		
VINYLKET	1	1			1				1																
XYLOSAN		1	4							2		2													

Tab. 54: Group contribution list for the Gani [326] group contribution method.

ID	>CH-	>CH 2	-CH3	- CH= C<	- CH= CH-	- CH= CH2	>C= (aro m)	-CH= (aro m)	CH3- ArC	-OH (alky l)	HO- ArC	- CH2- CO- (C)	CH3- CO- (C)	O=C H-	- CH2- COO -(C)	CH3- COO -(C)	>CH- O- (C)	- CH2- O- (C)	CH3- O- (C)	- COO H	5- ring corr.	6- ring corr.	CHC HO	c- C=O	ArCC HO	C- CH= CH	c- CHO H	ArC- O- CH3	
ACETALDY														1						1			1						
ACETICAC			1																	1									
ACETOL			1							1		1																	
ACETONE			1										1																
ACROLEIN						1								1									1						
ANISOLE							1	5											1										1
CMRYLALC		1			1		1	4		1	1																1		
CRESOL								4	1		1																		
EG		2									2																		
EGACET		2									1					1													
ETHANOL		1	1								1																		
FFA		12	1		2															1									
FORMALDY														1															
FORMICAC																				1									
FURFURAL							1	3						1			1												
GLYOXAL														2															
GUAIACOL							1	4			1								1										
HAA		1								1				1															
HEXADEC		14	2																										
HMF							1	2		1				1			1												
HMWL		6					8	12		3	2						3		5										5
KETENE												1																	
LEVOGLUC	4									3							1	1											
METCSONE		1	1	1								1									1			1					
METHANOL			1							1																			
MF							2	1						1			1				1				1				
MLINO		11	2		2										1														
PHENOL								5			1																		
SYNAPALD					1		4	2		1				1					2										
SYRINGOL						2	3				1								2										
VANILLIN							2	4			1			1					1										
VINYLKET	1	1	1											1									1						
XYLOSAN	3									2							1	1				1						2	

Tab. 55: Group contribution list for the Joback [325] group contribution method.

ID	-CH3	>CH2	>CH-	=CH2	=CH-	>CH2 (ring)	>CH- (ring)	=CH- (ring)	=C< (ring)	-OH (alkyl)	-OH (arom)	-O- (non- ring)	-O- (ring)	>C=O (non- ring)	>C=O (ring)	O=CH-	-COOH	-COO-
ACETALDY	1															1		
ACETICAC	1																1	
ACETOL	1	1								1				1				
ACETONE	2													1				
ACROLEIN				1	1											1		
ANISOLE	1							5	1			1						
CMRYLALC		1			2			4	2	1	1							
CRESOL	1							4	1		1							
EG		2								2								
EGACET	1	2									1							1
ETHANOL	1	1								1								
FFA	1	12			4												1	
FORMALDY																1		
FORMICAC																	1	
FURFURAL								3	1				1			1		
GLYOXAL																2		
GUAIACOL	1							4	2		1	1						
HAA		1								1						1		
HEXADEC	2	14																
HMF								2	2		1		1			1		
HMWL	5	6	3					12	12	3	2	7						
KETENE				1										1				
LEVOGLUC						1	5			3			2					
METCSONE	1					2		1	1						1			
METHANOL	1									1								
MF	1							2	2				1			1		
PHENOL								5	1		1							
SYNAPALD	2				2			2	4		1	1				1		
SYRINGOL	2							3	3		1	2						
VANILLIN	1							3	3		1	1				1		
VINYLKET	1	1			1									1				
XYLOSAN		1	4							2			2					

Tab. 56: Group contribution list for the Le Bas [348] group contribution method.

ID	#C	#H	#O except esters, ethers, acids	#O in methyl esters/ethers	#O in higher esters/ethers	#O acids	5-ring corr.	6-ring corr.	-OH (alkyl)	-OH (arom)
ACETALDY	2	4	1							
ACETICAC	2	4				2				
ACETOL	3	6	1						1	
ACETONE	3	6	1							
ACROLEIN	3	4	1							
ANISOLE	7	8	1					1		
CMRYLALC	9	10	2					1	1	1
CRESOL	7	7	1					1		1
EG	2	6							2	
EGACET	4	8		2					8	
ETHANOL	2	6	1						1	
FFA	18	32				2				
FORMALDY	1	2	1							
FORMICAC	1	2				2				
FURFURAL	5	4		1	1					
GLYOXAL	2	2	2							
GUAIACOL	7	8	1					1		1
HAA	2	4	1						1	
HEXADEC	16	34								
HMF	5	4	2				1			1
HMWL	37	44		4	3			4	3	2
KETENE	2	2	1							
LEVOGLUC	6	10	2						3	
METCSONE	5	6	1							
METHANOL	1	4	1							
MF	6	6	2				1			
PHENOL	6	6						1		1
SYNAPALD	11	12	2	2						1
SYRINGOL	8	10	2					1		1
VANILLIN	8	8	1	1				1		1
VINYLKET	4	6	1							
XYLOSAN	5	8	2		2				2	

Tab. 57: Group contribution list for the Li-Ma [340] group contribution method.

ID	-COOH	-COO-	>C=O (ring)	>C=O	-CHO	-O- (ring)	ArC-O-	-O- (No n-ring)	ArC-OH	-OH (ring)	-OH	=CH- (arom)	=C< (arom)	=CH- (ring)	=C< (Ring)	ArC=CH-	=CH ₂	=CH-	-CH ₂ - (ring)	>CH- (Ring)	ArC-CH ₃	ArC-CH<	-CH ₃ (ring)	-CH ₃	-CH ₂ -	>CH-
ACETALDY					1																			1		
ACETICAC	1																							1		
ACETOL				1							1													1	1	
ACETONE				1																				2		
ACROLEIN					1												1	1							1	
ANISOLE								1				1	1												1	
CMRYLALC									1		1	4	2			1		1								1
CRESOL											1	4	2								1					
EG											2															2
EGACET		1									1													1		2
ETHANOL											1													1		1
FFA	1																	4						1		12
FORMALDY					1																					
FORMICAC	1																									
FURFURAL					1			1				3	1													
GLYOXAL					2																					
GUAIACOL							1		1			4	2											1		
HAA					1						1															1
HEXADEC																								2		14
HMF					1			1	1			2	2													
HMWL							7		2		3	12	12									3	4			6
KETENE				1													1									
LEVOGLUC						2				3										1						5
METCSONE			1											1	1					2				1		
METHANOL											1													1		
PHENOL									1			5	1													
SYNAPALD					1		2		1			2	1			1		1								
SYRINGOL							2		1			3	3												2	
VANILLIN					1		1		1			3	3												1	
VINYLKET				1														1						1		1
XYLOSAN						2				2									1	4						

Tab. 58: Group contribution list for the Lydersen [328] group contribution method.

ID	-CH3	>CH2	>CH-	=CH2	=CH-	=C<	>CH2 (ring)	>CH- (ring)	>C< (ring)	=CH- (ring)	=C< (ring)	-OH (alkyl)	ArC- OH	-O- (non- ring)	-O- (ring)	>C=O (non- ring)	>C=O (ring)	O=CH-	-COOH	-COO-
ACETALDY	1																	1		
ACETICAC	1																		1	
ACETOL		1										1				1				
ACETONE	2															1				
ACROLEIN				1	1													1		
ANISOLE	1								1	5				1						
CMRYLALC		1			2					4	2	1	1							
CRESOL	1				4	2							1							
EG		2										2								
EGACET	1	2										1								1
ETHANOL	1	1										1								
FFA	1	12			4														1	
FORMALDY																		1		
FORMICAC																			1	
FURFURAL										3	1				1			1		
GLYOXAL																		2		
GUAIACOL	1									4	2		1	1						
HAA		1										1						1		
HEXADEC	2	14																		
HMF										2	2		1		1			1		
HMWL	4	6	3						12	12		3	2	7						
KETENE				1												1				
LEVOGLUC							1	5				3			2					
METCSONE	1						2			1	1						1			
METHANOL	1											1								
MF	1									2	2				1			1		
PHENOL										5	1		1							
SYNAPALD	2				2				4	2			1	2				1		
SYRINGOL	2									3	3		1	2						
VANILLIN	1									3	3		1	1				1		
VINYLKET	1	1			1											1				
XYLOSAN							1	4				2			2					

Tab. 59: Group contribution list for the UNIFAC [225,284,285] group contribution method.

ID	>CH-	>CH2	-CH3	>C=C<	-CH=C H-	-CH=C H2	>ArC=	-ArCH =	ArC- CH<	ArC- CH3	-OH	ArC- OH	-CH2- CO-	CH3- CO-	O=CH -	CH3- COO-	>CH- O-	-CH2- O-	CH3- O-	HCOO H	- COOH	Furfur al
ACETALDY			1												1							
ACETICAC			1																		1	
ACETOL			1								1		1									
ACETONE			1											1								
ACROLEIN						1									1							
ANISOLE							1	5											1			
CMRYLALC		1			1		1	4			1	1										
CRESOL								4		1		1										
EG		2									2											
EGACET		2									1					1						
ETHANOL		1	1								1											
FFA		12	1		2																1	
FORMALDY															1							
FORMICAC																				1		
FURFURAL																						1
GLYOXAL															2							
GUAIACOL							1	4				1							1			
HAA		1									1				1							
HEXADEC		14	2																			
HMF		1									1											1
HMWL		6					7	12	3		3	2					3		4			
KETENE														1								
LEVOGLUC	3	1									3						2					
METCSONE		1	1	1										1								
METHANOL			1								1											
MF										1												1
PHENOL								5				1										
SYNAPALD					1		3	2				1			1				2			
SYRINGOL							2	3				1							2			
VANILLIN							2	3				1			1				1			
VINYLKET	1	1	1												1							
XYLOSAN	3										2						1	1				

Property estimation parameters

$$C_{p,i}^{*,ig} = \begin{cases} C_{1i} + C_{2i}T + C_{3i}T^2 + C_{4i}T^3 & 280 \text{ K} \leq T \leq 1100 \text{ K} \\ 36029.20 + C_{5i}T^{C_{6i}} & T < 280 \text{ K} \end{cases}$$

Tab. 60: Parameters for the estimation of the ideal gas heat capacity ($C_p^{*,ig}$) using the Benson and the Joback methods. Values in $\text{J}\cdot\text{mol}^{-1}\cdot\text{K}^{-1}$, temperature in K. Estimated using Aspen Plus™ V12.

ID	BENSON						JOBACK					
	C ₁	C ₂	C ₃	C ₄	C ₅	C ₆	C ₁	C ₂	C ₃	C ₄	C ₅	C ₆
ACETALDY	19277.85	19277.85	-1.78×10-2	-1.51×10-5	4.58×10-1	1.87	12470.00	168.32	-7.80×10-2	1.05×10-5	2.10×10-1	2.01
ACACID	34626.29	34626.29	1.41×10-2	-3.30×10-5	6.53	1.50	5670.00	244.62	-1.58×10-1	4.06×10-5	1.46	1.74
ACETOL	32287.41	32287.41	-1.80×10-2	-3.25×10-5	10.71	1.50	12811.00	294.82	-1.51×10-1	2.53×10-5	10.25	1.50
ACETONE	13717.64	13717.64	-7.54×10-2	-1.77×10-6	7.55	1.50	7520.00	260.84	-1.21×10-1	1.55×10-5	5.48	1.56
ACROLEIN	15380.09	15380.09	-8.80×10-2	1.16×10-5	5.32	1.52	8570.00	243.30	-1.55×10-1	3.98×10-5	3.99	1.58
ANISOLE	-41754.01	-41754.01	-5.31×10-1	1.60×10-4	13.54	1.54	-11880.00	526.72	-2.77×10-1	4.28×10-5	16.81	1.50
CMRYLALC	-22373.32	-22373.32	-5.60×10-1	1.63×10-4	24.15	1.50	-57009.00	988.50	-8.68×10-1	3.12×10-4	26.16	1.50
CRESOL	-23913.73	-23913.73	-4.23×10-1	1.14×10-4	17.41	1.50	-38050.00	643.52	-5.03×10-1	1.63×10-4	8.77	1.60
EG	27865.56	27865.56	2.99×10-3	-2.22×10-5	4.08	1.50	11652.00	261.80	-1.46×10-1	3.22×10-5	8.15	1.50
EGACET	54825.62	54825.62	4.42×10-2	-9.10×10-5	18.98	1.50	1442.00	543.12	-4.23×10-1	1.37×10-4	18.65	1.50
ETHANOL	6638.87	6638.87	-1.09×10-1	1.83×10-5	7.55×10-1	1.85	6361.00	227.82	-1.15×10-1	2.24×10-5	7.81×10-1	1.85
FFA	-21614.89	-21614.89	-1.06×10+0	2.50×10-4	74.54	1.50	-37238.00	1804.62	-1.20×10+0	3.26×10-4	73.73	1.50
FORMALDY	26230.74	26230.74	4.73×10-2	-3.06×10-5	-3.05×10-1	1.50	-7030.00	176.40	-2.31×10-1	1.07×10-4	-2.01×10+0	1.50
FORMICAC	11436.64	11436.64	-8.68×10-2	2.17×10-5	2.10×10-5	3.50	-13830.00	252.70	-3.11×10-1	1.37×10-4	-9.40×10-2	1.50
FURFURAL	-18612.50	-18612.50	-2.33×10-1	2.74×10-5	2.06	1.78	-9500.00	437.00	-3.18×10-1	8.87×10-5	11.50	1.50
GLYOXAL	29999.62	29999.62	5.62×10-2	-6.09×10-5	3.92	1.50	23870.00	142.80	-7.10×10-2	8.40×10-6	4.79	1.50
GUAICOL	-35050.11	-35050.11	-6.78×10-1	2.23×10-4	22.37	1.50	-20800.00	681.32	-5.34×10-1	1.76×10-4	20.48	1.50
HAA	40445.79	40445.79	5.16×10-2	-4.99×10-5	7.46	1.50	17761.00	202.30	-1.08×10-1	2.03×10-5	6.47	1.50
HEXADEC	-37314.53	-37314.53	-8.48×10-1	1.50×10-4	65.89	1.50	-11656.00	1523.84	-8.47×10-1	1.79×10-4	67.56	1.50
HMF	13636.36	13636.36	-1.95×10-1	2.64×10-5	15.32	1.50	-18420.00	591.60	-5.74×10-1	2.22×10-4	15.17	1.50
HMWL	-162269.07	-162269.07	-3.68×10+0	1.20×10-3	162.55	1.50	110416.00	2824.70	-1.40×10+0	1.96×10-4	162.26	1.50
KETENE	14368.40	14368.40	-3.62×10-2	-2.94×10-6	5.08×10-6	3.73	-7880.00	238.90	-2.55×10-1	1.06×10-4	1.49×1012	6.36
LEVOGLUC	-80875.55	-80875.55	-1.05×10+0	3.69×10-4	27.47	1.50	-44960.00	872.90	-5.47×10-1	1.26×10-4	26.31	1.50
METCSONE	-41965.16	-41965.16	-2.43×10-1	2.37×10-5	3.03×10-1	2.14	-34430.00	598.12	-4.33×10-1	1.28×10-4	6.41	1.64
METHANOL	21320.87	21320.87	2.92×10-2	-3.03×10-5	1.92×10-5	3.48	7270.00	132.82	-6.10×10-2	1.05×10-5	5.28×1015	7.30
MF	-16523.48	-16523.48	-2.72×10-1	6.72×10-5	2.19	1.76	3890.00	472.52	-3.05×10-1	7.57×10-5	16.63	1.50
PHENOL	-36404.30	-36404.30	-4.52×10-1	1.36×10-4	3.49	1.73	-59690.00	709.00	-6.57×10-1	2.44×10-4	8.58×10-1	1.97
SYNAPALD	42013.88	42013.88	-2.88×10-1	5.50×10-5	28.38	1.50	1380.00	936.84	-6.94×10-1	2.19×10-4	38.01	1.50
SYRINGOL	-33695.93	-33695.93	-9.03×10-1	3.09×10-4	32.15	1.50	18090.00	653.64	-4.10×10-1	1.08×10-4	28.88	1.50
VANILLIN	-2128.09	-2128.09	-6.13×10-1	1.74×10-4	33.32	1.50	3990.00	691.32	-5.14×10-1	1.61×10-4	26.63	1.50
VINYLKET	7939.60	7939.60	-1.58×10-1	2.85×10-5	10.14	1.50	-20889.00	468.92	-4.24×10-1	1.60×10-4	3.32	1.69
XYLOSAN	-110563.03	-110563.03	-9.04×10-1	3.03×10-4	3.90×10-1	2.16	-55039.00	957.60	-1.03×10+0	4.23×10-4	22.52	1.50

$$C_{p,i}^* = \frac{B}{1 - \frac{T}{T_{ci}}} + C_{1i} + C_{2i}T + C_{3i}T^2 + C_{4i}T^3 \quad T_{min} \leq T \leq T_{max}$$

Tab. 61: Parameters for the estimation of the ideal gas heat capacity (C_p^{*ig}) using sourced data from the TDE. Estimated using Aspen Plus™ V12. Validity region: 200-1000 K.

ID	Temperature Unit	Unit	C ₁	C ₂	C ₃	C ₄	B
ACETOL	K	J·kmol ⁻¹ ·K ⁻¹	39496.00	200.25	-1.25×10 ⁻²	-4.07×10 ⁻⁵	7.55×10 ⁻¹⁹
EGACET	K	J·kmol ⁻¹ ·K ⁻¹	13346.00	438.58	-2.30×10 ⁻¹	3.60×10 ⁻⁵	7.81×10 ⁻¹⁸
FFA	K	J·kmol ⁻¹ ·K ⁻¹	38156.00	1398.85	-4.49×10 ⁻¹	-8.15×10 ⁻⁵	-8.95×10 ⁻¹⁸
GUAIACOL	K	J·kmol ⁻¹ ·K ⁻¹	16689.00	497.72	-2.14×10 ⁻¹	2.30×10 ⁻⁶	-2.69×10 ⁻¹⁸
HAA	K	J·kmol ⁻¹ ·K ⁻¹	30060.00	143.75	2.70×10 ⁻⁴	-3.75×10 ⁻⁵	3.21×10 ⁻¹⁸
HMF	K	J·kmol ⁻¹ ·K ⁻¹	12160.00	488.89	-2.63×10 ⁻¹	3.74×10 ⁻⁵	1.00×10 ⁻¹⁷
LEVOGLUC	K	J·kmol ⁻¹ ·K ⁻¹	3207.00	643.27	-2.66×10 ⁻¹	-6.29×10 ⁻⁶	9.21×10 ⁻¹⁸
METC5ONE	K	J·kmol ⁻¹ ·K ⁻¹	-17760.00	510.97	-2.78×10 ⁻¹	4.96×10 ⁻⁵	1.20×10 ⁻¹⁷
SYRINGOL	K	J·kmol ⁻¹ ·K ⁻¹	49793.00	500.06	-1.19×10 ⁻¹	-6.00×10 ⁻⁵	1.34×10 ⁻¹⁷
VANILLIN	K	J·kmol ⁻¹ ·K ⁻¹	26963.00	578.45	-2.80×10 ⁻¹	2.40×10 ⁻⁵	1.13×10 ⁻¹⁷
ANISOLE	°C	cal·mol ⁻¹ ·K ⁻¹	9703.00	430.55	-1.25×10 ⁻¹	-3.58×10 ⁻⁵	3.12×10 ⁻¹⁹

Tab. 62: Parameters for the estimation of the liquid heat capacity (C_p^{*l}) using sourced data from the TDE. Estimated using Aspen Plus™ V12.

ID	Temperature Unit	Unit	C ₁	C ₂	C ₃	B	T _{min}	T _{max}
ACACID	°C	cal·mol ⁻¹ ·K ⁻¹	186377.50	-1043.94	3.78	7094.07	289.69	580.00
ACETONE	°C	cal·mol ⁻¹ ·K ⁻¹	198716.90	-949.68	3.10	3801.56	178.16	497.90
ACROLEIN	°C	cal·mol ⁻¹ ·K ⁻¹	131499.30	-373.18	1.37	4770.36	185.49	517.44
ANISOLE	°C	cal·mol ⁻¹ ·K ⁻¹	185398.40	-344.65	1.48	5472.11	235.84	630.00
FFA	°C	cal·mol ⁻¹ ·K ⁻¹	442912.70	88.49	1.51	7524.64	267.73	770.00
FORMALDY	°C	cal·mol ⁻¹ ·K ⁻¹	137243.30	-601.87	1.74	4615.69	155.17	409.74
FURFURAL	°C	cal·mol ⁻¹ ·K ⁻¹	370931.00	-1884.31	5.01	5846.52	234.84	644.84
HEXADEC	°C	cal·mol ⁻¹ ·K ⁻¹	355214.00	439.14	-6.48×10 ⁻²	2006.81	291.33	707.94
MF	°C	cal·mol ⁻¹ ·K ⁻¹	176921.90	-146.50	7.82×10 ⁻¹	5390.86	250.00	684.04
VINYLKET	°C	cal·mol ⁻¹ ·K ⁻¹	99849.19	-249.50	1.28	4552.48	250.00	529.20
METC5ONE	K	J·kmol ⁻¹ ·K ⁻¹	31270.80	364.75	-7.41×10 ⁻³	4201.14	250.00	673.26

$$C_{p,i}^{*,l} = \frac{B}{1 - \frac{T}{T_{ci}}} + C_{1i} + C_{2i}T + C_{3i}T^2 + C_{4i}T^3 \quad T_{min} \leq T \leq T_{max}$$

Tab. 63: Parameters for the estimation of the liquid heat capacity ($C_{p,i}^{*,l}$) using the Růžička method. Temperature in K.. Estimated using Aspen Plus™ V12.

ID	C ₁	C ₂	C ₃	T _{min}	T _{max}		C ₁	C ₂	C ₃	T _{min}	T _{max}
ACETALDY	152.99	609.61	-8.95×10 ⁻¹	162	294	GUAIACOL	-155226.08	1850.91	-1.61	264	477
ACACID	45764.73	242.89	3.91×10 ⁻²	216	391	HAA	107842.52	-233.89	1.29	213	386
ACETOL	208127.98	-816.40	2.28×10 ⁺⁰	235	424	HEXADEC	389544.77	-120.51	1.57	310	560
ACETONE	109152.06	3.41	1.72×10 ⁻¹	182	329	HMF	244506.46	-1308.34	3.98	291	527
ACROLEIN	-72014.47	1857.96	-3.50×10 ⁺⁰	180	325	HMWL	-1517238.44	14078.26	-1.55×10 ⁺¹	995	1800
ANISOLE	-70198.58	1251.10	-1.17×10 ⁺⁰	236	427	KETENE	79934.04	20.54	-6.92×10 ⁻²	124	223
CMRYLALC	-185781.91	2919.22	-4.11×10 ⁺⁰	337	609	LEVOGLUC	498537.19	-2784.24	8.24	373	675
CRESOL	44485.95	844.17	-7.94×10 ⁻¹	263	475	METCSONE	84438.26	983.12	-1.80	230	416
EG	261893.76	-1696.15	4.54×10 ⁺⁰	260	471	METHANOL	139660.49	-871.77	2.35	187	338
EGACET	228885.16	-677.12	2.02×10 ⁺⁰	255	461	MF	132914.09	-3.15	3.80×10 ⁻¹	244	441
ETHANOL	151796.35	-749.91	2.12×10 ⁺⁰	194	351	PHENOL	-169894.54	1694.00	-1.35	252	455
FFA	469025.67	-358.95	1.85×10 ⁺⁰	343	621	SYNAPALD	-350107.39	4030.93	-4.86	343	620
FORMALDY	-31817.97	637.88	-1.06×10 ⁺⁰	140	254	SYRINGOL	-356918.63	3152.69	-3.12	296	535
FORMICAC	-120302.65	1326.59	-1.98×10 ⁺⁰	207	374	VANILLIN	-174514.08	2477.68	-2.65	312	564
FURFURAL	68283.74	196.95	-4.20×10 ⁻¹	240	435	VINYLKET	19112.56	1307.90	-2.42	184	332
GLYOXAL	-63635.93	1275.76	-2.11×10 ⁺⁰	189	342	XYLOSAN	177938.00	-1600.93	4.98	307	556

$$\ln p_i^{*,l} = C_{1i} + \frac{C_{2i}}{T} + C_{3i}T + C_{4i} \ln T + C_{5i}T^6 \quad T_1 \leq T \leq T_2$$

Tab. 64: Parameters for the estimation of the vapor pressure ($p_i^{*,l}$) calculated from experimental data and Nannoolal-Rarey estimates. Values in Pa, temperature in K. Estimated using Aspen Plus™ V12, and using the method described in [341].

ID	EXPERIMENTAL							NANNOOLAL-RAREY						
	C ₁	C ₂	C ₃	C ₄	C ₅	T ₁	T ₂	C ₁	C ₂	C ₃	C ₄	C ₅	T ₁	T ₂
ACETALDY	-5.15	-3575.38	-2.75×10 ⁻²	6.48	1.21×10 ⁻¹⁶	191.65	464.11	80.88	-4982.20	1.19×10 ⁻²	-9.81	-6.54×10 ⁻¹⁸	240.15	480.15
ACACID	-46645.47	1415992.79	-1.10×10 ¹	7.93×10 ³	0.00	328.90	390.87	158.37	-8844.59	2.85×10 ⁻²	-2.27×10 ¹	-1.68×10 ⁻¹⁷	240.15	480.15
ACETOL	-3075.83	119190.91	1.50×10 ⁻¹	4.66×10 ²	-2.24×10 ⁻¹⁴	273.22	305.95	217.90	-11595.27	4.15×10 ⁻²	-3.25×10 ¹	-2.52×10 ⁻¹⁷	240.15	480.15
ACETONE	-19.76	-3610.04	-2.81×10 ⁻²	8.86	9.13×10 ⁻¹⁷	213.75	487.65	112.25	-6441.14	1.93×10 ⁻²	-1.50×10 ¹	-1.24×10 ⁻¹⁷	240.15	480.15
ACROLEIN	12135.91	-264652.11	4.88	-2.22×10 ³	-2.50×10 ⁻¹⁴	260.00	286.00	112.77	-6604.75	1.90×10 ⁻²	-1.51×10 ¹	-1.18×10 ⁻¹⁷	240.15	480.15
ANISOLE	-2816.77	76270.59	-7.56×10 ⁻¹	4.90×10 ²	6.32×10 ⁻¹⁶	390.00	430.00	212.10	-11457.21	3.97×10 ⁻²	-3.15×10 ¹	-2.32×10 ⁻¹⁷	240.15	480.15
CMRYLALC	n.a.	n.a.	n.a.	n.a.	n.a.	n.a.	n.a.	529.70	-24318.11	1.12×10 ⁻¹	-8.47×10 ¹	-7.27×10 ⁻¹⁷	240.15	480.15
CRESOL	806.77	-34145.60	1.50×10 ⁻¹	-1.29×10 ²	-2.16×10 ⁻¹⁸	326.15	1846.15	174.23	-9577.84	3.19×10 ⁻²	-2.53×10 ¹	-1.88×10 ⁻¹⁷	240.15	480.15
EG	-91013.47	2401514.52	-2.72×10 ¹	1.60×10 ⁴	3.83×10 ⁻¹⁴	307.70	384.50	255.00	-13213.57	4.98×10 ⁻²	-3.87×10 ¹	-3.08×10 ⁻¹⁷	240.15	480.15
EGACET	-65402.02	1613235.12	-2.15×10 ¹	1.16×10 ⁴	4.62×10 ⁻¹⁴	301.30	346.30	234.95	-12237.76	4.59×10 ⁻²	-3.54×10 ¹	-2.95×10 ⁻¹⁷	240.15	480.15
ETHANOL	79.43	-7239.95	4.36×10 ⁻³	-8.33	2.77×10 ⁻¹⁸	160.00	510.00	117.85	-6940.22	1.97×10 ⁻²	-1.59×10 ¹	-1.16×10 ⁻¹⁷	240.15	480.15
FORMALDY	1788.68	-34717.11	9.13×10 ⁻¹	-3.38×10 ²	-1.13×10 ⁻¹⁴	163.75	250.85	76.66	-4609.43	1.14×10 ⁻²	-9.10	-7.19×10 ⁻¹⁸	240.15	480.15
FORMICAC	71.68	-5907.58	9.13×10 ⁻³	-8.06	-2.11×10 ⁻¹⁹	282.00	580.00	159.99	-8844.89	2.94×10 ⁻²	-2.29×10 ¹	-1.89×10 ⁻¹⁷	240.15	480.15
FURFURAL	693405.58	-27632900.90	1.17×10 ²	-1.12×10 ⁵	-1.48×10 ⁻¹⁴	549.85	638.35	232.40	-12146.20	4.52×10 ⁻²	-3.50×10 ¹	-2.92×10 ⁻¹⁷	240.15	480.15
GLYOXAL	766.32	-25197.75	2.08×10 ⁻¹	-1.29×10 ²	-3.68×10 ⁻¹⁶	274.00	340.00	143.59	-8352.91	2.46×10 ⁻²	-2.01×10 ¹	-1.27×10 ⁻¹⁷	240.15	480.15
GUAIACOL	-497.18	7120.82	-1.51×10 ⁻¹	9.15×10 ¹	1.38×10 ⁻¹⁶	325.55	478.15	315.86	-15794.12	6.33×10 ⁻²	-4.89×10 ¹	-4.00×10 ⁻¹⁷	240.15	480.15
HAA	11178.78	-285523.67	3.65	-1.98×10 ³	-7.78×10 ⁻¹⁵	295.85	355.98	207.91	-10942.49	4.04×10 ⁻²	-3.10×10 ¹	-2.72×10 ⁻¹⁷	240.15	480.15
HEXADEC	189.79	-15834.14	1.57×10 ⁻²	-25.10	9.86×10 ⁻¹⁹	292.15	720.15	9710.11	-484233.47	1.27	-1509.89	-6.45E-17	240.15	480.15
HMF	-19963.38	519064.35	-5.98	3.51×10 ³	8.42×10 ⁻¹⁵	313.40	368.10	867.41	-36931.90	1.90×10 ⁻¹	-1.42×10 ²	-1.28×10 ⁻¹⁶	240.15	480.15
HMWL	n.a.	n.a.	n.a.	n.a.	n.a.	n.a.	n.a.	3443.67	-125971.90	7.98×10 ⁻¹	-5.77×10 ²	-5.43×10 ⁻¹⁶	240.15	480.15
KETENE	82.00	-2407.96	2.83×10 ⁻²	-12.20	-3.97E-16	160.15	220.15	4067.04	-207933.45	5.20×10 ⁻¹	-628.65	-2.54E-17	240.15	480.15
LEVOGLUC	-64045.94	1787624.54	-1.75×10 ¹	1.11×10 ⁴	1.67×10 ⁻¹⁴	344.96	404.98	478.95	-22231.00	1.01×10 ⁻¹	-7.63×10 ¹	-6.73×10 ⁻¹⁷	240.15	480.15
METCSONE	24.18	-5449.43	0.00	0.00	0.00	298.15	430.70	205.22	-10932.33	3.93×10 ⁻²	-3.05×10 ¹	-2.49×10 ⁻¹⁷	240.15	480.15
METHANOL	-12515.13	295682.50	-4.32	2.25×10 ³	1.13×10 ⁻¹⁴	288.15	337.65	110.09	-6452.78	1.84×10 ⁻²	-1.46×10 ¹	-1.11×10 ⁻¹⁷	240.15	480.15
MF	n.a.	n.a.	n.a.	n.a.	n.a.	n.a.	n.a.	251.03	-12902.04	4.95×10 ⁻²	-3.81×10 ¹	-3.16×10 ⁻¹⁷	240.15	480.15
PHENOL	-86.52	-5355.89	-5.34×10 ⁻²	2.18×10 ¹	6.06×10 ⁻¹⁷	380.30	454.90	234.12	-12228.74	4.55×10 ⁻²	-3.53×10 ¹	-2.91×10 ⁻¹⁷	240.15	480.15
SYNAPALD	38.79	-3078.24	3.27×10 ⁻³	-4.65	2.24×10 ⁻¹⁹	410.00	830.00	706.81	-31008.27	1.53×10 ⁻¹	-1.14×10 ²	-1.02×10 ⁻¹⁶	240.15	480.15
SYRINGOL	-7605.21	201164.87	-2.16	1.33×10 ³	2.33×10 ⁻¹⁵	333.28	413.16	552.20	-25142.15	1.17×10 ⁻¹	-8.85×10 ¹	-7.69×10 ⁻¹⁷	240.15	480.15
VANILLIN	-8966.58	229189.05	-2.68	1.58×10 ³	3.70×10 ⁻¹⁵	324.92	382.26	464.83	-21736.96	9.73×10 ⁻²	-7.38×10 ¹	-6.33×10 ⁻¹⁷	240.15	480.15
VINYLKET	n.a.	n.a.	n.a.	n.a.	n.a.	n.a.	n.a.	380.22	-18378.33	7.80×10 ⁻²	-5.97×10 ¹	-5.01×10 ⁻¹⁷	240.15	480.15
XYLOSAN	116.32	-13603.43	-3.26×10 ⁻³	-1.27×10 ¹	2.60×10 ⁻¹⁸	460.00	740.00	337.28	-16607.60	6.84×10 ⁻²	-5.25×10 ¹	-4.33×10 ⁻¹⁷	240.15	480.15

Tab. 65: Parameters for the estimation of the vapor pressure (p_i^{*l}) using the Riedel and Li-Ma methods. Values in Pa, temperature in K. Estimated using Aspen Plus™ V12.

ID	RIEDEL							LI-MA						
	C ₁	C ₂	C ₃	C ₄	C ₅	T ₁	T ₂	C ₁	C ₂	C ₃	C ₄	C ₅	T ₁	T ₂
ACETALDY	55.93	-4823	0	-4.92	2.89×10 ⁻¹⁷	142	464	63.51	-4910.58	0	-6.21	6.21×10 ⁻¹⁷	294	464
ACACID	-71.34	-4511	-4.54×10 ⁻²	18.77	3.86×10 ⁻¹⁷	329	587	66.71	-6943.84	0	-6.28	1.88×10 ⁻¹⁷	391	595
ACETOL	386.77	-14897	1.06×10 ⁻¹	-63.56	-7.66×10 ⁻¹⁷	273	589	117.54	-11166.80	0	-13.18	4.18×10 ⁻¹⁸	424	616
ACETONE	56.16	-5205	0	-4.93	1.84×10 ⁻¹⁷	322	500	66.94	-5520.99	0	-6.63	4.12×10 ⁻¹⁷	322	500
ACROLEIN	56.52	-5126	0	-4.99	2.11×10 ⁻¹⁷	313	490	65.41	-5334.64	0	-6.42	4.37×10 ⁻¹⁷	313	490
ANISOLE	60.38	-6772	0	-5.37	5.38×10 ⁻¹⁸	409	619	61.50	-6896.07	0	-5.51	4.82×10 ⁻¹⁸	409	619
CMRYLALC	134.07	-18018	0	-14.51	1.95×10 ⁻¹⁸	609	824	118.20	-15210.45	0	-12.75	4.47×10 ⁻¹⁹	609	824
CRESOL	68.98	-8057.78	0	-6.42	4.04×10 ⁻¹⁸	436	661	108.11	-11092.57	0	-11.7	4.66×10 ⁻¹⁸	436	661
EG	-3911.31	114495	-9.09×10 ⁻¹	667.15	3.15×10 ⁻¹⁶	308	589	105.77	-11068.98	0	-11.49	1.50×10 ⁻¹⁸	471	719
EGACET	-3825.15	108040	-9.36×10 ⁻¹	657.36	3.59×10 ⁻¹⁶	301	617	78.07	-8140.36	0	-7.97	1.03×10 ⁻¹⁸	461	660
ETHANOL	81.34	-7220	0	-8.32	2.60×10 ⁻¹⁷	337	499	62.22	-6459.58	0	-5.42	1.87×10 ⁻¹⁷	337	499
FORMALDY	48.30	-3840	0	-3.91	4.78×10 ⁻¹⁷	254	418	60.42	-4159.18	0	-5.88	1.32×10 ⁻¹⁶	254	418
FORMICAC	86.19	-8340	0	-8.80	1.44×10 ⁻¹⁷	367	555	-121.94	5312.65	0	20.16	-2.19×10 ⁻¹⁷	367	555
FURFURAL	54656.23	-1919296	10.90	-9045.83	-2.44×10 ⁻¹⁵	413	638	54561.48	-1915878.33	10.88	-9030.21	-2.43×10 ⁻¹⁵	413	638
GLYOXAL	69.08	-6522	0	-6.60	1.63×10 ⁻¹⁷	342	526	80.33	-6649.19	0	-8.47	4.29×10 ⁻¹⁷	342	526
GUAIACOL	-81.69	-4782	-3.81×10 ⁻²	19.63	1.35×10 ⁻¹⁷	326	717	1730.00	-66087.42	3.40×10 ⁻¹	-282.41	-6.05×10 ⁻¹⁷	326	717
HAA	-16942.04	493498	-4.23	2904.36	2.09×10 ⁻¹⁵	296	557	115.16	-9814.66	0	-13.14	7.74×10 ⁻¹⁸	386	557
HEXADEC	106.91	-13144.27	0	-11.40	3.49×10 ⁻¹⁸	565	724	89.63	-11773.73	0	-9.05	1.93×10 ⁻¹⁸	565	724
HMF	-3712.70	110155	-8.17×10 ⁻¹	629.27	1.71×10 ⁻¹⁶	313	722	94.72	-11381.21	0	-9.84	2.73×10 ⁻¹⁸	527	726
HMWL	8.09	-8783	0	1.11	1.96×10 ⁻²²	1800	2769	3.74	0.00	0	2.64	-3.53×10 ⁻¹⁹	1800	2769
KETENE	55.99	-4839.15	0	-4.92	2.83×10 ⁻¹⁷	293	466	60.90	-4776.42	0	-5.83	5.54×10 ⁻¹⁷	293	466
LEVOGLUC	5952.18	-228571	1.07	-969.27	-1.04×10 ⁻¹⁶	345	857	-2.20	106.38	0	3.15	-7.32×10 ⁻¹⁷	675	857
METCSONE	1606.53	-57496	3.28×10 ⁻¹	-264.13	-7.26×10 ⁻¹⁷	298	687	1136.52	-42074.44	2.32×10 ⁻¹	-185.74	-5.37×10 ⁻¹⁷	298	687
METHANOL	-2670.55	73311	-6.88×10 ⁻¹	463.24	3.35×10 ⁻¹⁶	288	475	7.43	-3624.69	0	2.54	1.08×10 ⁻¹⁷	338	513
MF	75.15	-8595	0	-7.25	4.77×10 ⁻¹⁸	441	652	81.59	-8726.56	0	-8.26	7.43×10 ⁻¹⁸	441	652
PHENOL	-5321.66	181841	-1.05	884.11	2.02×10 ⁻¹⁶	380	635	-5611.04	192374.16	-1.11	931.54	2.11×10 ⁻¹⁶	380	635
SYNAPALD	118.33	-16887	0	-12.47	1.25×10 ⁻¹⁸	644	869	-15.86	-1039.54	0	4.48	1.03×10 ⁻²⁰	644	869
SYRINGOL	-1353.51	37374	-2.92×10 ⁻¹	230.94	5.28×10 ⁻¹⁷	333	728	-15.02	-863.35	0	4.48	3.14×10 ⁻²⁰	535	757
VANILLIN	-81.61	-6608	-3.74×10 ⁻²	19.85	8.01×10 ⁻¹⁸	325	794	-15.26	-910.36	0	4.48	2.29×10 ⁻²⁰	564	782
VINYLKET	63.10	-6046	0	-5.84	1.50×10 ⁻¹⁷	346	526	73.18	-6315.55	0	-7.43	3.11×10 ⁻¹⁷	346	526
XYLOSAN	179.17	-21166	0	-20.53	5.43×10 ⁻¹⁸	556	728	1.60	-5142.54	0	3.03	7.93×10 ⁻¹⁹	556	728

Tab. 66: Parameters for the estimation of the vapor pressure ($p_i^{*,l}$) using the Mani method. Values in Pa, temperature in K. Estimated using Aspen Plus™ V12.

ID	C ₁	C ₂	C ₃	C ₄	C ₅	T ₁	T ₂	ID	C ₁	C ₂	C ₃	C ₄	C ₅	T ₁	T ₂
ACETALDY	115.96	-6210.59	2.10×10 ⁻²	-15.74	-7.11×10 ⁻¹⁸	191.65	464.11	GUAIACOL	72.96	-9142.07	0	-6.90	2.61×10 ⁻¹⁸	275.55	716.68
ACACID	78.17	-8074.86	0	-7.73	9.31×10 ⁻¹⁸	278.90	587.25	HAA	200.90	-18611.59	0	-24.16	3.11×10 ⁻¹⁷	245.85	556.85
ACETOL	85.82	-8815.05	0	-8.74	9.95×10 ⁻¹⁸	223.22	589.06	HEXADEC	101.88	-12581.22	0	-10.75	3.34×10 ⁻¹⁸	242.15	724.21
ACETONE	59.23	-5413.46	0	-5.40	2.11×10 ⁻¹⁷	163.75	493.50	HMF	127.64	-15282.58	0	-13.91	4.14×10 ⁻¹⁸	263.40	722.23
ACROLEIN	65.84	-5868.65	0	-6.25	2.42×10 ⁻¹⁷	210.00	489.60	KETENE	5.70	-1003.02	0	1.96	5.87×10 ⁻¹⁸	110.15	465.60
ANISOLE	77.00	-8395.20	0	-7.56	6.67×10 ⁻¹⁸	340.00	619.41	LEVOGLUC	135.87	-18876.29	0	-14.64	1.55×10 ⁻¹⁸	294.96	856.72
CRESOL	-12.89	408.73	0	4.27	-2.05×10 ⁻¹⁹	175.48	661.42	METCSONE	53.53	-6708.02	0	-4.40	2.58×10 ⁻¹⁸	248.15	687.00
EG	163.09	-16008.12	0	-18.93	1.80×10 ⁻¹⁷	257.70	589.28	METHANOL	112.08	-9271.42	0	-12.53	4.69×10 ⁻¹⁷	238.15	475.49
EGACET	113.05	-11867.93	0	-12.30	9.67×10 ⁻¹⁸	251.30	617.16	MF	87.95	-9902.33	0	-8.93	5.49×10 ⁻¹⁸	289.05	651.99
ETHANOL	93.65	-8216.78	0	-9.99	2.96×10 ⁻¹⁷	110.00	499.11	PHENOL	104.46	-11299.19	0	-11.10	7.54×10 ⁻¹⁸	330.30	635.00
FFA	53.38	-9234.31	0	-4.35	3.65×10 ⁻¹⁹	463.51	950.98	SYNAPALD	168.84	-22969.40	0	-18.94	2.07×10 ⁻¹⁸	360.00	845.15
FORMALDY	48.41	-3847.76	0	-3.93	4.79×10 ⁻¹⁷	113.75	418.10	SYRINGOL	100.48	-12377.74	0	-10.45	3.18×10 ⁻¹⁸	283.28	727.73
FORMICAC	71.43	-7122.84	0	-6.84	1.13×10 ⁻¹⁷	232.00	561.24	VANILLIN	87.06	-11794.08	0	-8.65	1.65×10 ⁻¹⁸	274.92	793.56
FURFURAL	-371.80	35738.07	0	51.50	-2.66×10 ⁻¹⁷	499.85	625.18	XYLOSAN	229.78	-26855.31	0	-27.05	6.88×10 ⁻¹⁸	410.00	727.98
GLYOXAL	77.12	-7271.85	0	-7.69	1.70×10 ⁻¹⁷	224.00	530.66								

$$\ln p_i^{*,l} = \ln p_{c,i} + \frac{C_{1i}(1 - T_{r,i}) + C_{2i}(1 - T_{r,i})^{1.5} + C_{3i}(1 - T_{r,i})^{2.5} + C_{4i}(1 - T_{r,i})^{3.5}}{T_{r,i}} \quad T_{r,i} = \frac{T}{T_{c,i}} \quad T_{min} \leq T \leq T_{max}$$

Tab. 67: Parameters for the estimation of the vapor pressure ($p_i^{*,l}$) using sourced data from the TDE. Estimated using Aspen Plus™ V12.

ID	Temperature Unit	Unit	C ₁	C ₂	C ₃	C ₄	T _{min}	T _{max}	ID	Temperature Unit	Unit	C ₁	C ₂	C ₃	C ₄	T _{min}	T _{max}
ACETALDY	K	bar	-7.56	2.75	-3.13	-1.63	149.75	464.11	GUAIACOL	K	bar	-8.73	2.51	-4.51	-4.05	301.43	694.00
ACACID	K	bar	-7.69	6.43×10 ⁻⁴	3.08×10 ⁻¹	-5.96	289.69	594.79	HEXADEC	K	bar	-10.64	5.04	-8.57	-4.12	289.99	722.39
ACETOL	K	bar	-9.71	1.52	0	0	275.48	616.00	HMF	K	bar	-11.40	4.59	-9.73	-5.24	306.10	726.00
ACETONE	K	bar	-7.70	2.01	-2.48	-2.68	178.16	508.07	KETENE	K	bar	-3.25	-3.42	0	0	159.36	223.81
ACROLEIN	K	bar	-7.30	2.41	-3.45	-5.01×10 ⁻¹	185.49	528.00	METHANOL	K	bar	-8.74	1.54	-2.98	-4.81×10 ⁻¹	175.60	512.68
ANISOLE	K	bar	-8.29	3.42	-4.73	-1.69	235.84	646.10	MF	K	bar	-8.08	2.12	-3.43	-3.52	220.00	698.00
CMRYLALC	K	bar	-10.14	3.51	-7.11	-4.85	240.00	780.00	PHENOL	K	bar	-7.74	1.90	-4.31	-4.23	314.04	694.27
CRESOL	K	bar	-8.02	3.07	-7.47	0.00	307.92	704.57	SYNAPALD	K	bar	-10.70	3.97	-8.24	-5.06	260.00	845.00
EG	K	bar	-9.50	5.10	-8.91	3.49×10 ⁻¹	259.26	719.47	SYRINGOL	K	bar	-9.22	2.83	-5.37	-4.37	328.60	757.00
ETHANOL	K	bar	-8.40	3.30×10 ⁻¹	-3.67	-1.37×10 ⁻¹	97.65	514.56	VANILLIN	K	bar	-9.20	2.82	-5.34	-4.36	354.60	782.00
FFA	K	bar	-11.35	4.55	-9.62	-5.23	267.73	787.00	VINYLKET	K	bar	-6.86	1.56	-1.66	-2.25	180.00	540.00
FORMALDY	K	bar	-7.57	3.08	-3.57	-7.54×10 ⁻¹	155.17	418.10	XYLOSAN	K	bar	-9.37	2.94	-5.65	-4.46	220.00	724.00
FORMICAC	K	bar	-10.78	1.25	8.98	-1.87×10 ¹	281.44	587.96	EGACET	K	Pa	-9.72	3.78	-6.42	-4.26	200.00	660.00
FURFURAL	K	bar	-7.48	6.26×10 ⁻¹	-1.19	-6.61	234.84	658.00	METCSONE	K	Pa	-6.39	1.41	-1.08	-1.66	220.00	687.00

$$\Delta_{vap}H_i^*(T) = \Delta_{vap}H_i^*(T_{ref}) \left(\frac{1 - T/T_{ci}}{1 - T_{ref}/T_{ci}} \right)^{a_i + b_i(1 - T/T_{ci})} \quad T > T_{min}$$

Tab. 68: Parameters for the estimation of the standard enthalpy of vaporization ($\Delta_{vap}H_i^*$) using the presented methods. Values in $J \cdot mol^{-1} \cdot K^{-1}$, temperature in K. Estimated using Aspen Plus™ V12.

ID	CLAUSIUS-CLAYPERON					GANI					VETERE					DUCROS					LI-MA				
	$\Delta_{vap}H^*(T_{ref})$	T_{ref}	a	b	T_{min}	$\Delta_{vap}H^*(T_{ref})$	T_{ref}	a	b	T_{min}	$\Delta_{vap}H^*(T_{ref})$	T_{ref}	a	b	T_{min}	$\Delta_{vap}H^*(T_{ref})$	T_{ref}	a	b	T_{min}	$\Delta_{vap}H^*(T_{ref})$	T_{ref}	a	b	T_{min}
ACETALDY	3.37×10 ⁷	150	0.29	0.34	60	2.41×10 ⁷	298	0.38	0	119	2.70×10 ⁷	294	0.38	0	118	2.54×10 ⁷	298	0.38	0	119	2.61×10 ⁷	294	0.38	0	118
ACACID	4.92×10 ⁷	329	0.43	0.55	132	5.40×10 ⁷	298	0.38	0	119	3.81×10 ⁷	391	0.38	0	156	5.33×10 ⁷	298	0.38	0	119	n.a.	n.a.	n.a.	n.a.	n.a.
ACETOL	4.11×10 ⁷	273	0.42	-2.43	109	5.55×10 ⁷	298	0.38	0	119	3.92×10 ⁷	414	0.38	0	166	2.57×10 ⁷	298	0.38	0	119	5.07×10 ⁷	424	0.45	0	170
ACETONE	2.87×10 ⁷	322	0.38	0.00	129	2.99×10 ⁷	298	0.38	0	119	3.08×10 ⁷	298	0.38	0	119	2.87×10 ⁷	322	0.39	0	129	n.a.	n.a.	n.a.	n.a.	n.a.
ACROLEIN	2.78×10 ⁷	313	0.38	0.00	125	2.67×10 ⁷	298	0.38	0	119	2.50×10 ⁷	298	0.38	0	119	2.76×10 ⁷	313	0.38	0	125	2.76×10 ⁷	313	0.38	0	125
ANISOLE	3.58×10 ⁷	409	0.38	0.00	163	5.08×10 ⁷	298	0.38	0	119	4.09×10 ⁷	298	0.38	0	119	3.75×10 ⁷	409	0.38	0	163	3.75×10 ⁷	409	0.38	0	163
CMRYLALC	6.78×10 ⁷	649	0.42	-0.45	260	1.81×10 ⁸	298	0.38	0	119	6.05×10 ⁷	649	0.38	0	260	1.55×10 ⁸	298	0.38	0	119	n.a.	n.a.	n.a.	n.a.	n.a.
CRESOL	3.93×10 ⁷	436	1.91	-10.28	174	7.32×10 ⁷	298	0.38	0	119	3.90×10 ⁷	436	0.38	0	174	6.23×10 ⁷	298	0.38	0	119	4.91×10 ⁷	436	0.45	0	174
EG	6.10×10 ⁷	609	0.30	1.42	244	1.13×10 ⁸	298	0.38	0	119	5.81×10 ⁷	609	0.38	0	244	1.03×10 ⁸	298	0.38	0	119	6.60×10 ⁷	471	0.46	0	188
EGACET	5.82×10 ⁷	308	0.30	-1.90	123	6.52×10 ⁷	298	0.38	0	119	4.36×10 ⁷	430	0.38	0	172	6.69×10 ⁵	298	0.38	0	119	5.31×10 ⁷	461	0.46	0	184
ETHANOL	7.21×10 ⁷	301	0.41	2.01	121	6.34×10 ⁷	298	0.38	0	119	3.79×10 ⁷	425	0.38	0	170	3.11×10 ⁷	298	0.38	0	119	3.92×10 ⁷	337	0.44	0	135
FORMALDY	2.75×10 ⁷	155	0.32	0.42	62	1.97×10 ⁷	298	0.38	0	119	2.44×10 ⁷	254	0.38	0	102	1.97×10 ⁷	298	0.38	0	119	4.82×10 ⁷	765	0.33	0	306
FORMICAC	3.72×10 ⁷	367	1.28	-6.12	147	4.99×10 ⁷	298	0.38	0	119	3.79×10 ⁷	367	0.38	0	147	4.77×10 ⁷	298	0.38	0	119	2.37×10 ⁷	254	0.36	0	102
FURFURAL	1.68×10 ⁷	413	9.81	-58.92	165	4.62×10 ⁷	298	0.38	0	119	3.69×10 ⁷	413	0.38	0	165	4.53×10 ⁷	298	0.38	0	119	n.a.	n.a.	n.a.	n.a.	n.a.
GLYOXAL	3.23×10 ⁷	342	0.24	1.04	137	3.26×10 ⁷	298	0.38	0	119	3.15×10 ⁷	342	0.38	0	137	3.95×10 ⁷	298	0.38	0	119	n.a.	n.a.	n.a.	n.a.	n.a.
GUAIACOL	6.19×10 ⁷	326	0.35	0.74	130	8.69×10 ⁷	298	0.38	0	119	4.46×10 ⁷	489	0.38	0	196	8.01×10 ⁷	298	0.38	0	119	3.25×10 ⁷	342	0.38	0	137
HAA	1.67×10 ⁸	325	0.82	8.94	130	4.89×10 ⁷	298	0.38	0	119	3.74×10 ⁷	386	0.38	0	154	2.27×10 ⁷	298	0.38	0	119	n.a.	n.a.	n.a.	n.a.	n.a.
HEXADEC	5.36×10 ⁷	565	0.29	1.08	226	8.02×10 ⁷	298	0.38	0	119	5.12×10 ⁷	565	0.38	0	226	8.10×10 ⁷	298	0.38	0	119	4.78×10 ⁷	386	0.45	0	154
HMF	1.05×10 ⁸	313	0.52	2.74	125	7.07×10 ⁷	298	0.38	0	119	4.50×10 ⁷	493	0.38	0	197	7.34×10 ⁷	298	0.38	0	119	5.30×10 ⁷	565	0.46	0	226
HMWL	n.a.	n.a.	n.a.	n.a.	n.a.	4.10×10 ⁸	298	0.38	0	119	1.89×10 ⁸	1800	0.38	0	720	4.12×10 ⁸	298	0.38	0	119	n.a.	n.a.	n.a.	n.a.	n.a.
KETENE	2.54×10 ⁷	293	0.14	1.02	117	2.69×10 ⁷	298	0.38	0	119	2.72×10 ⁷	293	0.38	0	117	2.46×10 ⁷	298	0.38	0	119	n.a.	n.a.	n.a.	n.a.	n.a.
LEVOGLUC	8.51×10 ⁷	345	0.49	-3.02	138	1.05×10 ⁸	298	0.38	0	119	6.58×10 ⁷	675	0.38	0	270	9.87×10 ⁷	298	0.38	0	119	2.71×10 ⁷	293	0.38	0	117
METCSONE	4.34×10 ⁷	298	1.06	-2.44	119	4.40×10 ⁷	298	0.38	0	119	3.66×10 ⁷	410	0.38	0	164	4.63×10 ⁷	298	0.38	0	119	n.a.	n.a.	n.a.	n.a.	n.a.
METHANOL	3.40×10 ⁷	288	0.55	-3.58	115	3.55×10 ⁷	298	0.38	0	119	3.42×10 ⁷	314	0.38	0	126	3.74×10 ⁷	298	0.38	0	119	n.a.	n.a.	n.a.	n.a.	n.a.
MF	4.22×10 ⁷	441	0.24	0.80	176	3.94×10 ⁷	298	0.38	0	119	3.95×10 ⁷	441	0.38	0	176	4.21×10 ⁷	298	0.38	0	119	4.11×10 ⁷	338	0.44	0	135
PHENOL	4.22×10 ⁷	380	0.11	1.19	152	6.76×10 ⁷	298	0.38	0	119	3.64×10 ⁷	408	0.38	0	163	6.57×10 ⁷	298	0.38	0	119	n.a.	n.a.	n.a.	n.a.	n.a.
SYNAPALD	3.11×10 ⁷	644	-0.04	-0.73	257	1.32×10 ⁸	298	0.38	0	119	5.97×10 ⁷	644	0.38	0	257	1.02×10 ⁸	298	0.38	0	119	n.a.	n.a.	n.a.	n.a.	n.a.
SYRINGOL	7.52×10 ⁷	333	0.39	0.84	133	1.06×10 ⁸	298	0.38	0	119	4.57×10 ⁷	509	0.38	0	203	9.46×10 ⁷	298	0.38	0	119	n.a.	n.a.	n.a.	n.a.	n.a.
VANILLIN	7.82×10 ⁷	325	0.42	0.35	130	1.12×10 ⁸	298	0.38	0	119	5.25×10 ⁷	566	0.38	0	226	9.17×10 ⁷	298	0.38	0	119	n.a.	n.a.	n.a.	n.a.	n.a.
VINYLKET	3.16×10 ⁷	346	0.23	1.07	138	3.15×10 ⁷	298	0.38	0	119	3.06×10 ⁷	346	0.38	0	138	3.07×10 ⁷	298	0.38	0	119	n.a.	n.a.	n.a.	n.a.	n.a.
XYLOSAN	5.65×10 ⁷	556	0.00	0.09	222	8.57×10 ⁷	298	0.38	0	119	5.25×10 ⁷	556	0.38	0	222	8.92×10 ⁷	298	0.38	0	119	3.16×10 ⁷	346	0.40	0	138

$$\ln \Delta_{vap}H_i^* = C_{1,i} + (C_{2,i} + C_{3,i}T_{r,i} + C_{3,i}T_{r,i}^2) \ln(1 - T_{r,i}) \quad T_{r,i} = \frac{T}{T_{c,i}} \quad T_{max} \geq T \geq T_{min}$$

Tab. 69: Parameters for the estimation of the standard enthalpy of vaporization ($\Delta_{vap}H_i^*$) using sourced data from the TDE. Temperature in K. Estimated using Aspen Plus™ V12.

ID	Unit	C ₁	C ₂	C ₃	C ₄	T _{min}	T _{max}	ID	C ₁	C ₂	C ₃	C ₄	T _{min}	T _{max}	C ₁
ACETALDY	kcal·mol ⁻¹	17.49	0.68	-0.57	0.33	150	464	GUAIACOL	kcal·mol ⁻¹	18.25	0.65	-0.24	0.02	301	694
ACETOL	kcal·mol ⁻¹	17.70	0.83	-0.77	0.36	178	491	HEXADEC	kcal·mol ⁻¹	18.58	0.77	-0.11	-0.21	290	697
ACETONE	kcal·mol ⁻¹	17.38	-0.19	0.73	-0.20	185	510	HMF	kcal·mol ⁻¹	18.72	0.63	0.26	-0.48	306	726
ACROLEIN	kcal·mol ⁻¹	17.92	0.37	0.16	-0.13	236	624	METC5ONE	kcal·mol ⁻¹	17.71	0.97	-1.28	0.71	225	687
ANISOLE	kcal·mol ⁻¹	18.73	1.08	-0.66	0.04	240	780	METHANOL	kcal·mol ⁻¹	17.72	0.57	-0.75	0.55	176	495
CMRYLALC	kcal·mol ⁻¹	17.78	-1.18	2.61	-1.07	308	679	MF	kcal·mol ⁻¹	18.27	1.23	-1.26	0.50	220	675
EG	kcal·mol ⁻¹	18.05	-0.50	1.68	-0.81	259	719	PHENOL	kcal·mol ⁻¹	18.24	0.67	-0.08	-0.14	314	669
EGACET	J·kmol ⁻¹	18.47	1.14	-0.79	0.11	205	660	SYNAPALD	kcal·mol ⁻¹	18.98	1.53	-1.47	0.46	260	845
ETHANOL	kcal·mol ⁻¹	17.79	0.42	-0.60	0.55	100	515	SYRINGOL	kcal·mol ⁻¹	18.50	0.93	-0.59	0.11	329	730
FFA	kcal·mol ⁻¹	18.93	1.18	-0.70	0.00	268	761	VANILLIN	kcal·mol ⁻¹	18.48	0.52	0.27	-0.35	355	782
FORMALDY	kcal·mol ⁻¹	17.29	0.52	-0.46	0.34	155	418	VINYLKET	kcal·mol ⁻¹	17.66	1.09	-1.32	0.64	185	540
FORMICAC	kcal·mol ⁻¹	17.14	3.22	-8.15	5.37	298	493	XYLOSAN	kcal·mol ⁻¹	18.53	1.08	-0.74	0.13	220	724
FURFURAL	kcal·mol ⁻¹	18.55	2.52	-3.26	1.31	235	658								

$$\eta_i^{*,v} = C_{1,i} + C_{2,i}T + C_{3,i}T^2 + C_{4,i}T^3 \quad T_{min} \leq T \leq T_{max}$$

Tab. 70: Parameters for the estimation of the gas-phase viscosity ($\eta_i^{*,v}$) using sourced data from the TDE. Temperature in K. Estimated using Aspen Plus™ V12.

ID	Unit	C ₁	C ₂	C ₃	C ₄	T _{min}	T _{max}	ID	Unit	C ₁	C ₂	C ₃	C ₄	T _{min}	T _{max}
ACACID	cP	-1.05×10 ⁻⁵	9.25×10 ⁻⁸	-1.33×10 ⁻¹⁰	7.63×10 ⁻¹⁴	307	890	FURFURAL	cP	-5.57×10 ⁻⁷	2.44×10 ⁻⁸	-9.84×10 ⁻¹³	-1.35×10 ⁻¹⁵	440	980
ACETALDY	cP	-5.68×10 ⁻⁷	4.03×10 ⁻⁸	-1.23×10 ⁻¹²	-5.24×10 ⁻¹⁵	300	690	GUAIACOL	cP	-6.58×10 ⁻⁷	2.43×10 ⁻⁸	-1.36×10 ⁻¹²	-9.93×10 ⁻¹⁶	480	1040
ACETOL	cP	-7.45×10 ⁻⁷	3.05×10 ⁻⁸	-2.00×10 ⁻¹²	-1.54×10 ⁻¹⁵	430	920	HEXADEC	cP	-4.11×10 ⁻⁵	1.72×10 ⁻⁷	-1.97×10 ⁻¹⁰	7.88×10 ⁻¹⁴	584	1080
ACETONE	cP	-7.70×10 ⁻⁶	7.60×10 ⁻⁸	-1.10×10 ⁻¹⁰	8.03×10 ⁻¹⁴	338	760	HMF	cP	-8.92×10 ⁻⁷	2.78×10 ⁻⁸	-2.00×10 ⁻¹²	-8.13×10 ⁻¹⁶	530	1080
ACROLEIN	cP	-4.31×10 ⁻⁷	3.01×10 ⁻⁸	-3.06×10 ⁻¹³	-3.33×10 ⁻¹⁵	330	790	KETENE	cP	-2.71×10 ⁻⁷	4.09×10 ⁻⁸	2.78×10 ⁻¹²	-1.07×10 ⁻¹⁴	230	600
ANISOLE	cP	-5.41×10 ⁻⁷	2.47×10 ⁻⁸	-9.24×10 ⁻¹³	-1.46×10 ⁻¹⁵	430	960	METCSONE	Pa.s	-3.78×10 ⁻⁷	2.20×10 ⁻⁸	3.35×10 ⁻¹⁴	-1.54×10 ⁻¹⁵	420	1030
CMRYLALC	cP	-7.92×10 ⁻⁷	2.29×10 ⁻⁸	-1.54×10 ⁻¹²	-5.77×10 ⁻¹⁶	570	1160	METHANOL	cP	3.07×10 ⁻⁵	-1.50×10 ⁻⁷	3.55×10 ⁻¹⁰	-2.24×10 ⁻¹³	343	760
CRESOL	cP	-5.73×10 ⁻⁷	2.21×10 ⁻⁸	-1.02×10 ⁻¹²	-9.70×10 ⁻¹⁶	480	1050	MF	cP	-6.03×10 ⁻⁷	2.43×10 ⁻⁸	-1.01×10 ⁻¹²	-1.15×10 ⁻¹⁵	470	1040
EG	cP	-7.32×10 ⁻⁷	2.96×10 ⁻⁸	-1.05×10 ⁻¹²	-1.39×10 ⁻¹⁵	480	1070	PHENOL	cP	-6.34×10 ⁻⁷	2.67×10 ⁻⁸	-9.87×10 ⁻¹³	-1.33×10 ⁻¹⁵	460	1040
EGACET	Pa.s	-6.83×10 ⁻⁷	2.51×10 ⁻⁸	-1.69×10 ⁻¹²	-1.03×10 ⁻¹⁵	470	980	SYNAPALD	cP	-7.84×10 ⁻⁷	1.93×10 ⁻⁸	-1.43×10 ⁻¹²	-3.23×10 ⁻¹⁶	640	1260
ETHANOL	cP	1.39×10 ⁻⁵	-4.29×10 ⁻⁸	1.21×10 ⁻¹⁰	-6.54×10 ⁻¹⁴	363	770	SYRINGOL	cP	-7.21×10 ⁻⁷	2.27×10 ⁻⁸	-1.40×10 ⁻¹²	-6.77×10 ⁻¹⁶	540	1130
FFA	cP	-7.35×10 ⁻⁷	1.73×10 ⁻⁸	-1.69×10 ⁻¹²	-2.02×10 ⁻¹⁶	630	1180	VANILLIN	cP	-6.08×10 ⁻⁷	1.82×10 ⁻⁸	-1.13×10 ⁻¹²	-4.92×10 ⁻¹⁶	560	1170
FORMALDY	cP	-4.77×10 ⁻⁷	4.48×10 ⁻⁸	5.09×10 ⁻¹⁴	-8.45×10 ⁻¹⁵	260	620	VINYLKET	cP	-4.61×10 ⁻⁷	3.15×10 ⁻⁸	-2.43×10 ⁻¹³	-3.40×10 ⁻¹⁵	340	800
FORMICAC	cP	-3.24×10 ⁻⁶	4.06×10 ⁻⁸	3.78×10 ⁻¹²	-1.03×10 ⁻¹⁴	317	880	XYLOSAN	cP	-8.37×10 ⁻⁷	3.01×10 ⁻⁸	-1.54×10 ⁻¹²	-1.17×10 ⁻¹⁵	500	1080

$$\ln \eta_i^{*,l} = C_{1,i} + \frac{C_{2,i}}{T} + \frac{C_{3,i}}{T^2} + \frac{C_{4,i}}{T^3} \quad T_{min} \leq T \leq T_{max}$$

Tab. 71: Parameters for the estimation of the liquid-phase viscosity ($\eta_i^{*,l}$) using sourced data from the TDE. Values in cP, temperature in °C. Estimated using Aspen Plus™ V12.

ID	C ₁	C ₂	C ₃	C ₄	T _{min}	T _{max}
ACETALDY	-19.53	8297.15	-2.22×10 ⁶	2.17×10 ⁸	200	460
ACACID	-16.45	6669.10	-1.81×10 ⁶	2.03×10 ⁸	291	590
ACETOL	-14.67	4313.45	-7.86×10 ⁵	9.39×10 ⁷	270	610
CRESOL	-20.20	12657.14	-4.76×10 ⁶	7.18×10 ⁸	308	700
EGACET	-11.30	8504.43	-2.28×10 ⁶	2.65×10 ⁸	-3	357
ETHANOL	-16.28	4552.21	-6.91×10 ⁵	5.18×10 ⁷	159	503
FFA	-12.06	2798.89	-2.41×10 ⁵	3.81×10 ⁷	269	780
FURFURAL	-16.12	6683.69	-1.87×10 ⁶	2.19×10 ⁸	278	650
GUAIACOL	-17.08	8910.53	-3.17×10 ⁶	4.66×10 ⁸	320	690
HEXADEC	-13.32	4095.20	-1.06×10 ⁶	1.50×10 ⁸	293	720
HMF	-18.34	8753.69	-2.32×10 ⁶	3.19×10 ⁸	310	720
METCSONE	-3.95	713.16	1.34×10 ⁵	-1.20×10 ⁶	-3	407

$$\ln \eta_i^{*l} = A_i + \frac{B_i}{T} + C_i \ln T \quad T_{min} \leq T \leq T_{max}$$

Tab. 72: Parameters for the estimation of the liquid viscosity (η_i^{*l}) using the shown methods. Values in N·s·m⁻², temperature in K. Estimated using Aspen Plus™ V12.

ID	LETSOU-STIEL					ORRICK-ERBAR					NANNOOLAL-RAREY				
	A	B	C	T _{min}	T _{max}	A	B	C	T _{min}	T _{max}	A	B	C	T _{min}	T _{max}
ACETALDY	71.25	-3192	-12.10	294	459	-11.16	823	0.00	294	348	-11.80	807	0.15	273	373
ACACID	103.43	-5767	-16.23	391	581	-11.03	1144	0.00	391	446	-15.81	1766	0.64	273	373
ACETOL	143.41	-8292	-21.82	414	583	-13.52	2522	0.00	424	462	-23.55	3194	1.36	273	373
ACETONE	66.83	-3220	-11.32	322	495	-11.35	922	0.00	322	375	-12.83	965	0.26	273	373
ACROLEIN	-10.99	832	0.00	313	367	81.73	-3841	-13.53	313	485	-12.39	943	0.21	273	373
ANISOLE	-11.02	1128	0.00	409	465	92.76	-5376	-14.61	409	613	-14.69	1476	0.51	273	373
CMRYLALC	145.29	-11384	-21.02	609	815	-16.13	4296	0.00	609	618	-40.54	6438	3.08	273	373
CRESOL	98.90	-6050	-15.31	436	655	-13.41	2583	0.00	436	496	-22.19	2960	1.13	273	373
EG	138.61	-8118	-21.08	430	583	-15.83	3673	0.00	430	442	-24.30	3368	1.40	273	373
EGACET	134.64	-8003	-20.46	425	611	-13.84	2691	0.00	461	495	-24.43	3449	1.40	273	373
ETHANOL	136.35	-6742	-21.38	337	494	-13.52	2073	0.00	337	374	-17.33	2034	0.68	273	373
FORMALDY	63.34	-2564	-11.14	254	414	-11.40	724	0.00	254	314	-11.69	690	0.17	273	373
FORMICAC	118.43	-6295	-18.49	367	549	-10.99	1144	0.00	367	416	-15.44	1635	0.64	273	373
FURFURAL	97.03	-5671	-15.18	413	619	-11.01	1161	0.00	435	494	-18.40	2196	0.81	273	373
GLYOXAL	79.87	-4010	-13.10	342	521	-11.34	1173	0.00	342	394	-124.71	22523	10.48	273	373
GUAIALCOL	-14.68	2096	0.35	293	710	-6.67	1929	-0.87	293	538	-26.85	3905	1.70	273	373
HAA	193.60	-10765	-29.12	386	551	-13.08	2423	0.00	386	418	-21.94	2897	1.23	273	373
HEXADEC	214.62	-15771.59	-30.84	565	717	-11.87	1859.00	0.00	565	661	-17.01	1940.53	0.80	273	373
HMF	171.63	-11727	-25.07	493	715	-13.18	2860	0.00	527	545	-42.77	6589	3.70	273	373
HMWL	53.27	-11589	-7.46	1800	2741	-34.73	13347	0.00	1800	2077	34.54 ^a	0	0.00	273	373
KETENE	79.94	-3575.50	-13.38	293	461	-11.14	733.00	0.00	293	349	-12.76	1037.01	0.27	273	373
LEVOGLUC	539.49	-48137	-73.00	675	848	-16.68	5949	0.00	675	784	-44.31	7061	2.53	273	373
METCSONE	55.82	-3411	-9.28	410	680	-10.85	1030	0.00	410	515	-14.22	1367	0.43	273	373
METHANOL	64.23	-2353	-11.23	293	471	41.80	-1020	-8.03	293	357	-15.35	1685	0.54	273	373
MF	83.75	-5117	-13.21	441	645	-10.68	1211	0.00	441	489	-18.50	2228	0.83	273	373
PHENOL	93.41	-5457	-14.65	408	629	-13.41	2489	0.00	408	476	-21.93	2999	1.17	273	373
SYNAPALD	197.15	-16435	-27.77	644	860	-14.76	3809	0.00	644	652	-55.57	9102	4.83	273	373
SYRINGOL	139.47	-9600	-20.65	509	720	-13.95	2967	0.00	509	546	-41.53	6500	3.37	273	373
VANILLIN	147.46	-11058	-21.49	566	786	-14.22	3078	0.00	566	595	-31.70	4747	2.31	273	373
VINYLKET	83.49	-4217	-13.63	346	521	-10.93	931	0.00	346	395	-15.28	1611	0.59	273	373
XYLOSAN	494.59	-37724	-68.65	556	721	-13.22	4500	0.00	556	659	-32.97	5024	1.99	273	373

a: Due to unfeasible results when using this method, the liquid viscosity was capped at 1×10⁸ cP.



FREDERICO G. FONSECA

CHEMICAL/PROCESS ENGINEER, DR.-ING.
BORN ON 16/05/1991 IN LISBON, PORTUGAL

PROFILE

A fresh graduate, I have worked for several years in process engineering, with a special focus on project development and waste valorization for the production of fuels and energy. I consider myself to be particularly committed, hardworking and a team player, as well as enjoying taking on responsible roles in a team.

SKILLS

Trade-Specific Software

Aspen Plus 12, Origin Pro 2019,
OPUS 7, Mendeley

Common Use Software

Microsoft Office (Word, Excel, Powerpoint, Visio)
MatLab, LucidChart

Languages

Portuguese: native
English: working proficiency
German, Spanish: advanced

CHARACTER REFERENCES

Dr. Axel Funke

Group leader @ IKFT-KIT
axel.funke@kit.edu

Prof. Nicolaus Dahmen

Institute Department Leader @ IKFT-KIT
icolaus.dahmen@kit.edu

Prof. Ana Paula Soares Dias

Former group leader @ Lisbon Tech
apsoares@tecnico.ulisboa.pt


HOW TO REACH ME

(+49) 1575 0282838

fredericofonseca1991@gmail.com

Address: Blumentorstr. 6, 76227 Karlsruhe

 @fgfonseca  Frederico_Fonseca

 Frederico-Gomes-Fonseca

CAREER SUMMARY

Postdoctoral Researcher

KIT, Karlsruhe, Germany | Mar 2023 to present

- Determination of thermophysical properties and binary interaction parameters for relevant molecules in bio-oil
- Modeling of liquid-liquid extraction and fermentation
- Improvement of fast pyrolysis model

Ph.D. Student

KIT, Karlsruhe, Germany | Feb 2018 to Dec 2022

- Process simulation (Aspen Plus) of a fast pyrolysis unit (360 kg/h)
- Operation of a fast pyrolysis pilot (10 kg/h)
- Determination of reaction kinetics based on thermogravimetry
- Determination of thermophysical properties and binary interaction parameters for relevant molecules in bio-oil
- Mobility program: KMITL, Bangkok, Thailand (2019)
 - Development of a system for online measurement of ash/moisture content in biomass using NIR spectroscopy and PLS regression
- Conference speaker
 - EUBCE 2019, TSAE 2019, Pyro2021

Internship

Projecto Detalhe, Sintra, Portugal | Juli 2013

"Basic Engineering of a Tankpark in Matola, Mozambique" | Program: "Inovar em Engenharia"

EDUCATION

Lisbon Tech (University of Lisbon), Portugal

Master and Bachelor in Chemical Engineering (final grade 16/20)

- Attended from Sept. 2009 to Dec. 2015
- Minor: Process Engineering
- Member of the organizing committee of the XXVII Conferences on Chemical Engineering, Lisbon Tech

ACADEMIC CONTRIBUTIONS

Manuscripts

F.G. Fonseca, A. Anca-Couce, A. Funke, N. Dahmen, *Challenges in kinetic parameter determination for wheat straw pyrolysis*, Energies. 15 (2022) 7240. doi:doi.org/10.3390/en15197240.

C.C. Schmitt, F.G. Fonseca, M.C. Fraga, A.W. Jr, S. Karp, Á. Henrique, M. José, C. Rita, R. Moreira, D. Eiji, K. Raffelt, N. Dahmen, *Thermochemical and Catalytic Conversion Technologies for the Development of Brazilian Biomass Utilization*, Catalysts. 11 (2021) 1549.

F.G. Fonseca, A.P. Soares Dias, *Almond shells: Catalytic fixed-bed pyrolysis and volatilization kinetics*, Renew. Energy. 180 (2021) 1380–1390. doi:10.1016/j.renene.2021.08.104.

A.P. Soares Dias, F.G. Fonseca, M. Catarino, J. Gomes, *Biodiesel Glycerin Valorization into Oxygenated Fuel Additives*, Catal. Letters. (2021).

Y. Fan, F.G. Fonseca, M. Gong, A. Hoffmann, U. Hornung, N. Dahmen, *Energy valorization of integrating lipid extraction and hydrothermal liquefaction of lipid-extracted sewage sludge*, J. Clean. Prod. (2020).

A.U. Şen, F.G. Fonseca, A. Funke, H. Pereira, F. Lemos, *Pyrolysis kinetics and estimation of chemical composition of Quercus cerris cork*, Biomass Convers. Biorefinery. (2020). doi:10.1007/s13399-020-00964-y.

A.P. Soares Dias, F. Rego, F. Fonseca, M. Casquilho, F. Rosa, A. Rodrigues, *Catalyzed pyrolysis of SRC poplar biomass. Alkaline carbonates and zeolites catalysts*, Energy. 183 (2019) 1114–1122.

F.G. Fonseca, A. Funke, A. Niebel, A.P. Soares Dias, N. Dahmen, *Moisture content as a design and operational parameter for fast pyrolysis*, J. Anal. Appl. Pyrolysis. 139 (2019) 73–86.

Conference Proceedings

F.G. Fonseca, A. Funke, N. Dahmen, *Modeling Fast Pyrolysis of Waste Biomass: Improving Predictive Capability*, in: Pyroliq 2023, Engineering Conferences International, Hernstein (Austria), 2023

F.G. Fonseca, A. Anca-Couce, A. Funke, N. Dahmen, *Kinetic parameter determination for wheat straw pyrolysis*, in: EPYRO2021, Medicongress, Ghent, 2021.

F.G. Fonseca, A. Funke, W. Saechua, P. Sirisomboon, *Precision test for the spectral characteristic of FT-NIR for the measurement of water content of wheat straw*, IOP Conf. Ser. Earth Environ. Sci. 301 (2019) 012034.

F.G. Fonseca, A. Funke, N. Dahmen, *Aspen Plus modeling of Fractional Condensation schemes for production of Fast Pyrolysis bio-oil*, in: 27th Eur. Biomass Conf. Exhib., ETA-Florence Renewable Energies, Lisbon, 2019: pp. 681–683.

F.G. Fonseca, A. Funke, A. Niebel, A.P.S. Dias, N. Dahmen, *Moisture content as a design and operational parameter for fast pyrolysis*, in: 1. Dtsch. Doktorandenkolloquium Bioenergie, DBFZ Deutsches Biomasseforschungszentrum gemeinnützige GmbH, 2018: p. 286.